

NATIONAL INSTITUTE FOR FUSION SCIENCE

NIFS-SWJTU JOINT PROJECT FOR CFQS -PHYSICS AND ENGINEERING DESIGN- VER. 3.1 2020. NOV.

National Institute for Fusion Science, National Institutes of Natural Sciences
Institute of Fusion Science, School of Physical Science and Technology,
Southwest Jiaotong University
Hefei Keye Electro Physical Equipment Manufacturing Co. Ltd.

(Received - Dec. 28, 2020)

NIFS-PROC-119

Jan. 25, 2021

This report was prepared as a preprint of work performed as a collaboration research of the National Institute for Fusion Science (NIFS) of Japan. The views presented here are solely those of the authors. This document is intended for information only and may be published in a journal after some rearrangement of its contents in the future.

Inquiries about copyright should be addressed to the NIFS Library, National Institute for Fusion Science, 322-6 Oroshi-cho, Toki-shi, Gifu-ken 509-5292 JAPAN.

E-mail: tosho@nifs.ac.jp

<Notice about copyright>

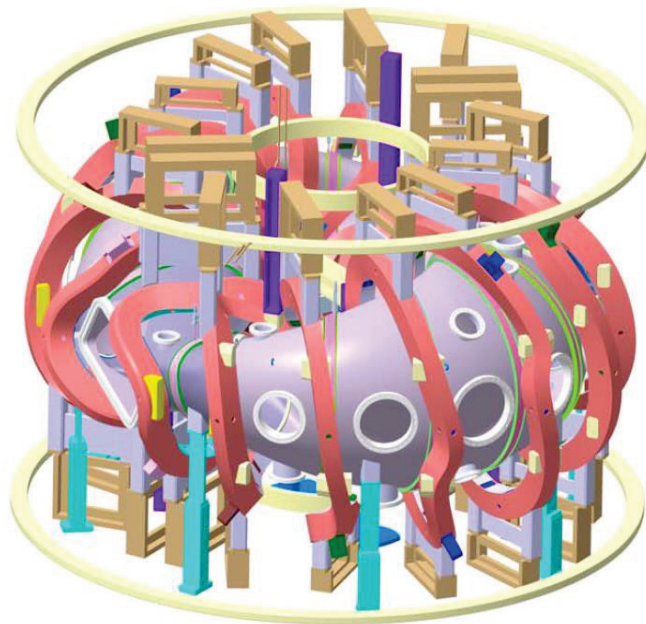
NIFS authorized Japan Academic Association For Copyright Clearance (JAC) to license our reproduction rights and reuse rights of copyrighted works. If you wish to obtain permissions of these rights, please refer to the homepage of JAC (<http://jaacc.org/eng/>) and confirm appropriate organizations to request permission.



NIFS-SWJTU JOINT PROJECT FOR CFQS

~PHYSICS AND ENGINEERING DESIGN~

VER. 3.1
2020. NOV.



National Institute for Fusion Science, National Institutes of Natural Sciences

Institute of Fusion Science, School of Physical Science and Technology, Southwest Jiaotong University

Hefei Keye Electro Physical Equipment Manufacturing Co. Ltd.

NIFS-SWJTU Joint project for CFQS: Physics and engineering design Ver 3.1

CFQS Team

**National Institute for Fusion Science, National Institutes of Natural Sciences
Institute of Fusion Science, School of Physical Science and Technology, Southwest Jiaotong
University
Hefei Keye Electro Physical Equipment Manufacturing Co. Ltd.**

Abstract

The National Institute for Fusion Science (NIFS) and Southwest Jiaotong University (SWJTU) concluded an agreement for international academic cooperation to promote cooperative research in helical fusion plasma research on July 3, 2017. Since then, NIFS and SWJTU have continued the design study of the quasi-axisymmetric stellarator CFQS as a joint project. NIFS and SWJTU have organized the steering committee to manage this joint project. This document summarizes achievements of physical and engineering design study of the CFQS up to the 3rd steering committee meeting, which was held on November 12, 2020 online, due to the effect of COVID-19.

Principal parameters of the CFQS is as follows: the major radius is 1 m, the magnetic field strength is 1 T, the aspect ratio is 4, and the number of toroidal period is 2. Magnetic field configuration is designed based on that of CHS-qa. Good MHD stability is confirmed. Good confinement property in the context of neoclassical theory is achieved by its quasi-axisymmetric configuration. Magnetic field coil system is designed for the CFQS, which consists of 16 modular coils. Supporting system is designed to withstand strong electro-magnetic force under 1 T operation, and it is improved to obtain wider space for heating and diagnostic systems. Analysis by using finite element method shows that the stress in the supporting structure is less than allowable level. Layout of main components, *e.g.* CFQS itself, diagnostic system, heating system, power supply in the torus hall is designed. For one of modular coils, mock up coil was constructed in the factory of Hefei Keye Electro Physical Equipment Manufacturing Co. Ltd., and various tests, such as heat run test and voltage isolation test were performed. Details are reported in this document.

Keywords: quasi-axisymmetric stellarator, helical device, modular coil, CFQS, joint project, NIFS, SWJTU

All figures are in color only CD-ROM(PDF).

Documentation Contributors

(Alphabetical order of family name)

HUANG	Jie	Southwest Jiaotong University (SWJTU)
ISOBE	Mitsutaka	National Institute for Fusion Science (NIFS)
KINOSHITA	Shigeyoshi	National Institute for Fusion Science (NIFS)
KOBAYASHI	Sakuji	National Institute for Fusion Science (NIFS)
LI	Yangbo	Southwest Jiaotong University (SWJTU)
LIU	Hai	Southwest Jiaotong University (SWJTU)
LIU	Haifeng	Southwest Jiaotong University (SWJTU)
MURASE	Takanori	National Institute for Fusion Science (NIFS)
NAGAOKA	Kenichi	National Institute for Fusion Science (NIFS)
NAKAGAWA	Sho	National Institute for Fusion Science (NIFS)
NAKATA	Motoki	National Institute for Fusion Science (NIFS)
OGAWA	Kunirhiro	National Institute for Fusion Science (NIFS)
OKAMURA	Shoichi	National Institute for Fusion Science (NIFS)
SHAO	Junren	Southwest Jiaotong University (SWJTU)
SHIMIZU	Akihiro	National Institute for Fusion Science (NIFS)
SUZUKI	Chihiro	National Institute for Fusion Science (NIFS)
TANOUE	Hiroyuki	National Institute for Fusion Science (NIFS)
WAN	Yi	Hefei Keye Electro Physical Equipment Manufacturing Co., Ltd. (Keye)
WANG	Xianqu	Southwest Jiaotong University (SWJTU)
XIONG	Guozhen	Southwest Jiaotong University (SWJTU)
XU	Yuhong	Southwest Jiaotong University (SWJTU)
YANG	Lang	Southwest Jiaotong University (SWJTU)
YIN	Dapeng	Hefei Keye Electro Physical Equipment Manufacturing Co., Ltd. (Keye)
YOSHIMURA	Yasuo	National Institute for Fusion Science (NIFS)

Acknowledgements

During our work of making physics and engineering design of CFQS device and environmental utilities, we were given a lot of useful information from scientists and engineers in the experimental groups of various devices in the world. We are very grateful for their advices and supports.

Dr. Hutch Neilson, Dr. Tom Brown, and others from NCSX program in Princeton Plasma Physics Laboratory, Princeton, USA.

Prof. David Anderson, Prof. Simon Anderson, and others from HSX program in University of Wisconsin - Madison, USA.

Prof. Thomas Klinger, Dr. Lutz Wegener, Dr. Thomas Rummel, and others from W7-X program in Max Planck Institute for Plasma Physics, Greifswald, Germany.

Prof. Ge Zhuang, Tao Lan and others from KTX program in University of Science and Technology of China, People's Republic of China.

TABLE OF CONTENTS

1	Introduction.....	8
1.1	Overview.....	8
1.2	Steering committee meeting.....	11
2	Research target.....	12
3	Physics design.....	13
3.1	MHD equilibrium.....	13
3.1.1	MHD equilibrium with VMEC code.....	13
3.1.2	MHD equilibrium with HINT code.....	17
3.2	QA-ness	24
3.3	MHD stability	27
3.3.1	Mercier stability	28
3.3.2	Ballooning mode.....	32
3.3.3	Kink mode.....	34
3.3.4	Tearing mode.....	36
3.3.5	Alfvén mode.....	37
3.4	Micro instability and anomalous transport.....	41
3.4.1	Maximum- J	41
3.4.2	Ion temperature gradient mode	46
3.5	Plasma rotation.....	51
3.6	Energetic particle and NBI deposition analysis	56
3.7	ECRH deposition analysis	60
3.8	Modular coil design and optimization by NESCOIL.....	63
3.9	Design of modular coils without torsions	69
3.10	Divertor configuration	76
4	Engineering design.....	86
4.1	Whole assembly.....	86
4.1.1	Specification for engineering design.....	86
4.1.2	Overall structure.....	89
4.1.3	Production flow.....	92
4.2	Coil system	93
4.2.1	System configuration	93
4.2.2	Modular coil.....	94
4.2.3	Poloidal field coil.....	100

4.2.4	Toroidal field coil.....	102
4.3	Vacuum vessel.....	105
4.3.1	Structure of main vacuum vessel	105
4.3.2	Port arrangement.....	108
4.4	Another component.....	111
4.4.1	External current lead.....	111
4.4.2	Supporting structure.....	111
4.4.3	Cooling water pipe.....	112
4.4.4	Baking heater for vacuum vessel	114
4.5	Verification of design.....	116
4.5.1	Numerical analysis of the modular coil and the support structure	116
4.5.2	Mockup of the modular coil MC4.....	118
4.5.3	Structural analysis of the vacuum vessel	120
4.5.4	Eddy current analysis on vacuum vessel.....	120
4.5.5	Real scale model of the vacuum vessel.....	123
4.6	Equipment related to the vacuum vessel.....	124
4.6.1	Limiter system	124
4.6.2	Vacuum pumping system	126
4.6.3	Wall conditioning system.....	126
4.6.4	Fuel gas supply system (Gas puff system).....	126
4.6.5	Vacuum management system.....	127
4.6.6	Shutter system to protect the glass windows.....	127
4.6.7	Vacuum test equipment.....	127
4.7	Power supply.....	128
4.7.1	Requirement to power supply system	128
4.7.2	Power supply for 0.1 T operation.....	130
4.7.3	Power supply for 1 T operation.....	131
4.7.4	Baking power supply	132
4.8	Pure water cooling system	133
4.9	Compressed air supply system.....	134
4.10	Liquid nitrogen supply system.....	134
4.11	Electron cyclotron resonance heating (ECRH) system	135
4.12	Neutral beam injection (NBI) heating system.....	137
4.13	Diagnostics system.....	138
5	Research plan and schedule	140
5.1	Physics research plan.....	140

5.1.1	Research plan for 0.1 T operation	140
5.1.2	Research plan for 1.0 T operation	140
5.2	Construction schedule	141

1 Introduction

1.1 Overview

The controlled nuclear fusion research is one of the most important issues for human beings because it is necessary to secure stable energy resources in order to enrich human life in the future. Fusion energy does not produce hydrocarbons and hence does not contribute to the global warming, which is one of the most serious environmental problems for Earth. The source of energy are isotopes of hydrogen, which are a common resource for the world because the hydrogen isotopes are obtained from seawater.

The development of technologies so far for making controlled nuclear fusion is based on two methods, namely, magnetic confinement of high temperature plasmas and the strong compression of high density plasmas with ultra-high intensity laser. For the magnetic confinement, high technology devices with strong magnetic field produced by large currents are used. This research started from the 1950s and varieties of different designs of magnetic confinement devices were proposed. After intensive research all over the world for more than a half century, two major magnetic confinement schemes have been established as candidates for the future fusion reactor design, namely, tokamak and stellarator.

These two designs have different advantages and disadvantages. Tokamak devices have better confinement property for high temperature plasmas because of their axisymmetric configuration of the magnetic field. However, tokamaks have essential problems of suffering current disruptions, which is very hazardous for the devices, and the high cost of current drive system because a large plasma current flowing in the plasma is a necessary element for the tokamak concept. On the other hand, stellarator does not have current disruption problems and does not need high cost current drive system because it does not require plasma current as a necessary element of a magnetic confinement concept. However, because of the lack of axisymmetry of the magnetic configuration, the confinement is degraded when the plasma temperature approaches the necessary conditions for the fusion reaction.

At present, large effort toward magnetic confinement of high temperature plasmas is focused on tokamak researches. In France, ITER, the largest facility of magnetic fusion research is now under construction as an international joint project. This device is a tokamak type and it is planned to produce 10 times larger fusion reaction energy than the electric energy consumed for maintaining high temperature plasmas in the device. This program is the final goal of the long way in making good plasma confinement using tokamak type devices. As a next step of fusion research toward the power reactor, we must solve many engineering problems. One of those significant issues is technology problems related to the plasma current (disruptions and current drive). It is strongly pointed out that we should have a multi-line research strategy for the future reactor design, namely, that we should

continue the stellarator research as a safe candidate for the fusion power plant free from the plasma current problems.

When the bright news of achieving high electron temperature in the tokamak device in Russia was distributed throughout the world fusion community in 1969, all plasma experimentalists began to work on tokamak experiments, thus giving up research with their own devices with different concepts from the tokamak. Since then, the main line of magnetic confinement fusion has been based on the tokamak concept. However, there were two continuous research activities for devices with the stellarator concept. In Kyoto University, in Japan, a series of devices with the names of Heliotron (A, B, C, D, DM, DR, E, and J) were built and the plasma parameters were improved continuously. In Germany, a series of devices with the name Wendelstein (1, 2, 3, ..., 6) were producing very promising data with stellarator configuration. In the final phase of these series, Wendelstein 7-A was built in Germany and started experiments in 1975. In Japan, Heliotron E was built and started experiments in 1980. Because the impact of experimental results from these devices were very large for the world fusion community, various types of stellarator programs were initiated in many countries in the 1980s.

In Japan, the designing work for Large Helical Device (LHD) started in 1985, and the construction of the device began in 1989. In Germany, the first design workshop for Wendelstein 7-X (W7-X) took place in 1987 and the first modular coil was ordered in 1998. These two world leading stellarator devices with super-conducting magnets are now in operation for experimental research in various topics of magnetic confinement with stellarator concept. In addition to these large devices, there were two medium size stellarators in operation from the 1980s to the 2000s both in Japan and in Germany. The roles of these devices were to conduct supporting experimental research in advance of the completion of construction and starting the experiments in larger-size major devices. Compact Helical System (CHS) was in operation from 1988 to 2006 and Wendelstein 7-AS was in operation from 1988 to 2002. The experimental results obtained in these devices before starting experiments in LHD and W7-X were very useful for planning experimental program in large devices. They also produced unique scientific results available only in the smaller size devices. In addition to these two experiments, many different types of stellarators were designed and built in other countries: in the United States, Advanced Toroidal Facility (ATF) with heliotron configuration and Helically Symmetric Experiment (HSX) with quasi-helical symmetric configuration started experiments in the 1980s. TJ-II in Spain and H-1 in Australia, both having the heliac configurations, started experiments in the 1980s. Among these devices, experiments in four devices are active at present, namely, LHD, W7-X, HSX, and TJ-II. Four other devices stopped experiments (ATF, W7-AS, CHS, and H-1).

The 1980s was an exciting period for stellarator research as many devices were designed and constructed. Fortunately, four devices continue in operation. However, we notice that it is too long for scientists in active research fields to keep running experiments in old devices designed and built more than 30 years ago even though the devices are in healthy condition for the experiments. In fact, there

were two research activities for the advanced design of stellarator concept in 1990s. In Japan, when CHS completed its initial phase of experimental program, the discussion for the next device after CHS was initiated in 1995. After making surveys for the possible candidates of the next devices, a plan for building a quasi-axisymmetric (QA) stellarator CHS-qa was chosen. Based on the physics and engineering design, a proposal of CHS-qa was completed in 2000 and submitted to the National Institute for Fusion Science (NIFS). Unfortunately, the proposal was not accepted because 2000 was just after the beginning of the LHD experiments and NIFS did not have financial and personnel capability to share in two large programs.

In Princeton Plasma Physics Laboratory (PPPL), a stellarator experiment program started in 1995 for building a medium size stellarator National Compact Stellarator Experiment (NCSX) in parallel to the existing spherical torus experiment, National Spherical Torus Experiment (NSTX). The design concept was a QA stellarator similar to CHS-qa. It had $N=3$ toroidal period number different from $N=2$ for CHS-qa. The proposal of the device construction was approved and PPPL started to build NCSX in 2000. Unfortunately, this program was cancelled in 2008 because of the rapid increase of the construction cost, which the United States government did not accept.

The advanced concept of QA stellarator is very attractive as it is a new scheme of stellarator configuration that had not been imagined by any scientists before 1994. A toroidal device of magnetic confinement must have rotating structures of magnetic field lines in a plasma toroid which can be produced either by a plasma current or by twisting of the plasma surface. Because a twisting shape is not axisymmetric, it is not naturally possible to make a twisting system as axisymmetric. A QA stellarator is not a hybrid device of tokamak and stellarator, either. When we design a hybrid system of two different concepts, all advantageous points and disadvantageous points are mixed together in general. However, the QA stellarator combines only advantageous points from both tokamak and stellarator, thus producing a new advantageous concept. Because such a new invention of the stellarator concept was not realized in the real experimental program in 2000, we now need to recover the lost 15 years by starting a new QA stellarator experiment with the Chinese First Quasi-axisymmetric Stellarator (CFQS).

The present design of the CFQS device incorporates numerous experiences we have learned in CHS-qa design work. In addition, we are adding many new design points that have been learned in theoretical and computational works during the past 15 years. The divertor configuration design, which is supposed be one of the most important research issues in advanced stellarator concept, was renewed from the CHS-qa design with a new concept of the island bundle divertor configuration. For the engineering design of the device and manufacturing, we will make use of new numerical technologies of mechanical design and of new engineering facilities in order to obtain very high accuracy of the three-dimensional shape of the device.

This program is a joint project conducted by NIFS in Japan and Southwest Jiaotong University (SWJTU) in China. We concluded the MoU in 2017 on NIFS and SWJTU Joint Project (NSJP) for CFQS experiment. In addition, we are working together with Hefei Keye Electro Physical Equipment Manufacturing Co., Ltd. in Hefei with their contribution in engineering design and manufacture of the device. Thus, in fact, the program is a joint project by three organizations in Japan and China. We have been working together for the physics and engineering design of CFQS device. SWJTU and the Keye company are primarily responsible for the engineering design and for manufacturing the device. NIFS is primarily responsible to contribute in preparing plasma heating system and diagnostic system. The experiment in the device will be conducted as international collaborations by NIFS, SWJTU and other researchers in foreign countries who will be interested in the challenging advanced stellarator program in Chengdu, China.

1.2 Steering committee meeting

In order to decide the policy of the joint project in each year, the steering committee meeting is regularly held. On May 30 2018, 1st steering committee meeting was held in SWJTU in Chengdu, China. In this meeting, the basic CFQS physics design, which was designed based on CHS-qa, was confirmed. Main parameters of CFQS, major radius, $R = 1$ m, aspect ratio, $A_p = 4$, and toroidal magnetic field strength, $B_t = 1$ T were decided.

On May 29 2019, 2nd steering committee meeting was held in SWJTU in Chengdu, China. In this meeting, the site for experimental building was discussed. Emei campus was one of possible sites to construct the experimental building for CFQS. Progress of engineering design was checked. And the progress of mockup modular coil construction, which was built for check of manufacturing feasibility and achieved accuracy, was confirmed. Real scale 3-D plastic model of 1/4 toroidal section vacuum chamber was made, in order to check the workability in the inside of chamber, and accessibility to plasma.

On Nov. 12 2020, 3rd steering committee meeting was held by online. As the site of experiment building for CFQS, SWJTU suggested its new campus in Tianfu new district in Chengdu. The experimental building will be constructed in this site near future. The construction of mockup modular coil was completed. To check the performance of the mock up modular coil, various tests, such as heat run test, and voltage isolation test were done.

This report summarizes the achievement of physics, engineering research, and the construction of CFQS up to this meeting. In the following sections, important items in the physics and engineering designs of CFQS will be described. We hope this report will provide sufficient information to all researchers in the world about our CFQS program and motivate them to participate in the joint program of NSJP.

2 Research target

The CFQS is an international joint project between SWJTU in China and NIFS in Japan. It is the first stellarator to be manufactured and assembled by the Hefei Keye Electro Physical Equipment Manufacturing Co. Ltd. in China. Whereas in China there have been several tokamaks built by national institutions, there is no stellarator up to now. As the stellarator is technically much more complicated than the tokamak, our first target is to construct the CFQS device successfully and make it in good operation status in SWJTU. Secondly, we want to scientifically prove the major advantage of a quasi-axisymmetric (QA) stellarator in confining plasmas with reduced magnetic field ripple, and hence, neoclassical transport in comparison with previous conventional stellarators. Thirdly, for complementing the two-dimensional (2-D) tokamak physics, we will thoroughly study the intrinsic three-dimensional (3-D) physics in the CFQS stellarator to improve our understanding on related 3-D issues appeared in the tokamak, which has primarily 2-D magnetic configuration.

The main focus of the CFQS research activities is on basic physics studies under the advanced QA configuration. The scientific subjects include neoclassical transport, macro-scale magnetohydrodynamics (MHD) instabilities (interchange, ballooning, kink, and tearing modes, *etc.*), micro instabilities (electron drift wave, ion temperature gradient (ITG) and electron temperature gradient (ETG) modes, and trapped electron mode (TEM), *etc.*) and turbulence-induced transport, nonlinear interaction and energy cascading of multi-scale turbulence and zonal flows, confinement scaling and isotopic effects, plasma rotations, and edge and divertor physics. Special attention will also be paid on MHD activities arising from the neoclassical bootstrap current and the maximum- J issue in the QA configuration.

3 Physics design

3.1 MHD equilibrium

3.1.1 MHD equilibrium with VMEC code

The characteristics of three-dimensional (3-D) magnetic field configuration is uniquely determined, if the geometry of LCFS, the radial profile of pressure and the toroidal current as a function of flux are given [3.1.1-1]. The equilibrium of the magnetic field configuration is obtained by the VMEC code [3.1.1-2]. This code calculates the equilibrium from the given last closed flux surface (LCFS), the pressure and the toroidal current profile. The geometry of the torus LCFS can be parameterized by the Fourier series as follows,

$$\begin{aligned} R(\theta, \phi, s) &= \sum R_{mn}(s) \cos(m\theta - N_p n\phi), \\ Z(\theta, \phi, s) &= \sum Z_{mn}(s) \sin(m\theta - N_p n\phi). \end{aligned}$$

Here, θ , ϕ , and s are the poloidal angle, toroidal angle, and the radial flux coordinate, respectively. m , n , are the poloidal and toroidal mode, respectively, and N_p is the toroidal periodic number of the magnetic field configuration. In other words, the geometry of the LCFS, namely, the characteristics of the magnetic field configuration equilibrium, is expressed numerically by the dataset of R_{mn} and Z_{mn} . In stellarator optimization, we consider these parameters (R_{mn} , Z_{mn}) as control parameters, and some specific characters of magnetic field configuration are optimized. For numerical optimization, characters of magnetic field configuration are expressed numerically. For example, the sum of non-axisymmetric components of magnetic field in the Boozer coordinates [3.1.1-3], the Mercier criteria of D_I , and the effective helical ripple ε_{eff} etc. are used for the numerical evaluation of the magnetic configuration. These values that characterize the magnetic field configuration are optimized by changing the control parameters, *i.e.*, (R_{mn} , Z_{mn}) by using a non-linear optimization method. The guiding center orbits of charged particles in stellarators are determined by the absolute value of the magnetic field in the Boozer coordinates [3.1.1-3,4], therefore the spectrum of magnetic field strength B_{mn} in the Boozer coordinates are important. If the magnetic field strength in this coordinate system, B , is axisymmetric, *e.g.* it depends on only the θ , the guiding center orbits in this coordinates also become axisymmetric. This configuration is called as a quasi-axisymmetric (QA) system, because the geometry of plasma boundary is three dimensional, however, in the Boozer coordinates the particle orbit becomes axisymmetric and the good particle confinement property like tokamaks can be achieved.

As the post CHS project, the QA device, CHS-qa, was designed in NIFS [3.1.1-5]. The parameters of this device were as follows: The toroidal periodic number (N_p) is 2, the toroidal magnetic field strength (B_t) is 1.5 T, the major radius (R) is 1.5 m, and the aspect ratio (A_p) is 3.2, which is called as the 2b32 configuration. This configuration was designed to have a good QA property with good

magnetic well and ballooning mode stability. Based on this configuration, new QA configuration is designed for the CFQS. N_p of 2, B_t of 1.0 T, and R of 1.0 m are chosen for the CFQS. From the engineering point of view, the same low-aspect-ratio of the CHS-qa is not easy to realize, so the plasma size is shrunk and A_p of 4 is selected. In Fig. 3.1.1-1, the vacuum magnetic surfaces calculated by VMEC code are shown. The coefficients R_{mn} and Z_{mn} for the CFQS are shown in Table 3.1.1-1. The radial profile of the rotational transform and the magnetic well are shown in Fig. 3.1.1-2. The profile of rotational transform is characterized by low shear, and the magnetic well property is realized in the all radial region.

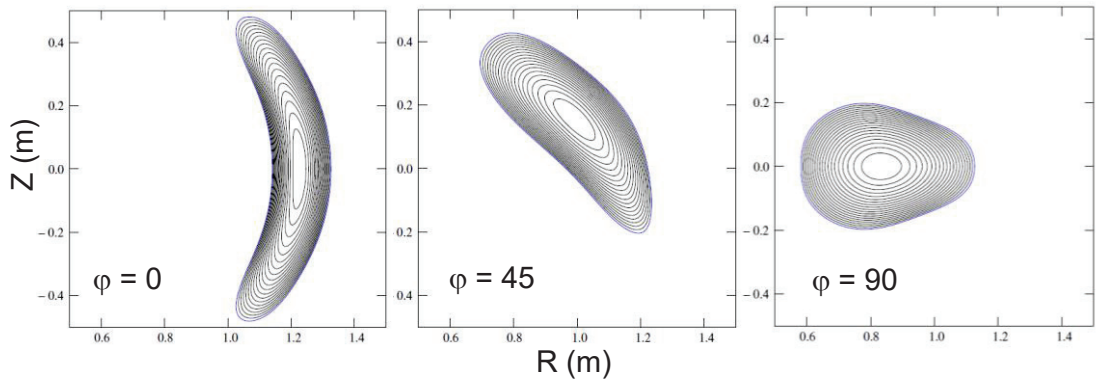


Fig. 3.1.1-1 CFQS magnetic flux surfaces in vacuum calculated by VMEC code at toroidal angles of 0, 45, and 90 degrees are shown.

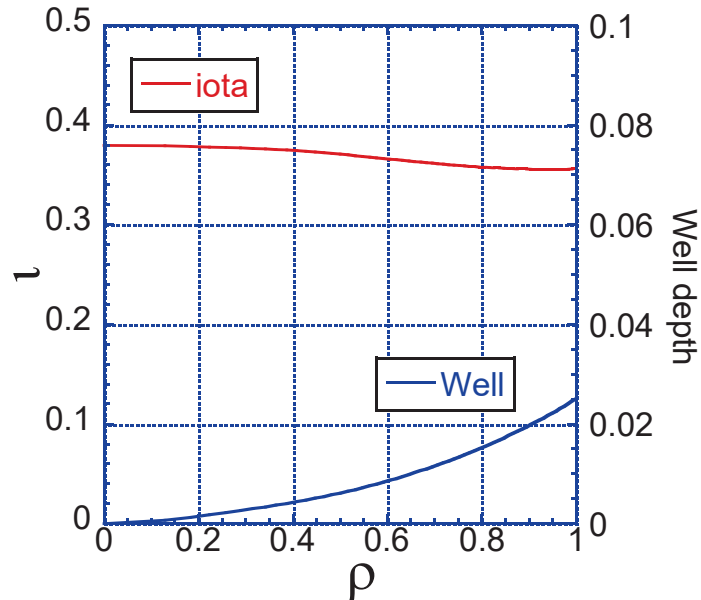


Fig. 3.1.1-2 Radial profiles of the rotational transform and magnetic well depth.

Table 3.1.1-1 Fourier components of R_{mn} , Z_{mn} for the CFQS boundary surface.

m	n	R_{mn}	Z_{mn}
0	0	1.000000E+00	0.000000E+00
0	1	1.391875E-01	-1.041401E-01
0	2	3.510066E-03	-2.047598E-03
0	3	-1.013876E-04	1.642899E-03
0	4	-9.175025E-05	1.845669E-05
1	-4	2.798909E-05	6.083008E-05
1	-3	-8.309604E-04	-1.061025E-03
1	-2	5.350281E-04	-1.240619E-03
1	-1	3.272968E-02	3.765426E-02
1	0	1.980512E-01	3.153157E-01
1	1	-1.190292E-01	1.059881E-01
1	2	-9.839016E-03	1.600162E-02
1	3	-1.036865E-04	-1.235699E-03
1	4	-1.774901E-04	-1.233294E-05
2	-4	-1.276662E-05	1.619552E-05
2	-3	-2.212222E-04	-1.655420E-04
2	-2	2.659139E-03	9.708512E-04
2	-1	5.392748E-03	3.943360E-03
2	0	2.368458E-02	5.220414E-03
2	1	4.800571E-02	1.879457E-02
2	2	1.418504E-02	-1.281654E-02
2	3	6.331471E-04	3.229137E-03
2	4	3.216150E-04	-3.067359E-05
3	-4	-2.244352E-05	-2.337868E-05
3	-3	2.247393E-06	7.071358E-05
3	-2	1.535243E-04	-7.055294E-05
3	-1	2.756543E-03	8.833038E-04
3	0	-3.334046E-03	3.224783E-03
3	1	-7.588701E-03	-6.650261E-03
3	2	-5.415940E-03	-2.327107E-03
3	3	-1.395157E-03	2.106916E-03
3	4	3.497018E-04	-6.340033E-04
4	-4	-1.132392E-05	4.601234E-06
4	-3	2.972533E-05	2.318047E-05
4	-2	-5.763365E-06	-6.467228E-05
4	-1	-8.356260E-05	-6.036524E-05
4	0	2.323114E-05	7.077580E-04
4	1	1.594329E-03	-9.755319E-04
4	2	-1.043988E-03	-2.935019E-03
4	3	-3.632249E-05	1.253345E-03
4	4	8.926982E-05	-2.034287E-04

5	-4	-1.660390E-06	-3.428524E-06
5	-3	2.634658E-06	4.226553E-06
5	-2	2.735705E-06	-5.476804E-07
5	-1	2.253818E-05	-1.345821E-05
5	0	-6.240069E-05	9.560246E-05
5	1	2.985376E-04	3.224349E-04
5	2	2.590860E-04	-7.446490E-05
5	3	2.474033E-04	2.527979E-04
5	4	9.280067E-05	-1.552233E-04
6	-4	1.525797E-05	-1.628272E-05
6	-3	-3.190926E-06	8.024808E-06
6	-2	7.765667E-06	-1.349779E-06
6	-1	-6.667636E-06	3.234683E-05
6	0	-4.959176E-05	-2.079634E-04
6	1	2.254973E-04	4.967132E-04
6	2	-1.654727E-04	-2.109075E-04
6	3	4.065117E-06	1.641132E-04
6	4	-1.144226E-05	-2.856708E-05
7	-4	-1.117052E-05	4.973842E-06
7	-3	-2.019870E-06	2.080768E-06
7	-2	1.753082E-06	9.119779E-07
7	-1	8.999813E-06	7.420079E-06
7	0	-2.983144E-05	-4.351131E-05
7	1	7.571942E-06	1.951069E-05
7	2	1.239090E-04	1.100027E-04
7	3	-4.699164E-05	-6.161755E-05
7	4	3.831545E-05	5.227709E-05

References

- [3.1.1-1] J. Nührenberg, R. Zille, *Physics Letters A* **129** (1988) 113.
[3.1.1-2] S. P. Hirshman, J. C. Whitson, *Physics of Fluids* **26** (1983) 3553.
[3.1.1-3] A. H. Boozer, *Physics of Fluids* **23** (1980) 904.
[3.1.1-4] A. H. Boozer, *Physics of Fluids* **24** (1981) 1999.
[3.1.1-5] S. Okamura *et al.*, *Nuclear Fusion* **41** (2001) 1865.

3.1.2 MHD equilibrium with HINT code

The HINT code is a three-dimensional MHD equilibrium code based on the relaxation method without requiring the nested flux surface [3.1.2-1]. In this section, the typical configuration of the CFQS plasma is studied using the HINT code. A brief introduction of the code has been given here.

In the new version of the HINT code, the cylindrical coordinate (R, ϕ, Z) with the right-handed system is used with a high numerical accuracy. The steady-state solution based on the relaxation method is employed to solve single-fluid nonlinear MHD equations [3.1.2-2,3,4]. The relaxation consists of the following two steps, including (A) plasma pressure relaxation and (B) magnetic field relaxation. In step A, no pressure gradient along the magnetic field is satisfied with $\mathbf{B} \cdot \nabla p = 0$ for relaxation process of the plasma pressure (p), where the magnetic field \mathbf{B} is fixed. In step B, magnetic field is calculated with fixed p , which is updated in the step A. The reduced MHD equations are used as

$$\frac{\partial \mathbf{v}}{\partial t} = -\nabla p + (\mathbf{j} - \mathbf{j}_0) \times \mathbf{B}$$

$$\frac{\partial \mathbf{B}}{\partial t} = \nabla \times [(\mathbf{v} \times \mathbf{B}) - \eta(\mathbf{j} - \mathbf{j}_0 - \mathbf{j}_{\text{net}})]$$

where, t is time, \mathbf{v} is plasma velocity, \mathbf{j} is the total current density, \mathbf{j}_0 is the current density produced by vacuum magnetic field, \mathbf{j}_{net} corresponds to the net toroidal current like the neoclassical bootstrap current, η is dissipative parameter and constant plasma density is assumed. From the step B, a new magnetic field \mathbf{B} is obtained, then substituting it into step A that can yield new p . Both \mathbf{B} and p are updated via once iteration. After the multiple iteration process of the two steps, the final equilibrium is obtained when plasma velocity and magnetic field satisfy $dv/dt \rightarrow 0$ and $dB/dt \rightarrow 0$ simultaneously. The new version of HINT with the modified scheme of the pressure relaxation is efficient to calculate QAS and low shear stellarators [3.1.2-2].

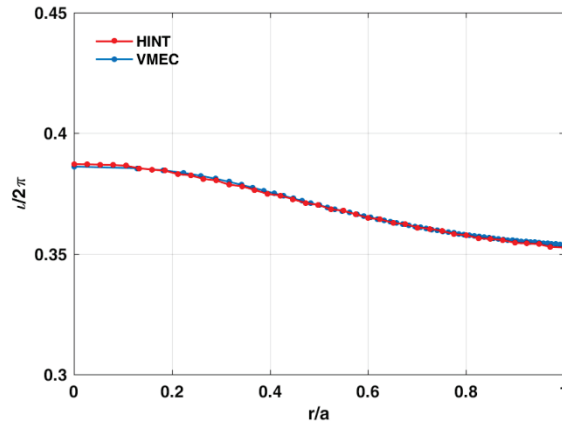


Fig. 3.1.2-1 Rotational transform ($t/2\pi$) in vacuum with normalized minor radius (r/a) for the HINT code and the VMEC code.

Fig. 3.1.2-1 shows a benchmark for CFQS equilibrium using the HINT and the VMEC code, where the rotational transform in vacuum for CFQS has been first given in previous work [3.1.2-5]. The VMEC free-boundary equilibrium result is in good agreement with the result of the HINT code for the zero pressure case. The typical rotational transform, $t/2\pi$, is smaller than 0.4, and this profile implies a weak shear comparing with other optimized stellarator configurations.

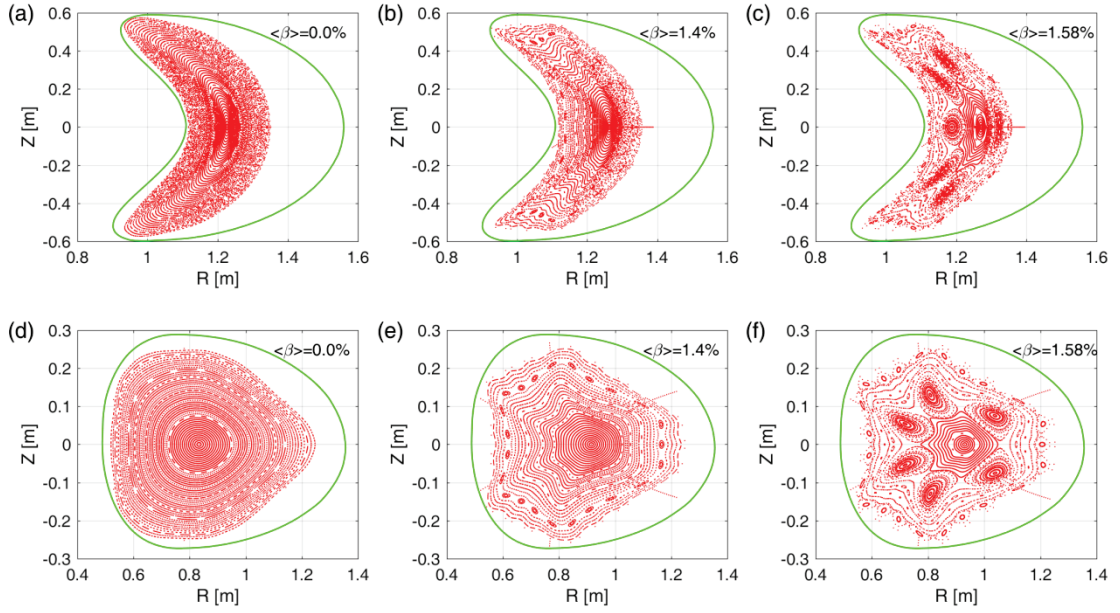


Fig. 3.1.2-2 Poincaré plots of magnetic flux surfaces calculated using HINT code for various volume averaged beta. (a)-(c) $\langle\beta\rangle = 0.0\%$, 1.4% , and 2.58% at $\phi = 0^\circ$. (d)-(f) $\langle\beta\rangle = 0.0\%$, 1.4% , and 2.58% at $\phi = 90^\circ$.

After the benchmark, we further calculate the finite beta equilibrium for the CFQS using the HINT code. The Poincaré plots of magnetic surfaces are shown in Fig. 3.1.2-2, where the green line describes the vacuum vessel (VV) shape. The different volume-averaged beta $\langle\beta\rangle$ are considered. In this calculation, a reference configuration with a general pressure profile as $\propto (1-\psi)^2$ is employed, where ψ is the toroidal flux. Comparison of the difference $\langle\beta\rangle$ cases shows that an ergodization of magnetic surfaces expands with $\langle\beta\rangle$ increases in the boundary plasma ergodic region. When the plasma beta is sufficiently large, the large magnetic island generates not only on boundary but also on many low-order rational surfaces such as $m/n = 4/2, 5/2$, and $6/2$, where m and n are the poloidal and toroidal mode number, respectively. The outer ergodic region expands towards plasma center, meanwhile, flux surfaces in high- β equilibrium tend to be more easily broken, which lead to plasma region shrinking. This suggests that the confinement of the edge plasma is significantly limited by the break of magnetic structure. On the other hand, however, $\langle\beta\rangle$ in Fig. 3.1.2-2(b) is larger than the design value of the CFQS regular operation as $\langle\beta\rangle = 1\%$ [3.1.2-5,6]. It is easily to predict that, in the low- β regime of $\langle\beta\rangle$ less than 1% , effective volume of the confinement region can be well retained in the present

equilibrium design. In order to reduce the outer magnetic surfaces loss caused by the outward shift of the surface position, an additional vertical field produced by external coils may be feasible for the CFQS to push the surface position back recovering the lost magnetic surfaces, as has been reported in reference [3.1.2-7,8].

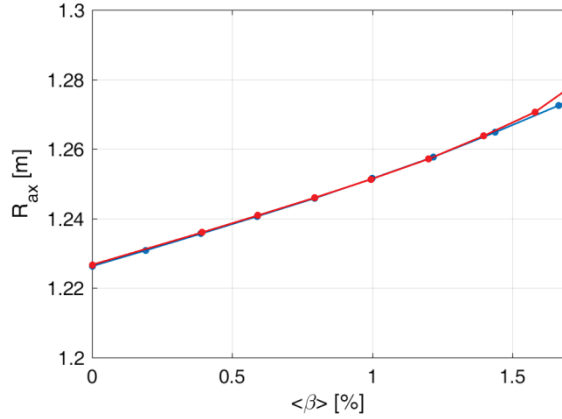


Fig. 3.1.2-3 The average position of the magnetic axis in major radius direction (R_{ax}) as a function of $\langle\beta\rangle$ calculated by the HINT (red line) and the VMEC code (blue line).

In fact, the finite beta effect not only on the edge, but also on every magnetic surfaces [3.1.2-2,9]. To explore the role of plasma beta and magnetic island in core region, we further calculate the magnetic axis shifts in the finite plasma beta cases by the HINT code and the VMEC code. The magnetic axis shift as a function of $\langle\beta\rangle$ is shown in Fig. 3.1.2-3, where the pressure profile is the same as that of Fig. 3.1.2-2. It is noted that when $\langle\beta\rangle < 1.4\%$, the result of the HINT code is quantitatively consistent with that of the VMEC code. The R_{ax} almost linearly depends on $\langle\beta\rangle$. In the high- β regimes of $\langle\beta\rangle$ larger than 1.5%, however, the shift is accelerated as a result of the $m/n = 6/2$ islands outward pushing. This point is confirmed in Fig. 3.1.2-2(c) and (f) in which many larger islands are produced on the left hand side of magnetic axis.

In CHS-qa, the estimated value of neoclassical bootstrap current reached to 100 kA for high- β discharges [3.1.2-10,11]. Since the CFQS is more compact quasi-axisymmetric system, substantial neoclassical bootstrap current is expected in high- β regime [3.1.2-6,12,13]. The HINT calculation of the equilibrium modified by neoclassical bootstrap current, therefore, is important to explore the configuration properties in detail. At first, the influence of neoclassical bootstrap current on MHD equilibrium of CFQS is investigated using the BOOTSJ code that calculates neoclassical bootstrap currents based on the drift kinetic model in non-axisymmetric magnetic configurations [3.1.2-14].

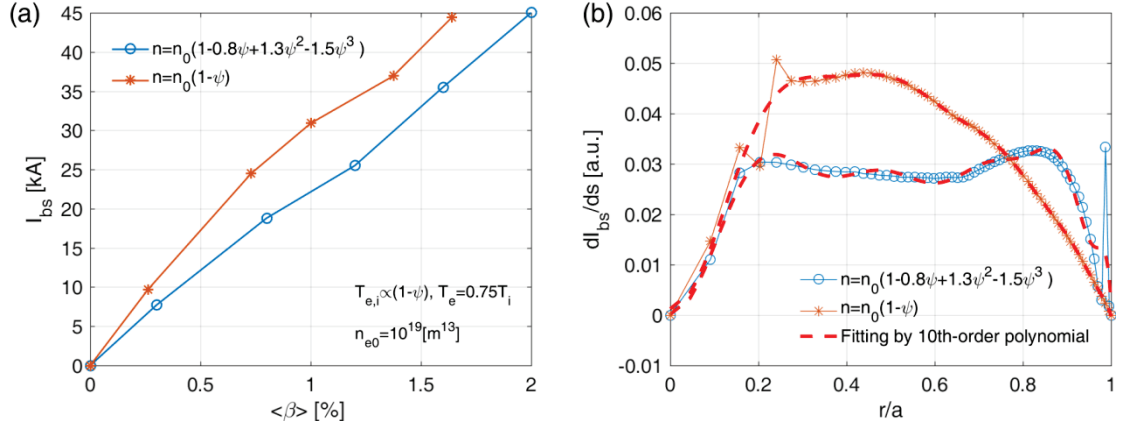


Fig. 3.1.2-4 (a) Neoclassical bootstrap current (I_{bs}) and (b) neoclassical bootstrap current density (dI_{bs}/ds) as a function of $\langle\beta\rangle$ for parabolic (Case 1) $n = n(0) \cdot (1 - \psi)$ and flat n_e profile (Case 2) $n = n(0) \cdot (1 - 0.8\psi + 1.3\psi^2 - 1.5\psi^3)$ calculated by the BOOTSJ code.

To study the effect of neoclassical bootstrap current, we consider two different density profiles with the fixed temperature profile of $T_{e,i} \propto (1 - \psi)$, corresponding to Case 1: parabolic profile ($n = n(0) \cdot (1 - \psi)$) and Case 2: flat density profile ($n = n(0) \cdot (1 - 0.8\psi + 1.3\psi^2 - 1.5\psi^3)$) as used in Fig. 3.1.2-4 (a) and (b), respectively. The parameters are the same as those used in Fig. 3.1.2-3 and then only the density profile is changed. From Fig. 3.1.2-4 (a) and (b), we can find the flattening of n_e profile can effectively reduce the neoclassical bootstrap current value and change the current density profile. The neoclassical bootstrap current almost linearly increases with $\langle\beta\rangle$ increases. For a general design of $\langle\beta\rangle \sim 1\%$, the amplitudes of neoclassical bootstrap current ~ 20 kA for Case 1 and ~ 30 kA for Case 2 are smaller than that in CHS-qa [3.1.2-6,8,12,13]. In Case 1, dI_{bs}/ds produced by the parabolic profile has a peak at $r/a = 0.4$ and results in the reversed magnetic shear, corresponding to advanced operation scenarios in tokamak. In Case2, dI_{bs}/ds rises toward the outer region and leads to a weak shear of $t/2\pi$ profile, which is similar to the result of reference [3.1.2-6].

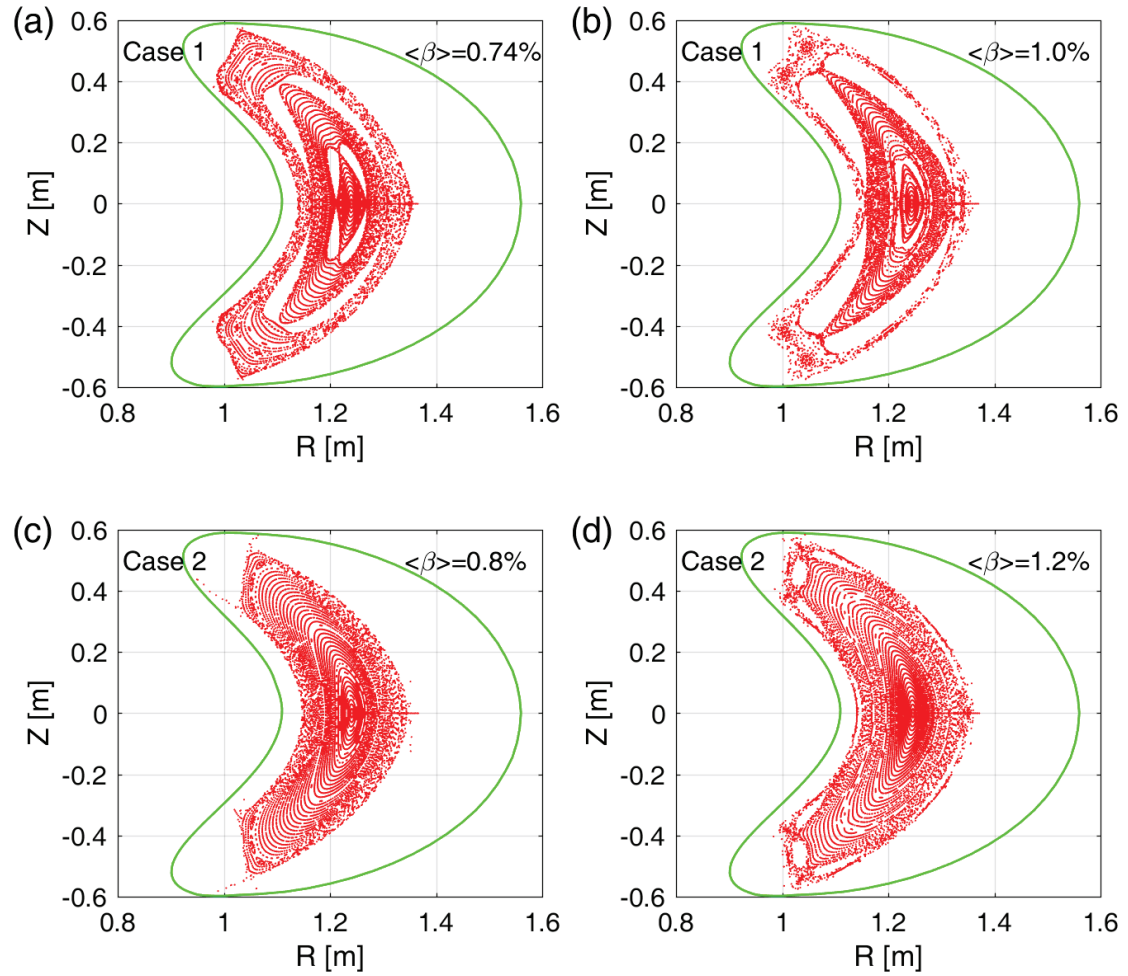


Fig. 3.1.2-5 Poincaré plots of magnetic surfaces for (a) Case 1 parabolic n_e profile with $\langle\beta\rangle = 0.74\%$, (b) Case 1 parabolic n_e profile with $\langle\beta\rangle = 1.0\%$, (c) Case 2 flat n_e profile with $\langle\beta\rangle = 0.8\%$, and (d) Case 2 flat n_e profile with $\langle\beta\rangle = 1.2\%$.

In general, in the 3-D MHD equilibrium, the magnetic island and stochasticization are driven by the nonlinear 3-D equilibrium response rather than the magnetic reconnection driven by the MHD instability [3.1.2-2,3,4,9]. It means that in the CFQS the neoclassical bootstrap current can enhance the rotational transform but does not have a direct contribution on the generation of equilibrium magnetic islands. To check the robustness of boundary magnetic structure and islands, we perform the HINT calculation for the CFQS including neoclassical bootstrap current, and give the Poincaré plots of magnetic surfaces in Fig. 3.1.2-5 for the two different n_e profile cases, where the parameter setting is introduced in Fig. 3.1.2-4.

For Case 1, as is shown in Fig. 3.1.2-5 (a) and (b), with increasing of $\langle\beta\rangle$, the shape of the LCFS is opened clearly. The edge field is ergodized as a result of the finite pressure effects. The magnetic island forms at the rational surface corresponding to $1/2\pi = 2/4$. For the high- β equilibrium, the

increasing of stochastic region results in the effective volume of the confinement region shrinking to insides of islands. It implies that the force balance is not easy to maintain by residual plasma after the stochastization of magnetic field lines in the more peaked pressure configuration of Case 1.

For Case 2, as is shown in Fig. 3.1.2-5 (c) and (d), we can find in the moderate flattened pressure equilibrium with $\langle\beta\rangle \sim 1.2\%$, the magnetic island and stochastization are suppressed effectively. Although the boundary island remains due to increasing plasma beta, the relatively good flux surfaces are still kept over the entire plasma area. This offers the possibility to expect the high- β equilibrium for CFQS. Meanwhile, a high effective confinement volume in high- β operation scenarios can be realized if the density profile can be controlled by electron cyclotron resonance heating, pellet injection and so on.

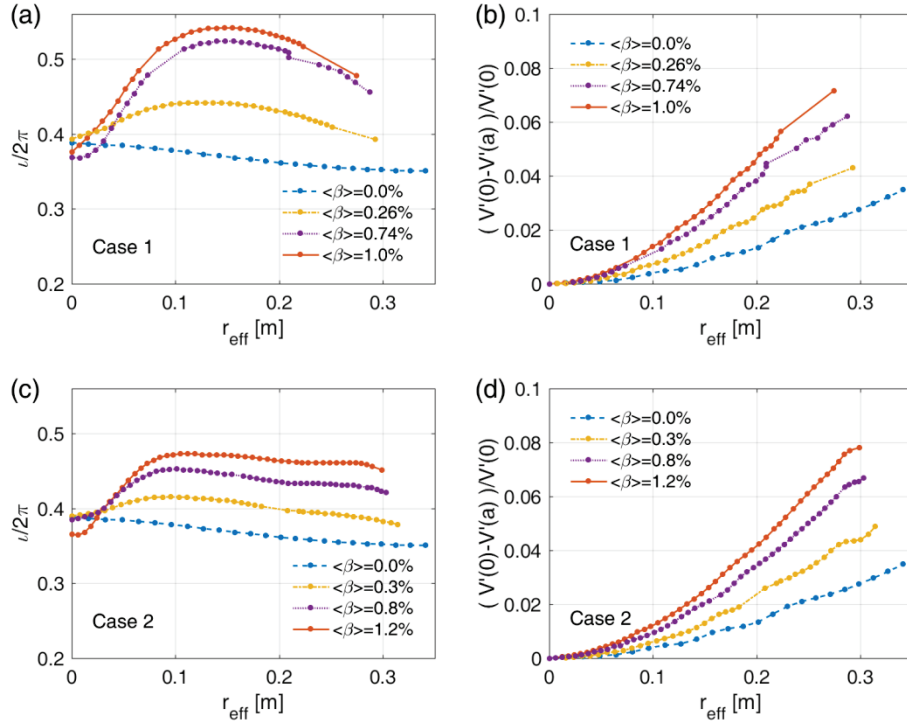


Fig. 3.1.2-6 (a) Rotational transform profiles and (b) magnetic well depth for different $\langle\beta\rangle$ in parabolic n_e profile. (c) Rotational transform profiles and (d) magnetic well depth for different $\langle\beta\rangle$ in flat n_e profile.

In previous works, it has been reported that the rotational transform can be enhanced by increasing the neoclassical bootstrap current in QAS [3.1.2-6,13]. Moreover, the enhanced rotational transform may play an important role in dynamics of the magnetic island. To explore the $\langle\beta\rangle$ dependence of rotational transform including neoclassical bootstrap current consistently, we present the results of $i/2\pi$ profile for various $\langle\beta\rangle$ in Fig. 3.1.2-6 (a) and (c). The magnetic well depth defined by $(V_p'(0)-$

$V_p'(a)/V_p'(0)$ to evaluate MHD property of QAS is shown in Fig. 3.1.2-6 (b) and (d), where V_p is the plasma volume with different effective radius and prime denotes the derivative of toroidal flux.

For Case 1, as $\langle\beta\rangle$ increased, the rotational transform crosses $\iota/2\pi=0.4, 0.5$, and the $\iota/2\pi$ profile is sensitive to the changes of $\langle\beta\rangle$ value, particularly in the small $\langle\beta\rangle$ regimes. On the rational surface, the modification of magnetic island near rational surface results in a vacancy region of iota profile in which the magnetic field line is closed insider islands rather than along its rotational transform. Moreover, it is also not possible to compute a $\iota/2\pi$ value further out due to the stochasticity of magnetic field lines in plasma edge region. Using the averaged effective radial position r_{eff} [m], we can easily find the confinement plasma region shrinking which corresponds to magnetic surface plotting of Fig. 3.1.2-5 (a) and (b). Fig. 3.1.2-6 (b) shows the effect of finite $\langle\beta\rangle$ on magnetic well depth. The magnetic well gradually rises from 3.5% to 6.7% on the LCFS, which qualitatively accords with the result of CHS-qa [3.1.2-10].

For Case 2, the iota profile flats in the intermediate region of $r_{eff} > 0.1$ [m] due to the profile effect of neoclassical bootstrap current. In a finite beta case, the magnetic well becomes deeper than that in vacuum equilibrium. Because the modified rotational transform suppresses plasma region shrinking, the well depth ($\sim 8\%$) for $\langle\beta\rangle = 1.2\%$ is also larger than that in Case 1 even with the low $\langle\beta\rangle = 1.0\%$. Then the magnetic well property is achieved throughout the entire plasma region.

References

- [3.1.2-1] S. P. Hirshman and J. C. Whitson Phys. Fluids **26** (1983) 3553.
- [3.1.2-2] Y. Suzuki *et al.*, Plasma Phys. Control. Fusion **59** (2017) 054008.
- [3.1.2-3] Y. Suzuki, J. Geiger, Plasma Phys. Control. Fusion **58** (2016) 064004.
- [3.1.2-4] Y. Suzuki *et al.*, Contrib. Plasma Phys. **50** (2010) 576.
- [3.1.2-5] H. F. Liu *et al.*, Plasma Fusion Res. **13** (2018) 3405067.
- [3.1.2-6] A. Shimizu *et al.*, Plasma Fusion Res. **13** (2018) 3403123.
- [3.1.2-7] K. Matsuoka *et al.*, Fusion Sci. Technol. **46** (2004) 378.
- [3.1.2-8] S. Okamura *et al.*, Nucl. Fusion **44** (2004) 575.
- [3.1.2-9] Y. Suzuki *et al.*, Nucl. Fusion **46** (2006) L19.
- [3.1.2-10] M. Isobe *et al.*, J. Plasma Fusion Res. SERIES **5** (2002) 360.
- [3.1.2-11] M. Isobe *et al.*, 28th EPS Conference on Controlled Fusion and Plasma Physics, Funchal, Portugal, 18-22 June 2001 ECA Vol.25A 761.
- [3.1.2-12] Y. Xu *et al.*, 27th IAEA Fusion Energy Conference (FEC 2018) Ahmedabad, India, 22-27 October 2018 EX/P5-23.
- [3.1.2-13] M. Isobe *et al.*, Plasma Fusion Res. **14** (2019) 3402074.
- [3.1.2-14] K. C. Shaing *et al.*, Phys. Fluids **B1** (1989) 148.

3.2 QA-ness

As stated above, the guiding center drift orbit is determined by the absolute value of \mathbf{B} in the Boozer coordinates, because in the guiding orbit equation only the absolute value of \mathbf{B} appears and the vector components of \mathbf{B} do not appear. The Fourier components of the CFQS magnetic field in the Boozer coordinates are shown in Fig. 3.2-1. The toroidal ripple component, B_{10} is dominant for the good QA property. The contour map of magnetic field strength in the toroidal and poloidal angle plane is shown in Fig. 3.2-2.

Due to the QA property, the neoclassical bootstrap current is driven by the neoclassical effect. The BOOTSJ code can give us the neoclassical bootstrap current in the collision less limit [3.2-1]. With the BOOTSJ code, the neoclassical bootstrap current is estimated for the CFQS. Fig. 3.2-3 shows the dependency of the neoclassical bootstrap current on the volume-averaged plasma beta $\langle\beta\rangle$. Here, low-density case ($n_{e0}=1.0 \times 10^{19} \text{ m}^{-3}$, $T_e = 10 T_i$), and high-density case ($n_{e0}=2.0 \times 10^{19} \text{ m}^{-3}$, $T_e = T_i$) are considered. Radial profiles for density and temperature are assumed to be parabolic, $n_e \propto (1-\rho^2)$ and $T_e, T_i \propto (1-\rho^2)$. For the beta scan, n_e is fixed, and T_e , and T_i are changed. When $\langle\beta\rangle$ reaches 1 %, the neoclassical bootstrap current of 30 kA is expected. For low-density case, the change of the rotational transform profile is shown in Fig. 3.2-4. The MHD instability, such as kink mode, will be studied in the future.

The neoclassical transport in the $1/\nu$ regime can be estimated by the NEO [3.2-2] code. By this code, so-called the effective helical ripple ε_{eff} is estimated in this work. The neoclassical diffusion coefficient D is proportional to $v_d \varepsilon_{eff}^{3/2}/\nu$. Here, v_d and ν are the drift velocity and the collision frequency, respectively. The radial profile of $\varepsilon_{eff}^{3/2}$ are shown in Fig.3.2-5. The magnetic configurations of the CFQS in this figure are calculated with VMEC on fixed boundary and free boundary condition. The $\varepsilon_{eff}^{3/2}$ of the CFQS are two or three order less than that of the CHS. Up to $\langle\beta\rangle$ of 1.5%, the good neoclassical confinement property is kept.

Fourier spectrum of B in Boozer coordinates

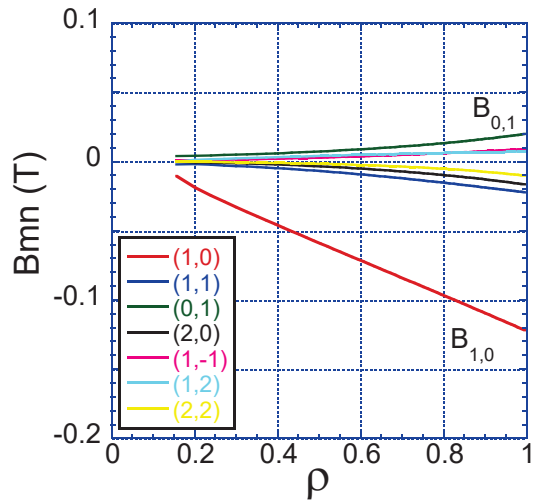


Fig. 3.2-1 Fourier spectrum of B in the Boozer coordinates.

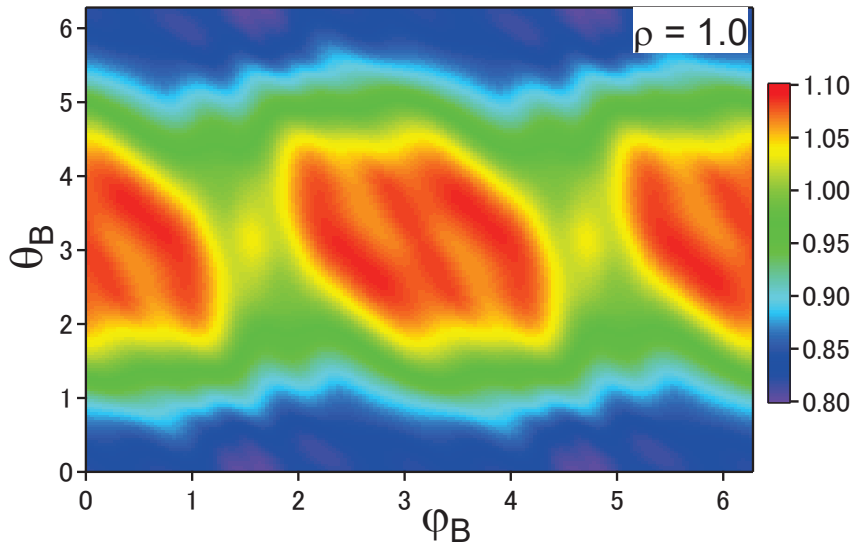


Fig. 3.2-2 Contour map of the magnetic field strength B in the Boozer coordinates on the LCFS of the CFQS.

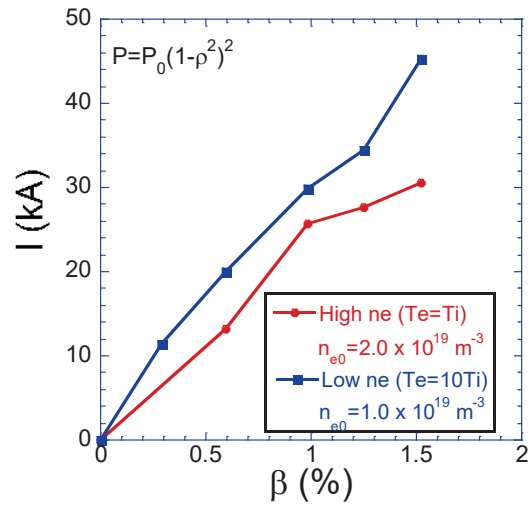


Fig. 3.2-3 Dependency of the neoclassical bootstrap current on the volume-averaged plasma beta.

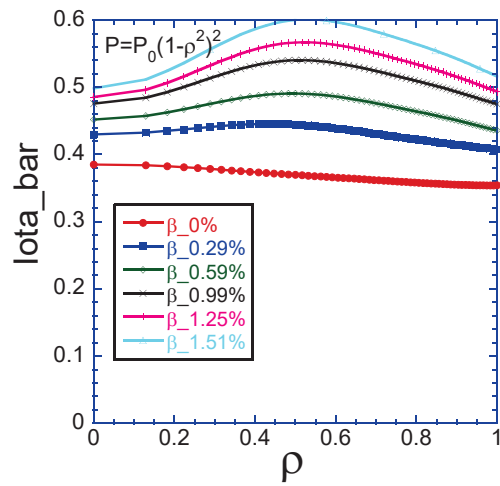


Fig. 3.2-4 Radial profile of the rotational transform considering the neoclassical bootstrap current.

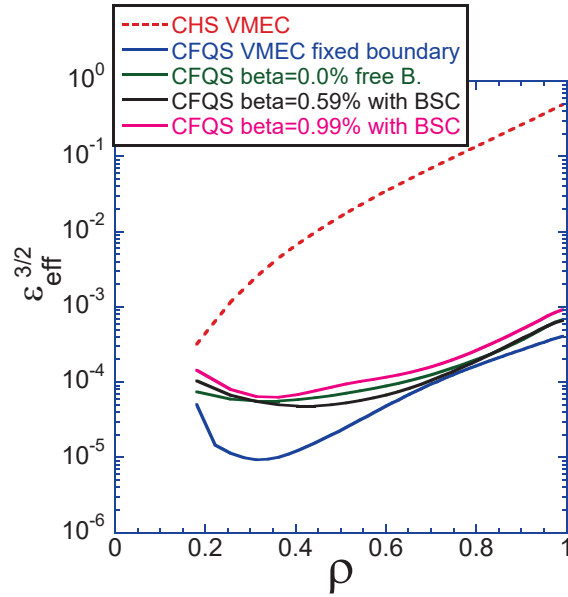


Fig. 3.2-5 Radial profiles of the effective helical ripple, $\epsilon_{\text{eff}}^{3/2}$. In the latter three cases, *i.e.*, green, black, and pink, the free-boundary calculation result of the VMEC are used to estimate $\epsilon_{\text{eff}}^{3/2}$.

References

- [3.2-1] K. C. Shaing *et al.*, Phys. Fluids **B 1** (1989) 148.
- [3.2-2] V. V. Nemov *et al.*, Phys. of Plasmas **6** (1999) 4622.

3.3 MHD stability

Key MHD stabilities in the design of a finite- β QA stellarator configuration are discussed in this section. Mercier stability, ballooning mode, kink mode, and tearing mode are investigated to determination of β limit. These four issues are not independent. The VMEC, COBRAVMEC, BOOTSJ, and TERPSICHORE codes are executed to estimate them [3.3-1~5].

References

- [3.3-1] S.P. Hirshman, and J.C. Whitson, Phys. Fluids **26** (1983) 3353.
- [3.3-2] A. H. Boozer, Phys. Fluids **24** (1981) 1999.
- [3.3-3] K.C. Shaing *et al.*, Phys. Fluids **B1** (1989) 1663.
- [3.3-4] R. Sanchez *et al.*, J. Comp. Physics **161** (2000) 576.
- [3.3-5] C. Mercier, Nucl. Fusion **1** (1960) 47.

3.3.1 Mercier stability

The Mercier criterion is a necessary condition for the stability of localized interchange modes in a toroidal plasma, according to the ideal MHD model [3.3.1-1]. These modes are localized around mode-rational surfaces, where the parallel wave vector vanishes, so as to minimize the magnetic field line bending energy. The driving force for these modes is the pressure gradient across surfaces with average unfavorable curvature. The Mercier stability criterion involves competition between the driving force and the stabilizing effect of magnetic shear. The Mercier criterion can be written as summation of four terms, corresponding to the contributions coming from the shear, magnetic well, net currents, and geodesic curvature, respectively.

Once the magnetic field coils have been designed it needs to be established that these coils actually reproduce the desired MHD equilibrium and its relevant properties. For this purpose, free boundary equilibria were computed for volume averaged $\langle\beta\rangle = 0$ and $\langle\beta\rangle = 2\%$. The cross sections of the plasma boundary obtained from free boundary equilibrium calculations (*i.e.* using the external magnetic field generated by the modular coils described in Sec. 4.2) are obtained. A comparison of the flux surfaces of the vacuum field and the $\langle\beta\rangle = 2\%$ solution (both VMEC) is presented in Fig. 3.3.1-1. It is observed that the Shafranov shift of the axis exists. The variation of Shafranov shift with $\langle\beta\rangle$ is displayed in the Fig. 3.3.1-2. When $\langle\beta\rangle$ equals to 1.7%, the Shafranov shift is about the half of the minor radius.

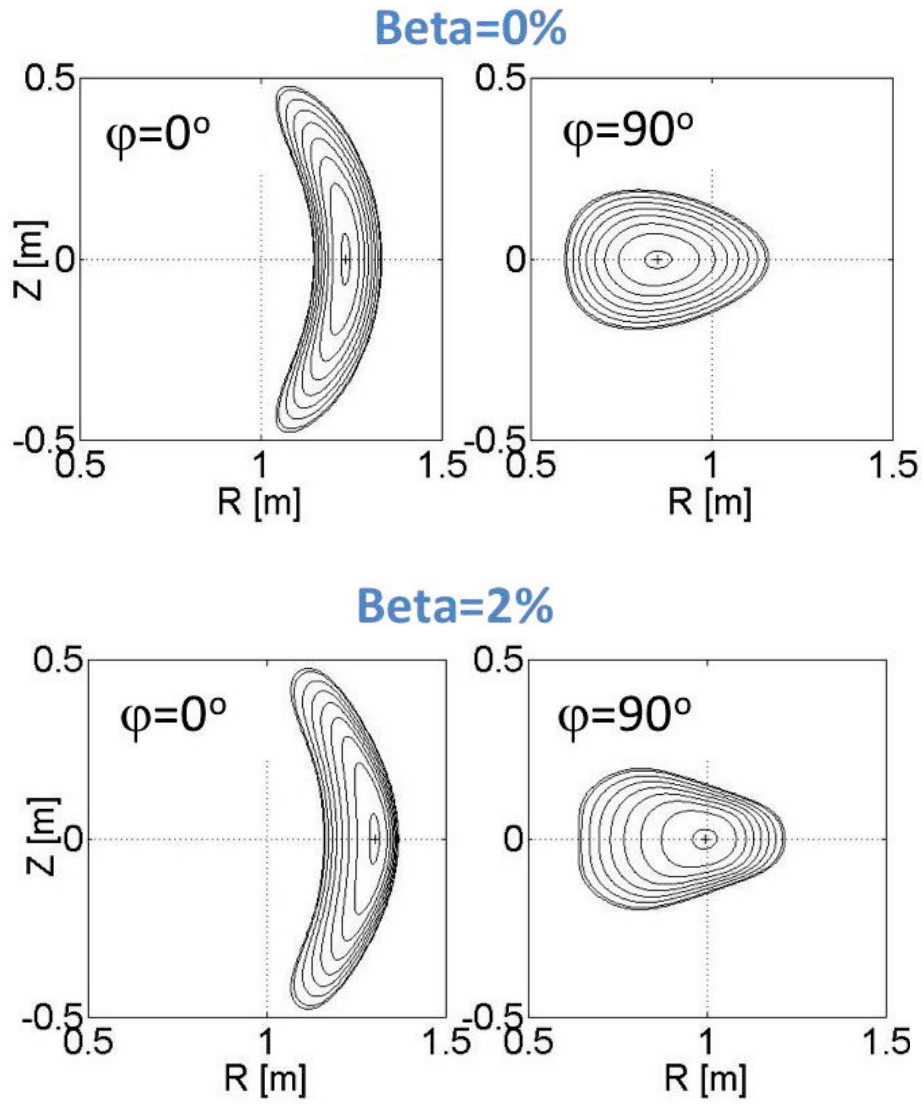


Fig. 3.3.1-1 Poloidal cross sections of the free-boundary equilibrium calculated by VMEC code with the plasma pressure free (top panel) and $\langle \beta \rangle = 2\%$ (bottom panel).

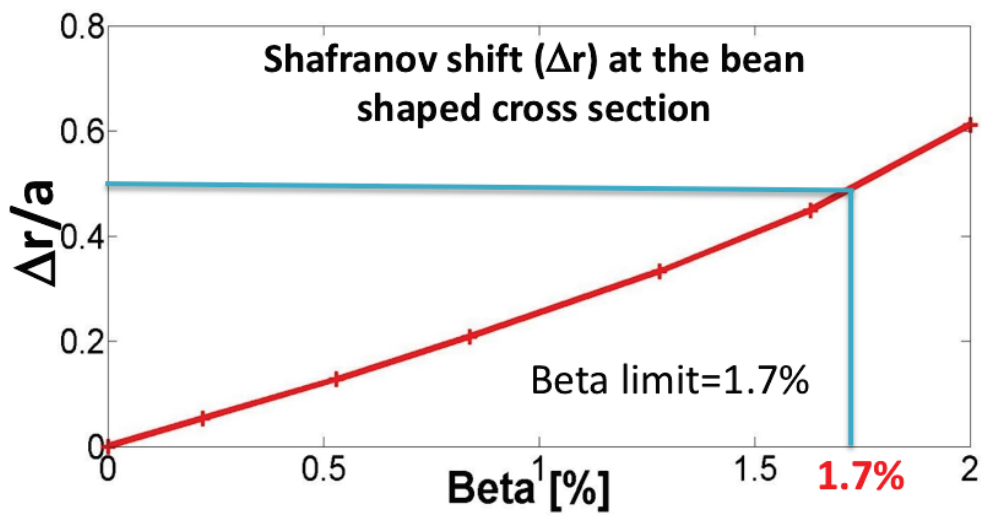


Fig. 3.3.1-2 Shafranov shift vs. $\langle \beta \rangle$ at the bean-shaped poloidal cross section.

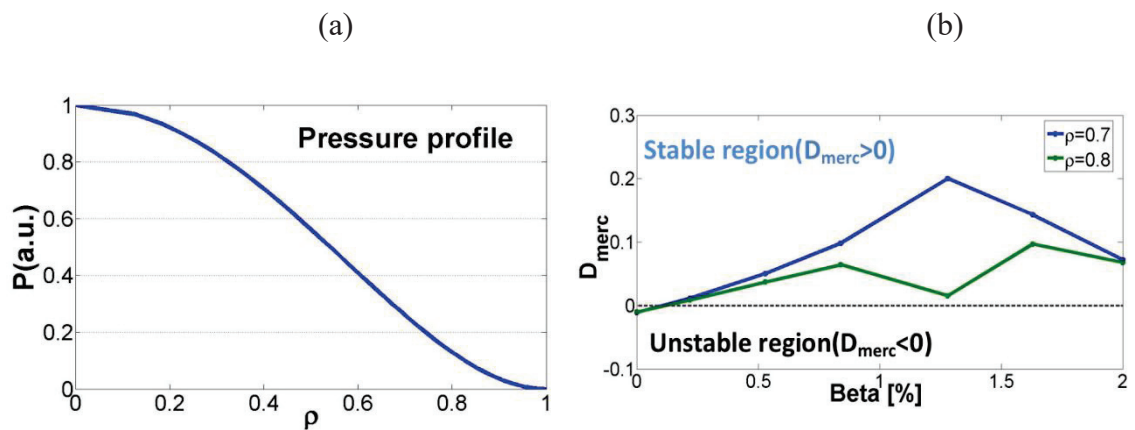


Fig. 3.3.1-3 (a) Assumed radial profile of plasma pressure (quadratic form) and (b) the variation of Mercier stability with $\langle \beta \rangle$ at two different radial position, *i.e.*, $\rho = 0.7$ and 0.8 .

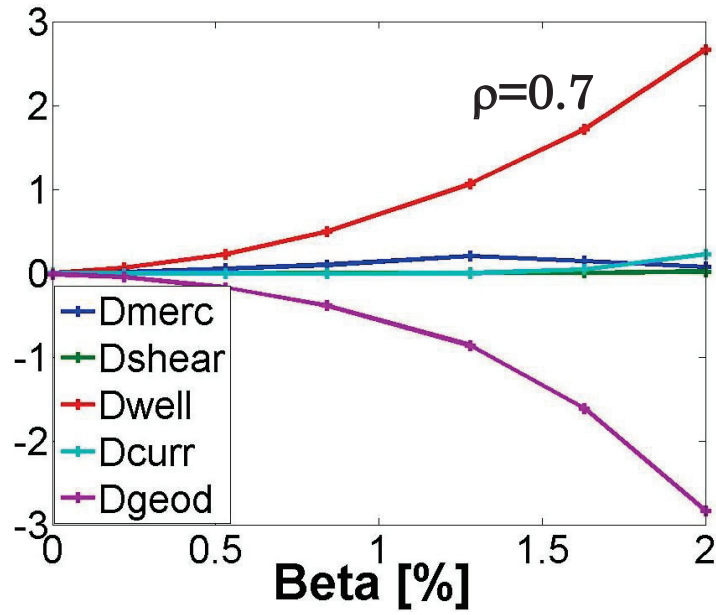


Fig. 3.3.1-4 Shear term, well term, current term and geodesic curvature term versus $\langle\beta\rangle$ at radial position $\rho = 0.7$, showing stabilization from the contribution of magnetic well.

The Fig. 3.3.1-3 (a) gives the input profile of plasma pressure $P(\rho) = P_0(1+\rho^2)^2$ for the VMEC calculation with the unfixed plasma boundary and Fig. 3.3.1-3 (b) displays the variation of Mercier stability with the volume-averaged beta at two different radial positions, *i.e.*, $\rho = 0.7$ and 0.8 . It shows that the interchange mode is stable up to $\langle\beta\rangle = 2\%$. The Mercier criterion can be expressed as $D_{merc} = D_{shear} + D_{well} + D_{curr} + D_{geod}$, where these terms correspond to the contributions coming from the shear, magnetic well, net currents, and geodesic curvature, respectively. In the Fig. 3.3.1-4, the variation of these four terms versus $\langle\beta\rangle$ at radial position $\rho = 0.7$ is shown, which depicts the stabilizing effect from the magnetic well ($D_{well} > 0$) is stronger than the destabilizing effect from the geodesic curvature term ($D_{geod} < 0$).

References

[3.3.1-1] C. Mercier, Nucl. Fusion **1** (1960) 47.

3.3.2 Ballooning mode

A principle aim of stellarator research is to understand the physical mechanisms that limit the plasma stored energy. The expectation is that pressure driven instabilities will be excited as the plasma energy increases relative to the magnetic energy. Since one of the advantages of stellarators is the avoidance of current driven instabilities, pressure driven instabilities may be critical in limiting stellarator operation. In theoretical studies of particular configurations, local criterion deduced from ideal MHD ballooning theory is often used to predict the plasma pressure limits of stellarators.

A feature related to second stability, which we call ‘self-stabilization’ for large pressure gradients after Ref. [3.3.2-1] has been observed in various stellarator experiments [3.3.2-2,3]. In these results, geometrical deformations associated with the Shafranov shift result in configurations which are stable with respect to Mercier modes as the plasma pressure increases. In this section, the COBRAVMEC code is utilized to calculate ideal ballooning stability for VMEC equilibria.

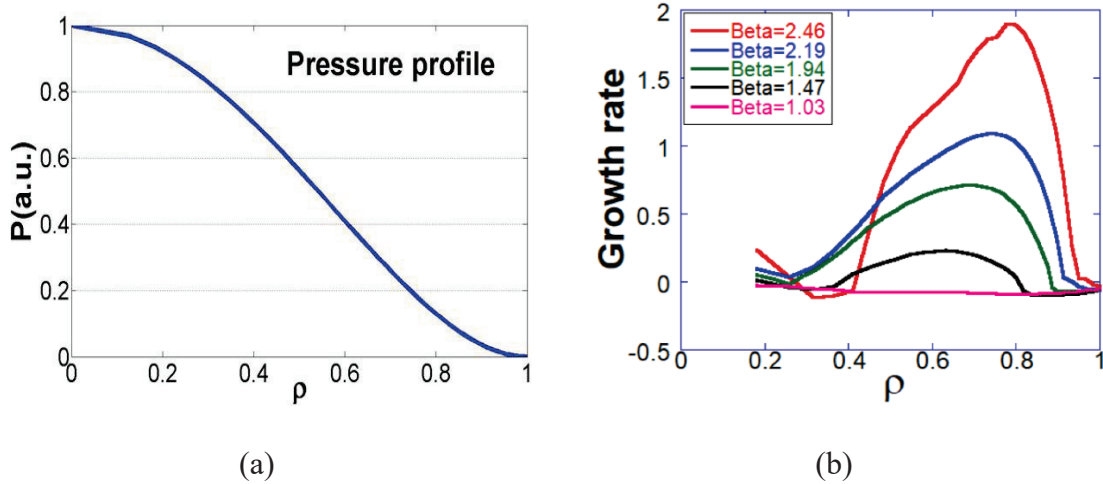


Fig. 3.3.2-1 (a) Assumed radial profile of plasma pressure (quadratic form), (b) Ballooning growth rates from COBRAVMEC as a function of the normalized flux for various volume-averaged beta, indicating the first stability boundary.

For the reference configuration, a quadratic pressure profile, $P(\rho) = P_0(1+\rho^2)^2$ was chosen. Ballooning growth rates as a function of the normalized flux label, ρ , are shown in Fig. 3.3.2-1 (a). As the plasma pressure increases, the plasma first becomes ballooning unstable at $\langle \beta \rangle$ of 1.03%, displayed in Fig. 3.3.2-1 (b). The region of instability grows until 3 %, where a region of second stability appears as shown in Fig. 3.3.2-2.

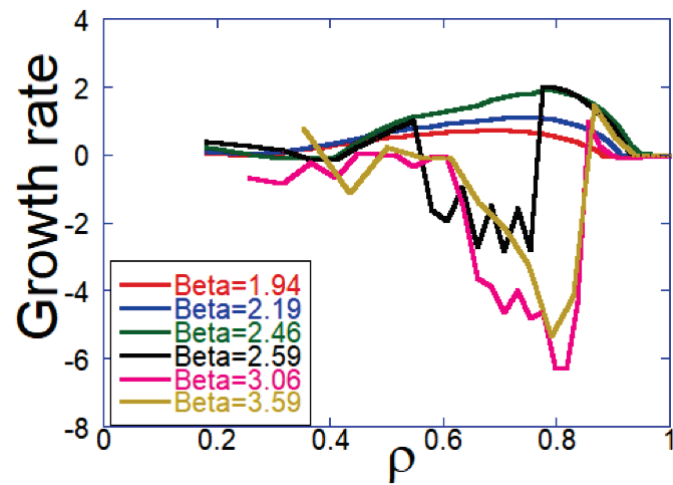


Fig. 3.3.2-2 Ballooning growth rates from COBRAVMEC as a function of the normalized flux for various volume-averaged beta, indicating the onset of second stability.

References

- [3.3.2-1] R. D. Hazeltine and J. D. Meiss, Plasma Confinement (Addison Wesley, Redwood City, 1992), pp. 309–312.
- [3.3.2-2] C. C. Hegna and S. R. Hudson, Phys. Plasmas **9** (2002) 2014.
- [3.3.2-3] R. Hudson and C. C. Hegna, Phys. Plasmas **10** (2003) 4716.

3.3.3 Kink mode

In a QA configuration, larger amount of neoclassical bootstrap current (BSC) flows and increases rotational transform due to its tokamak-like magnetic field structure. Therefore, the onset of an external kink mode should be carefully assessed in the ideal MHD stability analysis including plasma current. If a BSC profile is given, global low- n ideal MHD stability can be calculated with the TERPSICHORE code [3.3.3-1]. Since such a calculation for the CFQS configuration has not been performed yet, a typical example for the CHS-qa configuration [3.3.3-2] is described below.

A self-consistent BSC profile for a CHS-qa reference configuration has been calculated with SPBSC code [3.3.3-3]. We have solved finite beta equilibria including BSC assuming the fixed density and temperature profiles for three representative cases; (A) $n_e = 1.0 \times 10^{20} \text{ m}^{-3}$, $T_e = 1.04 \text{ keV}$, (B) $n_e = 0.2 \times 10^{20} \text{ m}^{-3}$, $T_e = 5.2 \text{ keV}$, (C) $n_e = 1.5 \times 10^{20} \text{ m}^{-3}$, $T_e = 1.04 \text{ keV}$ [3.3.3-4]. The resulting rotational transform is shown in Fig. 3.3.3-1 as a function of the normalized toroidal flux. Then the ideal global MHD stability has been analyzed with artificially changing the total parallel current while keeping its profile. The dependences of the most unstable eigenvalues on the total current are shown in Fig. 3.3.3-2 for the three representative cases. The onset of destabilization above 150 kA in the cases A and B clearly corresponds to the crossing of the edge rotational transform beyond 0.5 and 0.6. The associated amplitude of the dominant perturbation mode increases toward the edge, which clearly indicates the characteristics of an external kink instability. On the other hand, the global mode is kept stable up to 250 kA for the case C which has a different current profile. It indicates the possibility of stabilization of the external kink mode by controlling the current profile in a QA configuration.

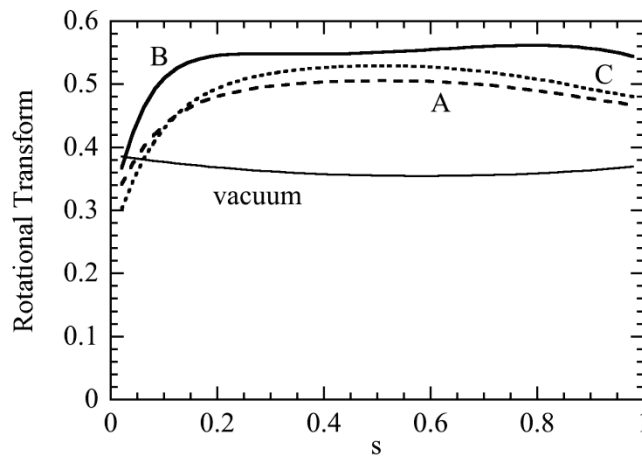


Fig. 3.3.3-1 Radial profiles of rotational transform for the three representative cases.

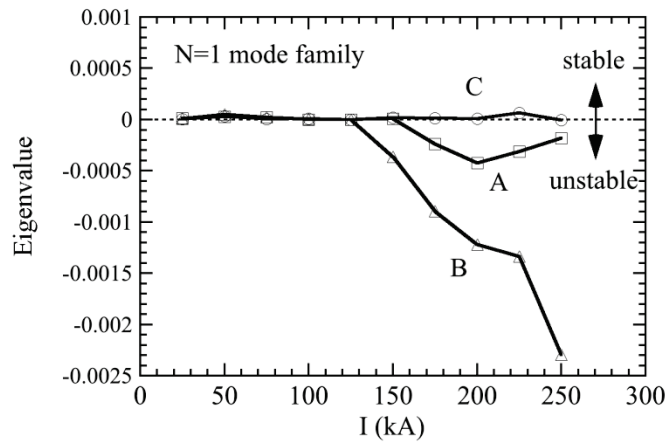


Fig. 3.3.3-2 Most unstable eigenvalues as functions of total current for the three representative cases.

References

- [3.3.3-1] D.V. Anderson *et al.*, *Int. J. Supercompt. Appl.* **4** (1990) 34.
- [3.3.3-2] C. Suzuki *et al.*, *J. Plasma Fusion Res. SERIES 6* (2004) 519.
- [3.3.3-3] K.Y. Watanabe *et al.*, *Nucl. Fusion* **35** (1995) 335.
- [3.3.3-4] M. Isobe *et al.*, *J. Plasma Fusion Res. SERIES 5* (2002) 360.

3.3.4 Tearing mode

The tearing mode stability, which is determined by Δ' , is analyzed for existing singular point in the plasma region with the same code described in Ref. 3.3.4-1 for the CHS-qa configuration [3.3.4-2]. Here, we consider a pressure less plasma in the cylindrical system with parabolic net toroidal current density J_z and check whether the tearing mode is stable or not at the rational surface of interest with increasing J_z . The tearing mode is stable for rational surfaces $n/m = 2/5, 3/7, 4/9$, and $1/2$ in the core domain (see Fig. 3.3.4-1) but the analyses indicate that it becomes unstable when singular point is in outer region ($r/a > 0.6$) for $n/m = 1/2$.

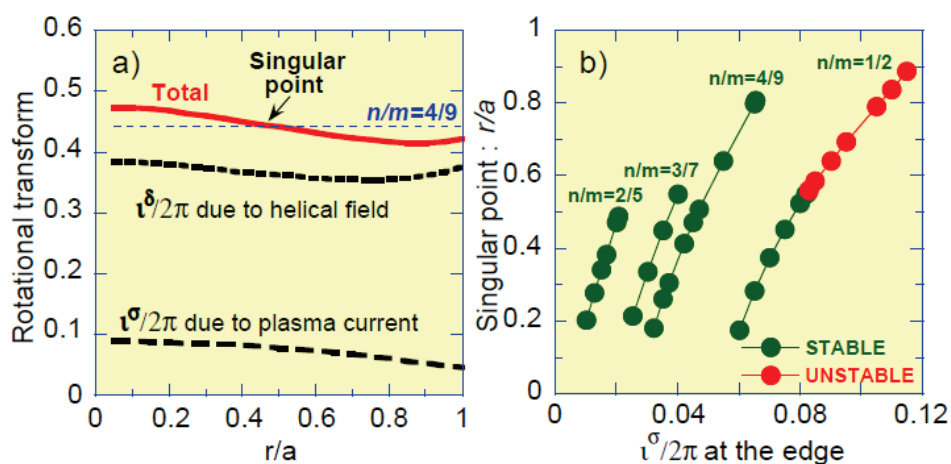


Fig. 3.3.4-1 (a) An example of rotational transform profile for tearing mode analysis for $n/m = 4/9$, and (b) Δ' analysis results are shown.

References

- [3.3.4-1] K. Matsuoka *et al.*, Nuclear Fusion **17** (1977) 1123.
- [3.3.4-2] M. Isobe *et al.*, 28th EPS Conference on Controlled Fusion and Plasma Physics, Funchal, Portugal, 18-22. June 2001, ECA Vol. **25A** (2001) 761.

3.3.5 Alfvén mode

To further study the MHD stability in CFQS configuration, we perform the MHD simulation by MEGA code without energetic particles. The module and equations of this code are same as that of reference [3.3.5-1,2]. The plasma pressure profile is calculated by HINT2 code in Fig. 3.3.5-1 (b) with the core averaged pressure value being 3.7×10^{-3} [3.3.5-3]. The random initial perturbation and small normalized dissipation coefficients ($= 1 \times 10^{-8}$) are adopted. From the Fig. 3.3.5-2, we can find that in this configuration the MHD mode is stable with the negative growth rate defined by $\gamma = d(\ln E_k)/dt$.

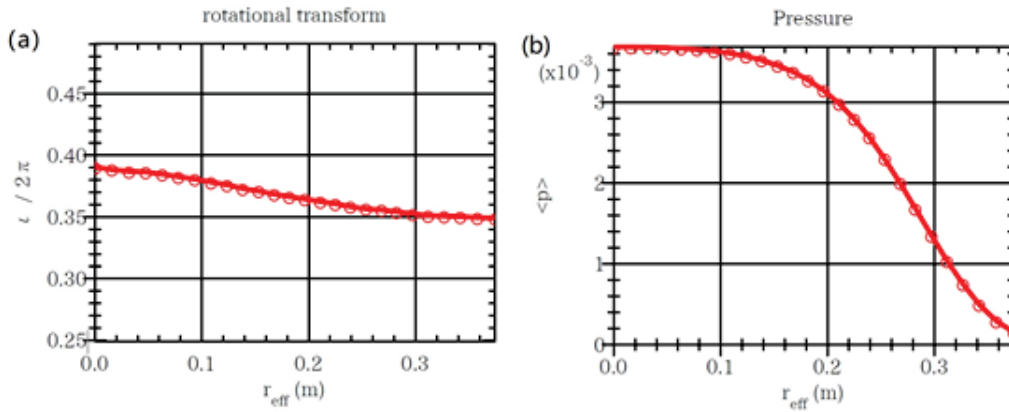


Fig. 3.3.5-1 Equilibrium profiles for (a) iota and (b) plasma pressure.

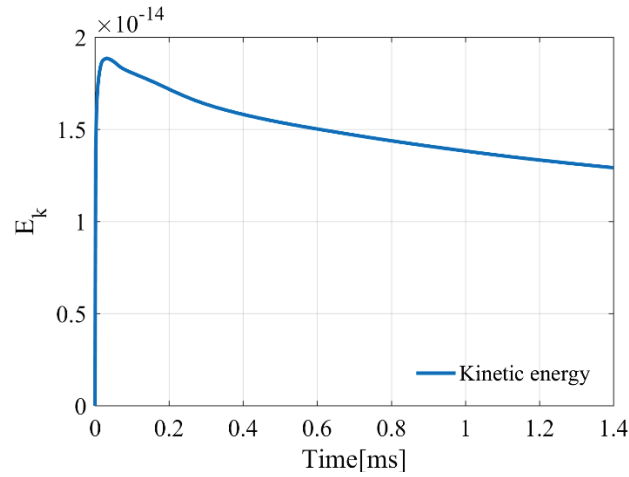


Fig. 3.3.5-2 Time evolution of kinetic energy.

MHD instability analysis is essential to evaluate the basic properties of QAS configuration [3.3.5-4~7]. Especially, the stability of external kink mode and ballooning mode has been paid close attention in the physical design and optimization of QAS. As an initial value MHD code, MEGA code is a powerful tool to study nonlinear MHD instabilities in 3-D tokamak and stellarator [3.3.5-2,8,9]. Therefore, the simulations of global MHD stability have been carried out for the optimized equilibrium

(Case 2) given in section 3.1.2 using MEGA code. In the simulations, the potential MHD stabilities are considered self-consistently adopting of an initial random perturbation. The plasma viscosity and diffusion coefficients are set to 10^{-5} to maintain numerical stability, which are assumed to be equal to each other. The plasma resistivity are given as 5×10^{-5} or other values. The growth rate and mode frequency are normalized by Alfvén frequency for Case 2 equilibrium. Alfvén time is $\sim 1.4 \times 10^{-7}$ second with plasma density being $1 \times 10^{19} \text{ m}^{-3}$. A Boozer coordinate system of the equilibrium was constructed for the spectral analysis of the simulation results [3.3.5-2].

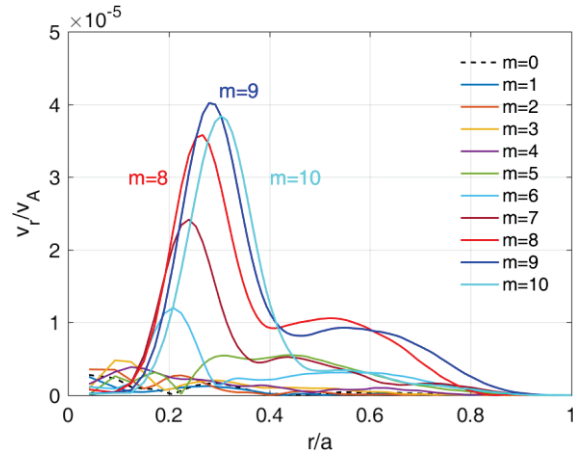


Fig. 3.3.5-3 The profiles of radial velocity for $m = 0 \sim 10$ and $n = -4$.

The radial eigenmode structures of the unstable mode with a dominated toroidal mode number $n = -4$ are shown in Fig. 3.3.5-3, where radial velocity v_r is normalized by Alfvén velocity v_A . The mode harmonics are dominated by $m = 8 \sim 10$. The peaking location is near the rational surface of $i/2\pi = 0.5$ and also close to the weak shear regions as shown in Fig. 3.1.2-6(c). The mode structure with a strong coupling is compared with conventional resistive ballooning modes as reported in such publications [3.3.5-9,10].

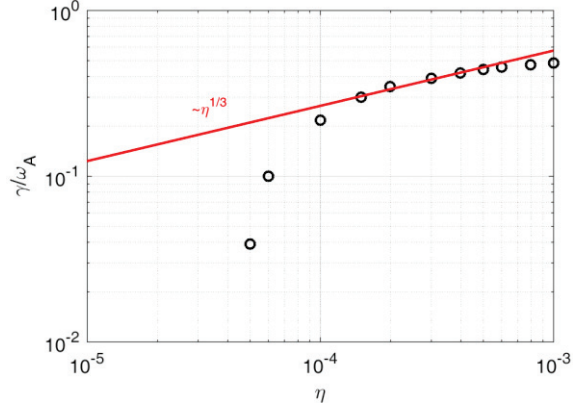


Fig. 3.3.5-4 The linear growth rate of the mode, $\gamma = d(\ln Ek)/dt$, as a function of plasma resistivity and the fitting by $\eta^{1/3}$ with $\langle\beta\rangle \sim 1.2\%$.

Considering the important role of resistivity in dynamics of the MHD mode, we show the resistivity dependence of mode growth rate in Fig. 3.3.5-4, where the linear growth rate $\gamma = d(\ln Ek)/dt$ is normalized by Alfvén frequency ω_A , η is plasma resistivity, and Ek is the kinetic energy. It is seen that, for the high- η regimes, the mode is unstable with a zero mode frequency. For the low- η regimes, the mode is stabilized in this equilibrium. In the resistivity-dominated region of $10^{-4} < \eta < 10^{-3}$, the $\eta^{1/3}$ scaling of growth rates obtained from the simulations is in agreement with the theoretical result of resistive ballooning modes in stellarator [3.3.5-11]. This suggests that the resistive MHD mode can be excited due to the finite plasma pressure in CFQS plasmas.

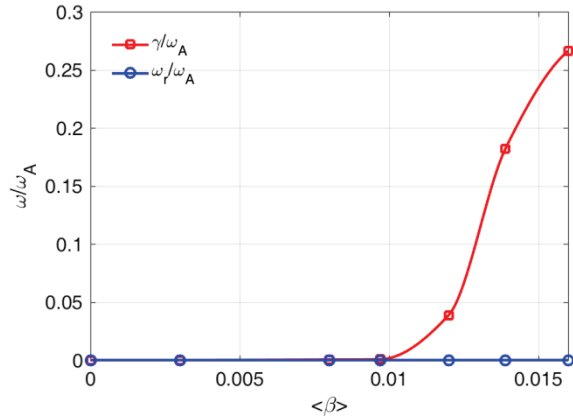


Fig. 3.3.5-5 Mode frequency and growth rate as a function of $\langle\beta\rangle$.

To clear the finite plasma pressure effects, we scan the growth rate and mode frequency as a function of $\langle\beta\rangle$ as shown in Fig. 3.3.5-5. A strong $\langle\beta\rangle$ dependence of the mode growth rate and zero mode frequency are found, corresponding to a pure MHD mode. On the other hand, the mode is stable when the $\langle\beta\rangle$ is smaller than $\sim 1\%$, which suggests a beta limit for the present design of CFQS. It has to be pointed out that the ideal external kink mode as one important MHD stability in QAS [3.3.5-5,12,13],

we have not discussed here, may be unstable when the boundary rotational transform exceeds 0.5 [3.3.5-5] and should be studied in future.

References

- [3.3.5-1] Y. Todo, N. Nakajima, M. Sato, and H. Miura, *Plasma Fusion Res.* **5** (2010) S2062.
- [3.3.5-2] Y. Todo, *et al.*, *Phys. Plasmas* **24** (2017) 081203.
- [3.3.5-3] Y. Suzuki, *et al.*, *Nucl. Fusion* **46** (2006) L19–L24.
- [3.3.5-4] S. Okamura *et al.*, *Nucl. Fusion* **41** (2001) 1865.
- [3.3.5-5] M. Isobe *et al.*, 28th EPS Conference on Controlled Fusion and Plasma Physics, Funchal, Portugal, 18-22 June 2001 ECA Vol.25A 761.
- [3.3.5-6] G. Y. Fu *et al.*, *Phys. Fluids* **B 4** (1992) 1401.
- [3.3.5-7] S. A. Henneberg *et al.*, *Nucl. Fusion* **59** (2019) 026014.
- [3.3.5-8] Y. Todo, H. L. Berk, B.N. Breizman, *Nucl. Fusion* **50** (2010) 084016.
- [3.3.5-9] Y. Todo *et al.*, *Plasma Fusion Res.* **5** (2010) S2062.
- [3.3.5-10] M. Sato *et al.*, *Nucl. Fusion* **57** (2017) 126023.
- [3.3.5-11] W. A. Cooper, *Physical Review A* **32** (1985) 3124
- [3.3.5-12] G. Y. Fu *et al.*, *Fusion Science and Technology* **51** (2007) 218.
- [3.3.5-13] C. Suzuki *et al.*, *J. Plasma Fusion Res. SERIES* **6** (2004) 519.

3.4 Micro instability and anomalous transport

3.4.1 Maximum- J

The turbulent fluctuation suppression in the CFQS has got emphasized considerably. The suppression of the turbulent transport due to the sheared flow induced fluctuation decorrelation has been widely investigated, theoretically, leading to the significant progress in the understanding of the improved confinement regime. The other possible mechanism for turbulent suppression has been proposed based on the stabilization of microinstabilities. Several kinds of microinstabilities appear when directions of the diamagnetic drift and ∇B drift (B is the magnetic field strength) are in the same direction for trapped particles [3.4.1-1, 2]. In an axisymmetric configuration, the relevant drift is in the toroidal direction (toroidal precession). The velocity of the toroidal precession can be expressed in terms of the second adiabatic invariance J [3.4.1-3]. Also, the stability condition for microinstabilities is derived [3.4.1-4] with a scalar plasma pressure P as

$$\nabla P \cdot \nabla J > 0,$$

which is frequently called the maximum- J condition; it reduces to $dJ/dr < 0$ for a usual pressure gradient with $dP/dr < 0$. This indicates that microinstabilities can be stabilized or suppressed if the toroidal precession of trapped particles is in a favorable ($dJ/dr < 0$) direction.

Orbits of blocked or helically trapped particles: These particles are located in the region of phase space near the locally trapped- passing boundary. These particles may be regarded as locally trapped for a few bounces but they are able to de-trap collisionlessly. A blocked particle's trajectory is not restricted to a single toroidal segment but extends to neighbouring sections. Such particles are also called transitioning [3.4.1-5]. An illustration of these three types of orbits and a comparison with particle orbits in an axisymmetric plasma is given in Fig. 3.4.1-1.

Without plasma the contour plot of J is shown as a function of the minor radius and the toroidal angle in the Fig. 3.4.1-2. The calculation of J is made by following the particle orbits starting from the outboard side of the torus with different toroidal angles. $\zeta_N = 0$ corresponds to the vertically elongated cross section and $\zeta_N = 0.5$ to the horizontally elongated cross section. When B_{ref} equals 0.95 T, there is no maximum- J region. Whereas B_{ref} equals 0.97 T, the maximum- J region comes up at the core area.

Radial profiles for density and temperature are assumed to be parabolic, $n_e \propto (1-\rho^2)$ and $T_e, T_i \propto (1-\rho^2)$. When $\langle \beta \rangle$ reaches 1 %, the neoclassical bootstrap current of 30 kA is expected. The change of the rotational transform profile with beta is shown in Fig. 3.4.1-3. As $\langle \beta \rangle$ increases the region of the reversal magnetic shear near the magnetic axis appears and increases. In these equilibria the contour plots of J are given with $B_{ref} = 0.91$ T in Fig. 3.4.1-4 and $B_{ref} = 0.93$ T in Fig. 3.4.1-5, respectively. It is found that as the beta increases the region of the maximum- J increases in the core region.

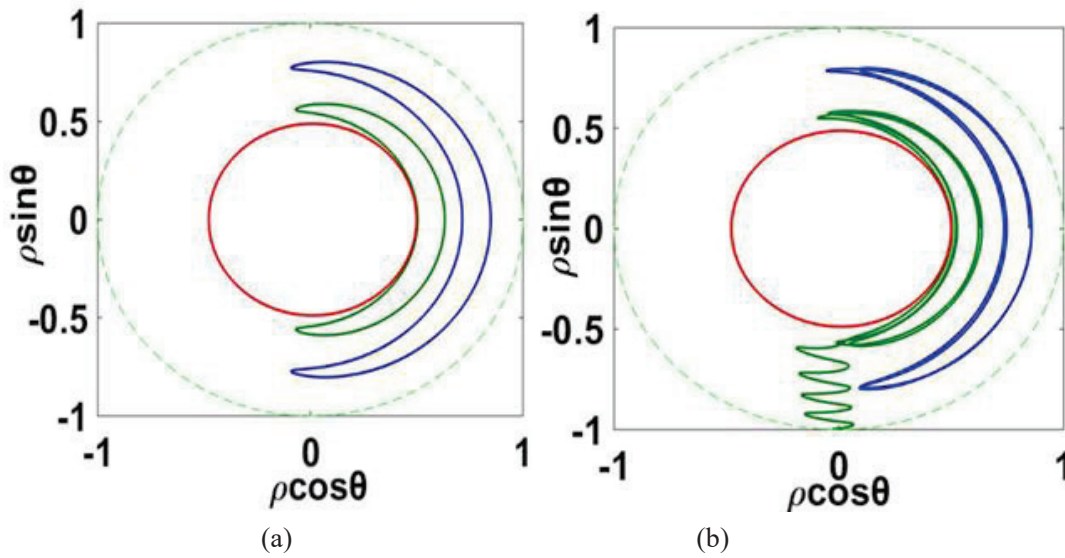


Fig. 3.4.1-1 Examples of the main orbit topologies in a perfect axisymmetric system and a CFQS. The dashed line represents the LCFS for each case. Guiding center (GC) orbits of (a) passing particle (red, $B_{ref} = 1.5$) and toroidally trapped particles (green, $B_{ref} = 0.94$ and blue, $B_{ref} = 0.98$) in axisymmetric equilibrium. GC orbits of (b) passing particle (red, $B_{ref} = 1.5$) and toroidally trapped particles (green, $B_{ref} = 0.94$ and blue, $B_{ref} = 0.98$) in the CFQS equilibrium. Particle (green) drifts radially due to ripple banana diffusion and is trapped in local ripple well, and is finally lost.

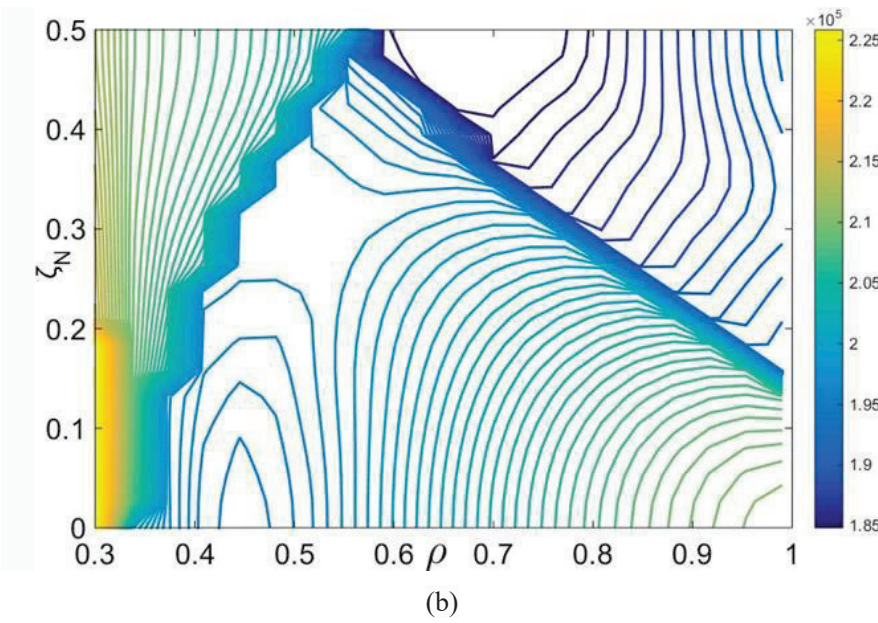
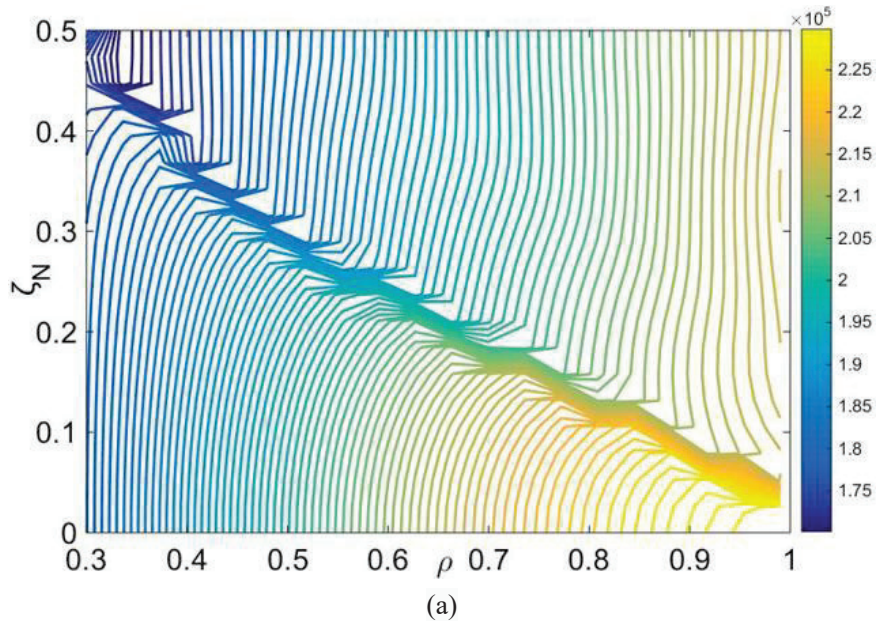


Fig. 3.4.1-2 Contour J on the (ρ, ζ_N) plane. (a) B_{ref} equal to 0.95 T, without maximum- J region (b) B_{ref} equal to 0.97 T, with maximum- J region.

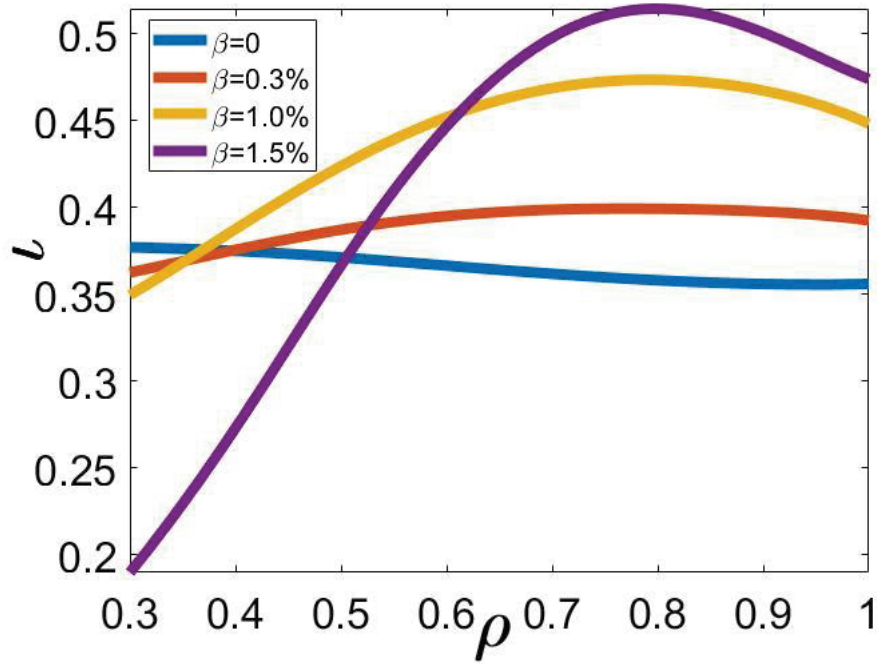


Fig. 3.4.1-3 Radial profile of the rotational transform considering the neoclassical bootstrap current.

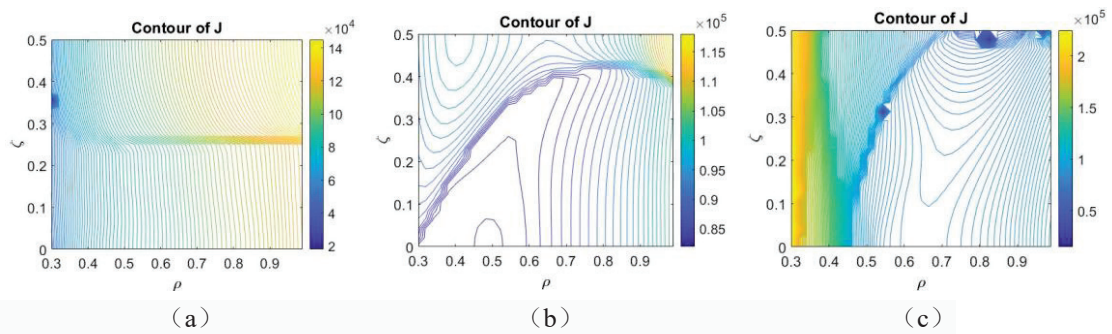


Fig. 3.4.1-4 Contour J on the (ρ, ζ) plane, B_{ref} equal to 0.91 T, $\langle \beta \rangle = 0.3\%$ for (a), $\langle \beta \rangle = 1.0\%$ for (b), and $\langle \beta \rangle = 1.5\%$ for (c).

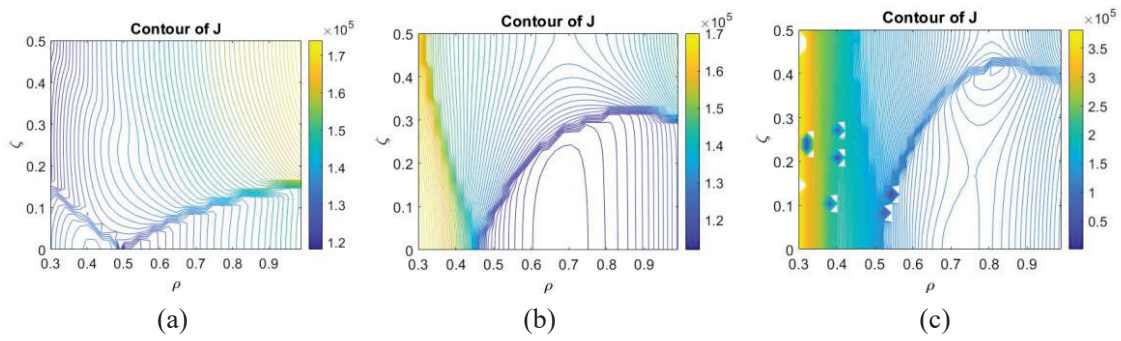


Fig. 3.4.1-5 Contour J on the (ρ, ζ) plane, B_{ref} equal to 0.93 T, $\langle \beta \rangle = 0.3\%$ for (a), $\langle \beta \rangle = 1.0\%$ for (b), and $\langle \beta \rangle = 1.5\%$ for (c).

References

- [3.4.1-1] H. P. Furth and M. N. Rosenbluth, 1969 Proc. Conf. 3rd Int. on Plasma Physics and Controlled Nuclear Fusion Research (Novosibirsk, 1968) vol. **1** (Vienna: IAEA) p 821.
- [3.4.1-2] B. B. Kadomtsev and O. P. Pogutse, 1970 Reviews of Plasma Physics vol. **5** (New York, London: Consultants Bureau) p 249.
- [3.4.1-3] B. B. Kadomtsev and O. P. Pogutse, Nucl. Fusion **11** (1971) 67.
- [3.4.1-4] R. J. Hastie *et al.*, Ann. of Phys. **41** (1967) 302.
- [3.4.1-5] C. D. Beidler *et al.*, Phys. Plasmas **8** (2001) 2731.

3.4.2 Ion temperature gradient mode

The linear ion temperature gradient (ITG)-driven instability is examined by means of the electromagnetic gyrokinetic Vlasov simulations with GKV [3.4.2-1], where a local flux-tube at the mid-minor radius of $\rho = 0.5$ in the vacuum equilibrium is considered. An axisymmetric limit with the same rotational transform, the magnetic shear, and the aspect ratio is compared to identify the impact of non-axisymmetric geometry on the microinstability properties, where the circular poloidal cross section is assumed for the simplicity. The linear growth rate spectra of the ITG mode at $R_{ax}/L_n = 0$ is shown in Fig. 3.4.2-1, where the electrons are assumed to be adiabatic here. It is found that the CFQS has more unstable ITG modes with higher growth rate $\gamma R_{ax}/\nu_{ti}$ in a wider range of the wavenumber space $k_{\theta}\rho_{ti}$, compared with that in the axisymmetric limit [3.4.2-2]. The difference is mainly associated with the geometric structures appearing in the squared perpendicular wavenumber $(k_{\perp}\rho_{ti})^2$, which provides the finite Larmor radius (FLR) stabilization of the ITG modes. It is known that the density gradient can also affect ITG modes. The linear growth rate spectra of ITG modes at $R_{ax}/L_n = 8$ is shown in Fig. 3.4.2-2. From Fig. 3.4.2-1 and Fig. 3.4.2-2, there is a critical temperature gradient for ITG modes. If R_{ax}/L_{ti} exceeds this critical gradient, the ITG mode is unstable. As R_{ax}/L_{ti} increases, ITG modes become more unstable, and as density gradient R_{ax}/L_n increases, the $k_{\theta}\rho_{ti}$ of the most unstable mode shifts to a higher $k_{\theta}\rho_{ti}$. Fig. 3.4.2-3 shows the relationship between the maximum growth rate of ITG modes and R_{ax}/L_n . From the figure it is found a moderate R_{ax}/L_n can destabilize ITG modes but for a large R_{ax}/L_n the growth of ITG mode is strongly suppressed. If R_{ax}/L_n is negative, *i.e.* a hollow density profile, even if R_{ax}/L_n is small, ITG modes are suppressed. The growth rate of ITG modes almost increases linearly with R_{ax}/L_{ti} for any R_{ax}/L_n . By fitting these lines, the threshold of the critical temperature gradient for ITG modes can be gotten. A negative R_{ax}/L_n enhances this threshold, and a positive R_{ax}/L_n can reduce the threshold firstly and then enhances the threshold as R_{ax}/L_n increases. From Fig. 3.4.2-4, the relationship between growth rate and R_{ax}/L_n is very clear. As R_{ax}/L_n increases, the growth rate firstly increases and then decreases. For a negative R_{ax}/L_n , ITG modes are always suppressed and their growth rate decreases as the absolute value of R_{ax}/L_n increases. From the previous results, a large R_{ax}/L_n or density peaking can strongly stabilize ITG modes [3.4.2-3].

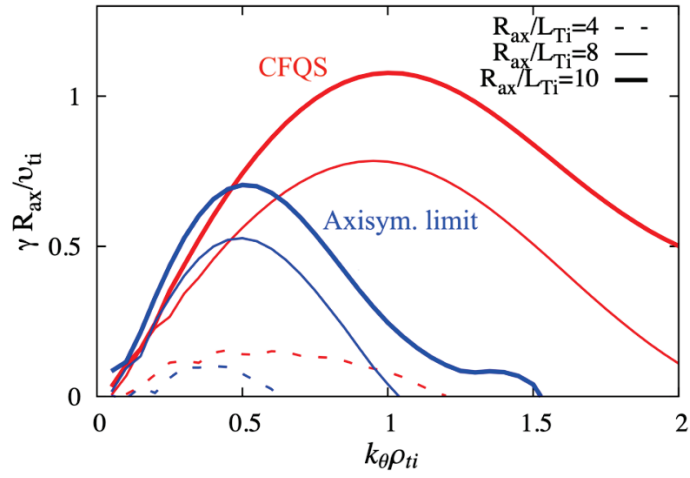


Fig. 3.4.2-1 Linear growth rate spectra for the ITG mode in CFQS and the axisymmetric limit (Axisym. limit) for several cases of the normalized ion temperature gradient parameters $R_{ax}/L_{Ti} = -R_{ax}d(\ln T_i)/dr$ at $R_{ax}/L_n = -R_{ax}d(\ln n)/dr = 0$.

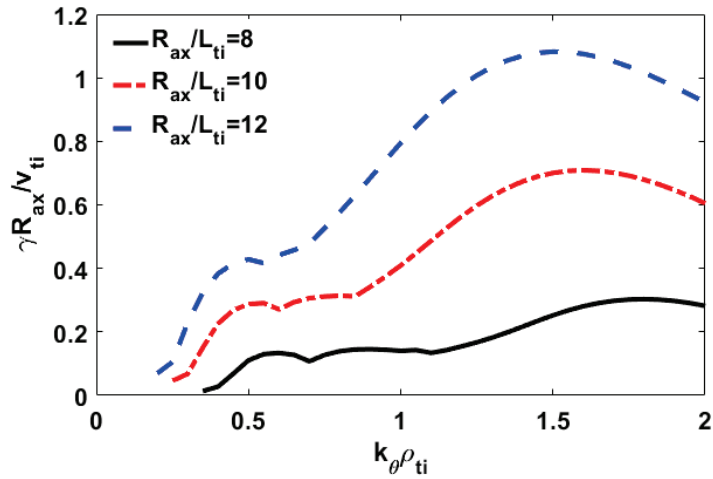


Fig. 3.4.2-2 Linear growth rate spectra for the ITG mode in CFQS for several cases of the normalized ion temperature gradient parameters R_{ax}/L_{Ti} at $R_{ax}/L_n = 8$.

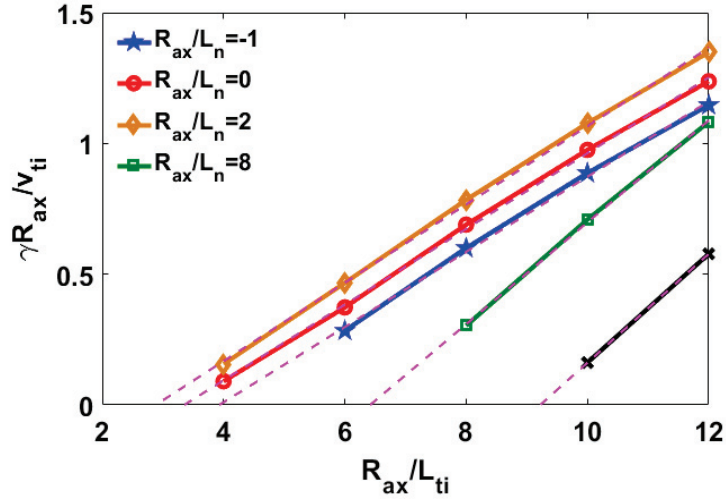


Fig. 3.4.2-3 The maximum growth rate of electrostatic ITG modes in CFQS vs. R_{ax}/L_{ti} for various R_{ax}/L_n . The dashed lines are the fitted lines of the corresponding lines of growth rate.

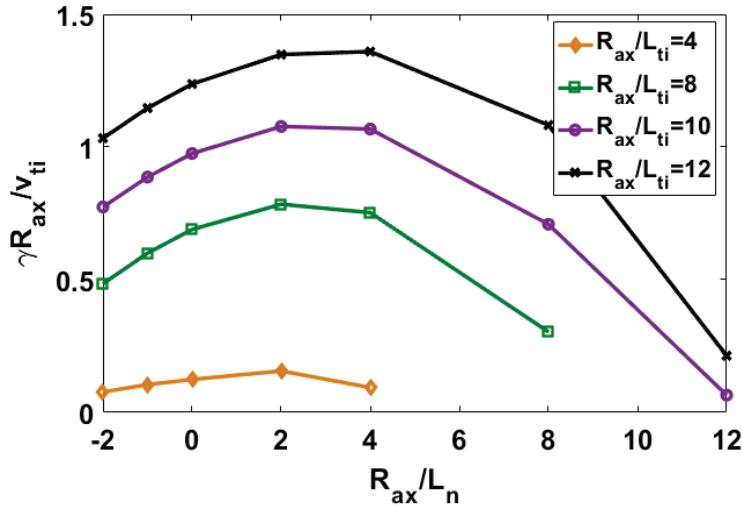


Fig. 3.4.2-4 The maximum growth rate of electrostatic ITG modes in CFQS vs. R_{ax}/L_n for various R_{ax}/L_{ti} .

To scan R_{ax}/L_n and R_{ax}/L_{ti} , the ITG growth rates vs. R_{ax}/L_n and R_{ax}/L_{ti} are shown in Fig. 3.4.2-5. The ITG mode with the largest growth rate is located at the region with the largest R_{ax}/L_{ti} and a moderate $R_{ax}/L_n \sim 4$. The growth of ITG mode depends on the competition between the driving of R_{ax}/L_{ti} and damping of R_{ax}/L_n . To compare with the NCSX results [3.4.2-4], the relationship between the growth rate of ITG modes and R_{ax}/L_{ti} and R_{ax}/L_n in CFQS and NCSX are very similar. It reveals that this relationship is rarely affected by the difference between the CFQS and NCSX magnetic configurations.

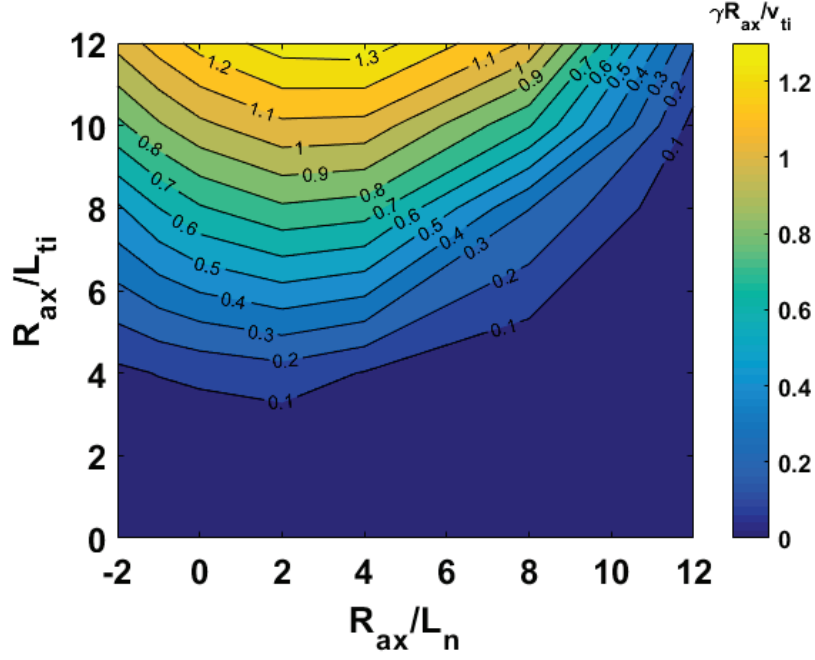


Fig. 3.4.2-5 The maximum growth rates of electrostatic ITG modes vs. R_{ax}/L_n and R_{ax}/L_{ti} .

The nonlinear ITG turbulence simulation has also been carried out. As shown in Fig. 3.4.2-6 (a), we observe that the saturated turbulent transport level Q_t/Q_{GB} in the CFQS is comparable or less than that in the axisymmetric limit. It is also found from Fig. 3.4.2-6 (b) that the CFQS indicates a relatively stronger zonal-flow generation W_{ZF}/W_{total} , in comparison to the axisymmetric limit. The magnetic fluctuations effects in the finite β cases, which can destabilize the kinetic ballooning modes (KBM) and microtearing modes (MTM), will be investigated in the future works.

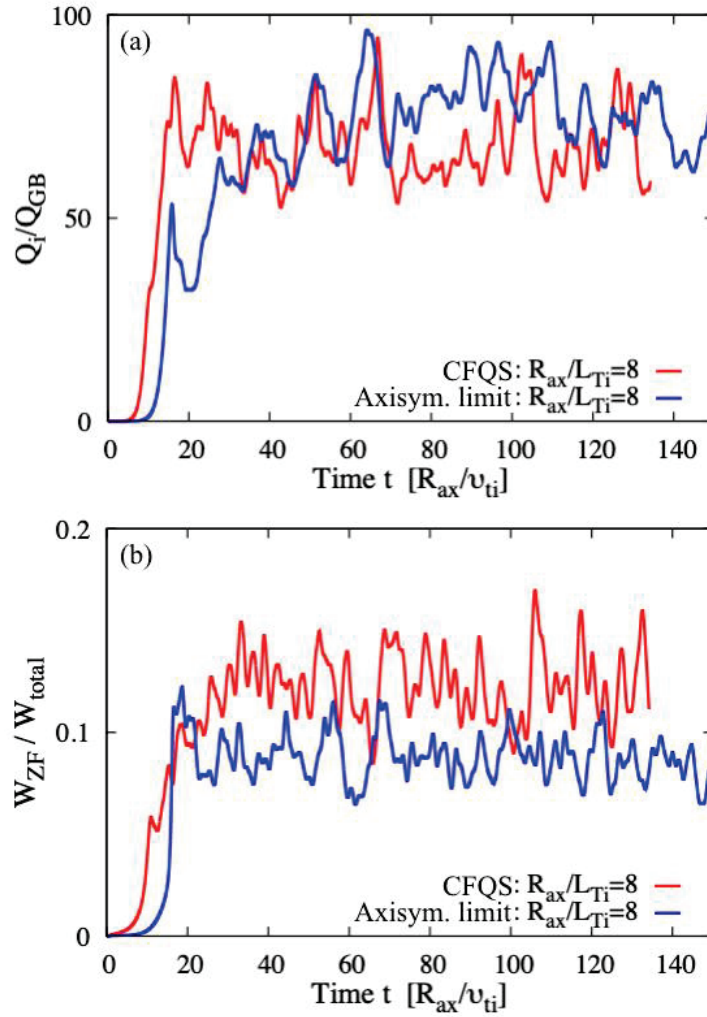


Fig. 3.4.2-6 Nonlinear GKV simulation results of (a) the ion turbulent heat flux Q_i / Q_{GB} and (b) the zonal flow energy normalized by the total energy W_{ZF} / W_{total} in the ITG-driven turbulence in the CFQS and the axisymmetric limit (Axisym. limit).

References

- [3.4.2-1] T. –H. Watanabe and H. Sugama, Nucl. Fusion **46** (2006) 24.
- [3.4.2-2] M. Nakata *et al.*, “Turbulent transport and zonal flow generation in quasi-axisymmetric stellarator”, The 27th International Toki Conference and the 13th Asia Pacific Plasma Theory Conference (2018) O-1.
- [3.4.2-3] Romanelli, M., Bourdelle, C., & Dorland, W. “Effects of high density peaking and high collisionality on the stabilization of the electrostatic turbulence in the Frascati Tokamak Upgrade”, Phys. Plasmas **11** (2004) 3845.
- [3.4.2-4] Baumgaertel, J. A. *et al.*, “Gyrokinetic studies of the effect of β on drift-wave stability in the National Compact Stellarator Experiment”, Phys. Plasmas **19** (2012) 122306.

3.5 Plasma rotation

In conventional helical devices, an impact of radial electric field on plasma confinement has extensively been investigated so far. It is one of the major issues also in a QA device because plasma rotation, which is closely related to radial electric field, can be driven more easily, and because anomalous transport can be possibly reduced by controlling plasma rotation/flow. Since the discovery of H-mode in tokamaks, the roles of shear flow on an improved confinement have been widely understood also in helical systems; *e.g.*, high ion/electron temperature modes [3.5-1,2]. Consequently, the reduction of anomalous transport by shear flow has become a general issue in toroidal plasmas.

Unlike tokamaks, radial electric field or plasma rotation in helical devices are determined by a solution of an ambipolar condition according to the neoclassical theory. Also, toroidal plasma rotation tends to be dissipated in conventional helical systems because of larger toroidal viscosity which originates from larger toroidal ripple of magnetic field strength [3.5-3]. According to theoretical studies on tokamaks, transport barriers are established by a positive feedback mechanism that reduces the transport coefficients through the increase in local pressure gradient. Radial electric field (or plasma flow), which is strongly correlated with the local pressure gradient, is a key parameter for the mechanism mentioned above. In order to promote such spontaneous growths of shear flow and pressure gradient, plasma flow should be free from any constraints.

In conventional helical devices such as CHS, plasma mainly rotates poloidally because of larger toroidal viscosity. In this situation, Pfirsch-Schlüter-type return flow should exist so as to satisfy incompressibility, which can possibly be dissipated by helical ripple [3.5-4]. Therefore, it is quite difficult to drive high speed plasma rotation in conventional helical systems due to large parallel viscosity both in toroidal and poloidal directions. Indeed, the radial electric field strengths observed in CHS and Heliotron-E are around 100 V/cm at most. Furthermore, the scale length of the radial electric field tends to be longer, which leads to weaker shear. Consequently, tokamak-like transition phenomena relevant to edge transport barrier have never been observed so far in helical systems.

In order to establish transport barriers, a magnetic configuration should be free from any constraints of plasma flow due to parallel viscosity. This expanded parameter range of plasma rotation is one of the reasons why we adopt the QA configuration, which is ideal for reducing toroidal viscosity as well as achieving low aspect ratio and incompressible flow at the same time.

In QA configuration, ripple trapped particles can be suppressed by reducing residual ripple. In such a situation, according to the neoclassical theory, confinement property is similar to that in an axisymmetric system. That is to say, values of radial electric field are never restricted by the ambipolar condition, which is a characteristic feature not found in the other optimized stellarators. As described below, the residual ripple in a QA configuration is drastically reduced in comparison with CHS.

In the earlier experiments in tokamaks and helical devices, it has been found that the plasma current, plasma rotation (or radial electric field) are well explained by the neoclassical theory, while

particle/heat transport is dominated by anomalous transport [3.5-5]. The plasma rotation interpreted by the neoclassical theory gives a good hint to study the anomalous transport. Also, it is important to study the neoclassical theory itself as it is still incomplete for non-axisymmetric systems. In addition, it would be also important to investigate whether the neoclassical theory can predict neoclassical bootstrap current, toroidal viscosity and radial electric field in a QA configuration with non-axisymmetric perturbation.

Neoclassical parallel viscosity is roughly proportional to the square of the magnetic field ripple strength defined by $\gamma^2 = \langle (\delta B / \delta s)^2 / B^2 \rangle$, where $\delta / \delta s$ is differential with respect to the flow direction and $\langle \rangle$ denotes averaging on a magnetic surface. This parameter should be quantitatively evaluated from the calculations including all of the Fourier components of the field strength B because higher order mode may largely contribute to the value of γ . Since the calculation of γ for the CFQS configuration has not been carried out yet, the results for the CHS-qa configuration [3.5-6] are shown hereafter. In principle, similar results are expected in the CFQS.

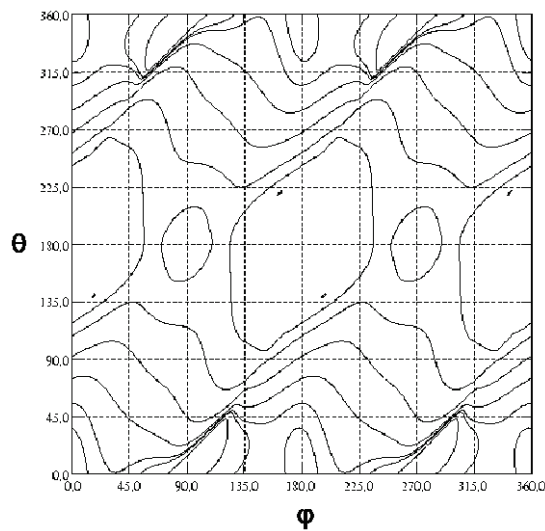


Fig. 3.5-1 Contour plot of B for the LCFS of CHS-qa (2w39) configuration.

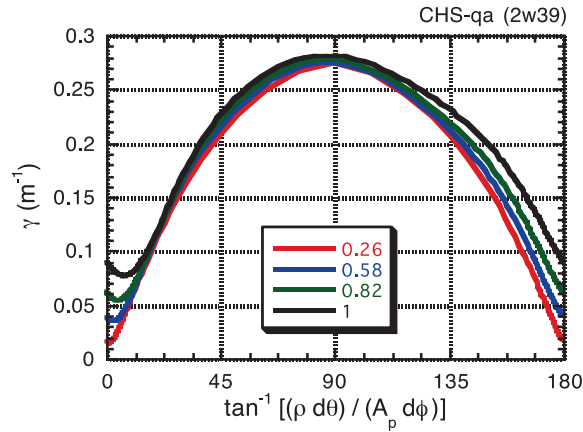


Fig. 3.5-2 Angle dependence of γ for CHS-qa (2w39) configuration.

Fig. 3.5-1 shows a contour plot of B on the LCFS of a reference configuration of CHS-qa (2w39). The grid data for B in cylindrical coordinates (R, Z, Φ) are constructed from the result of VMEC code calculation. Toroidal (ϕ) and poloidal (θ) angles are expressed in real coordinates, and $\theta = \tan^{-1}[(R - R_{ax}) / (Z - Z_{ax})]$, where R_{ax} and Z_{ax} are R and Z values at the magnetic axis in an equal ϕ plane, respectively. This means that the effect of the excursion of the magnetic axis is ignored in the calculation. We assumed a flow direction expressed by a straight line in this ϕ - θ plane. When averaging, we fixed the angle of $\delta/\delta s$ direction with respect to the toroidal direction ($=\tan^{-1}(r \theta / R \phi)$).

Fig. 3.5-2 shows the calculated dependence of γ on the flow direction at the four different flux surfaces (normalized minor radii of 0.26, 0.58, 0.82, and 1.0). As shown, the values of γ have peaks around 90 degrees in the QA configuration, which indicates larger parallel viscosity in the poloidal direction. In the toroidal direction, γ is less than 0.1 even in the LCFS, which implies that perpendicular/anomalous viscosity plays an important role for determining toroidal rotation speed in a similar way to tokamaks. Though the effect of coil ripples is not included in the present calculation, the angle minimizing γ is not zero but $1.1 \sim 6.8$ degrees unlike tokamaks, which is considered to be the effect of residual non-axisymmetric components.

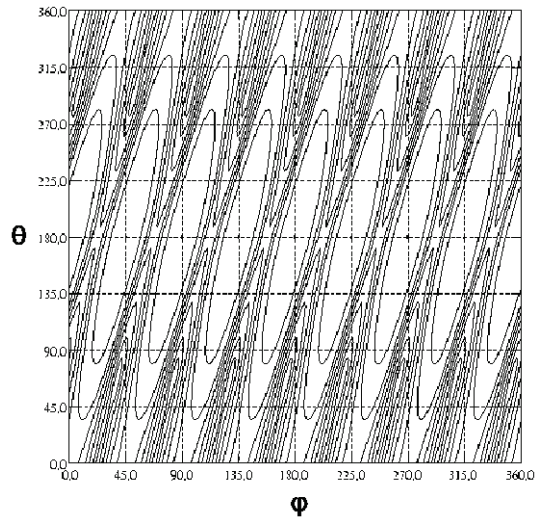


Fig. 3.5-3 Contour plot of B for the LCFS of CHS ($R_{ax} = 92.1$ cm) configuration.

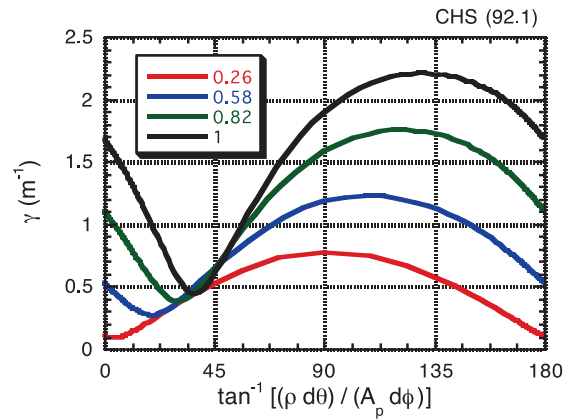


Fig. 3.5-4 Angle dependence of γ for CHS ($R_{ax} = 92.1$ cm) configuration.

For the comparison with a conventional helical device, the calculation of γ has been performed for a representative configuration of CHS. The contour of B on the LCFS and the results of the γ calculation are shown in Fig. 3.5-3 and Fig. 3.5-4, respectively, in a similar way to the CHS-qa. The angle minimizing γ is around 40 degrees, which indicates that the flow tends to be driven along the helical structure ($m = 2, n = 1$) of the CHS configuration. Nevertheless, this minimum value of γ in CHS is still larger than the maximum value of γ along the poloidal direction in CHS-qa. Therefore, high-speed toroidal rotation cannot be driven in CHS because of strong toroidal viscosity, as demonstrated in the previous CHS experiment.

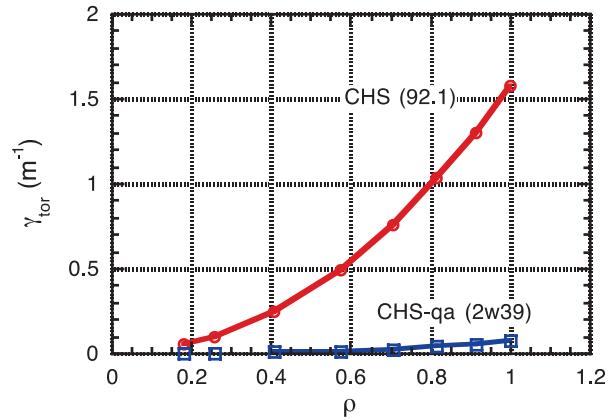


Fig. 3.5-5 Dependence of toroidal γ on minor radius for CHS-qa and CHS.

In reality, the direction of plasma flow cannot be expressed simply by a straight line in real coordinates. Experimental results in CHS suggests that the spontaneous rotation, which is driven without external momentum input (with NBI), tends to be driven along the direction minimizing parallel viscosity. In a QA configuration, this direction is the toroidal direction in the Boozer coordinates. Therefore, we have also calculated γ with the angle of $\delta/\delta s$ direction fixed in the Boozer coordinates. Fig. 3.5-5 shows γ in the toroidal direction as a function of normalized minor radius for CHS and CHS-qa. As shown, γ_{tor} in CHS-qa is much smaller than that in CHS, which implies tokamak-like nature of a QA configuration with respect to plasma rotation.

References

- [3.5-1] K. Ida *et al.*, Phys. Rev. Lett. **76** (1996) 1268.
- [3.5-2] A. Fujisawa *et al.*, Phys. Rev. Lett. **79** (1997) 1054.
- [3.5-3] K. Ida *et al.*, Phys. Rev. Lett. **67** (1991) 58.
- [3.5-4] S. Nishimura *et al.*, Phys. Plasmas **7** (2000) 437.
- [3.5-5] O. Okamoto, NIFS-PROC-**25** (1995).
- [3.5-6] C. Suzuki *et al.*, Plasma Phys. Control. Fusion **44** (2002) A225.

3.6 Energetic particle and NBI deposition analysis

Energetic alpha particles produced by the d-t reaction will play an essential role in sustaining a self-ignition condition in burning plasma in the future. When alpha particles are substantially lost from the plasma, the self-ignited state is easily terminated. Moreover, the localized heat load on the first wall due to the impact of the escaping alphas may seriously damage the device. Because of the reason above, a great deal of attention has to be paid to physics issues related to energetic ions such as the magnetic field ripple transport, anomalous transport and/or loss caused by MHD instabilities. Note that although neoclassical transport in CFQS is outstandingly reduced, it does not always guarantee good energetic-ion confinement. Since QAS is quite similar to tokamak in magnetic field structure, EP orbits in QAS is also quite similar to those in tokamak [3.6-1~5].

To obtain high plasma parameter and to study the beam ion confinement in QA configuration, the installation of neutral beam (NB) injector is planned with CFQS. Feasibility study of NB injection on CFQS is performed using the beam deposition calculation code and the guiding center orbit following code [3.6-6]. Fig. 3.6-1 shows the schematic drawing of the CFQS with NB injector. According to the CAD modeling including the coil case, the VV, and the coil supporting structure, the possible injection angle of NBI is from 44 degrees to 52 degrees [3.6-7]. Here, we considered to use an NB injector operated in the CHS [3.6-8] with injection energy and power of 30 keV and 0.9 MW.

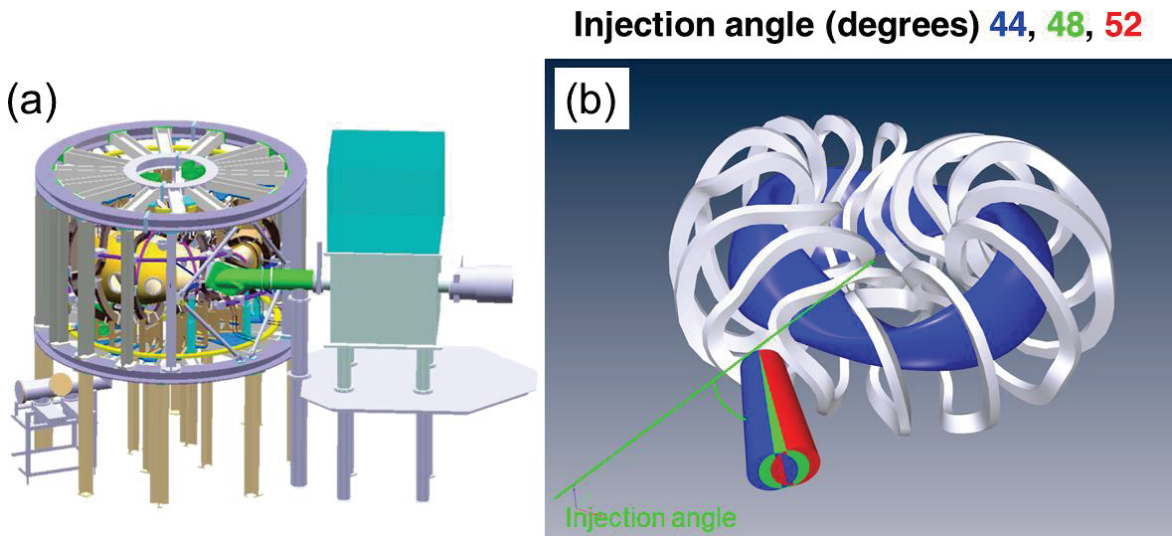


Fig. 3.6-1 (a) Schematic drawing of CFQS with NB injector, (b) Possible NB injection lines.

Deposition fraction on NB injection angle was surveyed by means of HFREYA code which is deposition calculation code using the Monte Carlo methods [3.6-9]. Here, the plasma parameter is assumed to be parabolic profile, *i.e.*, $\sim (1-(r/a)^2)^2$. The central electron temperature T_{e0} is given using central electron density n_{e0} with $T_{e0} = 2.0/n_{e0}$ (10^{19} m^{-3}) in order to maintain the plasma stored energy. We changed NB injection angle from 44 to 52 degrees with 2 degrees steps. Fig. 3.6-2 shows the

deposition fraction of NB injection as a function of line-averaged electron density (n_{e_avg}). The deposition fraction rapidly increase with n_{e_avg} at n_{e_avg} of less than $4 \times 10^{19} \text{ m}^{-3}$. The maximum deposition fraction is obtained with NB injection angle of from 44 to 48 degrees.

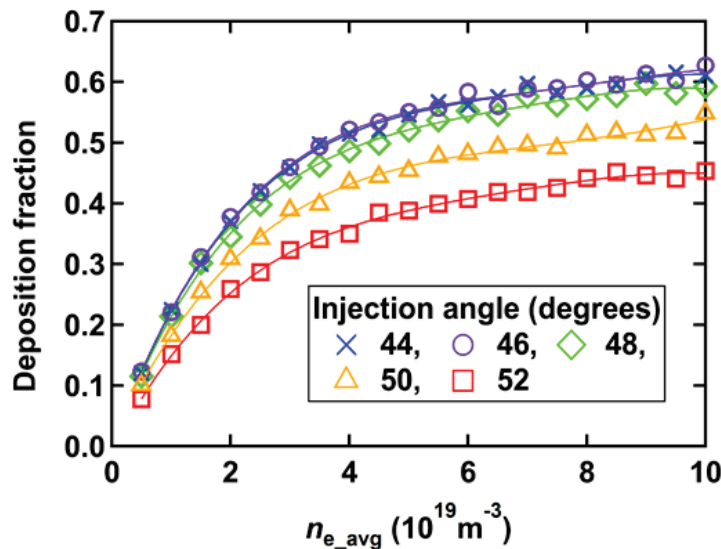


Fig. 3.6-2 Dependence of deposition fraction of NB on line-averaged electron density.

The beam ion orbit calculation is performed by the guiding center orbit following code in the Boozer coordinates DELTA5D [3.6-5] in order to evaluate the beam ion confinement. Fig. 3.6-3 shows the Poincaré plots of typical collisionless orbit of co-going transit ion (H^+) at B_t of 1 T in toroidal angles of 90 and 180 degrees. Here, beam ion energy and pitch angle are 30 keV and 22 degrees, respectively. The deviation of orbit from the magnetic flux surfaces is relatively large due to the relatively low magnetic field strength and the relatively low rotational transform. Beam ion confinement is evaluated using DELTA5D code including beam-plasma collision. Here, we randomly choose 1000 beam ions injected by co-inject NB and followed in thermalization time of beam ions (~ 50 ms). Time evolution of loss energy of beam ions as a function of time is plotted in Fig. 3.6-4 (a). Here, calculation is performed with n_{e_avg} of $2 \times 10^{19} \text{ m}^{-3}$. Loss energy gradually increases with time until t of 25 ms, and then is almost saturated. We obtained relatively low loss energy at the injection angle of 48 to 52 degrees. Fig. 3.6-4 (b) shows the loss energy at t of 50 ms as a function of n_{e_avg} . The loss energy slightly increase with the n_{e_avg} . The loss energy at 50 ms is relatively lower at the injection angle of 48 to 52 degrees when $n_{e_avg} < 4 \times 10^{19} \text{ m}^{-3}$. This is because the fraction of beam ions deposited in smaller R region, where the confinement of co-passing beam ion seems to be worse due to the large outward deviation of orbit becomes larger with the decrease of the injection angle. It seems that the injection angle of 48 degrees is more favorable regarding deposition and beam ion confinement.

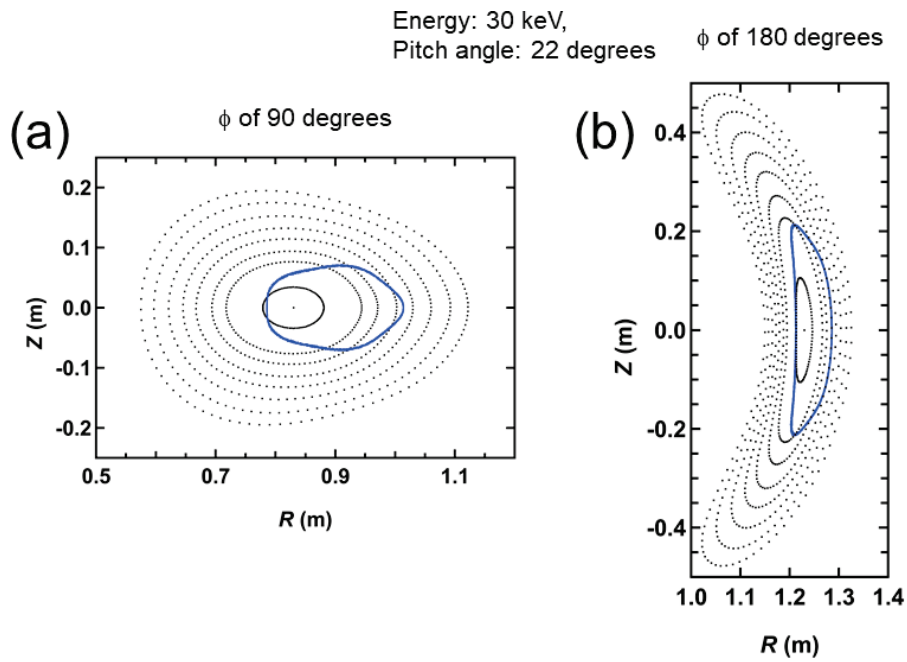


Fig. 3.6-3 Poincaré plots of typical co-going transit beam ion orbit at two different toroidal angles, (a) 90 degrees, and (b) 180 degrees.

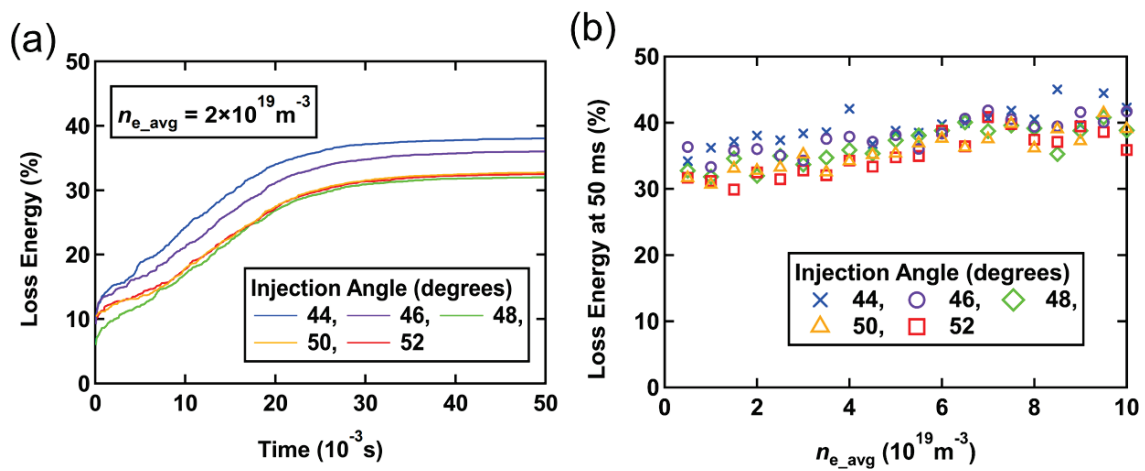


Fig. 3.6-4 (a) Time evolution of loss energy of beam ions. (b) Loss energy at 50 ms as a function of line-averaged electron density.

References

- [3.6-1] M.H. Redi *et al.*, Phys. Plasmas **6** (1999) 3509.
- [3.6-2] M. Isobe *et al.*, J. Plasma Fusion Res. SERIES **6** (2004) 622.
- [3.6-3] H.W. Kugel *et al.*, Fusion Sci. Technol. **51** (2007) 203.
- [3.6-4] S. Murakami *et al.*, Proceedings of 1997 International Symposium on Plasma Dynamics in Complex Electromagnetic Fields ~ for Comprehension of Physics in Advanced Toroidal

Plasma Confinement ~, 8-11 December, 1997. **IAE-RR-98 054**, March 1998, pp. 137-140.

[3.6-5] D. A. Spong *et al.*, Phys. Plasmas **18** (2011) 056109.

[3.6-6] K. Ogawa *et al.*, Plasma and Fusion Research **14** (2019) 3402067.

[3.6-7] S. Kinoshita *et al.*, Plasma and Fusion Research **14** (2019) 3405097.

[3.6-8] K. Matsuoka *et al.*, Plasma Phys. Control. Fusion **42** (2000) 1145.

[3.6-9] S. Murakami *et al.*, Trans. Fusion Technol. **27** (1995) 256.

3.7 ECRH deposition analysis

Electron cyclotron resonance heating (ECRH) power deposition and electron cyclotron current drive (ECCD) are analyzed using the ray-tracing code, TRAVIS [3.7-1]. For the analysis, a CFQS equilibrium file “wout.2b40R1mB01” was applied for the TRAVIS code. The frequency and the injected power of EC-wave in X-mode polarization are 54.5 GHz and 1 MW, respectively. As a test case, peaked electron temperature profile with T_{e0} of 3.5 keV and flat electron density profile with n_{e0} of $1.0 \times 10^{19} \text{ m}^{-3}$ were assumed. The T_e and n_e profiles are plotted in Fig. 3.7-1.

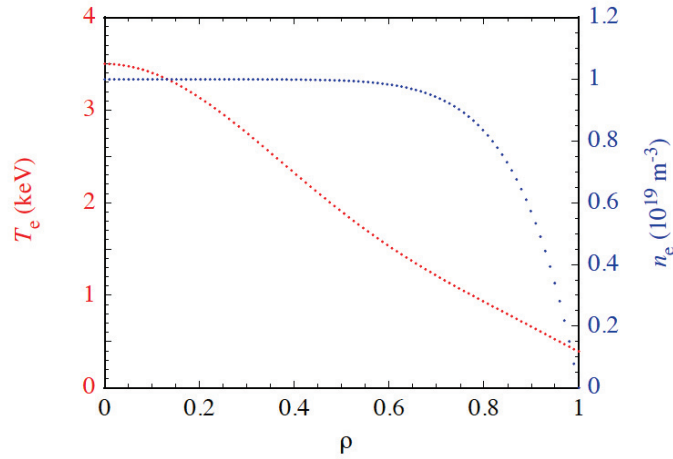


Fig. 3.7-1 Assumed electron temperature and density profiles for ECRH power deposition and ECCD analysis using the TRAVIS code.

Considering the dimension of the ECRH power injection port (CFQS O-8.5 port, ICF406), the size of 2-D steerable final plane mirror is determined as H134×W96 mm, the position of the center of the plane mirror is (R : major radial position = 1.55 m, T : toroidal position = 0 m, and Z : vertical position = -0.104 m) and the focused beam waist radius ($1/e$ radius of electric field amplitude) is 25 mm at the position ($R = 1.185$ m, $T = 0$ m, and $Z = 0$ m), in this analysis. Positive directions of T and Z are right side looking from outside of the torus and upper side, respectively. Using the 2-D steerable mirror, EC-wave power deposition control and ECCD can be realized.

Fig. 3.7-2 shows the controllability of power deposition position by scanning beam aiming position (R_f , T_f , Z_f). Here, R_f , T_f , and the magnetic field on axis at the bean-shape poroidal cross section, B , were fixed at 1.2 m, 0 m, and 0.975 T, respectively. Z_f was varied vertically as 0, -0.1, -0.2, and -0.25 m. The vertical axis of Fig. 3.7-2 is absorbed power density per volume, dP/dV (MW m^{-3}). By the variation of Z_f , the peak position of power deposition shifts toward outside as $\rho = 0$, ~ 0.2 , ~ 0.4 , and ~ 0.6 , respectively. Though the heating efficiency degrades with the outward shift of the power deposition position, high heating efficiency over 80 % can be expected in the wide range.

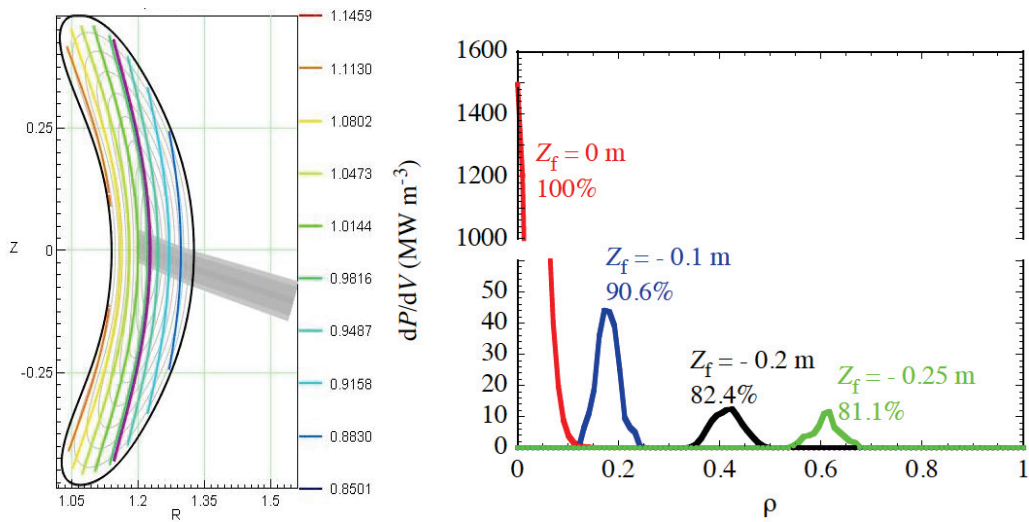


Fig. 3.7-2 Left: an example of a poloidal cross section plotted with an EC-wave beam path (here, $Z_f = 0$ m) and right: power deposition profiles with Z_f settings at 0, -0.1, -0.2, and -0.25 m.

Scanning EC-wave beam direction toroidally, dependence of EC-driven current I_{ECCD} against the parameter T_f is obtained as seen in Fig. 3.7-3. Here, R_f was fixed at 1.2 m. Z_f and B were slightly adjusted at each T_f , to keep on-axis heating and center-peaked current profile.

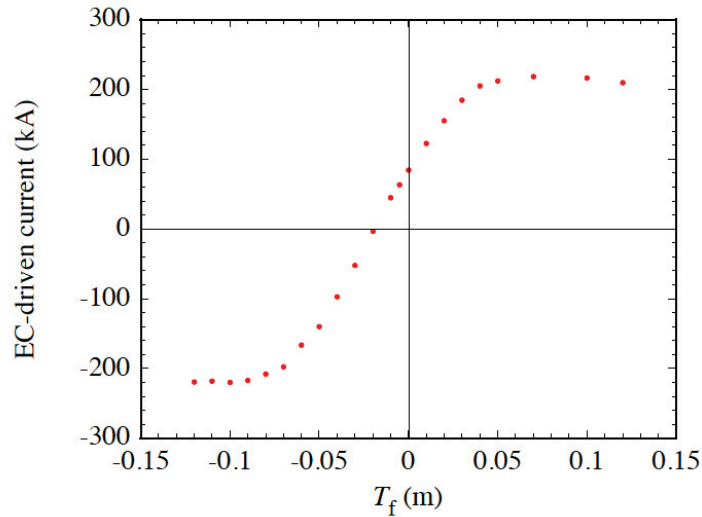


Fig. 3.7-3 EC-driven current as a function of T_f . Positive direction of current is clockwise looking from top side of the torus.

The magnitude of I_{ECCD} increases up to ~ 200 kA and then saturates with the magnitude of T_f . The asymmetry of I_{ECCD} about $T_f = 0$ m comes from the downward shift of the start position of the EC-wave beams (that is, center of the final plane mirror).

Thus, the 2-D steerable EC-wave beam injection system is expected to be available for a wealth of physical experiments in CFQS which require power deposition, current, and current profile controls.

References

[3.7-1] N.B. Marushchenko *et al.*, Phys. Plasmas **18**, 032501 (2011).

3.8 Modular coil design and optimization by NESCOIL

Vacuum equilibrium properties of a toroidal configuration are determined by the shape of the LCFS (plasma boundary). Generally, considering the nested magnetic flux surfaces, the VMEC code enables to solve the three dimensional MHD equilibrium accurately and efficiently. In order to achieve the target magnetic configuration, a modular coil system is necessary to be designed to reproduce the plasma boundary. Due to the Neumann boundary condition, the accuracy of the magnetic configuration induced by the coil system is dependent on the normal component of the magnetic field on the plasma boundary, which is expressed as where B is the vacuum magnetic field generated from the coil system on the plasma boundary and n is the normal unit vector of this surface. Via the minimization of on the plasma boundary, the modular coil geometry is optimized. Meanwhile, the engineering constraints are taken into account which are the minimum interval between adjacent coils and maximum curvature. This optimization process is accomplished by the NESCOIL code [3.8-1]. In the design of the coil system for the CFQS, the coil numbers, major radii and aspect ratio have been scanned to achieve an optimum modular coil system. The corresponding parameters of coil systems are listed in the Table 3.8-1. We have designed 10 magnetic configurations and 19 coil systems in total. The N_p of all configurations is the same, 2.0. Making a comparison among them, the configuration with the major radius (R_0) = 1.0 m, aspect ratio (A_p) = 4.0, magnetic field strength (B_t) = 1.0 T and minor radius (a) = 0.25 m is advantageous. In our work, the 20-coil, 16-coil, and 12-coil systems are designed. The results of filament-coil optimization are listed in the Table 3.8-2. In comparison of the physics and engineering constraints among them, the table indicates that the 16-coils system is preferable, which shows that the minimum interval between adjacent filament coils is the widest; the minimum radius of curvature is the largest and the magnetic flux surface generated is the closest to the target surface.

Table 3.8-1 Parameters for 10 magnetic configurations designed, showing the configuration with the major radius $R_0 = 1.0$ m, aspect ratio $A_p = 4.0$, magnetic field strength $B_t = 1.0$ T, and minor radius $a = 0.25$ m.

R_0 (m)	A_p	a (m)	B_t (T)	Num of modular coils
1.5	3.2	0.47	1.0	20
1.5	3.9(2w39)	0.38	1.0	20
1.5	4.0	0.38	1.0	20
1.5	5.0	0.30	1.0	20
1.2	3.8	0.32	1.0	20
1.2	4.0	0.30	1.0	24, 20, 16, 12
1.2	5.0	0.24	1.0	20
1.0	3.2	0.31	1.0	20, 16, 12
1.0	3.6	0.28	1.0	20, 16, 12
1.0	4.0	0.25	1.0	20, 16, 12
Total	Number of configurations:10		Number of coil systems:19	

Table 3.8-2 Parameters of three different types of coil systems for CFQS-2b40.

A_p	R_0 (m)	a (m)	Number of coils	Minimum distance between coils (cm)	Minimum radius of curvature (cm)	$\mathbf{B} \cdot \mathbf{n} / \mathbf{B} $	Current per coil (MA)	Cross section of coils (cm ²)
4.0	1	0.25	20	17.0	18.2	1.11%	0.2500	17×9
4.0	1	0.25	16	18.5	21.5	0.97%	0.3125	18×10
4.0	1	0.25	12	14.2	14.7	1.21%	0.4167	19×13

Fig. 3.8-1 gives the of 16-modular coil system. Due to $N_p = 2$ and stellarator symmetry, the whole torus consists of four symmetric sections. Therefore, the coils system possesses four different shaped modular coils. The centerline of each finite sized coil is assigned by the corresponding filament coil. The all 16 filament coils are from the results of the NESCOIL code. The coil cross section is rectangular and the area is $13.2 \times 6.9 \text{ cm}^2$ which includes copper conductor, and insulation.

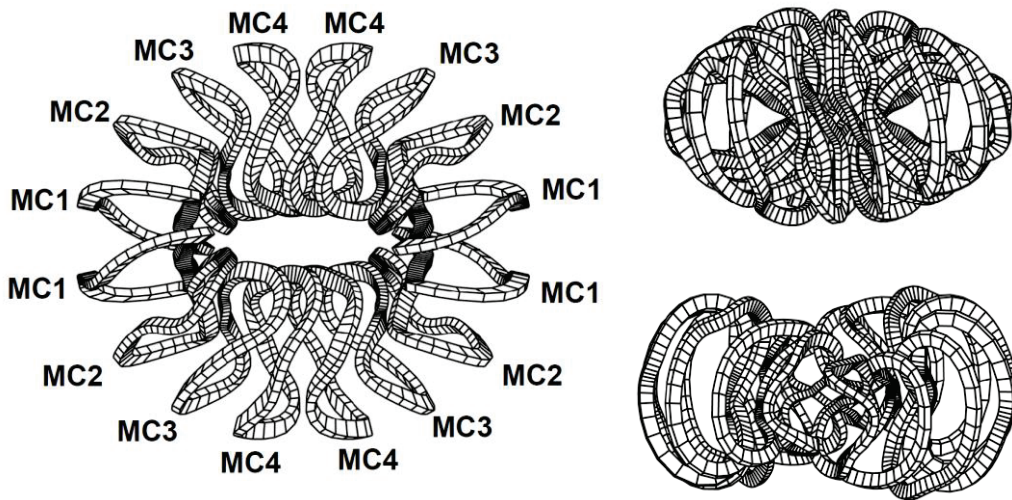


Fig. 3.8-1 Modular coils of the CFQS, the top view and side views at toroidal angle= 0° (vertical elongation), and 90° (horizontal elongation). The serial number of coils represents the various shapes of coils. The coil system comprises of four different shape coils.

In order to estimate the accuracy of the magnetic configuration induced by the 16-coil system, the coils generated magnetic flux surfaces, rotational transform and Fourier spectrum of the magnetic field strength are calculated. In Fig. 3.8-2, Poincaré plots of magnetic flux surfaces and rotational transform induced by the modular coils are analyzed, assuming the coils are filament ones. At the toroidal angle= 0° , 45° , and 90° , cross sections are displayed. The angle = 0° and 90° correspond to the vertically and horizontally elongated cross sections, respectively. The average of $\mathbf{B} \cdot \mathbf{n} / |\mathbf{B}|$ on the plasma boundary is below 1%, which cannot be reduced from the viewpoint of the engineering. The rotational transform profile and magnetic well induced by coils and target profile are compared in Fig. 3.8-2 (d). Horizontal axis ρ in this figure represents the normalized average minor radius. The figure shows a good agreement in rotational transform profile and magnetic well depth, between coils induced ones and target ones. From Fig. 3.8-2 (a)-(c), they depict a good coincidence in the shapes of a magnetic flux surface and that of target plasma boundary. It should be noted that the width of outmost flux surface

produced by modular coils is larger than that of target plasma boundary, which is beneficial to raise the plasma volume by movable limiters. In order to precisely estimate the QA property of the configuration, the magnetic field strength is decomposed into a Fourier spectrum in the Boozer coordinates. Fig. 3.8-3 (a) depicts the spectrum of the magnetic field strength based on the target magnetic configuration. To extinguish the small-amplitude components, the largest component B_{00} is omitted. In Fig. 3.8-3 (a), the magnetic field strength is 1.0 T. B_{10} is the dominant component resulting from the toroidicity. Other components, such as mirror ripple (B_{01}) and helical ripples (B_{11} , B_{12}), are much less than B_{10} , which indicates a tokamak-like QA configuration. In Fig. 3.8-3 (b), coil induced spectrum of magnetic field strength is given. On the basis of synthetical analyzation, the designed 16-coil system is well workable.

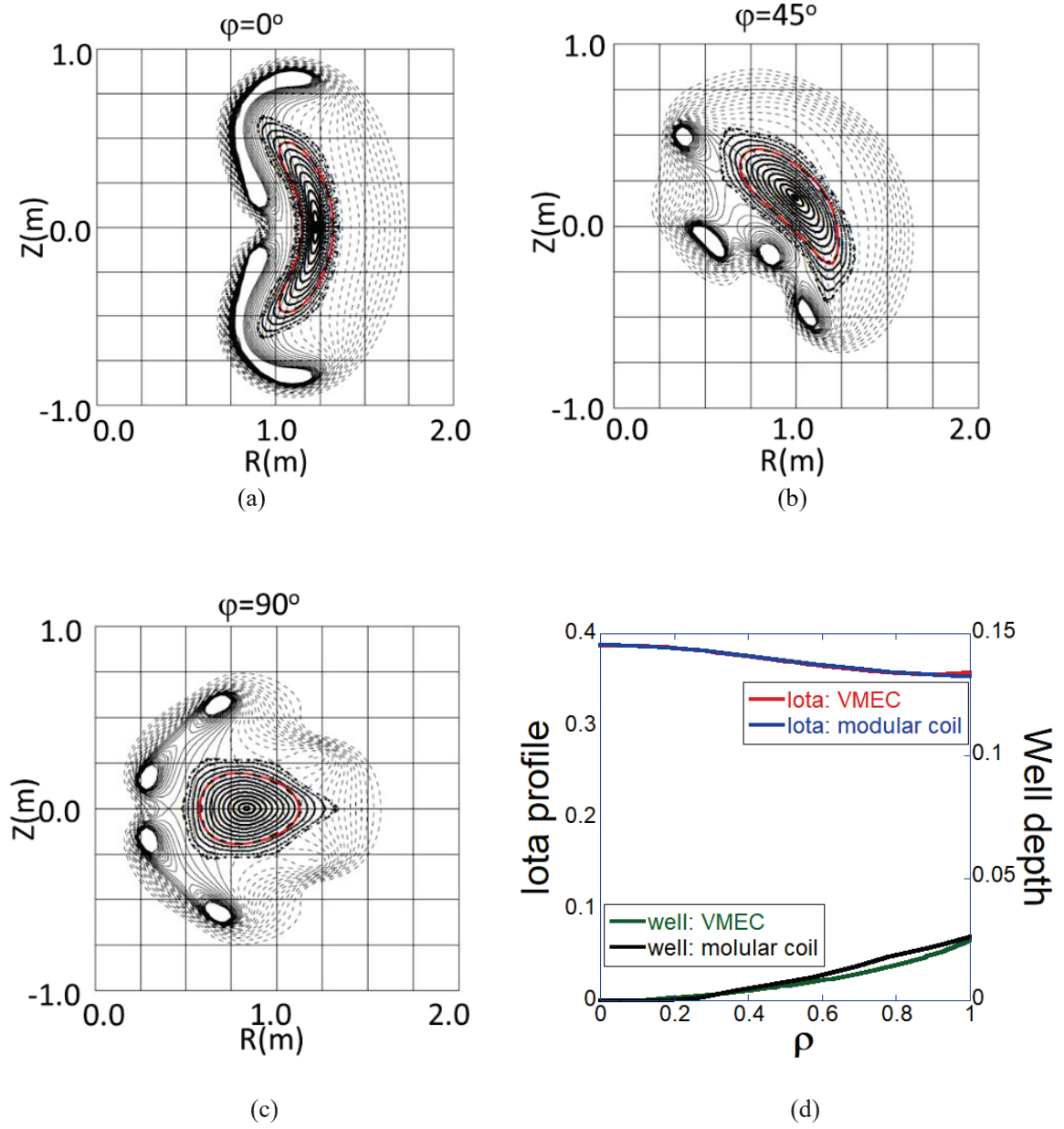


Fig. 3.8-2 Poincaré plots of magnetic flux surfaces at the toroidal angle $=0^\circ$, 45° , and 90° for (a)-(c) respectively. The red curve represents the target plasma boundary. (d) shows the comparison of the rotational transform and magnetic well between the configuration produced by modular coils and target one.

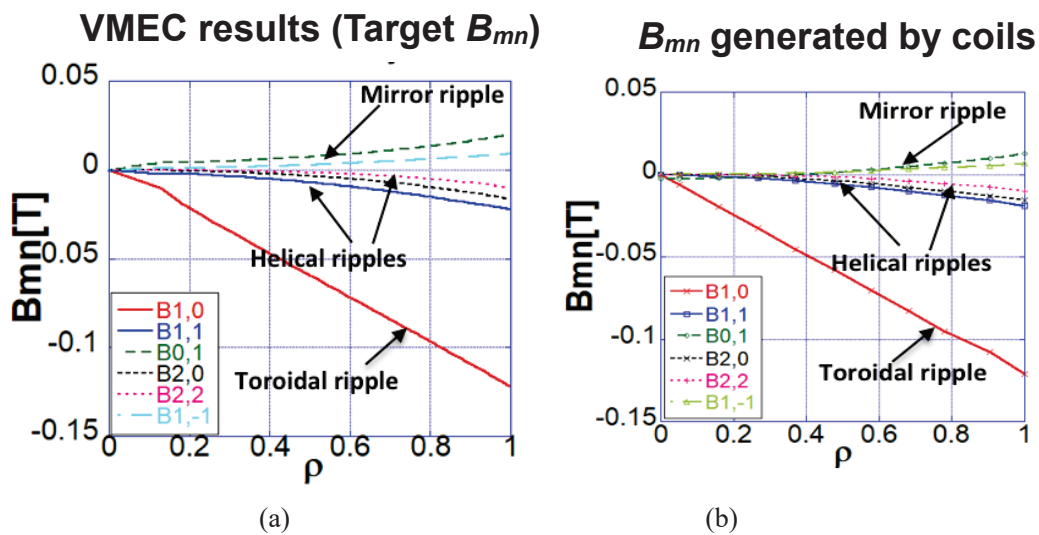


Fig. 3.8-3 Fourier spectrum of the magnetic field strength for the CFQS configuration in the Boozer coordinates. (a) B_{mn} from VMEC results (target spectrum), (b) B_{mn} generated by modular coils.

References

[3.8-1] M. Drevlak, Fusion Technology, **33** (1998) 106.

3.9 Design of modular coils without torsions

In the fabrication of coils, the coil's torsion has a great influence on the difficulty of manufacture. The greater the torsion, the coil is more complex. So, we have optimized the coil system by reducing the torsion.

We compute the torsion by these equations as follows:

For arbitrary point r_c in the modular coil cross section,

$$\mathbf{r}_c(l, \xi, \eta) = \mathbf{r}_G(l) + \xi \mathbf{u}(l) + \eta \mathbf{v}(l). \quad (3.9.1)$$

Tangential vector is as follows,

$$\mathbf{t}_c \equiv \frac{d\mathbf{r}_c}{dl_c} = \left(\frac{d\mathbf{r}_G(l)}{dl} + \xi \frac{d\mathbf{u}(l)}{dl} + \eta \frac{d\mathbf{v}(l)}{dl} \right) / \frac{dl_c}{dl}. \quad (3.9.2)$$

Here, $-x_w \leq \xi \leq x_w$ and $-y_w \leq \eta \leq y_w$.

We define vector,

$$\mathbf{b} = \mathbf{t}_c \times \mathbf{u} \quad \mathbf{n} = \mathbf{b} \times \mathbf{t}_c. \quad (3.9.3)$$

Torsion,

$$\tau(l) = -\mathbf{n} \cdot \frac{d\mathbf{b}}{dl_c}. \quad (3.9.4)$$

We rotate the cross section of coils and calculate the torsion after each rotation. Next, we can find the minimum torsion in our calculated result. When we get the minimum in all cross section, we finish the optimization of the coil.

The following figures (Fig. 3.9-1~8) show the torsion of the coil without optimization and with optimization, respectively.

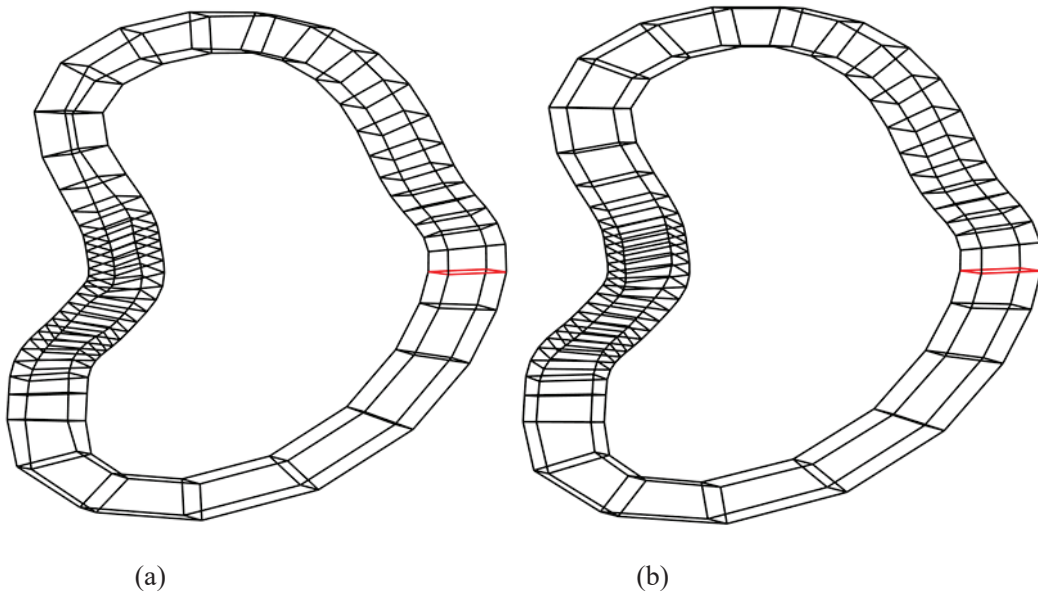


Fig.3.9-1 MC1 coil without optimization (a) and with optimization (b). The red line is the first cross section.

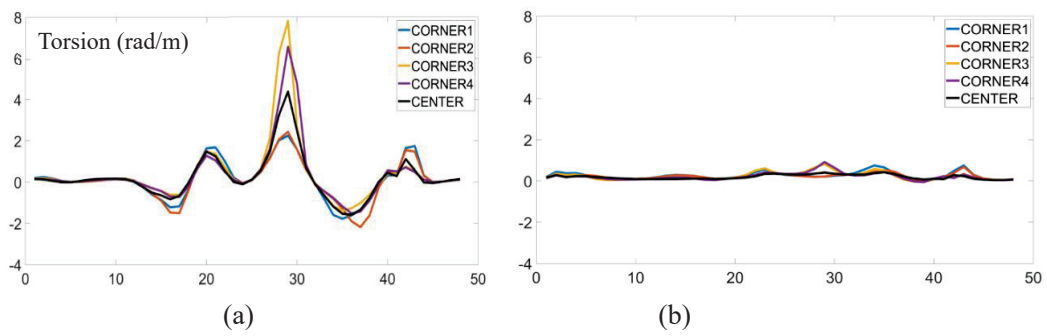


Fig. 3.9-2 Torsion of MC1 coil without optimization (a) and with optimization (b).

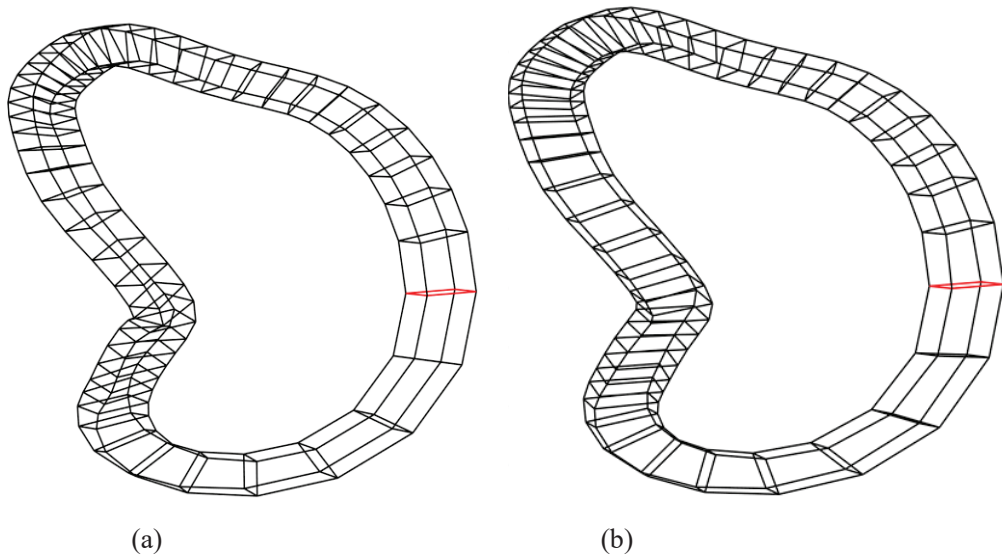


Fig. 3.9-3 MC2 coil without optimization (a) and with optimization (b).

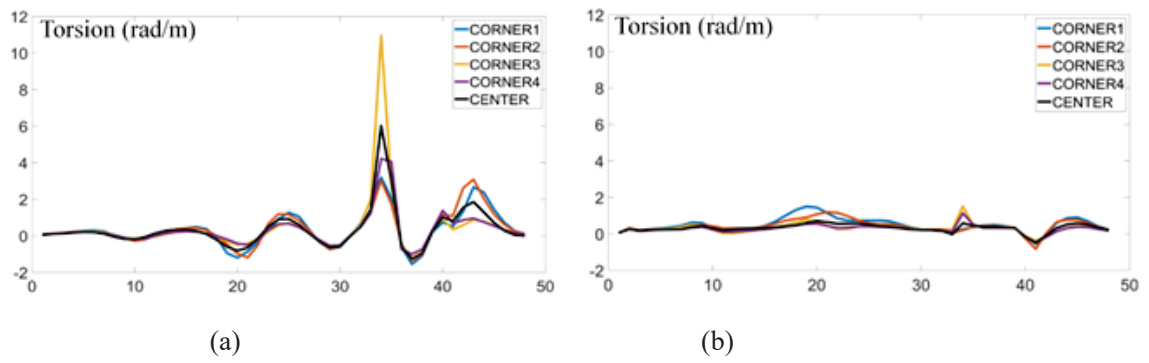


Fig. 3.9-4 Torsion of MC2 coil without optimization (a) and with optimization (b).

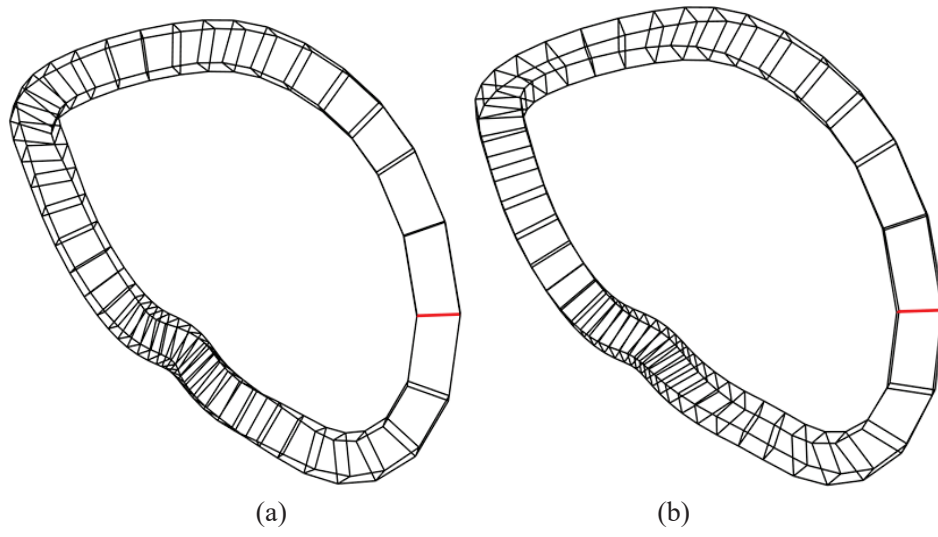


Fig. 3.9-5 MC3 coil without optimization (a) and with optimization (b).

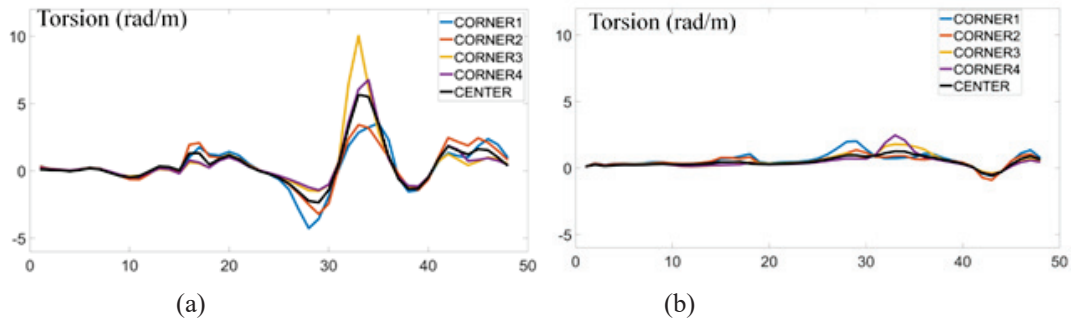


Fig. 3.9-6 Torsion of MC3 coil without optimization (a) and with optimization (b).

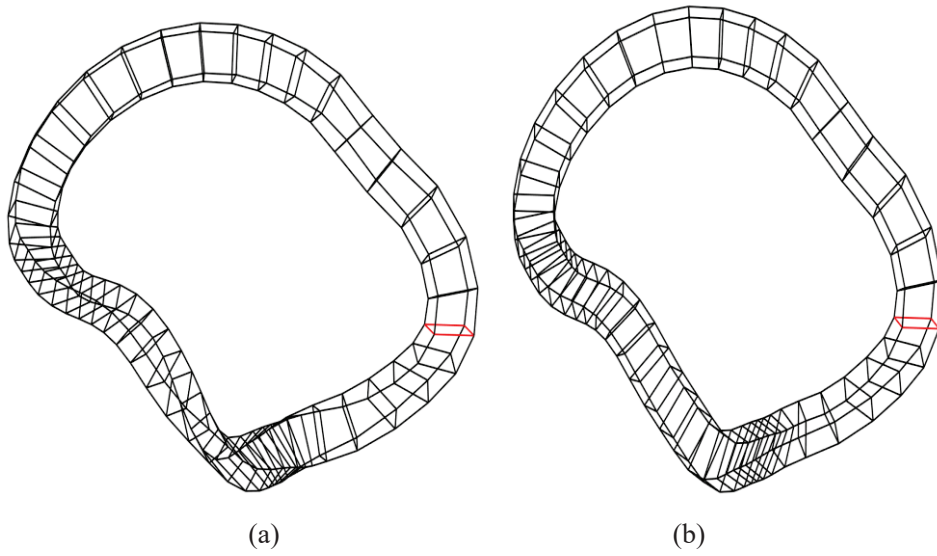


Fig. 3.9-7 MC4 coil without optimization (a) and with optimization (b).

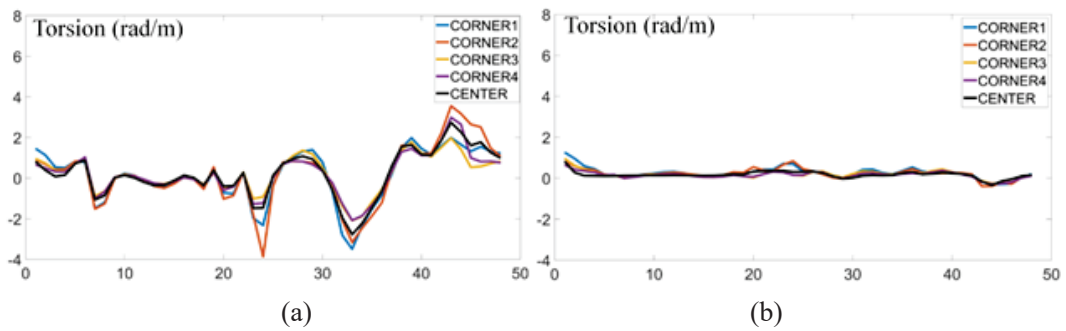


Fig. 3.9-8 Torsion of MC4 coil without optimization (a) and with optimization (b).

Through the figures above, it's clearly shown that the torsion has been well optimized.

In addition, curvature is also an important parameter for the coil system, of course, it is not a good parameter for the coil, the equations of curvature as follows:

$$k = \frac{|d\mathbf{t}_c|}{|dl_c|} = \left| \frac{d^2\mathbf{r}_c}{dl_c^2} \right|.$$

\mathbf{t}_c is calculated in equation (3.9.2) and \mathbf{r}_c is calculated in equation (3.9.1).

Then, we compare the curvature of coils without optimization and with optimization, respectively.

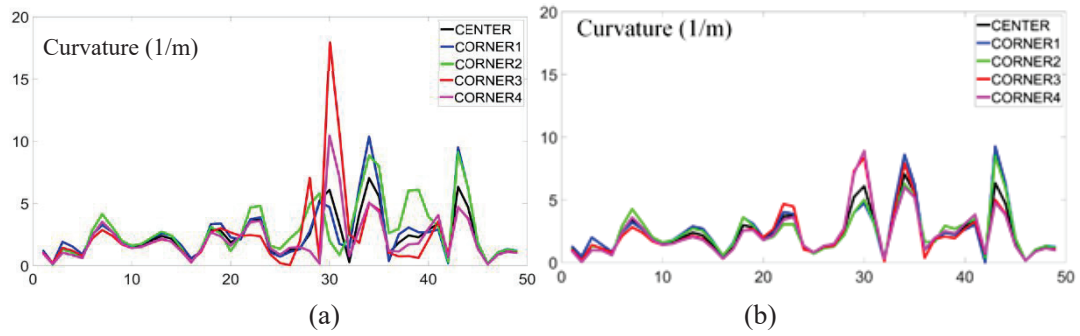


Fig. 3.9-9 Curvature of MC1 coil without optimization (a) and with optimization (b).

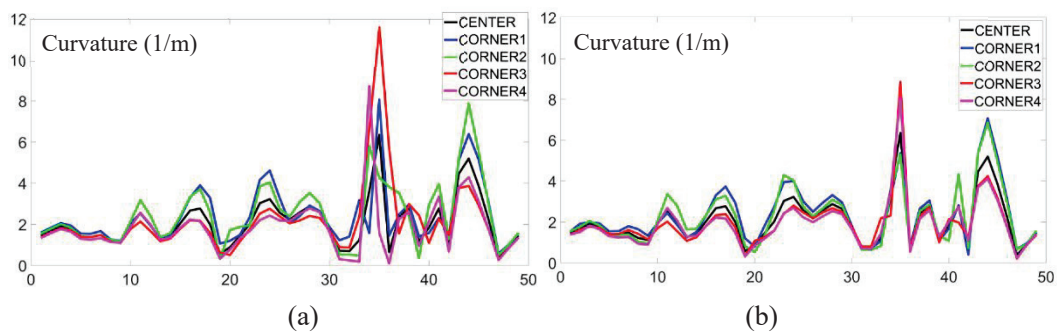


Fig. 3.9-10 Curvature of MC2 coil without optimization (a) and with optimization (b).

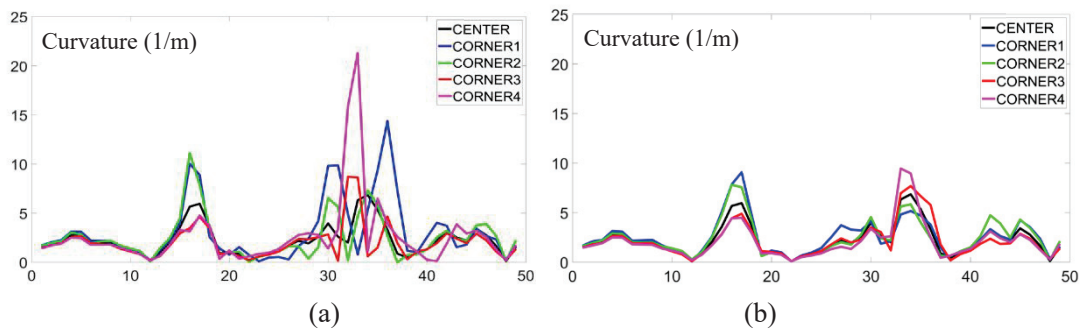


Fig. 3.9-11 Curvature of MC3 coil without optimization (a) and with optimization (b).

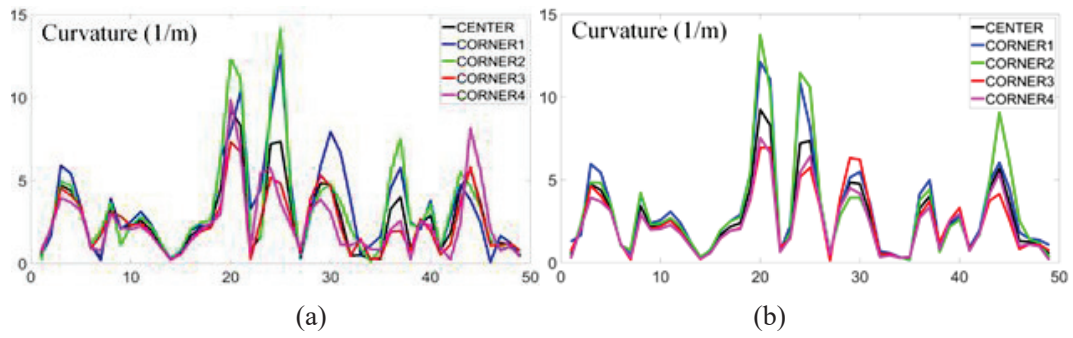


Fig. 3.9-12 Curvature of MC4 coil without optimization (a) and with optimization (b).

The above figures (Fig. 3.9-9~12) show that the coil optimization for torsion also have a good improvement in curvature. Fig. 3.9-13 shows the final results of modular coils with plasma boundary.

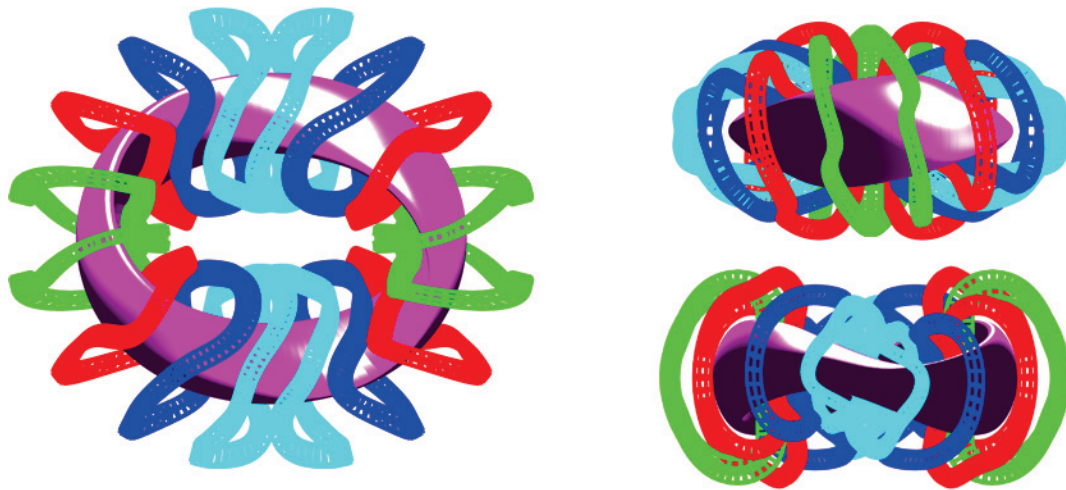


Fig. 3.9-13 Modular coils and plasma boundary of CFQS.

3.10 Divertor configuration

In designing the magnetic configuration of an experimental device, the first priority is placed on designing the configuration of the core confinement region. However, it is well known that without a proper design of magnetic configuration of the peripheral region the concept is not useful for the fusion reactor. This is called “divertor design” because the most important physics issue related to the peripheral magnetic configuration is particle and heat removal.

In tokamak research, the concept of divertor is almost established and all existing tokamak devices in the world have similar divertor configuration (single null divertor) with the direct extension to the tokamak demo design. There are still discussions for the new ideas of advanced configurations (double null divertor and snow flake divertor) but they have not been adopted in real experimental devices. In stellarator research, we do not have one established concept of divertor partly because we have varieties of stellarator configurations and divertor concept strongly depends on the magnetic configuration of core confinement region. In fact, for the two largest stellarator experiments, LHD and W7-X, these devices have different divertor structures. In LHD, the intrinsic helical divertor has divertor magnetic field lines connecting the ergodic boundary layer of the core confinement region and the divertor plates on the wall [3.10-1, 2, 3]. In W7-X, the island divertor provides a sophisticated divertor structure combined with small islands created near the boundary of the core confinement region [3.10-4, 5, 6, 7]. For the new stellarator CFQS in China, we are designing a new divertor configuration which provides a sufficiently long connection length of magnetic field lines between the plasma boundary and the wall.

Three poloidal cross sections of the LCFS of CFQS are shown in Fig.3.10-1. These figures are VMEC output as a target configuration of the modular coil design. Modular coils were designed to realize such a magnetic configuration with a choice of the number of coils around the torus as 16 [3.10-8, 9]. The success of this coil design was the most important contribution to the finding of a new divertor concept for CFQS. Fig. 3.10-2 shows the punctual plots of the vacuum magnetic field lines (magnetic surfaces) produced with these modular coils (for the third cross section in Fig.3.10-1). Red line shows the LCFS of the target configuration in the modular coil design. The magnetic field produced by the modular coils has many closed magnetic surfaces with a larger area beyond the target LCFS. The result of the magnetic structure outside of the LCFS (defined by VMEC) does not come from the target configuration. In fact, another modular coil design with 20 coils with the same target configuration gave similar magnetic surfaces inside LCFS but the boundary configuration is very different. It has a stochastic layer just outside of the LCFS with small islands ($n = 2/m = 6$) surrounded by the stochastic layer.

The blue (lower) line in Fig. 3.10-3 shows the profile of the rotational transform of the vacuum magnetic configuration produced by the 16 modular coils. A very flat profile for the outer region is important for creating large islands for the divertor configuration. The rotational transform profile of

W7-X is also flat, but not as flat as that of CFQS. The polarities of the weak shear of both devices are different, namely, the CFQS has a weak negative shear (in the stellarator terminology) at the boundary while W7-X has a positive shear. A black arrow shows the position of the averaged minor radius of the LCFS of the target configuration. Although we decided upon an aspect ratio of 4.0 for the CFQS device, it is technically possible to create a larger confinement region if we design the vacuum chamber with a sufficiently large size to provide space for such larger closed magnetic surfaces. A control of plasma boundary with a movable limiter might be a possible choice for the plasma operation in experiments.

When we introduce the auxiliary toroidal coils to provide additional toroidal field to the stellarator field produced with modular coils, the magnetic configuration is changed to include large islands at the boundary of the core confinement region shown in Fig. 3.10-4. The QA property is conserved with the additional toroidal field. The strength of the additional toroidal field is -0.055 times averaged toroidal field produced by modular coils. The rotational transform is increased to change the boundary value to 0.4 (shown by red (upper) line in Fig. 3.10-3). This is a typical magnetic configuration for any type of stellarator that has a rational value of the rotational transform near the boundary. However, essential differences between the configuration shown in Fig. 3.10-3 from many other cases are 1) large size of islands and 2) the completeness of the island magnetic surfaces. It is shown in Fig. 3.10-4 that clearly formed island bundle flux surrounds the core confinement region with a clearly defined interface of the magnetic field separatrix. This is the reason why we call such a configuration as “island bundle divertor (IBD)”. The entire magnetic confinement area is clearly separated into two regions: hot plasma region in the core and cold plasma region in the periphery.

Fig. 3.10-5 shows the divertor field line tracing, which is created in the following calculation procedures. We found first the LCFS of the core confinement region. Then we distributed many field line tracing starting points with a small deviation (5 mm for $R = 1\text{ m}$ torus) from the LCFS. Because the island magnetic surfaces are complete, there is no escaping field line in such a calculation. Fig. 3.10-5 shows blue line for one of the possible shapes of the vacuum chamber wall. If we install divertor plates at this wall position, the cold plasma in the island bundle flux can be absorbed at the divertor plates. Fig. 3.10-6 shows the divertor tracing with the wall target where the field line tracing is stopped. The pattern of the magnetic field line Poincaré plots is very similar to the tokamak divertor structure. In fact, the transport of the magnetic field lines is exactly the same as tokamak divertor, where the peripheral regions of the divertor are connected to the core confinement region with a clear magnetic separatrix, and magnetic field lines in divertor region have long connection length between the null point and the wall. Because the magnetic field lines go around through all five island bundle fluxes with very small incident angles to the wall, the distribution of the heat load on the divertor plates is determined by the precise geometric design of the shapes and the locations of divertor plates.

Fig. 3.10-7 shows the distribution of the connection lengths for magnetic field lines near the X point of inboard side at the toroidal angle ϕ of 90° . The horizontal axis corresponds to the major radius of the calculation point in the poloidal cross section and the vertical axis to the vertical positions (a major radius of the device is 1 m). Calculation was made at 500 points for both horizontal and vertical directions. Three areas are clearly separated by a sharp separatrix created by the islands. A yellow area on the right of X point is the core confinement region, two violet areas above and yellow X point are inside islands and almost black area on the left of X point is outside of islands. In the magnetic island areas, the connection lengths of magnetic field lines are in the range of 500 to 1000 m and there is no exceptional field line with shorter length. This is because the island magnetic surfaces are very regular and there is only little ergodic region between the core confinement region and the island divertor flux. This is a clear difference from the LHD-type divertor structure where there are some field lines with shorter length between the core region and the divertor plate because of the ergodicity of the boundary layer of the core confinement region.

The magnetic field lines located on the separatrix lines (with red color) are parts of the field lines escaping from the core confinement region (yellow color) through the separatrix interface between core and island region. These field lines finally hit the wall (shown by the boundary of the black color area) at the left side of the figure. The position of this strike point moves as the position of the island changes. When the rotational transform value is shifted with the change of the current in the auxiliary toroidal coils by 2%, the position of the strike point moves about 1.5 cm along the wall. This sensitivity of the island position is within the controllability of the rotational transform with the auxiliary toroidal coil.

Because the rotational transform of IBD region is 0.4, island bundles shown in Fig. 3.10-4 are connected together. In other words, this bundle flux is a single flux. Thus particles and heat flux transferred from the core confinement region to the IBD can be removed at any position in the torus. Because the space between the plasma and the wall is very narrow in the toroidal position of the crescent shape of plasma (the leftmost LCFS in Fig. 3.10-1), we can avoid installing divertor structure at this region and take advantage of installing it where the space is larger. As shown in Fig. 3.10-6, the number of divertor feet is as many as ten. Thus it is possible to reduce the maximum heat load at the divertor compared with the tokamak case, where the number of feet is two (in the case of a single null). On the other hand, because the divertor fields are all connected into a single structure, it is not necessary to install as many as ten divertor plates.

We have discussed so far the island divertor concept for CFQS based on the vacuum magnetic field produced by the external coils. Because the neoclassical bootstrap current is larger for the quasi-axisymmetric stellarator compared to other types of stellarator, it is necessary to find the operation scenario of the island divertor for the plasmas with finite beta. An example of the neoclassical bootstrap current calculation for CFQS is reported in the previous paper with planned experimental

parameters [3.10-9]. Fig. 3.10-8 shows an example of the calculated profiles of the rotational transform in the operation with finite beta value. The calculation is based on the VMEC code which is widely used for the calculation of three dimensional equilibria with given plasma current profile. The black line shows the profile for the vacuum equilibrium with zero beta. It is equivalent to the blue line in Fig. 3.10-3 plotted from the magnetic field line tracing for the vacuum field. The red line shows the rotational transform profile with the averaged beta value of 0.35 %. The neoclassical bootstrap current is calculated using BOOTSJ code [3.10-10] for the pressure profile shown by the blue curve in the Pascal unit. This shape of the pressure profile is assumed based on the typical density and temperature profiles observed in many stellarator experiments [3.10-9]. When these codes are used for calculating the rotational transform profile with neoclassical bootstrap current, the reliability of the profile data in the vicinity of the magnetic axis is not good. Therefore these line are shown by dots for that area. It passes the value of 0.4 ($n/m = 2/5$) at the edge, which is expected to form islands. However, because the VMEC code assumes the existence of clear magnetic surfaces, the discussions of island structure need more advanced theoretical work using HINT, which is beyond the scope of this paper.

The green dotted line shows an example of controllability for the rotational transform profile using auxiliary toroidal coil. This profile is an example of applying the additional toroidal field to shift up the profile from the one with neoclassical bootstrap current. Actually the expected operation would be either shifting up or shifting down the rotational transform profile to match to the value of 0.4 in order to create island divertor configuration for the plasma with beta value different from 0.35 %.

For such finite beta plasmas, it is necessary to make two different controls in order to create good island divertor configuration. The first one is to adjust the rotational transform value near plasma edge at 0.4, which is resonant to the $n/m = 2/5$ islands. This control is relatively easy using an adjustable power supply for the auxiliary toroidal coils. The second one is to control plasma pressure profile for obtaining a suitable neoclassical bootstrap current profile, which produces the rotational transform profile with very low negative shear. This control would be technically difficult but could be achievable with proper heating control, which will be an important research topic in the experiments. The duration of the plasma discharge planned in the CFQS program is 100 ms due to the limitation of the heating devices. The estimated rising time of the neoclassical bootstrap current is between 20 to 100 ms depending on the collisionality. Even if the fully developed equilibria with neoclassical bootstrap current is not possible for collisionless plasmas in the strict sense, the experimental analysis for this scientific topic will be possible.

Because theoretical analysis of the island divertor configuration needs the equilibrium calculation including island structure, the model calculation using HINT code [3.10-11] is now in progress and will be reported in the succeeding paper. The equilibrium calculations using VMEC for the rotational transform profiles with auxiliary toroidal coils were made for different volume-averaged beta values

up to 1.5 %. For higher beta than 0.35 %, the auxiliary toroidal field must be positive (same polarity as the basic toroidal field) in order to decrease the rotational transform at the plasma edge down to 0.4.

Since the island structure is in general very sensitive to the control of the rotational transform, the control of neoclassical bootstrap current in the stellarator operation will be essential to keep the IBD concept stable. However, we know that any plasma parameters and engineering parameters must be controlled extremely accurately in the future fusion reactor. The control of neoclassical bootstrap current would be within available control knobs in the fusion reactors.

References

- [3.10-1] Y. Takeiri *et al.*, Nucl. Fusion **57** (2017) 102023.
- [3.10-2] S. Masuzaki *et al.*, Fusion Sci. Tech. **50** (2006) 361.
- [3.10-3] M. Kobayashi *et al.*, Fusion Sci. Tech. **58** (2010) 220.
- [3.10-4] R. C. Wolf *et al.*, Nucl. Fusion **47** (2017) 102020.
- [3.10-5] H. Renner *et al.*, Plasma Phys. Contrl. Fusion **44** (2002) 1005.
- [3.10-6] Y. Suzuki, J. Geiger, Plasma Phys. Contrl. Fusion **58** (2016) 064004.
- [3.10-7] Y. Feng *et al.*, Nucl. Fusion **56** (2016) 126001.
- [3.10-8] H. Liu *et al.*, Plasma and Fusion Research Series **13** (2018) 3405067.
- [3.10-9] A. Shimizu *et al.*, Plasma and Fusion Research Series **13** (2018) 3403123.
- [3.10-10] K. C. Shaing *et al.*, Phys. Plasma **B1** (1989) 148.
- [3.10-11] Y. Suzuki *et al.*, Nuclear Fusion **46** (2006) L19.

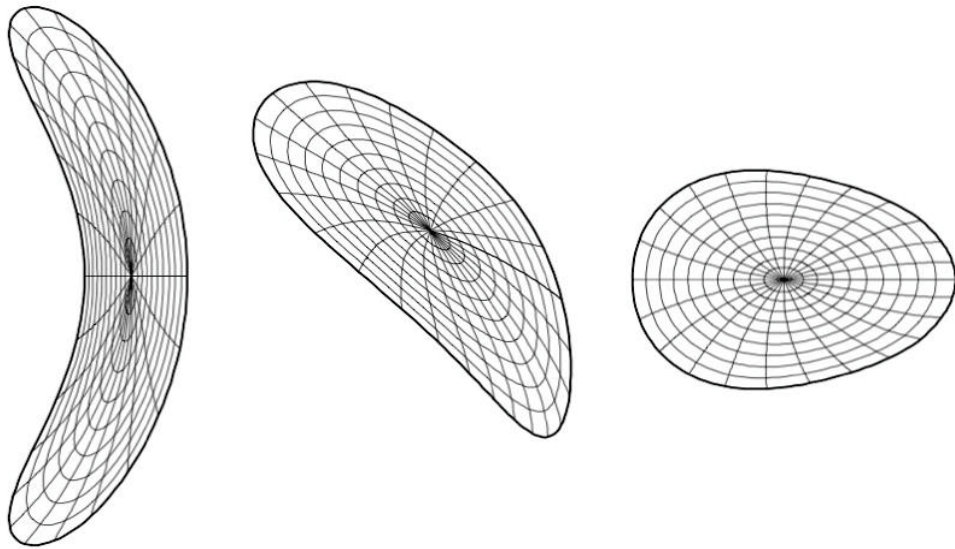


Fig. 3.10-1 LCFS for CFQS advanced stellarator design. Cross sections for three toroidal positions are shown.



Fig. 3.10-2 Punctual plots of magnetic surfaces for CFQS configuration produced by 16 modular coils. Red line corresponds to the LCFS of the 3rd plot in Fig. 3.10-1.

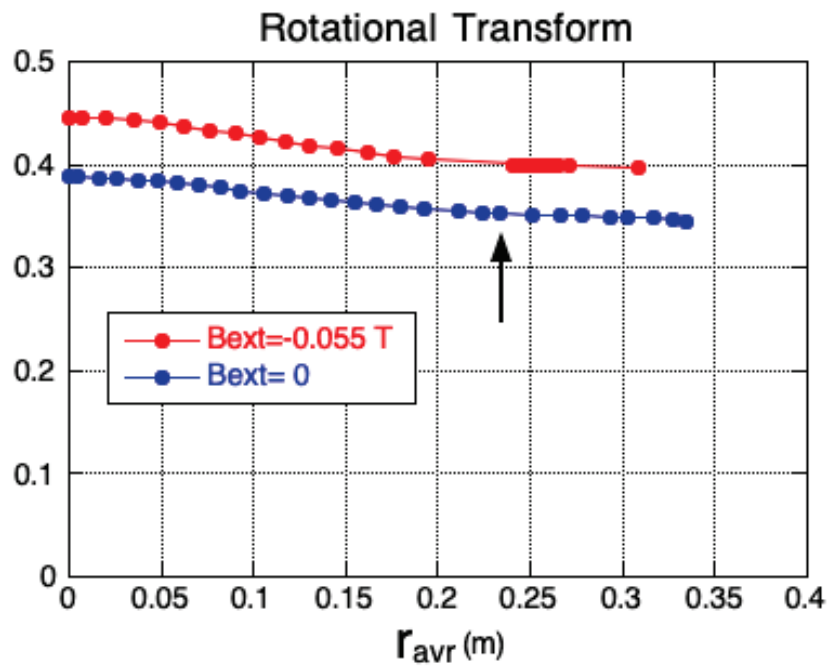


Fig. 3.10-3 Blue [lower] line: Rotational transform profile of vacuum field of CFQS. Arrow indicates the position of LCFS of target configuration. Red [upper] line: Rotational transform profile of island divertor configuration ($n/m = 2/5$) with additional toroidal field.

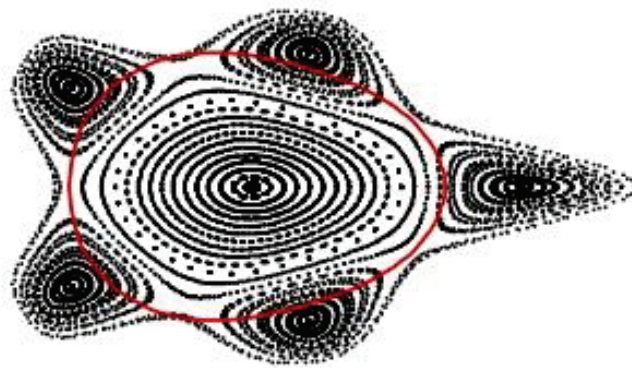


Fig. 3.10-4 Magnetic configuration of island bundle divertor.

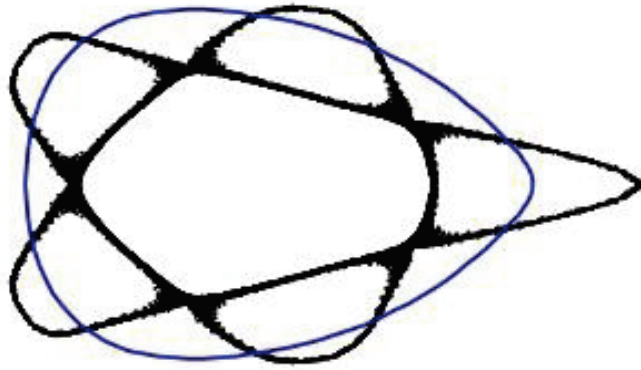


Fig. 3.10-5 Divertor field line tracing for island bundle divertor. Blue line shows one example of vacuum chamber wall position for locating divertor plates.

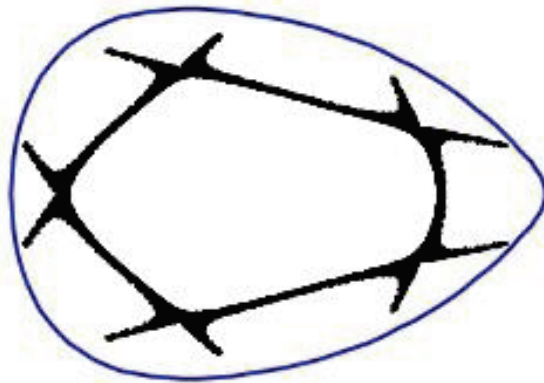


Fig. 3.10-6 Divertor field line tracing with assumed existence of divertor targets.

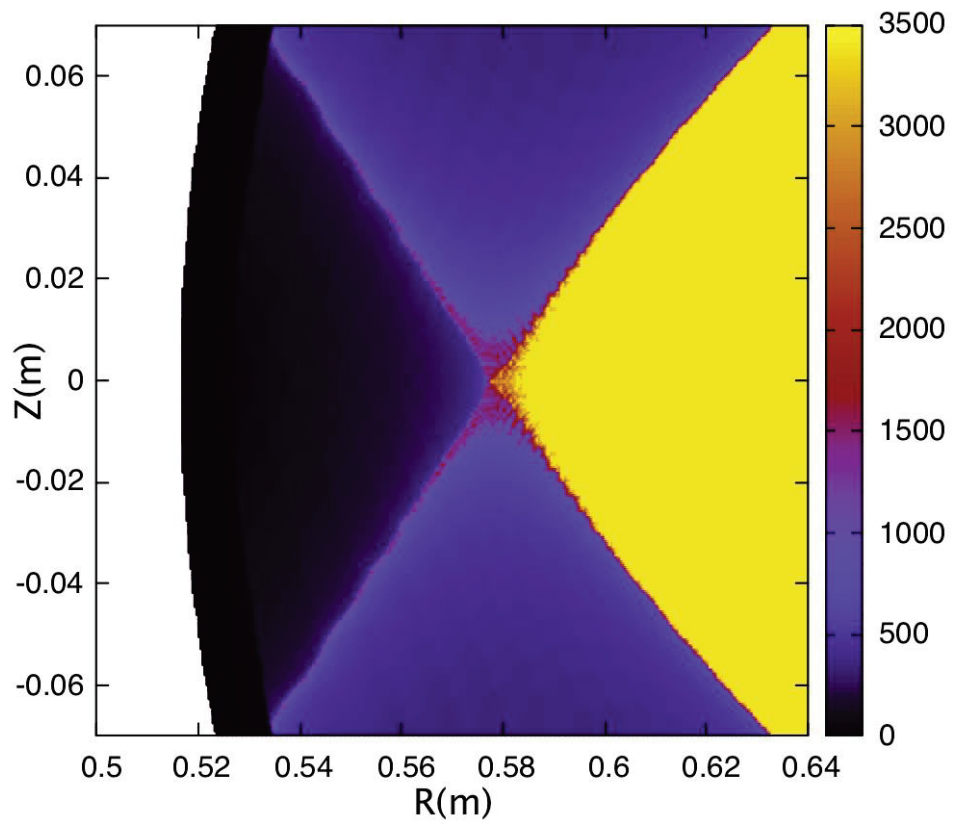


Fig. 3.10-7 Distribution of connection length near one of X-points in the island divertor of CFQS.

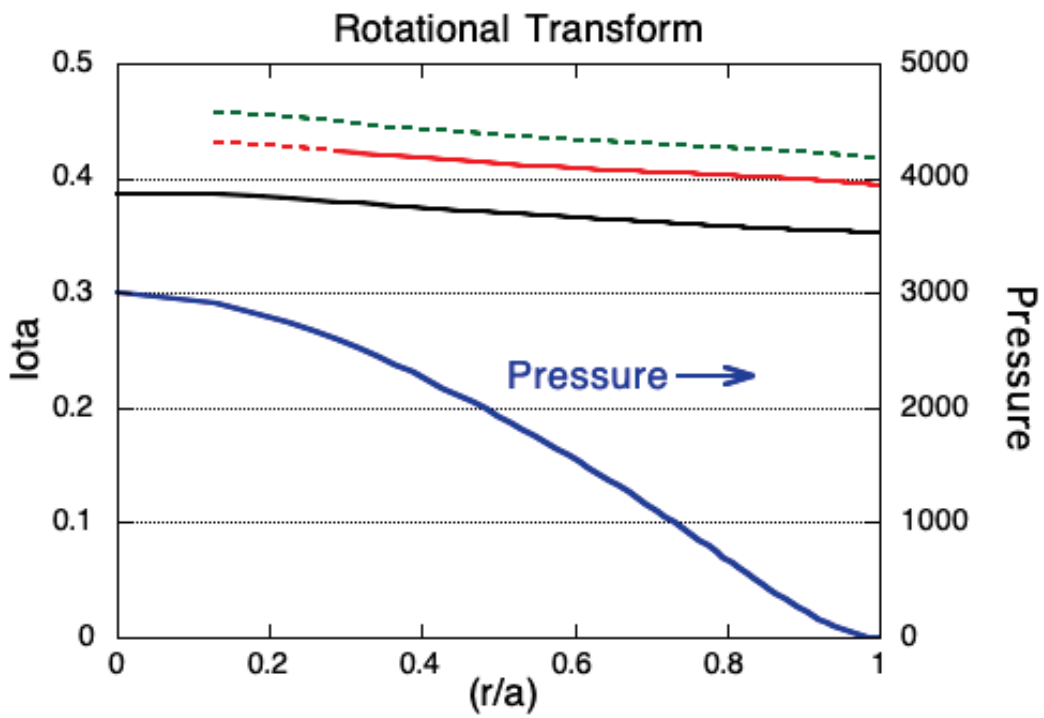


Fig. 3.10-8 Rotational transform profiles calculated by VMEC code. Black line shows the profile for the vacuum field (zero beta). Red line shows the profile with neoclassical bootstrap current calculated for beta value of 0.35 % and the pressure profile shown by blue curve. Green line shows an example of profile control using auxiliary toroidal field to shift up the red profile by reducing the toroidal field produced by modular coils.

4 Engineering design

4.1 Whole assembly

4.1.1 Specification for engineering design

The CFQS design is based on 2b32 CHS-qa configuration, and reduces the major radius, increases the aspect ratio, and reduces the magnetic field slightly to reduce costs and make it easier to manufacture. Table 4.1.1-1 shows physical main parameters of the CFQS. We can achieve low magnetic shear and a shallow well structure throughout the entire region as mentioned in the chapter for the equilibrium. The dominant ripple is the toroidal mode $B_{1,0}$, which indicates a tokamak-like or QA configuration. The CFQS project aims to confirm the effectiveness of this equilibrium. The aspect ratio of CFQS is the smallest in helical devices, and the coil shape is very complicated. They are the disadvantages that make engineering relatively harder than other devices. For example, the work area in the central region is very narrow and special structural idea is necessary for assembling the CFQS. The electromagnetic force will be locally large although the magnetic field in the plasma is not so large and only 1 T. Therefore, a strong reinforcement structure is required. They are engineering disadvantages for cost reduction. As described later, the direction of the electromagnetic force is unlike the tokamak. Special design is required because vertical and toroidal components are generated in the electromagnetic force.

Table 4.1.1-2 gives technical data of the CFQS. A basic QA configuration can be produced by four types of modular coils (for total of 16). However, to allow flexibility of configuration, we will install four poloidal field coils (to move the magnetic axis horizontally) and twelve toroidal field coils (to change the rotational transform). The coil currents are driven by nine power supplies in the rated operation conditions. The power supplies, the diagnostics and the heating apparatus are different in the experimental phase, but the main body of the CFQS is common. It will be constructed under the rated operation conditions.

The plasma heating apparatus is intended to provide for tangential neutral beam injection (NBI) of 40 kV, 1 MW, and electron cyclotron resonance heating of 54.5 GHz, 450 kW. For plasma diagnostics, we will use a Thomson scattering system, a microwave interferometer, a charge exchange spectroscopy, a heavy ion beam probe, and magnetic measurements, among others.

Table 4.1.1-1 Comparison of physical specifications for stellarators.

No	Parameters	CFQS	W7-X	HSX
1	Type	QA	QI	QH
2	Major radius (m)	1.0	5.5	1.2
3	Minor radius (m)	0.25	0.5	0.15
4	Aspect ratio	4	11	8
5	Magnetic field (T)	1	3	1
6	Toroidal periodic number	2	5	4
7	Rotational transform	0.35~0.38	0.85~1	1~1.1
8	Magnetic well depth	0~0.025		
QA; Quasi-axisymmetric configuration QI; Quasi-isodynamic configuration QH; Quasi-helical symmetric configuration				

Table 4.1.1-2 Technical data of the CFQS.

No	Device	Initial		Rated operation			
1	Plasma heating	2.45 GHz 20 kW ECRH		54.5 GHz 450 kW ECRH 40 kV 1 MW NBI Pulse 0.1 s			
2	Coil	MC	TFC	MC	PFC	TFC	
	Cross section	63 × 126	54 × 10	63 × 126	94.5 × 42	54 × 10	
	Magnetic field (T)	0.09	-	1	-	-	
	Number of coils	16	12	16	4	12	
	Turns	72	16	72	32	16	
	Current (A/turn)	434	217	4,340	4,340	2,170	
	Total current (kAT)	450	42	5,000	556	417	
	Current density (A/mm ²)	conductor only	7.4	11.4	74	74	114
		with insulator and coolant	3.9	6.4	39	35	64
	Rectangular wave equivalent time (s)	Continuous		1.1 s	0.38 s	0.19 s	
	Period (s)	-	-	300 s			
	Number of PS	4	3	4	2	3	
	Operation voltage (V)	227(MC1)	59(TF10)	2150(MC1)	1420(OV)	500(TF10)	
	Power capacity (kW)	320	30	36,000	7,940	2,940	
Power source	Commercial		Motor generator				
3	Diagnostics	Magnetic probe Electrostatic probe Spectrometer Interferometer		Thomson scattering FIR interferometer VUV spectrometer HIBP, CXRS <i>etc.</i>			
4	Vacuum vessel	0.45 m × 1.2 m at vertical elongated section					
	Material	SUS316 thickness 6 mm					
	Number of ports	42 or more					
	One turn resistance	0.4 mΩ (by ANSYS/Maxwell)					
	Baking temperature	130 °C					
	Vacuum pump	1500 ℓ/s TMP × 2					

4.1.2 Overall structure

Fig. 4.1.2-1 to Fig. 4.1.2-5 show schematics of the CFQS with power supplies. The CFQS body is approximately 2800 mm high between a top frame and a bottom frame and has an outer diameter of 4300 mm. The electromagnetic force applied to the modular coils is supported by a cage-type support structure, with diagonal beams to absorb the overturning force and two central pillars to absorb the centripetal force. The mass of the device body is about 30 tons. These devices will be installed in a torus hall with power supplies, as shown in Fig. 4.1.2-3. Fig. 4.1.2-4 and Fig. 4.1.2-5 indicate main dimension of the CFQS. To install various equipment's around the CFQS body, stages with a height of approximately 2.3 m and a width of 10 m will be installed. The center height of the body is planned to be 3.5 m from the floor, and we are going to create large space under the device to install measuring instruments and related equipment.

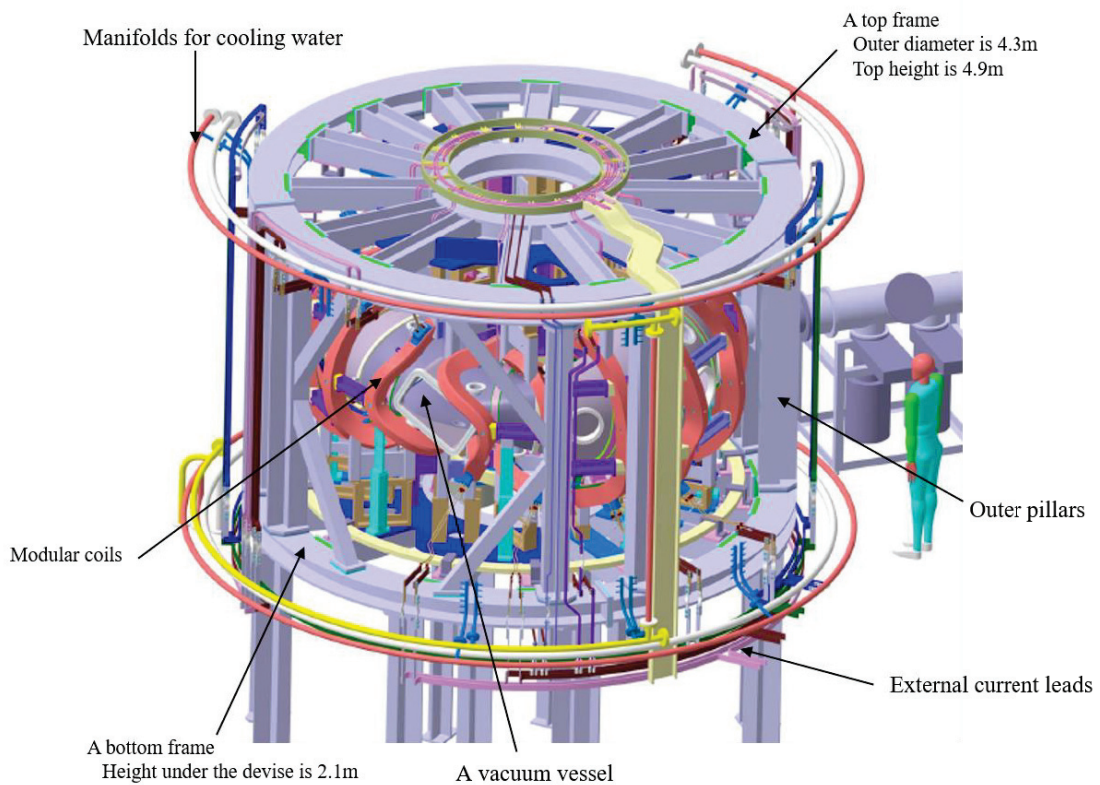


Fig. 4.1.2-1 Schematic of the CFQS.

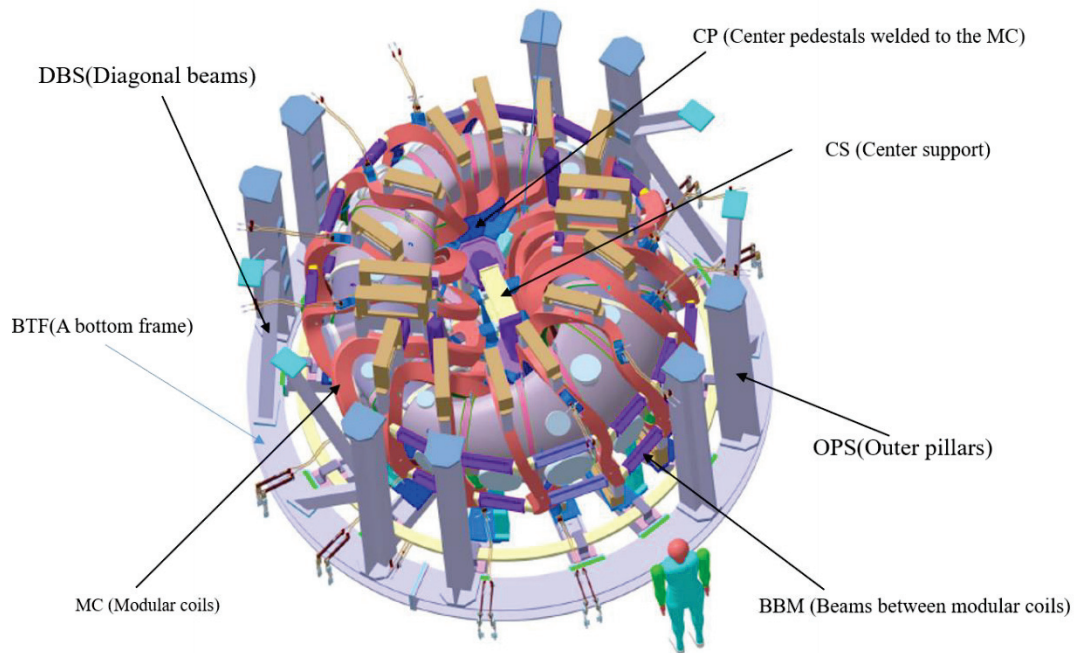


Fig. 4.1.2-2 Inside a cage-type support structure.

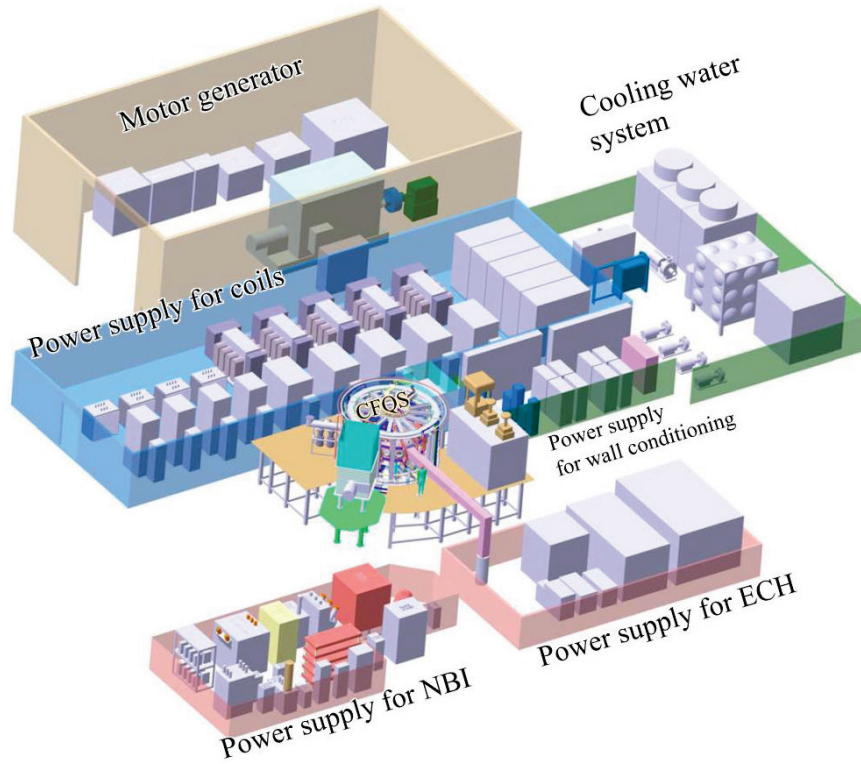


Fig. 4.1.2-3 Layout in an experimental building.

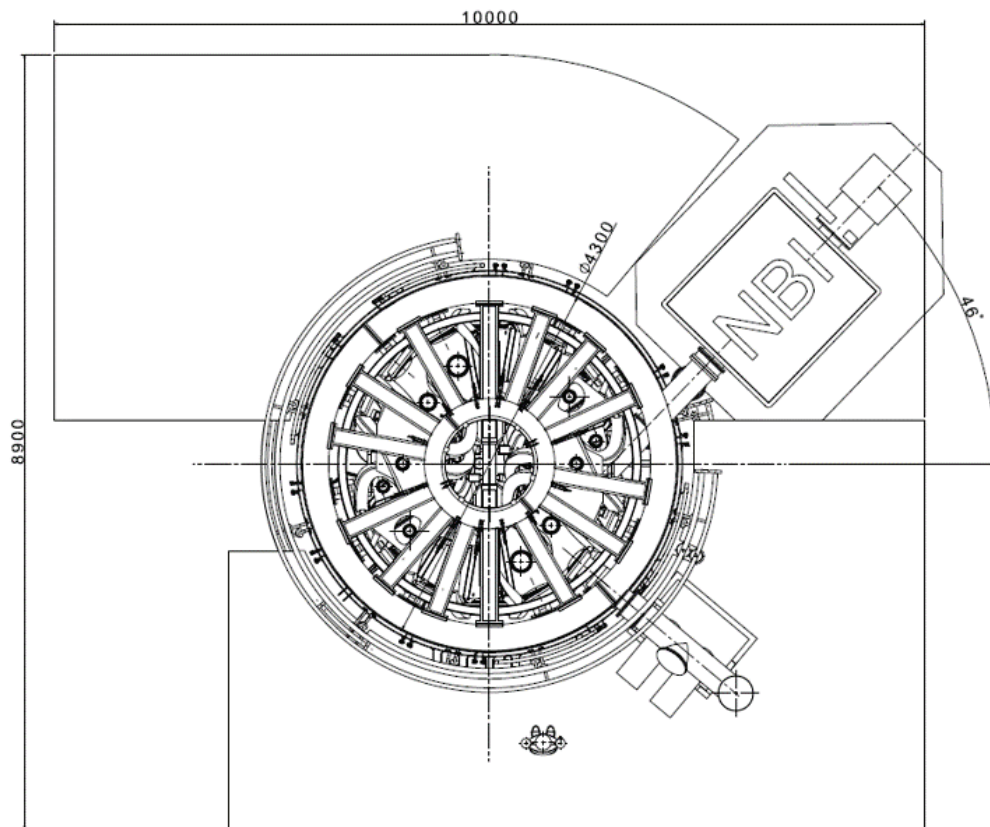


Fig. 4.1.2-4 Top view of the CFQS.

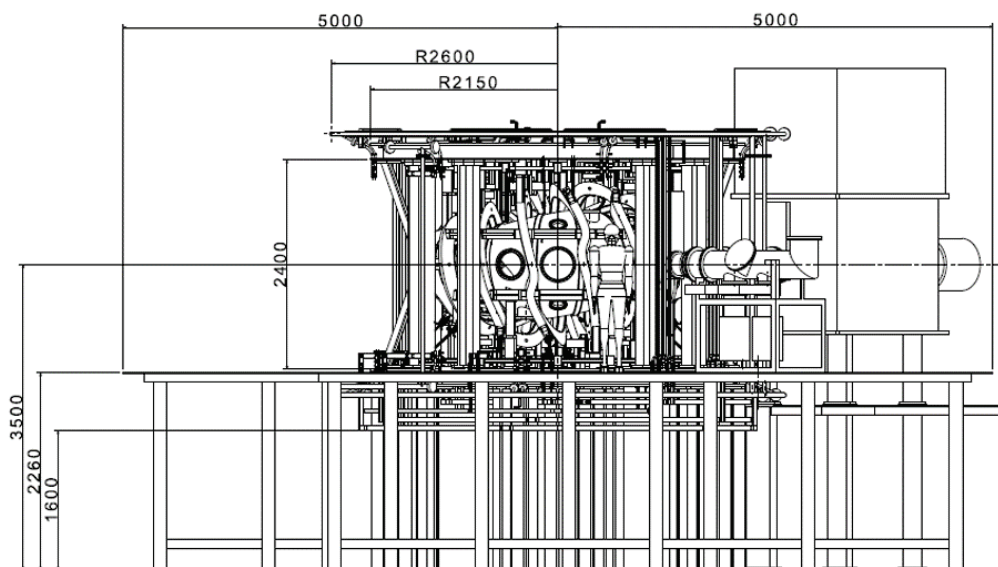


Fig. 4.1.2-5 Front view of the CFQS.

4.1.3 Production flow

Proposed production flow is shown in Fig. 4.1.3-1 and Fig. 4.1.3-2.

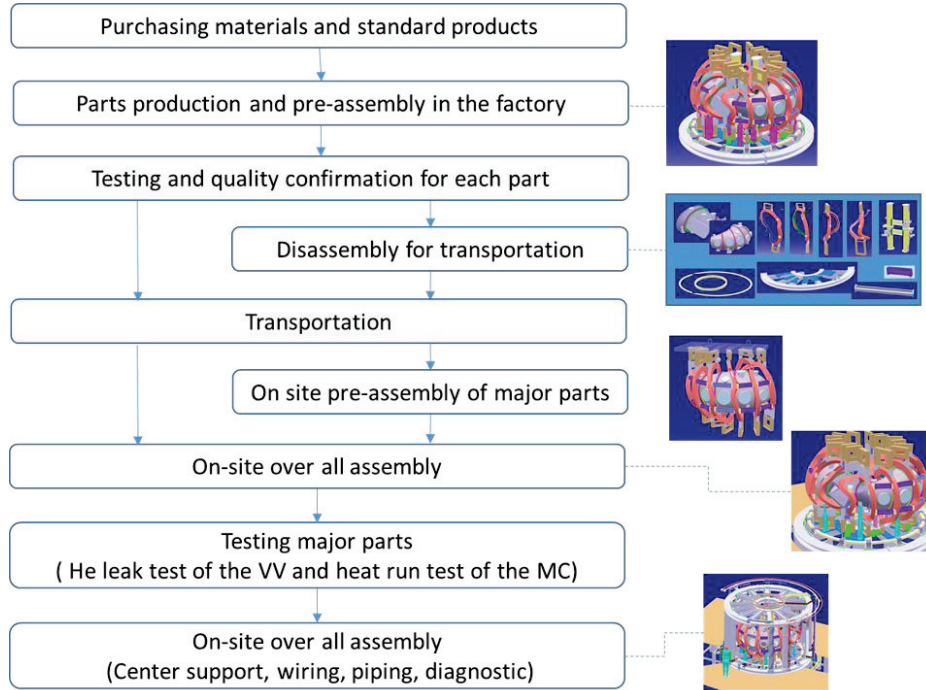


Fig. 4.1.3-1 Overall production flow.

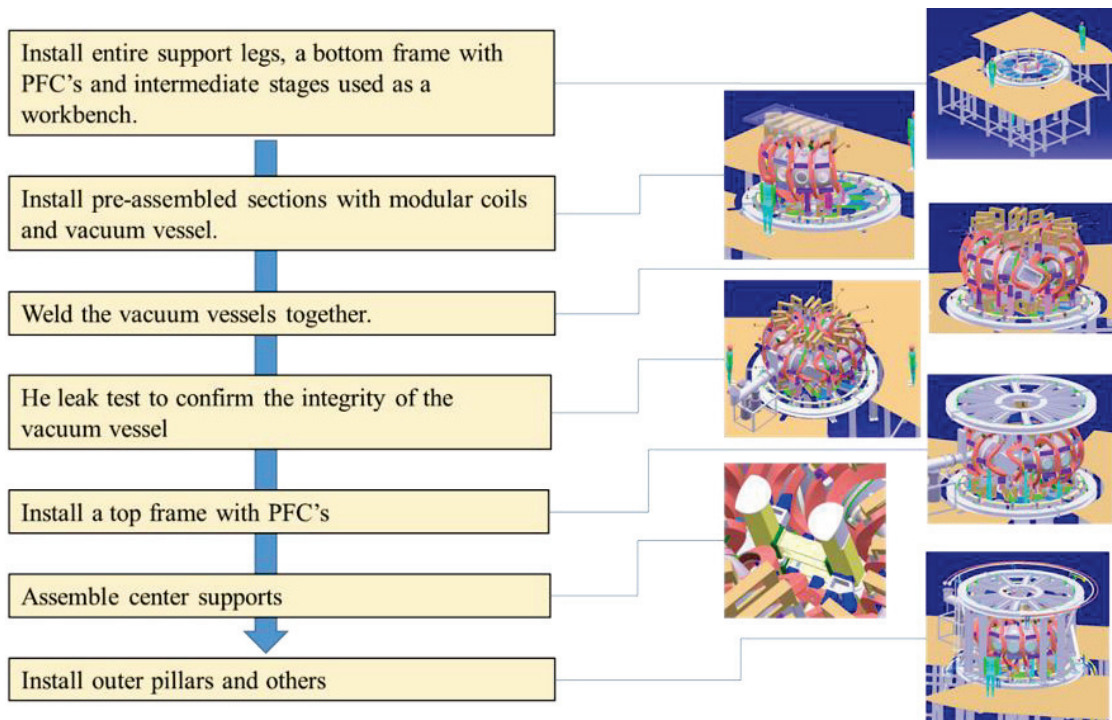


Fig. 4.1.3-2 Assembly flow on site.

4.2 Coil system

4.2.1 System configuration

Schematic of the coil system is shown in Fig. 4.2.1-1. It shows 16 modular coils (brown), 4 poloidal field coils (yellow) and 12 toroidal field coils (pink). The LCFS is shown in beige. A basic QA configuration can be produced by four types of modular coils with different shape. However, to allow flexible configuration, we will install four poloidal field coils (to move the magnetic axis horizontally) and twelve toroidal field coils (to change the rotational transform).

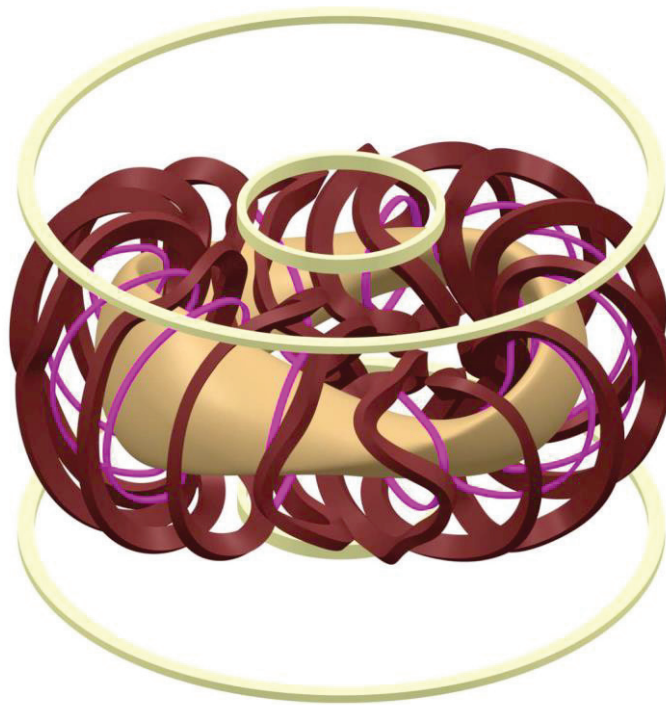


Fig. 4.2.1-1 Schematic of three coil systems.

4.2.2 Modular coil

Table 4.2.2-1 shows the main parameters of modular coil. Shapes of the modular coils are shown in Fig. 4.2.2-1 and their cross section is in Fig. 4.2.2-2. Since the current density is very high, the conductor temperature rises about 20 degrees per second of operation. To absorb this heat before next shot, the coils are cooled by pure water.

Very large magnetic forces are applied to the modular coils. The forces' magnitude and direction may be very complicated, and their characteristics are not easy to describe. They are like those of a tokamak's toroidal field coil, but the modular coils are more difficult to analyze and operated under more severe conditions because even the components that are negligible for tokamaks cannot be ignored. The strength of the coil conductor and insulation alone is not expected to be sufficient for large forces, it is reinforced with a SUS case like the tokamak's toroidal field coil.

The structure of the coil and the case is shown in Fig. 4.2.2-3. To reduce costs, the case is planned to consist of two parts, L shape plate and lid. The L shape plate has a barrier on the outside to interfere the coil when it is covered in the case. To solve this assembly concern, the modular coil shape is devised. Its design method is shown below.

- The center trajectory is calculated with the NESCOIL system.
- The cross-sectional area is defined in consideration of the limit of current density.
- The twisting angle of the normal vector for the current carrying surface (CCS) is optimized from the viewpoint of manufacturability.

We had checked first a design that a longer axis (the normal vector) was perpendicular to the CCS as shown in Fig. 4.2.2-4, and found a problem in the assembly process. We have optimized the angle to eliminate the interference problem, its result is shown in Fig. 4.2.2-5.

Fig. 4.2.2-6 shows joint of conductors. To reduce the number of power supplies, the three conductors are electrically connected in series outside the coil by the copper blocks of joint_1 and the joint_2. And in order not to increase the head loss of cooling water, the inlet and outlet of cooling water will be provided for each conductor. Therefore, the number of electric circuits is 1 per coil, and the number of cooling water flow paths is 3 per coil.

Table 4.2.2-1 Parameter for modular coil.

Category	Parameters	unit	MC1	MC2	MC3	MC4	Remarks
Electrical design	DH	mm	126	126	126	126	not include earth isolation
	DW	mm	63	63	63	63	not include earth isolation
	Number of coils		4	4	4	4	
	Cross-sectional area of conductor	mm ²	58.83	58.83	58.83	58.83	
	Turns	/coil	72	72	72	72	
	Length of conductors	m/turn	4.39	4.33	4.20	4.01	Obtained by CATIA
		m/coil	316	312	302	289	
	Resistance	mΩ	435.7	429.5	415.6	401.2	Obtained by Maxwell for 4 coils adding margin of 5%
	Inductance	mH	82.5	81.1	78.7	76.0	
Time constant	s	0.189	0.189	0.189	0.189		
Maximum operation voltage	kV	2.4	2.4	2.4	2.4	110% of the start-up voltage	
Cooling design	Number of cooling circuits	/coil	3	3	3	3	
	Length of cooling pipe	m	105.4	103.9	100.8	96.2	Average ; about 100m
	Flow velocity	m/s	1.9	1.9	1.9	1.9	
	Flow rate	m ³ /s	2.39E-05	2.39E-05	2.39E-05	2.39E-05	
	Loss head	m	185.1	182.5	177.0	168.9	Hazen Williams' equation
Pulse operation	Current	kA/turn	4.34	4.34	4.34	4.34	Current wave form
	Current density	A/mm ²	73.8	73.8	73.8	73.8	startup exponential
	Start-up voltage	kV	2.151	2.119	2.052	1.981	Flattop constant
	Flat-top voltage	kV	1.891	1.864	1.804	1.741	Damping exponential
	Decay voltage	kV	0.997	0.985	0.95	0.918	
	Discharge period	s	300	300	300	300	
	Current rise time	s	0.4	0.4	0.4	0.4	
	Flat top time	s	0.6	0.6	0.6	0.6	
	Stored magnetic energy	MJ	0.777	0.764	0.742	0.715	0.5LI ²
	Energy consumption	MJ	9.144	9.014	8.718	8.418	integral(RI ²)
	Rectangular wave equivalent time	s	1.114	1.114	1.114	1.114	
	Maximum PS power	MW	9.338	9.194	8.905	8.596	
	Adiabatic temperature rise	k	35.8	35.8	35.8	35.8	In a short pulse
Time averaged current	kA/turn	0.264	0.265	0.264	0.264		
Time averaged current density	A/mm ²	4.496	4.497	4.495	4.496		
Steady operation	Current	kA/turn	0.434	0.434	0.434	0.434	
	Current density	A/mm ²	7.38	7.38	7.38	7.38	
	Voltage	kV	0.189	0.186	0.18	0.174	
	Stored magnetic energy	MJ	7.77E-03	7.64E-03	7.41E-03	7.15E-03	0.5LI ²
	PS power for flat top	kW	82.0	80.7	78.1	75.5	
	Average temperature rise	k	68.7	67.6	65.4	63.2	
	Start-up voltage	kV	0.227	0.224	0.216	0.209	Assumed roughly 120% of the flat top.

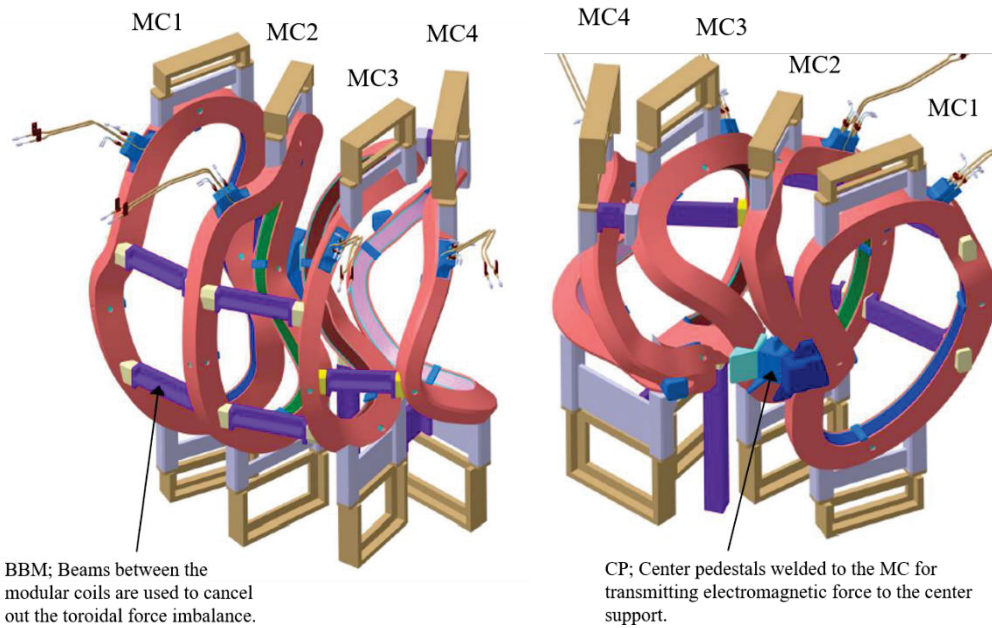
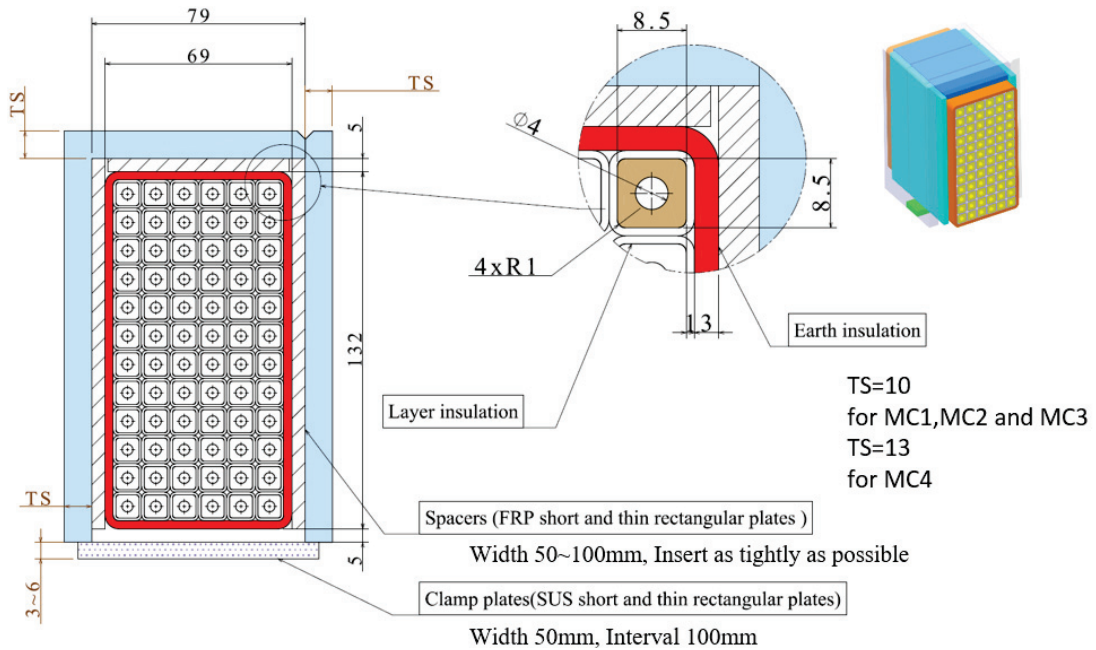
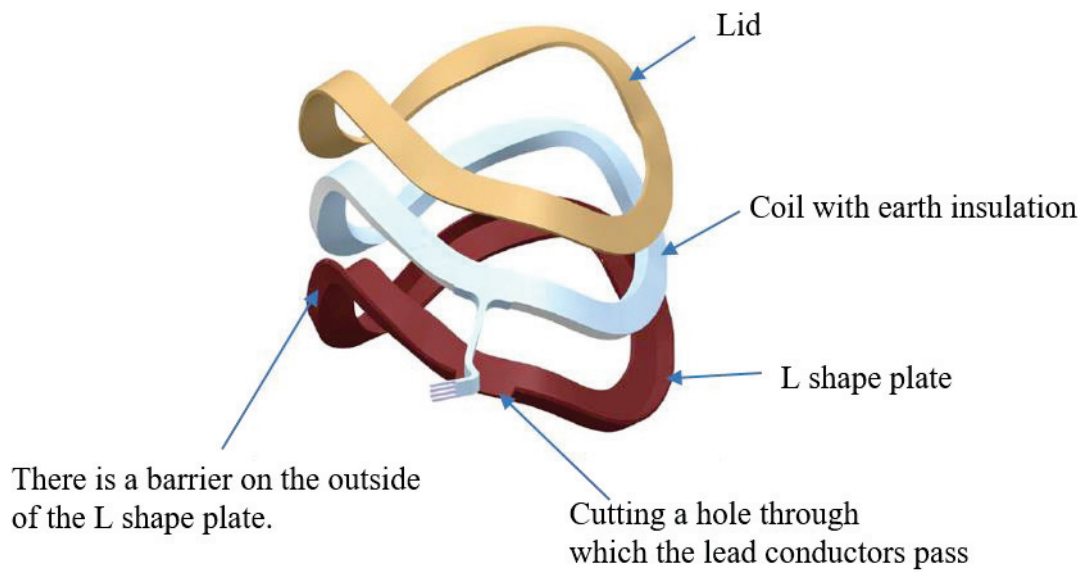


Fig. 4.2.2-1 Modular coil system, showing legs, SUS cases, current leads, BBM, and CP.



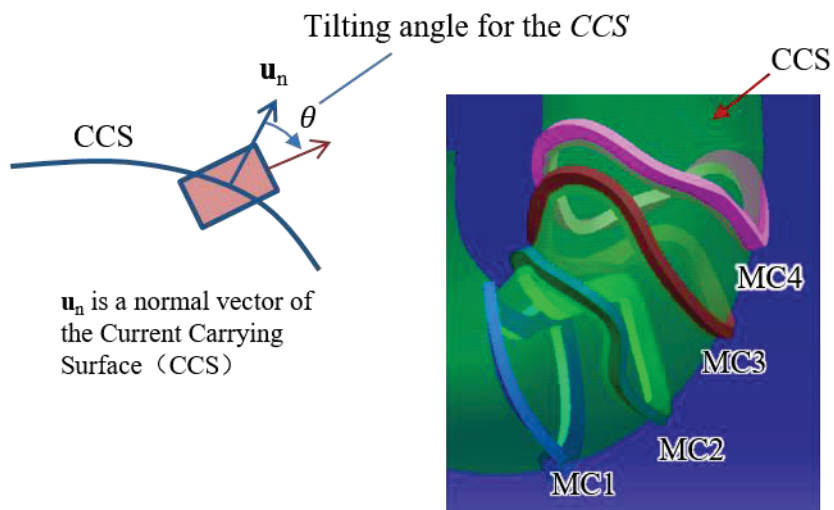
A coil is covered in two plates (blue, L shape plate and lid) which are joined by welding. Some FRP spacers (hatting) are inserted for adjusting gap. The clamp plates are added to reinforce of the coil case and prevent the lid plate from opening.

Fig. 4.2.2-2 Cross section of the modular coil.



The barrier of the L shape plate may interfere with the coil when it is put in the case.

Fig. 4.2.2-3 Coil case and coil with insulation.



The tilting angle θ should be designed to prevent the coil from touching the case.

Fig. 4.2.2-4 Normal direction of the rectangular cross section.

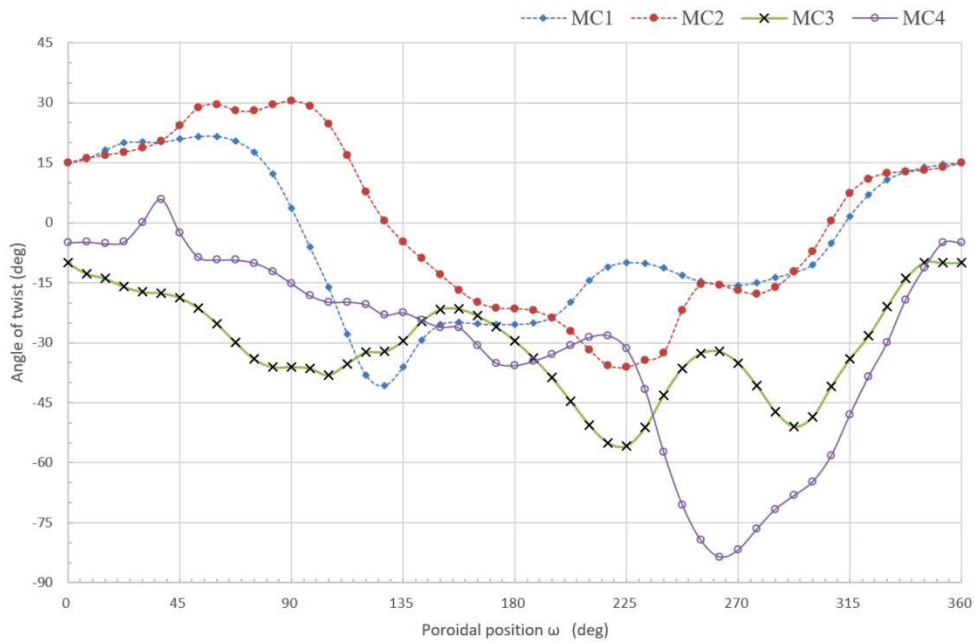


Fig. 4.2.2-5 Twisting angle of the cross-section.

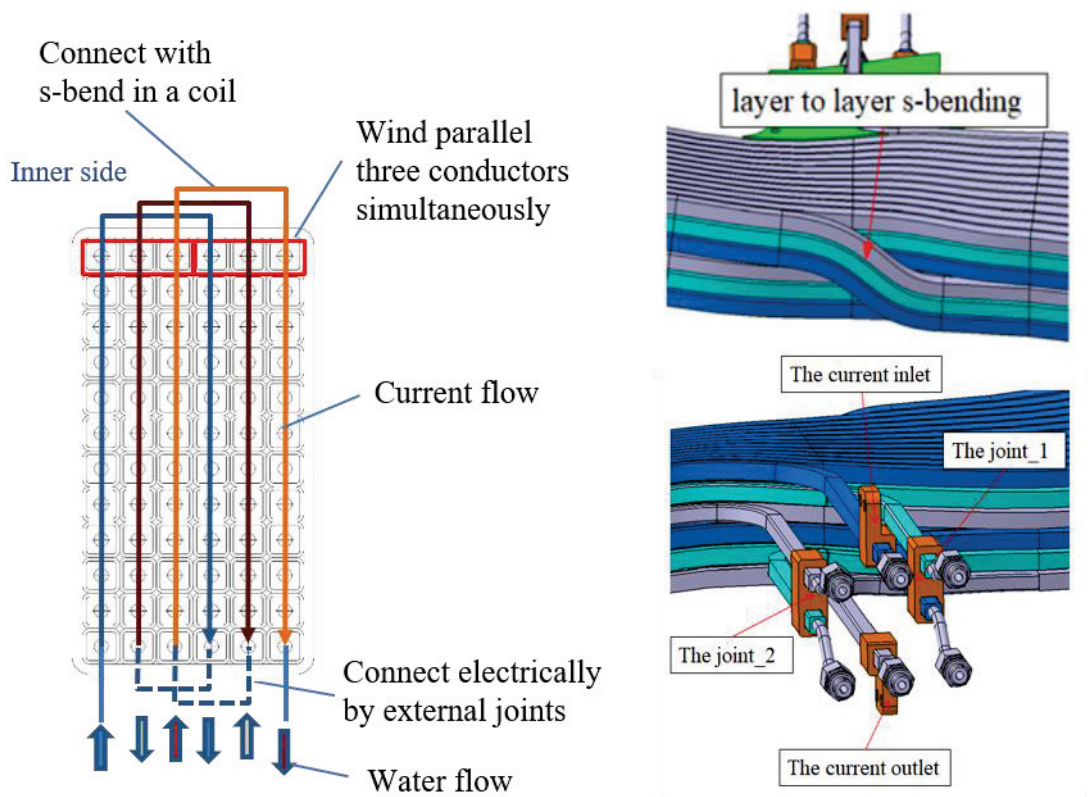


Fig. 4.2.2-6 Joints for the modular coil conductor.

Fig. 4.2.2-7 shows coil leads and coil support with coil case. Shape of the coil lead is not easy to decide properly in a desk study, because it is necessary to bend intricately considering interference with peripheral parts and fixing place. Therefore, the conductor shape will be adjusted according to the surrounding structure during installation. To prepare for this, leave 500 mm to 800 mm as an extra length and cut the conductor at an appropriate place during installation. After adjusting the length and bending them, the go and return conductors are wrapped with glass tape and fixed with a resin. Pedestals for transmitting electromagnetic force to the support structure are welded on the coil case, but the contact surfaces will be machined to ensure the accuracy. Since the coil position is adjusted during installation, leave a peep hole in the coil case so that the reference markers on the coil insulation can be recognized.

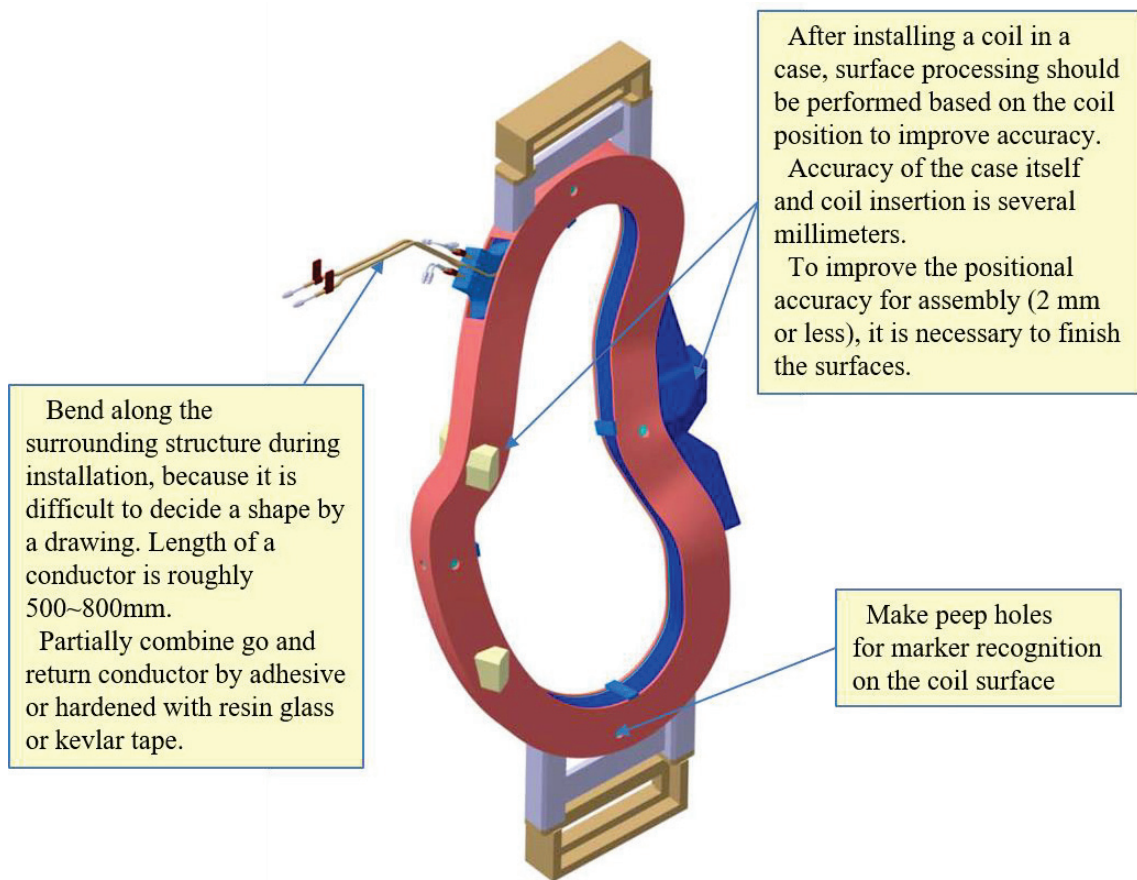


Fig. 4.2.2-7 Structure of the current leads and the coil case, and manufacturing procedure.

4.2.3 Poloidal field coil

Two pairs of PFCs will be installed to the CFQS. Main purpose of poloidal field coils is to apply vertical field to change the position of magnetic axis. Parameters of poloidal field coils are shown in Table 4.2.3-1. Layout and cross section of the PFCs are shown in Fig. 4.2.3-1 and Fig. 4.2.3-2. As shown in the figures, the PFC is 32-turn water cooled coil, IV is solenoid wound and OV is pancake wound.

The vertical magnetic field necessary for plasma control is not clear. We assume 10% of total modular coil current as a design specification for the PFC.

Table 4.2.3-1 Parameters of PFCs.

Category	Parameters	unit	IV	OV	Remarks
Electrical design	R		0.536	1.695	
	DR	mm	48	90	not include earth isolation
	DZ	mm	90	48	not include earth isolation
	Number of coils		2	2	
	Cross-sectional area of conductor	mm ²	58.83	58.83	
	Turns	/coil	32	32	
	Length of conductors	m/turn	3.40	10.60	
		m/coil	108.8	339.2	
	Resistance	mΩ	73.0	230.6	
	Inductance	mH	5.00	18.85	
	Time constant	s	0.068	0.082	
Maximum operation voltage	kV	0.6	2.2		
Heat resistance class		A	A		
Cooling design	Number of cooling circuits	/coil	1	2	
	Length of cooling pipe	m	108.8	169.6	
	Flow velocity	m/s	1.9	1.5	
	Flow rate	m ³ /s	2.39E-05	1.88E-05	
	Loss head	m	191.1	192.3	Hazen Williams' equation
Pulse operation	Current	kA/turn	4.34	4.34	Current wave form
	Current density	A/mm ²	73.8	73.8	startup exponential
	Start-up voltage	kV	0.413	1.418	Flat top constant
	Flat-top voltage	kV	0.317	1.001	Damping exponential
	Decay voltage	kV	0	0	
	Discharge period	s	300	300	
	Current rise time	s	0.1	0.1	
	Flat top time	s	0.3	0.3	
	Stored magnetic energy	MJ	0.047	0.178	0.5LI ²
	Energy consumption	MJ	0.523	1.671	integral(RI ²)
	Rectangular wave equivalent time	s	0.380	0.385	
	Maximum PS power	MW	1.79	6.151	
	Adiabatic temperature rise	k	12.21	12.36	In a short pulse
Time averaged current	kA/turn	0.155	0.155		
Time averaged current density	A/mm ²	2.627	2.642		
Steady operation	Current	kA/turn	0.3	0.3	
	Current density	A/mm ²	5.10	5.10	
	Voltage	V	21.9	69.18	
	Stored magnetic energy	MJ	2.25E-04	8.48E-04	0.5LI ²
	PS power for flat top	kW	6.6	20.8	
	Average temperature rise	k	33.0	66.0	
	Start-up voltage	kV	26.28	83.016	Assumed roughly 120% of the flat top.

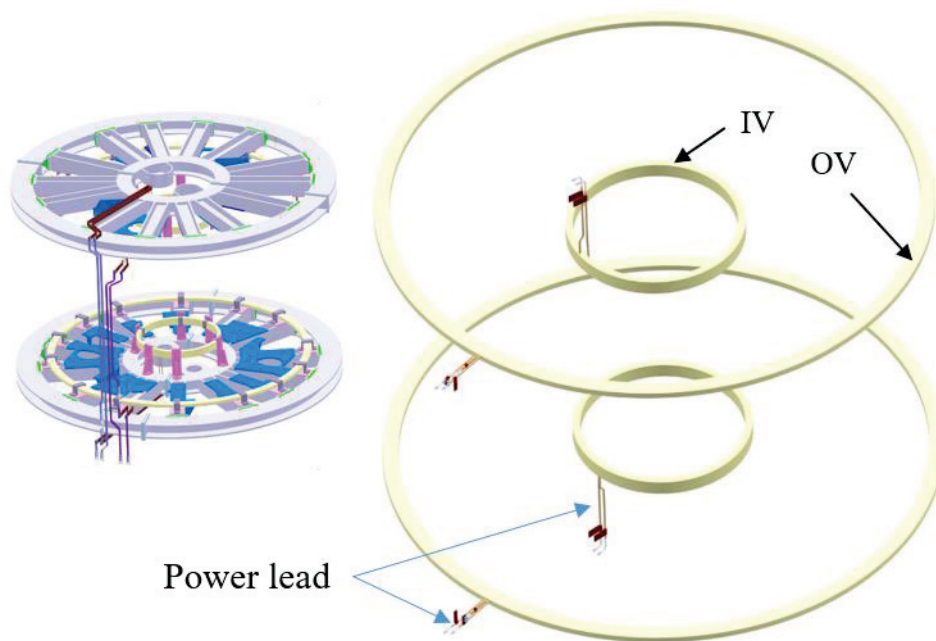


Fig. 4.2.3-1 Layout of poloidal field coil system.

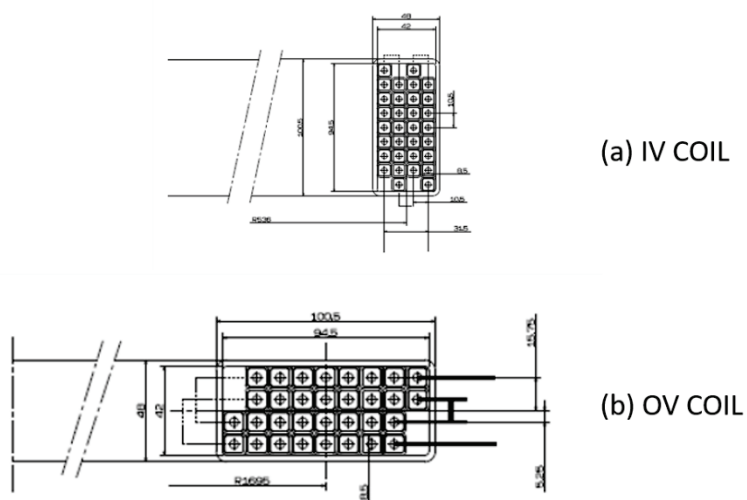


Fig. 4.2.3-2 Cross section of the poloidal field coils.

4.2.4 Toroidal field coil

Auxiliary TFCs will be installed to CFQS to control the rotational transform. At present design, we have designed total of 12 TFCs with three types. Parameters of TFCs are shown in Table 4.2.4-1. The shape of the coil and the position of the current lead are shown in Fig. 4.2.4-1 to Fig. 4.2.4-3. They have been designed to wind a solid conductor directly on the vacuum vessel (VV) by the solenoid wind method. The coil installation space is not enough, so we decided to use a design to be cooled by heat conduction from the VV without water cooling.

Table 4.2.4-1 Parameters of TFCs.

Category	Parameters	Unit	TFC10	TFC32	TFC70
Electrical design	DH	mm	10	10	10
	DW	mm	54	54	54
	Number of coils		4	4	4
	Cross-sectional area	mm ²	19.0	19.0	19.0
	Turns	/coil	16	16	16
	Length of conductors	m/turn	3.390	3.150	2.588
		m/coil	54.2	50.4	41.4
	Resistance	mΩ	228.1	210.0	173.6
	Inductance	mH	3.000	2.700	2.160
	Time constant	s	0.013	0.013	0.012
	Maximum operation voltage	kV	0.6	0.6	0.6
	Test voltage	kV	2.2	2.2	2.2
Heat resistance class		B	B	B	
Cooling design	Number of cooling circuits	/coil	0	0	0
	Length of cooling pipe	m	0	0	0
	Flow velocity	m/s	0	0	0
	Loss head	m	0	0	0
Pulse operation	Current	kA/turn	2.17	2.17	2.17
	Current density	A/mm ²	114.2	114.2	114.2
	Start-up voltage	kV	0.507	0.465	0.384
	Flat top voltage	kV	0.495	0.456	0.377
	Decay voltage	kV	0.000	0.000	0.000
	Discharge period	s	300	300	300
	Current rise time	s	0.05	0.05	0.05
	Flat top time	s	0.15	0.15	0.15
	Stored magnetic energy ($0.5 LI^2$)	MJ	0.007	0.006	0.005
	Energy consumption (integral (RI^2))	MJ	0.203	0.187	0.154
	Rectangular wave equivalent time	s	0.189	0.189	0.189
	Maximum PS power	MW	1.100	1.009	0.832
	Adiabatic temperature rise in a pulse	k	14.5	14.5	14.5
Time averaged current	kA/turn	0.054	0.054	0.054	
Time averaged current density	A/mm ²	2.864	2.865	2.866	

The TFC was designed according to the following policy.

- Shortening the pulse width reduces the temperature rise in a shot because there is not enough space to install water cooled coil. If the temperature rise is large, the experiment on that day

- will be stopped when the maximum temperature exceeds 90 °C.
- Increasing the number of turns and reducing the current to make the leads thinner because there is no space to thick current leads.
 - It is difficult to determine the wiring route by design because it must pass through a complicated and narrow gap between modular coils. Therefore, the wiring route should be adjustable according to the actual product. The insulated wire as the current lead and the coil may be connected by solderless terminals.
 - The total current is about 8 % of the modular coil

It is obvious that the water-cooled coil is desirable to realize the low magnetic field long-time operation. For that purpose, it is necessary to increase the coil cross-sectional area, which makes winding difficult and there is a concern that the TFC may interfere with the MC. In addition, the development of a water-cooled current lead, which should be thin and flexible as in the current design, will not be easy. Originally, the TFC was supposed to be an experiment with a short pulse, so it was judged that the experiment could be performed with natural air cooling. However, we want to expect cooling due to heat conduction from the VV, so we plan to design the TFC insulation as thin as possible.

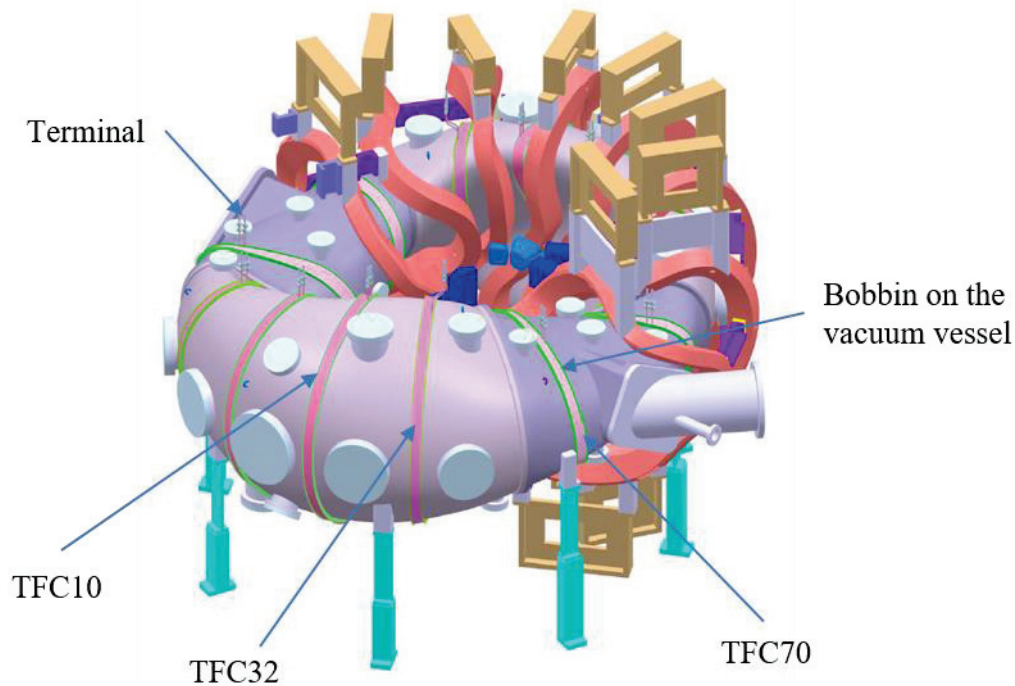


Fig. 4.2.4-1 Schematic of TFC.

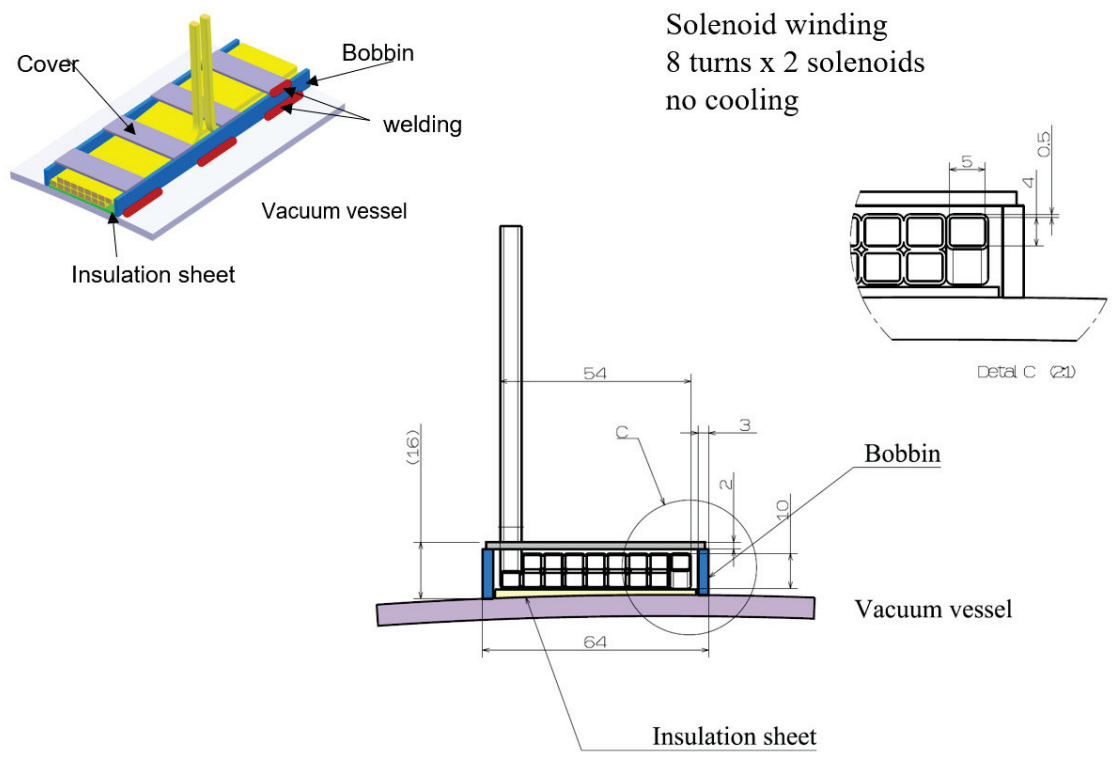


Fig. 4.2.4-2 Cross section of TFC.

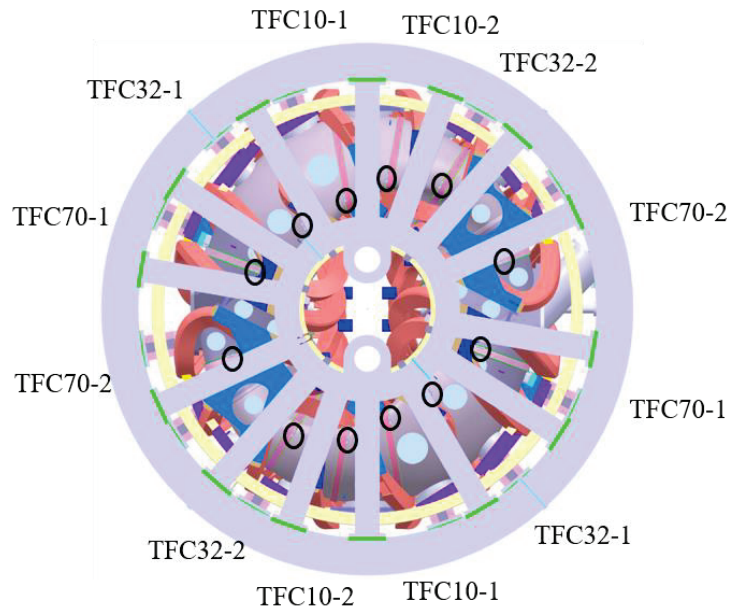


Fig. 4.2.4-3 Terminal position of the TFC.

4.3 Vacuum vessel

4.3.1 Structure of main vacuum vessel

Fig. 4.3.1-1 shows a schematic of the main VV, which will be manufactured by welding together four sections of two types in the toroidal direction. It is supported by eight leaf type legs. The flanges used for welding are also shown in the figure. Since the electromagnetic forces on the VV are expected to be small, it will be fabricated from SUS316L with relatively thin walls of 6 mm.

As a result, the one-turn resistance is roughly 0.3 mΩ which we believe to be sufficiently large while not producing significant joule heating. The walls will be conditioned by baking them at 130-150 °C via sheath heaters.

The main VV is fixed on the cage-type support structure by eight leaf-type legs, added to allow for the VV's thermal expansion during baking. It also has twelve winding bobbins to wind the TFCs.

The shape of inner surface is shown in Fig. 4.3.1-2. The cross-sectional area is much larger than that of the 2b32 reference surface that is defined for the island bundle divertor experiment, and minimum space required from a physical point of view. The LCFS of standard 2b40 equilibrium is narrower than the 2b32 surface. The minimum gap between the 2b32 plane and the inner surface of main VV is about 30 mm. Please refer to Appendix-A 3.1 of this booklet for the specific shape of main VV at different toroidal angles.

Dimension of VV is shown in Fig. 4.3.1-3. The width and height of the inner surface are both at least 450 mm, which is sufficient for people to work inside. Using such a large VV also helps to make the experiment more flexible.

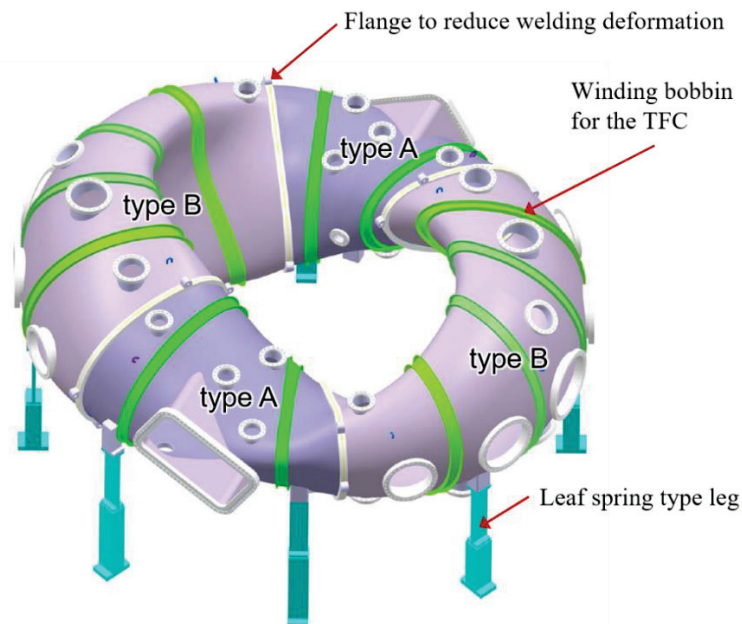
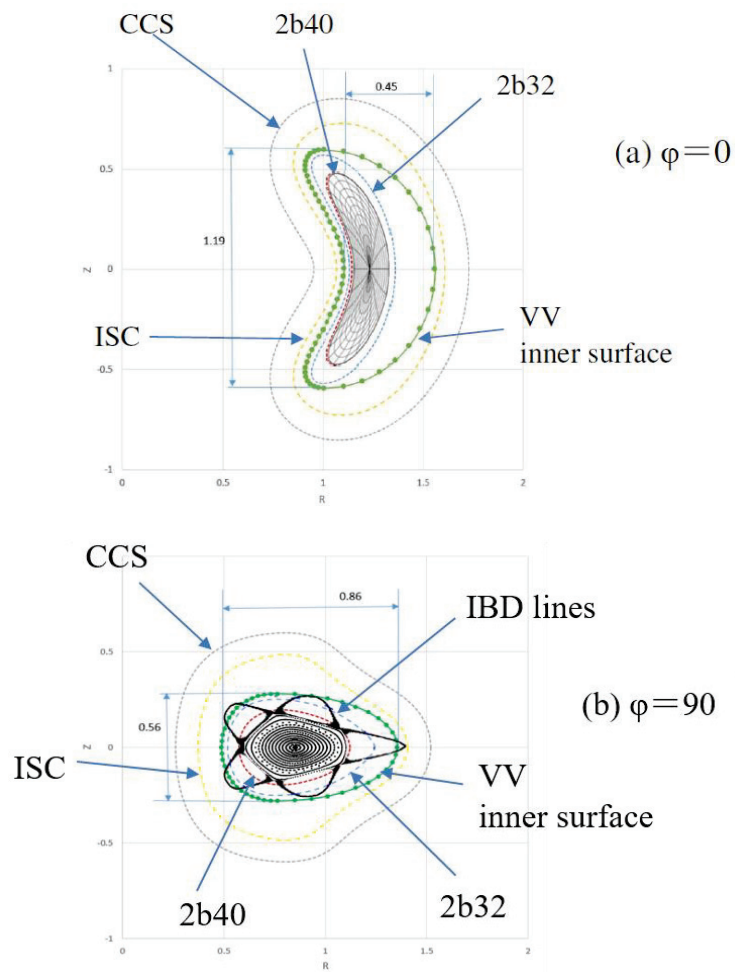


Fig. 4.3.1-1 Schematic of the VV.



- 2b40 shows an LCFS of the standard equilibrium,
- 2b32 shows a reference surface of the IBD configuration (aspect ratio;3.2),
- CCS shows the current carrying surface on which the center of modular coil is placed,
- ISC shows an innermost peripheral surface of the modular coil,
- IBD shows the island bundle divertor configuration.

Fig. 4.3.1-2 Cross section of the main VV inner surface.

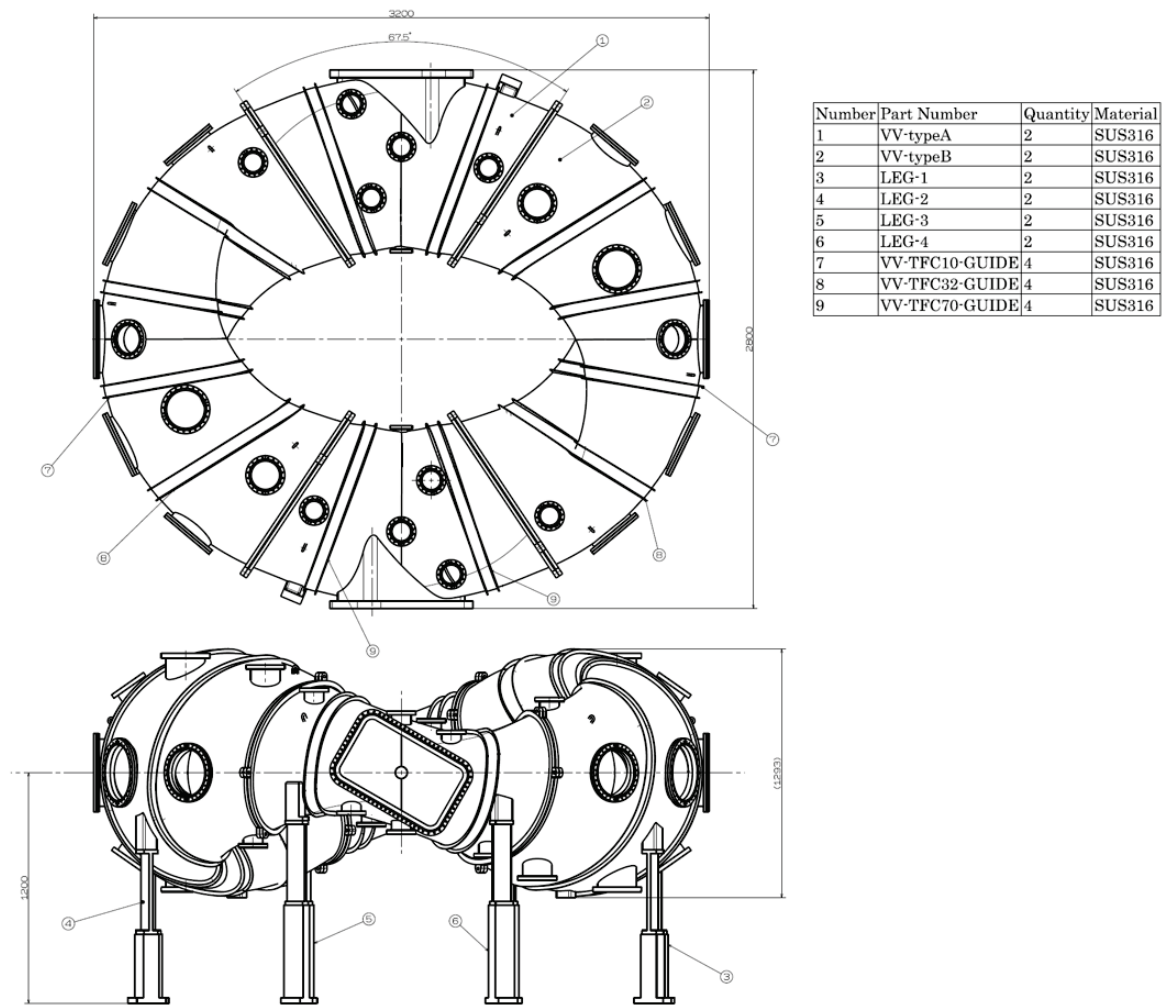


Fig. 4.3.1-3 Dimension of the VV.

4.3.2 Port arrangement

More than 42 large ports with a diameter of at least 114 mm, will be provided for heating and measurement. Two of them are large rectangular ports with an opening diameter (inner size) of 340 mm × 580 mm, both for a worker to enter, for NBI, and for Thomson scattering diagnostics. As small ports of 70 mm or less in diameter are unexamined, there is a possibility that they can be added in the future if it will be necessary for the experiment. Table 4.3.2-1 and Fig. 4.3.2-1 show the port list and their positions.

The design goal or policy to define ports as follows.

- Make it possible to divert as many CHS assets as possible.
- Allow one worker to enter the VV and work inside.
- To weld together split places of the VV.
- To install measurement equipment like magnetic probes.
- To install some plates to protect VV from heat.
- Establish as many and large ports as possible to make the experiment more flexible.

To achieve this purpose, we examined the location and size of the ports. However, small ports with a diameter of 70 mm or less may not be considered and may be increased further.

Table 4.3.2-1 Port list.

No	Name	Flange size	Center position			Note	Old name
			Φ	Height	Radius		
1	I-090	$\Phi 114$	90	0	450	n_e (μ wave)	I5
2	I-270	$\Phi 114$	270	0	450	Thomson	I13
3	O-000U	$\Phi 203$	0	55°	565	not penetrate	O1U
4	O-000	$\Phi 406$	0	0	1600		O1
5	O-000L	$\Phi 203$	0	-55°	565	not penetrate	O1L
6	O-023	$\Phi 356$	22.5	0	1570		O2
7	O-045	$\Phi 305$	45	0	1500	Vacuum pump	O3
8	O-090S	440×680	90	0	1400	NBI and n_e (μ wave)	O5
9	O-135	$\Phi 305$	135	0	1500		O7
10	O-158	$\Phi 356$	157.5	0	1570		O8
11	O-180U	$\Phi 203$	180	55°	565	not penetrate	O9U
12	O-180	$\Phi 406$	180	0	1600	ECRH	O9
13	O-180L	$\Phi 203$	180	-55°	565	not penetrate	O9L
14	O-203	$\Phi 356$	202.5	0	1570		O10
15	O-225	$\Phi 305$	225	0	1500	HIBP	O11
16	O-270S	440×680	270	0	1400	Thomson	O13
17	O-315	$\Phi 305$	315	0	1500		O15
18	O-338	$\Phi 356$	337.5	0	1570		O16
19	U-018	$\Phi 253$	18	620	1180		U1.5
20	U-045	$\Phi 203$	45	560	1000	CXRS & MSE	U3
21	U-063	$\Phi 152$	63	440	1000	not penetrate	U4
22	U-090	$\Phi 152$	90	320	1000	vertical through	U5
23	U-102IN	$\Phi 152$	102	280	750	not penetrate	U5.5a
24	U-102	$\Phi 152$	102	220	1250		U5.5
25	U-130	$\Phi 152$	130	390	1200		U7
26	U-198	$\Phi 253$	198	620	1180		U9.5
27	U-225	$\Phi 203$	225	560	1000	HIBP	U11
28	U-243	$\Phi 152$	243	440	1000	not penetrate	U12
29	U-270	$\Phi 152$	270	320	1000	vertical through	U13
30	U-282IN	$\Phi 152$	282	280	750	not penetrate	U13.5a
31	U-282	$\Phi 152$	282	220	1250		U13.5
32	U-310	$\Phi 152$	310	390	1200		U15
33	L-050	$\Phi 152$	50	-390	1200		L3.5
34	L-078	$\Phi 152$	78	-220	1250		L4.5
35	L-078IN	$\Phi 152$	78	-280	750	not penetrate	L4.5a
36	L-090	$\Phi 152$	90	-320	1000	vertical through	L5
37	L-117	$\Phi 152$	117	-440	1000	not penetrate	L6
38	L-135	$\Phi 203$	135	-560	1000	CXRS(ref)	L7
39	L-162	$\Phi 253$	162	-620	1180		L8
40	L-230	$\Phi 152$	230	-390	1200		L11.5
41	L-258	$\Phi 152$	258	-220	1250		L12.5
42	L-258IN	$\Phi 152$	258	-280	750	not penetrate	L12.5a
43	L-270	$\Phi 152$	270	-320	1000	vertical through	L13
44	L-297	$\Phi 152$	297	-440	1000	not penetrate	L14
45	L-315	$\Phi 203$	315	-560	1000		L15
46	L-342	$\Phi 253$	342	-620	1180		L16

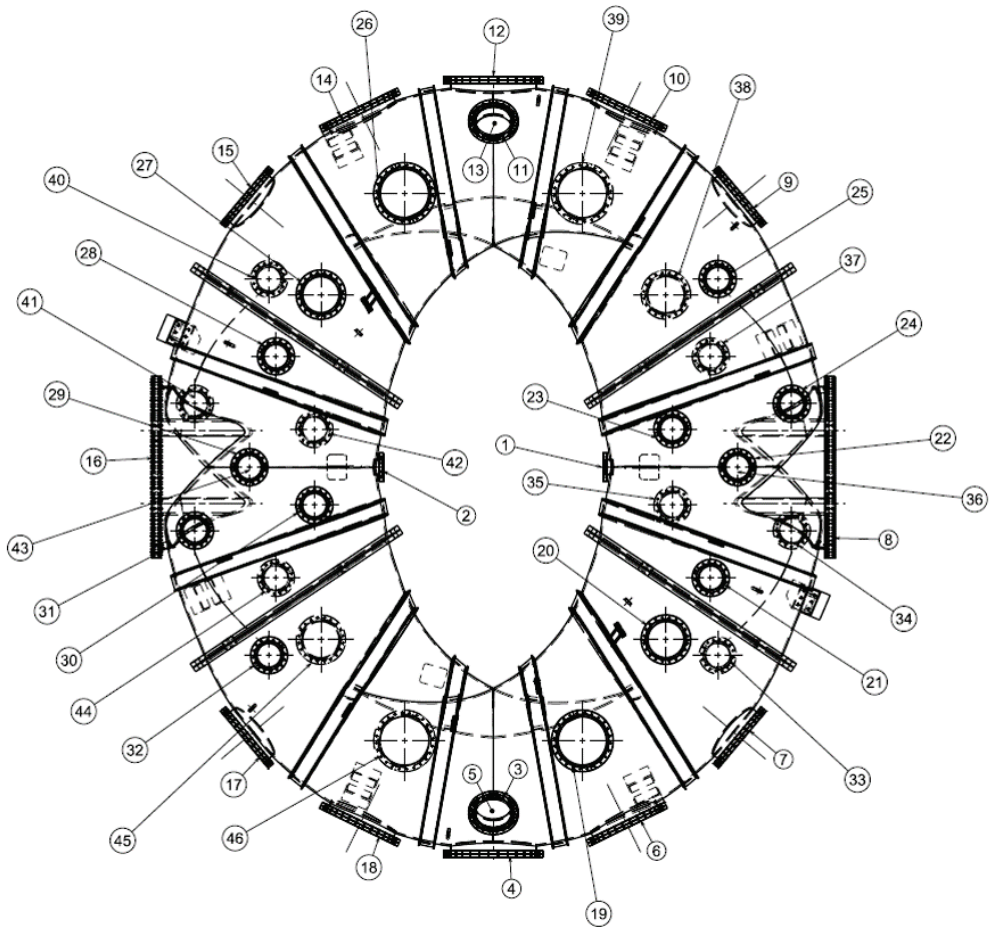


Fig. 4.3.2-1 Port arrangement.

4.4 Another component

4.4.1 External current lead

The 32 coils will be installed in the CFQS, but it is not realistic to wire all those current leads to a control power supply room because very large space is necessary. We think that it is preferable to connect the coils with copper bus bar near the CFQS body to minimize space of the wiring and to reduce cost. Busbars save space but are difficult to design because they are inflexible. Fig. 4.4.1-1 shows wiring plan of the current lead. The water-cooling coils of PFC and MC are connected by copper busbars and flat braid flexible terminals which may absorb thermal displacement and assembly error. The TFCs with complicated wiring routes are connected by flexible electric wires covered with insulation coating.

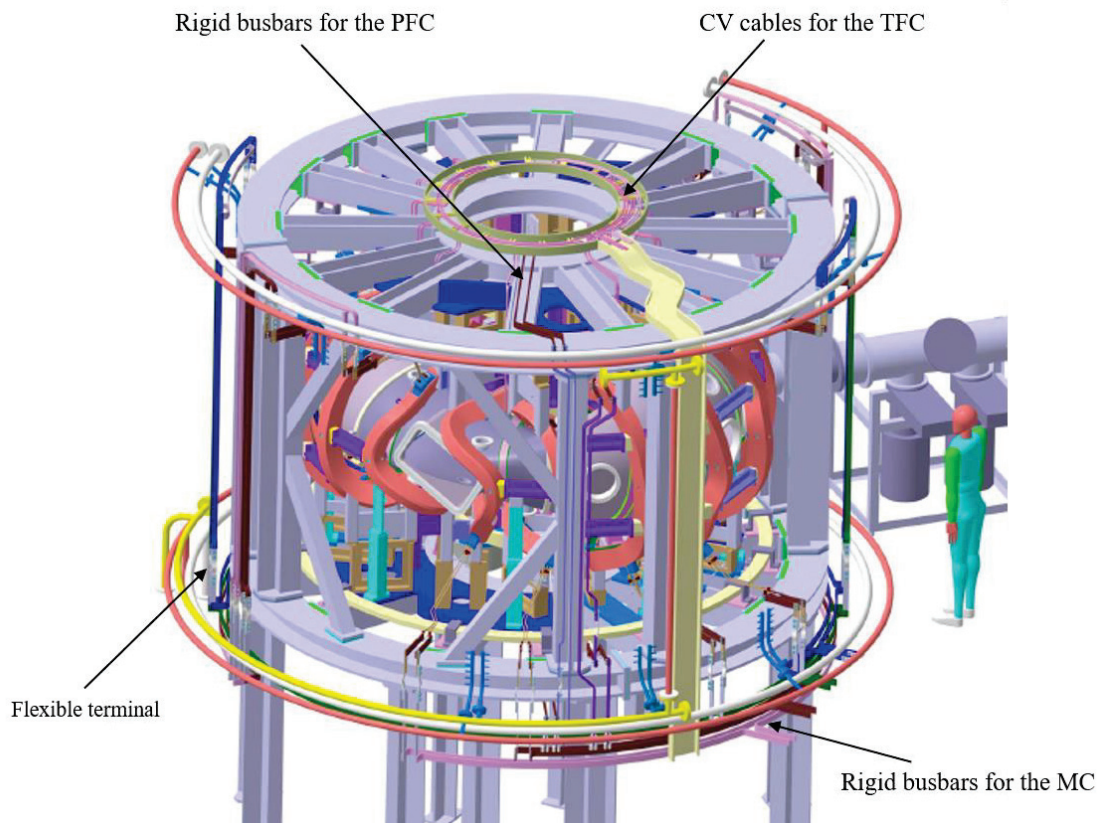


Fig. 4.4.1-1 External current leads for coils.

4.4.2 Supporting structure

The cage type support structure and the cooling water pipes are shown in Fig. 4.4.2-1. A cage type structure prevents deformation of the modular coils. It also has, among other components, a VV, other coils, and a diagnostic system attached on it.

Large tokamaks are typically designed with TFC wedges to support the centripetal forces. Since the CFQS cannot take this approach due to shape of constraints, it instead absorbs such a large force with some pedestals (PRF) and the central connection board (CCB). There is a big rectangular hole in it to access the inside port on the VV.

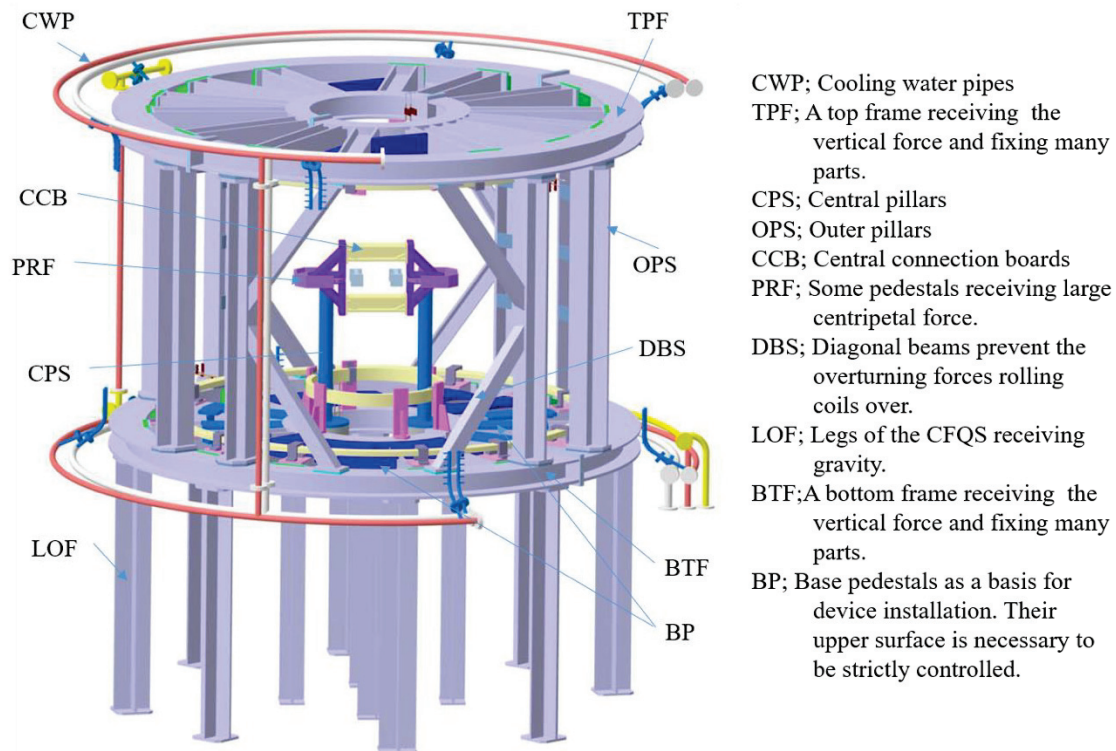


Fig. 4.4.2-1 Cage type support structure.

A cage type structure with diagonal beams (DBS) that prevents deformation of the modular coils by the overturning moments or vertical forces and handle the entire load. For use in future NBI experiments, we adopted a design that does not have pillars (OPS) around the large rectangular ports. Instead, the open spaces are surrounded with the diagonal beams. The central connection boards (CCB) absorb the large force mainly the centripetal component with the pedestals (PRF). The central pillars (CPS) are installed to support the PRFs during assembly work.

The base pedestals (BP) are flat plates on which the VV and the modular coils are installed. Their upper surface becomes the installation reference for other parts, so it should be strictly controlled, such as improving flatness by machining and marking reference points for coil placement.

4.4.3 Cooling water pipe

To cool the coils, it is necessary to disperse 108 cooling pipes (hoses) around the CFQS. The size and arrangement of a manifold (an assembly of branch pipes) for connecting them to the cooling water device are determined as shown in Fig. 4.4.3-1.

Design policy and requirement are as follows.

- Flow rate in a manifold; 5 m³/hr for the MC and 1 m³/hr for the PFC.
- Material; SUS304 or SUS316 pipe with Sch20 (Maximum pressure=2 MPa or more).
- Loss head in a manifold; 10 m or less.
- A welding flange with gasket seal is used to improve reliability. Do not use screw-in flange.
- Provide a function to adjust the flow rate and monitor flow rate for each type of coil. It is not necessary to adjust the flow rate for each channel for cost reduction. The flow rate in each channel will be measured by a portable ultrasonic flow meter, and the flow balance between channels is adjusted by an orifice or the like.
- Fix c-shaped manifold extended in the toroidal direction on the support frame.
- Connect the manifold and coil with insulated nylon or PFA hose with a heat resistance of 100 °C or higher. Applying metal reinforced hose is prohibited because high voltage is applied to the coil.

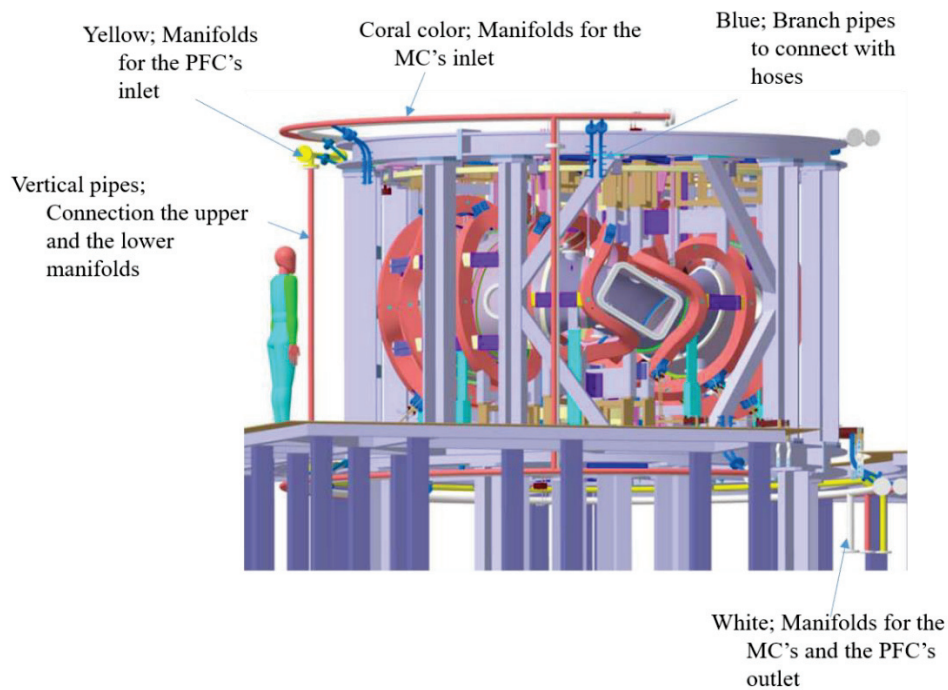


Fig. 4.4.3-1 Cooling water pipe.

4.4.4 Baking heater for vacuum vessel

For baking of the VV, we will wind some sheath heaters on the VV surface. Total required baking power for CFQS VV is estimated approximately 25 kW. The power is referred by CHS baking system since the volume of the CFQS VV is almost equivalent to that of CHS.

Baking regions are distinguished 8×2 sections based on 12 Toroidal field coils (TFC) and 4 flanges to connect 4 sections as shown in Fig. 4.4.4-1. Each heater is wound separately so as not to leap over them, and has its own power system to make it easier to control the temperature. Each baking heater winding route is arranged as shown in Fig. 4.4.4-2. The heating capacity of each section was set so that the amount of heat per unit mass was almost constant. Diameter of each sheath heater is 4.8 mm and its resistance is 1.55 Ω/m . The heater length was estimated from the 3-D CAD model of Fig. 4.4.4-2. It is mounted on the surface of VV with an interval of about 100 mm. Table 4.4.4-1 shows the specification of the baking heaters, such as heater length, required capacity and voltage.

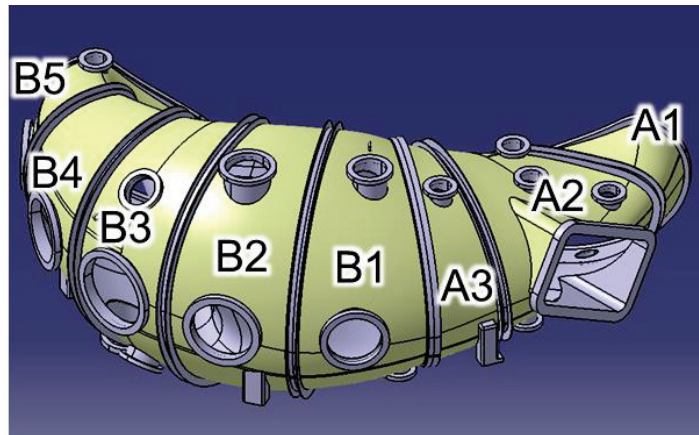


Fig. 4.4.4-1 Divided region of the VV.

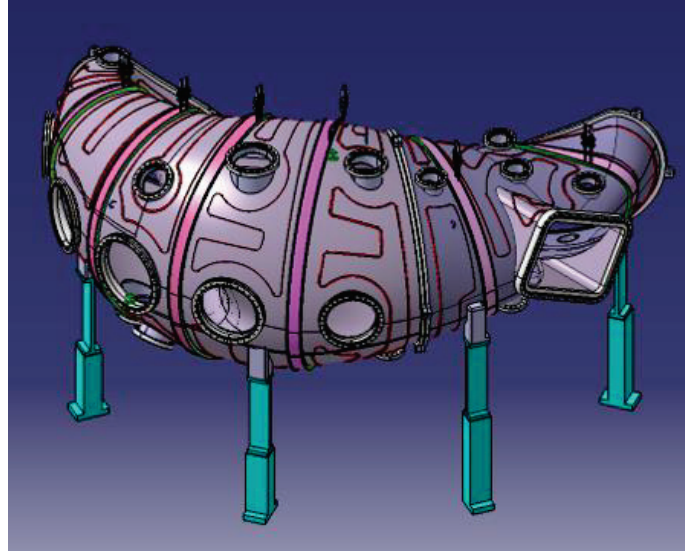


Fig. 4.4.4-2 Preliminary winding route design.

Table 4.4.4-1 Specification of baking heaters.

Region	Required capacity [kW]	Heater length [m]	Resistance [Ω]	Maximum voltage [V]	Maximum current [A]	Heating capacity [kW]
A1	0.98	4.8	7.4	110	14.8	1.6
A2	2.42	11.3	17.6	220	12.5	2.8
A3	1.05	4.8	7.4	110	14.9	1.6
B1	1.67	10.1	15.7	220	14.0	3.1
B2	1.63	10.7	16.7	220	13.2	2.9
B3	1.46	11.6	18.0	220	12.2	2.7
B4	1.62	10.9	16.9	220	13.0	2.9
B5	1.67	10.1	15.7	220	14.0	3.1
Sum	12.5	74.3				20.7
Diameter of each sheath heater is 4.8 mm and its resistance is 1.55 Ω /m.						

4.5 Verification of design

4.5.1 Numerical analysis of the modular coil and the support structure

A strong support structure is necessary for keeping device in a safety state during operation. As for magnetic confinement fusion device, the electromagnetic (EM) force is the main load on coil system, which is the key component of whole device. Therefore, we need to understand the EM force on coil system and then design a reliable support structure.

There are three types of coils in CFQS, modular coil, poloidal field coil and toroidal field coil. The modular coil is a major part of coil system. It has the most complicate shape and largest total current, so our analysis mainly focuses on them. We have confirmed the design validity of the modular coil system and mechanical support structure by the numerical analysis with the ANSYS Mechanical and the ANSYS Maxwell.

Fig. 4.5.1-1 shows a 3-D model for the analysis. Stress distribution on the support structure with the EM force is shown in the Fig. 4.5.1-2. It is obvious that the maximum stress on the supporting structure is about 100 MPa that is less than the design guideline for the CFQS.

The detail of the electromagnetic force and the structural analysis are shown in Appendix-A 2.6 and 2.9.

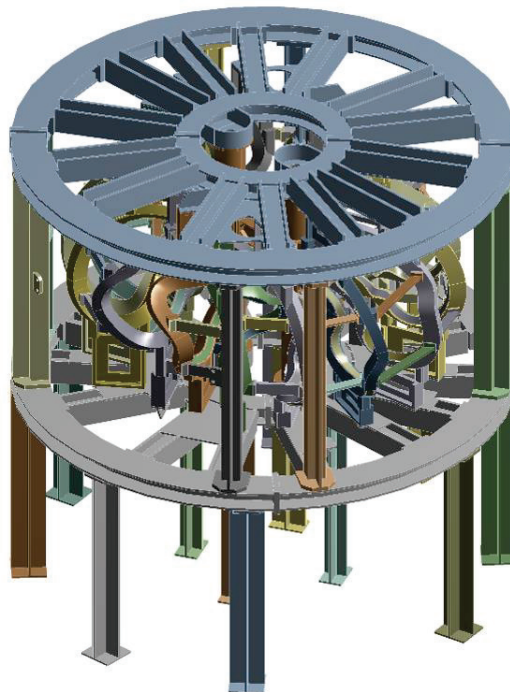
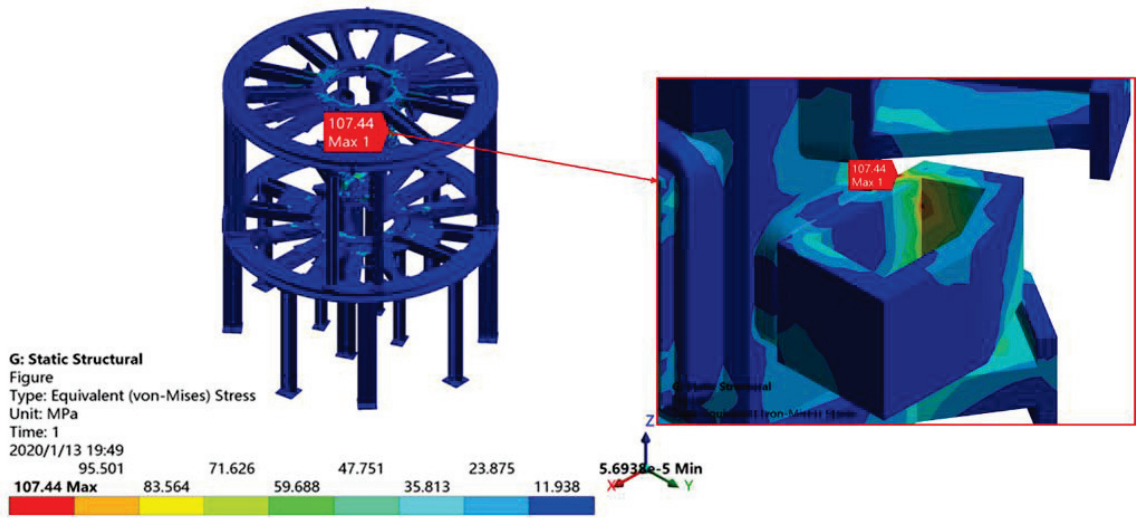
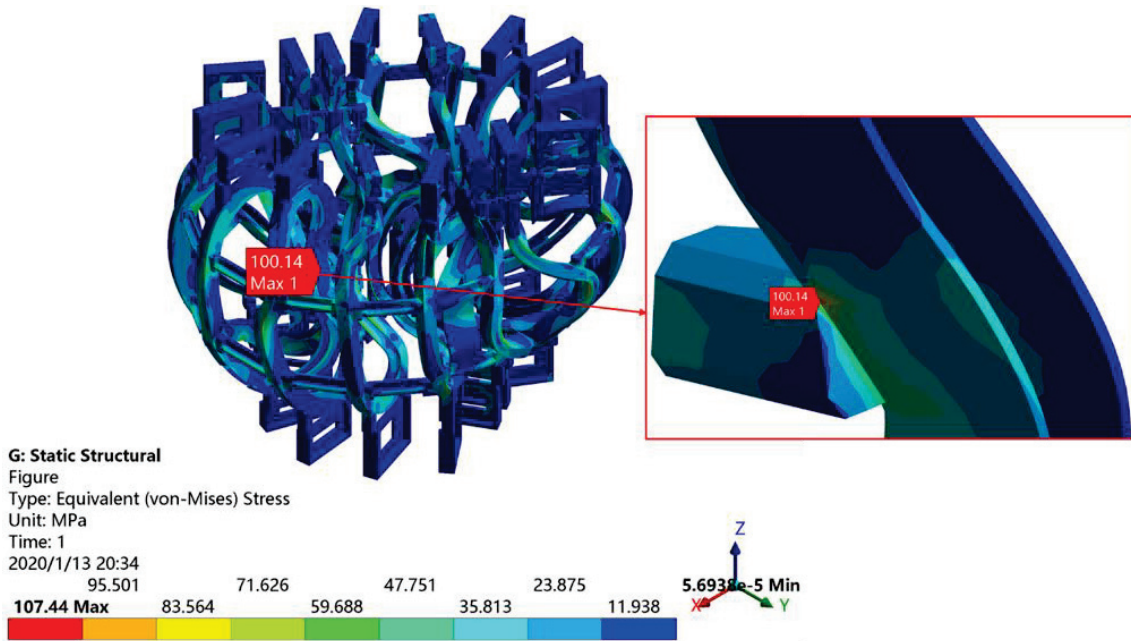


Fig. 4.5.1-1 3-D model of support structure for the analysis.



(a) Support frame and center support



(b) Coil support

Fig. 4.5.1-2 Stress distribution on the support structure.

4.5.2 Mockup of the modular coil MC4

The total number of the CFQS modular coil is 16. The number of MC4 coil is 4, and the MC4 is the most complex coil. So, the MC4 mockup coil was manufactured firstly, the manufacturability and the validity of the design were confirmed. Fig. 4.5.2-1 shows the mockup coil and the mould for the VPI process.

An electric current was actually applied to the coil as shown in Fig. 4.5.2-2 and Fig. 4.5.2-3, and the change in coil temperature was measured. Since the experimental results are consistent with the theoretically estimated characteristics, it was confirmed that the coil fabrication was appropriate.

Detail of the mockup coil is shown in Appendix-A 5.4.

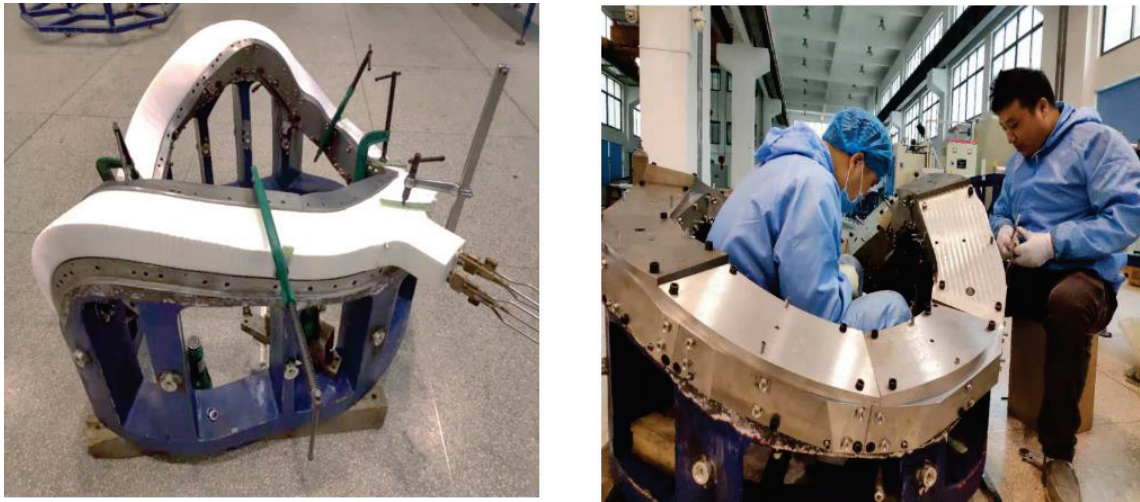


Fig. 4.5.2-1 Picture of the mockup coil.

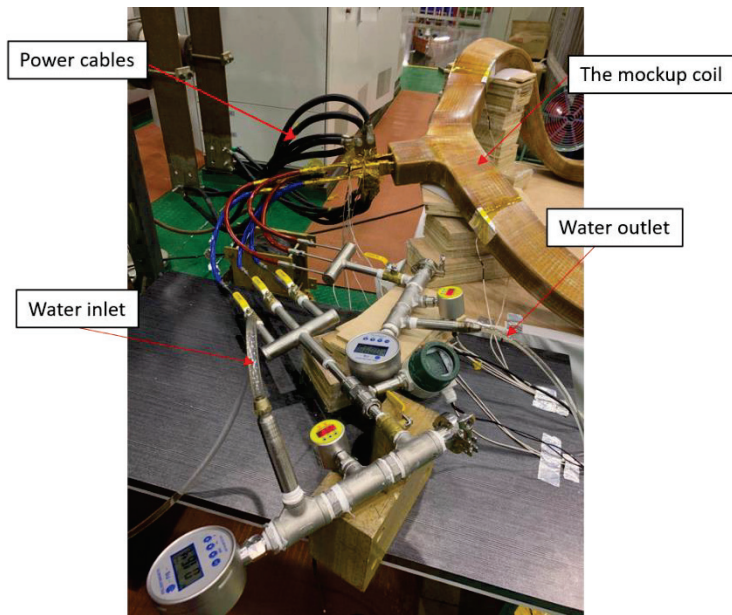
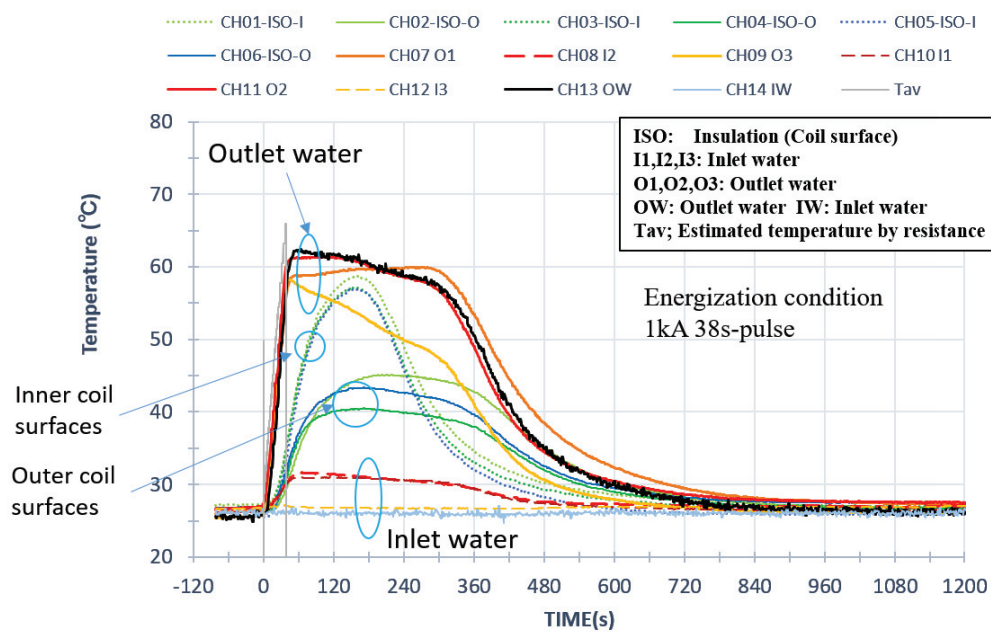


Fig. 4.5.2-2 Setting of the heat run test.



Note; The temperature change of the cooling water can be classified into two stages of -2 degrees/min and -8 degrees/min. It appears to be related to the time it takes for the water to circulate (a few minutes) and the time delay associated with heating the insulation. Greatly reduces the cooling time with water. It takes about 15 minutes to recover.

Fig. 4.5.2-3 Result of heat run test.

4.5.3 Structural analysis of the vacuum vessel

On plasma operation, the VV is exposed to several loads, such as an atmospheric pressure, a thermal stress, and electromagnetic forces of eddy current. The most important of these is the vacuum force, and it is necessary to confirm that the deformation and stress due to that force are within a reasonable range. Due to its complexity of shape, it is hard to predict the mechanical behavior of the VV. Therefore, we have performed structural analyses to validate the reliability of VV with use of ANSYS, a commercial finite element analysis software for the engineering simulation.

Fig. 4.5.3-1 shows the results of a structural analysis applied atmospheric pressure. The maximum stress is 87.4 MPa which is less than design guideline of stress and the maximum deformation is 1.03 mm. The location of maximum stress and maximum displacement is at the root of the port.

Please refer to Appendix-A 3.3 for the analysis results and analysis conditions (boundary conditions, *etc.*) for other loads.

In this analysis, it was assumed that the port was connected to the plate of the VV by full welding. Incomplete welding is likely to be applied for the purpose of cost reduction, so the effects of this will be considered separately.

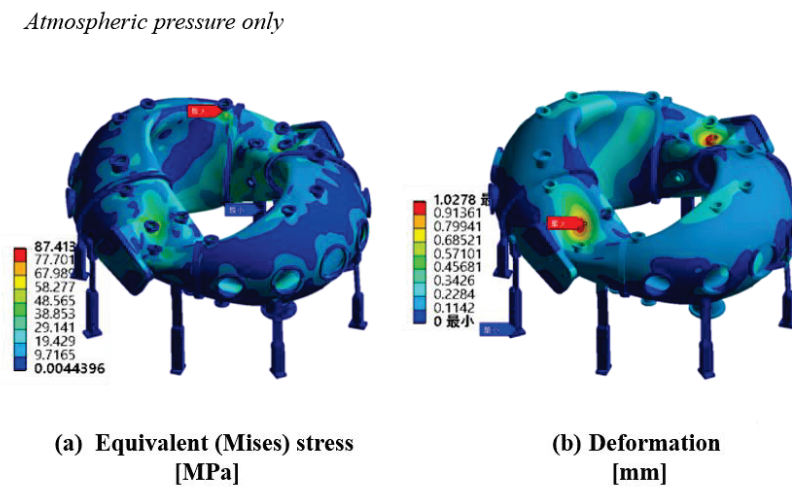


Fig. 4.5.3-1 Example of the structural analysis.

4.5.4 Eddy current analysis on vacuum vessel

In the CFQS using normal conducting coils, since the energization time of magnetic field coils is limited by the balance between heat generation and cooling performance of coils, the plasma discharge duration is also limited. Hence, the influence of the eddy current generated on the VV may be exerted during the plasma discharge.

The eddy current on the VV is induced by the current change of the external coil, such as the modular coil, the toroidal field coil, and the poloidal field coil. A VV in which eddy currents do not flow is

preferable because eddy currents disturb the target magnetic field distribution of the external coil, but it is difficult in practice. Therefore, the strategy is to delay the generation of plasma until the induced eddy current decays and its effect can be ignored. To judge whether the strategy is appropriate, the time constant of the eddy current was evaluated by eddy current analysis.

Fig. 4.5.4-1 shows waveform of the external coil current and the eddy current on the VV. The figure shows the eddy currents when three types of coil current change as the external coil. Fig. 4.5.4-2 shows the eddy current distribution on the VV. The eddy current disappeared in about 20 ms after the external coil became constant at 40 ms. In other words, the effect of eddy current can be ignored if the plasma experiment is started after waiting about 20 ms when the external coil current becomes constant. The change in eddy current is expressed as a time constant of 4 ms for the TFC and the MC, and 5 ms for the PFC.

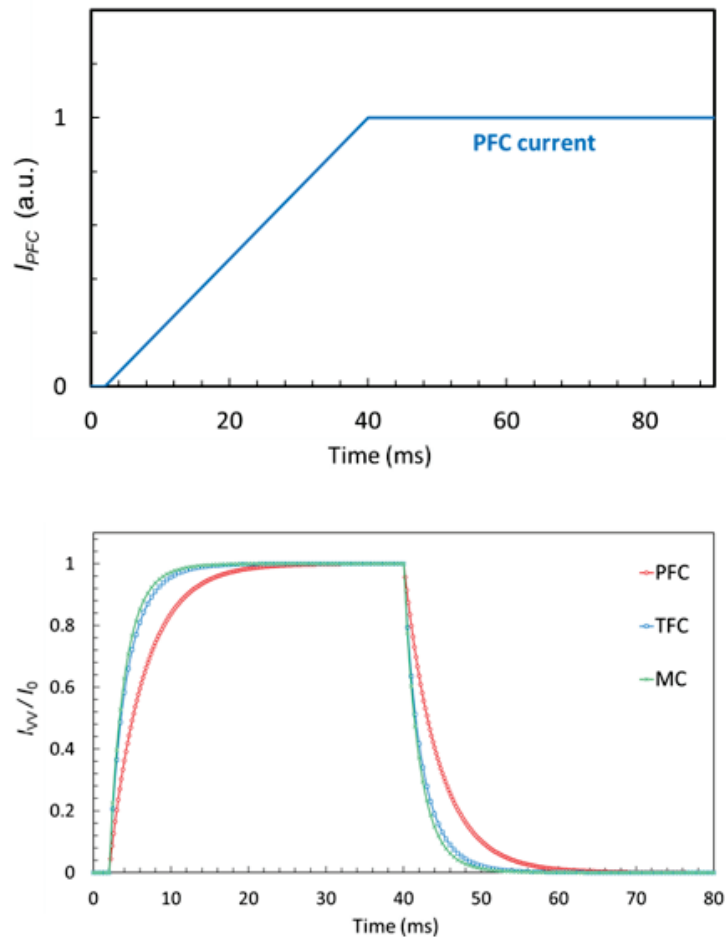


Fig. 4.5.4-1 Example of time-varying waveform of external coil current and eddy current.

Eddy current density by PFC at 40 ms

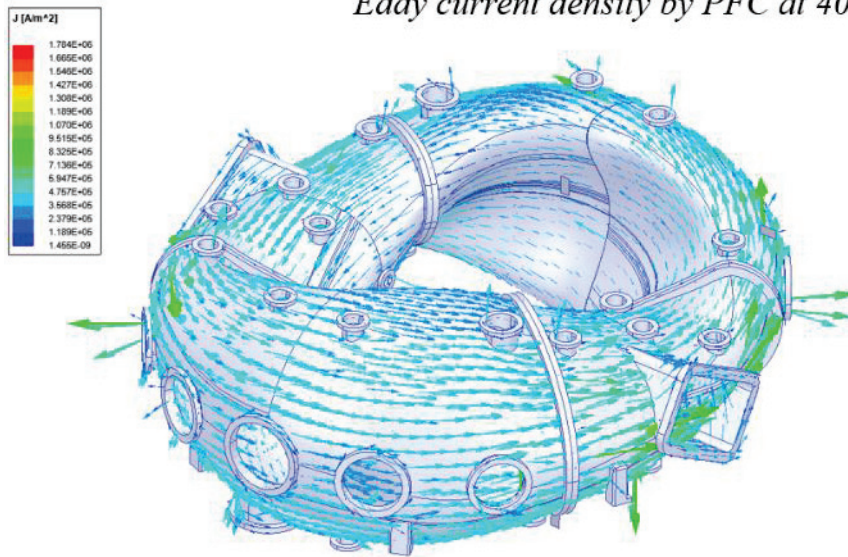


Fig. 4.5.4-2 Example of eddy current distribution.

4.5.5 Real scale model of the vacuum vessel

Real scale model of VV type A has been manufactured by 3-D printer. Since the size of the VV is large, a real scale model cannot be made by 3-D printer all at once. Therefore, the type A VV has been cut into 16 pieces (Fig. 4.5.5-1) to print by 3-D printer.

Each of 16 pieces has been made by 3-D printer in Keye company (Fig. 4.5.5-2). These 16 pieces are being assembled (Fig. 4.5.5-3).

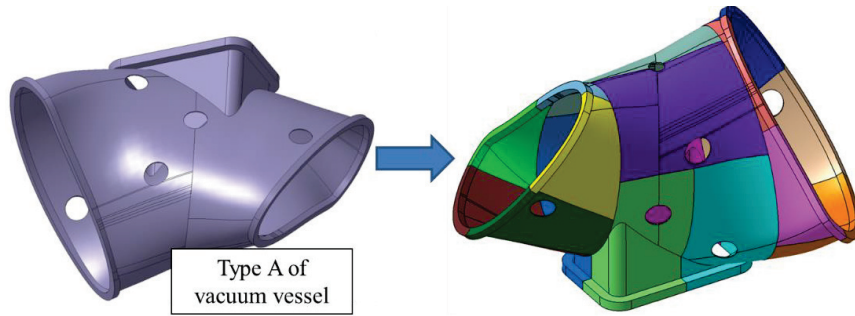


Fig. 4.5.5-1 Type A of VV is cut into 16 pieces to print by 3-D printer.

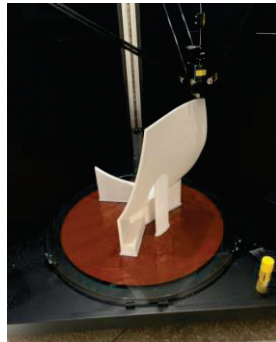


Fig. 4.5.5-2 3-D printer to fabricate real scale VV model.



Fig. 4.5.5-3 Pictures of assembled real scale 3-D VV model.

4.6 Equipment related to the vacuum vessel

4.6.1 Limiter system

As in other magnetically confined fusion devices, the plasma in the CFQS is confined within closed magnetic flux surfaces and a boundary exists between plasmas and the machine-wall components. This boundary is generally called the scrape-off layer (SOL), which is determined by a solid surface (limiter) or topologically by magnetic field perturbations (divertor) [4.6.1-1]. In the SOL the impurities originated from plasma-facing components (PFCs) may cause a lot of problems, such as huge radiative power loss and dilution of fuel particles, it is therefore a crucial task to reduce impurities released from the PFC and prevent them from entering the plasma core region.

For the divertor configuration, plasma particles and energy leaving the confinement region are guided to the divertor target plate by open field lines. In stellarators, this divertor configuration can be intrinsically developed on the base of special edge magnetic structures arising from the small radial magnetic field resonant with rational surfaces [4.6.1-2]. Nevertheless, the stellarator divertor geometries may differ from each other, depending on the global magnetic shear. In the case of low-shear there exist chains of the island divertor, while in high-shear case the overlapping of island chains may form a stochastic layer [4.6.1-3]. In CFQS, the vacuum rational transform is designed between $2/6$ and $2/5$ from the core to the edge to avoid low-order rational surfaces, thus, the magnetic shear is quite low. It is expected from calculations that at the periphery of the CFQS, an island bundle divertor configuration will be formed under certain discharge conditions.

In different from the divertor, the limiter configuration is to use a solid surface to define the edge of the plasma. Depending on the shape and the positioning of the solid diaphragm, the limiters are generally divided into (a) poloidal limiter; (b) rail limiter and (c) toroidal limiter, as depicted in Fig. 4.6.1-1. The poloidal limiter is the simplest concept with a circular hole defined by a diaphragm normal to the toroidal magnetic field. The diameter of the hole is thus smaller than that of the VV. Inside the hole the field lines are closed, while outside the hole the field lines are truncated by the diaphragm and the plasma density and temperature are radially decreasing due to parallel losses of particle and energy flux onto the limiter in the SOL. Consequently, the limiter primarily serves to protect the wall from erosion by plasma heat loads. For withstanding heavy heat load, the limiter itself is usually made of a refractory material, such as carbon, tungsten, or molybdenum.

In the CFQS stellarator, although an innate divertor configuration exists in the plasma boundary, we intend to put two sets of the poloidal limiter inside the VV for defining the plasma and protecting the wall. These two limiters will be installed at two approximately opposite toroidal locations of the torus. One limiter has a fixed diameter with a minor radius $a = 27$ cm. For the other one, its diameter is adjustable, and the minor radius can be varied within a range of $r = (20-27)$ cm. Because the CFQS is free of major plasma disruptions, there is little thermal shock occurred during the operation. Thus,

the sputtering and arcing rates from limiters are expected to be very low. The material for the limiters can be C, W or Mo.

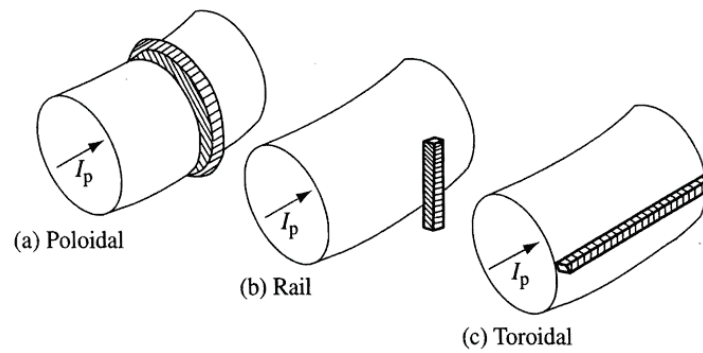


Fig. 4.6.1-1 Schematic of different types of the limiter.

References

- [4.6.1-1] J. Wesson, Tokamaks, fourth edition, Oxford University Press, 2011.
- [4.6.1-2] Y. Xu, “A general comparison between tokamak and stellarator plasmas”, Matter and Radiation at Extremes **1** (2016) 192.
- [4.6.1-3] Y. Feng *et al.*, “Comparison between stellarator and tokamak divertor transport”, Plasma Phys. Control. Fusion **53** (2011) 024009.

4.6.2 Vacuum pumping system

Pumping system in CHS will be transferred to CFQS. As shown in the below figure, rotary pump is used for rough pumping, then the turbo molecular pump gets involved.

Rotary pump is used for 20-30 Pa, then start the turbo molecular pump, to reduce the time reach the work pressure. Two turbo molecular pumps are used to achieve and sustain high degree of vacuum as shown in Fig. 4.6.2-1.

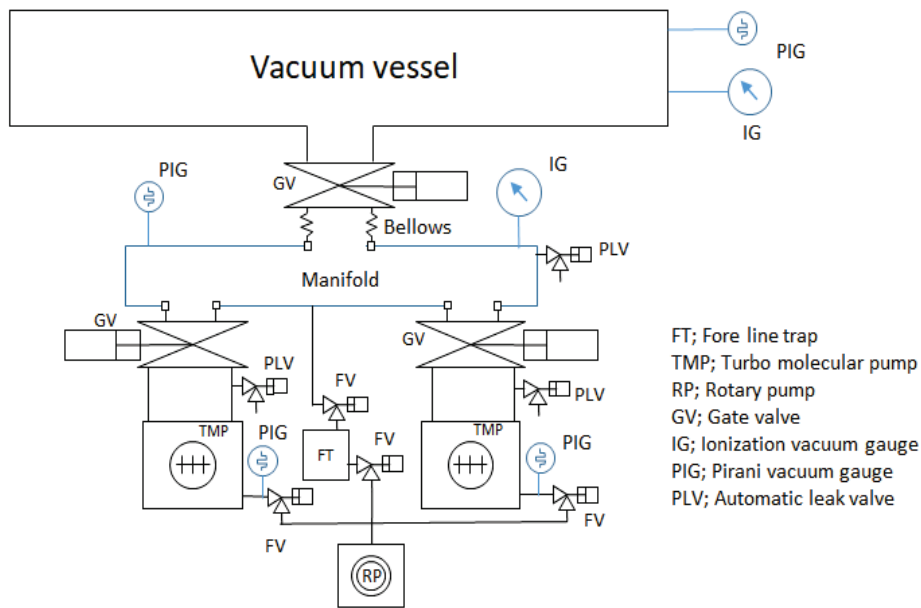


Fig. 4.6.2-1 Sketch of vacuum pumping system.

4.6.3 Wall conditioning system

Wall conditioning is important to produce plasma after the maintenance of VV.

Typical wall conditioning method is discharge cleaning by 2.45 GHz microwave heating system. The resonance magnetic field strength of this frequency is 0.0875 T, and steady state magnetic field is favorable for this purpose. Microwave is generated by magnetron and transferred by wave guide.

For other wall conditioning, glow discharge with helium or hydrogen, and titanium getter may be applied.

4.6.4 Fuel gas supply system (Gus puff system)

To generate plasma, it is necessary to control the supply amount of high purity gas. To do that, high-speed control valve system to adjust gas injection rate with gas purification function to remove impurities from the injected gas is required. The equipment that does them is commonly called a gas puff system.

Normally, hydrogen gas is injected for plasma generation, but noble gas such as helium or argon may be injected depending on the experimental purpose. Nitrogen gas may be injected to calibrate the measuring instrument. In addition, a large amount of nitrogen gas or dry air may be injected to open the inside of the VV to the atmosphere.

Thus, since various kinds of gases are injected for various purposes, it is likely that an equipment for performing them will be required. Detail will be designed in the future.

4.6.5 Vacuum management system

Vacuum management is very important to produce high-performance plasma, and instruments for that purpose and protective functions in case of trouble are required.

Typical instrument is high speed ionization vacuum gauge, quadrupole mass spectrometer, helium leak detector, and so on. As a vacuum protection device, a gate valve system for interrupting the vacuum in an emergency is essential. Detail will be designed in the future.

4.6.6 Shutter system to protect the glass windows

Glass windows may be attached for plasma measurements. The plasma may cause the glass window to be coated with some film, making it difficult for light to pass through. To prevent such a problem, it is preferable to add a movable shutter on the vacuum side of the glass window and close the shutter when the glass window is not used. Since there is a high possibility that the glass window will be coated at the time of the wall conditioning with titanium getter or glow discharge, the shutter should be closed in such a case.

4.6.7 Vacuum test equipment

As the experiment progresses, various equipment will be added to the VV port. To reduce the risk of vacuum leaks causing damage to working equipment, it is essential to confirm that newly added equipment has no leak in a unit test. The test chamber with a vacuum pumping unit should be prepared separately from the CFQS body for a unit leak test.

4.7 Power supply

4.7.1 Requirement to power supply system

Chinese power environment is different from Japan as shown in Table 4.7.1-1. To relocate some equipment's of the CHS for CFQS experiments, it is reasonable to prepare converters, mainly transformers, for solving the difference in voltage. Although it is possible to install individual transformers for each used device, it is considered that cost reduction can be achieved by putting them together, because there are many devices scheduled to be used.

Table 4.7.1-2 shows summary of required power. Fig. 4.7.1-1 shows the preliminary one line diagram of power supply system for the CFQS. Where, the parts surrounded by the red broken line indicate the equipment's for the NBI.

Table 4.7.1-1 Comparison of power environment

	Frequency	HV	LV 1f	LV 3f
NIFS in Japan	60(West Japan)	6.6 kV	100 V	200 V
SWJTU in China	50	10 kV	220 V	380 V

HV; High voltage

LV; Low voltage

Table 4.7.1-2 Total electric power to be required

No	Power board	Voltage	Phase	Total capacity	Use
1	HV	10 kV	3Φ	5 MVA	250 kW for the MG 4 MVA for the NBI
2	LV	380 V	3Φ	1 MVA	700 kVA for PS for 0.1 T 300 kVA for cooling water
3	LV	220 V	1Φ	Not clear	Diagnostic, control <i>etc.</i>

To apply large currents to the CFQS coils, a short pulse large capacity power supply of about 60 MVA and 1 s of a pulse length is required. Since it is difficult to supply this power from the commercial power source, a current source with energy storage function is required. The power supply system in Fig. 4.7.1-1 has a generator driven by an induction motor. Please refer to Appendix-A 4.3 for examples of the motor generator system.

A high-power electron cyclotron heating (ECRH) system is required to generate high temperature plasma. Since the ECRH system will be able to use a capacitor bank power supply and the instantaneous power can be designed small, we believe that it will receive from a low voltage power board.

In the initial experiments after the CFQS construction is completed, we have a plan to carry out measurement experiments of plasma shape with low magnetic field and longtime discharge. At that stage, the power system in the shaped box in Fig. 4.7.1-1 may be required.

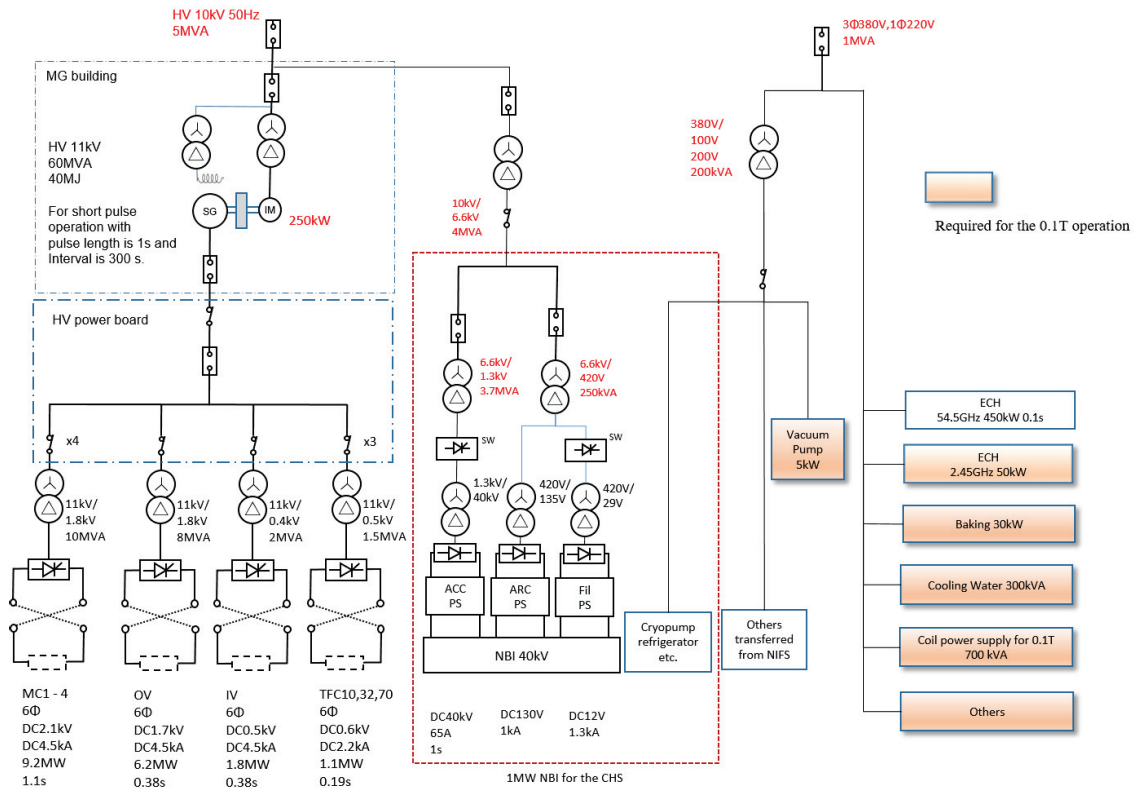


Fig. 4.7.1-1 Power system for the CFQS.

4.7.2 Power supply for 0.1 T operation

In the initial experiments, we have a plan to carry out measurement experiments of plasma shape with low magnetic field and continuous discharge. At that stage, we think the power supply shown in Fig. 4.7.2-1 is enough. It mainly consists of voltage adjusters and 6 phase diode rectifiers for modular coil (MC), and DC power supplies with six phase Thyristor-controlled units for Toroidal field coil (TFC). The power board at least 700 kVA power capacity is also required as power source. Please refer to Appendix-A 4.2 for detail of the circuit diagram and layout.

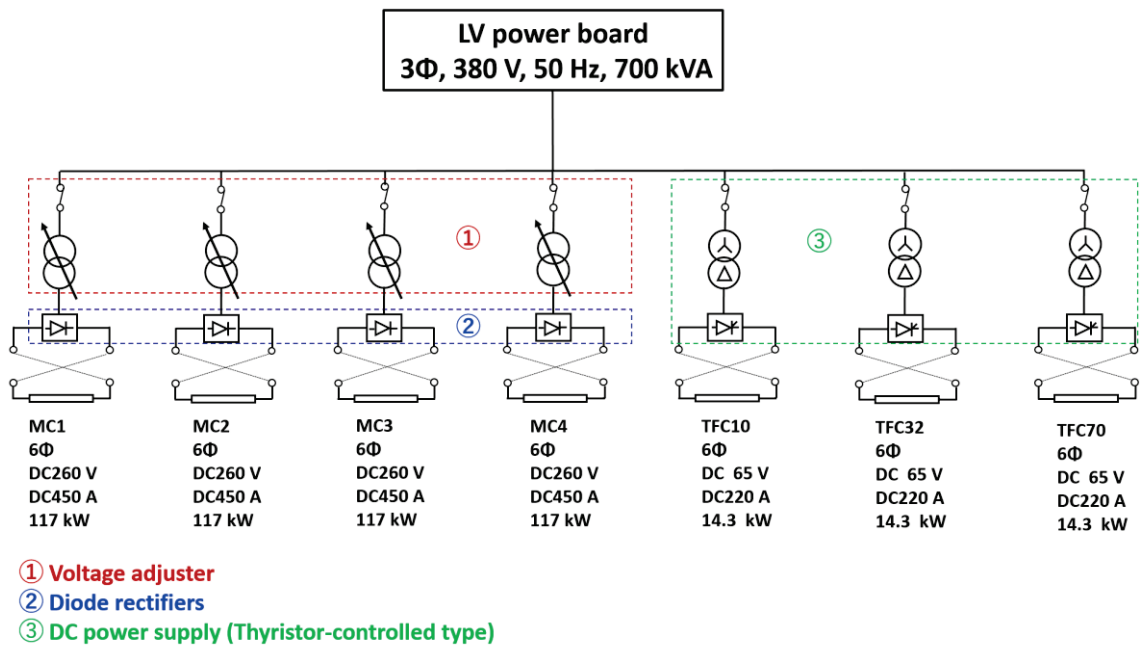


Fig. 4.7.2-1 Power supply system for initial operation of 0.1 T.

4.7.3 Power supply for 1 T operation

To apply large currents to the CFQS coils, a short pulse large capacity power supply of about 60 MW and 1s of a pulse length is required. Since it is difficult to supply this power from the commercial power source directly, a current source with energy storage function should be employed. The power supply with Induction motor (IM) and synchronous generator (SG) may be most suitable type for 1.0 T operation because it can store large amount of electrical energy and supply power with good controllability. Discussions about comparison of power supply candidates focusing on capacity, space, cost, and operation control are described in Appendix-A 4.3.

Fig. 4.7.3-1 shows the designed power supply system for rated operation (1.0 T). The circuit mainly consists of IM, SG, the inverter for IM and SG revolution control, the excitation system for SG, six phase Thyristor-control units and polarity switching circuits. Please refer to Appendix-A 4.3 for detail of the circuit diagram and layout.

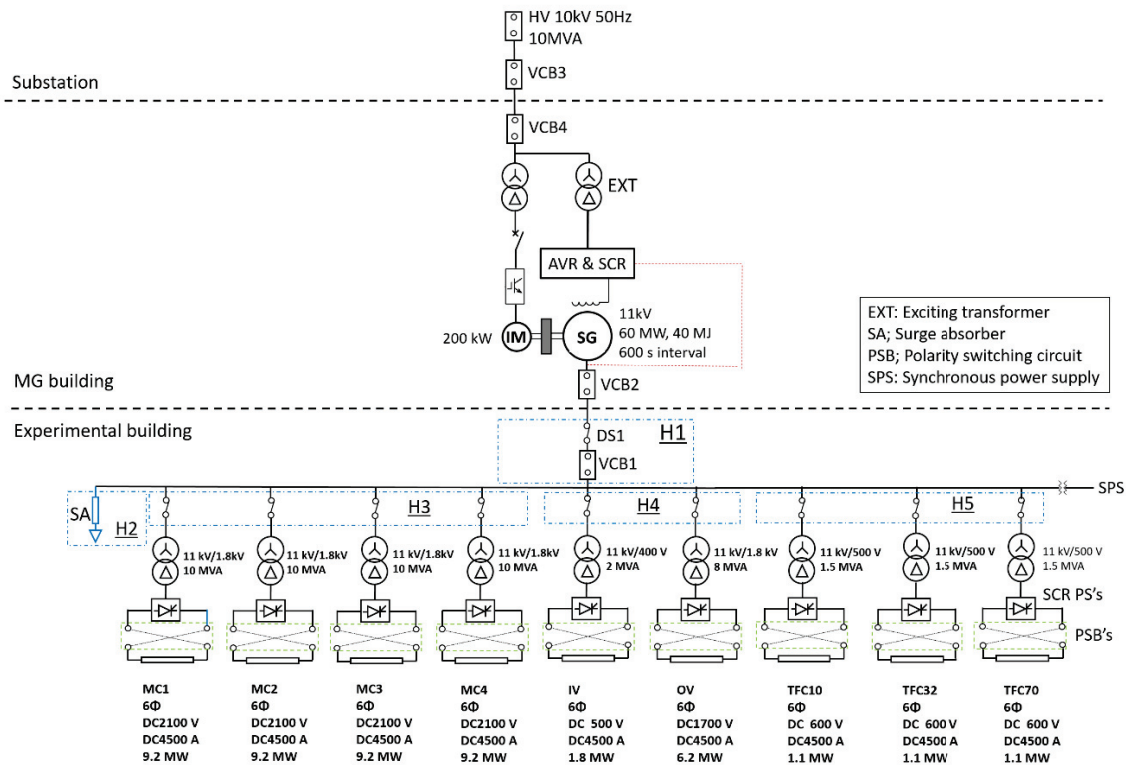


Fig. 4.7.3-1 Designed circuit diagram of power supply system with IM and SG.

4.7.4 Baking power supply

Total required baking power for CFQS VV is estimated approximately 25 kW. We designed the power supply satisfying the electrical conditions for baking as represented in Fig. 4.7.4-1. It mainly consists of AC power regulators (APR) which can change the applied voltage and applied power (up to AC220 V, 2.3 kW) for each baking heater, a magnet contactor (MC) for emergency shutdown to prevent overheating, molded case circuit breakers (MCCB) for each baking switching and transformer (TR) for insulation.

The baking sections of A1 and A3 as shown in Fig. 4.4.4-1 are connected in series because these volumes are relatively small compared with other sections. APR output is controlled by a temperature indication controller (TIC) which monitors surface temperature of VV. Surface temperature is monitored by not only TIC but also the other temperature monitoring system with over 64 measurement spots. The details of the other monitoring system will be designed later. MC is operated to stop baking when any surface temperature of VV exceeds critical value.

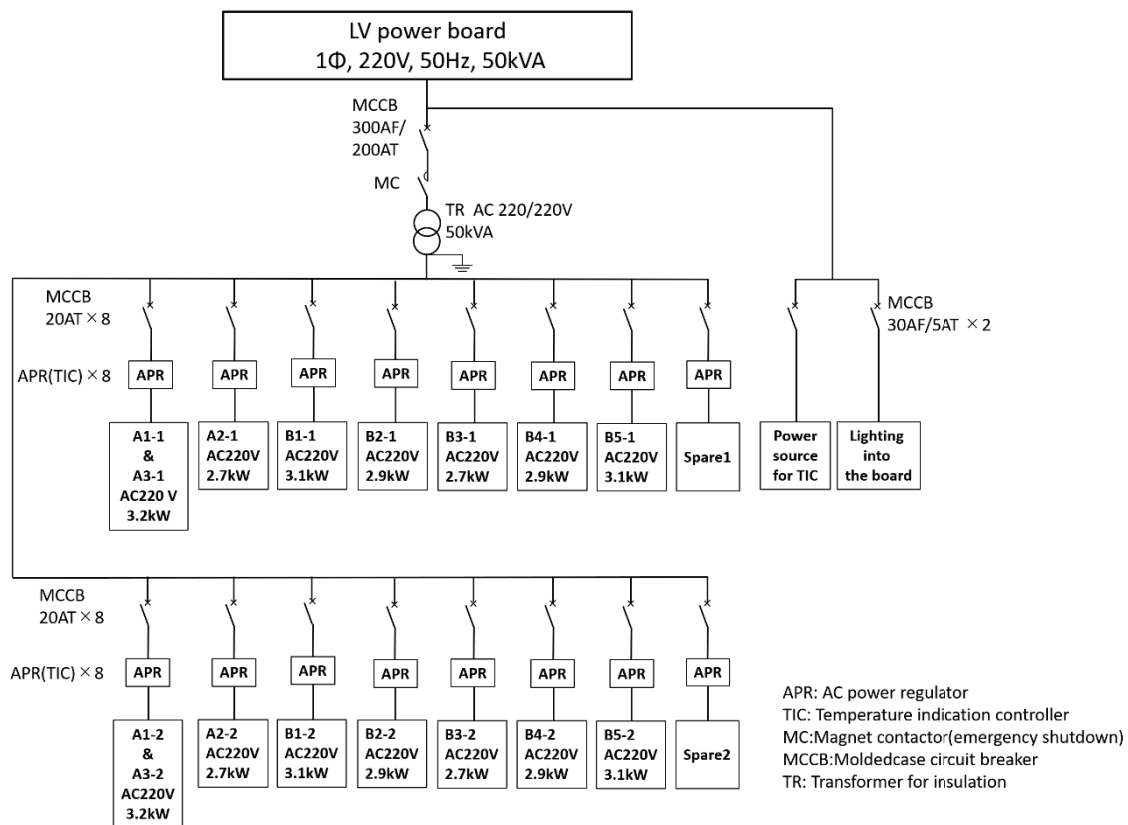


Fig. 4.7.4-1 Designed circuit diagram of the baking system.

4.8 Pure water cooling system

Pure water-cooling system is required to cool magnetic coil system, heating system, diagnostic system, and pumping system. And industrial water system to cool the motor generator may be also required. Fig. 4.8-1 shows preliminary layout of the pure water cooling system.

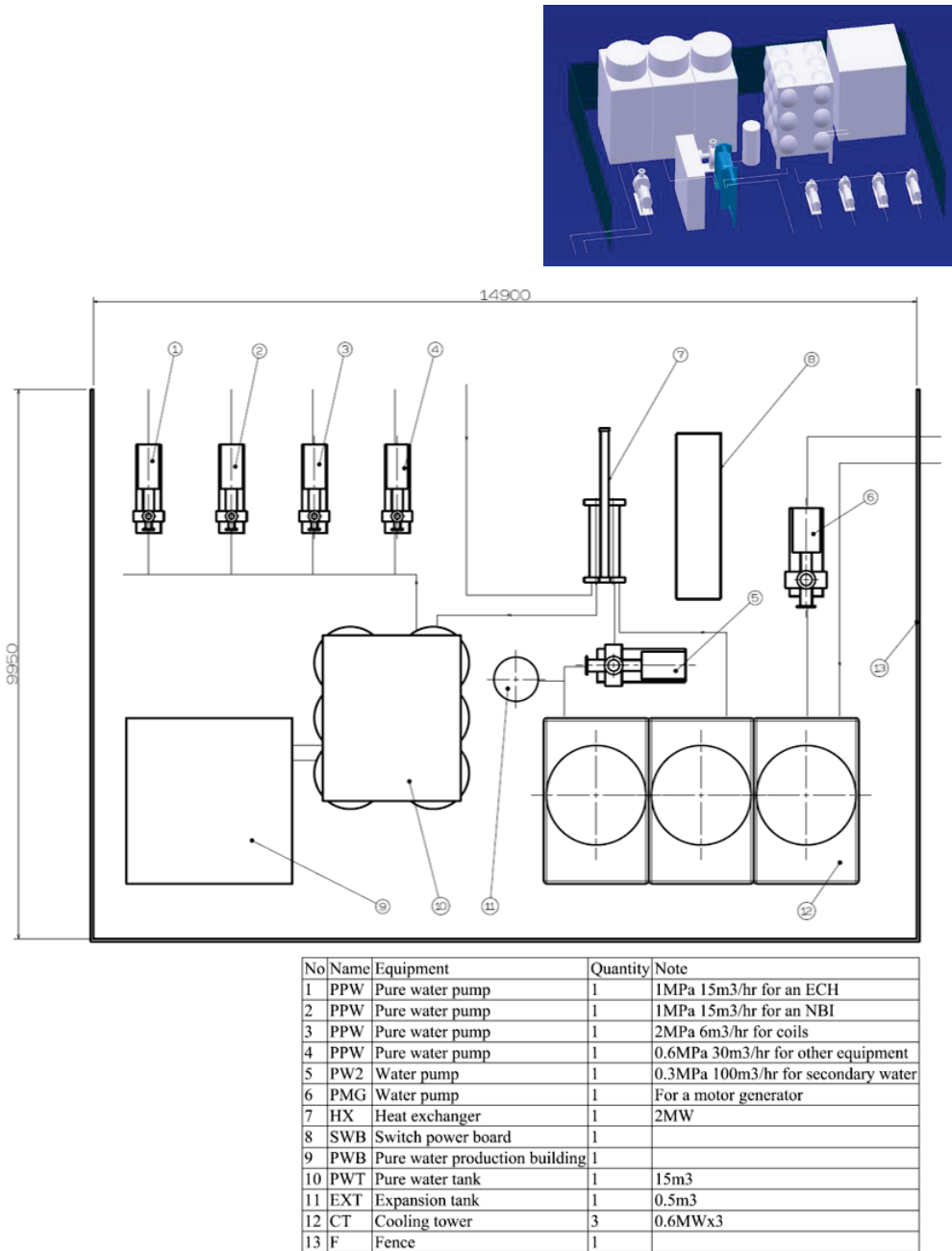


Fig. 4.8-1 Preliminary layout of pure water cooling system.

4.9 Compressed air supply system

Compressed air supply system is mainly used to control the gate valve. Detail will be designed in the future.

4.10 Liquid nitrogen supply system

Liquid nitrogen is often used for various purposes in fusion devices. They are nitrogen trap for removing impurities, pre-cooling of superconducting device, cooling of heat shields, and so on. If desired, liquid nitrogen can be purchased in a Dewar bottle, but when the amount used is large, there are many cases where a liquid nitrogen production device is prepared.

The need for such equipment will be considered separately.

4.11 Electron cyclotron resonance heating (ECRH) system

The main component of the electron cyclotron resonance heating (ECRH) system is gyrotron. The gyrotron which was used for CHS experiment and will be used in CFQS experiment has an oscillation frequency of 54.5 GHz and the maximum output power of up to 450 kW. The maximum pulse length is 100 ms. Fig. 4.11-1 shows the single line diagram of ECRH system and Fig. 4.11-2 shows a preliminary layout of the ECRH system for the CFQS. It is necessary to secure a large area (100 m² for the power supply) near CFQS to install the ECRH system. The detail of the ECRH system for the CHS is summarized in Appendix-B 3.5.

The EC-waves generated by the gyrotron effectively and locally heat the electrons at a position on the EC-wave beam path where the resonance condition ($n\omega_{ce} = \omega - k_{\parallel}v_{\parallel}$ and $\omega_{ce} \equiv eB/m_e$) is satisfied. Here, integer n denotes harmonic number, ω_{ce} is electron cyclotron angular frequency, e is a unit charge of an electron, B is the strength of magnetic field, m_e is the mass of an electron with relativistic effect, ω is angular frequency of EC-waves, and k_{\parallel} and v_{\parallel} are the components of wave number and electron velocity parallel to the magnetic field line, respectively. Applying the frequency of 54.5 GHz, the resonance condition for $n = 2$ (second harmonic resonance) is satisfied with $B = 0.97$ T.

In the case of the CHS experiment, the EC-wave power was transmitted from the gyrotron to the CHS VV by a quasi-optical transmission line. The transmission line was furnished with focusing and plane mirrors, polarizer mirrors to control transmitted wave's polarization arbitrarily, and vacuum window to keep the vacuum condition in CHS.

By use of the power transmission and injection systems, effective and localized ECRH with power deposition control, electron cyclotron current drive (ECCD), and electron Bernstein wave heating may be realized. For that purpose, two dimensionally steerable power injection system with beam focusing is necessary. To realize the power injection system, at least, two mirror antenna system (one is plasma facing two-dimensional (2-D) steerable plane mirror, and the other is beam focusing mirror) inside the VV is required. The dimensions of the mirrors depend on the focused beam waist size at the plasma core region and the distance between the plasma and the mirrors. The antenna design should be optimized under the available circumstance of CFQS VV design, to realize the beam waist size as small as possible in the plasmas.

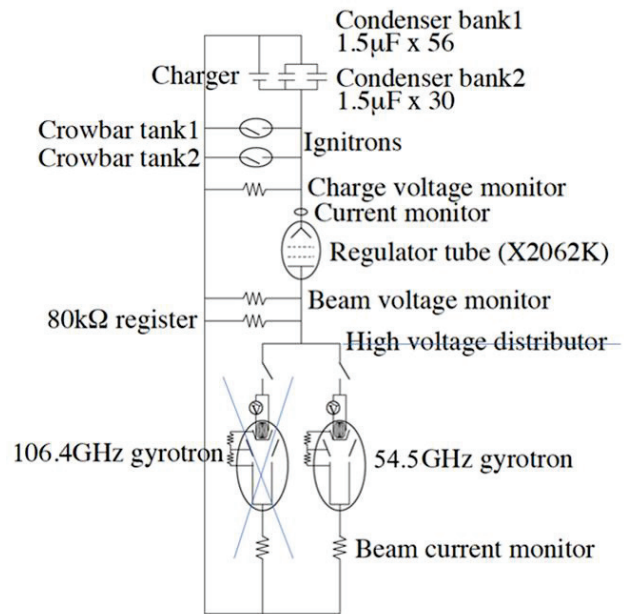


Fig. 4.11-1 Single line diagram of ECRH.

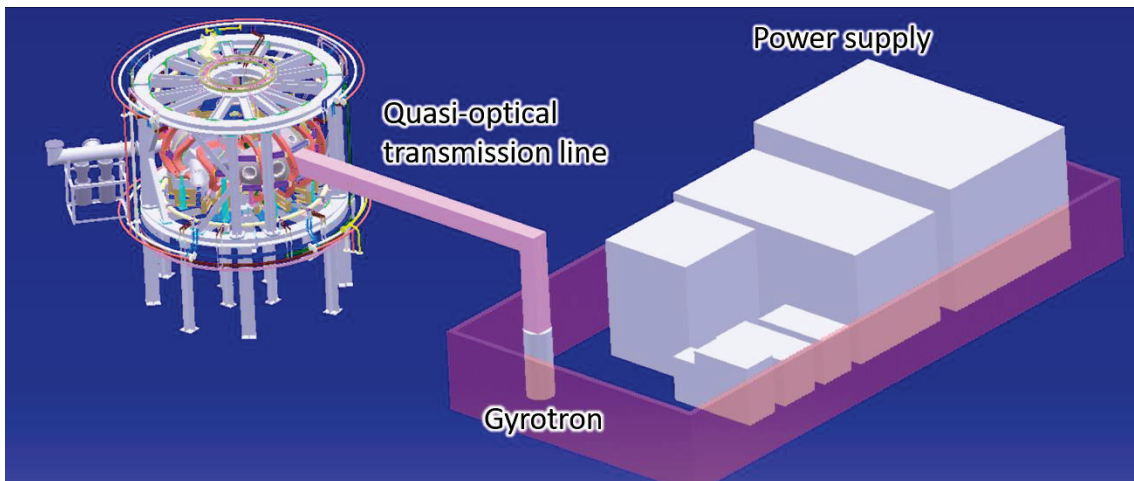
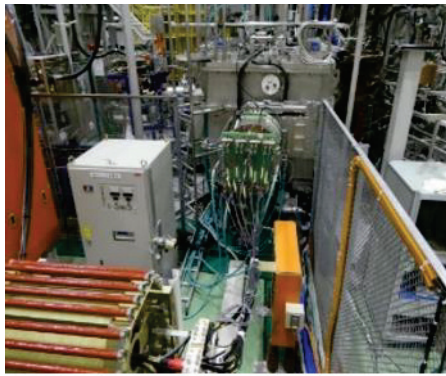


Fig. 4.11-2 Preliminary layout of ECRH system for CFQS.

4.12 Neutral beam injection (NBI) heating system

Neutral beam injection (NBI) is a powerful tool for plasma heating and drive of the plasma current and flow. To study energetic particle physics, tangential NBI is an inevitable device. Tangential port with diameter of 300 mm is recommended to install NBI. Fig. 4.12-1 shows the NBI#2 system that will be moved for the CFQS experiment in the future and Fig. 4.12-2 shows a preliminary layout of the NBI system for the CFQS. It is necessary to secure a large area (100 m² for the power supply and 10 m² for the ion source) near CFQS to install the NBI system.

The detail of the NBI system is summarized in Appendix-B 3.4.



(a) Back side view



(b) Side view

Fig. 4.12-1 NBI for the CHS.

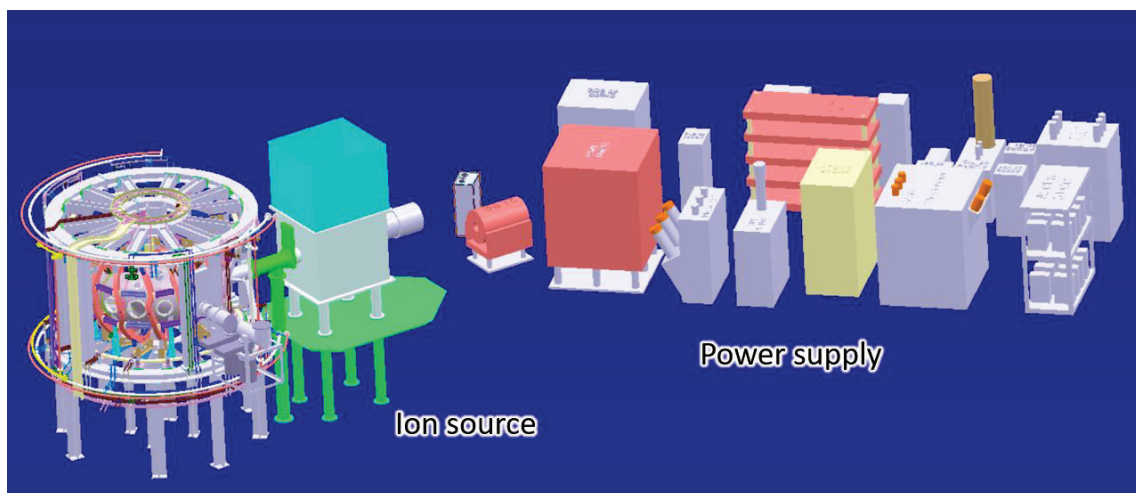


Fig. 4.12-2 Preliminary layout of NBI system for CFQS.

4.13 Diagnostics system

Diagnostics are indispensable for studying high temperature plasma physics in modern fusion research. There are a lot of interesting topics to be studied; transitions to improved confinement modes, formation of transport barriers, and their impact on plasma turbulence, *etc.* Roles of diagnostics are increasing in the studies on high temperature plasma properties, not only for fusion but also for basic physics.

CFQS is an innovatively designed device to achieve tokamak-like confinement properties and helical-like stability at the same time. Plasmas produced in the CFQS will become a good target for researches which aim at achieving cost-effective stable burning plasmas. High-quality data based on detailed measurements should be obtained for comprehensive understanding of toroidal plasmas.

As mentioned above, anomalous transport and improved confinement modes are important issues for understanding toroidal plasmas. Based on the successful results of the advanced diagnostics in CHS and LHD, we will employ advanced diagnostic systems such as heavy ion beam probe (HIBP) and microwave reflectometry to study the spatio-temporal turbulence structure, the structures of electric field, and plasma flow. After the installation of NBI in the future, we will consider developing charge exchange spectroscopy (CXS) for the measurement of radial electric field and plasma flow velocity to study the relation between toroidal rotation and momentum input.

Also, physics of density limit is important in helical devices because confinement property of helical systems is improved as the density increases following the scaling law. Therefore, higher priorities are given for the diagnostics of edge plasma, MHD instability behavior and radiation power, including magnetic probe, bolometer, *etc.*

For basic diagnostics, microwave interferometer should be firstly developed to measure the electron density. Thomson scattering is also important to study the physics of transport barriers. Multi-dimensional measurement is useful for studying internal structure of basic plasma parameters. Therefore, the development of 2-D and/or 3-D measurements will be performed as far as possible. So that the structure and non-linear development of plasmas can be observed in detail.

Diagnostics planned in the CFQS are listed in Table 4.13-1 and Table 4.13-2. Assignment of ports to these diagnostics is planned as shown in the section about the VV. Some of the ports should be specifically designed for HIBP and Thomson scattering because these diagnostics require special geometries.

Table 4.13-1 Basic diagnostics planned in the CFQS.

Parameters	Diagnostics	Remarks
Electron density	Microwave interferometer Far-infrared interferometer Thomson scattering	150 GHz Multichannel
Electron temperature	Thomson scattering Electron cyclotron emission	Multichannel
Ion temperature	Charge exchange spectroscopy	After NBI installation
MHD	Magnetic probe	
Edge plasma	Langmuir probe H α detector	
Radiation power	Pyroelectric detector Resistive bolometer AXUV photodiode array	20 channels
Stored energy	Diamagnetic loop	
Plasma Current	Rogowski coil	
Impurities	Vacuum ultraviolet spectroscopy	
Vacuum magnetic surface	Beam fluorescence measurement system	
Shape of plasma	CCD camera	

Table 4.13-2 Advanced diagnostics planned in the CFQS.

Parameters	Diagnostics	Remarks
Electric potential/field	Heavy ion beam probe	
Plasma rotation	Charge exchange spectroscopy	After NBI installation
Lost ions	Lost ion probe	
Turbulence	Heavy ion beam probe (HIBP) Microwave reflectometer	Multichannel

5 Research plan and schedule

The CFQS manages to offer available solutions to critical challenges for toroidal confinement fusion: it provides a steady-state, disruption-free reactor concept as well as neoclassically optimized magnetic configurations. With respect to the magnetic configurations, the CFQS is designed and operated to achieve three types of advanced configurations, *i.e.*, quasi-axisymmetric, mirror linked, and divertor configurations. To guarantee the safety of the facility operation and accuracy of each magnetic configuration two steps are scheduled to operate CFQS, which are the low magnetic field operation and standard magnetic field operation.

5.1 Physics research plan

5.1.1 Research plan for 0.1 T operation

The research plan for the 0.1 T operation is as follows,

- i. Operate all the diagnostics and auxiliary systems, *e.g.*, electron gun, CCD camera, interferometer, probes, visible light, *etc.*
- ii. Achieve flexible magnetic configurations, *i.e.*, quasi-axisymmetric configuration, mirror linked configuration as well as divertor configuration; check the accuracy of magnetic field configurations in vacuum by mapping experiment.
- iii. Verify optimization of neoclassical transport and whether the tokamak-like fundamental transport properties are realized or not.

5.1.2 Research plan for 1.0 T operation

The research plan for the 1.0 T operation is as follows,

- i. Neoclassically optimized magnetic configurations.
- ii. Turbulence and transport research.
- iii. Island bundle divertor.
- iv. Plasma-materials interactions in 3-D systems.
- v. Energetic-particle confinement.
- vi. Equilibrium and stability at high- β .
- vii. Impurity confinement and accumulation.
- viii. Optimize the coil system for the next generation stellarator.

5.2 Construction schedule

- Phase I; Physics design and main machine design
 - Configuration
 - Neoclassical transport
 - MHD
 - Modular coils
 - Vacuum vessel
 - Supporting structure *etc.*
- Phase II; Fabrication of CFQS, transfer essential heating, and diagnostic systems from NIFS to SWJTU
 - NBI
 - Gyrotron
 - Interferometer
 - X-ray diagnostic *etc.*
- Phase III; Commissioning, verify construction accuracy, and obtain first plasma.
- Phase IV; Magnetic configuration studies and heating experiments in 0.1 T operation.
- Phase V; Magnetic configuration studies and heating experiments in 1.0 T operation.

During FY 2022, the first plasma of the CFQS will be achieved.

NIFS-SWJTU JOINT PROJECT FOR CFQS
~PHYSICS AND ENGINEERING DESIGN~

VER. 3.1

2020. NOV.

APPENDIX-A

~BASIC DESIGN~



NIFS; National Institute for Fusion Science

SWJTU; Institute of Fusion Science, School of Physical Science and Technology Southwest Jiaotong University

Hefei Keye; Hefei Keye Electrical Physical Equipment Manufacturing Co., Ltd.

Table of contents

1	General information	4
1.1	Abbreviation.....	4
1.2	Guideline of allowable limit value of stress and strain for the CFQS.....	5
2	Coils	6
2.1	Design of coils.....	6
2.1.1	Conductor	6
2.1.2	Insulation	6
2.1.3	Stiffened shell (Reinforcement plate).....	7
2.1.4	Winding structure	7
2.1.5	Temperature rise in one shot and cooling method.....	11
2.2	Impedance of each coil.....	12
2.3	Resistance of each coil	14
2.4	Pressure drop and average temperature rise of cooling water for coils.....	15
2.5	Optimization of the twisting angle of each modular coil	17
2.6	Electromagnetic force analysis on modular coils.....	21
2.6.1	Coil system for the CFQS and analysis method	21
2.6.2	Magnetic field distribution on the modular coils.....	21
2.6.3	EM force components of the modular coil	21
2.7	Eddy current analysis on modular coil case	31
2.8	Validating the ANSYS/Maxwell result for inductance	32
2.9	Finite element analysis for support structure.....	33
2.10	External current lead	37
2.11	Cooling water piping.....	41
3	Vacuum vessel.....	46
3.1	Cross section of vacuum vessel for CFQS	46
3.2	Design of leaf-spring type leg	52
3.2.1	Design values.....	52
3.2.2	Buckling load and safety factor	52
3.2.3	Bending stress with the forced displacement.....	53
3.3	Structural analysis of vacuum vessel.....	55
3.4	Eddy current analysis of vacuum vessel.....	58
3.4.1	Time constant of eddy current and its effect on plasma discharge	58
3.4.2	EM force on vacuum vessel and structural analysis	59
3.5	Effect of mesh size in FEM analysis for the vacuum vessel	65
3.6	Eddy current analysis for inductive heating of the vacuum vessel.....	67
3.7	Required length of the baking heater for vacuum vessel	69
4	Power supply for coils.....	71

4.1	Current wave form to estimate required power capacity.....	71
4.2	Trial design of coil power supply for 0.1T operation.....	76
4.3	Trial design of coil power supply for 1T operation.....	78
4.3.1	Designed circuit diagram and the layout of MG building	78
4.3.2	Specifications of SG, IM, and a flywheel.....	80
4.3.3	Comparison of coil power supply systems	82
5	Mockup of a modular coil	87
5.1	Engineering design of the mock-up coil.....	87
5.1.1	Conductor and insulation design	87
5.1.2	Mockup coil design.....	88
5.1.3	Design of conductor joint	89
5.1.4	Joint of cooling water pipe	90
5.1.5	Filler block design	90
5.2	The coil winding manufacture line.....	91
5.3	The winding mould design	92
5.4	Result of manufacturing and test for the MC4 mockup coil	94
5.4.1	The manufacture process	94
5.4.2	The dimension measurement on the winding mould	95
5.4.3	Impulse test.....	96
5.4.4	Heat run test.....	100
5.4.5	High voltage test.....	106
5.4.6	Dimension measurement after heat run test.....	107
5.4.7	Summary of the MC4 mock up coil manufacture.....	109
6	Plastic model developed by 3D printer	110
7	Mass list of the CFQS main parts.....	114
8	Preliminary production flow of the CFQS	115
8.1	Overall production flow	115
8.2	Production flow of vacuum vessel in a factory	116
8.3	Pre-assembly procedure of modular coils and vacuum vessel on site.....	119
8.4	Overall assembly procedure on site.....	121

1 General information

1.1 Abbreviation

This document includes various abbreviation words. The following table shows their meaning.

No	Abbreviation	Description
1	A/F	Arc and filament
2	ACC or ACL	Acceleration
3	ACSW	Acceleration Thyristor switch
4	AVP	Auxiliary vacuum pump
5	BLA	Beam line auxiliary control board
6	BMAG or BNDMAG	Bending magnet
7	CB	Control board or Circuit breaker
8	COOL OIL	Cooling oil equipment
9	CRYOP	Cryogenic pump
10	CTRL or CP	Control panel
11	DCC	DC capacitor
12	DCL	DC reactor, DC inductor or Deceleration
13	DCM	DC generator and motor
14	DS	Disconnecter
15	ECH	Electron cyclotron heating
16	EQ	Equipment
17	GS	Grounding switch
18	GTO	Gate turnoff Thyristor
19	HSYG	Horizontal synchronous generator
20	HV	High voltage
21	IM	Induction motor
22	IS	Ion source
23	ISO	Isolation
24	LHe	Liquid helium
20	LN2	Liquid nitrogen
26	LV	Low voltage
27	MC	Modular coil
28	NBI	Neutral beam injector
29	PFC	Poloidal field coil
30	PS	Power supply
31	RP	Rotary pump
32	REFCR	Refrigerator for cryogenic pump
33	SB	Surge blocker
31	SCR	Thyristor
32	SIM	Self-excited induction generator and motor
33	SW or SWB	Switch, switch board or power board
34	TB	Table or Terminal box
35	TCB	Temperature converter board
36	TFC	Toroidal field coil
37	TMP	Turbo molecular pump
38	TRF	Transformer
39	VCB	Vacuum circuit breaker
40	VD	Voltage divider
41	VP or VPS	Vacuum pumping system
42	VSYG	Vertical synchronous generator
43	VV or VC	Vacuum vessel or Vacuum chamber

1.2 Guideline of allowable limit value of stress and strain for the CFQS

Although there is no publicly determined standard for fusion research, it is convenient to define something as guidelines. The stress component of the fusion device is complicated and its analysis not sufficient. So, it is not easy to step in detail on technical standards. We may only follow the basic idea, but we should think about the details flexibly. The fusion research often follows the ASME III. Even in the CFQS project, we will be better to follow the same guideline.

Table 1.2.1 may be used as a guideline for CFQS, that is a just guideline, not a necessary and sufficient condition. If it cannot be satisfied, it may be sometimes used on condition that the integrity is confirmed in the periodic inspections.

Table 1.2.1 Design guideline of typical materials.

Material		SUS316	C1020 -O	C1020 -1/2H	Resin	Composite (Coil)	FRP
Young's Modulus	(GPa) E	197	100	100	1~3	100	100
Design Stress	(MPa) S_m	137	50	90	-	30	50
Design Strain	ε					<0.1%	
Tensile Strength	(MPa) σ_u	520	230	270	10~100	200	2000
Yield Strength	(MPa) σ_y	205	80	250	-	80	500
Elongation	(%)	40	50	25	1~2	1~2	5
Poisson's ratio	ν	0.3	0.34	0.34	-	0.3	0.3
Density	(kg/m ³) ρ	7800	8960	8960	1100	8000	1500
Thermal expansion	α	1.73×10^{-5}	1.65×10^{-5}	1.65×10^{-5}	5×10^{-5}	1.65×10^{-5}	2.0×10^{-5}
Comments		300k	OFC	OFC	after curing	OFC + isolation	Varies

$S_m = \min(2/3 \sigma_y, 1/3 \sigma_u)$ -- ASME III criterion

The S_m is changed according to operating temperature.

If possible, it is desirable that strain ratio ε is less than 0.1 % or 0.5 % at worst for the coil

Because the material properties of a coil (that is on copper and insulation composite) differ greatly from structural material, the ASME III should not be strictly applied for them. The strength of the coil is affected by the working method and the heat treatment conditions in addition to the selection of the material. As these data are not released to the public, they need to be acquired by developers themselves through element prototyping and inspection. It is difficult to decide the guidelines when it is not done, but it is inconvenient if we have no guidelines. So, we will temporarily extend the ASME III to the coil but also consider the unique properties. Those are

- The conductor is very flexible and cannot be cut in a short time even if it exceeds the yield strength.
- The insulation (especially cured resin close to glass) is easy to crack and should be restricted by strain.
- It is more reliable to minimize the deformation of the coil within the measurable range. The target of the deformation is 1 mm or less.

2 Coils

2.1 Design of coils

2.1.1 Conductor

1) Modular coil (MC) and poloidal field coil (PFC)

Material; Hollow copper square tube (OFC-O, equivalent JIS-C1020)

Oxygen free copper annealed

Tensile strength; 239 MPa, Elongation; 45 %, Hardness; 48HB

Cross section Fig. 2.1.1

Cross-sectional area of cooling hole $S_{H2O} = \pi D^2/4 = 12.566 \text{ [mm}^2\text{]}$

Cross-sectional area of conductive section

$$S_{CU} = 8.5 \times 8.5 - 12.566 - (2 \times 2 - \pi \times 1 \times 1) = 58.825 \text{ mm}^2$$

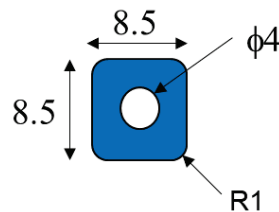


Fig. 2.1.1 Cross section of a conductor.

2) Toroidal field coil (TFC)

Material; Copper square solid conductor with insulation coating

Cross section Cross-sectional area is about 20 mm²

2.1.2 Insulation

1) MC and PFC

Heat-resistant classification class; F for the MC, A for the PFC

Vacuum pressure impregnation (VPI)

Layer insulation

Thickness; 1 mm

Fiber glass tape 16 mm \times 0.2 mm, half lap \times 2

Polyimide tape (Kapton) 10 mm \times 0.05 mm, half lap \times 2

Ground insulation

Thickness; 3 mm or less to be determined according to the voltage

2) TFC

Heat-resistant classification class; B or F
Enamel clothing *etc.* to be determined.

2.1.3 Stiffened shell (Reinforcement plate)

1) MC

SUS U-shaped case partially connected by short and thin rectangular plate
Thickness; 10 mm for the MC1, MC2, and MC3; 15 mm for the MC4

2) PFC(IV) and PFC(OV)

Nothing

3) TFC

Nothing.
Clamping fixed in a bobbin on the vacuum vessel

2.1.4 Winding structure

1) MC

- Winding method; Three double pancakes with winding parallel simultaneously
- Cross section; Fig. 2.1.2
- Structure of winding start and winding end; Fig. 2.1.3
- Conductor and cooling water pipe joints; Fig. 2.1.4

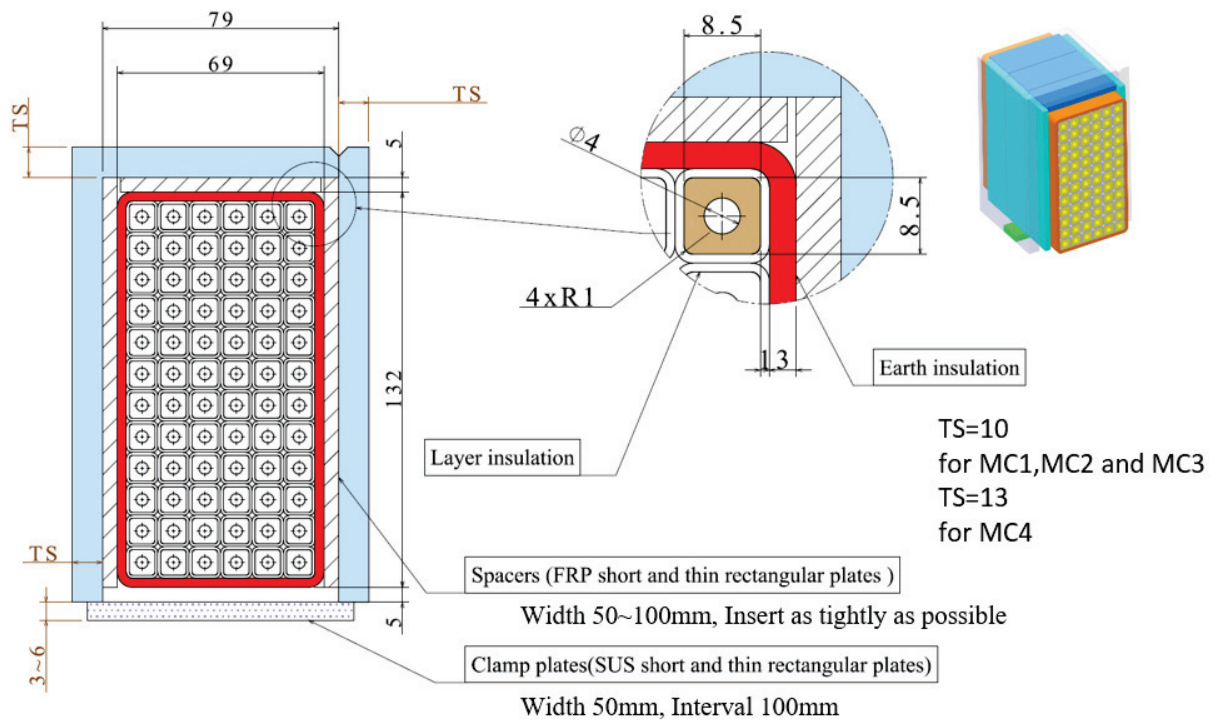


Fig. 2.1.2 Cross section of the modular coil.

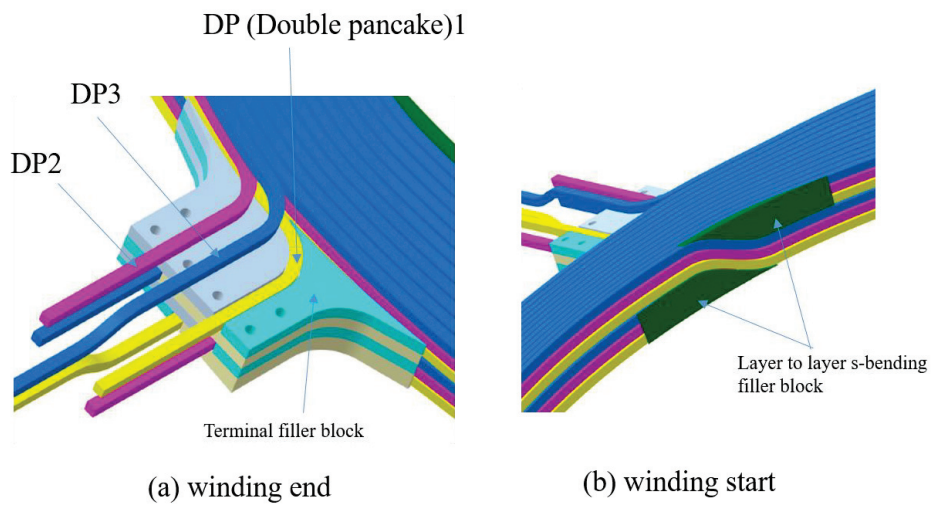


Fig. 2.1.3 Structure of winding start and winding end.

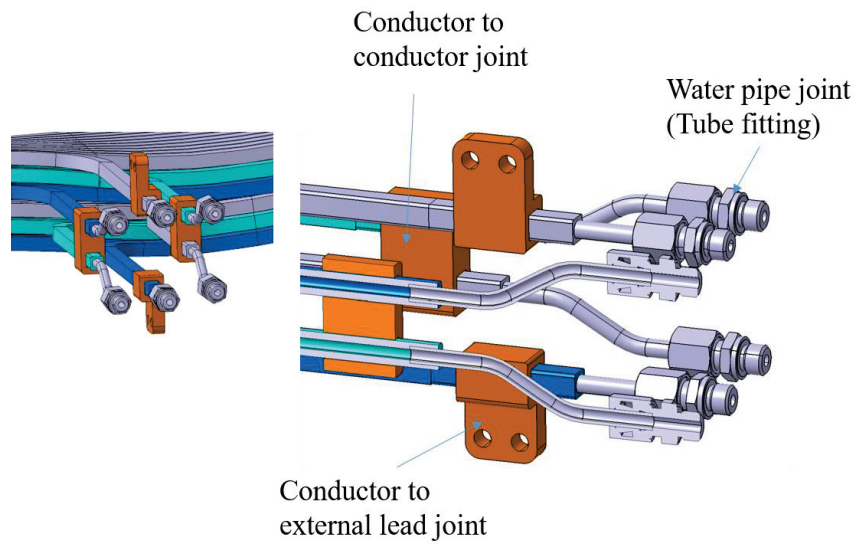


Fig. 2.1.4 Conductor and cooling water pipe joints.

2) PFC

- Winding method;
 - Four solenoid winding for the IV
 - Two double pancakes with winding parallel simultaneously for the OV
- Cross section; Fig. 2.1.5
- Structure of winding start and winding end; Fig. 2.1.6 and Fig. 2.1.7

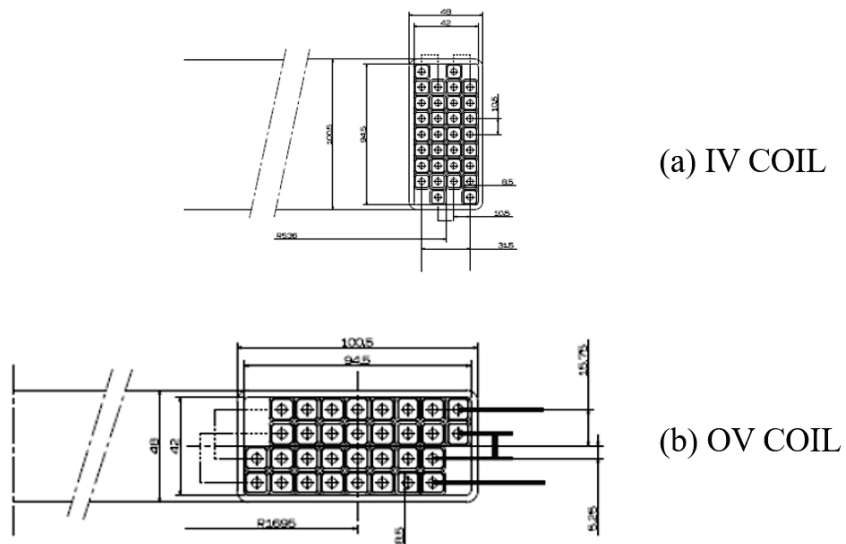


Fig. 2.1.5 Cross section of the PFC.

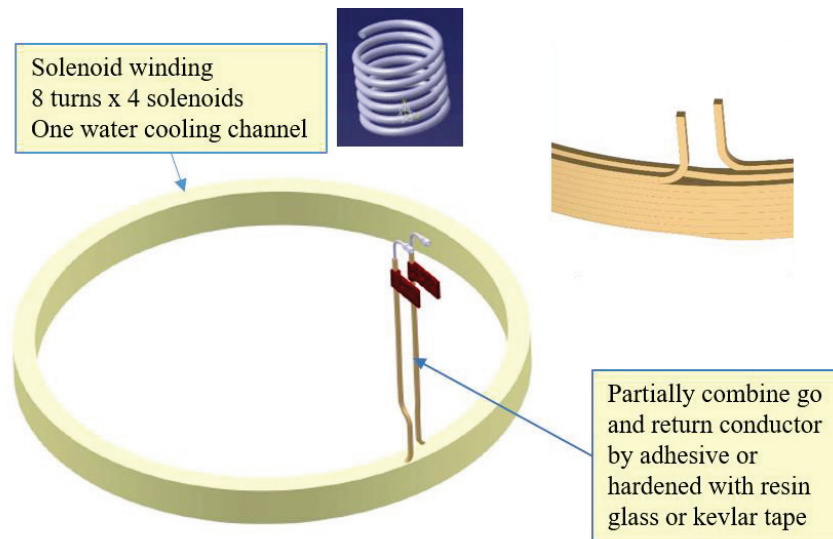


Fig. 2.1.6 Structure of winding start and winding end for the IV.

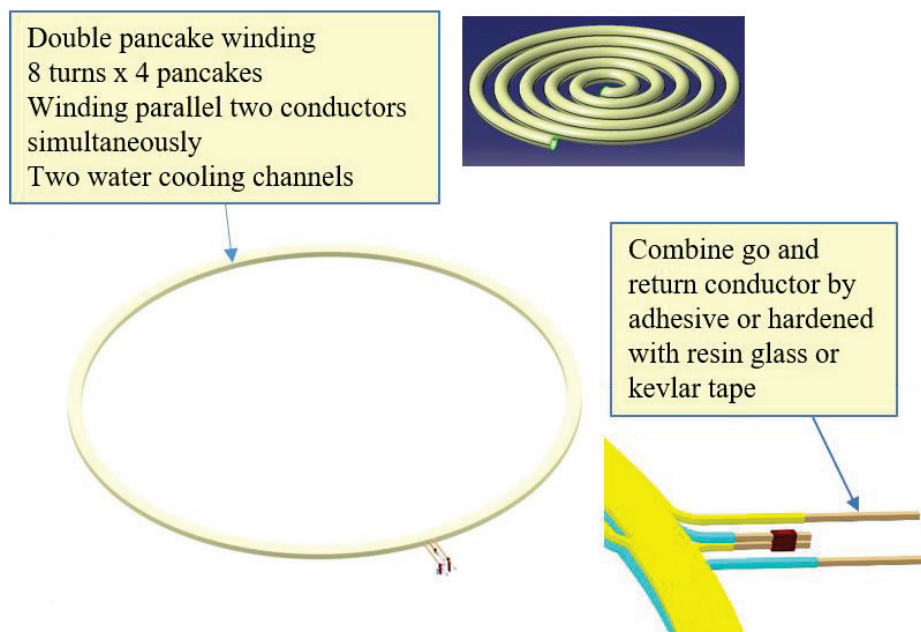


Fig. 2.1.7 Structure of winding start and winding end for the OV.

3) TFC

- Winding method; Two solenoid winding with no cooling channel
- Cross section; Fig. 2.1.8 and Fig. 2.1.5
- External lead joint; Connecting with insulated cables by solderless terminal

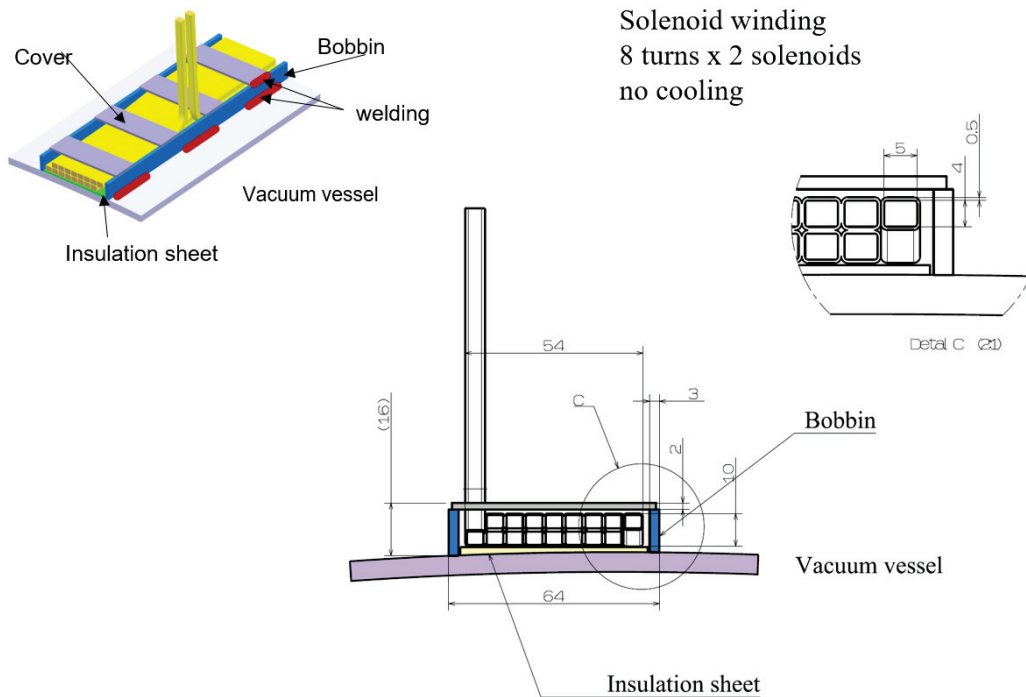


Fig. 2.1.8 Cross section of the TFC.

2.1.5 Temperature rise in one shot and cooling method

The design plan is shown in Table 2.1.1. The time average current density is low enough to be cooled by natural air cooling. Since the temperature rise in one shot of the MC is very large, water cooling is used to shorten the cooling time constant. Although the current density of PFC is not high, it is also water cooled because the air-cooling efficiency seems to be poor due to the large cross section.

Table 2.1.1 Temperature rise in one shot and cooling method.

Coil name	unit	MC	PFC	TFC
Cross section of the coil	mm ²	63 × 126	94.5 × 42	54 × 10
Pulse length (Square wave conversion time)	s	1.11	0.38	0.2
Pulse period	s	300	300	300
Maximum current	A	4,340	4,340	2,170
Time average current	A	264	155	54
Maximum current density	A/mm ²	74	74	114.2
Time average current density	A/mm ²	4.5	2.6	2.9
Temperature rise in a shot	k	36	12	15
Cooling method		Water	Water	Natural air
Cooling time (Expected empirical value)		Typically, 5 to 10 minutes		Typically 1 hour

2.2 Impedance of each coil

Table 2.2.1 Inductance matrix for each coil group.

Turns	72				32		16		
Number of coils	4	4	4	4	2	2	4	4	4
Name	MC1	MC2	MC3	MC4	IV	OV	TFC10	TFC32	TFC70
MC1	58.87	14.15	5.77	3.72	0.07	0.85	-5.16	-1.73	-0.43
MC2	14.15	49.45	11.69	5.82	0.27	0.21	-2.00	-3.68	-0.72
MC3	5.77	11.69	47.41	13.86	-0.27	-0.48	-0.74	-1.68	-1.89
MC4	3.72	5.82	13.86	52.57	-0.60	-0.66	-0.45	-0.76	-3.32
IV	0.07	0.27	-0.27	-0.60	4.28	0.72	0.00	0.00	0.00
OV	0.85	0.21	-0.48	-0.66	0.72	18.13	0.00	0.00	0.00
TFC10	-5.16	-2.00	-0.74	-0.45	0.00	0.00	2.683	0.262	0.057
TFC32	-1.73	-3.68	-1.68	-0.76	0.00	0.00	0.262	2.335	0.108
TFC70	-0.43	-0.72	-1.89	-3.32	0.00	0.00	0.057	0.108	1.996

Obtained at May 2019 by NIFS after the design change of reducing the maximum curvature and tilting the normal direction to the current carrying surface. They were obtained by ANSYS/Maxwell. Each value includes margin of 5 %. Unit of inductance is mH.

Table 2.2.2 Combined inductance and resistance for each coil group.

Name	Turns	Number of coils	S	L	R
			mm ²	mH	mΩ
MC1	72	4	58.83	82.52	435.67
MC2	72	4	58.83	81.12	429.50
MC3	72	4	58.83	78.74	415.62
MC4	72	4	58.83	75.97	401.23
IV	32	2	58.83	5.00	73.00
OV	32	2	58.83	18.85	230.59
TFC10	16	4	19.00	3.00	228.13
TFC32	16	4	19.00	2.70	210.00
TFC70	16	4	19.00	2.16	173.57

Obtained by ANSYS/Maxwell. Each value includes margin of 5 %. Unit of inductance and resistance is mH and mΩ, respectively. The resistance was obtained with resistivity at 75 °C.

Table 2.2.3 Inductance matrix for each coil obtained by the ANSYS/Maxwell.

	MC1-1	MC1-2	MC1-3	MC1-4	MC2-1	MC2-2	MC2-3	MC2-4	MC3-1	MC3-2	MC3-3	MC3-4	MC4-1	MC4-2	MC4-3	MC4-4	IV-L	IV-U	OV-L	OV-U	T32-1	T32-2	T32-3	T32-4	T70-1	T70-2	T70-3	T70-4	T10-1	T10-2	T10-3	T10-4		
MC1-1	2215	14	13	461	462	15	14	160	157	21	17	71	70	36	25	39	-1	8	34	54	-254	-9	-9	-85	-41	-15	-11	-22	-754	-8	-8	-295		
MC1-2	14	2216	461	13	15	462	160	14	21	157	71	17	36	70	39	26	8	-1	54	34	-9	-254	-85	-9	-15	-41	-22	-11	-8	-754	-295	-8		
MC1-3	13	461	2215	14	14	160	462	15	17	71	157	21	26	39	70	36	-1	8	34	54	-9	-85	-254	-9	-11	-22	-41	-15	-8	-295	-754	-8		
MC1-4	461	13	14	2215	160	14	15	462	71	17	21	157	39	26	36	70	8	-1	54	34	-85	-9	-254	-22	-11	-15	-41	-295	-8	-8	-754			
MC2-1	462	15	14	160	2166	19	13	73	451	31	14	41	158	62	21	27	-8	35	15	7	-702	-11	-9	-38	-100	-25	-10	-14	-300	-9	-8	-95		
MC2-2	15	462	160	14	19	2166	73	13	31	451	41	14	62	158	27	21	35	-8	7	15	-11	-702	-38	-9	-25	-100	-14	-10	-9	-300	-95	-8		
MC2-3	14	160	462	15	13	73	2166	19	14	41	451	31	21	27	158	62	-8	35	15	7	-9	-38	-702	-11	-10	-14	-100	-25	-8	-95	-300	-9		
MC2-4	160	14	15	462	73	13	19	2166	41	14	31	451	27	21	62	158	35	-8	7	15	-38	-9	-11	-702	-14	-10	-25	-100	-95	-8	-9	-300		
MC3-1	157	21	17	71	451	31	14	41	2079	60	11	28	463	140	16	18	-17	-11	-7	-43	-301	-17	-9	-20	-313	-56	-9	-11	-92	-12	-10	-39		
MC3-2	21	157	71	17	31	451	41	14	60	2079	28	11	140	462	18	16	-11	-17	-43	-7	-17	-301	-20	-9	-56	-313	-11	-9	-12	-92	-39	-10		
MC3-3	17	71	157	21	14	41	451	31	11	28	2079	60	16	18	462	140	-17	-11	-7	-43	-9	-20	-301	-17	-9	-11	-313	-56	-10	-39	-92	-12		
MC3-4	71	17	21	157	41	14	31	451	28	11	60	2079	18	16	140	462	-11	-17	-43	-7	-20	-9	-17	-301	-11	-9	-56	-313	-39	-10	-12	-92		
MC4-1	70	36	26	39	158	62	21	27	463	140	16	18	1988	399	15	14	-27	-34	-24	-44	-95	-36	-12	-14	-502	-162	-11	-11	-37	-19	-14	-21		
MC4-2	36	70	39	26	62	158	27	21	140	462	18	16	399	1986	14	15	-34	-27	-44	-24	-36	-95	-14	-12	-162	-502	-11	-11	-19	-37	-21	-14		
MC4-3	25	39	70	36	21	27	158	62	16	18	462	140	15	14	1985	399	-27	-34	-24	-43	-12	-14	-95	-35	-11	-11	-502	-161	-14	-21	-37	-19		
MC4-4	39	26	36	70	27	21	62	158	18	16	140	462	14	15	399	1987	-34	-27	-44	-24	-14	-12	-36	-95	-11	-11	-161	-502	-21	-14	-19	-37		
IV-L	-1	8	-1	8	-8	35	-8	35	-17	-11	-17	-11	-27	-34	-27	-34	1971	19	275	59	0	0	0	0	0	0	0	0	0	0	0	0	0	
IV-U	8	-1	8	-1	35	-8	35	-8	-11	-17	-11	-17	-34	-27	-34	-27	19	1971	59	275	0	0	0	0	0	0	0	0	0	0	0	0	0	
OV-L	34	54	34	54	15	7	15	7	-7	-43	-7	-43	-24	-44	-24	-44	275	59	8124	306	0	0	0	0	0	0	0	0	0	0	0	0	0	0
OV-U	54	34	54	34	7	15	7	15	-43	-7	-43	-7	-44	-24	-43	-24	59	275	306	8125	0	0	0	0	0	0	0	0	0	0	0	0	0	0
T32-1	-254	-9	-9	-85	-702	-11	-9	-38	-301	-17	-9	-20	-95	-36	-12	-14	0	0	0	2138	7	5	22	69	16	6	9	180	5	5	53	5		
T32-2	-9	-254	-85	-9	-11	-702	-38	-9	-17	-301	-20	-9	-36	-95	-14	-12	0	0	0	0	7	2138	22	5	16	69	9	6	5	180	53	5		
T32-3	-9	-85	-254	-9	-38	-702	-11	-9	-20	-301	-17	-9	-12	-14	-95	-36	0	0	0	0	5	22	2138	7	6	9	69	16	5	53	180	5		
T32-4	-85	-9	-9	-254	-38	-9	-11	-702	-20	-9	-17	-301	-14	-12	-36	-95	0	0	0	0	22	5	7	2137	9	6	16	69	53	5	5	180		
T70-1	-41	-15	-11	-22	-100	-25	-10	-14	-313	-56	-9	-11	-502	-162	-11	-11	0	0	0	0	69	16	6	9	1766	77	6	7	24	9	7	13		
T70-2	-15	-41	-22	-11	-25	-100	-14	-10	-56	-313	-11	-9	-162	-502	-11	-11	0	0	0	0	16	69	9	6	77	1766	7	6	9	24	13	7		
T70-3	-11	-22	-41	-15	-10	-14	-100	-25	-9	-11	-313	-56	-11	-11	-502	-161	0	0	0	0	6	9	69	16	6	7	1766	77	7	13	24	9		
T70-4	-22	-11	-15	-41	-14	-10	-25	-100	-11	-9	-56	-313	-11	-11	-161	-502	0	0	0	0	9	6	16	69	7	6	77	1767	13	7	9	24		
T10-1	-754	-8	-8	-295	-300	-9	-8	-95	-92	-12	-10	-39	-37	-19	-14	-21	0	0	0	0	180	5	5	53	24	9	7	13	2280	5	5	207		
T10-2	-8	-754	-295	-8	-9	-300	-95	-8	-12	-92	-39	-10	-19	-37	-21	-14	0	0	0	0	5	180	53	5	9	24	13	7	5	2279	207	5		
T10-3	-8	-295	-754	-8	-8	-95	-300	-9	-10	-39	-92	-12	-14	-21	-37	-19	0	0	0	0	5	53	180	5	7	13	24	9	5	207	2279	5		
T10-4	-295	-8	-8	-754	-95	-8	-9	-300	-39	-10	-12	-92	-21	-14	-19	-37	0	0	0	0	53	5	5	180	13	7	9	24	207	5	5	2279		

Each coil is composed of one turn. Unit of inductance is nH.

2.3 Resistance of each coil

The resistance is estimated by the equation.

$$R = \rho_e L / S_{cu}$$

where

Resistivity; $\rho_e = 1.724 \times 10^{-8}$ [Ωm Cu at room temperature]

Resistivity; $\rho_e = 1.895 \times 10^{-8}$ [Ωm Cu at 75°C]

Length of conductor; L [m]

Cross Section of a conductor; S_{cu} [m^2]

The resistance of modular coil is also obtained by ANSYS/Maxwell with the condition of the cross section of a conductor = 126.5×10^{-6} that is an average value including isolator and cooling hole. Since there are large differences of the condition between the formula and the Maxwell, results of the Maxwell are multiplied by $126.5/58.825=2.15$.

Table 2.3.1 Resistance of modular coil without margin.

Name	S_{cu} (mm^2)	Total length (m) of conductors for four coils	R ($m\Omega$) at 75°C		R ($m\Omega$) at room temperature	
			Formula	Maxwell	Formula	Maxwell
MC1	58.825	1263	404	415.0	368	378
MC2		1248	400	409.0	364	372
MC3		1209	388	395.8	353	360
MC4		1155	368	382.1	335	348

Table 2.3.2 Resistance of poloidal coils and toroidal coils without margin.

Name	S_{cu} (mm^2)	Number of coils \times turns for each coil	Total length (m) of conductors	R ($m\Omega$) at 75 °C by formular	R ($m\Omega$) at room temperature by formular
IV	58.825	2×32	217.6	69.5	63.2
OV		2×32	678.4	219.6	199.8
TFC32	19.00	4×16	216.8	217.2	197.7
TFC70		4×16	201.6	200.0	182.0
TFC10		4×16	165.6	165.3	150.4

2.4 Pressure drop and average temperature rise of cooling water for coils

Pressure drop (loss head) is calculated by the Hazen Williams' equation below.

$$h_f = 10.67 \cdot L \frac{(Q/C)^{1.85}}{D^{4.87}} .$$

Average temperature rise of cooling water is calculated by the equation below.

$$\begin{aligned} \Delta T_{water} &= \frac{\text{Average heat input}}{(\text{Flow rate})(\text{Density})(\text{Specific heat capacity})} \\ &= \frac{\Delta W}{t_{period}} \cdot \frac{1}{(Q_0 \rho C_h)} . \end{aligned}$$

where

h_f = Loss head (m)

L = Length of one cooling tube (m)

Q and Q_0 = Flow rate in a tube (m³/s)

C = Roughness coefficient (Hazen-Williams coefficient)

D = Inside tube diameter (m)

ΔW = Heat generation in one pulse (J)

t_{period} = Discharge period (s)

ρ = Density of water (kg/m³)

C_h = Specific heat capacity (J/kg K)

Table 2.4.1 Pressure drop, and average temperature rise of the cooling water.

Parameters		unit	Inlet			Outlet		
			MC	PFC(IV)	PFC(OV)	ALL		
Coil	Length of one cooling tube	L	m	100	108.8	169.6		
	Size of cooling hole in a conductor	D	mm	4	4	4		
	Flow velocity of water	u	m/s	1.9	1.9	1.5		
	Number of cooling tubes for a coil	n		3	1	2		
	Flow rate in a hole	Q	m^3/s		2.39E-05	2.39E-05	1.88E-05	
			ℓ/min		1.43	1.43	1.13	
	Loss head (Hazen Williams' equation)	h_f	m	175.62	191.07	192.34		
	Pressure drop	ΔP	MPa	1.71	1.87	1.88		
	Number of coils	m		16	2	2		
	Resistance of a coil at 75°C	R	Ω	0.105	0.036	0.116		
	Pulse operation							
	Current	I	kA	4.34	4.34	4.34		
	Pulse length (Square wave conversion)	Δt	s	1.11	0.38	0.38		
	Discharge period	t_{period}	s	300	300	300		
	Heat generation of a coil in one pulse	ΔW	MJ	2.20	0.26	0.83		
	Heat generation all in one pulse		MJ	35.12	0.52	1.66		
	Average temperature rise of the cooling water	ΔT_w	k	24.5	8.6	17.6		
	Steady operation							
	Current	I	kA	0.434	0.3	0.3		
	Average heat generation of a coil	P	kW	19.8	3.2	10.4		
Average temperature rise of the cooling water	ΔT_w	k	66.2	32.5	66.4			
Mani fold	Spec of main pipe			40A Sch20	40A Sch20	50A Sch20		
	Inner diameter of pipe	D_0	mm	42.6	42.6	53.5		
	Length of main pipe (Preliminary)	L_0	m	200	200	200		
	Flow rate in a pipe	Q_0	m^3/s		1.15E-03	1.23E-04	1.27E-03	
			m^3/hr		4.13	0.44	4.57	
	Flow velocity of water	v_0	m/s	0.804	0.086	0.565		
	Loss head (Hazen Williams' equation)	h_f	m	4.495	0.073	1.790		
Pressure drop	ΔP	MPa	0.044	0.001	0.017			
Physical property	Roughness coefficient of hole	C		130	130	130	130	
	Density of water	ρ	kg/m^3	996	996	996	996	
	Gravitational acceleration	g	m/s^2	9.8	9.8	9.8	9.8	
	Specific heat capacity of water	C_h	$J/kg.k$	4186	4186	4186	4186	

$$Q = Au = u \times \frac{(\pi D^2)}{4}$$

$$h_f = 10.67 \times L \times \frac{(Q/C)^{1.85}}{D^{4.87}}$$

$$\Delta P = \rho \times g \times h_f$$

$$\Delta T_w = \frac{\Delta W}{t_{period} (nQ) \rho C_h} \times 1$$

$$Q_0 = \sum n \times m \times Q$$

$$v_0 = Q_0 / \left(\frac{\pi D_0^2}{4} \right)$$

2.5 Optimization of the twisting angle of each modular coil

The twisting angle of the normal vector for the current carrying surface (CCS) was optimized from the viewpoint of manufacturability. The results are shown in Fig. 2.5.1, Fig. 2.5.2, Fig. 2.5.3, and Table 2.5.1 below.

The definition of curvature on the three-dimensional (3-D) surface is as follows by the differential geometry.

- Gaussian curvature $\sqrt{K} = \sqrt{k_1 k_2}$
- Mean curvature $H = (k_1 + k_2)/2$
- Maximum curvature $\text{Max}(k_1, k_2)$

Where, $k_1 k_2$ are principal curvatures. $\text{Max}(k_1, k_2) \gg \text{Min}(k_1, k_2)$ indicates near cylindrical bending (single dimensional bending), and $\text{Max}(k_1, k_2) = \text{Min}(k_1, k_2)$ indicates bowl or saddle bending (two dimensional bending). It is better that the minimum curvature radius $1/\text{Max}(k_1, k_2)$ is as large as possible, and it is desirable that it is 5 times or more the conductor diameter to prevent the conductor cross section from being deformed during winding.

The twist angle was determined according to the following procedure.

- The angle was changed continuously so that the curvature and the torsion in the Frenet-Serret formular did not increase abruptly.
- The initial angle was selected so that they would not interfere when the coil was inserted into the case as you can see by comparing Fig. 2.5.3 and Fig. 2.5.4.
- The gap between the coils and the gap with the vacuum vessel were evaluated on 3-D CAD, and the solution with an appropriate size was manually selected.

It seems that the obtained result may not be a logical optimum solution, but it is considered that the selection is an appropriate choice that is practically problem-free as can be seen by comparing with Table 2.5.2.

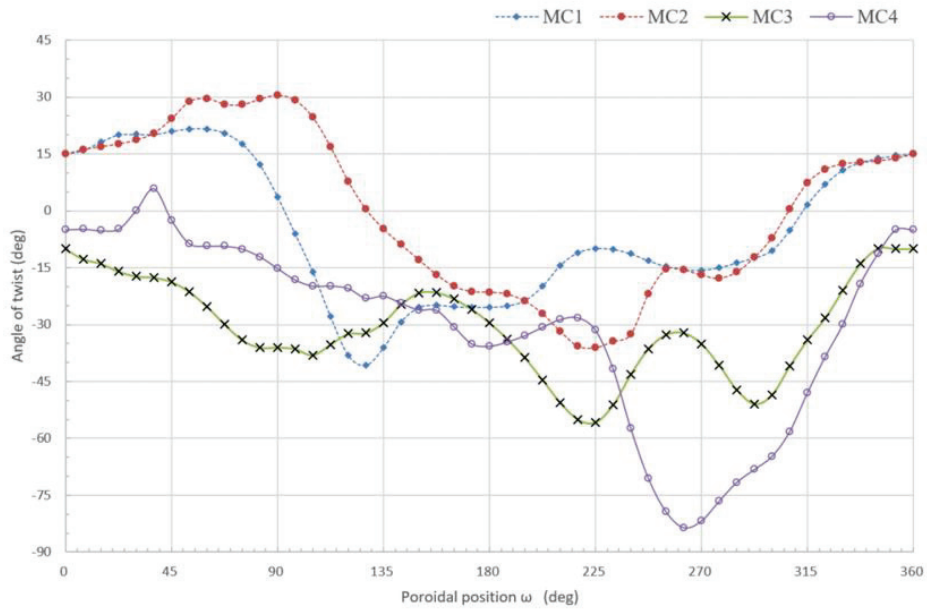
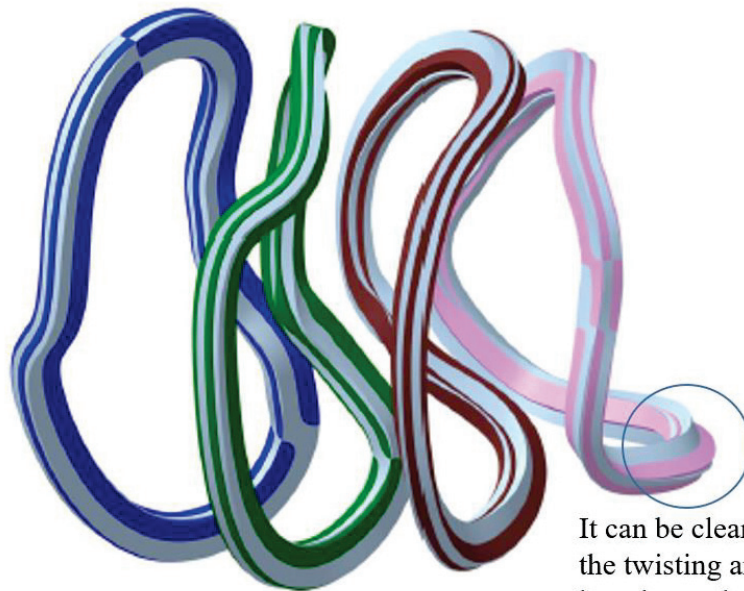


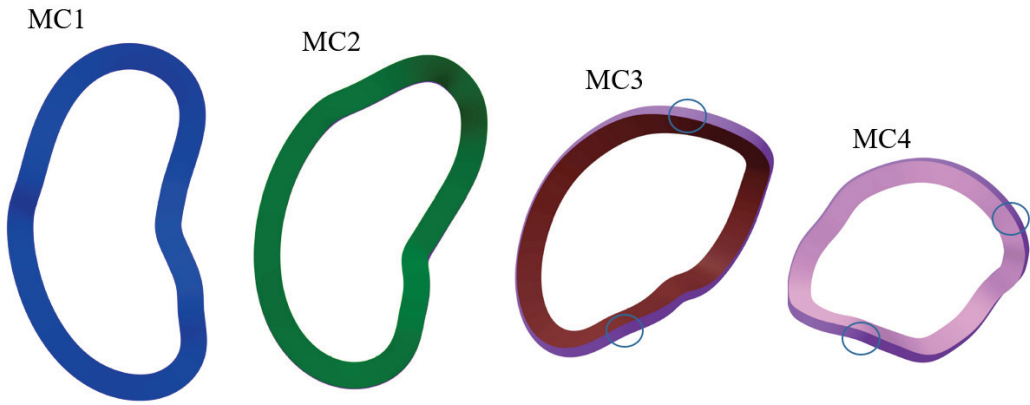
Fig. 2.5.1 Twisting angle of each modular coil.



It can be clearly seen that the twisting angle of MC4 has changed about 90 degrees from before optimization.

Fig. 2.5.2 Comparison of coil shapes.

Gray coils show shape before optimization with the twisting angle = 0, and others show shape after optimization.



The inner and outer walls are not visible because they are parallel to view direction.

Only the outer walls (purple parts) are visible because they are open faces.

It shows that the coil does not contact the case when the coil is inserted.

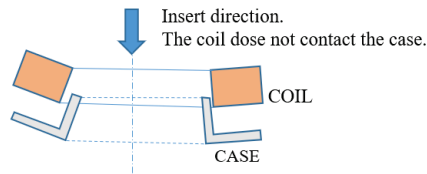
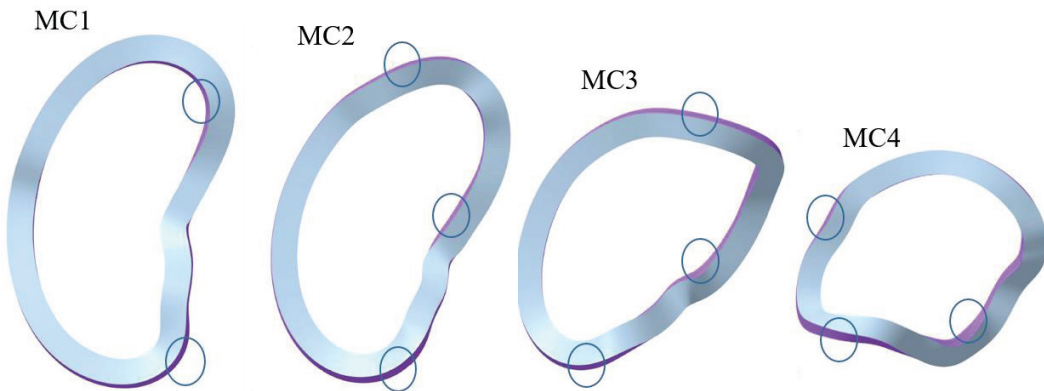


Fig. 2.5.3 Orthogonal direction view of the optimized coils.



The inner and outer walls (purple parts) are visible. It shows that the coil contacts the case when the coil is inserted.

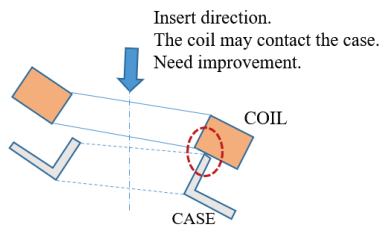


Fig. 2.5.4 Orthogonal direction view of the unoptimized coils.

Table 2.5.1 Curvature and gap of the optimized result.

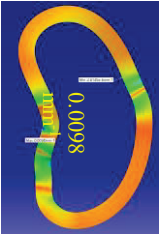



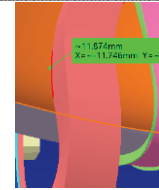
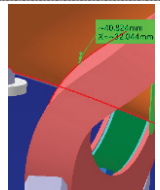
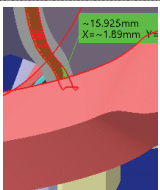
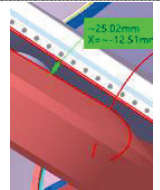
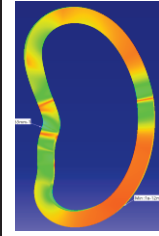
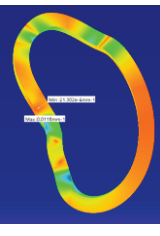
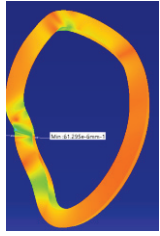
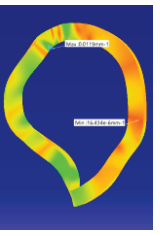
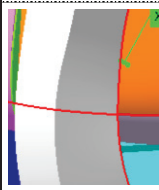
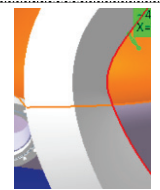
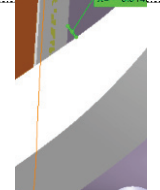
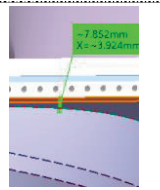
No		MC1 (type X)	MC2 (type X)	MC3 (type H)	MC4 (type G)	Criterion
Minimum curvature radius on the 3D surface (mm)	1/Gaussian	207	105.5	387.6	704.2	> 50
	1/Mean	191	103.2	275.5	230.9	
	1/Max(k ₁ ,k ₂)	100	80	141.8	155.5	
						
Minimum gap between coils with coil case (mm)	MC1-MC1	74.2				> 20 Tolerance+ margin
	MC1-MC2	43.8				
	MC2-MC3		48.1			
	MC3-MC4			37.6		
	MC4-MC4				76.0	
Minimum gap between vacuum vessel with coil case (mm)		12(With shell)	41(With shell)	16(With flange)	25(With OP)	> 10 (Tolerance)
						
Feature		The bottom surface is orthogonal to floor		A coil may interfere with coil case when the coil is put in the case		

Table 2.5.2 Curvature and gap with the twisting angle = 0 before optimization.

No		MC1 (type B)	MC2 (type B)	MC3 (type B)	MC4 (type B)	Criterion
Minimum curvature radius on the 3D surface (mm)	1/Gaussian	27 NG	125	71	200	> 50
	1/Mean	26 NG	118	71	167	
	1/Max(k ₁ ,k ₂)	22 NG	83.3	55 Marginal	83	
						
Minimum gap between coils with coil case (mm)	MC1-MC1	23.6 Marginal				> 20 Tolerance+ margin
	MC1-MC2	15.3 NG				
	MC2-MC3		16.7 NG			
	MC3-MC4			34.6		
	MC4-MC4				116.4	
Minimum gap between vacuum vessel with coil case (mm)		21(With shell)	49(With shell)	25(With flange)	8(With OP) NG	> 10 (Tolerance)
						
Feature		A coil will interfere with coil case when the coil is put in the case				

2.6 Electromagnetic force analysis on modular coils

2.6.1 Coil system for the CFQS and analysis method

A strong support structure is necessary for keeping device in a safety state when operating it. As for magnetic confinement fusion device, the electromagnetic force is the main load on coil system, which is the key component of whole device. Therefore, we need to understand the electromagnetic force on coil system and then design a reliable support structure.

There are modular coils, poloidal (vertical) field coils and toroidal field coils in this device. Fig. 2.6.1 shows the coil system of CFQS. The modular coils are a major part of coil system, they have the most complicate shape and largest total current, so our analysis focus on them. The following Table 2.6.1 shows the total current of the modular coil and each coil name of modular coils is shown in Fig. 2.6.2. In our analysis, the ANSYS Maxwell and ANSYS Workbench system was used.

2.6.2 Magnetic field distribution on the modular coils

Fig. 2.6.3 shows the magnetic field strength on each coil. In this figure, the distribution of the magnetic field on each coil is not uniform, and the magnetic field strength on the inboard side is larger than on the outboard side. The maximum magnetic strength reaches about 2.2 T, which is located on the inboard side of MC3. It is clearly seen that the distribution of the EM force will be irregular on MCs during the machine operation.

2.6.3 EM force components of the modular coil

The EM force distributions on different type of MCs are shown in Fig. 2.6.4. The results indicate that the EM force are larger on the high-field side of the MCs as we expected.

To make it easy for predicting the behavior of coils through the result depicted in Fig. 2.6.4, the EM forces on MCs are roughly divided into centripetal (radial), toroidal, and vertical components based on a cylindrical coordinate system as shown in Fig. 2.6.5. From Fig. 2.6.6 to Fig. 2.6.9 show the distribution of different force components on different type of coils. For different type of coils, the magnitude of each force component is different due to the coil shape and position.

Table 2.6.2 shows three major electromagnetic force components on the modular coil. As we all know, the CFQS is a tokamak-like device. So, we summarized the characteristics of the CFQS in Table 2.6.3 in comparison with tokamak toroidal field coil. But we need further observation because these results show only components applied on gravity center of each coil. Here, the magnetic field components are as follows.

1) Centripetal force

It is a component that tends to move the coil toward the center of the device. The torus device has a strong magnetic field on the center side. The centripetal force is mainly generated by the difference in hoop force between the center side and the outer side. In the TFC design of a tokamak, the supporting structure that withstands this component is most important.

2) Toroidal force

Sum of toroidal components that is a vertically symmetry component. It is caused by the coil being pulled from the neighbor. The tokamak does not generate this component because the TFC is pulled with the same force from the left and right.

3) Vertical force

This is sum of vertical components that is a vertically asymmetry component. Since the normal tokamak TFC is designed to have a vertically symmetrical shape, this component is almost small. Since the CFQS uses vertically asymmetric modular coils, it is necessary to design it in consideration of supporting this component.

4) Overturning force

A component that turns (rotates) the coil in the toroidal direction. It is mainly caused by the interaction of the TFC current and the PFC field in the tokamak. Since this force does not disappear even when the total force of the TFC is added, a large rotational moment is generated. In the TFC design of a tokamak, the supporting structure that withstands this component is very important. It is caused by vertical asymmetry of the coil shape in the CFQS. There is this component when we look at each coil, but the whole is canceled, and the rotational moment is lost.

For designing support structure, detail of the force distribution on coils is required. From these results, we can understand the force distribution on modular coils as shown in Table 2.6.2 and Table 2.6.3. It will be helpful for us to design and improve our support structure.

Fig. 2.6.10 shows the vertical and horizontal force on the modular coil. The horizontal force that causes the centripetal force component is dominant in the MC1 and the MC2, and the vertical force is big enough not to ignore in the MC3. Strong supports are required to resist the centripetal and vertical components, and corresponding supports must be adopted for the toroidal components.

Table 2.6.1 Currents in different coils.

Coil type	Total current in a coil (kA Turns)	Number of coils	Total current (kA Turns)
Modular coil	312.5	16	5,000

Table 2.6.2 Major components of EM force on modular coils.

Coil name		MC1 1	MC2 1	MC3 1	MC4 1	Note	
Coil position	Cartesian coordinate	x(mm)	1202.9	973.4	593.3	207.0	
		y(mm)	215.1	582.5	801.3	891.5	
		z(mm)	52.5	146.1	165.5	75.9	
Center of gravity	Major radius	R(mm)	1222.0	1134.4	997.0	915.2	
	Toroidal angle	φ (degrees)	10.1	30.9	53.5	76.9	
EMF (N)		F_x	-162.46	-103.65	-29.39	34.56	
		F_y	-43.47	-106.26	-99.97	-49.27	
	Vertical	F_z	-18.70	-60.86	-93.46	-39.20	
	Horizontal	F_h	168.17	148.44	104.20	60.18	$\sqrt{F_x^2+F_y^2}$
	Centripetal	F_R	-167.57	-143.51	-97.84	-40.18	$F_x*\cos(\varphi)+F_y*\sin(\varphi)$
	Toroidal	F_T	-14.19	-37.95	-35.86	-44.81	$F_y*\cos(\varphi)-F_x*\sin(\varphi)$
	Total	F	169.21	160.43	139.97	71.83	$\sqrt{F_x^2+F_y^2+F_z^2}$
Proportion (%)	Vertical	P_z	11.1	37.9	66.8	54.6	$\text{abs}(F_z/F)$
	Centripetal	P_R	99.0	89.5	69.9	55.9	$\text{abs}(F_R/F)$
	Toroidal	P_T	8.4	23.7	25.6	62.4	$\text{abs}(F_T/F)$

Table 2.6.3 Difference of EM force between tokamak and modular coil.

Force component	TFC Tokamak	Modular coil CFQS
Vertical force	Small	Large on some coils (MC3)
Centripetal force	Very large	Large on some coils (MC1, MC2)
Toroidal force	Almost zero	Large on some coils (MC4)
Overturning force	Very large	Small (Canceled as all coils)



Fig. 2.6.1 CFQS coil system.

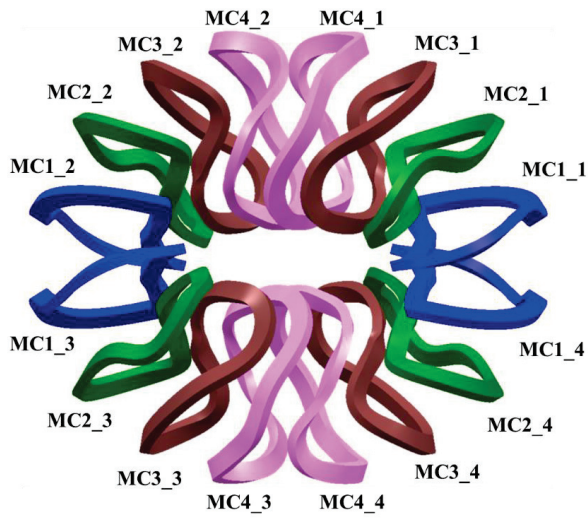


Fig. 2.6.2 Top view of modular coils.

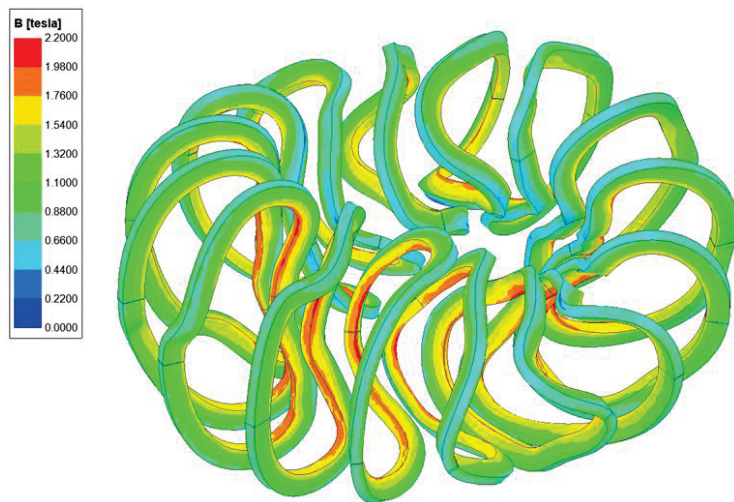


Fig. 2.6.3 Distribution of the magnetic field strength on the modular coil.

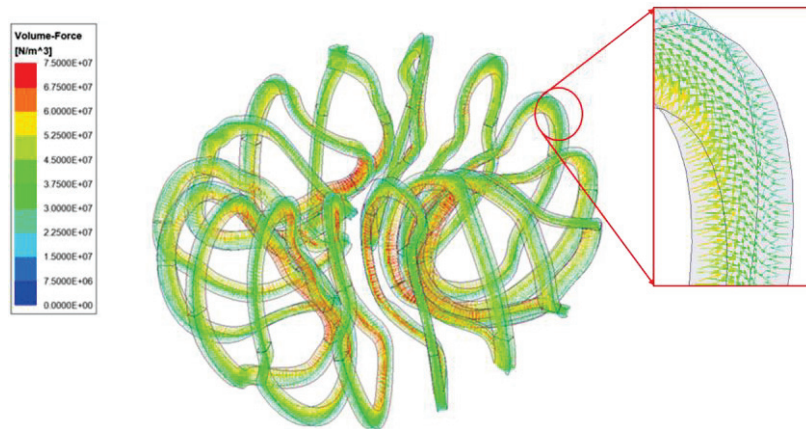


Fig. 2.6.4 EM force distribution on the MCs.

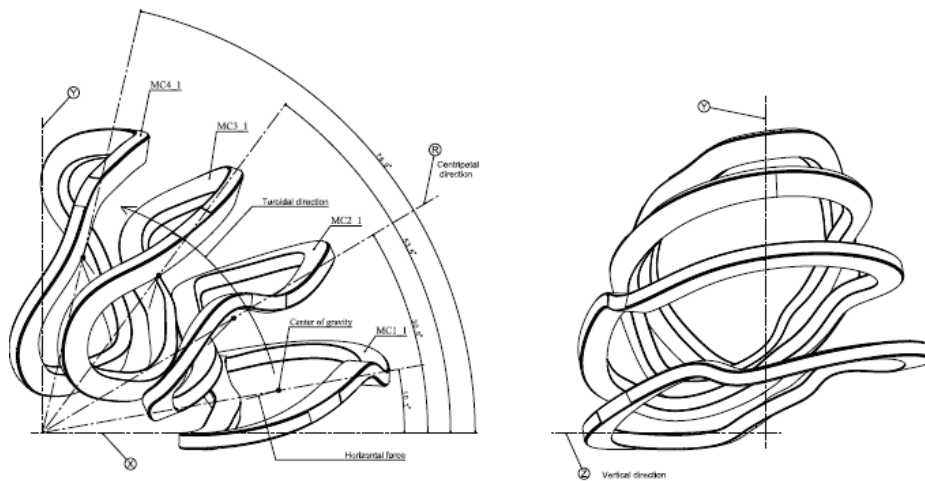
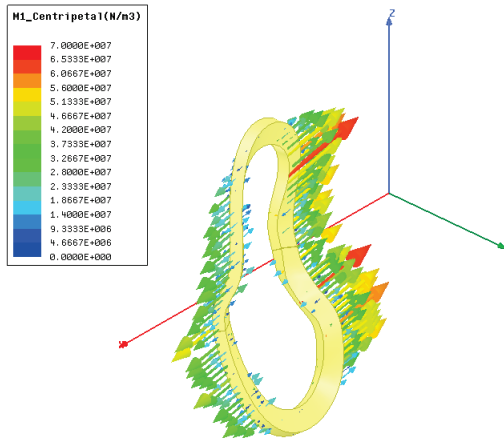
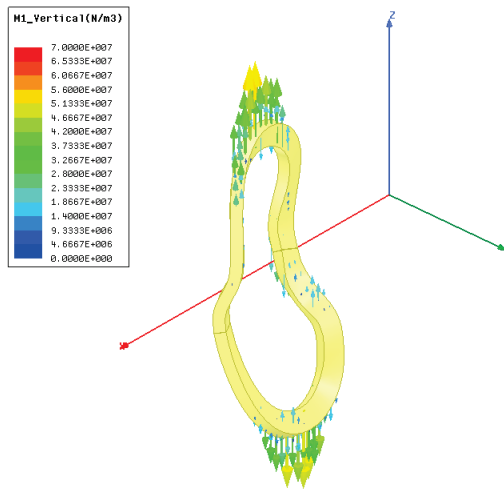


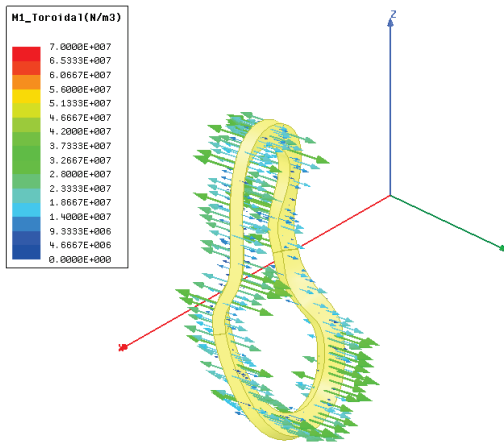
Fig. 2.6.5 Definition of coordinate system.



(a) Centripetal component.

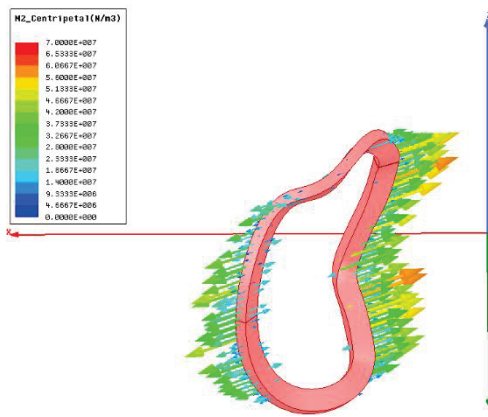


(b) Vertical component.

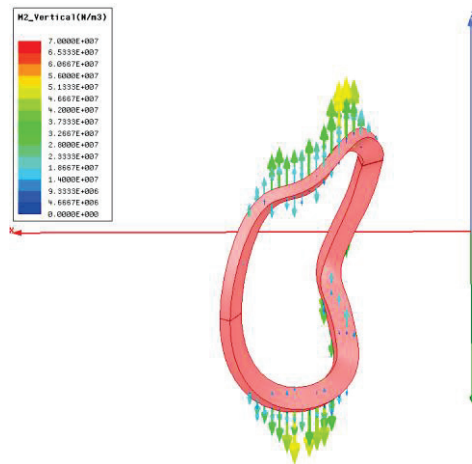


(c) Toroidal component.

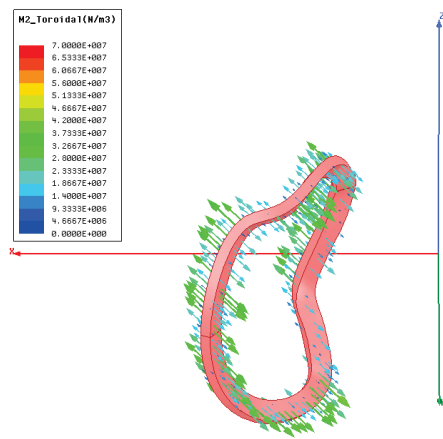
Fig. 2.6.6 EM force on MC1.



(a) Centripetal component.

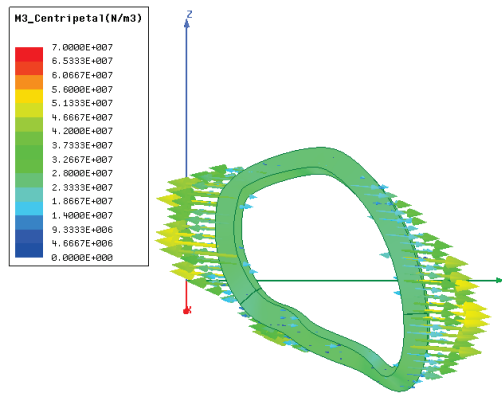


(b) Vertical component.

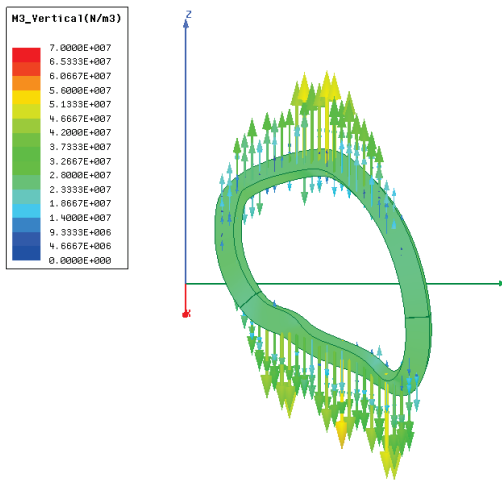


(c) Toroidal component.

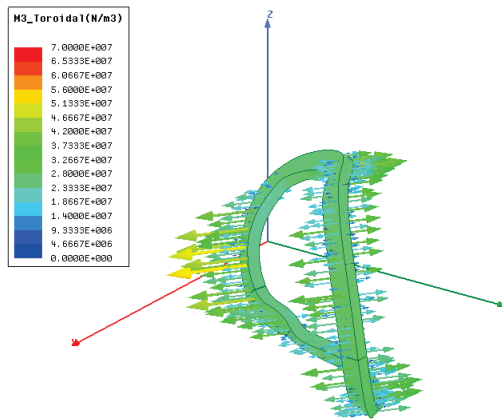
Fig. 2.6.7 EM force on MC2.



(a) Centripetal component.

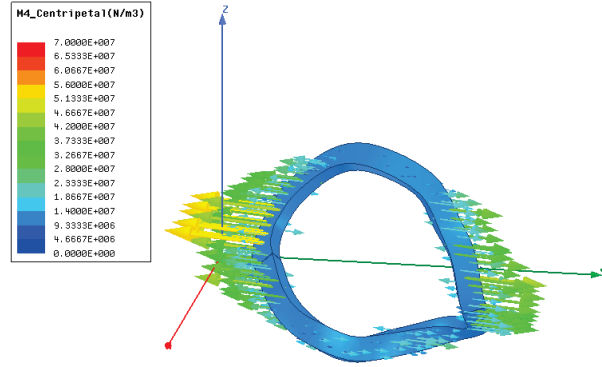


(b) Vertical component.

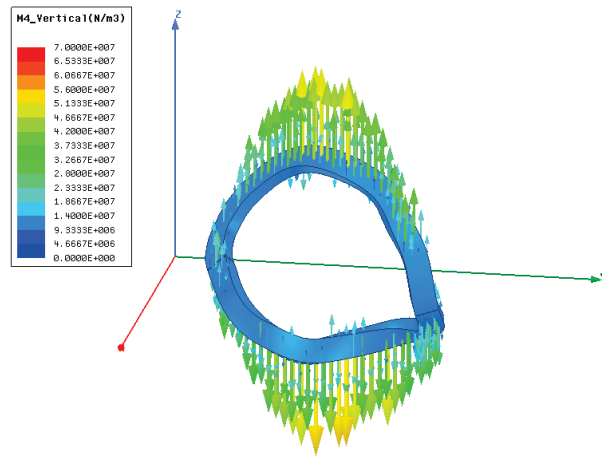


(c) Toroidal component.

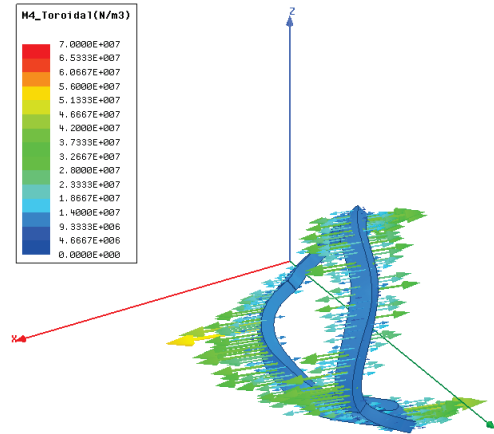
Fig. 2.6.8 EM force on MC3.



(a) Centripetal component.



(b) Vertical component.



(c) Toroidal component.

Fig. 2.6.9 EM force on MC4.

					Unit: kN
Component		MC1_1	MC2_1	MC3_1	MC4_1
Vertical	F_z	-18.70	-60.86	-93.46	-39.20
Centripetal	F_R	-167.57	-143.51	-97.84	-40.18

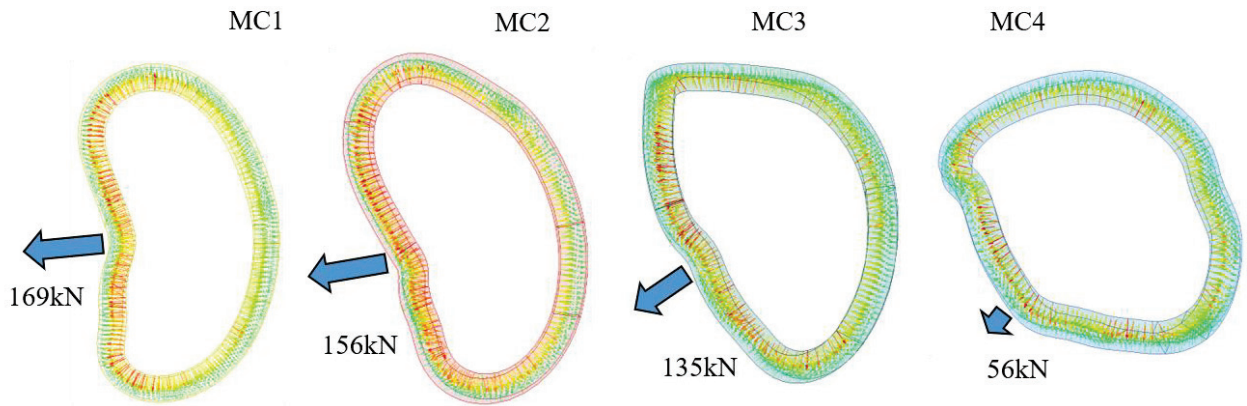


Fig. 2.6.10 Vertical and horizontal force on the MC.

2.7 Eddy current analysis on modular coil case

A time constant of an eddy current on a modular coil case was obtained. Fig. 2.7.1 shows the MC4 and its coil case. Thickness of the coil case is 13 mm and the material stainless steel. A current is applied in a cross section of the coil according to a waveform shown in Fig. 2.7.2.

The eddy current is obtained by integrating over a cross section. As a result, a time constant of the eddy current on coil case is estimated to be 2.5 ms, that is much shorter than the flat top length of the coil current. So, the effect of the coil case on the magnetic field is negligible.

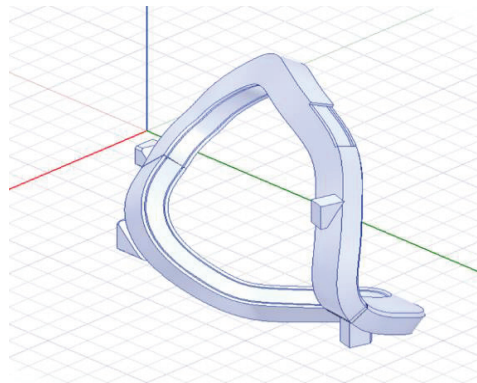


Fig. 2.7.1 MC4 and its coil case.

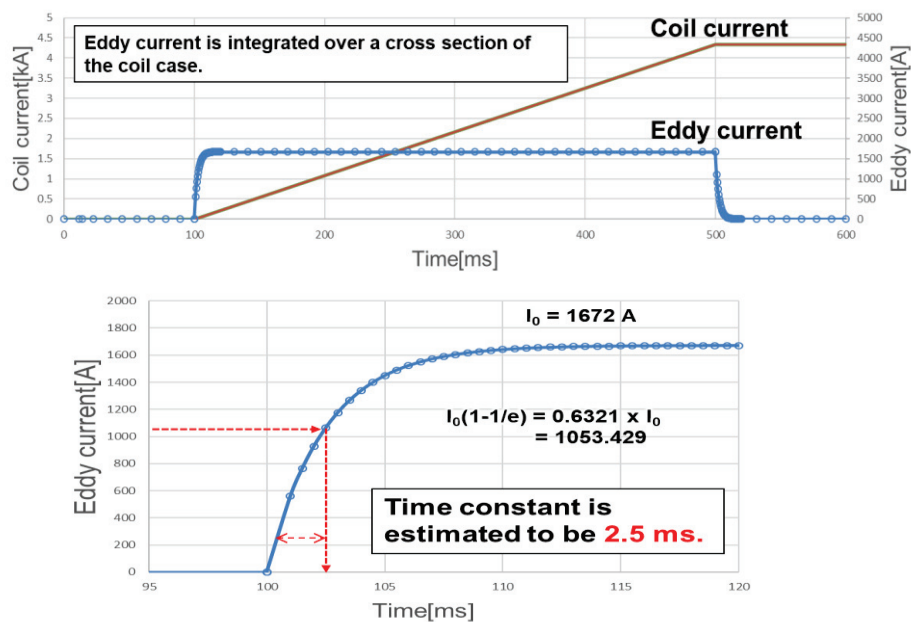


Fig. 2.7.2 Time evolution of eddy current on the coil case.

2.8 Validating the ANSYS/Maxwell result for inductance

The inductance can be analytically estimated by the solenoid formula with the Nagaoka coefficient.

$$L = K \times 4\pi \times 10^{-7} \times \mu_r \times N^2 \times S / L_{length}$$

where K is a Nagaoka coefficient, μ_r is a relative permeability, N is the number of turns, S is a cross section of inside area of coil and L_{length} is a coil width.

• MC1

$$S = \pi \times 0.92 \times \frac{1.62}{4} = 1.17$$

$$L_{length} = 0.069$$

$$\frac{D}{L_{length}} \sim \frac{0.61}{0.07} = 9$$

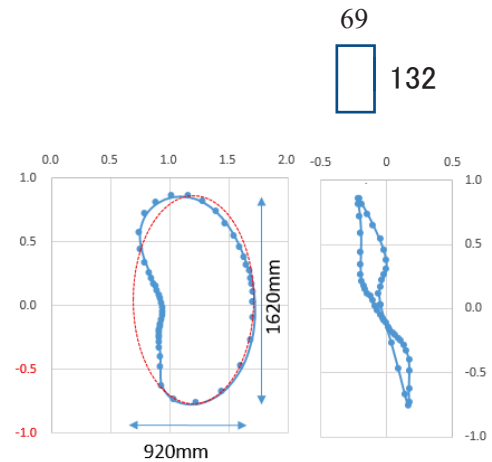
$$K = 0.2$$

$$L = \frac{0.2 \times 4\pi \times 10^{-7} \times 72^2 \times 1.17}{0.07} = 0.021[H]$$

Obtained by the formula

$$L = 2216 \times 10^{-9} \times 72^2 = 0.0115[H]$$

Obtained by the ANSYS/Maxwell



• MC4

$$S = \pi \times 1.03 \times \frac{1.16}{4} = 0.94$$

$$L_{length} = 0.069$$

$$\frac{D}{L_{length}} \sim \frac{0.55}{0.07} = 7.9$$

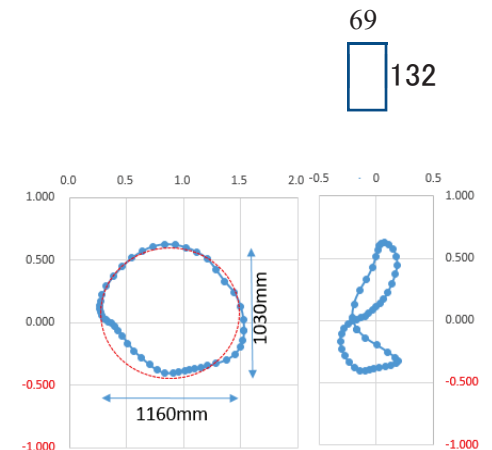
$$K = 0.2$$

$$L = \frac{0.2 \times 4\pi \times 10^{-7} \times 72^2 \times 0.94}{0.07} = 0.017[H]$$

Obtained by the formula

$$L = 1985 \times 10^{-9} \times 72^2 = 0.0103[H]$$

Obtained by the ANSYS/Maxwell



The results of the ANSYS/Maxwell are considered reasonable, which shows a value slightly larger than the roughly estimated value.

2.9 Finite element analysis for support structure

The finite element analysis has been widely used for structural analysis in many fusion devices. Usually, the analysis result is considered as a reference to estimate the quality of the supporting structure design and help designers to make optimization. Here, previous result of electromagnetic force analysis was coupled into ANSYS mechanical, and deformation, von-Mises stress and elastic strain were evaluated. As a result, we can confirm the validity of the supporting structure.

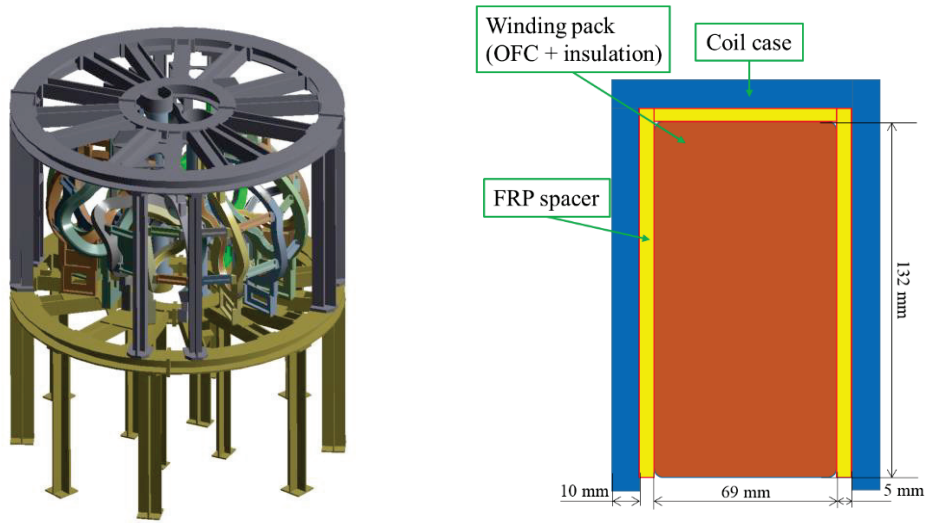
Fig. 2.9.1 (a) shows the three-dimensional global model of the CFQS. In this model, the vacuum vessel is not included in calculation. Fig. 2.9.1 (b) shows the simplified cross-section of the winding packs. In simulation, the bottom surface of twelve base legs is set as fixed boundary, and all parts are bonded together except for the coil case, FRPs and winding packs, since the coil case is not a closed one. In the real situation, the contact areas of winding packs and FRPs are frictional. But in our simulation, we set the contact condition as frictionless (the winding pack is not well supported, and the relative move could be large) as we want to know the property of the supporting structure in the worst situation. For the contact areas between coil cases and FRPs, we assume no separation (no relative move on perpendicular direction) because the FRPs should fulfill the initial gap between the coil case and winding packs. The load condition includes the deadweight of the device and EM forces applied on MCs.

In our design, lots of small parts are used in supporting coil system. To make analysis easier, we divide whole structure into three major parts, 1) support frame, 2) center support, 3) coil support. Fig. 2.9.2 shows the three major parts. According to previous result of electromagnetic force analysis, these three parts support different force components. Support frame is mainly used for supporting vertical force and whole device, center support resists the large centripetal force, coil supports resist toroidal force, overturning force, and coil's bending, moreover, they resist the centripetal force also.

In Fig. 2.9.3, three contour plots show the relevant result. The distribution of deformation on winding pack indicates that the maximum deformation is about 0.902 mm, which occurs on MC4. Therefore, we consider that the deformation will not affect the property of the entire MC system significantly. The maximum stress and elastic strain on the winding pack is about 66 MPa and 0.06 %, respectively. They are also located on MC4, and both values are less than our design values. In the winding pack, the coils are formed by two parts, *i.e.*, OFC and resin insulation. But in this simulation the coils are replaced by one composite material. Therefore, both design values for stress and elastic strain should be satisfied. The distribution of the stress and elastic stress on coils indicate that both stress and strain are in the tolerable range.

To make sure the support structure is reliable, we need to check the stress, strain, and deformation of the device.

Fig. 2.9.4 shows the stress distribution on the supporting frame and coil cases. It is obvious that the maximum stress on the supporting structure is 107.44 MPa. The maximum stress on the supporting frame and coil cases is located on the center support element and connection elements on MC1, respectively. The results indicate that the property of the supporting structure satisfies our design guideline.



(a) Simplified CFQS global model.

(b) Simplified cross-section of the winding pack.

Fig. 2.9.1 Simplified model of the supporting structure and modular coils.

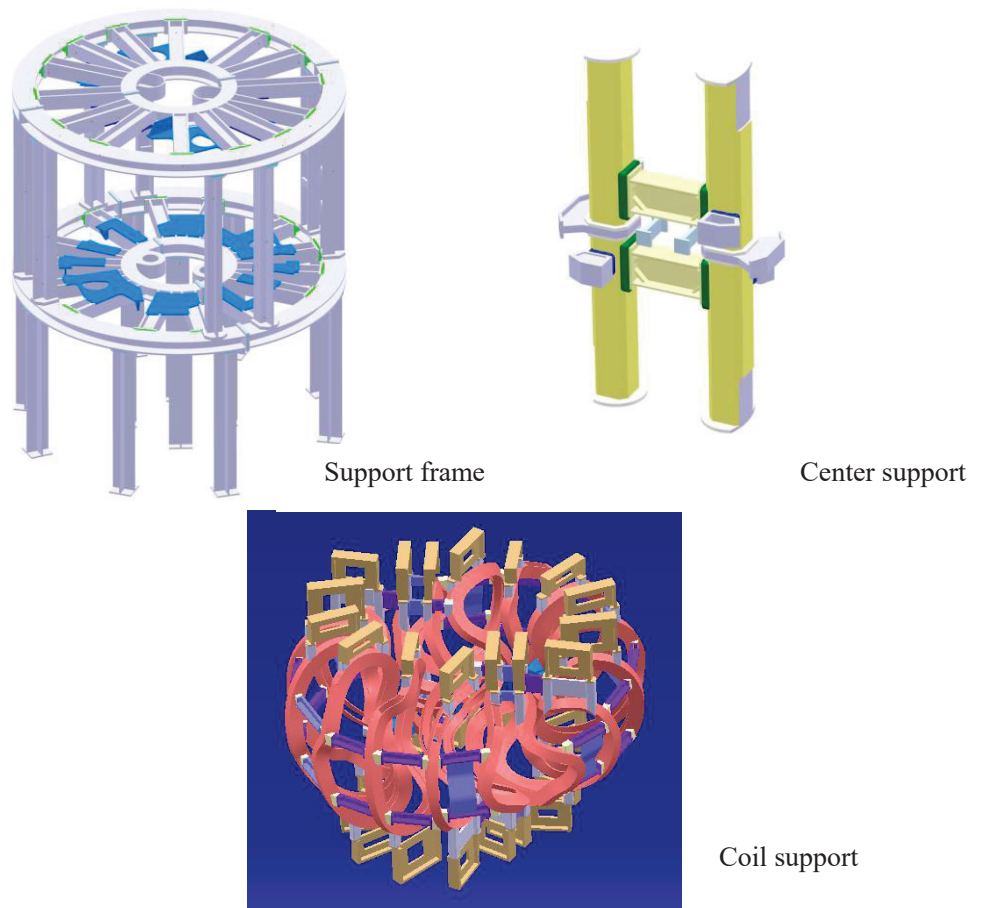
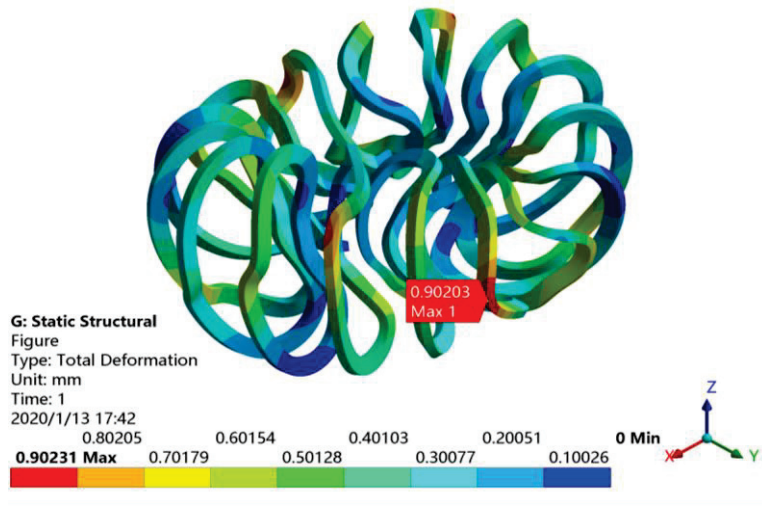
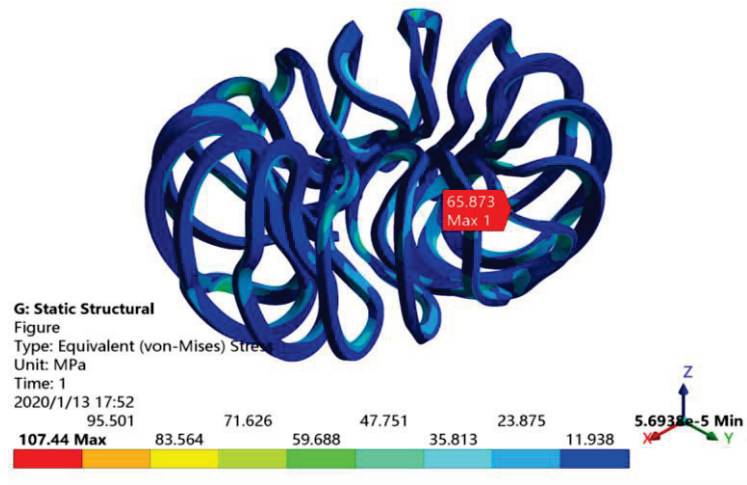


Fig. 2.9.2

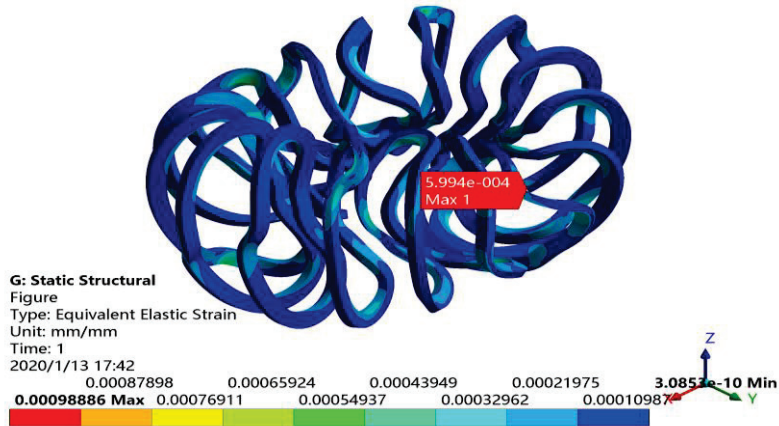
Three major parts of support structure.



(a) Deformation.

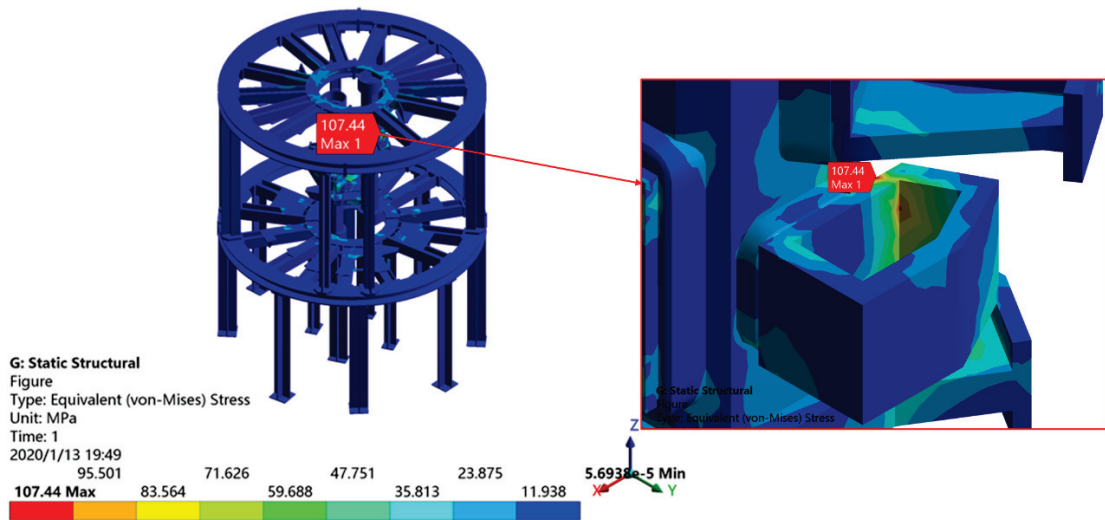


(b) Stress.

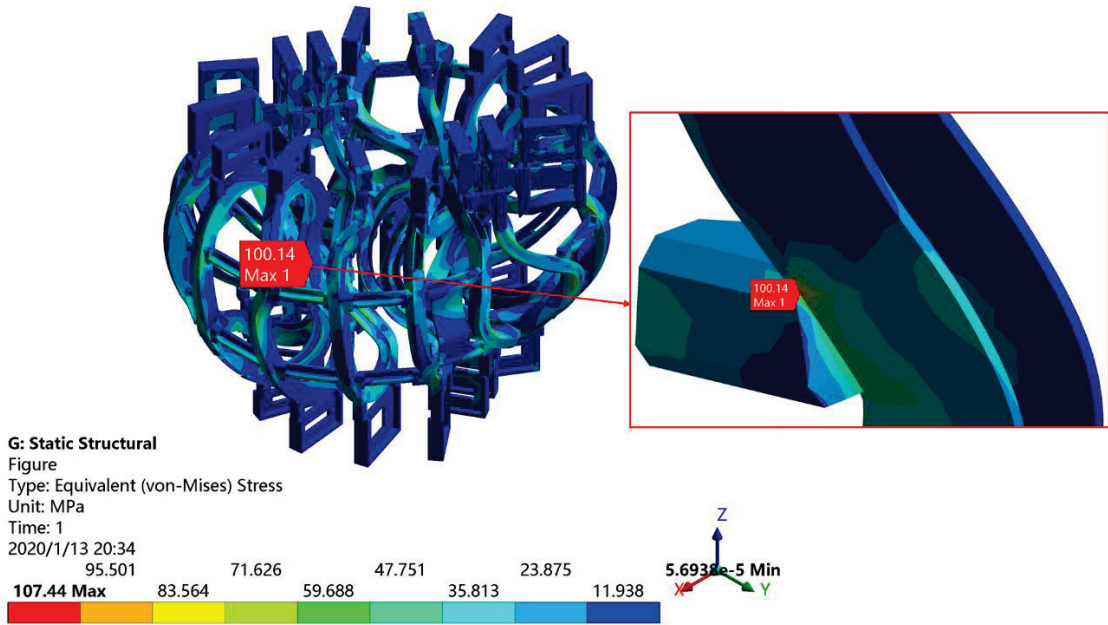


(c) Strain.

Fig. 2.9.3 FEA result for winding packs (MC).



(a) Supporting frame.



(b) Coil support.

Fig. 2.9.4 FEA result for supporting structure.

2.10 External current lead

The 32 coils will be installed in the CFQS, but it is not realistic to wire all those current leads to a control power supply room because very large space is necessary. We think that it is preferable to connect the coils with copper bus bar near the CFQS body to minimize space of the wiring and to reduce cost. Busbars save space but are difficult to design because they are inflexible. Fig. 2.10.1 shows wiring plan of the current lead. The water-cooling coils of PFC and MC are connected by copper busbars and flat braid flexible terminals which may absorb thermal displacement and assembly error. The TFCs with complicated wiring routes are connected by flexible electric wires covered with insulation coating.

Requirement for external current lead are summarized in Table 2.10.1 and Table 2.10.2. Example of wiring plan for each coil system are shown in Fig. 2.10.2, Fig. 2.10.3, and Fig. 2.10.4.

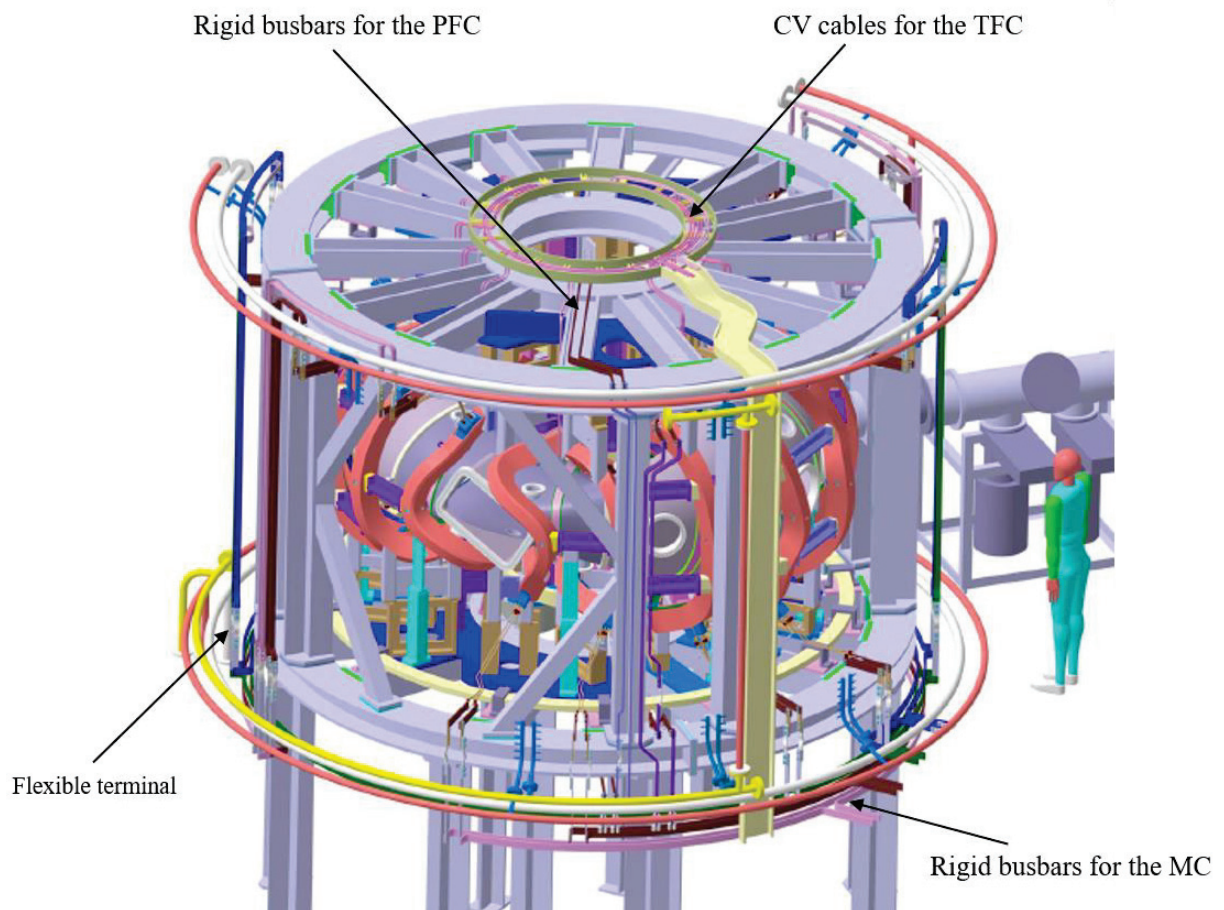


Fig. 2.10.1 External current leads for coils.

Table 2.10.1 Requirement for solid bus bar.

No	Item	Requirement	Criteria	Notes
1	Rigidity	Rigid which does not easily deform		
2	Displacement and stress	They are within allowable range for the repulsive force between returning conductors	Stress < 20 MPa	To prevent insulation breakdown
			Deflection < 2 mm	To prevent interference with other parts
			Natural frequency > 20 Hz	seismic and stiffness evaluation criteria
3	Cross section	No excessive temperature rise without cooling	Adiabatic temperature rise < 5k	In a shot for the short pulse operation
			Current density < 2A/mm ²	For continuous operation
4	Connection method	Multiple bolt fastening	Size of bolt ≥ M10	
			Number of bolts ≥ 2 for one place	

Table 2.10.2 Requirement for cable and flexible terminal.

No	Item	Requirement	Criteria	Notes
1	Cross section	Current in continuous operation is below the capacity except in special cases	$S \geq 200 \text{ mm}^2$	434 A for the MC and the PFC
			$S \geq 38 \text{ mm}^2$ (must) or 60 mm ² (desirable)	217 A for the TFC
2	Connection method	Multiple bolt fastening	Size of bolt ≥ M10	
			Number of bolts ≥ 2 for one place	
3	Allowable voltage	Above the operating voltage	≥ 6000 V	2400 V for the MC 2200 V for the OV 600 V for the IV
			≥ 600 V	600 V for the TFC
4	Allowable temperature	Above the operating temperature	≥ 90 °C	CV cable

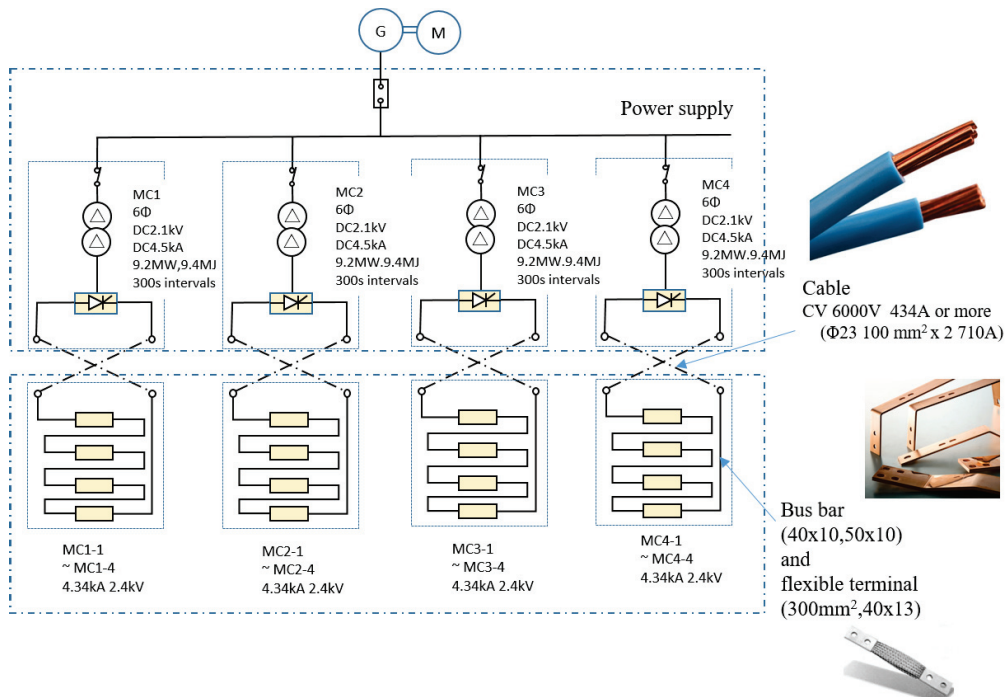


Fig. 2.10.2 Wiring plan for the modular coil.

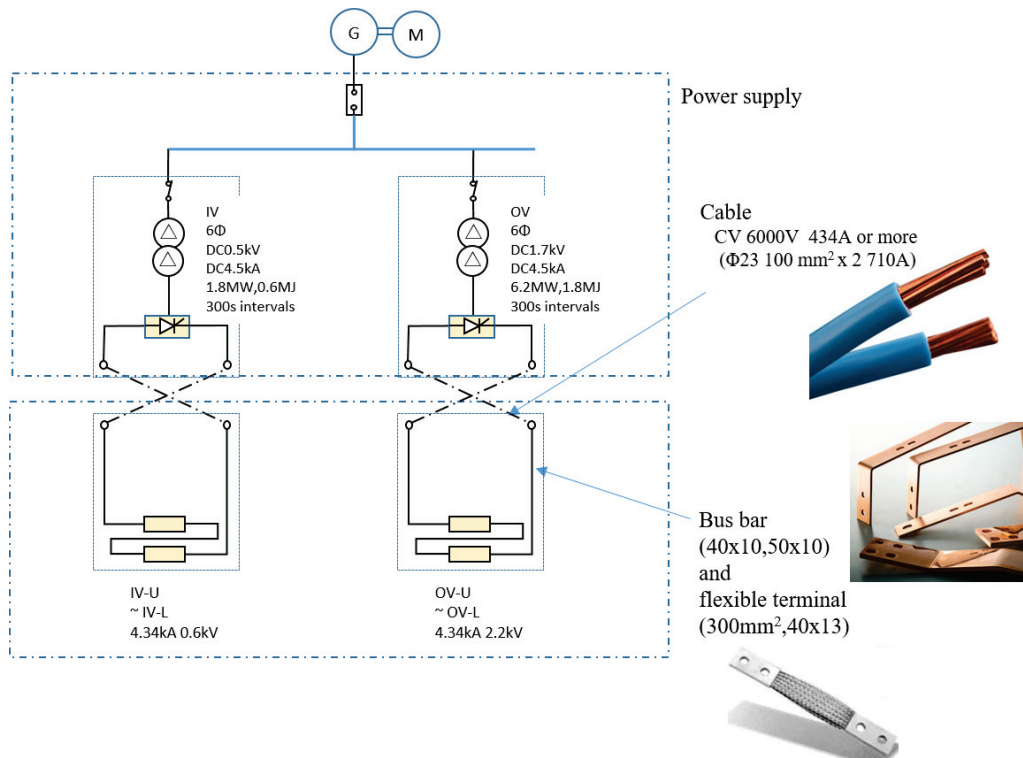


Fig. 2.10.3 Wiring plan for the PFC.

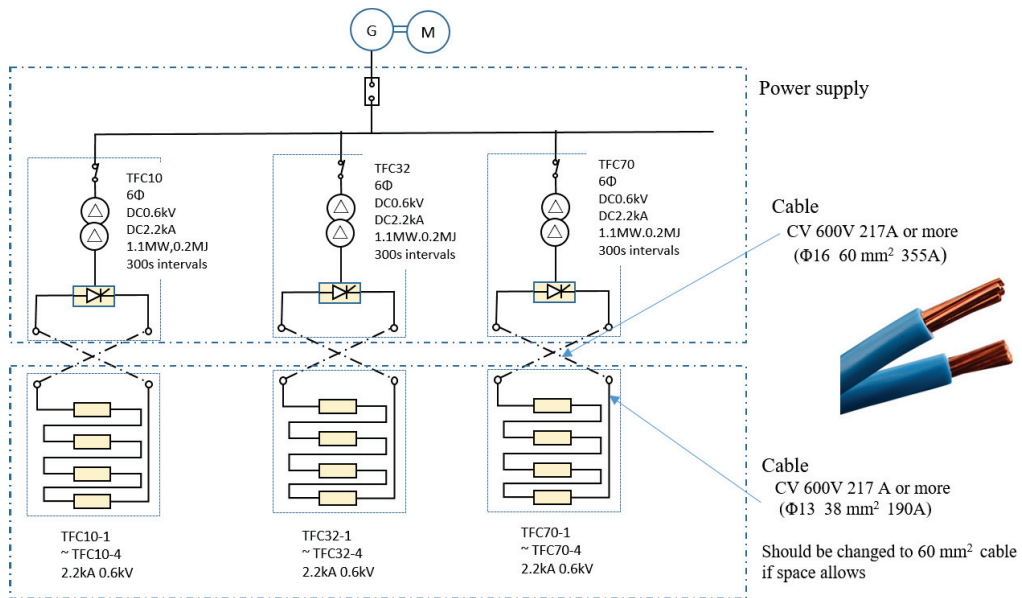


Fig. 2.10.4 Wiring plan for the TFC.

2.11 Cooling water piping

In order to cool the coils, it is necessary to disperse 108 cooling pipes (hoses) around the CFQS. The size and arrangement of a manifold (an assembly of branch pipes) for connecting them to the cooling water device were determined as shown in Table 2.11.1, and Fig. 2.11.1 to Fig. 2.11.5.

Design requirements were as follows.

- (a) Flow rate in a manifold; 5 m³/hr for the MC's and 1 m³/hr for the PFC's. Minimum flow required obtained by calculation is 4.57 m³/hr in total.
- (b) Length of a main pipe; 100 m or less
- (c) Maximum pressure; 20 atm or less
- (d) A welding flange with gasket seal is used to improve reliability. Do not use screw-in flange (or threaded flange) as much as possible.
- (e) Inject pure water from below CFQS body
- (f) Use SUS304 pipe with Sch20
- (g) Provide a function to adjust the flow rate for each type of coil. It is not necessary to adjust the flow rate for each channel. If necessary, adjust the flow rate by the orifice.
- (h) Install a flow meter on the manifold so that the flow rate of the entire the MC's and the PFC's can be monitored. Monitoring for each channel is not required for cost reduction. The flow rate in each channel will be measured by a portable ultrasonic flow meter, and the flow balance between channels is adjusted by an orifice or the like
- (i) Fix c-shaped manifold extended in the toroidal direction on the support frame.
- (j) Connect the manifold and coil with insulated nylon or PFA hose with a heat resistance of 100 °C or higher. Applying metal reinforced hose is prohibited because high voltage is applied to the coil.

Table 2.11.1 Average temperature rise, and pressure drop in manifolds.

Parameters		unit	Inlet			Outlet	
			MC	PFC(IV)	PFC(OV)	ALL	
Coil	Length of one cooling tube	L	m	100	108.8	169.6	
	Size of cooling hole in a conductor	D	mm	4	4	4	
	Flow velocity of water	u	m/s	1.9	1.9	1.5	
	Number of cooling tubes for a coil	n		3	1	2	
	Flow rate in a hole	Q	m^3/s	2.39E-05	2.39E-05	1.88E-05	
			ℓ/min	1.43	1.43	1.13	
	Loss head (Hazen Williams' equation)	h_f	m	175.62	191.07	192.34	
	Pressure drop	ΔP	MPa	1.71	1.87	1.88	
	Number of coils	m		16	2	2	
	Resistance of a coil at 75°C	R	Ω	0.105	0.036	0.116	
	Pulse operation						
	Current	I	kA	4.34	4.34	4.34	
	Pulse length (Square wave conversion)	Δt	s	1.11	0.38	0.38	
	Discharge period	t_{period}	s	300	300	300	
	Heat generation of a coil in one pulse	ΔW	MJ	2.20	0.26	0.83	
	Heat generation all in one pulse		MJ	35.12	0.52	1.66	
	Average temperature rise of the cooling water	ΔT_w	k	24.5	8.6	17.6	
	Steady operation						
	Current	I	kA	0.434	0.3	0.3	
	Average heat generation of a coil	P	kW	19.8	3.2	10.4	
Average temperature rise of the cooling water	ΔT_w	k	66.2	32.5	66.4		
Mani fold	Spec of main pipe			40A Sch20	40A Sch20	50A Sch20	
	Inner diameter of pipe	D_0	mm	42.6	42.6	53.5	
	Length of main pipe (Preliminary)	L_0	m	200	200	200	
	Flow rate in a pipe	Q_0	m^3/s	1.15E-03	1.23E-04	1.27E-03	
			m^3/hr	4.13	0.44	4.57	
	Flow velocity of water	v_0	m/s	0.804	0.086	0.565	
	Loss head (Hazen Williams' equation)	h_f	m	4.495	0.073	1.790	
Pressure drop	ΔP	MPa	0.044	0.001	0.017		
Physical property	Roughness coefficient of hole	C		130	130	130	130
	Density of water	ρ	kg/m^3	996	996	996	996
	Gravitational acceleration	g	m/s^2	9.8	9.8	9.8	9.8
	Specific heat capacity of water	C_h	$J/kg.k$	4186	4186	4186	4186

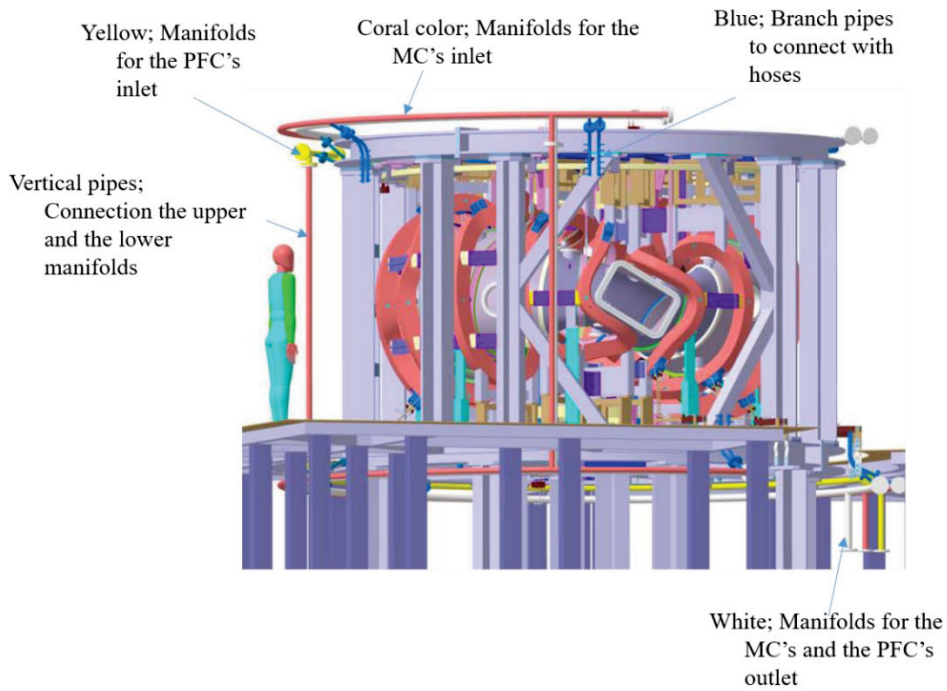


Fig. 2.11.1 Cooling water piping.

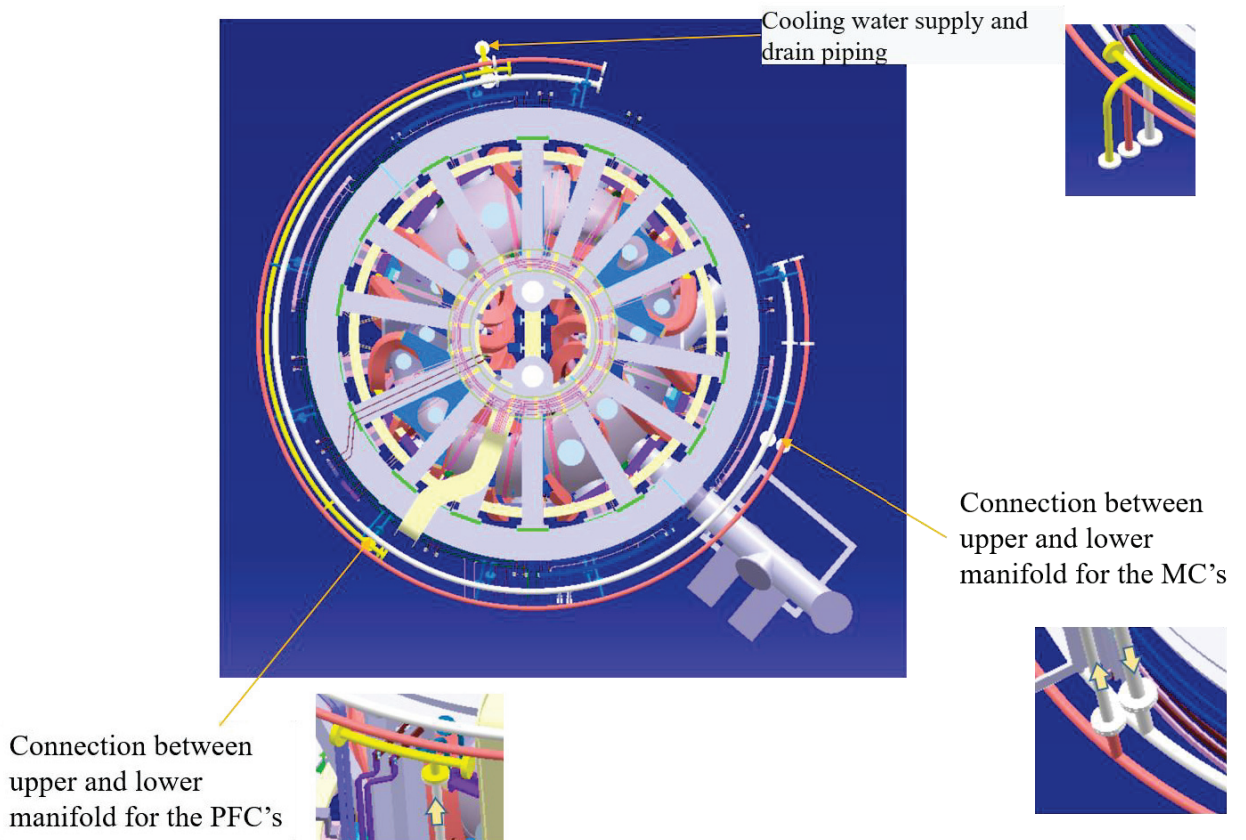


Fig. 2.11.2 Placement of manifold for the cooling water.

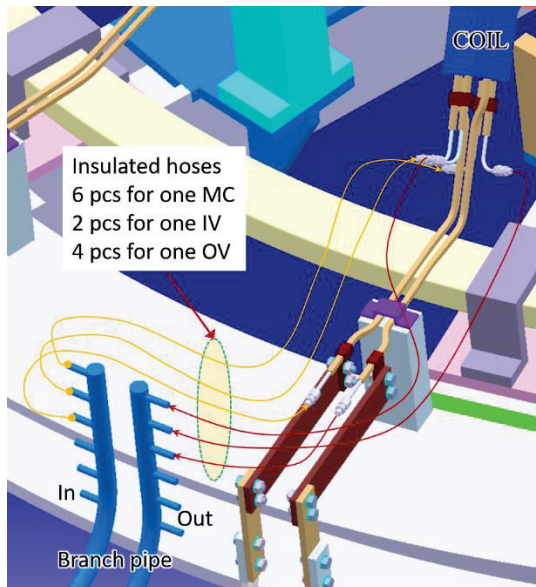


Fig. 2.11.3 Connecting the cooling water hoses.

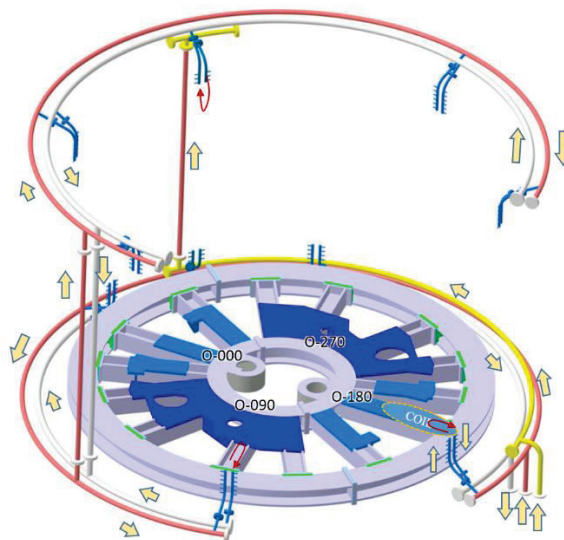


Fig. 2.11.4 Cooling water flow direction.

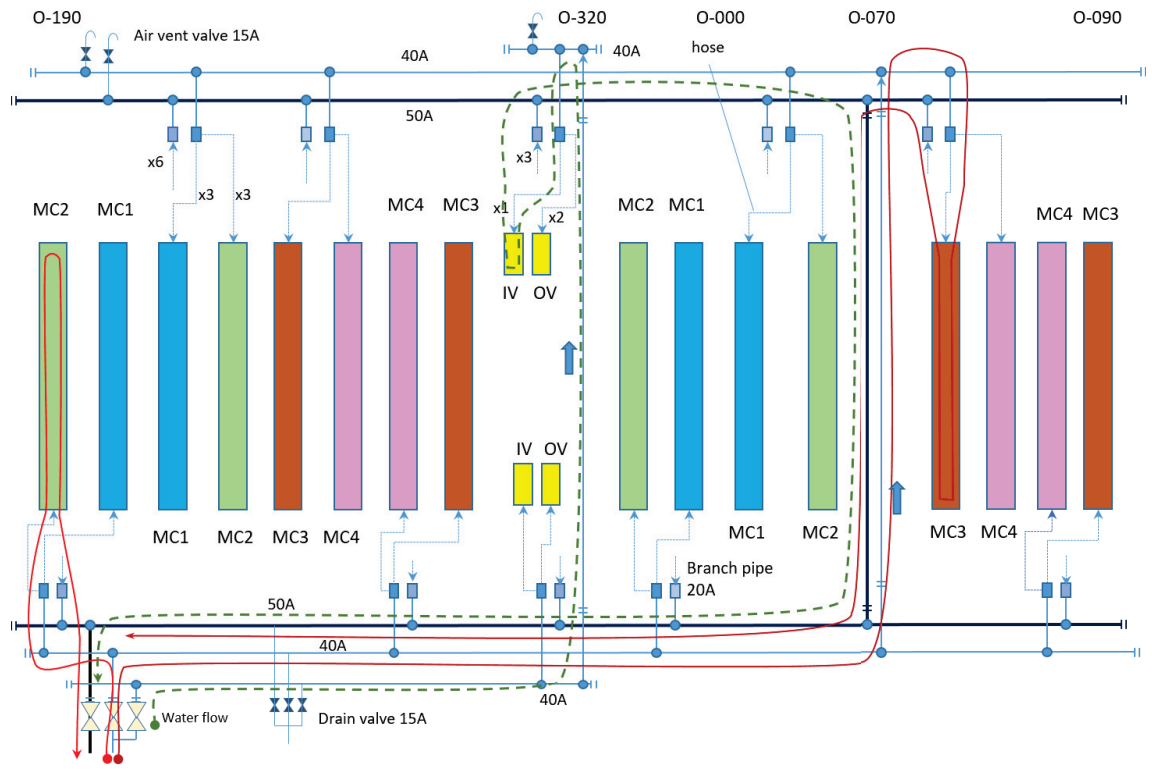


Fig. 2.11.5 Example of cooling water flow path.

3 Vacuum vessel

3.1 Cross section of vacuum vessel for CFQS

The shape of inner surface is shown at different toroidal angle in this chapter. Fig. 3.1.1 shows how to define the shape and others show cross sectional shape at different angles.

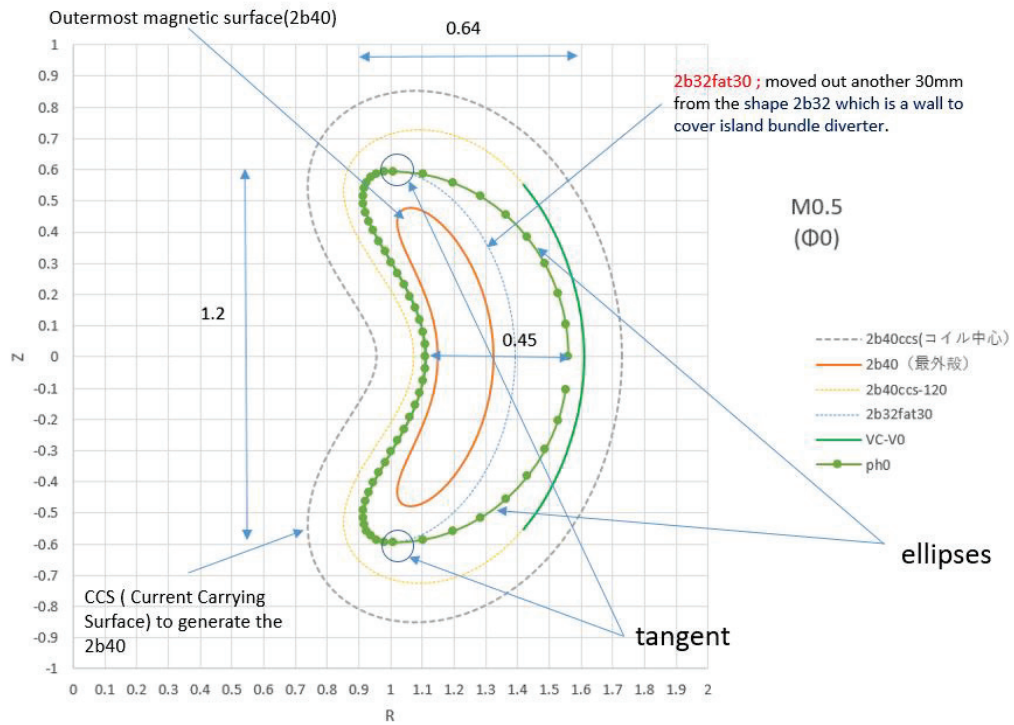


Fig. 3.1.1 Drawing with showing how to define inner shape of main vessel.

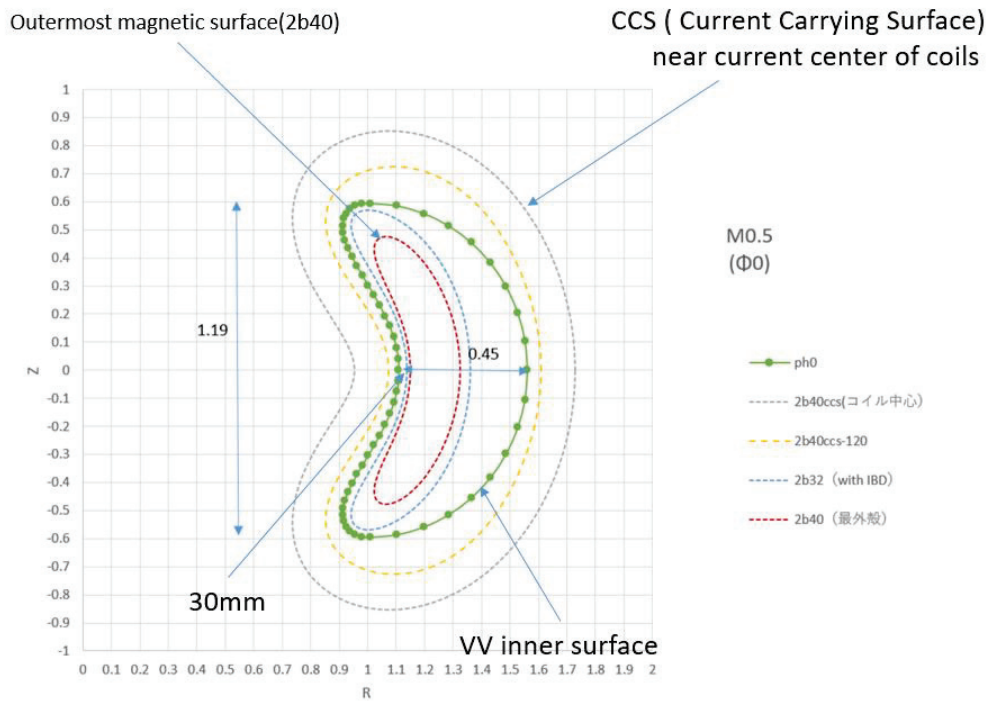


Fig. 3.1.2 Shape of main vessel at 0 degrees.

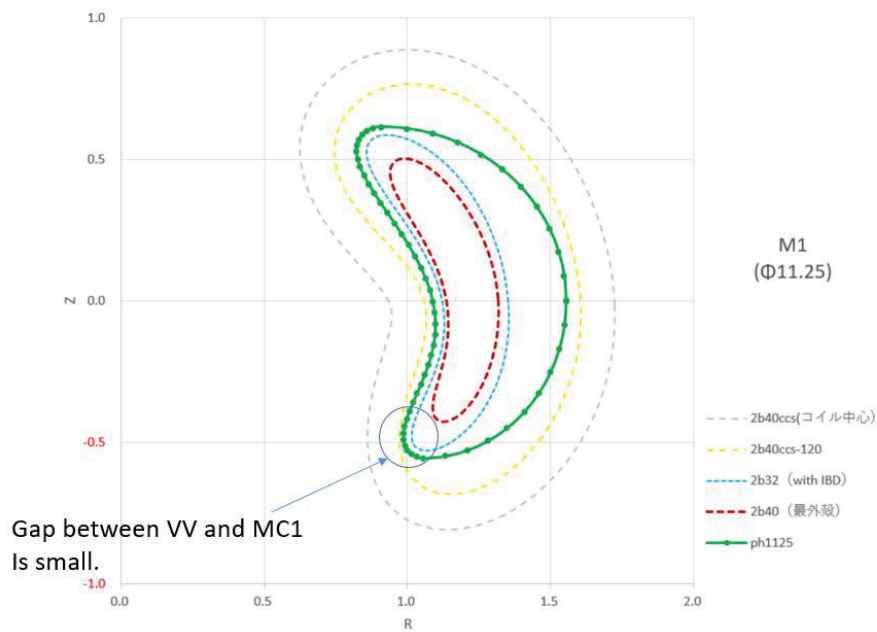


Fig. 3.1.3 Shape of main vessel at 11.25 (1/8 × 90) degrees.

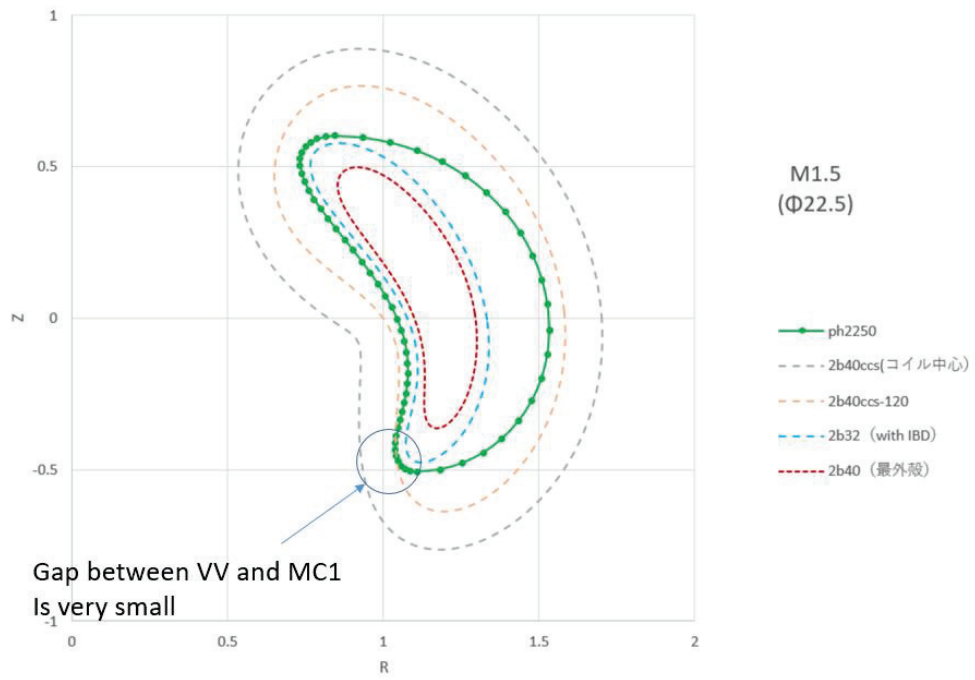


Fig. 3.1.4 Shape of main vessel at 22.5 ($2/8 \times 90$) degrees.

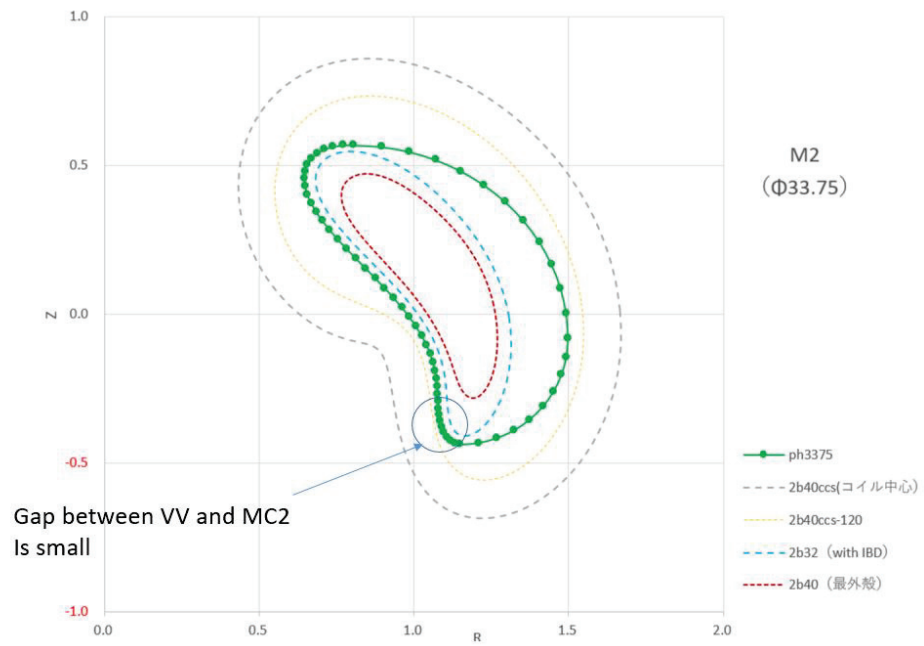


Fig. 3.1.5 Shape of main vessel at 33.75 ($3/8 \times 90$) degrees.

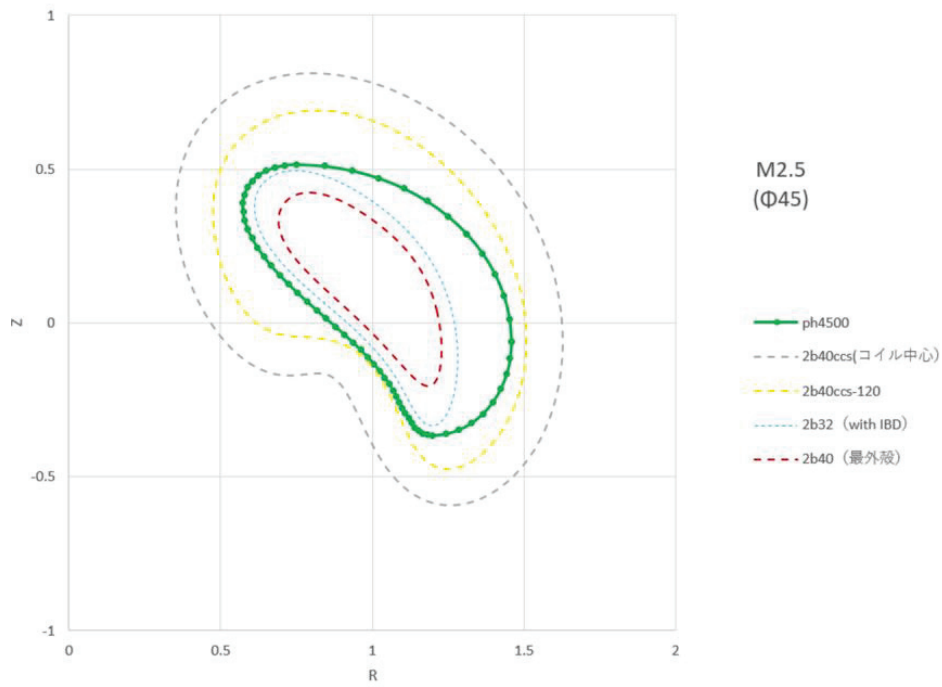


Fig. 3.1.6 Shape of main vessel at 45 ($4/8 \times 90$) degrees.

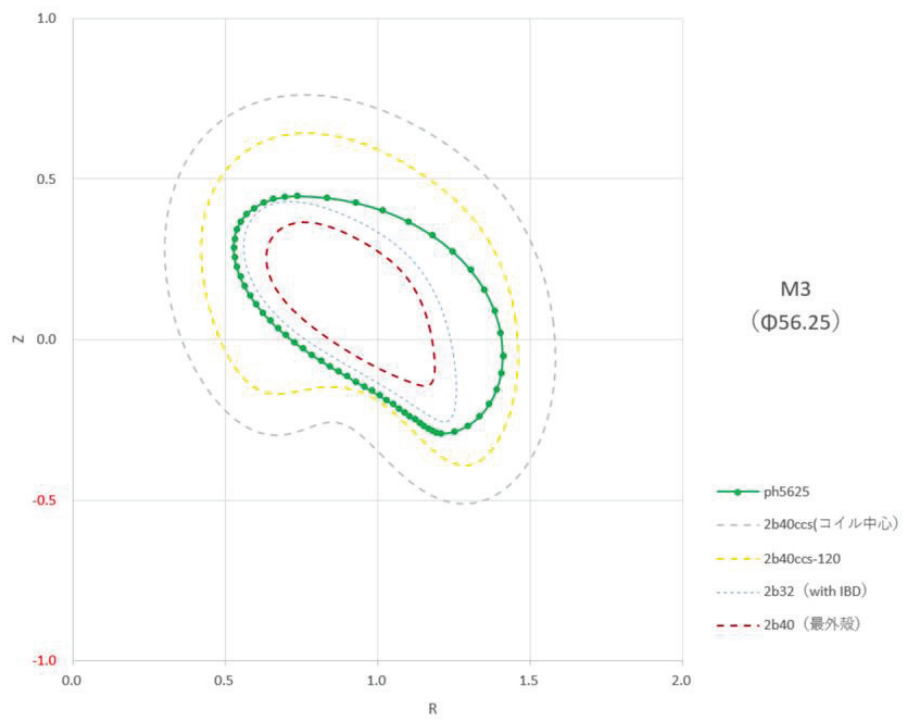


Fig. 3.1.7 Shape of main vessel at 56.25 ($5/8 \times 90$) degrees.

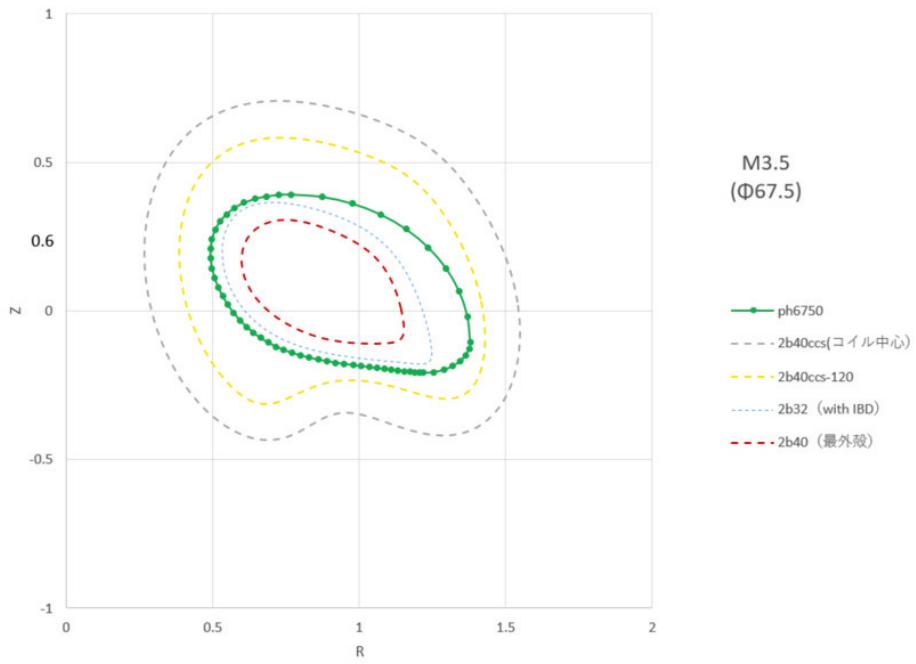


Fig. 3.1.8 Shape of main vessel at 67.5 (6/8 × 90) degrees.

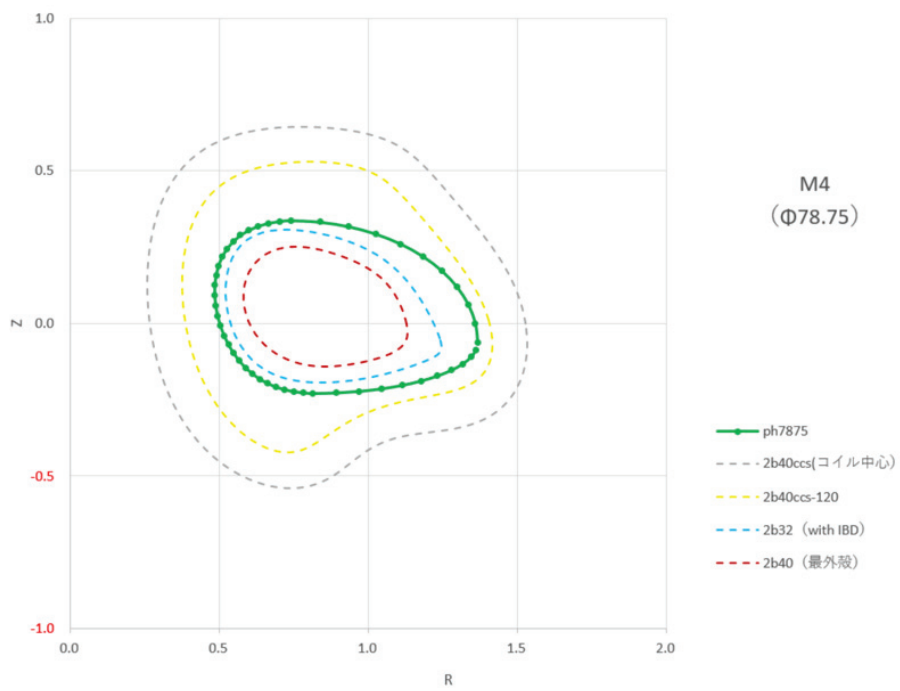


Fig. 3.1.9 Shape of main vessel at 78.75 (7/8 × 90) degrees.

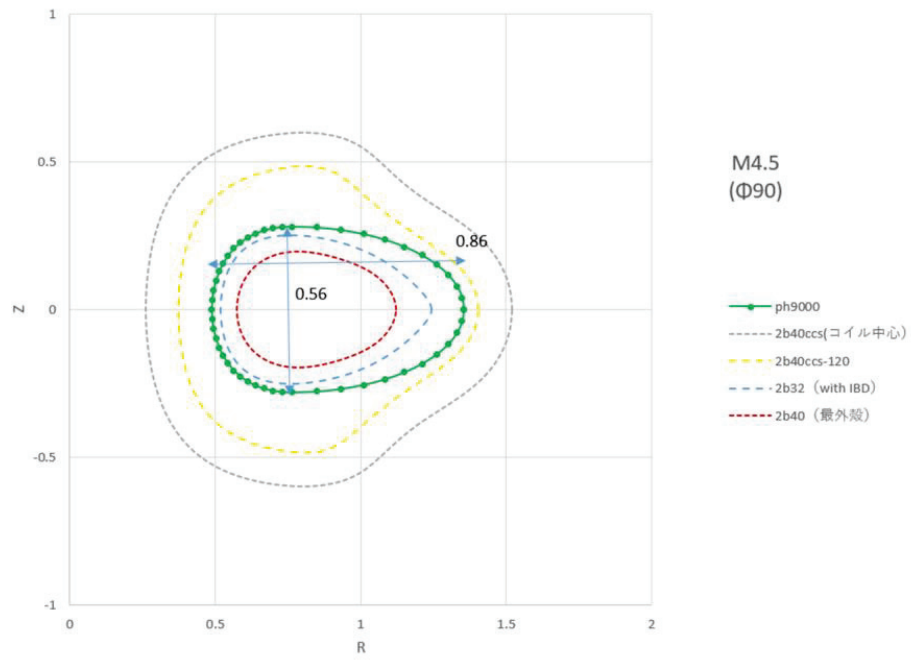


Fig. 3.1.10 Shape of main vessel at 90 degrees.

3.2 Design of leaf-spring type leg

To absorb the heat expansion deformation by the baking, the vacuum vessel is supported by eight leaf spring type legs. Since the leaf spring type leg will receive a compressive load, it is necessary to evaluate its buckling and bending stress. This chapter introduces the results of analysis and evaluation by hand calculation.

3.2.1 Design values

Design values of the leaf spring are as follows.

- Beam thickness; $H=20$ mm
- Beam width; $B=100$ mm
- Beam length $L=400$ mm
- Number of legs; 8
- Material; SUS316L
- Design temperature; 150 degrees C
- Young's modulus; $E = 193$ GPa
- Design allowable stress; $S_m = 115$ MPa
- Yield stress; $\sigma_y = 173$ MPa
- Support load; $F = 500$ kg. The weight of the vacuum vessel is about 4000 kg with extra 1400 kg of additional devices, so one leg shares 500 kg.
- Forced displacement by the baking; $\delta = 2$ mm

The thermal expansion of the stainless steel is $1.73 \times 10^{-5}/\text{degree}$. The major radius increases by an average of 0.17 % ($=1.73 \times 10^{-5} \times 100$) when the temperature of the vacuum vessel rises 100 degrees during baking. Since the major radius of the CFQS is 1 m, the amount of forced displacement is assumed to be 2 mm.

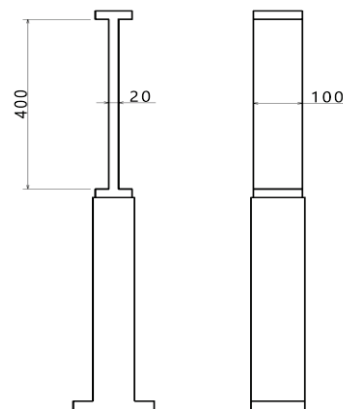


Fig. 3.2.1 Design dimension of the leg.

3.2.2 Buckling load and safety factor

The buckling load is calculated as follows by the formula of the beam fixed at two ends.

$$P_{cr} = \pi^2 EI / (KL)^2$$

$$\sigma_{cr} = \frac{P_{cr}}{A} = \pi^2 E / (KL/r)^2 < \sigma_y$$

Where

- P_{cr} ; Euler's critical load (longitudinal compression load on column).
- E ; Modulus of elasticity of column material (Young's modulus).
- I ; Minimum area moment of inertia of the cross section of the column.
- L ; Unsupported length of column.
- K ; Column effective length factor. $K = 0.5$ for the beam fixed at two ends. The value of K may change in the range of 0.5 to 2 at fixed conditions at both ends. In the worst case, the critical load will be 1/16 times, so it is necessary for the design to have a sufficient margin.
- σ_{cr} ; Critical buckling stress.
- A ; Area cross section.
- r ; Radius of gyration, $r = \sqrt{I/A}$.

Substituting the design values,

- Moment of inertia; $I = BH^3/12 = (20^3 \times 100) \times 10^{-12} = 6.67 \times 10^{-8} \text{ m}^4$.
- Radius of gyration; $r = \sqrt{6.67 \times 10^{-8} / (0.02 \times 0.1)} = 0.00577 \text{ m}$.
- Slenderness ratio; $KL/r = (0.5 \times 0.4) / 0.00577 = 34.7$.
- Critical buckling stress; $\sigma_{cr} = \pi^2 \times 193 \times 10^9 / 34.7^2 = 1.58 \text{ GPa}$.
- Buckling load; $P_{cr} = 3.16 \text{ MN} = 322 \text{ tons}$. The safety factor for buckling is about 644 (= 322000/500), which is sufficient.

3.2.3 Bending stress with the forced displacement

The bending stress of beam fixed at two ends can be obtained by expanding the model fixed at one end. The deflection at the unsupported end of the model (b) in Fig. 3.2.2 is calculated as follows.

$$y = \frac{WX^3}{3EI}$$

$$\sigma_b = \frac{M}{Z}$$

$$M = WX$$

Where

- y ; Displacement at the top of the model (b).
- σ_b ; Bending stress at the fixed end of the model (b).
- W ; Load at unsupported end of the model (b).
- X ; Beam length of the model (b).
- E ; Young's modulus.
- I ; Moment of inertia.
- M ; Bending moment at the fixed end of the model (b).

- Z ; Section modulus of the beam = $I/(H/2)$.
- H ; Thickness of the beam.

The bending stress of the model (a) is equal to a result with

$$y = 0.5 \times \text{the displacement at the top of the model (a).}$$

$$X = 0.5 \times \text{the beam length of the model (a).}$$

Substituting the design values,

$$W = \frac{y \times 3EI}{X^3} = \frac{(0.002/2) \times 3 \times 193 \times 10^9 \times 6.67 \times 10^{-8}}{(0.4/2)^3} = 4825 \text{ N}$$

$$\sigma_b = \frac{4825 \times (0.4/2)}{(6.67 \times 10^{-8} / (0.02/2))} = 145 \text{ MPa}$$

The compressive stress is easily obtained by

$$\sigma_m = \frac{(\text{Supprt load; } F) \times 9.8}{(\text{Cross sectional area; } A)} = \frac{500 \times 9.8}{0.02 \times 0.1} = 2.45 \text{ MPa}$$

The membrane plus bending stress is

$$\sigma_m + \sigma_b = 147 \text{ MPa} < \sigma_y = 1.5 \times S_m = 173 \text{ MPa (Allowable limit value)}$$

It satisfies the design guideline of the allowable limit value of stress for the CFQS.

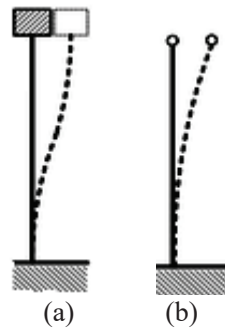


Fig. 3.2.2 Bended shape of a beam.

(a) a beam fixed at two ends and (b) fixed at one end and other free.

3.3 Structural analysis of vacuum vessel

On plasma operation, the vacuum vessel (VV) is exposed to several loads, such as an atmospheric pressure and a thermal stress. Due to its complexity of shape, it is hard to predict the mechanical behavior of VV which is receiving these loads. Therefore, we have performed structural analyses to validate the reliability of VV with use of ANSYS, a commercial finite element analysis software for the engineering simulation.

In this analysis, we have chosen 3 load cases as shown in Table 3.3.1. The temperature distribution required as a thermal load is obtained by heat transfer analysis in advance, which is shown in Fig. 3.3.1(a). For simplicity, the vacuum vessel and bottom surfaces of legs have been fixed to 122 °C and 22 °C, respectively. Fig. 3.3.1(b) shows boundary conditions and load conditions for structural analysis. Atmospheric pressure (0.1 MPa) is applied on the outer surface as shown in red and the bottom surfaces of eight legs are fixed for constraint condition. Furthermore, gravitational acceleration is applied on the entire vacuum vessel considering a self-weight.

Fig. 3.3.2 to Fig. 3.3.4 show the results of each cases. In case 1, the maximum stress is 87.4 MPa which is less than design stress and the maximum deformation is 1.03 mm. In case 2, the maximum stress is 128 MPa near the leaf spring type legs, which is acceptable. In case 3, significant stress does not appear.

Therefore, it is confirmed that there is no problem for structural integrity on these conditions.

Table 3.3.1 Load condition and analysis result.

	Atmospheric pressure (MPa)	Thermal load (Temperature rise) during baking	Self-weight	Maximum stress (MPa)	Maximum deformation (mm)
Case 1	0.1	Nothing-	Ignored	87.4	1.03
Case 2	0	100 °C	Ignored	128	3.07
Case 3	0.1	100 °C	Included	126	3.04

Load conditions

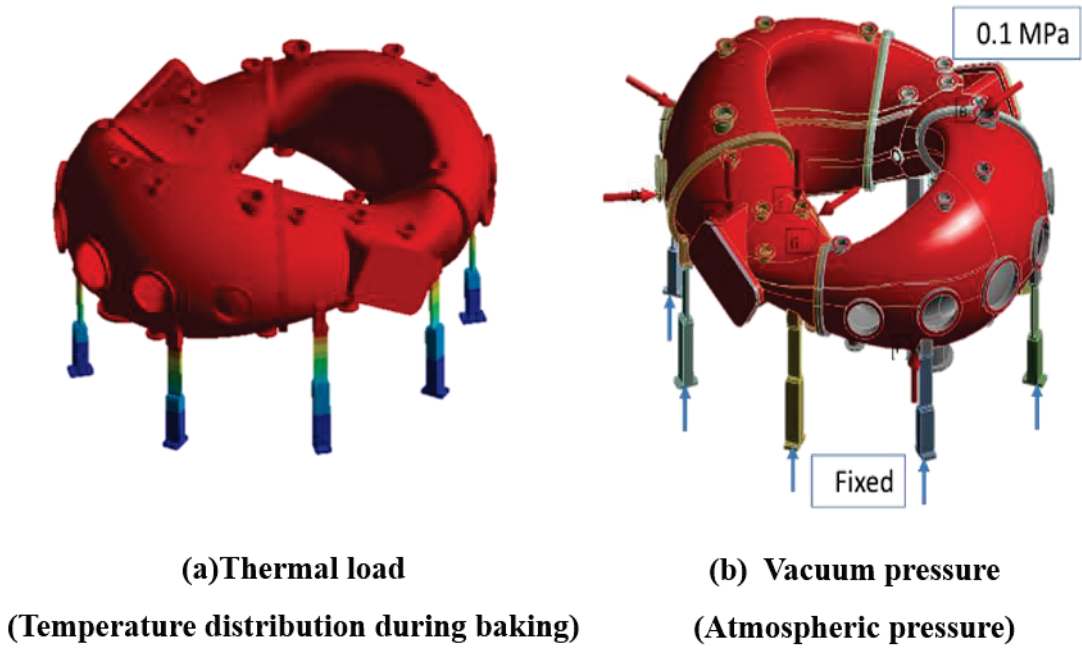


Fig. 3.3.1 Load conditions.

Atmospheric pressure only

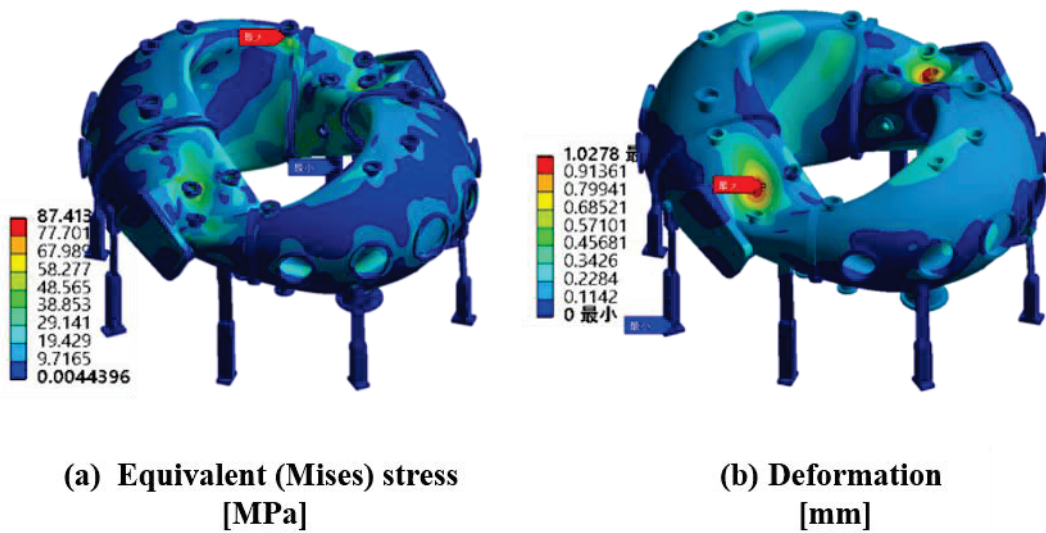


Fig. 3.3.2 Result of case 1 (Atmospheric pressure).

Thermal load only

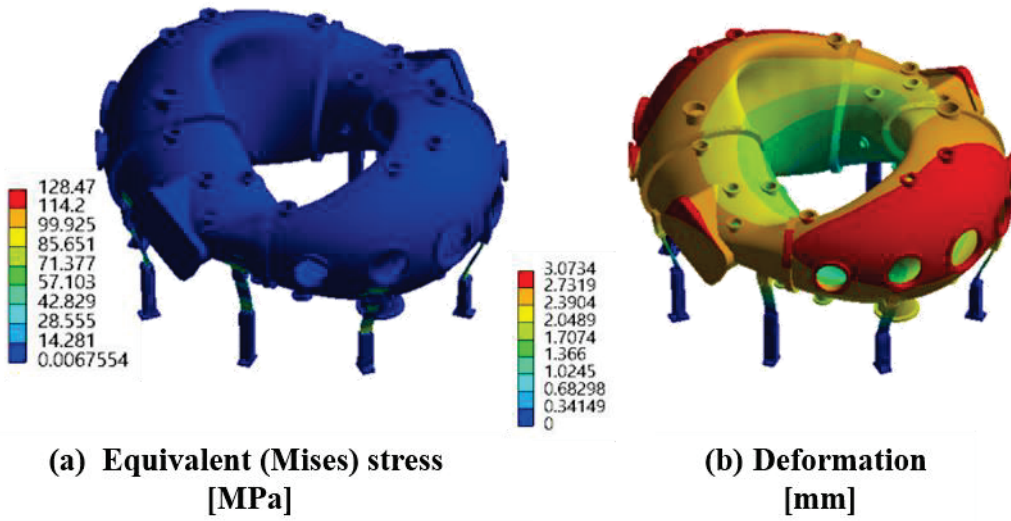


Fig. 3.3.3 Result of case 2 (Thermal load only).

Atmospheric pressure and thermal load

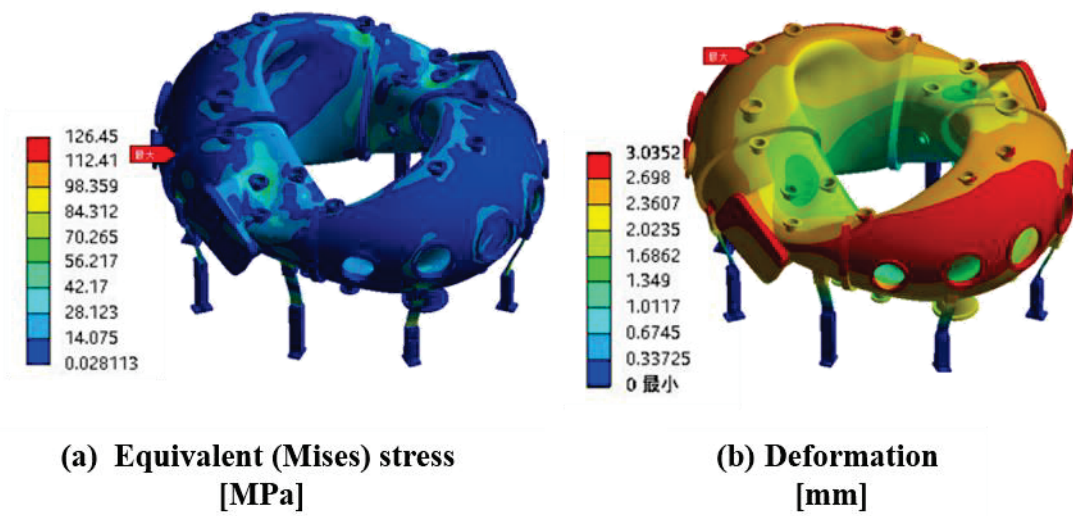


Fig. 3.3.4 Result of case 3 (Atmospheric pressure + thermal load).

3.4 Eddy current analysis of vacuum vessel

In the CFQS using normal conducting coils, since the energization time of magnetic field coils is limited by the balance between heat generation and cooling performance of coils, the plasma discharge duration is also limited. Hence, the influence of the eddy current generated on the VV may be exerted during the plasma discharge.

3.4.1 Time constant of eddy current and its effect on plasma discharge.

Eddy current is induced on the VV by the current change of the external coils. This relationship can be approximately expressed by the following equivalent circuit equation.

$$L \frac{dI_{VV}}{dt} + RI_{VV} = V = M \frac{dI_{EXT}}{dt} .$$

Where I_{VV} is a total eddy current induced on the VV, I_{EXT} is a current flowing in external coil like the modular coil, the poloidal field coil and the toroidal field coil. L and R are the inductance and resistance of the VV, respectively, and M is the mutual inductance between the external coil and the VV. Here, when the right-hand side of the equation is constant, that is, when the external coil current increases / decreases at a constant rate, the equation can be analytically solved, and the eddy current is given by the following equation.

$$I_{VV} = I_0 \left(1 - e^{-\frac{t}{\tau}} \right) .$$

Where, I_0 is the maximum value of the eddy current, and τ is the time constant of the eddy current determined by L/R .

Note that the time constant τ does not depend on the current value of the external coil and can be a useful method for evaluating the time to reach flattop or the remaining time of the eddy current. As shown in Fig. 3.4.1, when $t = \tau$, the value of the eddy current is approximately 63 % of the maximum value and when $t = 5\tau$, the eddy current is approximately 99 % of the maximum value. Therefore, if the plasma discharge is performed at a time of 5τ or more after the rise of the external coil current, we can consider that the influence of the eddy current is almost eliminated.

The eddy current induced on the VV by the PFC was calculated. The PFC current was set to increase linearly from the time of 2 ms to 40 ms, and then was set to be constant as shown in Fig. 3.4.2. Fig. 3.4.3 shows the calculation meshes used in this FEA. In this eddy current analysis, transient analysis is required to calculate the eddy current. To accurately evaluate the change in the eddy current, it is necessary to make the time step fine. The time step Δt was set to 0.2 ms in this analysis. A rectangular computational domain was designed to enclose the CFQS VV and the external coils. Also, on its boundaries, the Neumann condition ($\partial A / \partial n = 0$) was applied.

Fig. 3.4.4 shows a result of the eddy current density distribution at the time of 40 ms with the PFC current change as an example. The eddy current flows counterclockwise as seen from the top, and a relatively high current density appears near diagnostics ports. This result is consistent with the theoretically expected trend. To calculate the total eddy current induced on the VV, it is necessary to integrate the current density in a cross-section perpendicular to the direction in which the eddy current flows. Fig. 3.4.5 shows an integral cross section for calculating the total eddy current.

Similar calculations were performed with the TFC and the MC current change, and the results are shown in Fig. 3.4.6 which shows the time evolution of the total eddy current on the vacuum vessel. From the current

waveform, the time constant τ is approximately 4 ms for the PFC and 2 ms for the MC and the TFC, respectively. Fig. 3.4.7 shows a typical current scenario of the MC current and the PFC current in the CFQS experiment. The plasma discharge begins to start 50 ms after the PFC current reaches the flat top. The impact on the plasma discharge is expected to be negligibly small, because the eddy current ($5\tau \sim 20$ ms) is small enough to ignore at the start of plasma discharge.

3.4.2 EM force on vacuum vessel and structural analysis

Electromagnetic (EM) force is generated on the VV by the interaction of the eddy current and mainly magnetic field produced by the MC. The effect of the EM force is evaluated by structural analysis. Major component of the eddy current can be classified into a poloidal current and a toroidal current. The former is mainly induced by the MC current and the latter by the PFC current. The TFC current also induces a poloidal eddy current, but since its magnetomotive force is smaller than that of MC, it will be ignored below.

The typical current scenario of the PFC and the MC as shown in Fig. 3.4.7 was assumed in this analysis. The current change rates of the MC and the PFC are 10.75 kA/s and 43 kA/s, respectively. The maximum current of the MC is 4.3 kA with 72 turns. Regarding the PFC, the maximum current is 4.3 kA with 32 turns. The EM force and the EM stress under this current scenario were investigated by using ANSYS Maxwell and ANSYS Mechanical. In this EM analysis, transient analysis is also required to calculate the EM force induced by the time variation of the MC and the PFC.

Fig. 3.4.8 shows the time evolution of the maximum EM force per volume (N/m^3) on the VV under the typical current scenario mentioned above. The EM force increases almost linearly with the rise of the MC current and is maximized at the end of the MC current, since the eddy current induced by the MC is almost constant after 10 ms as shown in Fig. 3.4.6. The EM force is generated again with the rise of the PFC current. We find that the EM force by the PFC is smaller than that of the MC. Moreover, we also find that the direction of the EM force during the falling of the MC currents ($t = 1,100$ ms) is opposite to that at startup ($t = 500$ ms). It is more dangerous since the direction of force at the start is the same as the direction of vacuum pressure.

The force in this analysis can be converted into the EM pressure on the VV. The EM pressure is about 0.4 atm in consideration of the thickness of the stainless-steel plate of 6 mm. Although the EM pressure is lower than the atmospheric pressure (1 atm), it is not a negligible value. Therefore, a structural analysis was performed with the EM force and the atmospheric pressure by using ANSYS Mechanical. Fig. 3.4.9 shows the boundary conditions in this analysis. Fig. 3.4.10 shows the distribution of stress generated. The maximum stress of about 97.2 MPa occurs near the upper diagnostic port. Since the stress with vacuum pressure only is 87.4 MPa as shown in another section, the increase in stress by the EM force is about 10 %. The stress of 97.2 MPa is less than the guideline of allowable stress of stainless steel at room temperature (117 MPa). Furthermore, since the maximum stress is within an elastic deformation range, there is also no possibility that the VV will break due to repeated stress fluctuations.

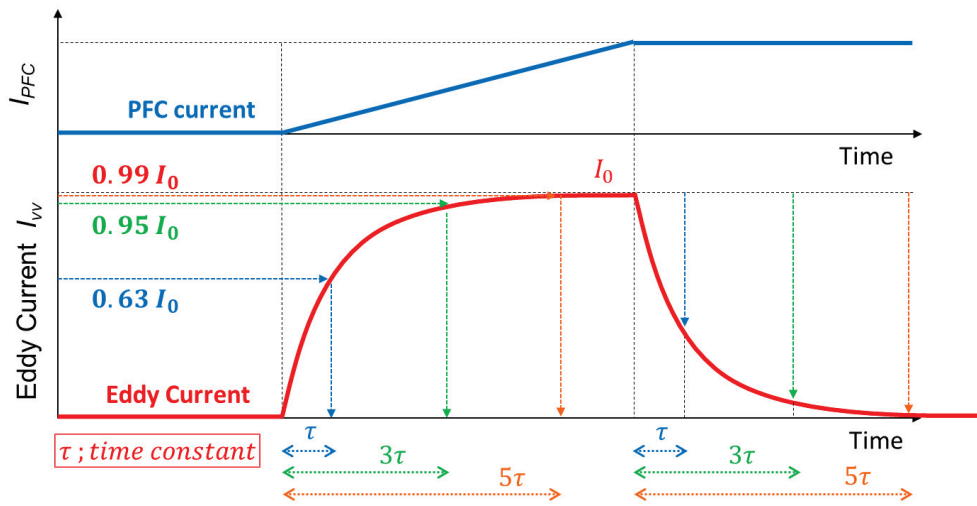


Fig. 3.4.1 A time evolution of eddy current due to PFC.

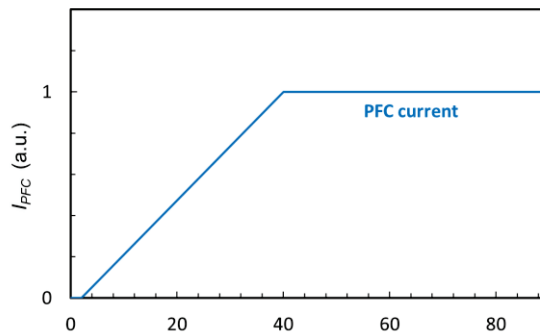


Fig. 3.4.2 PFC current to calculate time constant of the eddy current.

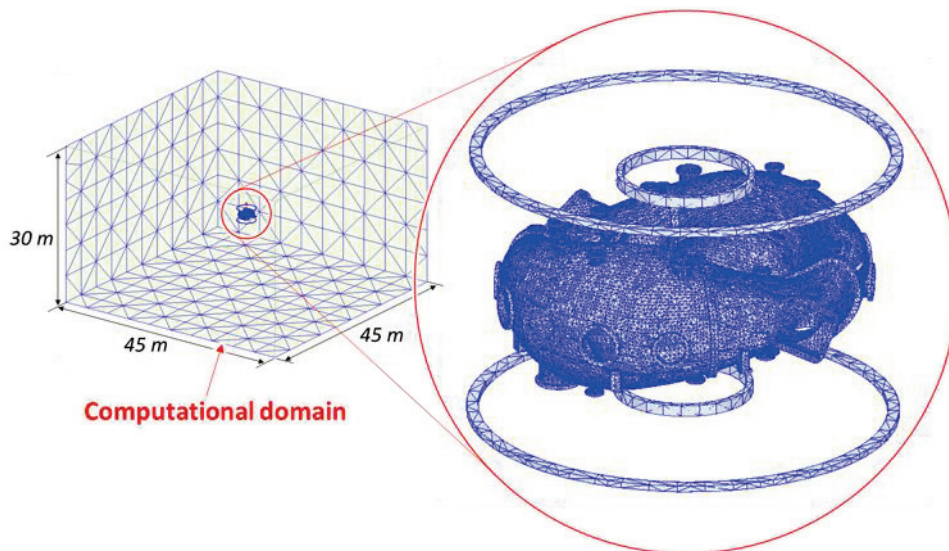


Fig. 3.4.3 Computational meshes of vacuum vessel, PFC and computational domain.

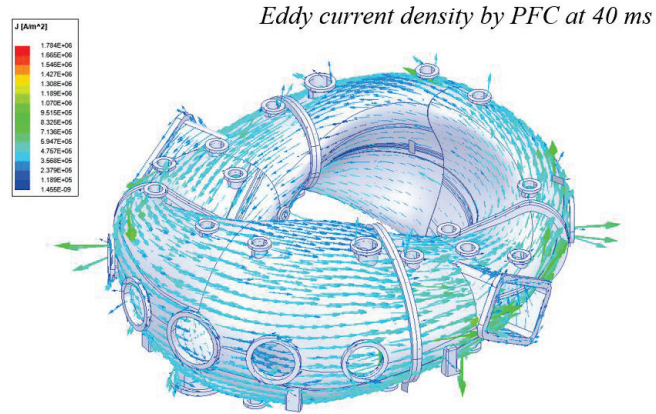


Fig. 3.4.4 Distribution of eddy current density.

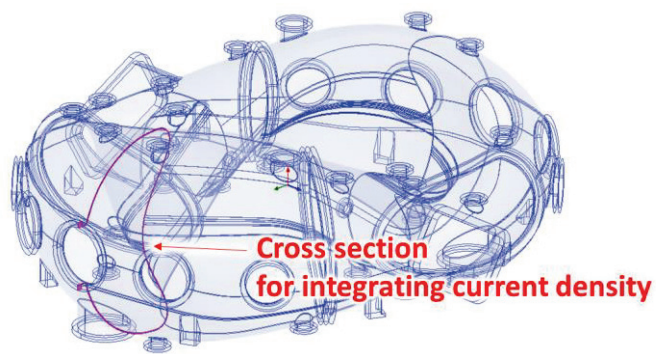


Fig. 3.4.5 Cross section to obtain total eddy current.

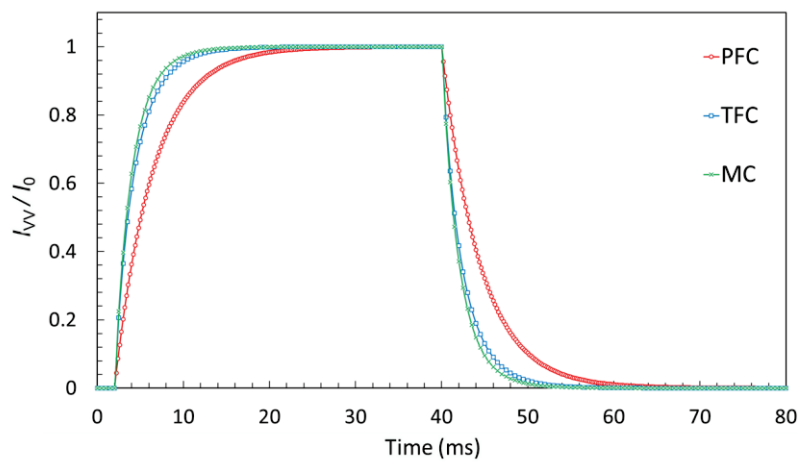
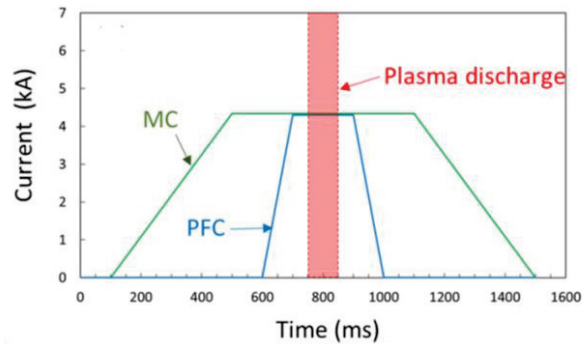
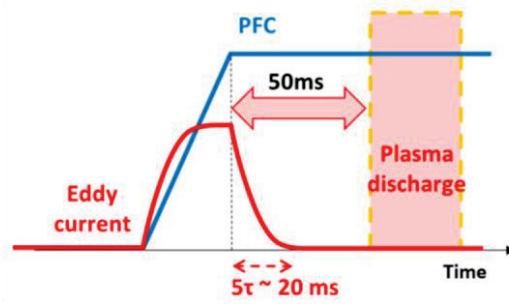


Fig. 3.4.6 Time evolution of total eddy current induced by each external coil.

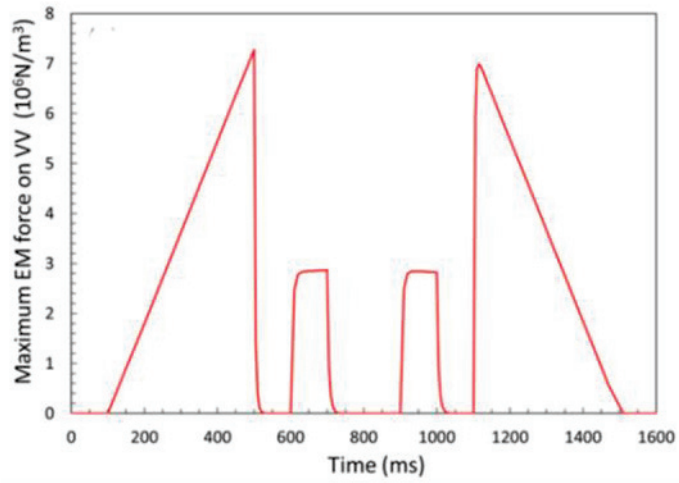


(a) Coil current waveform

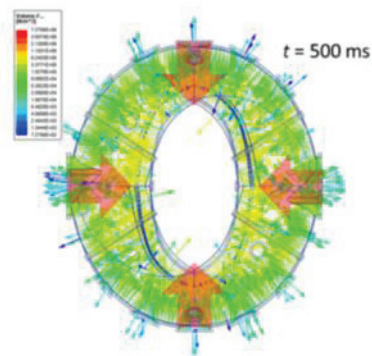


(b) Relationship of the eddy current and the plasma discharge

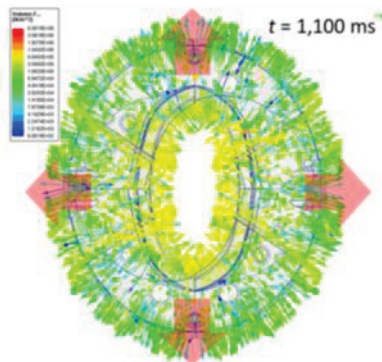
Fig. 3.4.7 Typical scenario of plasma experiment.



(a) Time evolution of maximum EM force



(b) EM force distribution at 500 ms



(c) EM force distribution at 1100 ms

Fig. 3.4.8 Time evolution of EM force on the VV under the typical scenario.

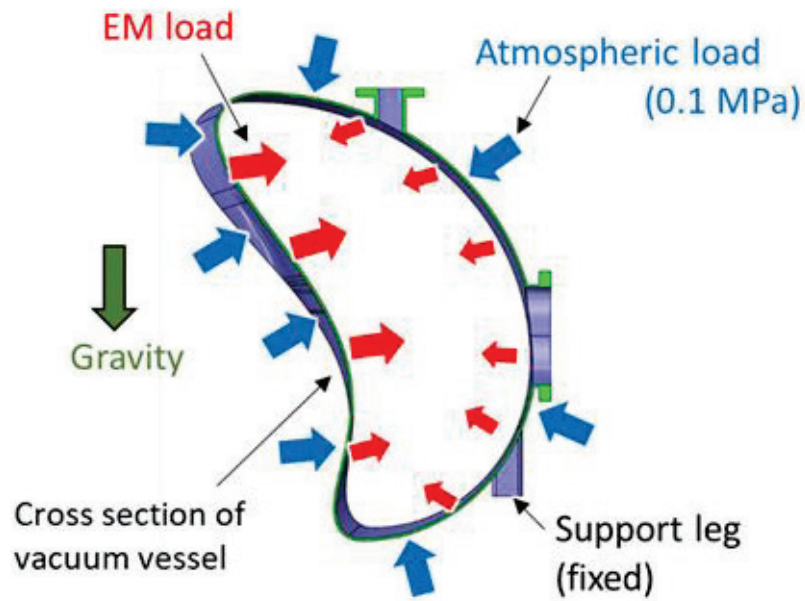


Fig. 3.4.9 Boundary conditions for the structural analysis with the EM load and atmospheric load.

EM load and atmospheric pressure

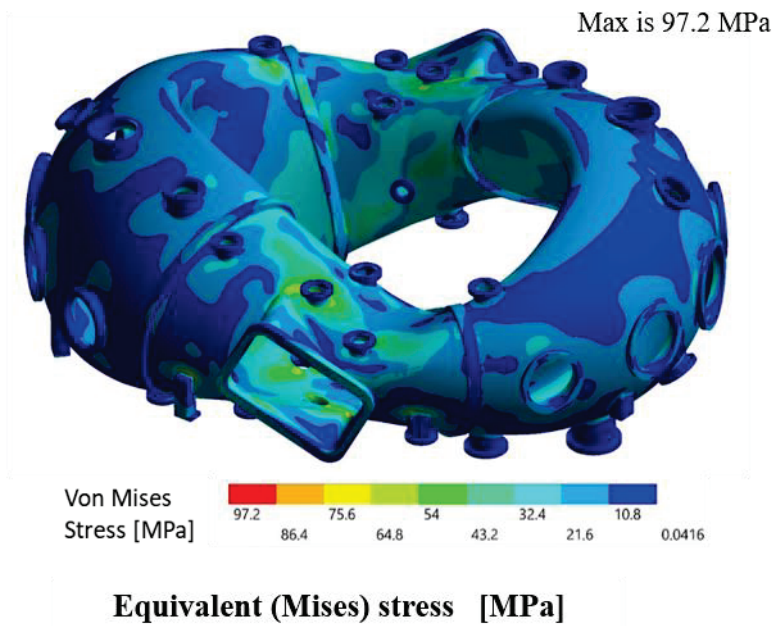
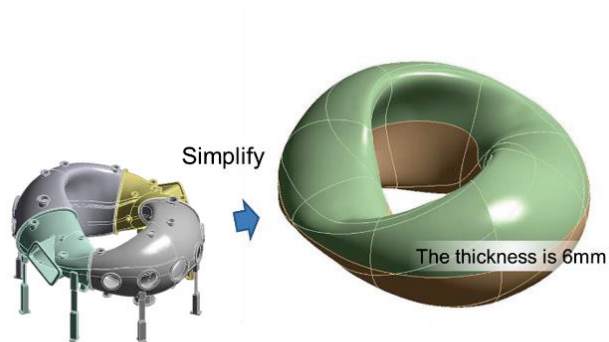


Fig. 3.4.10 Distribution of von Mises stress on the VV with the EM load and atmospheric load.

3.5 Effect of mesh size in FEM analysis for the vacuum vessel

A mesh size is one of the most important factors in FEM since a result of FEM depends on mesh size significantly. Therefore, we have conducted preliminary analysis with a simplified model and estimated reasonable mesh size for the analysis of the CFQS vacuum vessel (VV). Fig. 3.5.1 shows the model and analysis condition. We have investigated how the result changes with mesh refinement.

The results are summarized in Fig. 3.5.2. The vertical lines show the maximum deformation and stress, and the horizontal one the number of elements. According to this figure, as the mesh size decreases, the result of solid element shown as red circle seems to converge, and in case of less than 25 mm, it agrees with the result of shell element. From this result, we can assume that the mesh size should be less than 25 mm in the analysis of VV



(a) Simplified model



(b) Simplified load condition

Fig. 3.5.1 Simplified model.

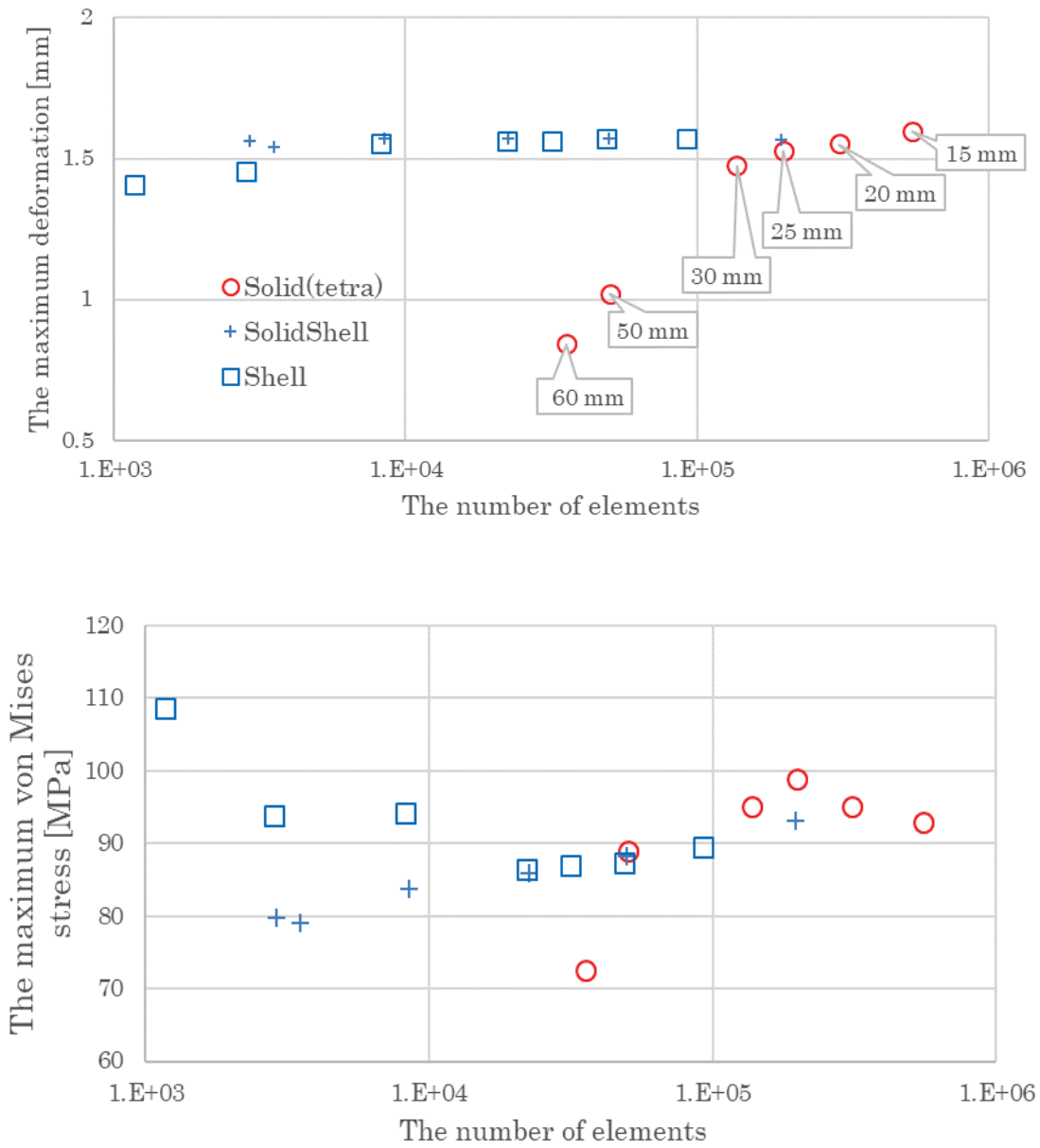


Fig. 3.5.2 Relationship between FEM analysis results and number of meshes.

3.6 Eddy current analysis for inductive heating of the vacuum vessel

Gases such as nitrogen, oxygen, hydrogen, water vapor, and carbon dioxide are adsorbed on the inner wall of a VV under the atmospheric pressure, and these adsorbed gases are released as outgas from a VV inner wall during the vacuum pumping. Since these outgases hinder the high vacuum pumping process, it is necessary to heat up the entire VV by heaters such as tape-shaped heaters around the outer wall of the VV in general, and to release the adsorbed gas attached to the inner wall. Regarding a baking method for the CFQS VV, usage of an induction heating with an eddy current generated in the VV has been proposed. 16 MCs are connected in a series and an AC is applied to the MC to generate heat by resistance loss of eddy current generated in the VV. We must check the feasibility of adopting the induction heating in the CFQS from the engineering point of view.

In this analysis, the AC analysis is required to calculate the heat generation of the CFQS VV by the induction current induced by the MCs. In general, when an AC flows through a conductor, a skin effect appears in which the current density is high at the surface of the conductor and gradually decreases with distance from the surface. If the skin depth δ is smaller than the thickness of the VV (6 mm), it can be considered that the eddy current concentrates on the VV surface. In this case, since a layered thin and fine mesh is required on the surface of the VV even in the FEA, the skin depth must be considered in advance. Here, skin depth δ can be calculated by the following equation.

$$\delta = \sqrt{\frac{2}{2\pi f \mu_r \mu_0 \sigma}} \cdot$$

Where f is the AC frequency, μ_r is the relative magnetic permeability, μ_0 is the vacuum magnetic permeability, and σ is the electric conductivity of the VV. When the skin depth is calculated using Equation 1, for example in the case of $f = 2$ kHz, the skin depth δ is approximately 9 mm. Therefore, since the skin depth is larger than the plate thickness of the VV, we considered that the current concentration due to the skin effect does not occur on the CFQS VV surface.

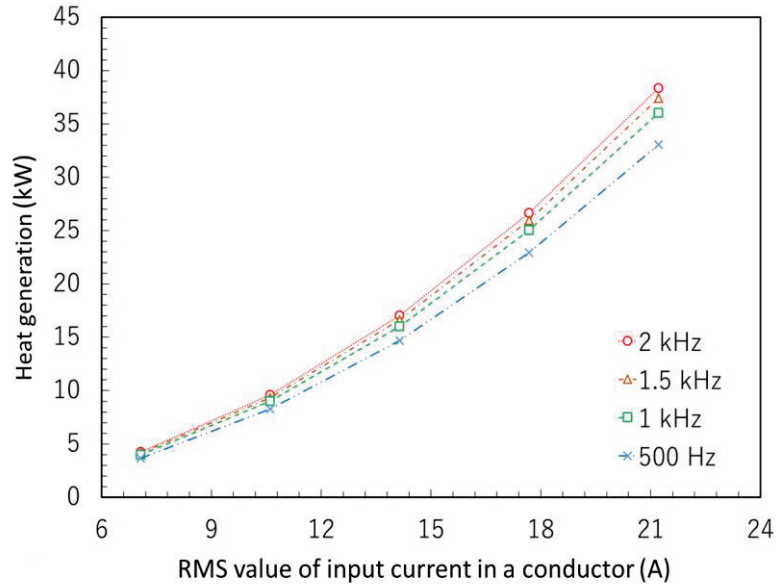
The heat generation of the CFQS VV with the current value and AC frequency of MC changing was investigated by using ANSYS Maxwell as shown in Fig. 3.6.1. The Root Mean Square (RMS) value I_{AC} of input current in a conductor was changed from about 7 A to 21 A, and the AC frequency was investigated at 500 Hz, 1 kHz, 1.5 kHz, and 2 kHz. Fig. 3.6.2 shows an example of the heat distribution of the VV obtained by this analysis in the case of $f = 1$ kHz and $I_{AC} = 7$ A.

The heat generation is more strongly dependent on the current value than the AC frequency. Here, the heat generation required for baking in the CFQS VV is 25 kW. This value is determined based on the actual value of VV baking system of CHS which has a similar size to the CFQS. In this case, the current required for the CFQS VV baking can be obtained to be about 18 A. The voltage applied in the MC is obtained by this current value I_{AC} and AC resistance ωL as follows.

$$V_{MC} = I_{AC} \cdot \omega L$$

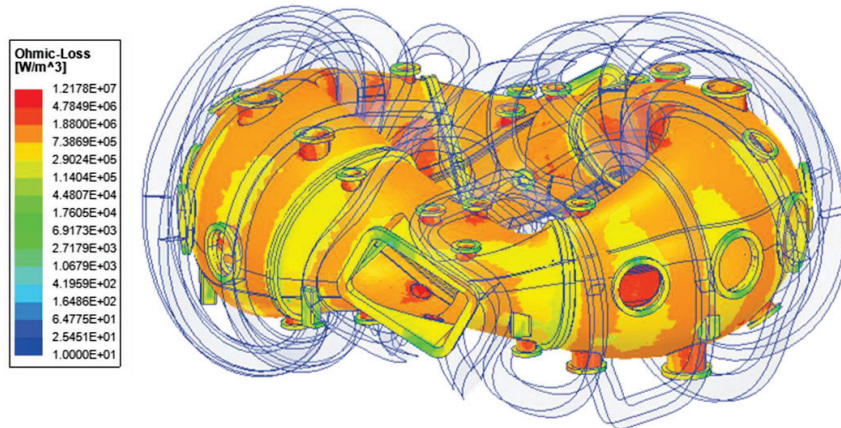
Where ω is the angular frequency represented as $2\pi f$. The inductance L of the MCs arranged in series was calculated to be about 0.3 H by using ANSYS Maxwell. Substituting $I_{AC} = 18$ A, and $f = 1$ kHz, the applied voltage on the MC is obtained to be approximately 34 kV.

As a result, this voltage value exceeds the operation voltage of DC 2.4 kV. Therefore, we found that the induction heating method could not be adopted in the CFQS. An alternative method should be considered as a next option, for example, the sheathed heater system.



Number of MC and turns are 16 and 72, respectively.

Fig. 3.6.1 Heat generation with changing RMS value of input current.



$$I_{AC} = 7 \text{ A}, f = 1 \text{ kHz}$$

The maximum heat generation in VV is approximately $1.2e7 \text{ W/m}^3$.

Fig. 3.6.2 Distribution of the heat generation.

3.7 Required length of the baking heater for vacuum vessel

Since the baking heater is outsourced by specifying the length, it is necessary to evaluate the required length in advance. However, since the shape of the vacuum vessel is complicated and the wiring path of the heater is not simple, it is not easy to evaluate the required length.

It was a little tough to estimate a length of the baking heater. We know creating 3-D model is the best way to estimate the length however it usually takes a lot of times and efforts to create complicated 3-D path in a CAD. In the early stage, we used strings and 3-D printed model to consider a suitable winding route and to estimate the length of baking heater. Following pictures in Fig. 3.7.1 show 1/10 scale 3-D printer models with wound strings instead of heaters.

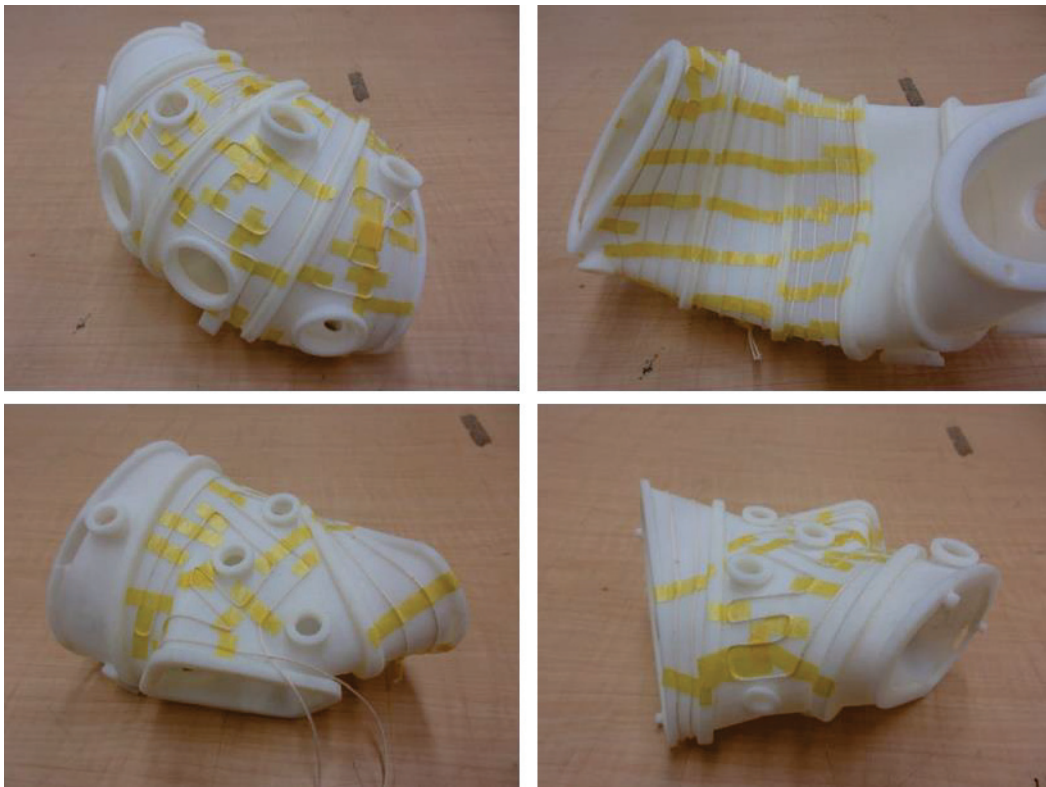


Fig. 3.7.1 3-D printed models with wounded strings instead of the heaters.

After determining the approximate winding policy using 3-D printer models, the heater route was determined on 3-D CAD accordingly as shown in Fig. 3.7.2. Table 3.7.1 shows a comparison between the heater length estimated by the 3-D printer model with strings and that estimated in 3-D CAD. As you can see from this table, there is no significant difference except for B2. In this region, heater path is modified to some extent.

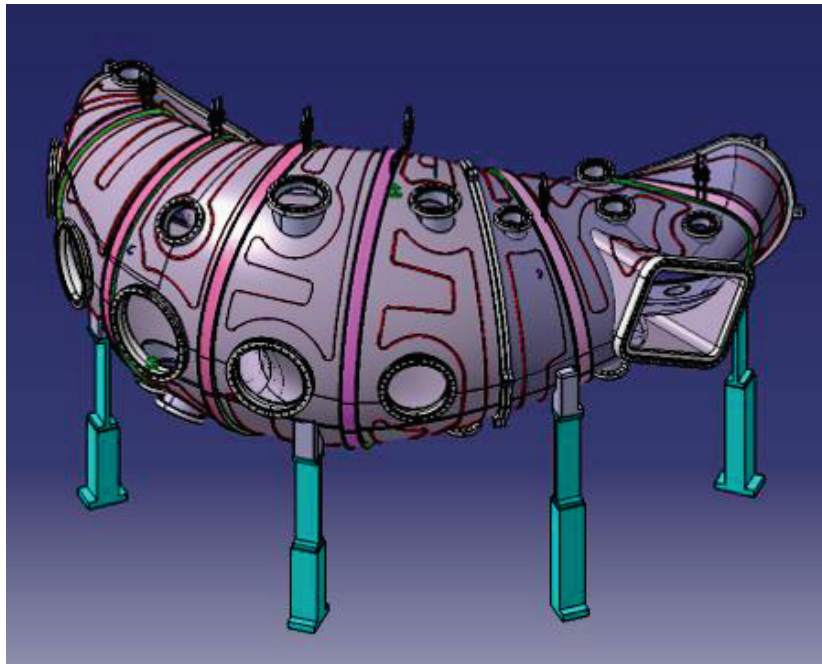
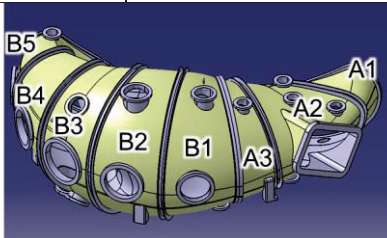


Fig. 3.7.2 Preliminary winding route design of the baking heater.

Table 3.7.1 Comparison of the heater length estimated.

Region	Heater length [mm]		Difference
	3-D printer model with strings	3-D CAD	
A1	4,750	4,788	-0.8 %
A2	12,000	11,325	6.0 %
A3	-	4,752	-
B1	10,750	10,105	6.4 %
B2	12,200	10,746	13.5 %
B3	12,200	11,621	5.0 %
B4	-	10,883	-
B5	-	10,105	-



4 Power supply for coils

4.1 Current wave form to estimate required power capacity

The required specification of the power supply system for coils is shown in Table 4.1.1. They are estimated by the following procedure.

Table 4.1.1 Required specification of power supply system for coils.

Coil group	0.1 T (continuous operation)	1 T (Pulse operation)
MC1	117 kW (DC 260 V, 450 A)	9.2 MW (DC 2100 V, 4500 A, 9.4 MJ)
MC2	117 kW (DC 260 V, 450 A)	9.2 MW (DC 2100 V, 4500 A, 9.4 MJ)
MC3	117 kW (DC 260 V, 450 A)	9.2 MW (DC 2100 V, 4500 A, 9.4 MJ)
MC4	117 kW (DC 260 V, 450 A)	9.2 MW (DC 2100 V, 4500 A, 9.4 MJ)
TFC10	14.3 kW (DC 65 V, 220 A)	1.1 MW (DC 600 V, 2200 A, 0.2 MJ)
TFC32	14.3 kW (DC 65 V, 220 A)	1.1 MW (DC 600 V, 2200 A, 0.2 MJ)
TFC70	14.3 kW (DC 65 V, 220 A)	1.1 MW (DC 600 V, 2200 A, 0.2 MJ)
OV	76.5 kW (DC 170 V,450 A) **	6.2 MW (DC 1700 V,4500 A, 1.8 MJ)
IV	23 kW (DC 50 V,450 A) **	1.8 MW (DC 500 V,4500 A, 0.6 MJ)
Total required power	~600 kW	~60 MW
Total required energy	—	~40 MJ
Power source	Commercial power source 3Φ AC 380 V, 50 Hz	Motor generator (MG) 3Φ AC 10 kV
MC; Modular coil, TFC; Toroidal field coil, IV and OV; Poloidal field coil **, If necessary and there is enough room in the project budget.		

To study the specifications of the coil power supply, the current waveform of each coil was defined. Fig. 4.1.1 shows an equivalent circuit and assumed current and voltage waveform. In the actual operation, the waveform of the CFB using the feedback control circuit will be desirable, but here, for simplicity, the waveform of the CVC by the constant voltage power supply for which an analytical solution exists is used. The current waveform is represented by a combination of exponential functions.

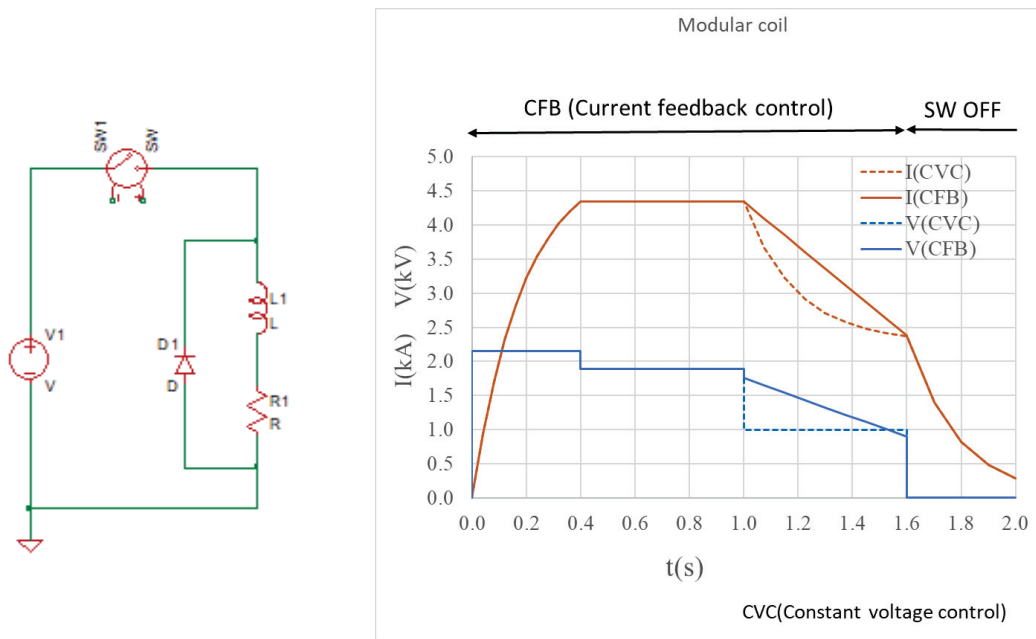


Fig. 4.1.1 Equivalent circuit and voltage / current waveform.

- Current ramp up phase ($t-t_0 < \Delta t_{up} = 0.4$ s , $t_{start}=0$ for the MC)

$$I(t) = \frac{V_{up}}{R} \left\{ 1 - \exp\left(-\frac{t - t_{start}}{\tau}\right) \right\}$$

$$V_{up} = V_{flat} / \left\{ 1 - \exp\left(-\frac{\Delta t_{up} - t_{start}}{\tau}\right) \right\}$$

$\tau = L/R$; Time constant of coil

t_{start} ; Energization start time

- Flat top phase ($t - \Delta t_{up} < \Delta t_{flat} = 0.6$ s for the MC)

$$I(t) = V_{flat} / R$$

- Decay phase ($t - t_1 = t - \Delta t_{up} - \Delta t_{flat} < \Delta t_{decay} = 0.6$ s for the MC)

$$I(t) = I(t_1) \exp\left(-\frac{t - t_1}{\tau}\right) + \frac{V_{down}}{R} \left\{ 1 - \exp\left(-\frac{t - t_1}{\tau}\right) \right\}$$

$$t_1 = \Delta t_{up} + \Delta t_{flat}$$

- Shut down phase ($t > t_2 = \Delta t_{up} + \Delta t_{flat} + \Delta t_{decay} = 1.6$ s for the MC)

$$I(t) = I(t_2) \exp\left(-\frac{t - t_2}{\tau}\right)$$

$$t_2 = \Delta t_{up} + \Delta t_{flat} + \Delta t_{decay}$$

Table 4.1.2 shows parameters to define waveform for each type of coil and Fig. 4.1.2 shows typical example of current waveform. Fig. 4.1.3 to Fig. 4.1.5 show current and voltage waveform for each coil.

Here, the purpose of the two-step fall of the MC current will be described. As with other coils, the power can be turned off at the end of the flat top. It reduces the heat generation energy of the coil and is therefore rational from the viewpoint of coil cooling. However, to reduce the electromagnetic force applied to the vacuum vessel by eddy current, a two-stage shutdown was adopted.

When the coil current changes, an eddy current is induced in the vacuum vessel. An electromagnetic force acts on the vacuum vessel due to the interaction between the eddy current and the magnetic field generated by the MC current. The eddy current is proportional to the time change rate of the coil current, and the magnetic field is proportional to the MC current. In the case of approximation by an exponential function, the current change rate becomes maximum and the electromagnetic force is maximized at the start of the coil current decay, and the evaluation at that time is important. Since the only way to reduce the electromagnetic force is to reduce the current decay rate at that time, a two-step waveform was used. However, in actual operation, since fine waveform control by current feedback control can be performed, the product of the MC current and the current change rate is limited without being limited to the two-step waveform.

Table 4.1.3 shows the result of eddy current analysis on the vacuum vessel. According to the analysis, the influence of the eddy current due to the MC current change is larger, and it is safer to limit the change rate of the MC current. Therefore, the voltage of the two-step decay was determined so that the product of the current and the current change rate was 47 kA²/s.

Table 4.1.2 Parameters that define the waveform.

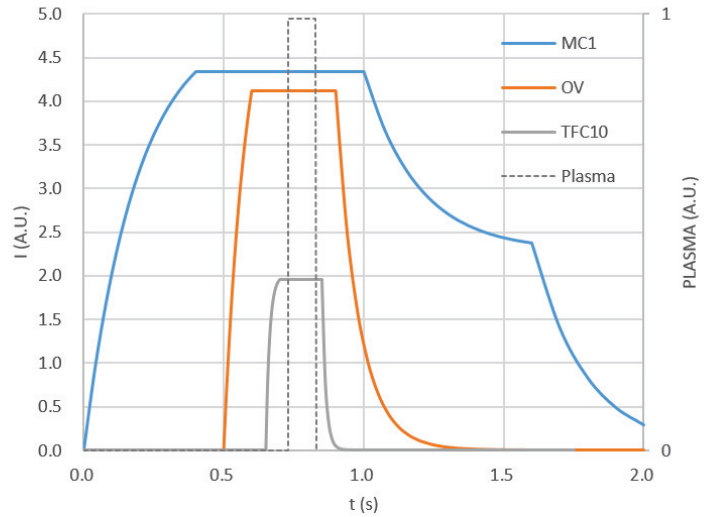
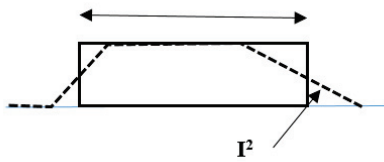
Item	Symbol	Unit	MC	PFC	TFC	Plasma
Energization start time	t_{start}	S	0	0.5	0.7	0.73
Current ramp up duration	Δt_{up}	S	0.4	0.1	0.05	0
Flat top duration	Δt_{flat}	S	0.6	0.3	0.15	0.1
Current decay duration	Δt_{decay}	S	0.6	0.0	0.0	0
Flat top (maximum) current	I_{flat}	kA	4.34	4.34	2.17	-
Time constant of coil	τ	s	0.19	0.07~0.08	0.01	-
Voltage at the flat top	V_{flat}	kV	1.8~1.9	0.3~1.0	0.4~0.5	-

Table 4.1.3 Results of eddy current analysis of vacuum vessel.

Item	MC	PFC	TFC
BMC	1 T (4.34 kA)	1 T (4.34 kA)	Ignore, because eddy current component is similar and total current is much smaller than the MC.
Current change rate	10.85 kA/s	43.4 kA/s	
Electromagnetic force	43.8 kPa (0.45 atm)	16.8 kPa (0.17 atm)	
Design value of force	< 43.8 kPa (0.45 atm)	< 43.8 kPa (0.45 atm)	
Design value of coil current change	$I \times dI/dt$ < 4.34*10.85=47 kA ² /s	dI/dt < 113 kA/s with BMC=1 T	
Natural damping with coil time constant	99 kA ² /s	62 kA/s	
Evaluation	NG. The change rate should be reduced. Two-step shutdown is supposed.	OK	

	RWET
Plasma	0.1
MCOIL	1.114
PFC	0.38
TFC	0.19

RWET (Rectangular wave equivalent time)
Pulse width of square wave with the same Joule heating energy



Adjusted the waveform of MC current at the time of current decay to reduce the force applied to the vacuum vessel by eddy current. Although an exponential function waveform is assumed for ease of calculation, a linear change waveform with current feedback control is desirable.

Fig. 4.1.2 Defined current waveform for calculation.

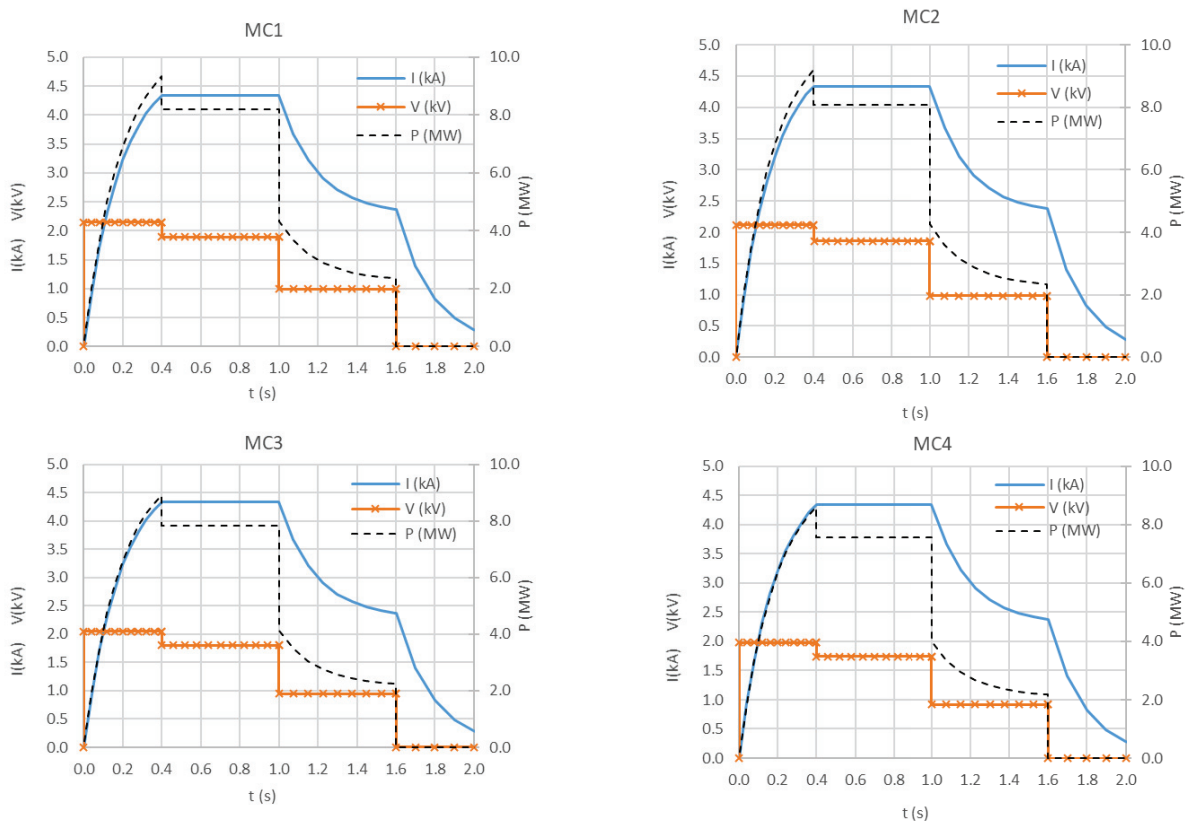


Fig. 4.1.3 Current and voltage waveform for the MC power supply.

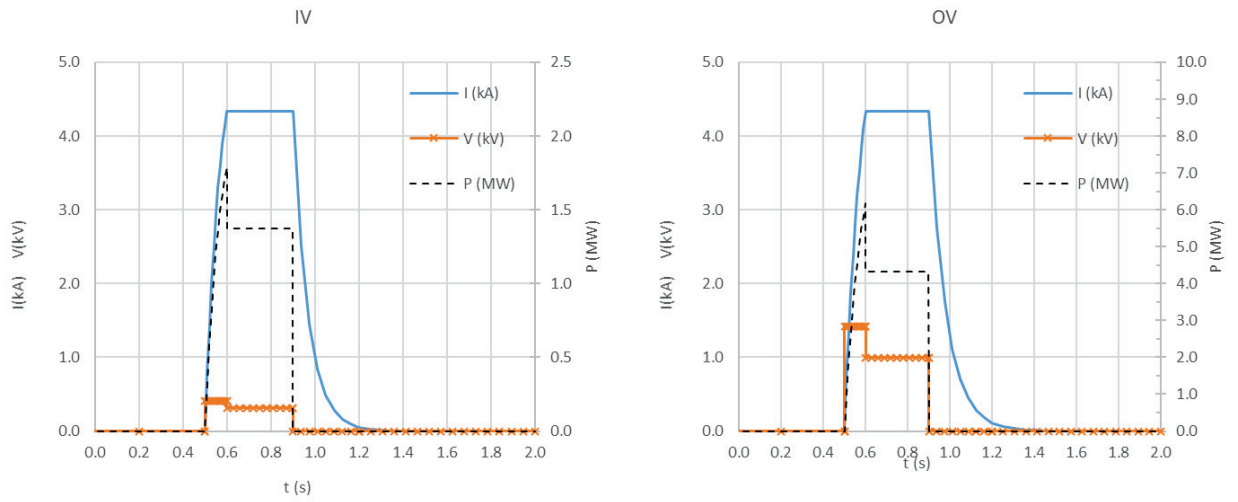


Fig. 4.1.4 Current and voltage waveform for the PFC power supply.

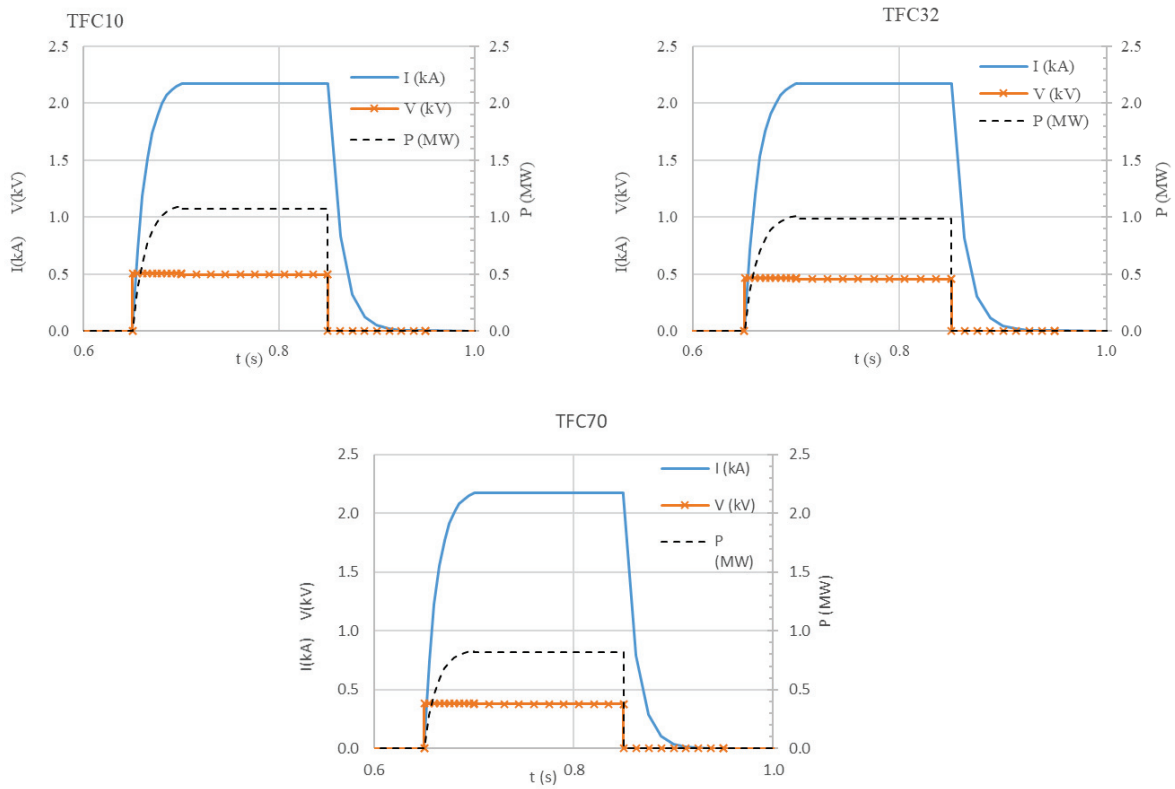


Fig. 4.1.5 Current and voltage waveform for the TFC power supply.

4.2 Trial design of coil power supply for 0.1 T operation

Initially, it was planned to execute a 0.1 T experiment using part of the 1.0 T power supplies. However, the experimental plan was changed to a plan to perform 0.1 T operation first to understand the characteristics of the generated magnetic surface. The power supply system for 1.0 T operation has not been determined yet due to its complicated configurations. On the other hands, the design of the power supply system for continuous 0.1 T operation needs to be determined immediately. Therefore, we decided that the power supply system for 0.1 T and 1 T are completely separated. It means that both systems do not share any electrical components. The power supply system for 0.1 T will be used for discharge cleaning after the initial experiment phase.

Fig. 4.2.1 shows the preliminary designed circuit diagram of the power supply system for 0.1 T. It mainly consists of voltage adjusters and 6 phase diode rectifiers for the MC, and DC power supplies with six phase Thyristor-controlled units for the TFC. Since a Thyristor-control rectifier unit with high capacity may be expensive, the rectifier for the MC is adopted a diode type. The DC power supply for TFC is composed of a Thyristor unit and a transformer. The power board at least 700 kVA power capacity is also required as power source.

Based on the circuit diagram, the layout of power supply system for 0.1 T is estimated as shown in Fig. 4.2.2. Manufacturer catalogs in Japan referred to each size of electrical component. The sizes of voltage adjuster and diode rectifier unit for MC are estimated as W1200×H1900×D700, W1200×H1449×D600, respectively. The Thyristor unit and the transformer for TFC are estimated as W600×H1800×D450 and W550×H700×D600. Space for the baking system with W2000×D700 is also installed in the layout. The size is referred from baking system for CHS. Maximum height of all equipment is approximately 2.0 m.

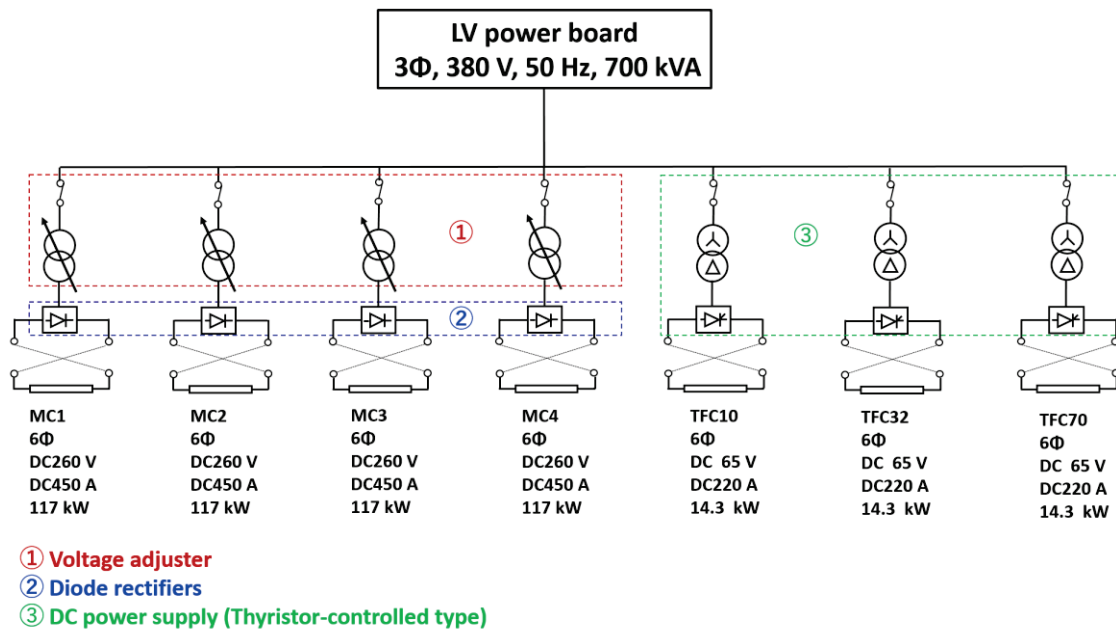


Fig. 4.2.1 Circuit diagram of the power supply system for 0.1 T.

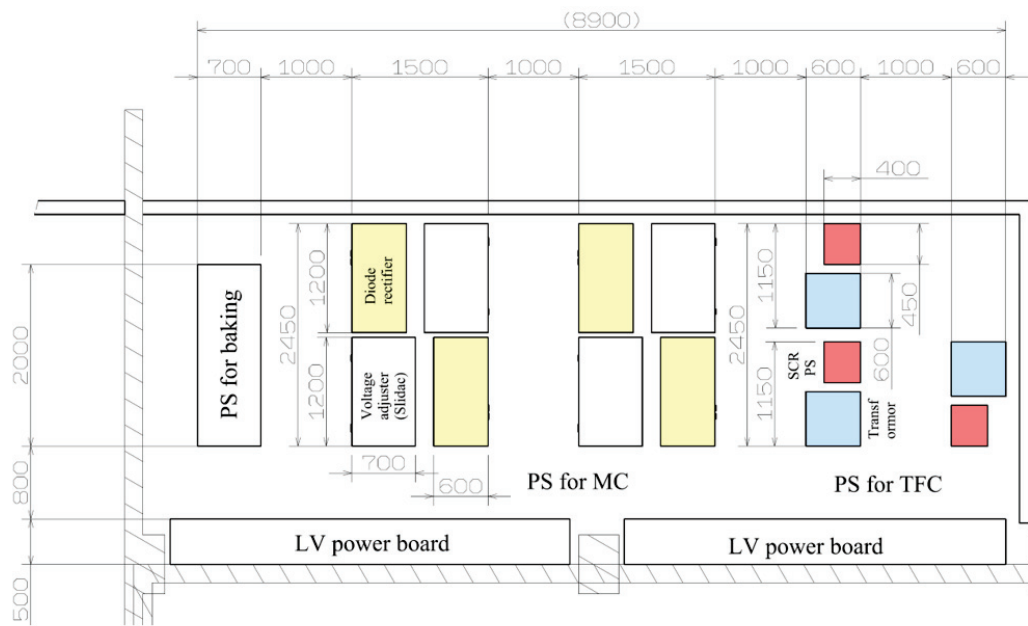


Fig. 4.2.2 Layout of the power supply system for 0.1 T.

4.3 Trial design of coil power supply for 1 T operation

4.3.1 Designed circuit diagram and the layout of MG building

Based on rough estimation, we designed circuit diagram of the power supply system with IM and SG as represented in Fig. 4.3.1. The circuit mainly consists of IM, SG, the inverter for IM and SG revolution control, the excitation system for SG, six phase Thyristor-control units, and polarity switching circuits. Typical SG with two pole, 50 Hz, 51 MVA rated output, 11 kV of operation voltage is selected by a manufacturer catalog. Although total required power for all coils is around 60 MW, the selected SG may cover the power because required output time is only several seconds. The static exciting system consisting of an exciting transformer (EXT), an automatic voltage regulator (AVR), and SCR is adopted for SG excitation control. The excitation system has rapid responsiveness for SG voltage control.

We also designed the layout of MG building including IM, SG, and some control equipment's as shown in Fig. 4.3.2. This design is based on the data of products with similar specifications published in the commercial catalog. Re-evaluation according to the specific product design is necessary.

The maximum height of equipment in the MG building is 3.7 m (height of SG). Manufacturer catalogs in Japan are referred to size of IM, SG, the inverter with 280 kVA for IM revolution control, and the three-phase transformer with 300 kVA for power receiving to IM. The size of EXT, AVR, SCR and oil feeder for SG bearings are based on a short circuit generator system (275 MVA) equipped in a certain Japanese manufacturer. M1 and M2 circuit breaker panels equipped in CHS power receiving system are referred to the size of VCB2 and VCB4. More details of designs should be proceeded with a manufacturer.

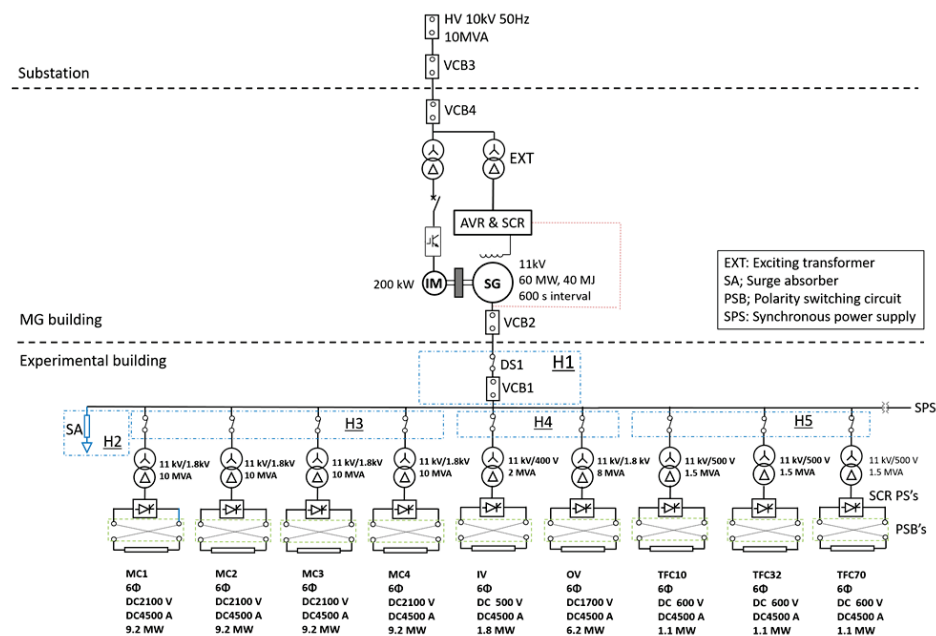
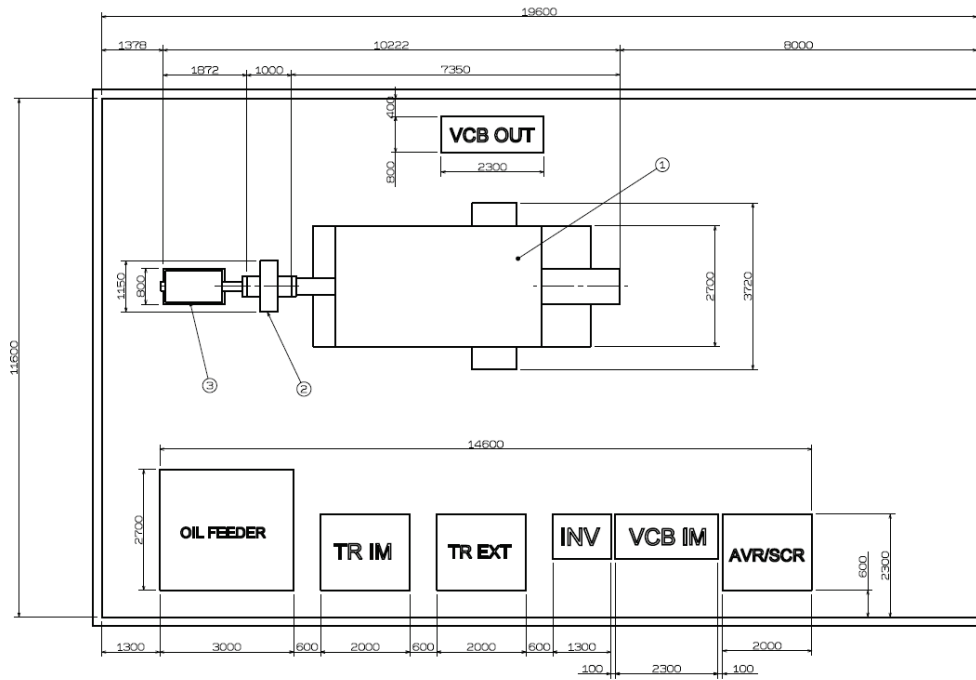


Fig. 4.3.1 Designed circuit diagram of power supply system with IM and SG.



No	Name	Equipement	Note
1	SG	Synchronous generator	51MVA 11kV 40-60Hz 68MJ
2	FW	Flywheel	26MJ
3	IM	Induction motor	200kW

Fig. 4.3.2 Designed layout of MG building.

4.3.2 Specifications of SG, IM, and a flywheel

Estimation results of specifications of IM, SG and a flywheel are summarized in Table 4.3.1. We have estimated stored energy in SG for CFQS by calculating of inertia moment of SG equipped in NIFS (250 MVA). The formula of inertia moment is followed:

$$J_x = \frac{1}{8} m \cdot D^2 = \frac{\pi}{32} \rho \cdot L \cdot D^4 \text{ [kg} \cdot \text{m}^2], \quad (1)$$

where J_x , m , D , ρ are inertia moment, mass of a rotor, diameter of a rotor and volume density of a rotor made of iron (8000 kg/m³) respectively. The calculated value of J_x of NIFS SG is 289,540 kg m². Based on the calculation result, we estimated the J_x value of CFQS SG by calculating the ratio of rotor size and mass between NIFS SG and CFQS SG. Then, stored energy K_s of CFQS SG is calculated from the following formula:

$$K_s = \frac{1}{2} \times J_{CFQS} \times (2\pi f)^2 \text{ [J]}, \quad (2)$$

where f is frequency with 50 Hz (3000 rpm). J_{CFQS} is inertia moment of CFQS SG with 1386.8 kg m². The calculated value of stored energy for CFQS SG is 68.4 MJ. Given 38 Hz of CFQS SG frequency after kinetic energy transfer to electrical power, only 28.9 MJ which cannot cover the required total energy for coils (40 MJ) is obtained. Therefore, the flywheel compensating stored energy for coil energization should be adopted. Required stored energy of the flywheel at 50 Hz (3000 rpm) is 26.2 MJ. Inertia moment of the flywheel J_{FLY} is $J_{FLY} = 531.5 \text{ kg m}^2$ obtained by Eq. (1). We designed the size of flywheel made of iron with 1150 mm diameter and 400 mm thickness (~3300 kg, 549 kg m²).

We also estimated required operation power for the IM. Given 600 s acceleration time (shot to shot) for number of revolutions of SG rotor and the flywheel from 2280 rpm to 3000 rpm, required torque for the IM is obtained as following formula:

$$T_{IM} = \frac{2\pi \times (J_{CFQS} + J_{FLY})}{60} \times \frac{N_2 - N_1}{600} \text{ [N} \cdot \text{m]}, \quad (3)$$

where N_1 and N_2 show number of revolutions [rpm]. In this case, N_2 is 3000 rpm and N_1 is 2280 rpm. Calculated value of required torque for IM between 2280 rpm to 3000 rpm is 240.9 Nm. On the other side, if SG rotor and the flywheel are accelerated from 0 rpm to 3000 rpm in 1800 s, required torque for IM is 334.6 Nm. Consequently, required maximum mechanical output of IM is 105.2 kW. The value is calculated by

$$P_m = \frac{T_{IM} \times N}{9.545}, \quad (4)$$

where N is number of revolutions. Required input power for IM is estimated around 200 kW because some loss factors such as copper loss, iron loss and windage need to be considered.

Table 4.3.1 Summary of the estimation result of IM and SG specifications.

Component	Parameter	Unit	Value
Generator	Number		1
	Capacity	MVA	51
	Voltage	kV	11
	Power factor	%	90%
	Frequency	Hz	38-50
	Revolution	rpm	2250-3000
	Number of poles	p	2
	Stored energy (Rotor)	MJ	68.4
Motor	Number		1
	Capacity	kW	200
	Voltage	kV	0.44
	Number of poles	p	2
Flywheel	Density	kg/m ³	8000
	Diameter	m	1.15
	Height	m	0.4
	Weight	kg	3,322
	Stored energy	MJ	26.2
	Release energy (Rotor + Flywheel)	MJ	40.0
Accelerating torque	Accelerating time (Shot to Shot)	s	600
	Accelerating time (Start-up)	s	1800
	Torque (Shot to Shot)	Nm	240.9
	Torque (Start-up)	Nm	334.6
	Mechanical output from a Motor (Shot to Shot)	kW	75.7
	Mechanical output from a Motor (Start-up)	kW	105.2

4.3.3 Comparison of coil power supply systems

For the 1 T operation, power supply system with up to 60 MW and 40 MJ capacity is required. It is rarely allowed to provide such massive electrical power directly from power grids due to overload (up to 10 MVA). Therefore, energy storage systems must be employed as shown in Fig. 4.3.3. Of course, AC/DC SCR control converter or rectifiers and PWM chopper circuit system must be utilized for controlling each coil current.

There are mainly four options which may satisfy the electrical conditions for the 1 T operation. The comparison is summarized in Table 4.3.2. IM and SG type may be the most appropriate power storage system. Discussions for each candidate focusing on capacity, space, cost, and operation control are described as follows.

1) Capacitor bank

Fig. 4.3.4 shows the power supply system with capacitor banks. This type has been widely adopted for small fusion devices and its configuration is comparatively simple. However, because high voltage capacitors have small energy density per volume, the problem of installation space for capacitors cannot be ignored. Consequently, capacitor bank is impractical for power supply system of 1 T operation. Details of discussions are described as follows.

The size of a capacitor depends on its type. Recently, although the energy storage density of a capacitor is greatly increased such as an electrolytic capacitor with small size, it is limited to 500 V or less. The modular coil of the CFQS is required to be applied over DC 1000 V. Thus, there is no choice but to be selected an oil capacitor with extremely large size.

Total required energy for MC is approximately 38 MJ with 2400 V. Given 3000 V charging voltage of capacitor bank before discharge and 2700 V after discharge, oil capacitors with about 44.4 F capacity is required. Charging voltage for capacitor bank need to be more than 2400 V even after discharge because of discharge current control. The total required capacitor including TFC and PFC capacity is estimated about 46.8 F 210 MJ based on above voltage conditions. If general oil capacitor with 78 μF , 3510 V rated voltage and size of $0.175 \text{ m} \times 0.620 \text{ m} = 0.11 \text{ m}^2$ is adopted, total required number of capacitors is about 600,000. Therefore, at least 66,000 m^2 space for capacitors is required. It should not be accommodated in the experimental building. Even though given 10 kV charging voltage is applied to capacitor bank, total required capacitance, number of capacitor and space is estimated about 0.9 F, 10,000, respectively.

Moreover, a Pulse Width Modulation (PWM) switching circuit must be installed between the capacitor bank and coils to control the coil current. Since the switching circuit generates ripples, it is necessary to evaluate the power supply by the combination of the capacitors and the switching circuit.

2) DC motors

Fig. 4.3.5 shows the power supply system of DC motors case. Since a DC motor is an old technology, procurement of new motors may be difficult. There is no other way but to find for used motors. However, since lifetime of a typical DC motor is limited by a brush, the used motor has relatively high risk of breakdown. Furthermore, over 100 number of DC motors with extremely large installation space may be required to cover the total energy of coils because it is difficult to procurement of over 200 kW used motors. Besides, simultaneous operation control of 100 number of DC motors may be impractical. Thus, DC motor should be inappropriate for power supply system of 1 T operation.

3) Self-excited induction generators (SEIG)

Fig. 4.3.6 shows the power supply system of SEIG type. Murayama et al. adopted this type for power storage system of a small fusion device [Fus. Eng. Des. **148**, 111270 (2019)]. The system is utilized squirrel cage IM as a motor/generator (MG) instead of SG. The advantage utilizing the IM with squirrel cage casting structure is robustness derived from the simple structure with no wearing parts except for bearings. Moreover, it can generate electricity with capacitor self-excitation phenomena which does not require excitation control system. However, in the case of CFQS, large installation space for the high voltage capacitors with up to 30 MVAR capacity may be required to obtain the suitable output voltage of SEIG. It is difficult to be accommodated in the experimental building.

Furthermore, we need to compensate the voltage drop of SEIG during the coil energization by connecting additional self-exciting capacitors in parallel at the start of the discharge phase. If additional capacitors are connected to SEIG before the discharge phase, output voltage of SEIG is significantly increased and it leads to insulation breakdown and overheat. Therefore, high voltage switching devices with high responsiveness and their control systems should be prepared. There is no achievement of implementation of power supply with SEIG for large or middle-sized fusion device (over 10 MW case) in Japan.

4) An induction motor and a synchronous generator

IM and SG type as shown in Fig. 4.3.7, which has been utilized for various fusion experimental devices in Japan may be most suitable as a power storage system for 1.0 T operation. It can store large amount of electrical energy over 100 MJ and supply power with good controllability. We decided on principal specifications and designed the circuit diagram and layout of power supply system with IM and SG energy storage system.

Table 4.3.2 Comparison of power storage systems for the 1 T operation.

Power storage candidate	Evaluation	Evaluation reason
Capacitor banks	Impractical	Extremely large number of capacitors (over 600,000) and their installation space is required.
DC motors	Impractical	Large number of motors (over 100) and their installation space is required. Simultaneous operation technique needs to be developed.
SEIG (Self-excited induction generator)	Marginal	There is no achievement of implementation of power supply with SEIG for large or middle-sized fusion device (over 10 MW case) in Japan. Large number of capacitors with rapid responsiveness switching systems for self-excitation control need to be prepared.
IM and SG	Appropriate	It has been utilized for various fusion experimental devices in Japan. It can store large amount of electrical energy over 100 MJ and supply power with good controllability.

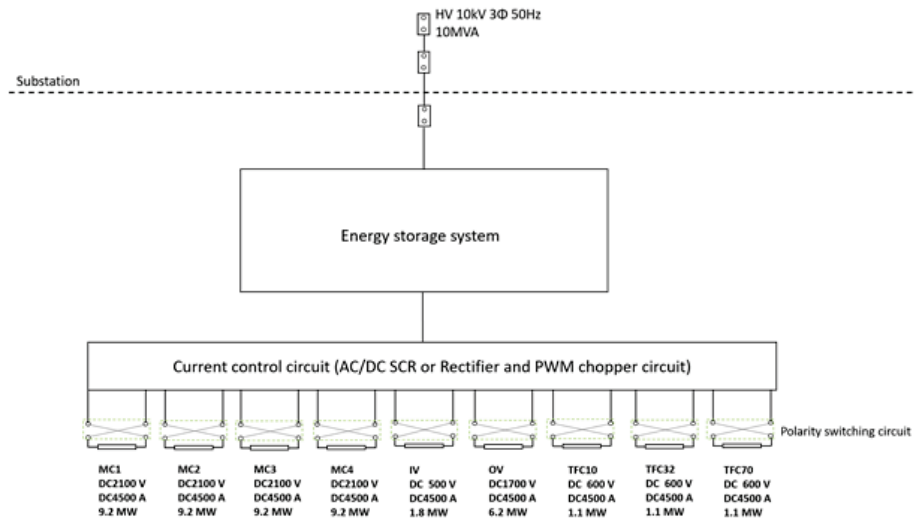


Fig. 4.3.3 Configurations of power supply system for 1.0 T operation.

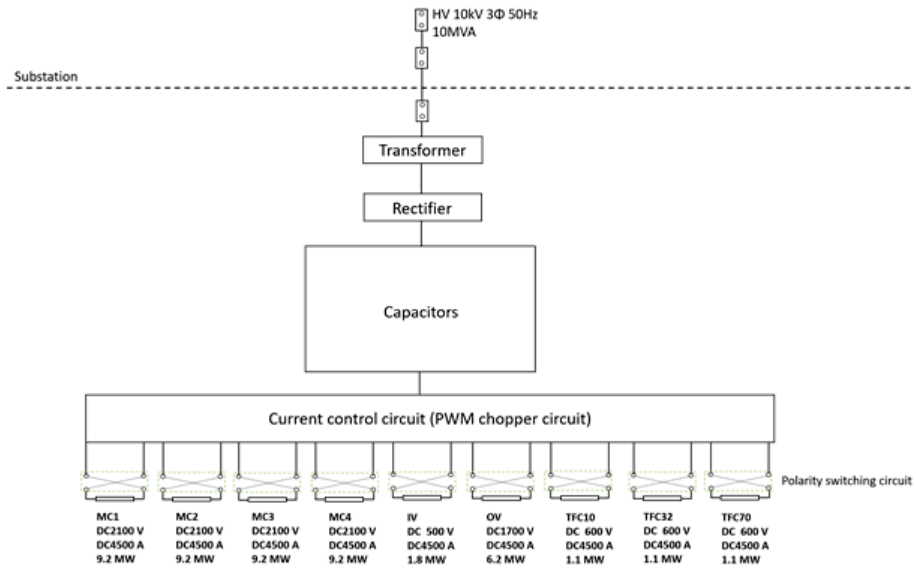


Fig. 4.3.4 Capacitor bank type power supply.

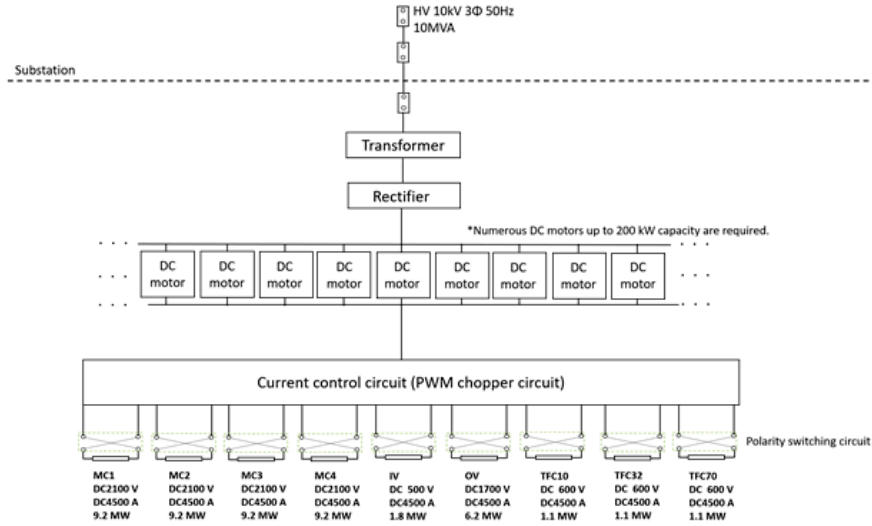


Fig. 4.3.5 Power supply with DC motors.

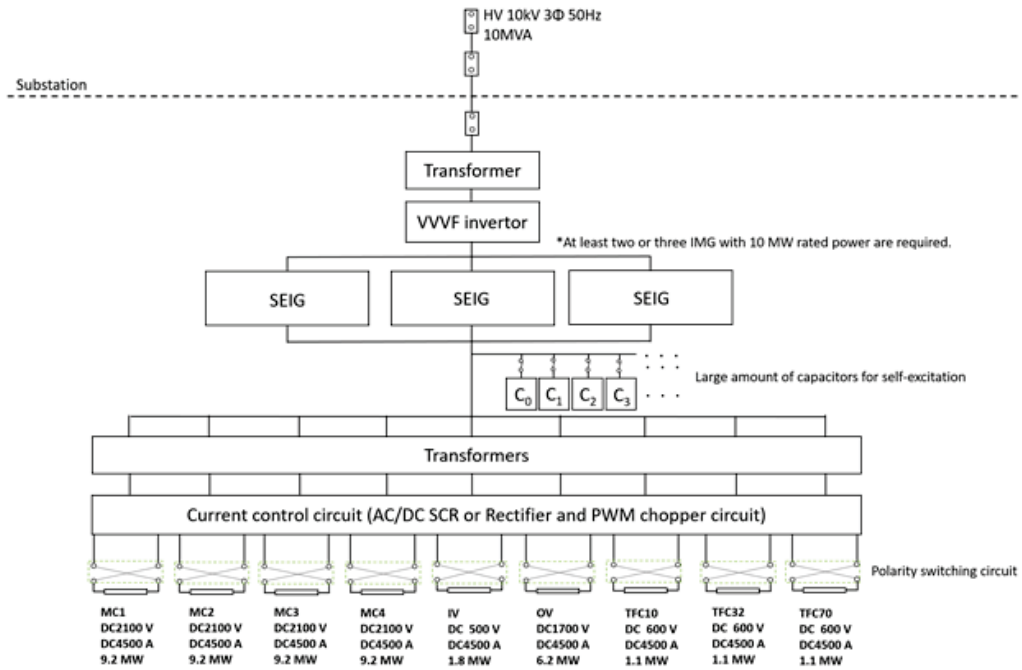


Fig. 4.3.6 Power supply with the SEIG.

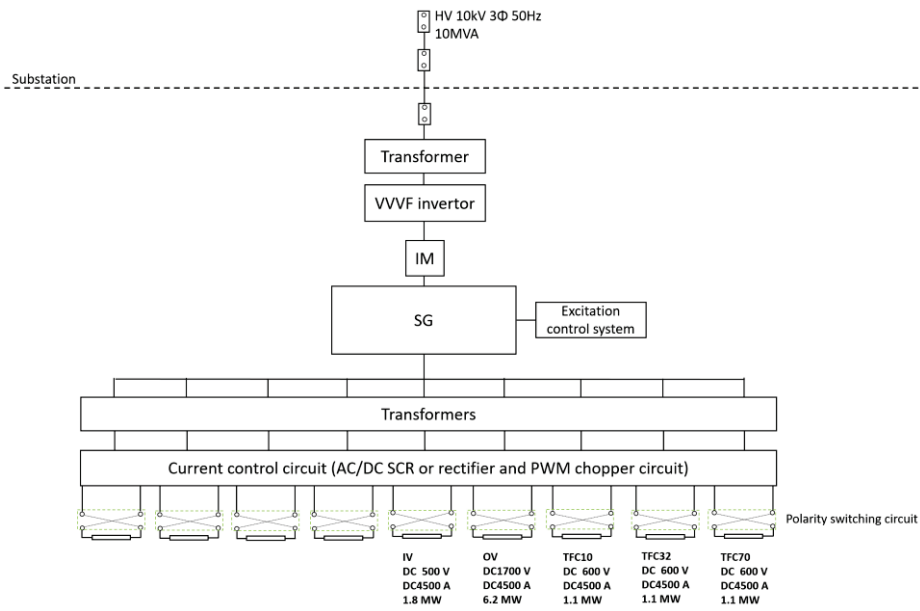


Fig. 4.3.7 Power supply with IM and SG.

5 Mockup of a modular coil

The total number of the CFQS modular coil is 16. The number of MC4 is 4, and the MC4 is the most complex coil. So, the MC4 mockup coil was manufactured firstly.

5.1 Engineering design of the mock-up coil

5.1.1 Conductor and insulation design

The coil cross section is shown in Fig. 5.1.1 and the total turns is 72. The conductor dimension used for the mockup coil is $8.5 \times 8.5 \times \Phi 4$ mm, the layer insulation thickness is 1 mm, and the ground insulation is 3 mm.

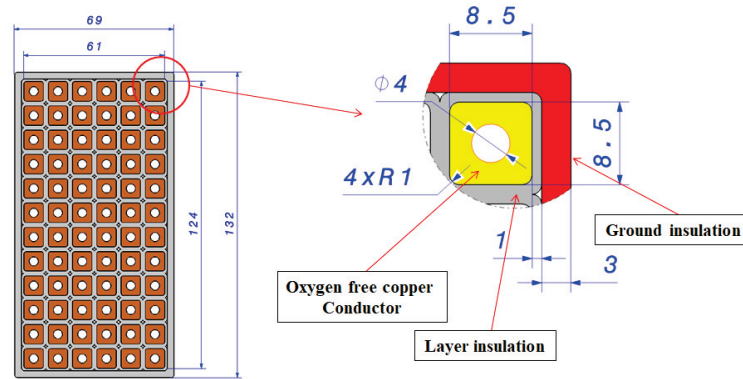


Fig. 5.1.1 Conductor and insulation.

Eight units Cu conductors have been purchased; each unit length is about 100 m. The material of the conductor for the mockup coil is oxygen-free copper and the chemical composition is shown in Table 5.1.1. The Cu content is 99.97 % and oxygen content is 0.0008 %. The mechanical performance of the conductor is shown in Table 5.1.2. The tensile strength is 239 MPa, and elongation is 45 %. The dimension tolerance of the conductor is $8.5 \times 8.5 \times \Phi 4 \pm 0.08$ mm.

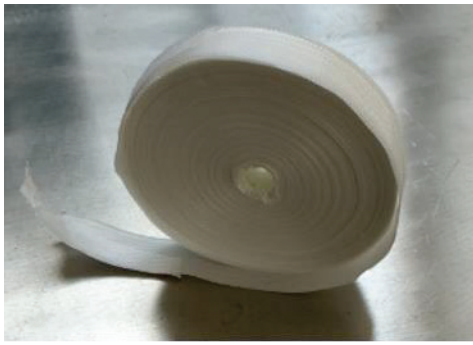
Table 5.1.1 Chemical composition of the Cu conductor.

化学成分 (%) Chemical Composition	Cu	O							
标准值 Standard Requirement	≥99.97	≤0.002							
实测值 Test	99.97	0.0008							

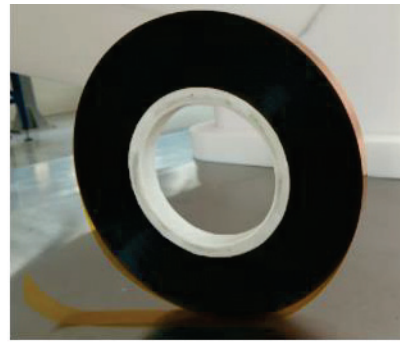
Table 5.1.2 Mechanical performance of the Cu conductor.

试验项目 Test	外观·尺寸 Visual & Dimension	抗拉强度 Rm(Mpa) Tensile Strength	延伸率 A(%) Elongation	导电率 (%) Electrical	气压 Pneumatic Pressure	耐击穿电压	钢珠通试
标准值 Standard Requirement		≥205	≥35	≥100	合格		通过
实测值 Test	合格	239	45	100	合格		通过
检验员签章 Inspector:	技术条件 Technical Conditions:		备注 Remark :		上海上大众鑫科技发展有限公司 SHANGHAI STARKING SCIENCE AND TECHNOLOGY CO., LTD 质保部 Quality Department		

The main material for the insulation is fiber glass tape and polyimide (Kapton) as shown in Fig. 5.1.2. The width and thickness of the fiber glass tape and the Kapton are 16 mm × 0.2 mm and 10 mm × 0.05 mm respectively for the mockup coil.



(a) Fiber glass tape
 16mm x 0.2mm x 50m
 Tensile strength 1920N/25mm



(b) Polyimide (Kapton) tape
 10mm x 0.05mm x 2000m
 Tensile strength 115MPa

Fig. 5.1.2 Insulation materials.

5.1.2 Mockup coil design

The structure design of the MC4 mockup coil is shown in Fig. 5.1.3. It mainly consists of coil main body, layer to layer S-bending, turn to turn S-bending, coil joints, and joint filler blocks.

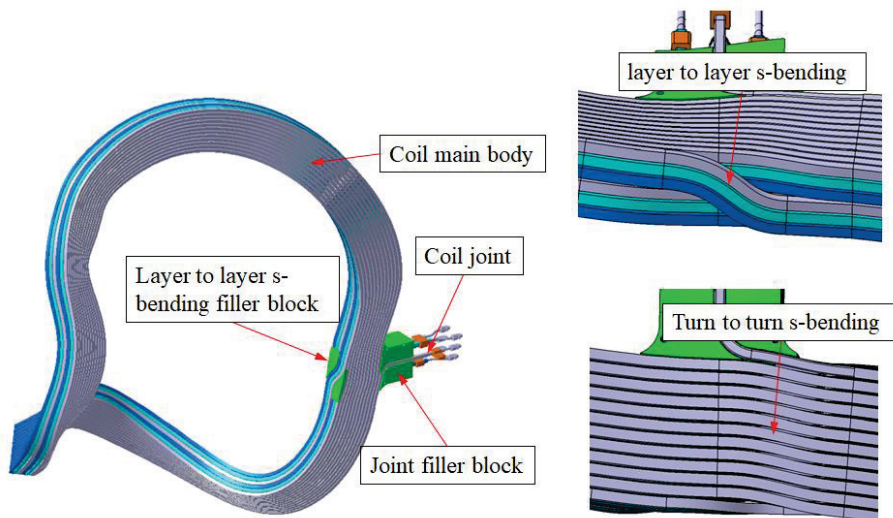


Fig. 5.1.3 Mockup coil design.

5.1.3 Design of conductor joint

Three double pancakes are connected each other near terminal as shown in Fig. 5.1.4. Detail of joints are shown in Fig. 5.1.5. Two types of copper block are designed to connect conductors. One of them is for connection between pancakes and other is for current lead. Two square holes are designed on the copper block and the conductor can be inserted from one side. After inserting of the conductor, the copper block will be welded with the conductors by silver brazing.

Location the copper blocks is shown in Fig. 5.1.6. The distance between the copper joint and coil main body is about 100 - 140 mm. To avoid damage, the insulation by the high temperature of the brazing, the copper block should keep larger than 100 mm distance with the coil insulation.

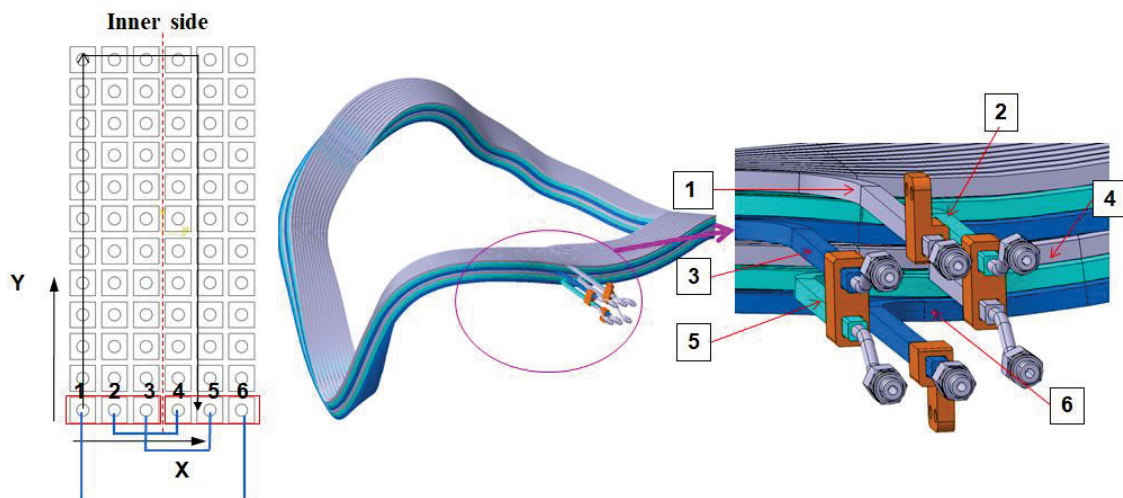


Fig. 5.1.4 Coil joint.

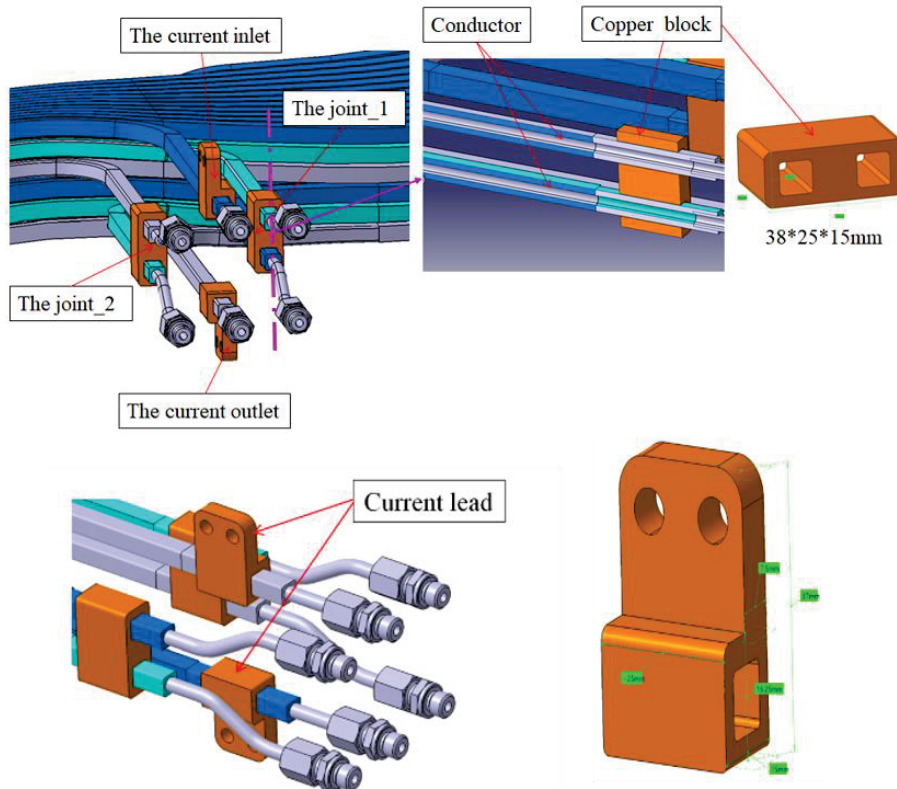


Fig. 5.1.5 Detail of the conductor joint.

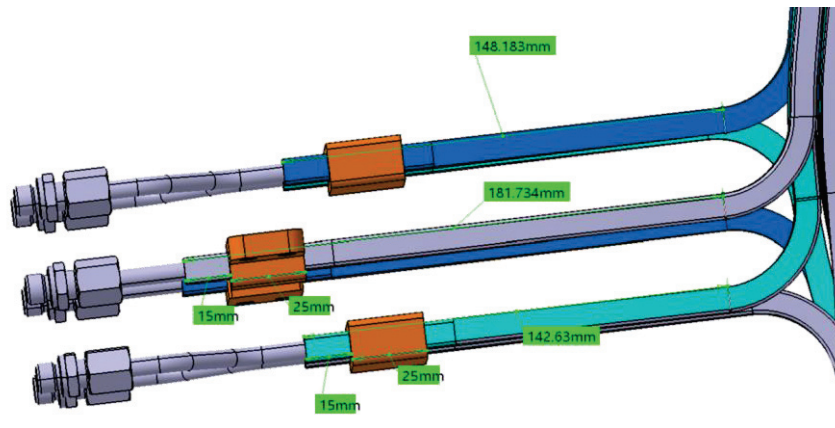


Fig. 5.1.6 Location of the copper block.

5.1.4 Joint of cooling water pipe

A $\Phi 6 \times \Phi 4$ pipe is designed for the water-cooling pipes as shown in Fig. 5.1.7. The material of the pipes is stainless steel. The terminal of the conductors will be drilled a $\Phi 6$ mm hole for inserting of the pipe. A standard water pipe joint is selected for the cooling water and the material is also stainless steel. The pipes will also be welded with the conductors by silver brazing.

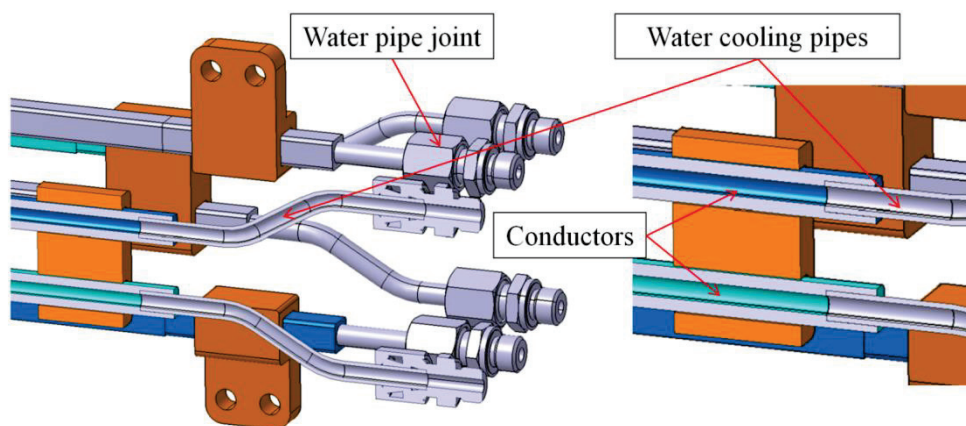


Fig. 5.1.7 Cooling water pipe joint.

5.1.5 Filler block design

The function of the S-bending filler block is to fill the gap of the S-bending area to provide a smooth surface for wrapping the 3 mm ground insulation. The detail of the filler blocks is shown in Fig. 5.1.8. The function of the joint filler block is :

- To fix all the joint conductors together to resist electromagnetic force.
- To fill the gap of the joint area for wrapping the 3 mm ground insulation.

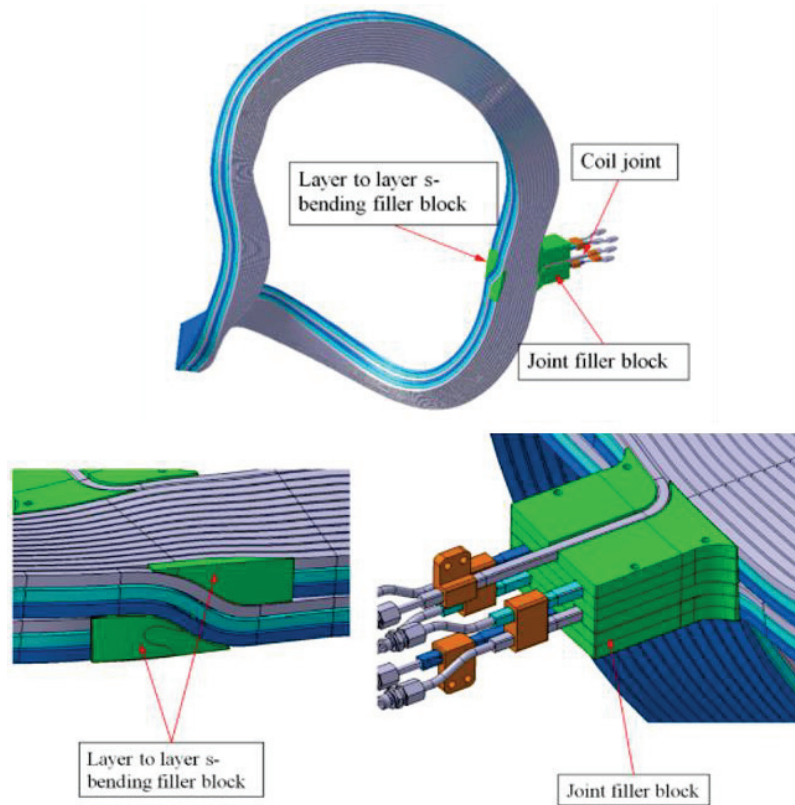


Fig. 5.1.8 Coil filler block.

5.2 The coil winding manufacture line

The conceptual design of the coil winding manufacture line for the mock up coil is shown in Fig. 5.2.1. It mainly includes rotating platform, winding mould and clamping, copper conductors, insulation wrapping, and conductor straightening.

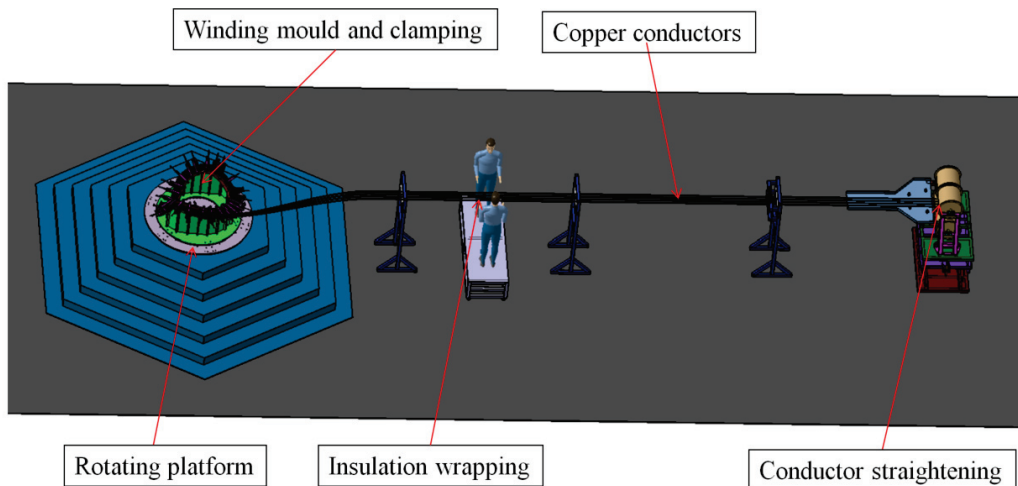


Fig. 5.2.1 Conceptual design of the coil winding manufacture line.

5.3 The winding mould design

The winding mould has been designed base on the MC4 coil profile shape, it consists of inner mould and bottom mould as shown in Fig. 5.3.1 The inner mould contains 12 types blocks. Fourteen grooves are designed on the bottom mould, as shown in Fig. 5.3.2. The function of grooves is for installation of the bottom plate of the clamping_2. The clamping_2 will be used to fix the coil after finishing the coil winding. The usage of the winding mould is divided into 2 stage as shown in Fig. 5.3.3:

- 1st stage: It will be used for the coil winding.
- 2nd stage: It will be used for coil VPI.

After finishing the coil winding, the mockup coil will be fixed by the clamping_2 and removed from the winding mould. And then the mockup coil will be wrapped with the 3 mm ground insulation without winding mould. And the winding mould “L” surface will be machined 3 mm (ground insulation thickness) for the VPI. Before VPI, the mockup coil will be wrapped with 3 mm ground insulation and will be put on the winding mould again and adjust the shape of the coil by clamping.

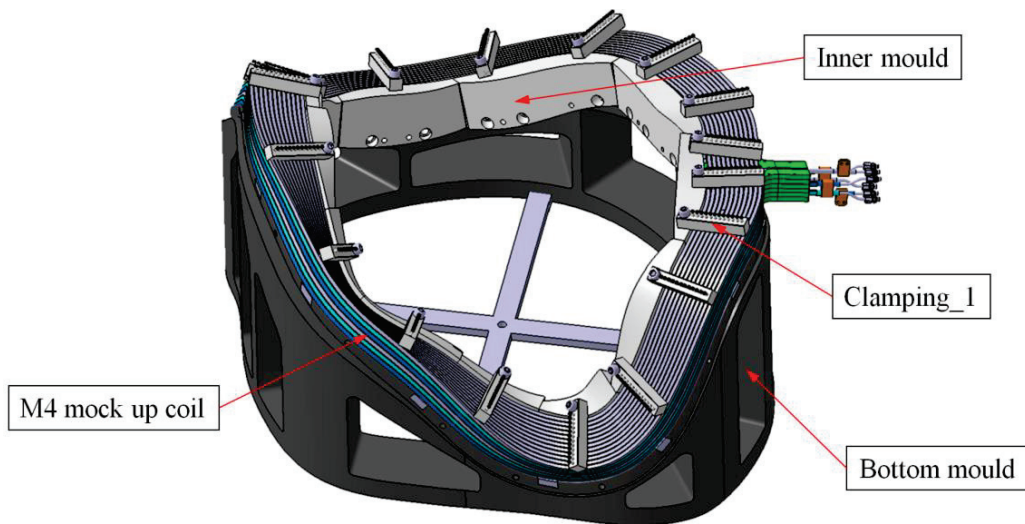


Fig. 5.3.1 The winding mould for MC4 mockup coil.

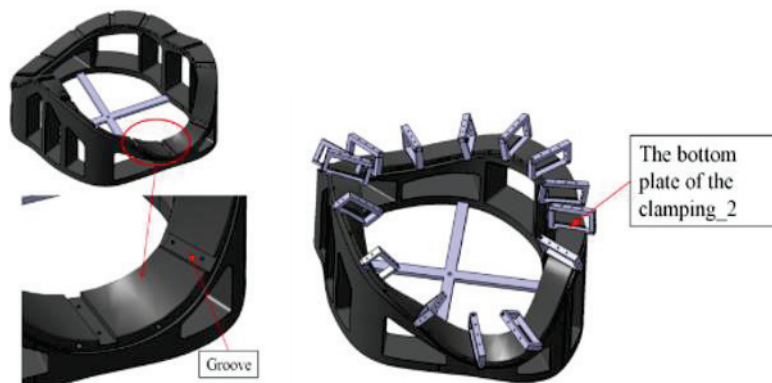


Fig. 5.3.2 The bottom mould design.

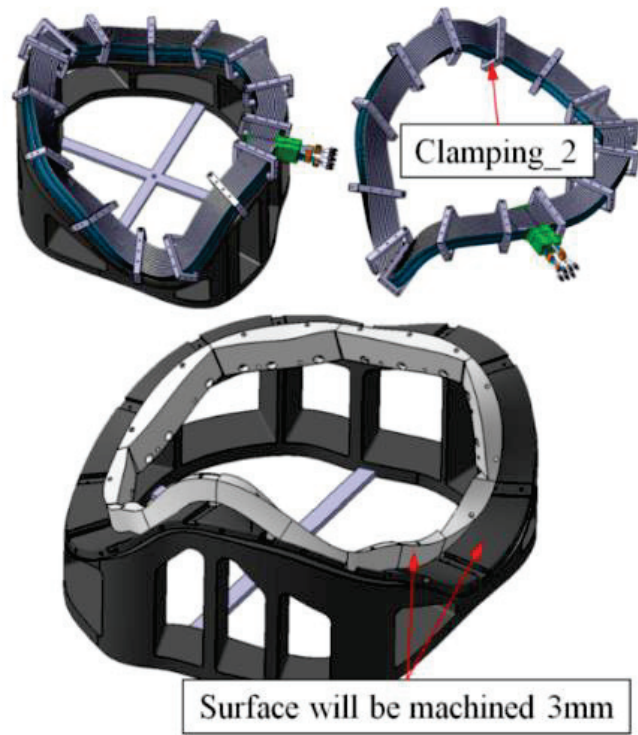


Fig. 5.3.3 The usage of the winding mould.

5.4 Result of manufacturing and test for the MC4 mockup coil

5.4.1 The manufacture process

The manufacture process of the MC4 mockup coil is shown in the Fig. 5.4.1, and the main manufacture points is shown in the Fig. 5.4.2.

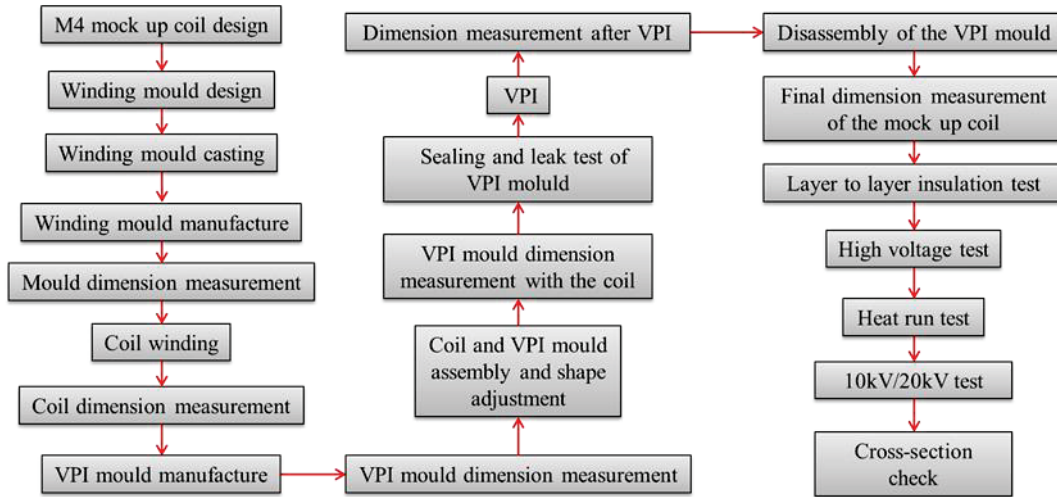


Fig. 5.4.1 The manufacture process of the MC4 mockup coil.

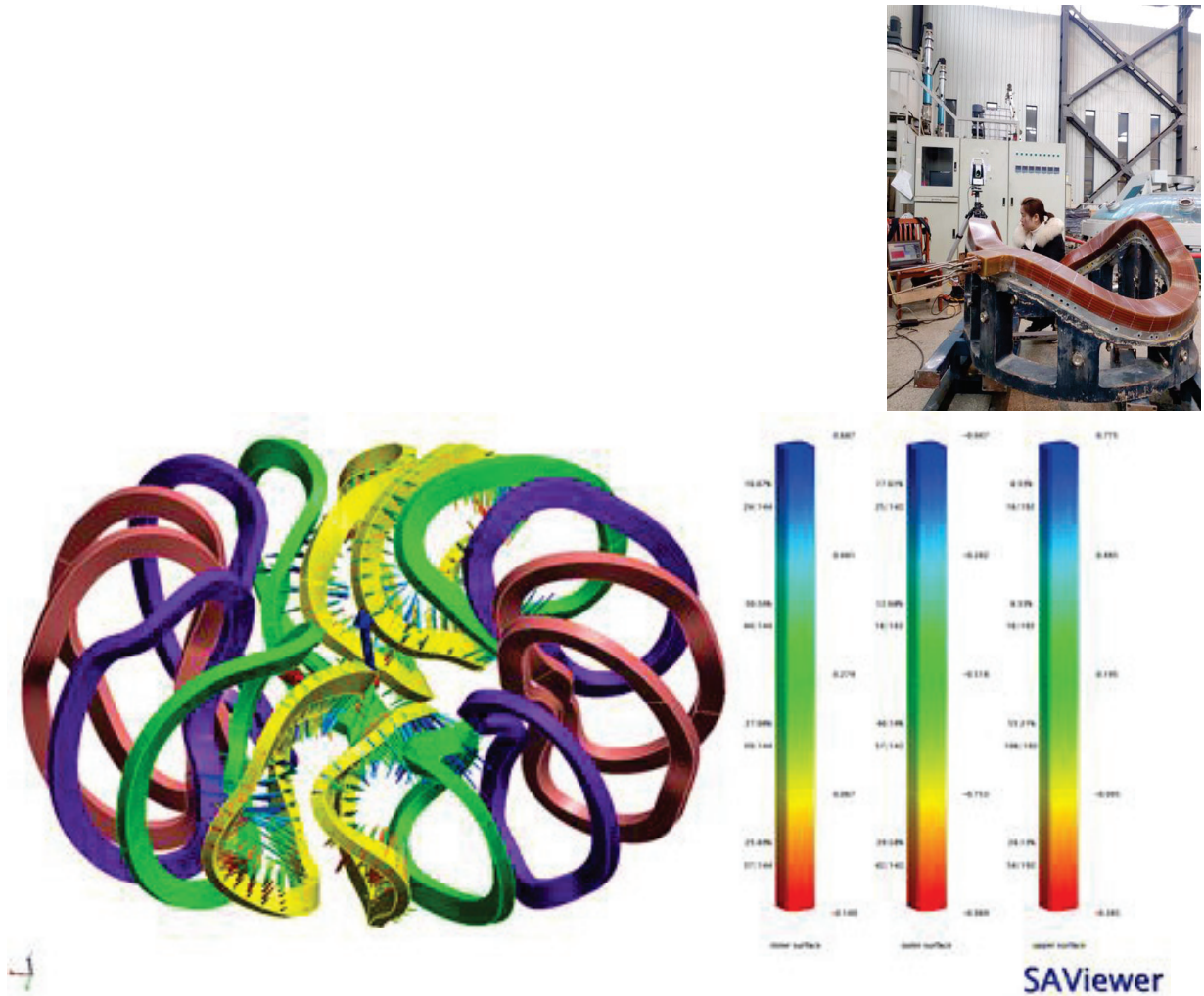


Fig. 5.4.2 The main manufacture points of the MC4 mockup coil.

5.4.2 The dimension measurement on the winding mould

After VPI the dimension of MC4 mockup coil has been measured on the winding mould, the deviation is shown in the Fig. 5.4.3.

- The deviation of the upper surface of the coil is -0.39~0.77 mm;
- The deviation of the outer surface of the coil is -0.13~0.98 mm;
- The deviation of the inner surface of the coil is -0.19~0.66 mm.



**Fig. 5.4.3 The dimension measurement result of the MC4 mockup coil.
(On the winding mould after VPI)**

5.4.3 Impulse test

In order to inspect the turn to turn insulation, the impulse tests were performed. The connecting schematic diagram for the impulse test is shown in the Fig. 5.4.4.

The test process as follow:

- 1) **Cut the series connection of the mockup coil, and perform the test of 1, 2, and 3.**
- 2) **Connect the A and B to perform the test of 4.**
- 3) **Connect the B and C to perform the test of 5.**
- 4) **Connect the A, B, and C to perform the test of 6.**

Fig. 5.4.5 shows example of wave form of the impulse test. The X axis shows number of sampling time point and Y shows voltage. The sampling frequency is 3.12 MSA/s (0.32 μ s/sample) and the number of time points displayed is 6000, which corresponds to 1.92 ms. Time between grids is 0.32 ms.

The test results are shown in Fig. 5.4.6 to Fig. 5.4.11. The waveforms show that the oscillation attenuation trend of all test waveforms are basically same, so the turn to turn insulation is qualified.

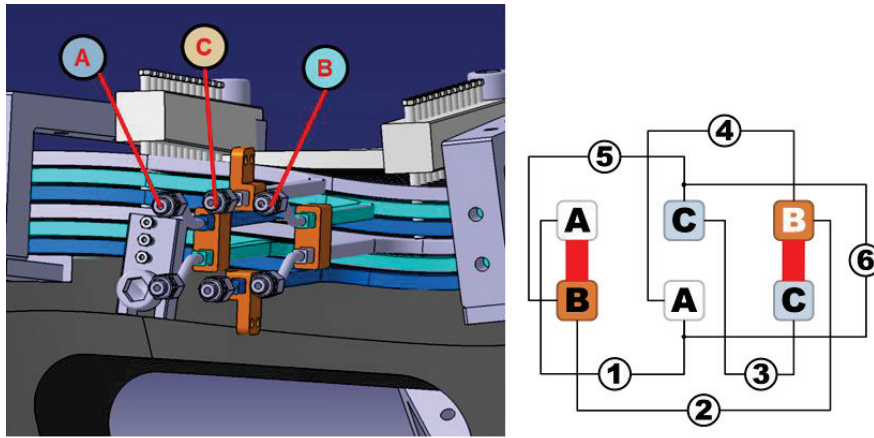


Fig. 5.4.4 The connecting schematic diagram for the impulse test. Marks A, B, and C indicate the names of conductors. Marks ① to ⑥ indicate the name of the test. Test 1 is the test of conductor A, test 2 is the test of conductor B, test 3 is the test of conductor C, test 4 is the test of conductor A+B, test 5 is the test of conductor B+C, and test 6 is the test of conductor A+B+C.

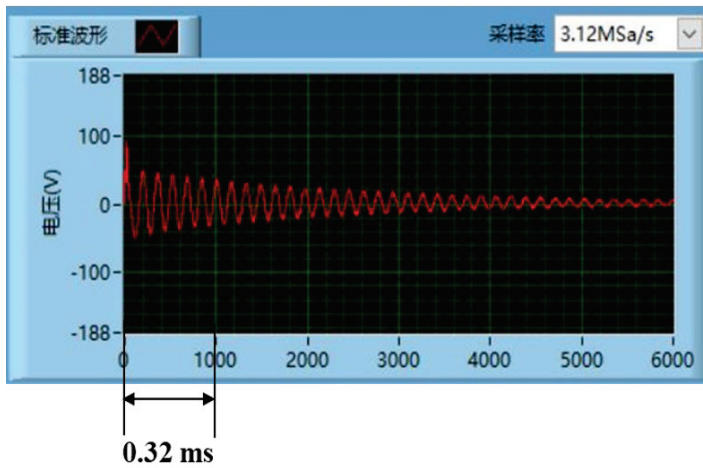


Fig. 5.4.5 Impulse test wave form.

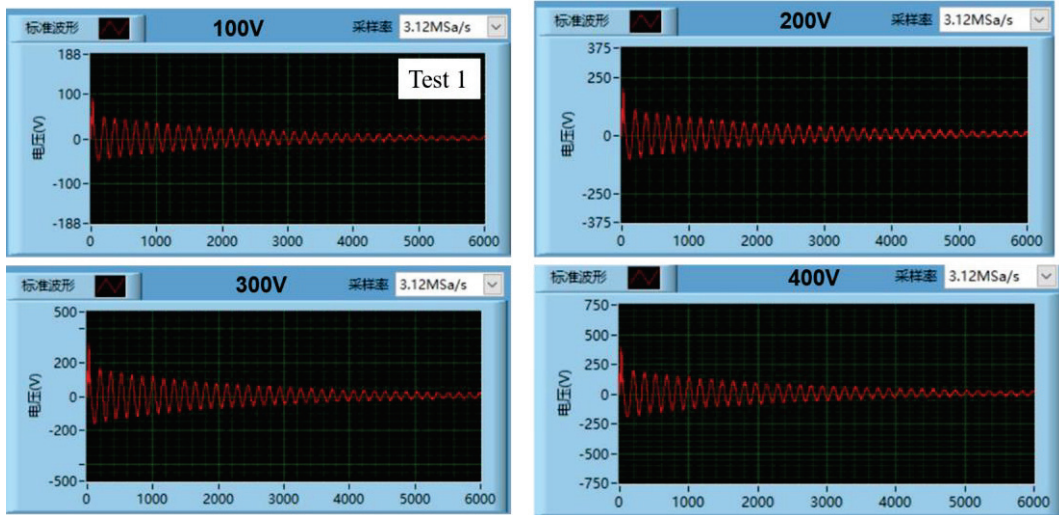


Fig. 5.4.6 Impulse test result of the TEST1.

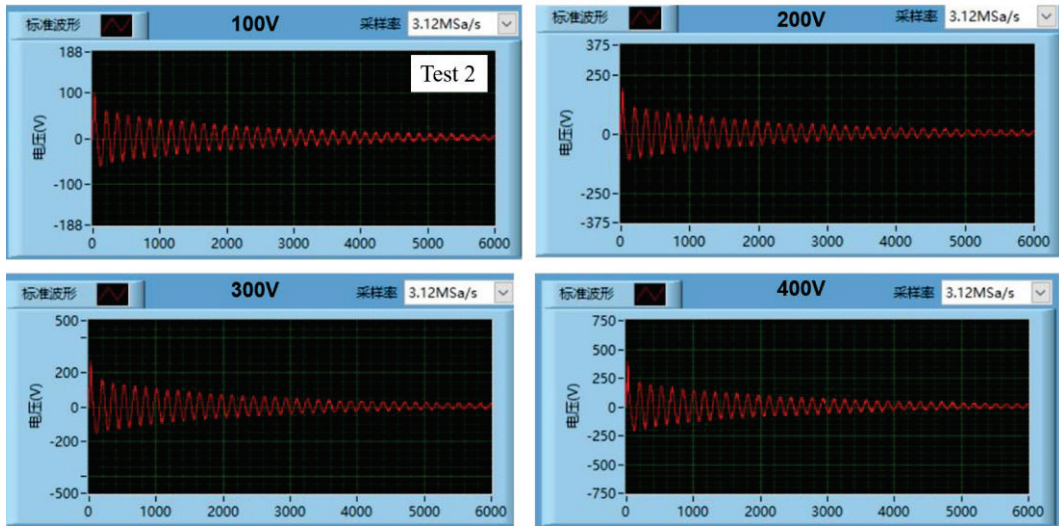


Fig. 5.4.7 Impulse test result of the TEST2.

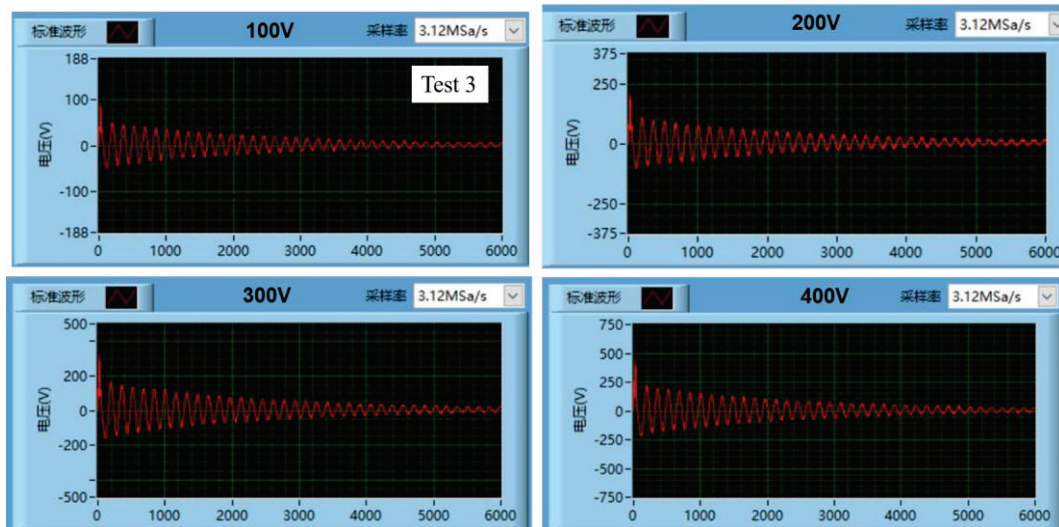


Fig. 5.4.8 Impulse test result of the TEST3.

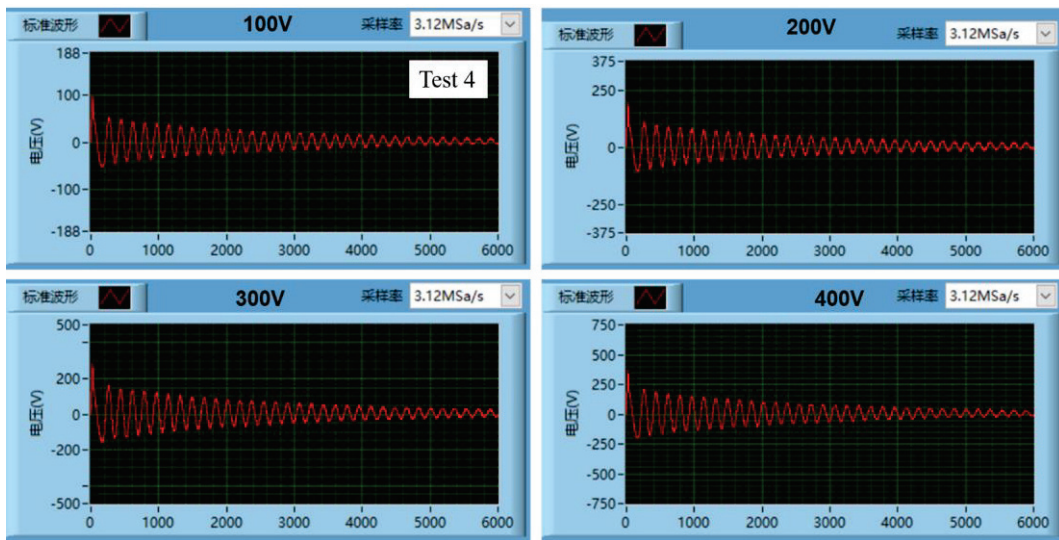


Fig. 5.4.9 Impulse test result of the TEST4.

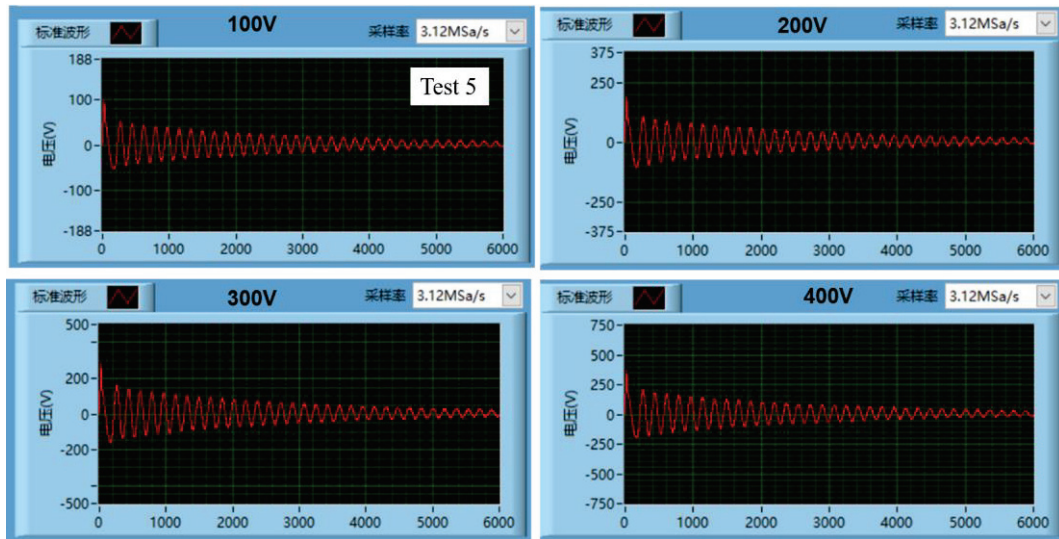


Fig. 5.4.10 Impulse test result of the TEST5.

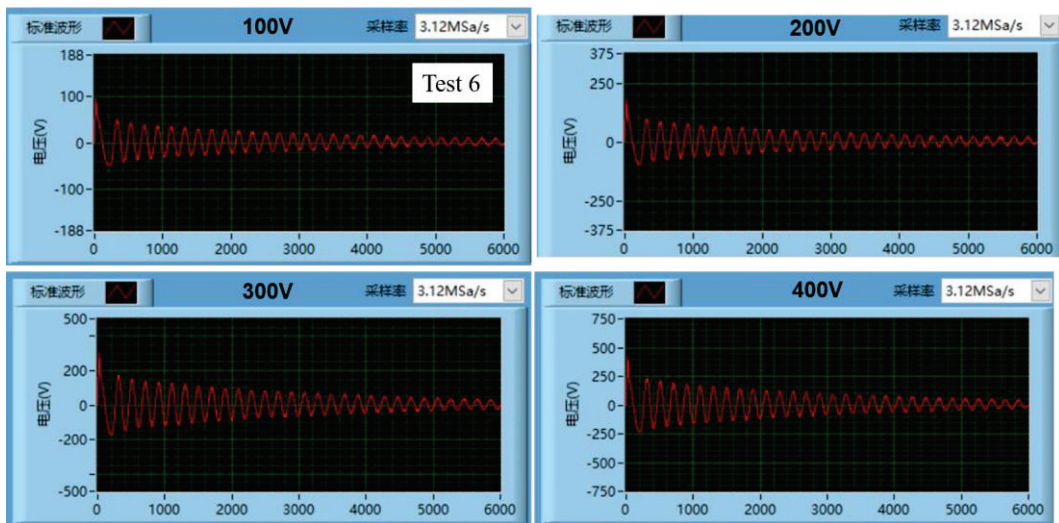


Fig. 5.4.11 Impulse test result of the TEST6.

5.4.4 Heat run test

In order to verify the cooling design, the heat run test has been performed, the sketch of the heat run test system is shown in Fig. 5.4.12 and Fig. 5.4.13. The maximum pressure of the cooling water is about 1 MPa.

The heat run test have been performed under 4 kinds of conditions.

- (a) 1 kA/38 s whose heat generation is equivalent to that for the 1.0 T operation (4.34 kA and 2 s).

1) Without cooling water

2) With 3.9 L/min. water flow

- (b) 500 A/120 s which corresponds to the steady operation condition (434 A).

3) Without cooling water

4) With 4.2 L/min. water flow

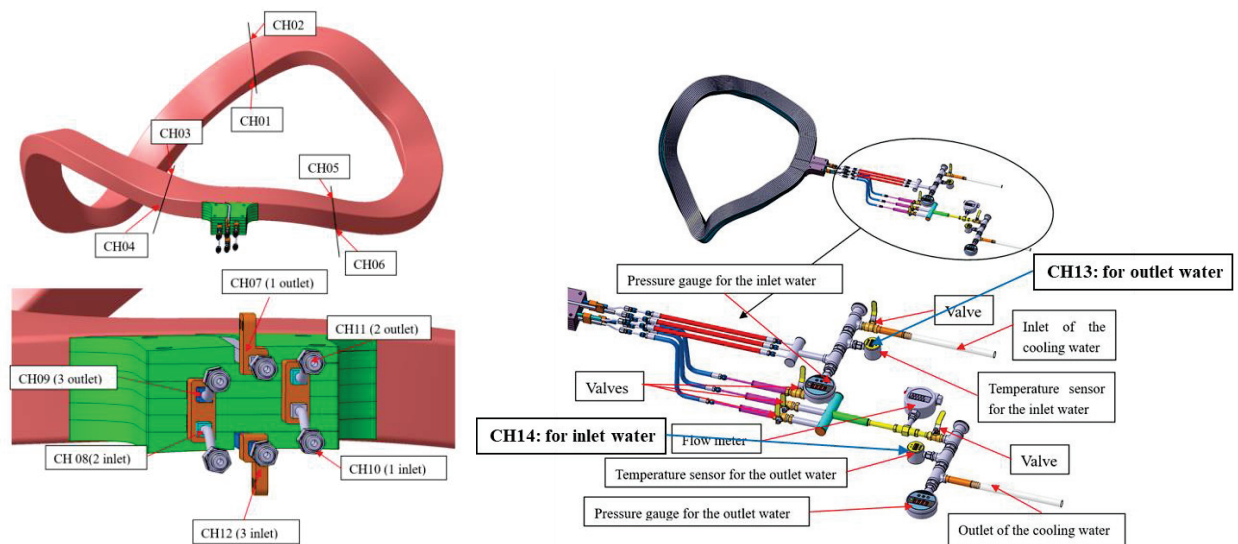


Fig. 5.4.12 Sketch of the coil test system and the temperature sensor distribution.

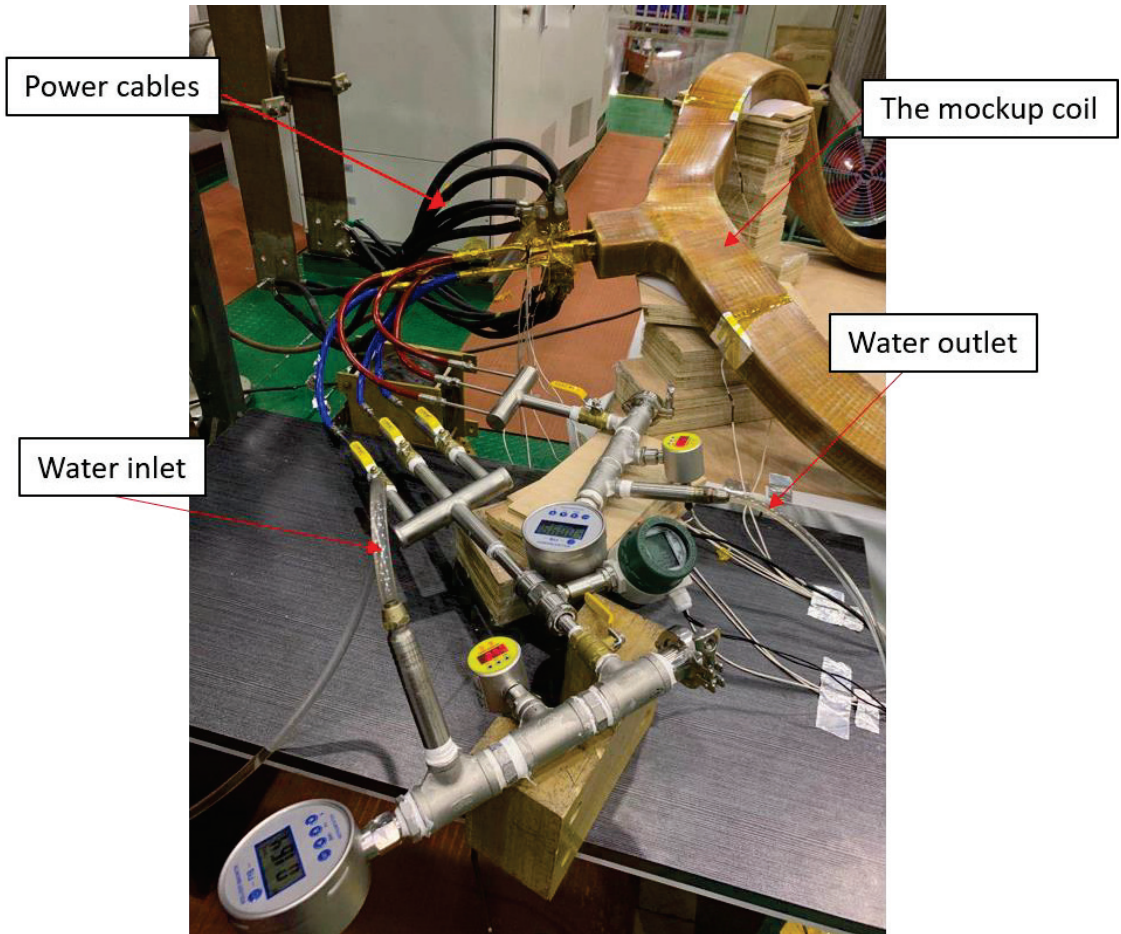


Fig. 5.4.13 Heat run test of the MC4 mockup coil.

1) Heat run test result of 1 kA/38 s without cooling water

- Maximum of temperature rise on the insulation surface is 38 °C.
- The temperature on the insulation surface reaches its maximum about 2 minutes after the end of current.
- The temperature drop rate without cooling water is very slow (15 °C /hour). Once the temperature rises, it takes about half a day to recover.

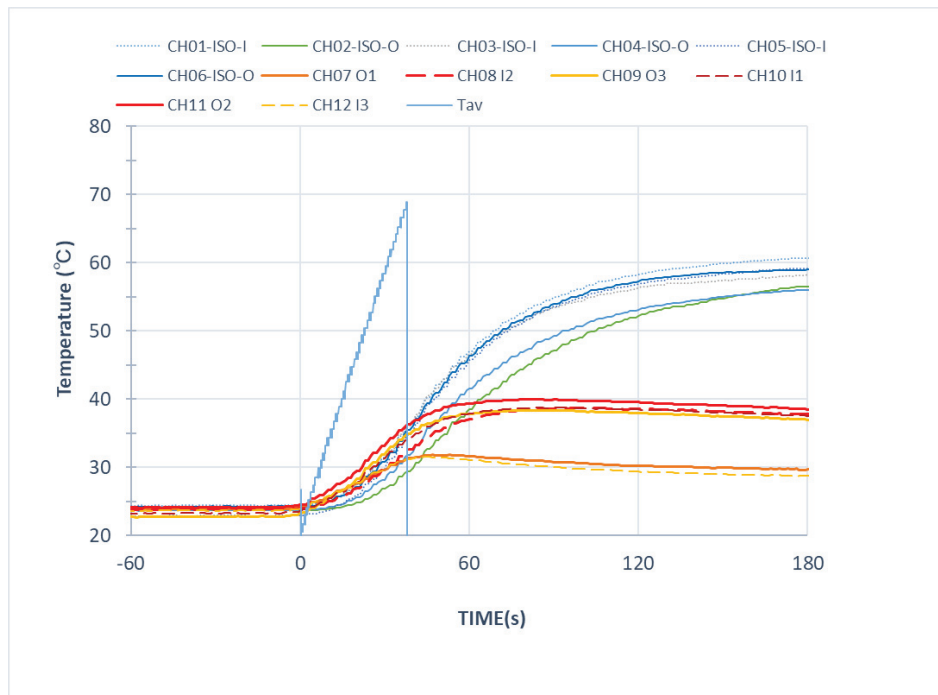


Fig. 5.4.14 Temperature rise curve of 1 kA/38 s without cooling water.

2) Heat run test result of 1 kA/38 s with cooling water

- Maximum temperature rise on the insulation surface is 35 °C. It shows that the temperature rise does not depend on the presence or absence of cooling water.
- The required cooling time greatly reduces for cooling water. It takes about 15 minutes to recover.

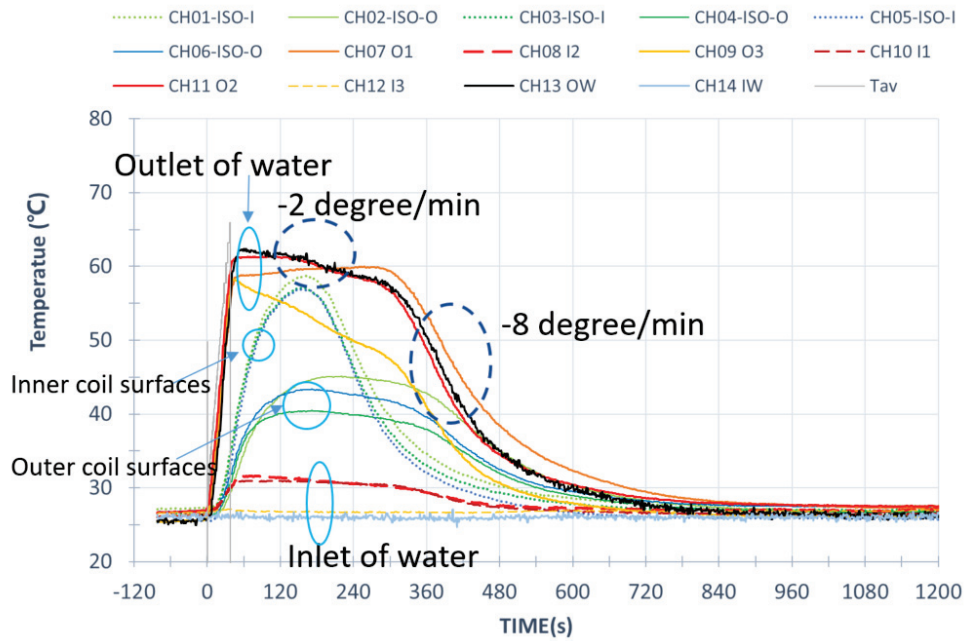


Fig. 5.4.15 Temperature rise curve of 1 kA/38 s with 3.9 L/min. cooling water.

3) Heat run test result of 500 A/120 s without cooling water

- Maximum of temperature rise on the insulation surface is 28 °C.
- It takes about 3 hours to recover.

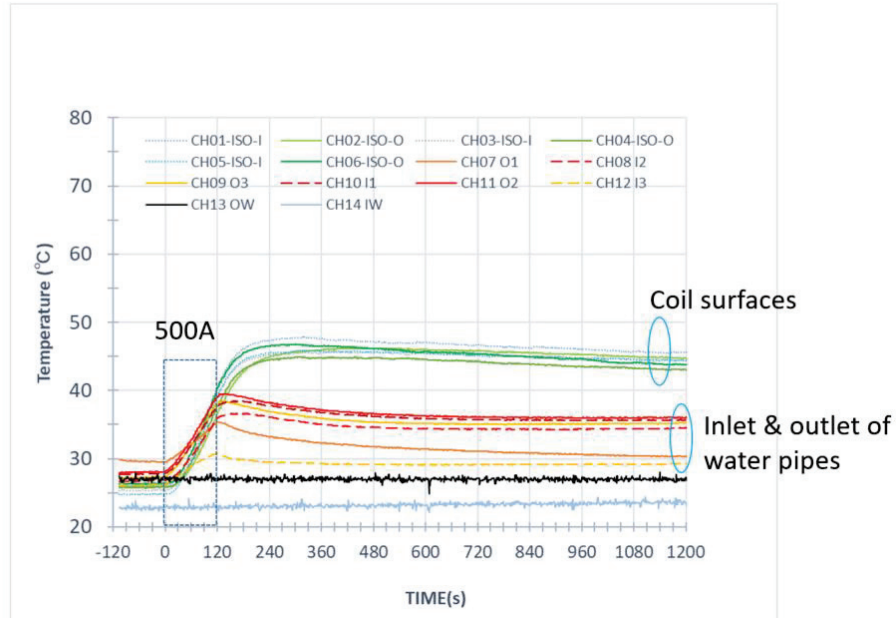


Fig. 5.4.16 Temperature rise curve of 500 A/120 s without cooling water.

4) Heat run test result of 500 A/120 s with cooling water

- Maximum of temperature rise on the insulation surface is 28 °C.
- It takes about 8 minutes to recover;
- The temperature continues to rise after 2 minutes of operation, and it is estimated that the allowable temperature will be reached in about 5 minutes. For continuous operation for 30 minutes or more for discharge cleaning, the cooling water should be increased to saturate at an appropriate temperature.
- It suggests that to improve the cooling effect, the pressure of the cooling water system in the real coil should be increased from 1 MPa to 2 MPa.

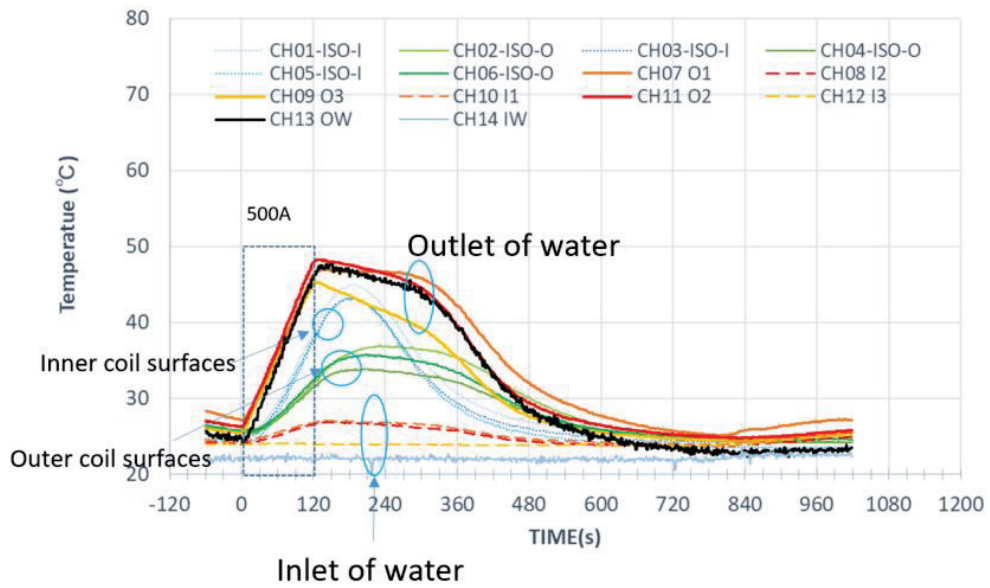


Fig. 5.4.17 Temperature rise curve of 1 kA/38 s with 4.2 L/min. cooling water.

5.4.5 High voltage test

To understand the insulation ability, a voltage higher than necessary was applied at the end of a series of tests, and it was confirmed that there was sufficient margin in insulation capacity.

1) Layer to layer isolation test with DC 10 kV

The ground test voltage to confirm the validity of this coil is DC 5.8 kV. If the same insulation performance can be ensured only by layer insulation, the ground insulation will be able to simplify more. To confirm that possibility, we planned a test in which a voltage of DC 10 kV was applied between adjacent conductors. Fig. 5.4.18 shows a picture of the test.

We cut series connection of 3 parallel conductor in the current lead area and apply DC 10 kV between each two conductors of 3 parallel. A high voltage DC generator (DHV-100 kV/5 mA) was used for the DC 10 kV test.

Three types of tests were carried out, and it was confirmed whether the leakage current at DC 10 kV was less than 17 μA (17 μA between the A and the B, 1 μA between the B and the C, or the A and the C).

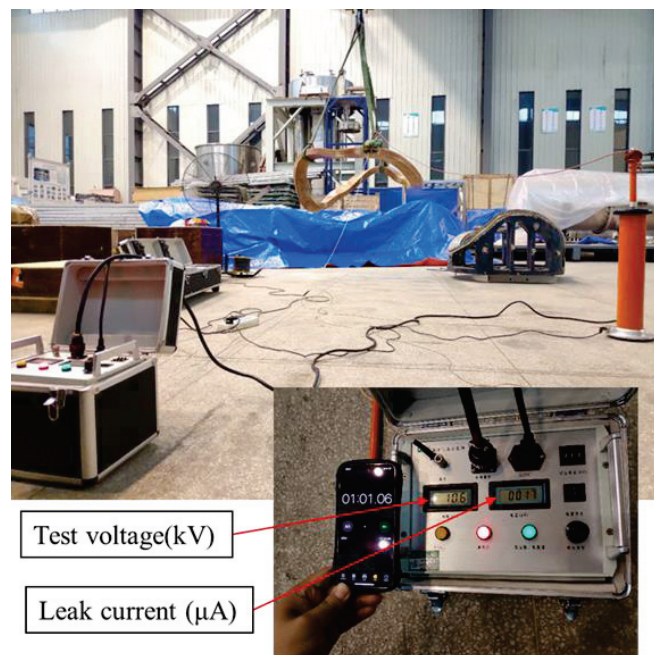


Fig. 5.4.18 Layer to layer isolation test with DC 10 kV.

2) Ground isolation test with DC 20 kV

If there is sufficient margin, it may be possible to simplify ground insulation. To confirm that possibility, we planned a test in which a voltage of DC 20 kV, which was 3.4 times the required test voltage, was applied between the conductor and the ground. The leakage current at DC 20 kV was not observed, and it was confirmed that there was sufficient margin in the ground insulation capacity.

5.4.6 Dimension measurement after heat run test

After heat run test, the dimension of the coil without restraint has been measured. The measurement result as follow:

- The deviation of the upper surface of the coil is -1.93~2.86 mm;
- The deviation of the outer surface of the coil is - 0.72~3.21 mm;
- The deviation of the inner surface of the coil is -3.26~0.69 mm.

Compare with the dimension measurement result after VPI, the coil deviation is very large. The reason is not clear, but it is said that it may be the effect of deformation due to removal from the winding frame or the measurement error.

In any case, it should be considered that there is a high possibility that a deviation of about ± 3 mm will occur. Since the standard tolerance of tolerance grades V (very coarse) or C (coarse) is several mm, the deviation of 3 mm is considered a reasonable value.

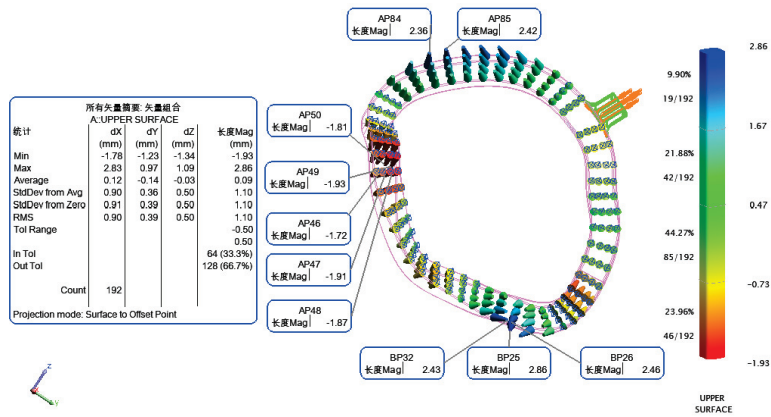


Fig. 5.4.19 The dimension measurement result of the upper surface.
(Without restraint after heat run test)

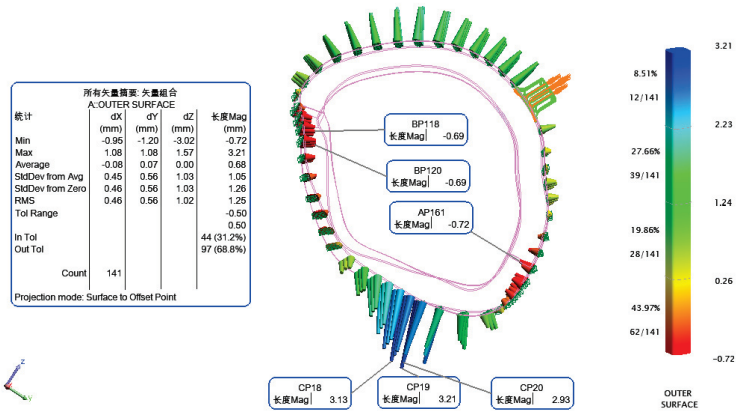


Fig. 5.4.20 The dimension measurement result of the outer surface.
(Without restraint after heat run test)

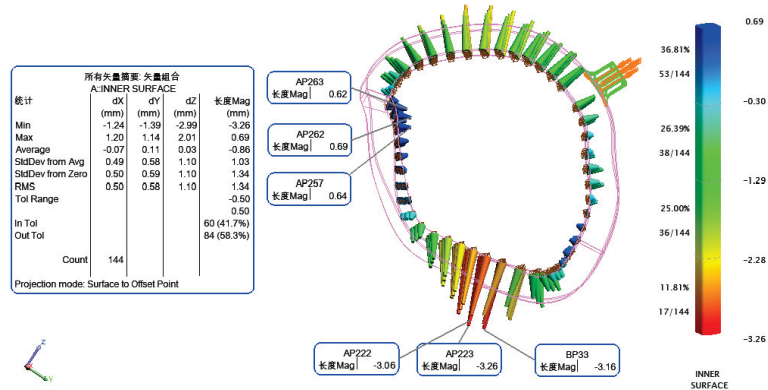


Fig. 5.4.21 The dimension measurement result of the inner surface.
(Without restraint after heat run test)

5.4.7 Summary of the MC4 mock up coil manufacture

- (a) The manufacture and test of the MC4 mockup coil have been finished.
- (b) The final dimension deviation of the mockup coil is about 3 mm.
- (c) The impulse test results show that the layer to layer insulation is qualified.
- (d) The heat run test shows that the characteristics of temperature changes are as expected theoretically.
- (e) When operating for a long time for discharge cleaning, it is better to increase the flow rate of cooling water in order to improve the cooling performance. For that purpose, it is necessary to increase the pressure of the cooling water device.
- (f) The withstand voltage of layer insulation is DC10 kV or more. Since it can withstand the operating voltage by itself, it is possible to simplify the ground insulation.
- (g) The withstand voltage of ground insulation is DC 20 kV or more. So, the ground insulation ability is enough and if can be simplified if necessary.

6 Plastic model developed by 3-D printer

Various reduced models were developed on the 3-D printer to validate the device fabrication and assembly procedures.



Fig. 5.4.1 Outermost magnetic surface of plasma.

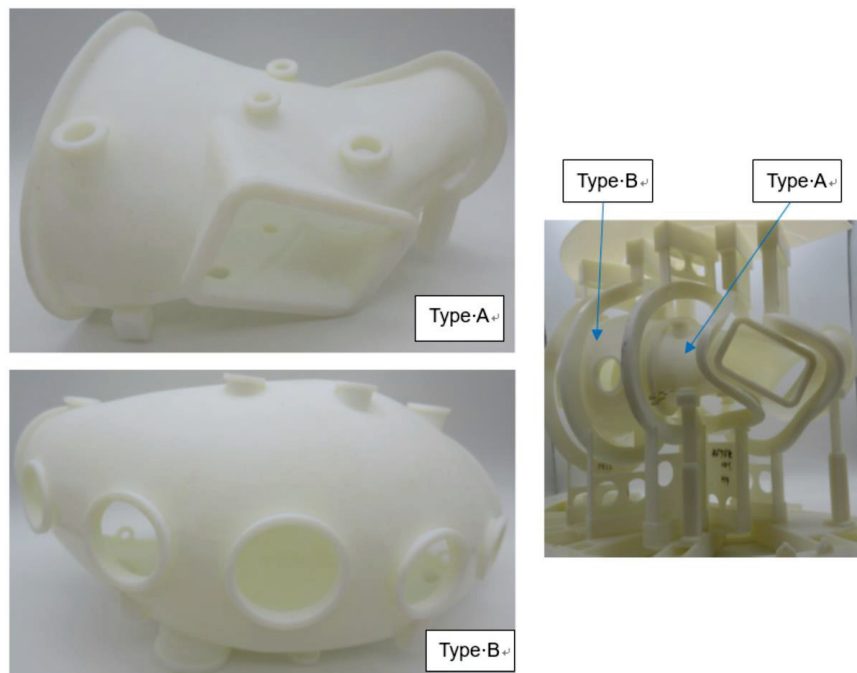


Fig. 5.4.2 Vacuum main vessel. (Preliminary; port size and position will be changed.)

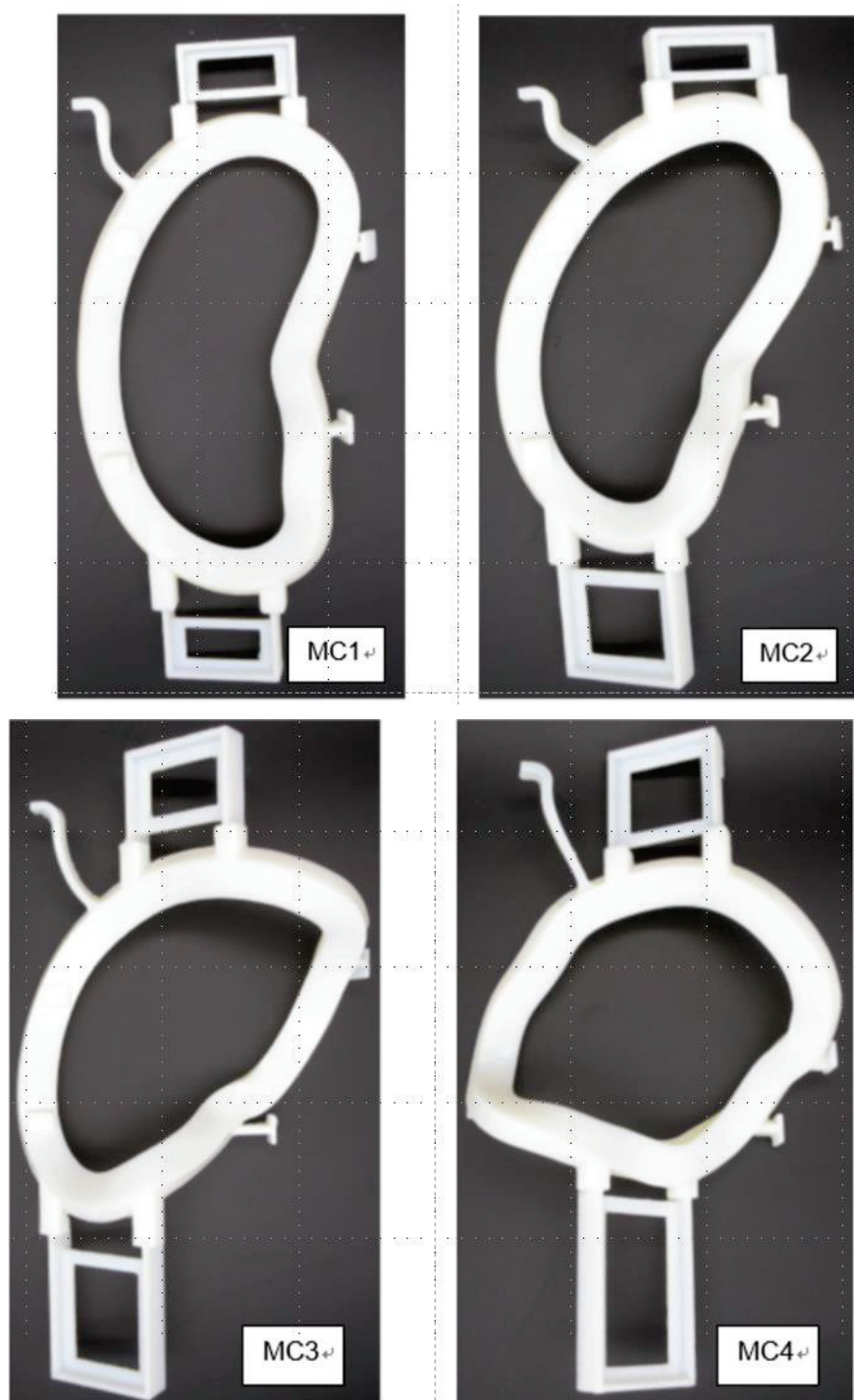


Fig. 5.4.3 Modular coil with case and support. (Latest at 2019/05/15).

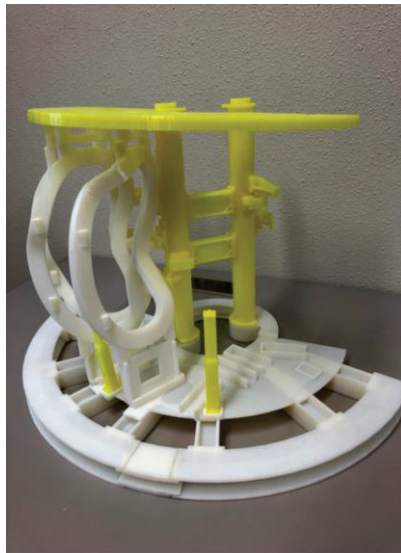


Fig. 5.4.4 Coil supports (Preliminary).

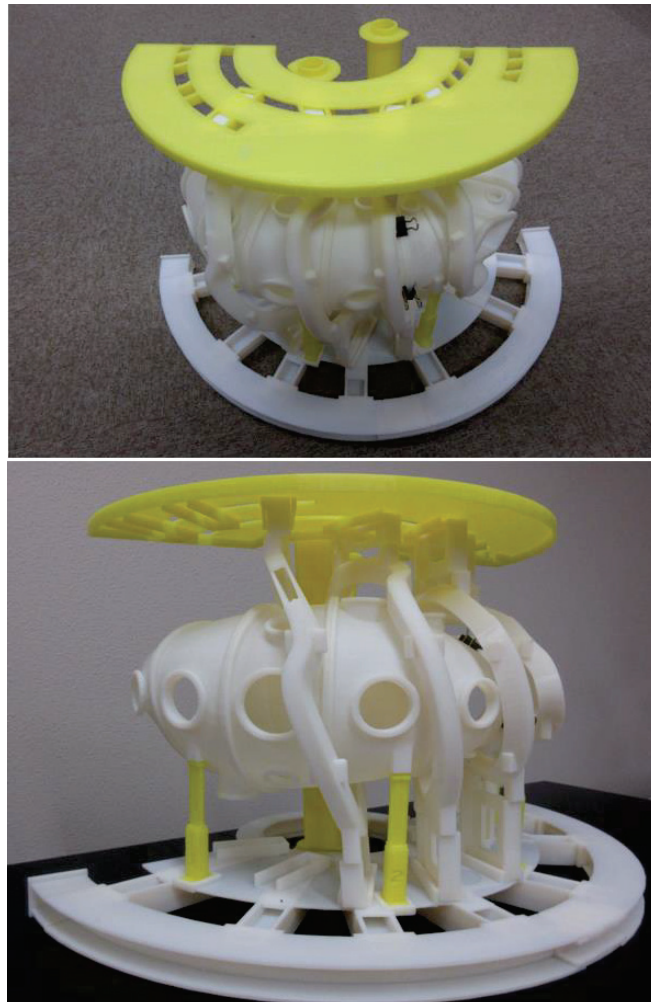


Fig. 5.4.5 Modular coils, vacuum vessel and coil supports (Preliminary).

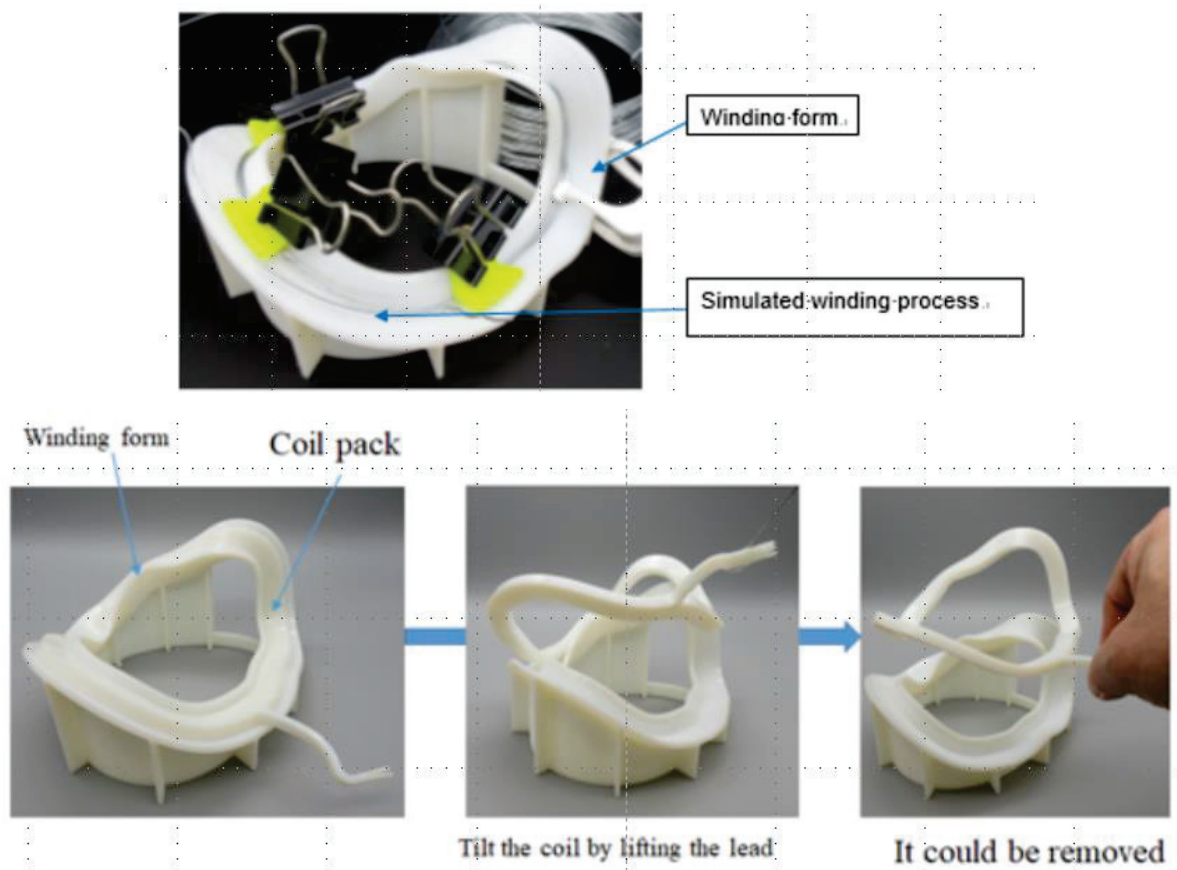
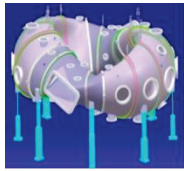

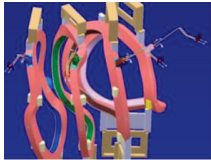
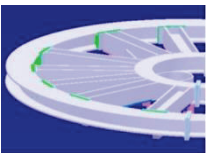
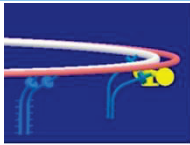
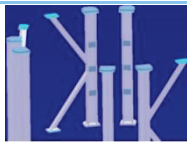
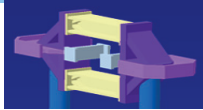





Fig. 5.4.6 Simulation of removing coil pack from winding frame for modular coil.

7 **Mass list of the CFQS main parts**

The mass list is shown in the table below to study transportation and crane work.

No	Product	Part	Mass(kg)	Quantity	Total(kg)	Picture
1	Vacuum vessel with TFC's and legs	Type A	420	2	2,250	
		Type B	705	2		
2	NBI port flange		49	2	98	
3	Modular coils	MC1	503	4	8,300	
		MC2	491	4		
		MC3	519	4		
		MC4	562	4		
4	Top and bottom frames with manifold	Top	4744	1	9,588	
		Bottom	4844	1		
5	Manifolds	Top	103	1	250	
		Bottom	147	1		
6	Pillars with diagonal beam	Pillar	313	8	5,186	
		beam	50	8		
		Leg out	201	8		
		Leg in	168	4		
7	Center support		180	1	180	
8	PFC	IV	130	2	1044	
		OV	392	2		
9	External current leads		405	1	405	
10	Beams between the M-coils		524	1	524	
11	Others (extra)		1655	1	2,175	
12	Sum				30,000	

8.1 Overall production flow

Fig. 8.1.1 shows overall production flow for the CFQS. Although it depends on the installation location and road conditions along the way, it is considered difficult to transport about 30 tons of CFQS all at once. After confirming the quality of individual parts at the factory, it is planned to disassemble and transport the individual parts and reassemble them on site.

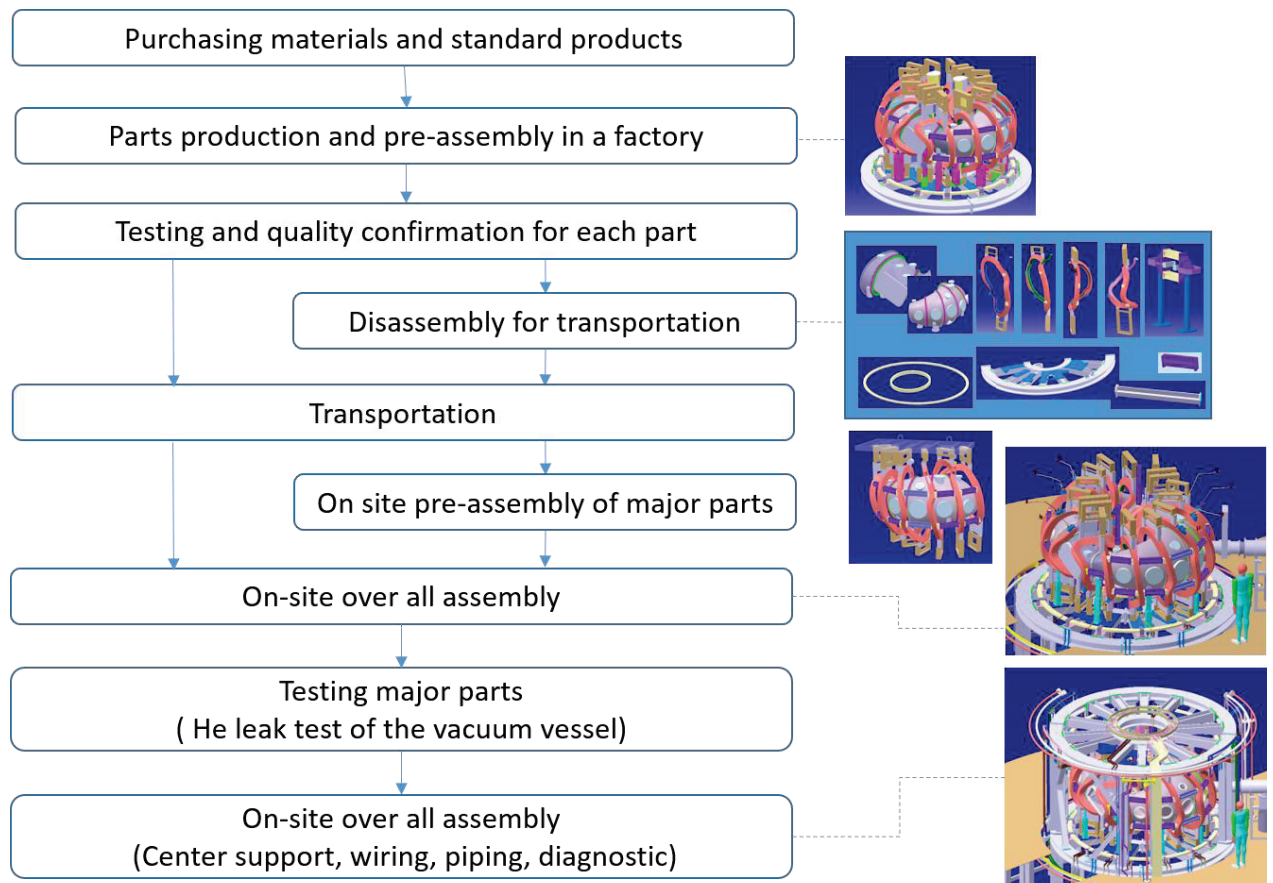


Fig. 8.1.1 Overall production flow.

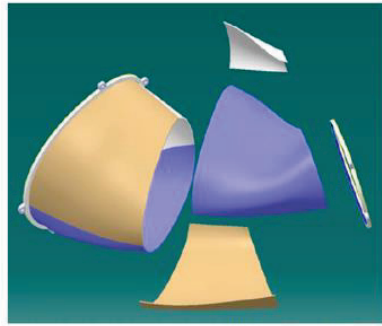
8.2 Production flow of vacuum vessel in a factory

We drew up a design plan to carry out manufacturing process of the vacuum vessel and conduct various equilibrium experiments. The important points are as follows.

- Minimizing field work for cost saving and reducing lead-time on site.
- Providing inspection process in the middle of the production and reducing the risk of backtracking work (all over again).
- Thinking about how to respond to problems and designing a structure that can be repaired or modified.
- Making it possible to utilize the space inside the vacuum vessel. It is difficult to access the vacuum vessel from the outside because a large number of parts, mainly coils, are installed nearby.
- Providing a large port for entering the inside of the vacuum vessel, and ensuring a workable cross-sectional area.
- If a defect will be found during on-site work, it will take a lot of time and cost to deal with it. To reduce the risk, we will assemble the main parts in a factory and make sure there will be no interferences or vacuum leaks. Since it is difficult to transport the entire vacuum vessel as a whole, we will disassemble and transport the individual parts and reassemble them on site.

Each section of vacuum vessel is manufactured by welding six plates bent with mould and two large flanges to prevent welding deformation as shown in Fig. 8.2.1. Fig. 8.2.2 shows an example of the bending press mold and the welding jig.

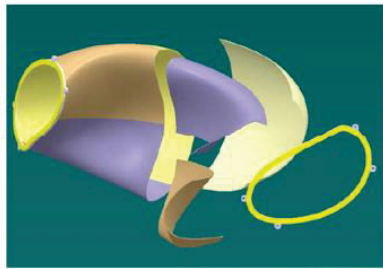
Fig. 8.2.3 and Fig. 8.2.4 show the procedure to product one section of the vacuum vessel and the pre-assembly process To minimize the work at the site, the manufacturing procedure is made to maximize the completion in the factory by making full use of press, welding, and machining. It is planned that the factory will check the validity of each part by a leak test and only weld between the sections will be done on site.



VC-divA-No-port.CATProduct

Type A

- Toroidal angle ; 67.5 degree
- Pieces
 - ✓ Three types of six plates bent with mold
 - ✓ One type of two flanges machined



VC-divB-No-port.CATProduct

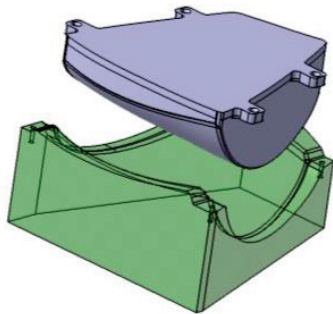
Type B

- Toroidal angle ; 112.5 degree
- Pieces
 - ✓ Three types of six plates bent with mold
 - ✓ One type of two flanges machined

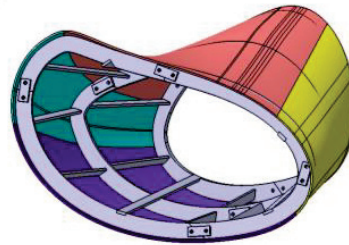
Fig. 8.2.1 Material pieces divided plan for vacuum vessel manufacturing.

It will be reviewed in the detailed design of the mockup.

(Eight pieces divided per one sector.)



(a) Mould for press working



(b) Jig to assemble the pressed plates for welding

Fig. 8.2.2 Example of mould and jig design for welding.

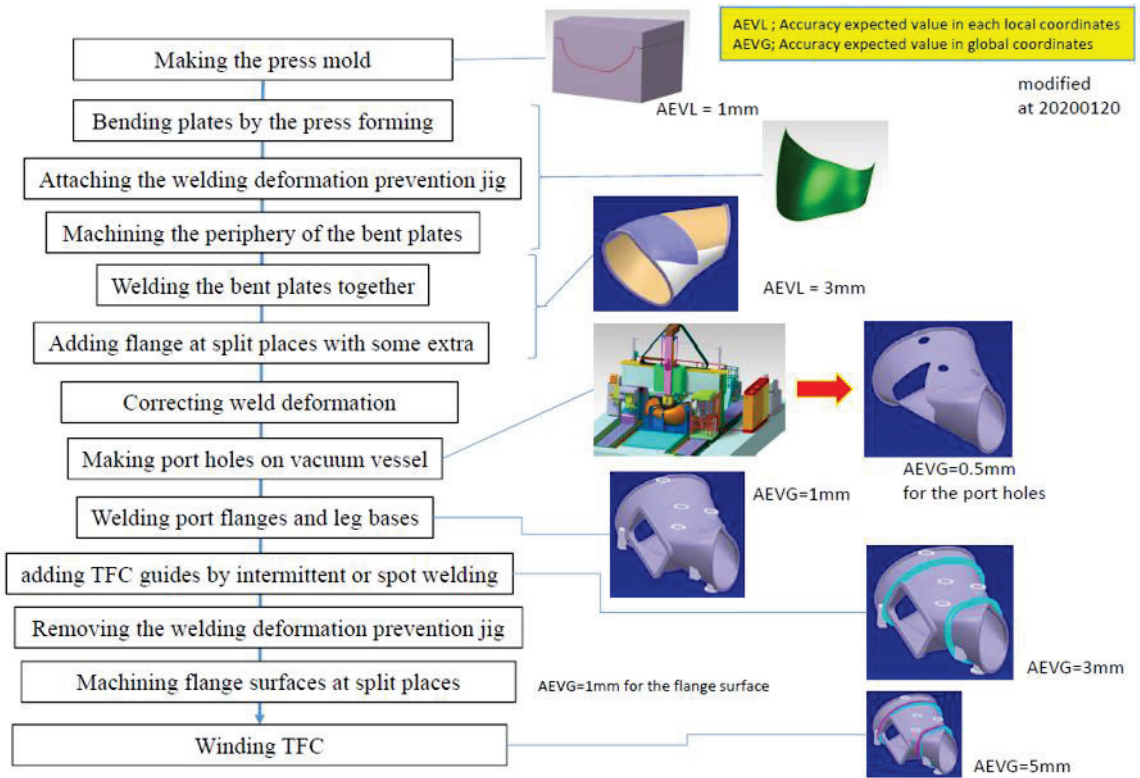


Fig. 8.2.3 Procedure to product one section of vacuum vessel.

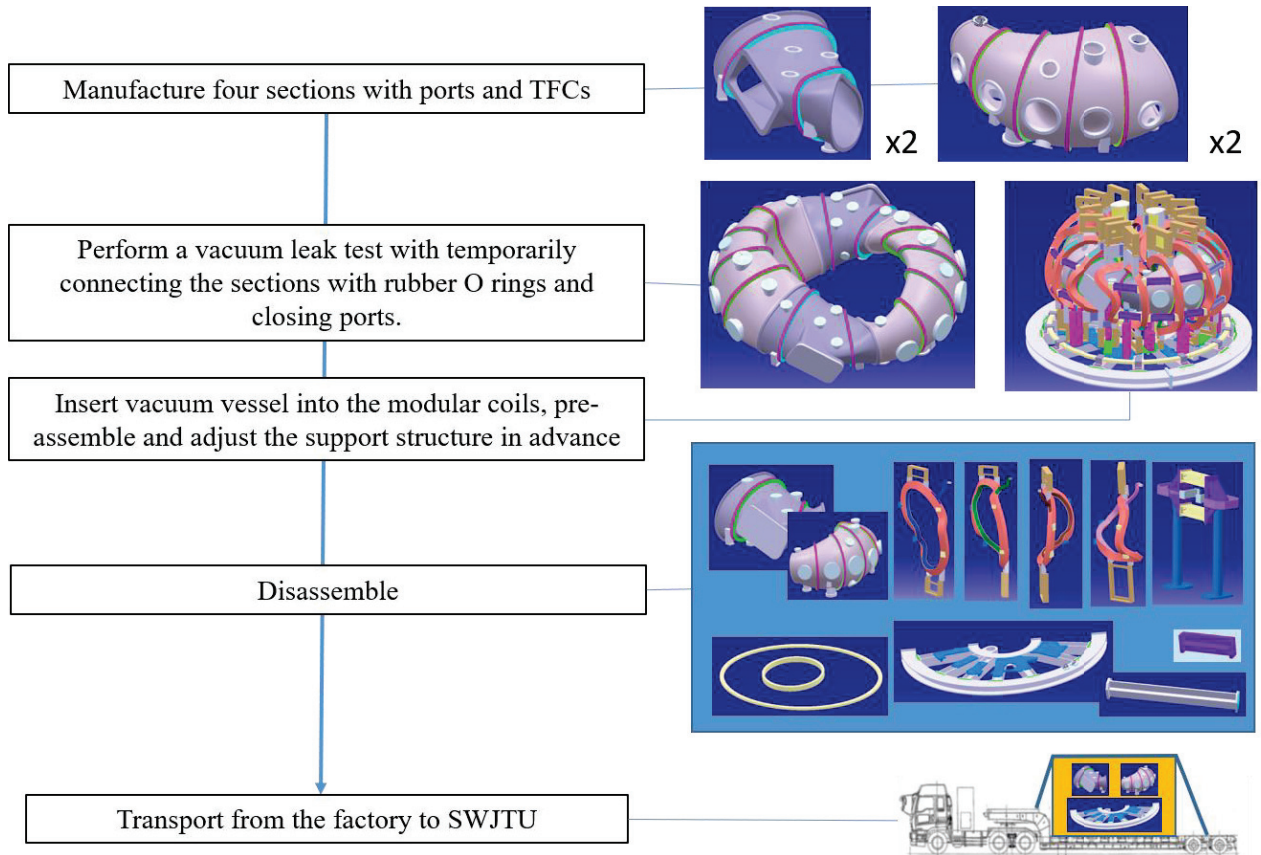


Fig. 8.2.4 Pre-assembly process of vacuum vessel in a factory.

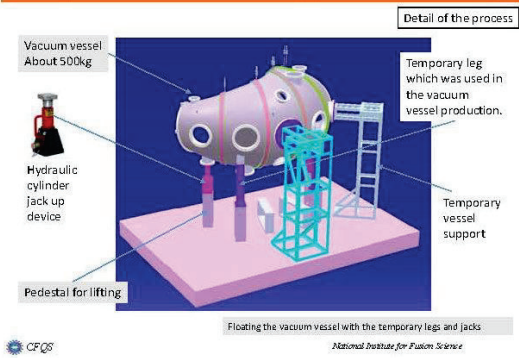
8.3 Pre-assembly procedure of modular coils and vacuum vessel on site

Before installing the modular coils and the vacuum vessel, it is necessary to pass the vacuum vessel through the coils. The work is planned to be done in a location different from the installation position in the same building. Although this work can be performed in the factory, it is difficult to safely carry the assembled parts together. Therefore, it is planned to transport each part and reassemble them on site after the defects in the temporary assembly are extracted in the factory. Since this pre-assembly work is complicated and delicate, confirmation of work steps and work training should be conducted in the factory.

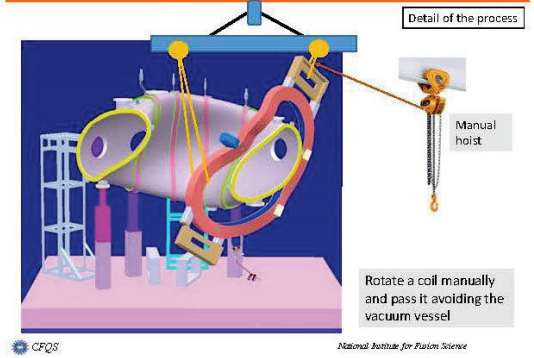
Fig. 8.3.1 shows the pre-assembly process of the modular coils and the vacuum vessel. In step 1, the vacuum vessel part is fixed with appropriate jigs on the workbench desirable to be composed of a surface plate which is a flat plate used as the main horizontal reference plane for precision inspection. The coil is inserted while rotating it in steps 2, 3, 4 and 5, but since the vacuum vessel has a complicated twisted shape, delicate adjustment work is required to move the coil. It is possible to develop a special transport machine for that work, but to reduce costs, it is also possible to work with an overhead crane and the manual hoist as shown in the figure. Since it is necessary to frequently attach and detach the legs of the vacuum vessel to pass the coil, a jig such as a hydraulic jack will be prepared to facilitate the work. In step 6, the whole is fixed to the upper temporary base and suspended by an overhead crane.

It is considered that the vacuum vessel and the coils can be suspended integrally by assembling in such a procedure. Steps 7 and 8 show a state in which two types of vacuum vessels and coils are suspended.

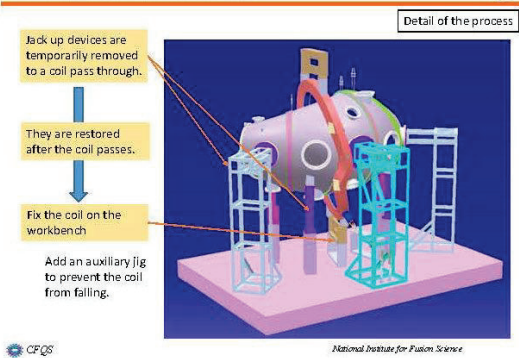
1. Prepare the vacuum vessel of the type B



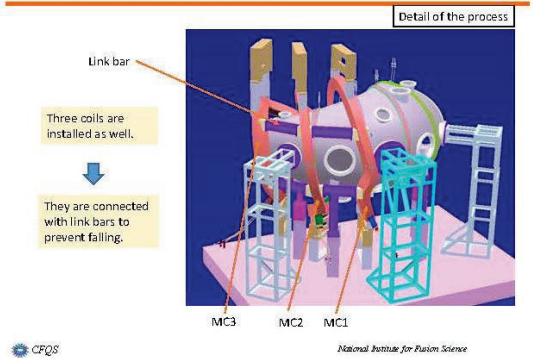
2. Rotate a coil and pass it around the vacuum vessel



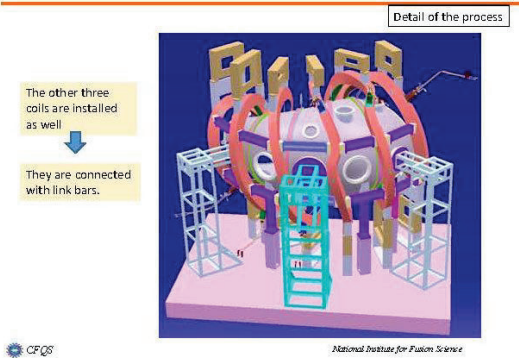
3. Fix a coil on the workbench



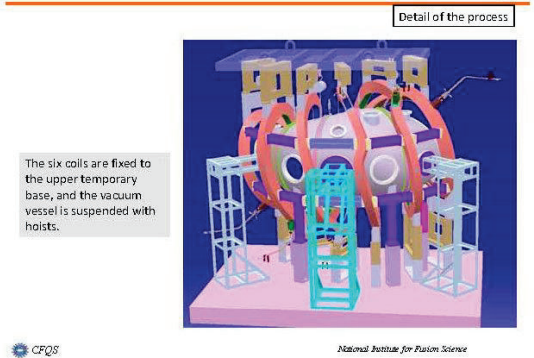
4. Fix three coils on the workbench



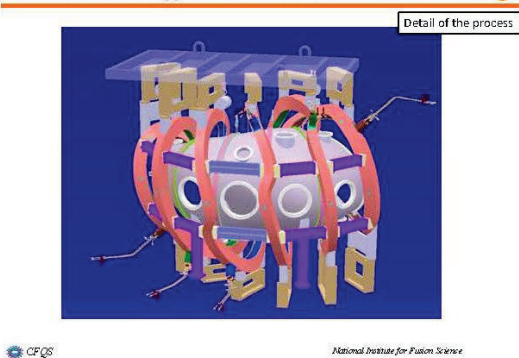
5. Install and fix six coils on the workbench



6. Lift the vacuum vessel and the coils



7. The unit of the type-B vessel with six coils



8. The unit of the type-A vessel with two coils

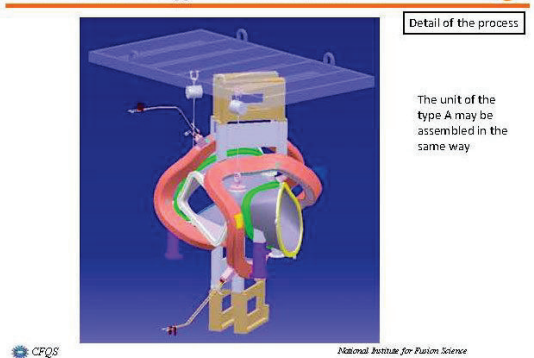


Fig. 8.3.1 Pre-assembly process of modular coils and vacuum vessel on sit.

8.4 Overall assembly procedure on site

Fig. 8.4.1 and Fig. 8.4.2 show detail of overall assembly flow on site.

Steps 1 to 6 are procedures for assembling the reference stand on which the devices are installed. In these steps, the entire support legs, the bottom frame with the PFC's and the intermediate stages as a workbench are installed. Here, since the upper surface of the base pedestal (BP) in the step 4 serves as a basis for device installation, it is necessary to strictly control the position of the reference point (defined on the surface by design). Therefore, measure the positions of the main points with a laser tracker, *etc.*, and if the error from the design value is large, correct it. If the error in the vertical direction is large, the upper surface of the BP is processed, or a spacer is sandwiched between the BP and the bottom frame (SHIM adjustment). If the horizontal displacement is large, remark the reference point (datum target) with the global coordinates.

In the steps 7 to 9, the four pre-assembly parts of the vacuum and the modular coil are installed, and the four sections of vacuum vessel are welded together. Here, the coils and the vacuum vessels are still temporarily fixed. This is because the vacuum vessel may be thermally deformed during the welding operation. Also, when a defect such as a vacuum leak is found in the next step, it is necessary to move the coil a little to perform the repair work, so these fixing works will be performed in later steps.

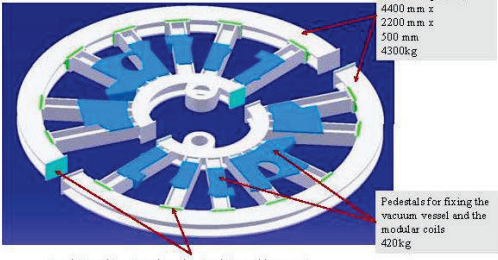
A leak test is performed in step 10 to finally confirm the validity of the vacuum vessel assembly procedure. In the subsequent steps 11 and 12, the support legs are replaced, and the position is adjusted, and the vacuum vessels and the coils are finally fixed. For the location adjustment, the laser tracker, and the distance measurement from the reference points on the BP (datum target) are performed. The most important in position adjustment is the center of gravity of the modular coil, and its accuracy is targeted to be less than 1 mm. The installation angle of the coil in the toroidal direction is also important, and the target is an accuracy of 1 degree. The vacuum port flange is also important, but it is difficult to adjust it to the design position. Therefore, the side surface of the flange is marked so that the actual position of the design reference can be known.

In the steps 13, 14 and 15, the remaining many parts are installed in sequence. In these steps, the top frame, the upper PFC's, the center supports, the outer pillars, the water piping, the various measurement wiring, the power cables, the power busbars, and others are installed.

1. Assemble bottom and top frames

Detail of the process

This picture shows the bottom frame assembly process. The top frame is also assembled in the same way.



Frames with the insulation plates ;
4400 mm x
2200 mm x
500 mm
4300kg

Pedestals for fixing the
vacuum vessel and the
modular coils
420kg

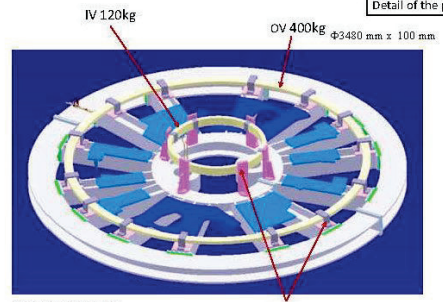
Insulation plates to reduce the circulating eddy current



National Institute for Fusion Science

2. Install PFC's on the frame

Detail of the process



IV 120kg

OV 400kg ϕ 3480 mm x 100 mm

Total about 5,000kg

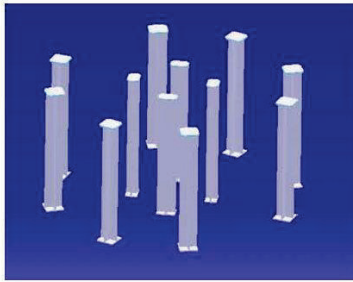
PFC supports



National Institute for Fusion Science

3. Install entire support legs on the floor

Detail of the process



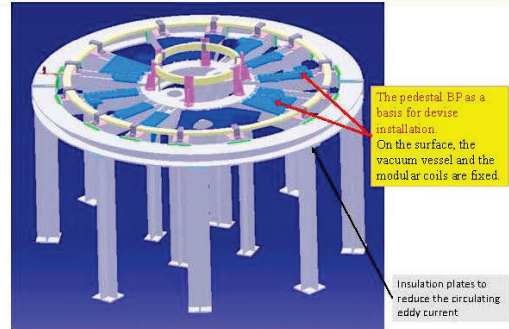
Entire support legs
• Approximately 2.1m
in height
• Quantity 12
• Fix to the foundation
plate embedded in
the floor with bolts
• About 200kg per
piece



National Institute for Fusion Science

4. Install the bottom frame

Detail of the process



The pedestal BP as a
basis for devise
installation
On the surface, the
vacuum vessel and the
modular coils are fixed

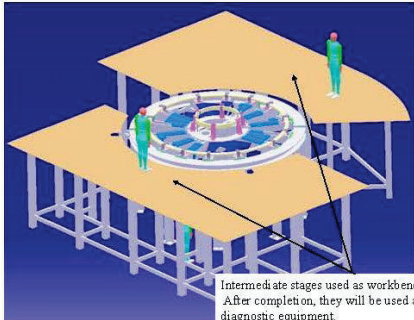
Insulation plates to
reduce the circulating
eddy current



National Institute for Fusion Science

5. Install the intermediate stages

Detail of the process



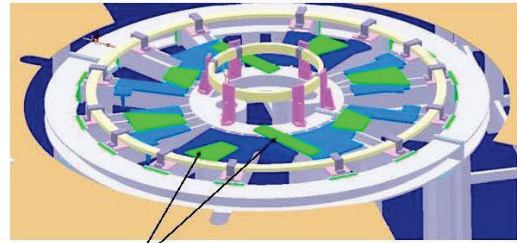
Intermediate stages used as workbench.
After completion, they will be used as a base for
diagnostic equipment.



National Institute for Fusion Science

6. Cover the opening

Detail of the process



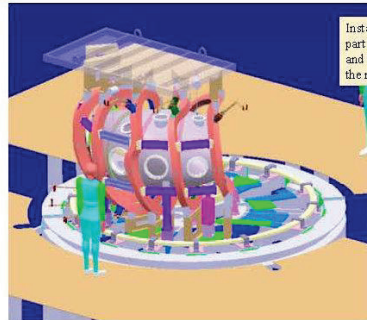
Covers to prevent workers from falling.
They will be also used as the vacuum vessel
fixing base during temporary installation.



National Institute for Fusion Science

7. Install a pre-assembly part

Detail of the process



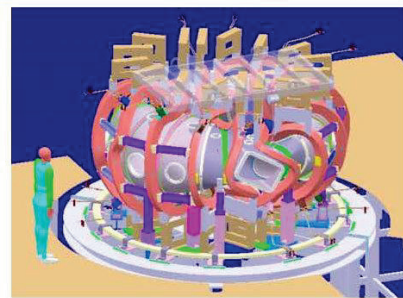
Install one pre-assembly
part with the modular coils
and the vacuum vessel on
the reference pedestal BP



National Institute for Fusion Science

8. Install other three pre-assembly parts

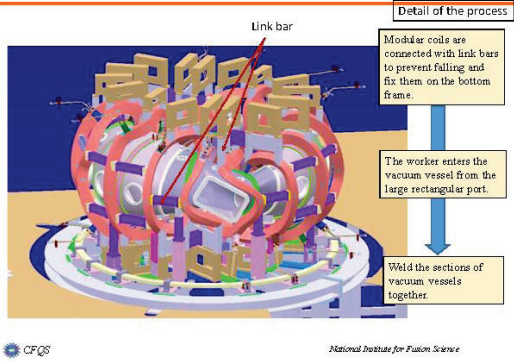
Detail of the process



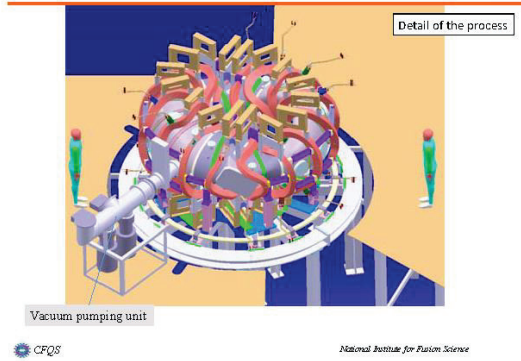
National Institute for Fusion Science

Fig. 8.4.1 Detail of assembly flow on site (1/2).

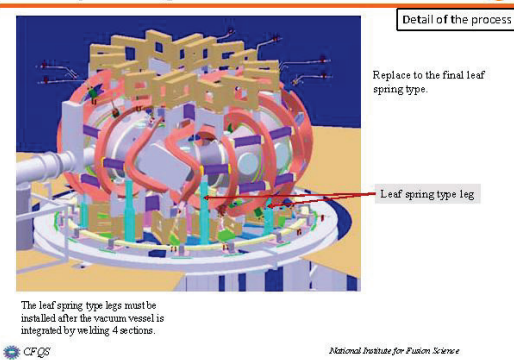
9. Temporary fix the modular coils and the vacuum vessel



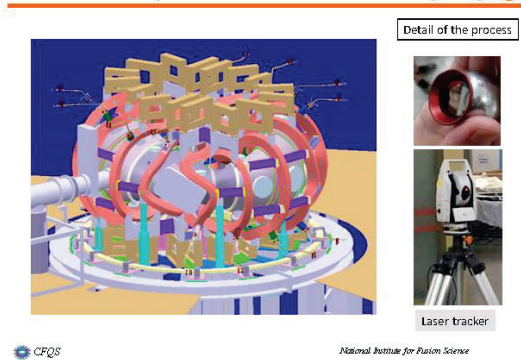
10. Leak test confirms the integrity of the vacuum vessel



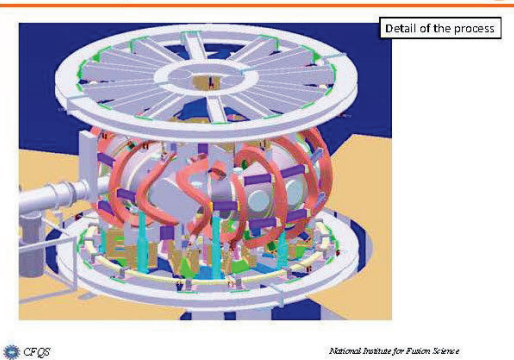
11. Replace the legs for the vacuum vessel



12. Measure the position of the coil and fix it after adjusting



13 Install a top frame and PFC's



14. Install center support



15 Install outer pillars and others

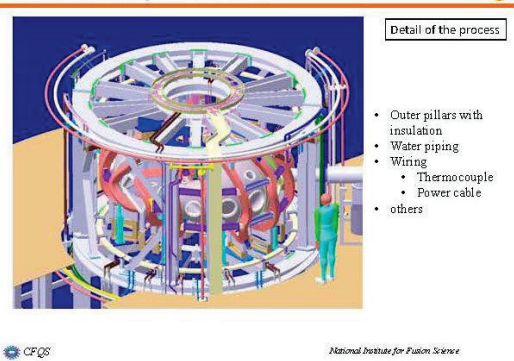


Fig. 8.4.2 Detail of assembly flow on site (2/2).

NIFS-SWJTU JOINT PROJECT FOR CFQS
~PHYSICS AND ENGINEERING DESIGN~

VER. 3.1
2020. NOV.

APPENDIX-B

~RELATED GENERAL INFORMATION~

DESIGN STANDARDS AND INFORMATION OF CHS
USED AS A REFERENCE IN THE CFQS DESIGN
(INFORMATION MAY NOT BE AFFECTED BY THE CFQS DESIGN)



NIFS; National Institute for Fusion Science

SWJTU; Institute of Fusion Science, School of Physical Science and Technology Southwest Jiaotong University

Hefei Keye; Hefei Keye Electrical Physical Equipment Manufacturing Co., Ltd.

TABLE OF CONTENTS

1	General.....	3
1.1	ASME III criterion as a reference.....	3
1.2	Physical property of austenite stainless steel (SUS).....	4
1.3	Physical property of pure copper.....	5
1.4	Motor generator for fusion device.....	8
2	Standard parts	9
2.1	O-ring for vacuum	9
2.2	SUS pipe and flange	10
2.3	Electrical cable	11
2.4	Solderless terminal	12
2.5	Flexible terminal (Standard type).....	13
3	CHS	14
3.1	Layout of torus hall for the CHS	14
3.2	Power system for the CHS	16
3.3	Vacuum pumping system for the CHS	18
3.4	NBI system for the CHS.....	22
3.5	ECRH system for the CHS.....	27
3.6	Power supply to bake vacuum vessel for the CHS.....	31
3.7	Cooling water system for the CHS.....	32
4	Analytical expression.....	34
4.1	Formula of adiabatic temperature rise	34
4.2	Formula to combine two wires	35

1 General

1.1 ASME III criterion as a reference

ASME III defines the following criterion to get allowable limit value of stress. It may be evaluated by the following procedure because it is difficult to distinguish stress components by the FEM calculation.

- $P_m + P_L + P_b + Q < 3 S_m$, absolute requirement everywhere.
- $P_m < S_m$, should be satisfied in major area.
- $P_m + P_b < 1.5 S_m$, local or thermal stress is permitted
- $P_m + P_b > 1.5 S_m$, may be permitted in extremely limited area

Here, S_m is a design stress strength obtained by the material properties and P_m, P_L, P_b, Q are stress components obtained by the stress analysis as a von Mises stress. Here technical terms are defined below.

- S_m is a design stress strength that is a reference intensity allowed to load by setting is given as the efficient design. It is obtained from the equation $S_m = \min (2/3 \sigma_y, 1/3 \sigma_u)$, where σ_y is a proof stress or offset yield strength that is a stress changing from elastic deformation to permanent deformation. σ_u is a tensile strength that is a maximum tensile stress appearing in the material before breaking.
- P_m is a primary general membrane stress that is an average value of stress in a cross section. Discontinuities and stress concentration are excluded.
- P_L is a primary local membrane stress that is an average value of stress by discontinuities.
- P_b is a primary bending stress that is a stress component proportional to the distance from the centroid in a cross section. Discontinuities and stress concentration are excluded.
- Q is a secondary stress (bending and membrane stress) that is a self-equilibrium stress generated in discontinuity of structure.

1.2 Physical property of austenite stainless steel (SUS)

There are slight differences in mechanical properties due to differences in composition. We should choose them according to our purpose.

The SUS 304 is the most distributed and inexpensive. However, as the permeability may increase, caution is required for nuclear fusion. It turns into magnetic material by bending or rolling. It is better not to use it in a magnetic field. We are worried about distorting the magnetic field profile.

The SUS316 and the SUS316L is more stable than the SUS304. The SUS316L is SUS316 with low carbon and has slightly better cold workability and corrosion resistance but it is a little expensive and a little weaker.

Table 1.2.1 Characteristics of typical SUS materials.

	SUS304(JIS G 4303)	SUS316(JIS G 4305)	SUS316L (JIS G 4305)
Material composition	Cr 18-20 % Ni 8-10.5 % Mn less than 2 % C less than 0.08 %	Cr 16-18 % Ni 10-14 % Mo 2-3 % Mn less than 2 % C less than 0.08 %	Cr 16-18 % Ni 12-15 % Mo 2-3 % Mn less than 2 % C less than 0.03 %
Mechanical properties at room temperature (MPa)	$\sigma_y = 205$ $\sigma_u = 520$ $S_m = 129$	$\sigma_y = 205$ $\sigma_u = 520$ $S_m = 129$	$\sigma_y = 175$ $\sigma_u = 480$ $S_m = 114$
Magnetic permeability	$\mu = 1.004 \sim 1.1$ or more	$\mu = 1.004$	$\mu = 1.004$

1.3 Physical property of pure copper

The temperature characteristics of pure copper are important. Particularly in coil design, it is necessary to consider the change in resistivity, so for convenience, an approximate expression is given here.

Table 1.3.1 Physical property of pure copper.

Temperature [K]	Electric resistivity [Ωm]	Specific heat [J/kg K]	Density [kg/m^3]
10	4.00E-10		
80	1.60E-09		
100	3.00E-09		
150	6.50E-09	322	8,990
250	1.25E-08	376	8,950
300	1.55E-08	386	8,880
600	3.55E-08	425	8,780

Ref. JSME Data Book : Heat Transfer 4th Edition, I. Hirata, Journal of the Cryogenic Society of Japan (1970)

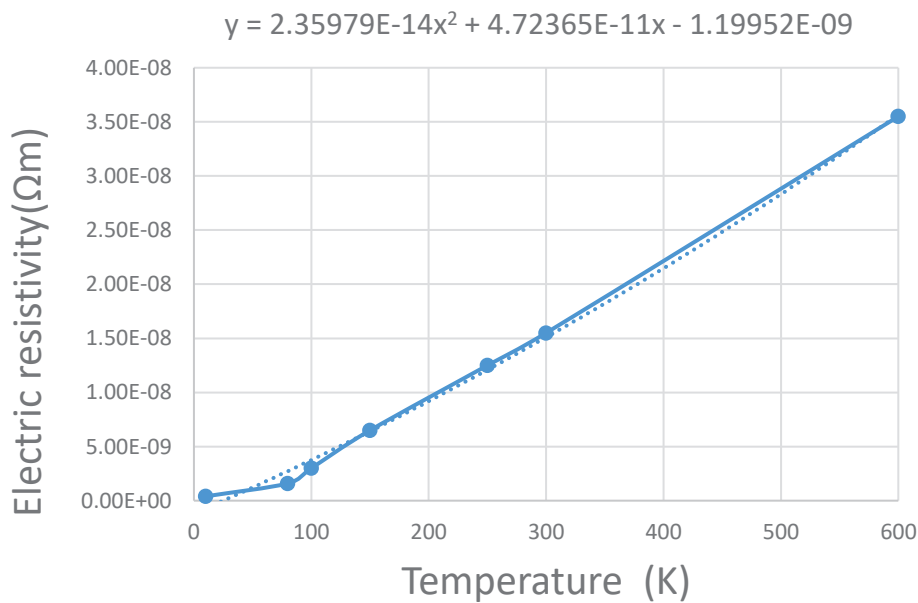


Fig. 1.3.1 Temperature characteristics of electrical resistivity by a quadratic function approximation.

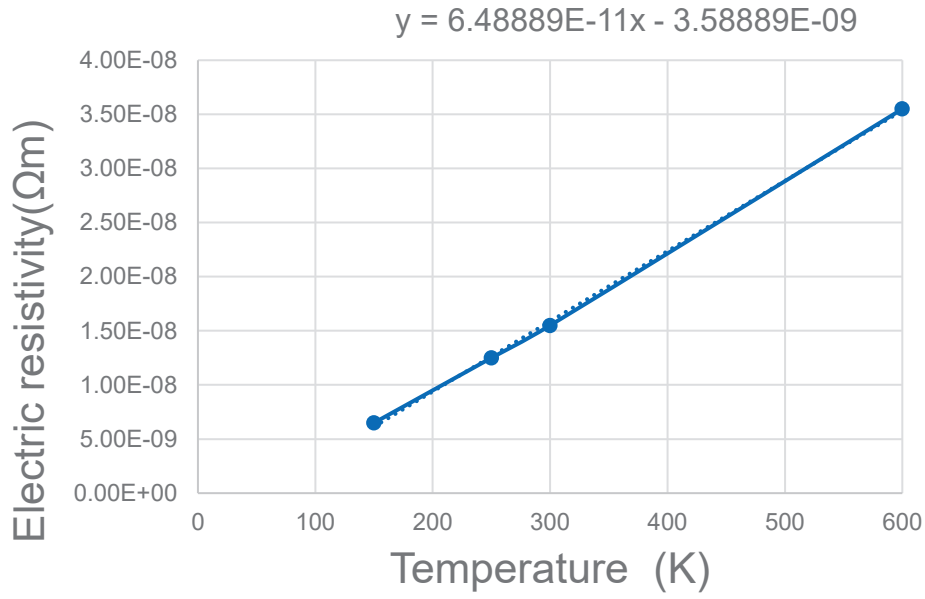


Fig. 1.3.2 Temperature characteristics of electrical resistivity by a Linear function approximation.

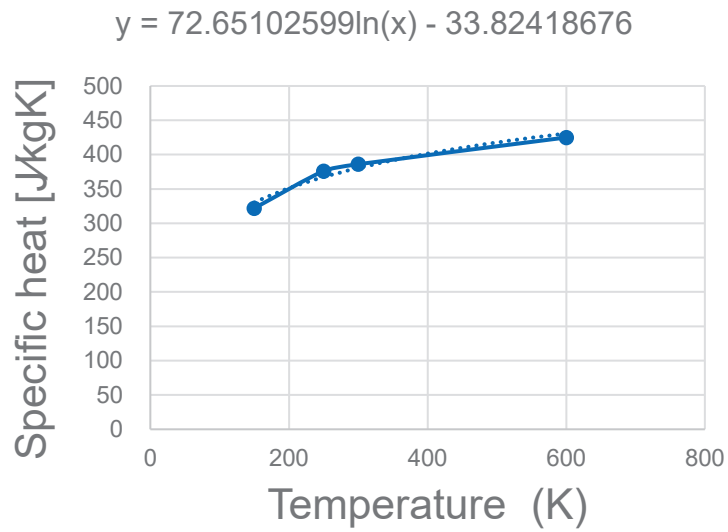


Fig. 1.3.3 Temperature characteristics of specific heat.

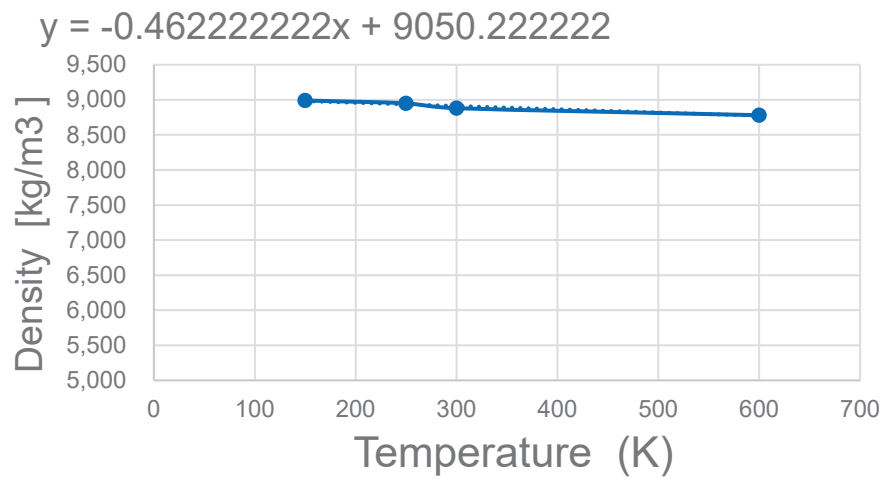


Fig. 1.3.4 Temperature characteristics of density.

1.4 Motor generator for fusion device

An energy storage device is required for the CFQS. For reference, the table below shows the capabilities of motor generators used in other equipment.

Table 1.4.1 Motor generator for fusion device.

No	Fusion device	Generator		Drive	
		Capacity	Spec	Capacity	Spec
1	TRIAM-1M Kyushu University	125 MVA 60 MJ	3Φ VSYG 6.6 kV 11 kA 67-59 Hz 670-590 rpm	1.4 MW	3Φ IM
2	Heliotron-J Kyoto University	330 MVA 300 MJ	3Φ VSYG 18 kV 10.58 kA 65-50 Hz 650-500 rpm	3.2 MW	3Φ IM
3	JT-60 HMG QST	400 MVA 2.5 GJ	3Φ VSYG 18 kV 12.83 kA 77.6-54.2 Hz 582-406 rpm	15 MW	3Φ IM
4	JT-60 PMG QST	500 MVA 1.3 GJ	3Φ VSYG 18 kV 16 kA 77.6-54.2 Hz 582-406 rpm	7 MW	3Φ IM
5	JT-60 TMG QST	215 MVA 4 GJ	3Φ VSYG 18 kV 6.9 kA 80-56 Hz 600-420 rpm	19 MW	Inverter drive
6	Gamma 10 University of Tsukuba	250 MVA 800 MJ	3Φ VSYG 18 kV 8 kA 77.6-54.3 Hz 582-407 rpm	2.4 MW	3Φ IM
7	LHD and CHS NIFS	250 MVA 1.4 GJ	3Φ VSYG 18 kV 8 kA 93-58 Hz 701-435 rmp	8.5 MW	3Φ IM
8	HL-2A SWIP, Chengdu (CHS Nagoya University)	125 MVA 200 MJ	3Φ HSYG 3 kV 24 kA 120-96 Hz 3600 rpm	2.5 MW	3Φ IM
9	HL-2A SWIP, Chengdu	300 MVA 1.35 GJ	6Φ VSYG 3 kV 29 kA 100-67 Hz 500-335 rpm	8.5 MW	3Φ IM
10	HL-2A SWIP, Chengdu	90 MVA 250 MJ	3Φ HSYS 1650-1488 rpm	2.5 MW	3Φ IM
11	HSX University of Wisconsin - Madison	84 MVA 42 MWp Over 20 MJ	DCM 30 motors 1.68kV 50kA		DCM
12	PLATO Kyushu University	810 kW _{-peak} 2.8 MJ (stored) 384 kJ (release)	3Φ SIM 2 motors 60 Hz-3600 rpm	72 kW	Inverter drive
*	CFQS NSJP	50 MW _{-peak} 35 MJ (released) 55 MJ (stored)			

$$MVA = kV \times kA \times \sqrt{3}$$

Capacity of the above equipment is excessive for the CFQS.

VSYG; Vertical synchronous generator HSYG; Horizontal synchronous generator
DCM; DC generator and motor SIM; Self-excited induction generator and motor
IM; Induction motor

2 Standard parts

2.1 O-ring for vacuum

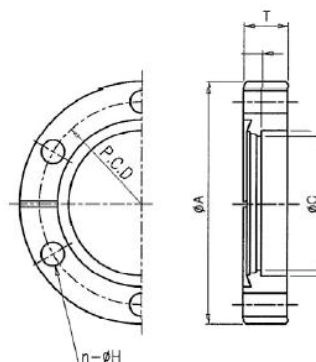
Depending on the operating temperature, it is necessary to select the material of O ring properly. Operating temperature is as follows.

- Nitrile rubber (NBR); -50 ~ 80°C. unusable at baking temperature 100 ~ 150 °C.
 - Fluorine rubber (FKM, Viton); -15 ~ 200 °C. may be usable, but worry about low temperature damage due to liquid nitrogen or cryogenic gas that is sometimes used for evacuation.
 - Metal O-ring; -250 ~ 650 °C. can be used at wide range of temperature. See attached URL and the table.
- ▶ http://www.mitsubishi-cable.co.jp/en/products/group/seal/semicon_e.html
 - ▶ http://www.mitsubishi-cable.co.jp/ja/products/group/seal/pdf/61_metal_o-ring.pdf
 - ▶ http://www.seals.de/downloads/Metall_Ringe_GB.pdf
 - ▶ https://www.canon-anelva.co.jp/english/products/component/catalog/pdf/catalog_vol_2_en.pdf

Table 2.1.1 ConFlat Fixed flanges.

Name	A	C	T	ΦH	N	PCD	bolt	pipe
ICF34	34	16	7.5	4.5	6	27	M4×20L	Φ19.1×Φ16.7
ICF70	70	38.5	12.7	6.7	6	58.9	M6×35L	Φ41×Φ38
ICF114	114	61	17.5	8.4	8	92.2	M8×45L	Φ63.5×Φ60.2
ICF152	152	97	20	8.4	16	130.3	M8×50L	Φ101.6×Φ95.6
ICF203	203	148.5	22	8.4	20	181.1	M8×55L	Φ153×Φ147
ICF253	253	198.5	25	8.4	24	231.9	M8×60L	Φ203×Φ197
ICF305	305	250	28	8.4	32	284	M8×70L	Φ250×Φ244
ICF356	356	295	28.5	10.5	30	325.4	M10×70L	Φ295×Φ289
ICF406	406	350	28.5	10.5	30	381	M10×70L	Φ350×Φ344

ConFlat is a registered trademark of Varian Co.



2.2 SUS pipe and flange

Table 2.2.1 SUS pipe and flange.

ND		SUS PIPE								W FLANGE (20K)			
		OD (mm)	Thickness (mm)						JIS	OD (mm)	Thick ness (mm)	JIS	
A	B		SCH 5s	SCH 10s	SCH 20s	SCH 40	SCH 80	SCH 120					SCH 160
6	1/8	10.5	1.0	1.2	1.5	1.7	2.4			G 34 59 TP			B 22 20
8	1/4	13.8	1.2	1.65	2.0	2.2	3						
10	3/8	17.3	1.2	1.65	2.0	2.3	3.2				90	14	
15	1/2	21.7	1.65	2.1	2.5	2.8	3.7		4.7		95	14	
20	3/4	27.2	1.65	2.1	2.5	2.9	3.9		5.5		100	16	
25	1	34.0	1.65	2.8	3.0	3.4	4.5		6.4		125	16	
32	1-1/4	42.7	1.65	2.8	3.0	3.6	4.9		6.4		135	18	
40	1-1/2	48.6	1.65	2.8	3.0	3.7	5.1		7.1		140	18	
50	2	60.5	1.65	2.8	3.5	3.9	5.5		8.7		155	18	
65	2-1/2	76.3	2.1	3.0	3.5	5.2	7.0		9.5		175	20	
80	3	89.1	2.1	3.0	4.0	5.5	7.6		11.0		185	22	
90	3-1/2	101.6	2.1	3.0	4.0	5.7	8.1		12.7		195	24	
100	4	114.3	2.1	3.0	4.0	6.0	8.6	11.1	13.5		210	24	
125	5	139.8	2.8	3.4	5.0	6.6	9.5	12.7	15.9		250	26	
150	6	165.2	2.8	3.4	5.0	7.1	11.0	14.3	18.2		280	28	
200	8	216.3	2.8	4.0	6.5	8.2	12.7	18.2	23.0		330	30	
250	10	267.4	3.4	4.0	6.5	9.3	15.1	21.4	28.6	400	34		
300	12	318.5	4.0	4.5	6.5	10.3	17.4	25.4	33.3	445	36		
350	14	355.6	4.0	5.0	8.0	11.1				G 34 68 TPY	490	40	
400	16	406.4	4.5	5.0	8.0	12.7					560	46	
450	18	457.2	4.5	5.0	8.0	14.3					620	48	
500	20	508.0	5.0	5.5	9.5	15.1					675	50	

ND; Nominal Diameter,

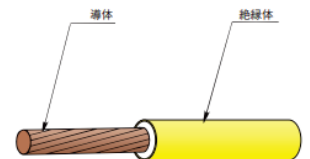
OD; Outer Diameter

Unless otherwise specified, the CFQS will use SCH20 piping for cooling water system and SCH5s piping for vacuum system.

2.3 Electrical cable

Table 2.3.1 Electrical cable.

Type	Twist	Nominal cross section	Finish outer diameter	Conductor outer diameter	Allowable current	Density	Test voltage	Number of strands	Strand diameter
		mm ²	mm	mm	A	A/mm ²	V		mm
600 V IV cable HIV cable	Single wire	0.79	2.6	1	16	20.37	1500		
		1.13	2.8	1.2	19	16.80	1500		
		2.01	3.2	1.6	27	13.43	1500		
		3.14	3.6	2	35	11.14	1500		
		5.31	4.6	2.6	48	9.04	1500		
		8.04	5.6	3.2	62	7.71	1500		
		12.57	6.8	4	81	6.45	2000		
		19.63	8.2	5	107	5.45	2000		
	Stranded wire	0.9	2.8	1.2	17	18.89	1500	7	0.4
		1.25	3	1.35	19	15.20	1500	7	0.45
		2	3.4	1.8	27	13.50	1500	7	0.6
		3.5	4.1	2.4	37	10.57	1500	7	0.8
		5.5	5	3	49	8.91	1500	7	1
		8	6	3.6	61	7.63	1500	7	1.2
		14	7.6	4.8	88	6.29	2000	7	1.6
		22	9.2	6	115	5.23	2000	7	2
		38	11.5	7.8	162	4.26	2500	7	2.6
		60	14	10	217	3.62	2500	19	2
		100	17	13	298	2.98	2500	19	2.6
150	21	16.1	395	2.63	3000	37	2.3		
200	23	18.2	469	2.35	3000	37	2.6		
600 V CV cable	Stranded wire	5.5	8	3	58	10.55	1500	7	1
		8	8.6	3.6	72	9.00	1500	7	1.2
		14	9.5	4.4	100	7.14	2000	Circular compression stranded	
		22	11	5.5	130	5.91	2000		
		38	13	7.3	190	5.00	2500		
		60	16	9.3	255	4.25	2500		
		100	19	12	355	3.55	2500		
		150	23	14.7	455	3.03	3000		
200	26	17	545	2.73	3000				
3300V CV cable	Stranded wire	8	13	3.4	78	9.75	9000		
		14	14	4.4	105	7.50	9000		
		22	15	5.5	140	6.36	9000		
		38	17	7.3	195	5.13	9000		
		60	21	9.3	260	4.33	9000		
		100	23	12	355	3.55	9000		
		150	26	14.7	455	3.03	9000		
200	30	17	540	2.70	9000				



Type	Explanation	Operating temperature
IV	Wire insulate by Vinyl	Less than 60 °C
HIV	Heat-proof wire Insulate by Vinyl	Less than 75 °C
CV	Cross-linked polyethylene insulated Vinyl sheathed	Less than 90 °C

2.4 Solderless terminal

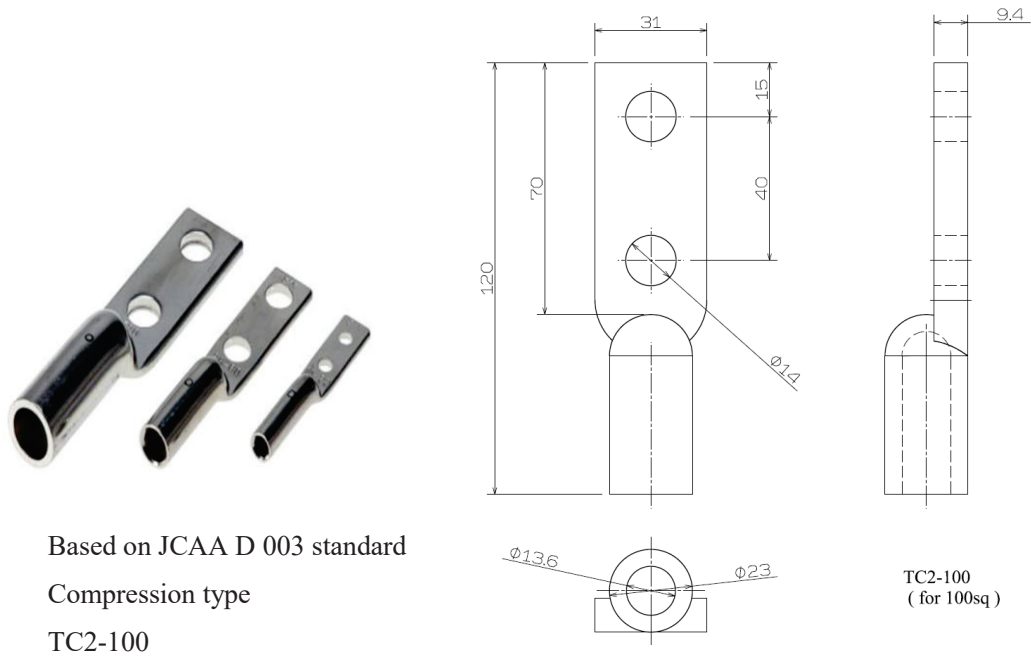


Fig. 2.4.1 Compression type solderless terminal TC2-100 for wire 100SQ.

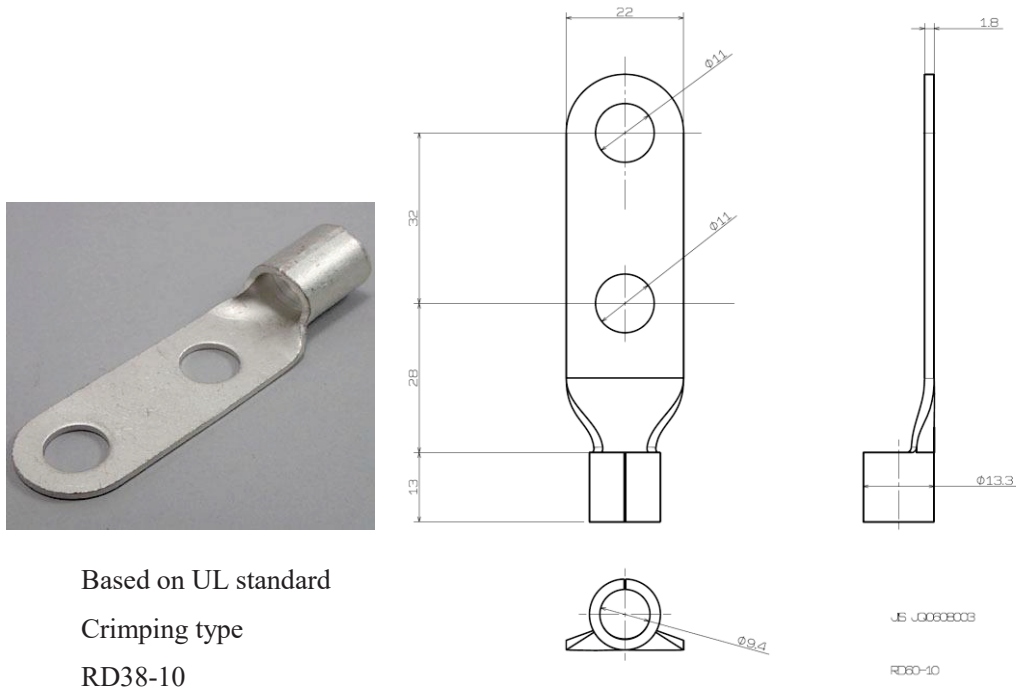


Fig. 2.4.2 Crimping type solderless terminal RD38-10 for wire 38SQ.

2.5 Flexible terminal (Standard type)

Many types are on the market for the purpose of absorbing the amount of displacement due to thermal expansion and contraction, absorbing the vibration generated by electrical equipment, and improving workability during assembly. For convenience, representative dimensions of flexible terminals which are likely to be applicable in the CFQS design are shown as an example.

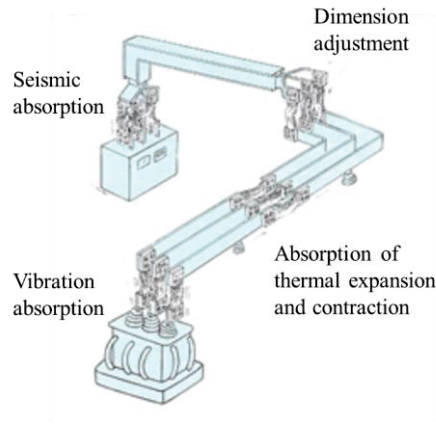


Fig. 2.5.1 Application example of flexible terminal.

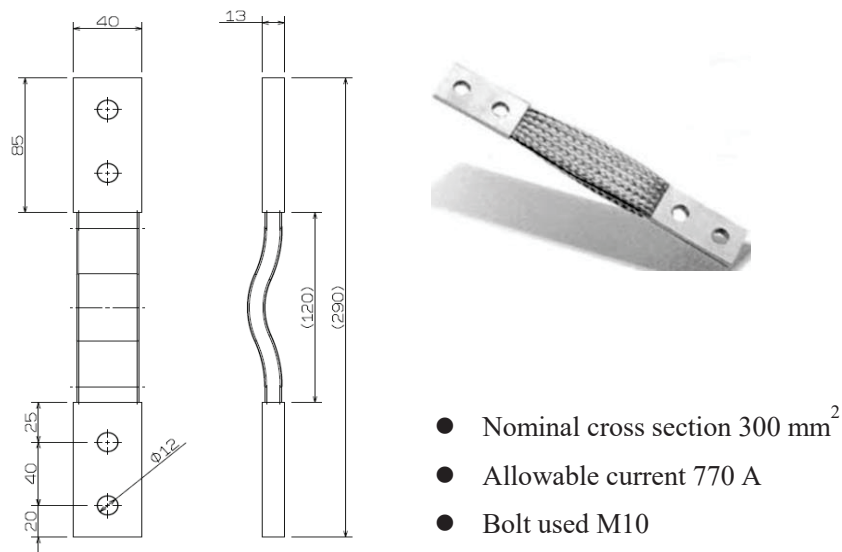


Fig. 2.5.2 Example of a standard type flexible terminal.

3 CHS

3.1 Layout of torus hall for the CHS

The CFQS laboratory will be designed with reference to the structure of the development and experiment building with the CHS installed in NIFS. For reference, the layout of the CHS laboratory is shown below.



Fig. 3.1.1 Body of the CHS (installed in Nagoya University at 1987).

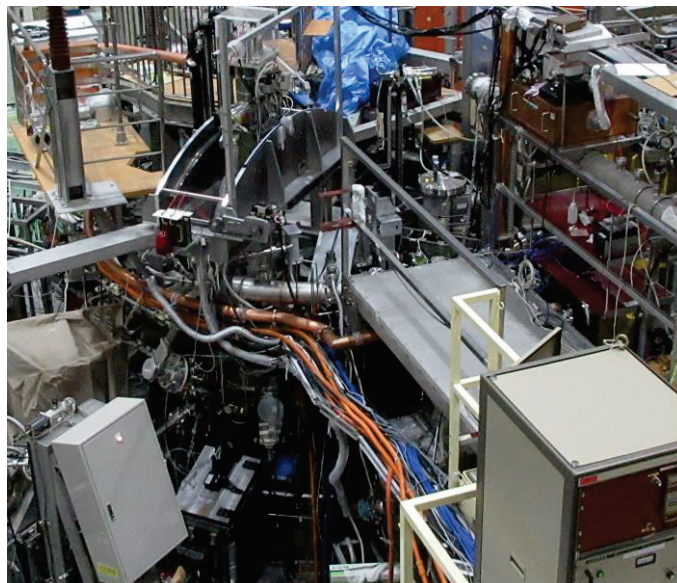


Fig. 3.1.2 Body and equipment's of the CHS (installed in NIFS).

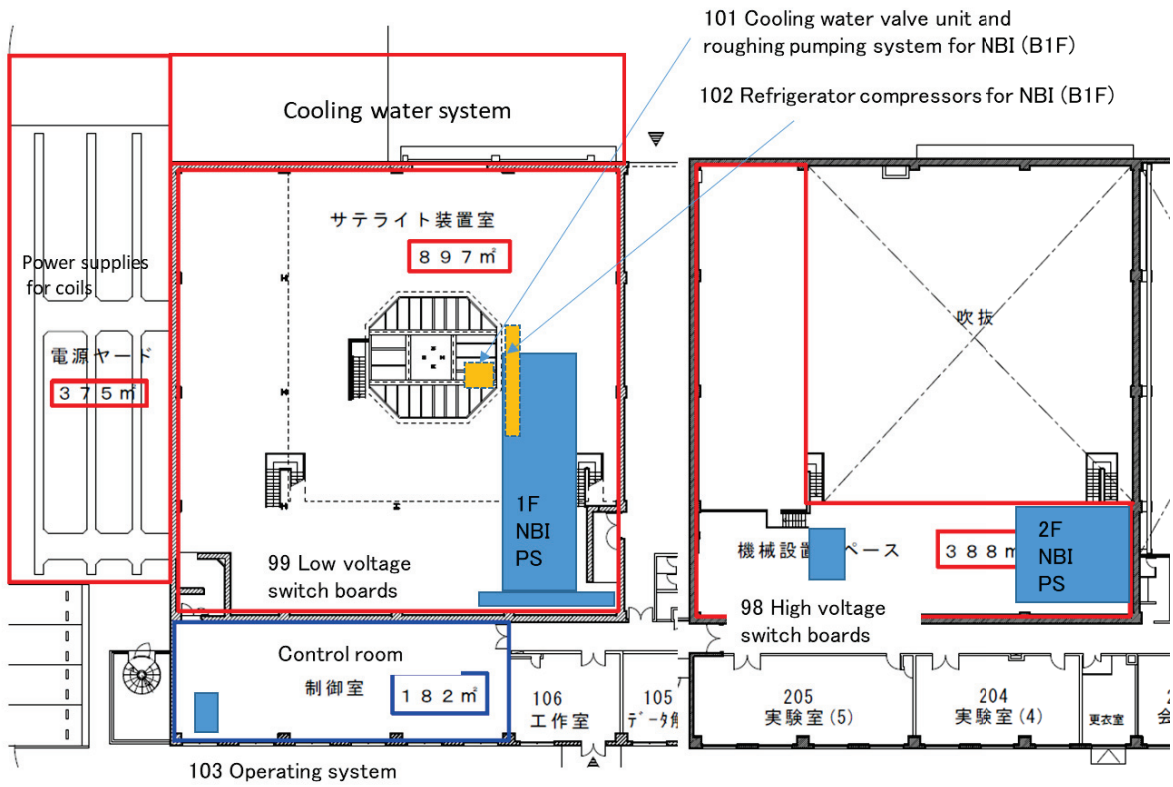


Fig. 3.1.3 Layout of torus hall for the CHS with the NBI system.

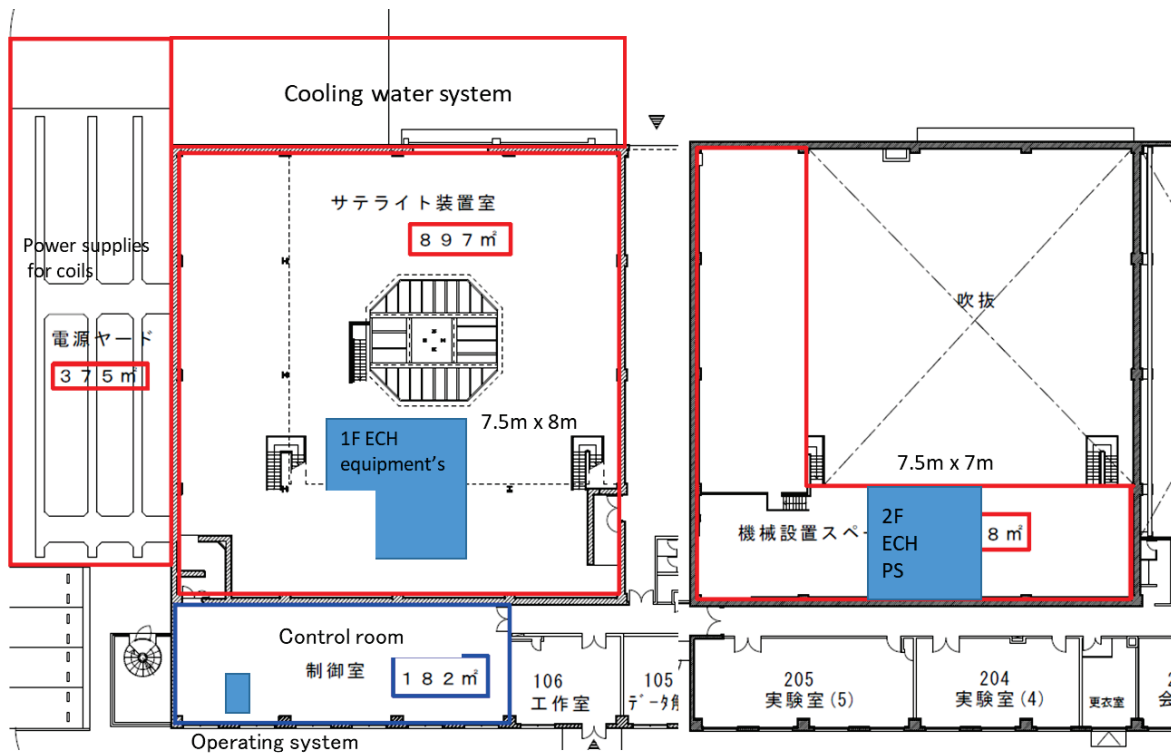


Fig. 3.1.4 Layout of torus hall for the CHS with the ECRH system.

3.2 Power system for the CHS

It should be noted that the commercial voltage is different in Japan and China as shown in Table 3.2.1. To transfer the CHS equipment to CFQS, transformers will be needed to adjust for voltage differences. Table 3.2.2 and Fig. 3.2.1 shows a list of low-voltage power board related to main equipment relocating from the CHS to the CFQS. It is necessary to prepare a power board to supply these voltages with the CFQS. Fig. 3.2.1 shows the one-line diagram of the CHS power supply system.

Table 3.2.1 Difference of power environment.

	Frequency	High voltage	Low voltage 1Φ	Low voltage 3Φ
NIFS	60 (West Japan)	6.6 kV	100 V	200 V
China	50	10 kV	220 V	380 V

Table 3.2.2 Load list of low voltage power board.

No	V	Sys	Use	Load	No	V	Sys	Use	Load
Row 1					Row 3				
u1	200 V	ECRH	Charger	24	L6	200 V	NBI-2	DCL CB	8
u4	200 V	NBI-2	GTO PS	8	Row 4				
u5	100 V	ECRH	1Φ SWB	12	L1	200 V	NBI-2	SB Gas	8
R1	100 V	NBI-2	AVP CB	1.6	R1	200 V	NBI-2	REFCR	8
R2	100 V	NBI-2	BLA CB	1.6	L2	200 V	NBI-2	REFCR	8
R3	100 V	NBI-2	TCB	1.6	R2	200 V	NBI-2	REFCR	8
L9	100 V	ECRH	CTRL	1.6	L3	200 V	NBI-2	REFCR	8
R9	100 V	ECRH	LN2	0.8	R3	200 V	NBI-2	REFCR	8
Row 2					L4	200 V	NBI-2	REFCR	8
R1	200 V	NBI-2	DCL	16	R4	200 V	NBI-2	REFCR	8
R2	200 V	NBI-2	GTO LV	16	L5	200 V	NBI-2	REFCR	8
R3	200 V	NBI-2	BMAG	16	R5	200 V	NBI-2	AVP	8
R4	200 V	NBI-2	AVP	4.8	Row 5				
R5	200 V	NBI-2	SCR CB	4.8	L5	200 V	ECRH	COOL OIL	5.28
					b1	200 V	ECRH	3Φ SWB	35.2

Board name; KIT-1A-13. The unit of load is kVA.

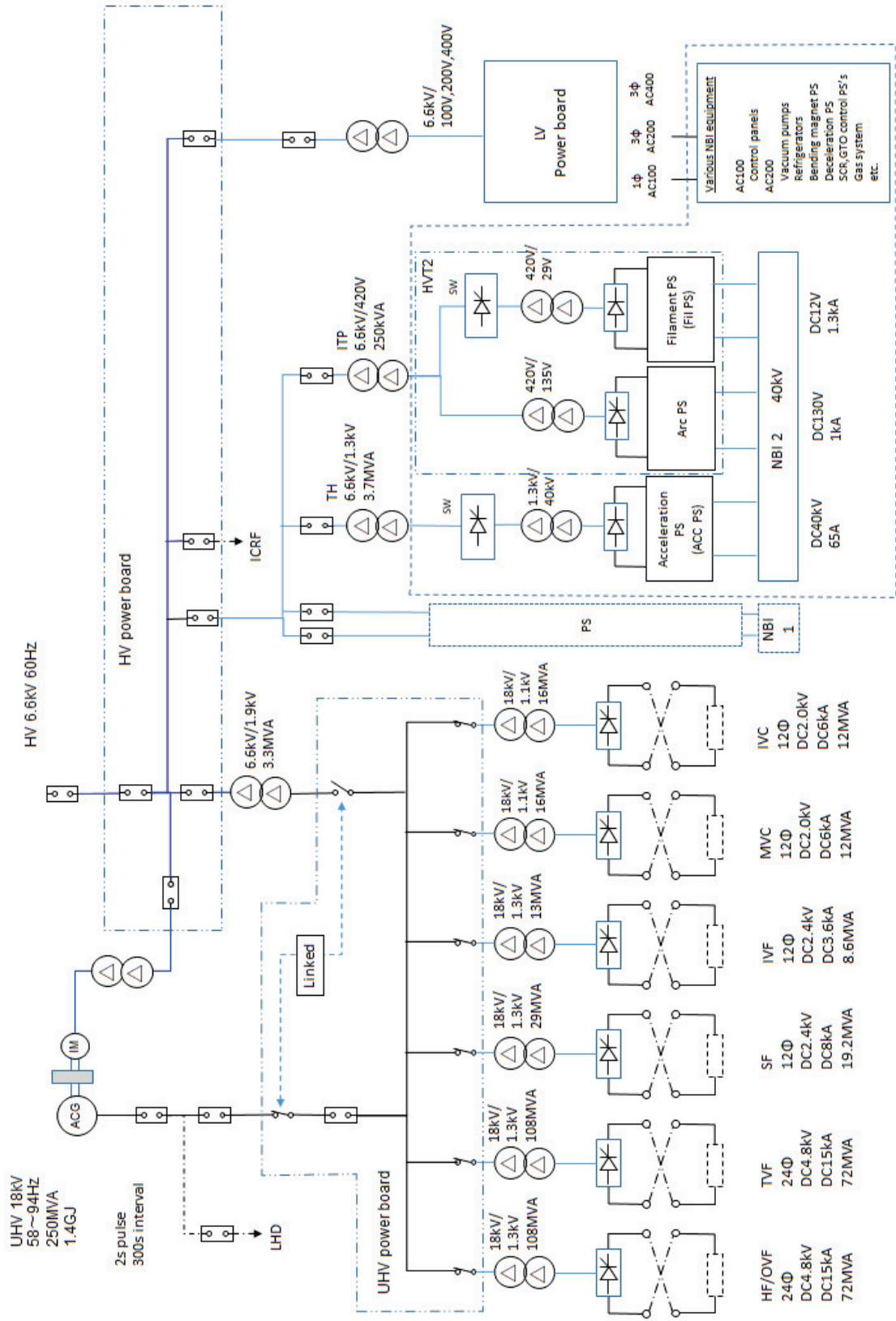


Fig. 3.2.1 One line diagram of power supply system.

3.3 Vacuum pumping system for the CHS

We plan to transfer the vacuum pumping unit for CHS in NIFS to CFQS. Their main specification is shown below. To use this unit with CFQS, modification adding some parts will be required as shown in Table 3.3.1.

Table 3.3.1 Main parameters for the vacuum pumping system.

No	Item	Contents
1	Input power supply	AC 220 V, 50/60 Hz, 1Φ/3Φ, 20 A (at startup)
2	Cooling water	8 kgf/cm ² G, 5 ℓ/min or more, 27 °C or less
3	Compressed air	7 kgf/cm ² G, 20 Nm ³ /h
4	Turbo molecular pump (TMP)	Number of units 2 Model; TH1502VW (Osaka Vacuum Ltd.) Exhaust speed; 1500 ℓ/s Ultimate pressure; 1×10 ⁻⁷ Pa Cooling method; water cooling Allowable temperature; 120 °C
5	Rotary pump (RP)	Number of units 1 Model; T2063A (Adixen/Alcatel) Exhaust speed; 1420 ℓ/min(60Hz) 1180 ℓ/min(50Hz)

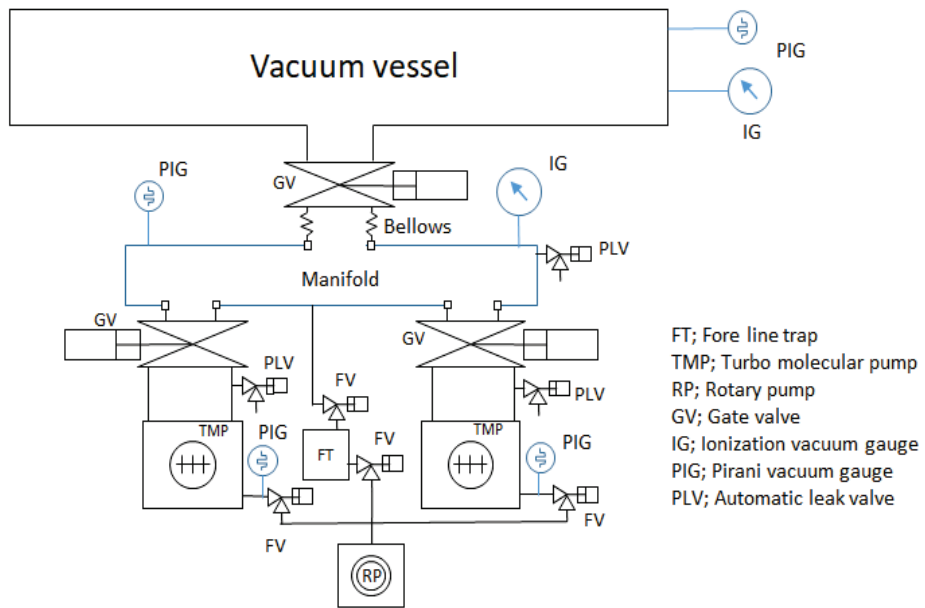


Fig. 3.3.1 System diagram of vacuum pumping unit.

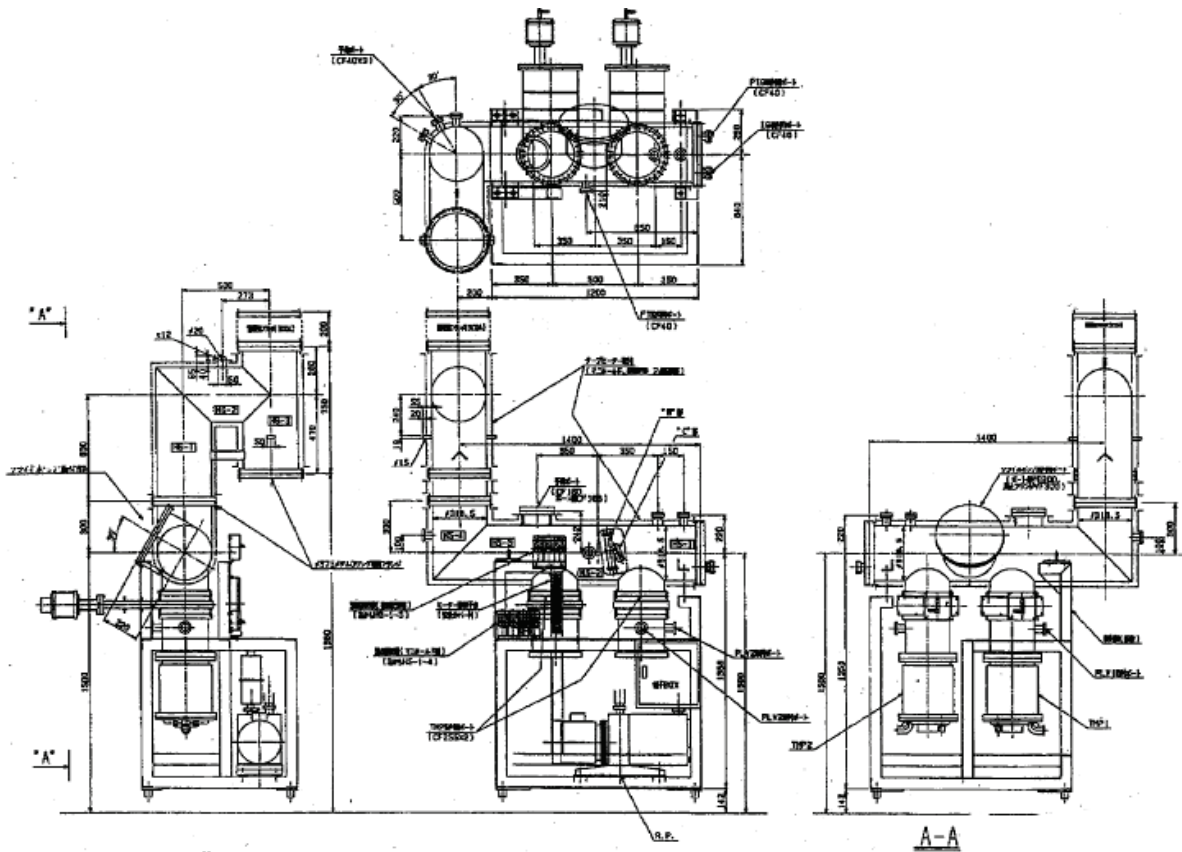


Fig. 3.3.2 Vacuum pumping unit for the CHS.

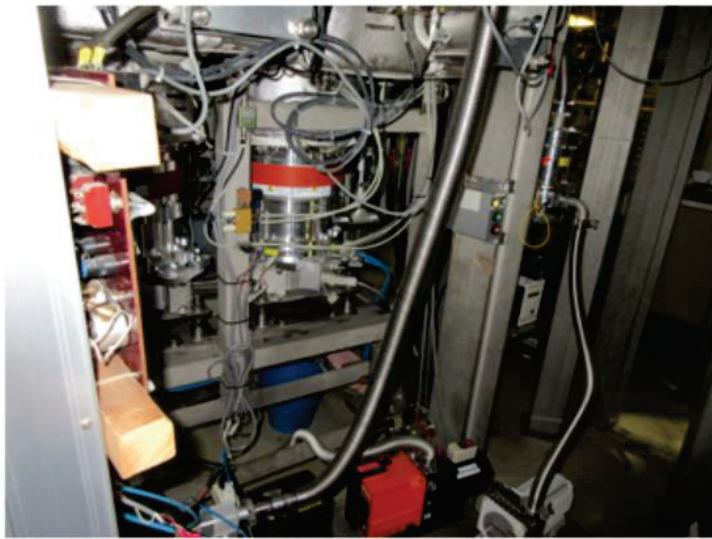
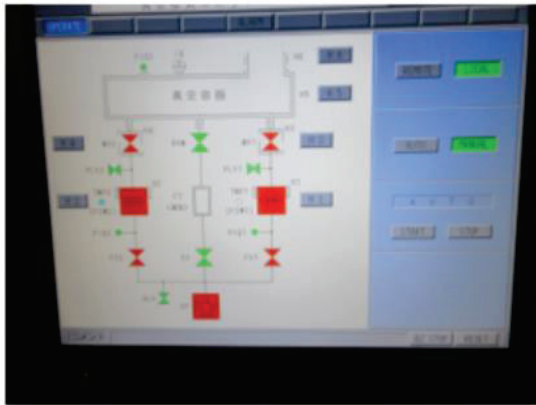
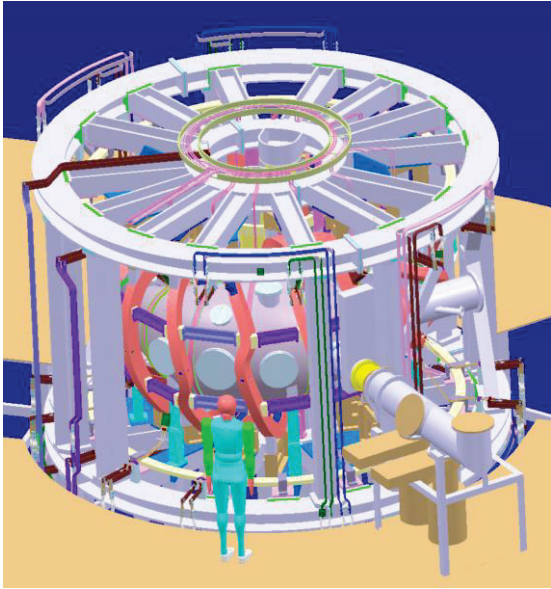
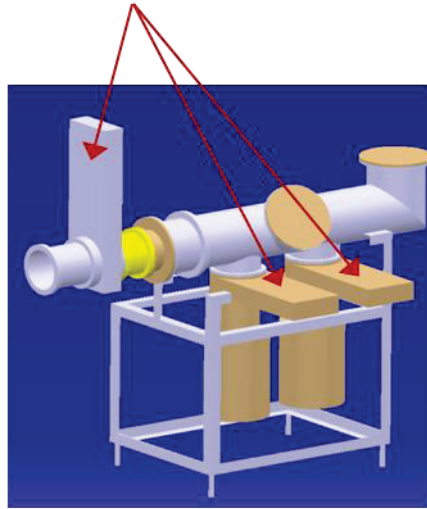


Fig. 3.3.3 Picture of vacuum pumping system.



Gate valve



1500ℓ/s TMP x 2

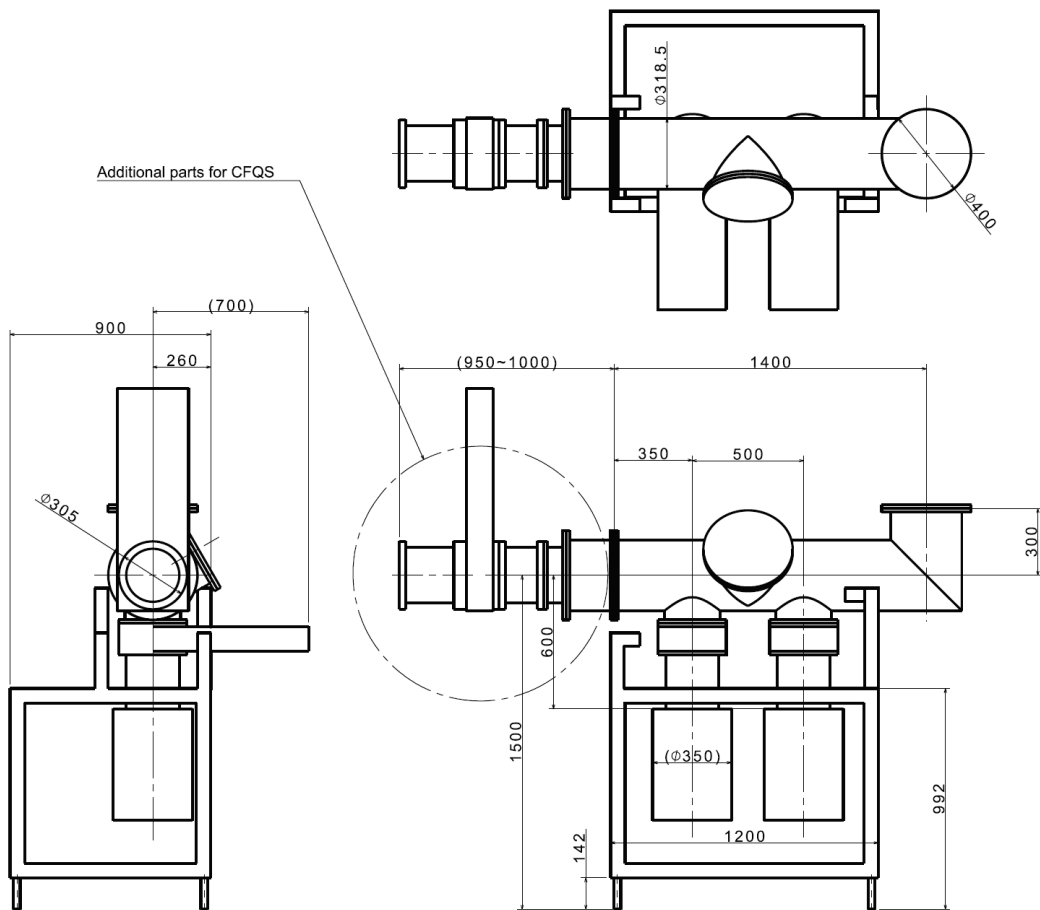


Fig. 3.3.4 Layout of the vacuum pumping unit for the CFQS.

3.4 NBI system for the CHS

There is a plan to transfer the NBI system from the CHS to the CFQS. A configuration of the NBI and power supply for the CHS is shown below.

Table 3.4.1 Power capacity of the NBI-2.

Name	Voltage	Output Current	Capacity of input transformer
Acceleration power supply	AC6.6 kV/DC 40 KV	65 A	3.7 MVA
Arc power supply	AC6.6 kV/DC 135 V	1 kA	250 kVA
Filament power supply	AC6.6 kV/DC 12 V	1.32 kA	
Deceleration power supply	AC 200 V		26 kVA
Bending magnet power supply	AC 200 V		20 kVA
Refrigerator for cryogenic pump	AC 200 V		64 kVA
Low voltage 1Φ (Others)	AC 100 V		4.8 kVA
Low voltage 3Φ (Others)	AC 200 V		50 kVA

Table 3.4.2 Technical specifications of NBI.

No	Item	Specification
1	Beam specie	H/D
2	Beam energy	20-40 kV
3	Port-through power	1 MW
4	Beam duration	1 s
5	Ion source	Filament-arc discharge with cusp magnets
6	Beam acceleration area	φ 300 mm
7	Aperture radius	φ 5 mm
8	Current density	250 mA/cm ²
9	Beam optics	Conversing beam via offset aperture
10	Focal length of the beam	3.0 m
11	Beam divergence angle	1 degree
12	Diameter of drift tube	φ 250 mm
13	Neutralization	Gas cell
14	Main vacuum pump	Cryosorption panel (326 m ³ /s)
15	Diagnostics	Calorimetric beam profile measurement

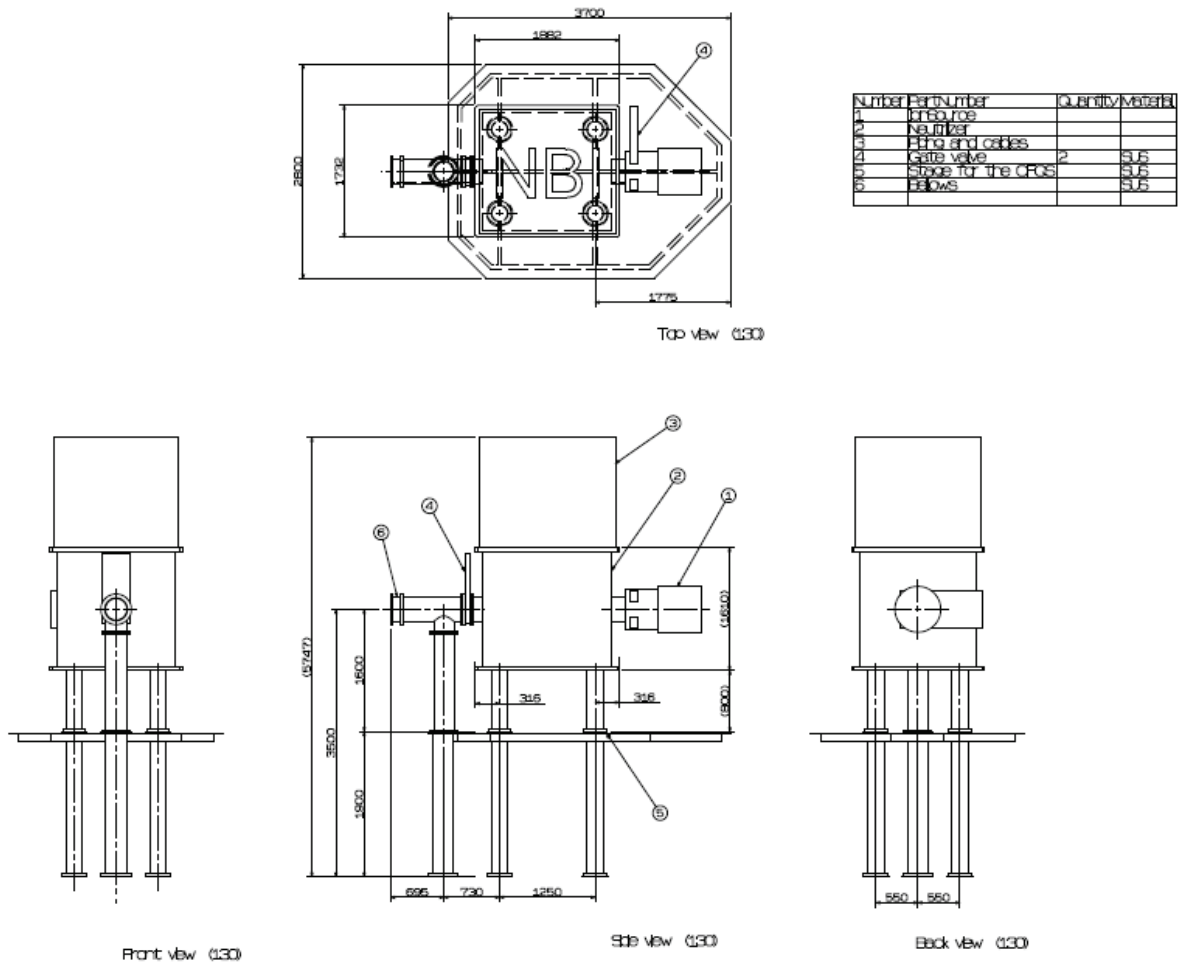


Fig. 3.4.1 Ion source of the NBI-2 system.

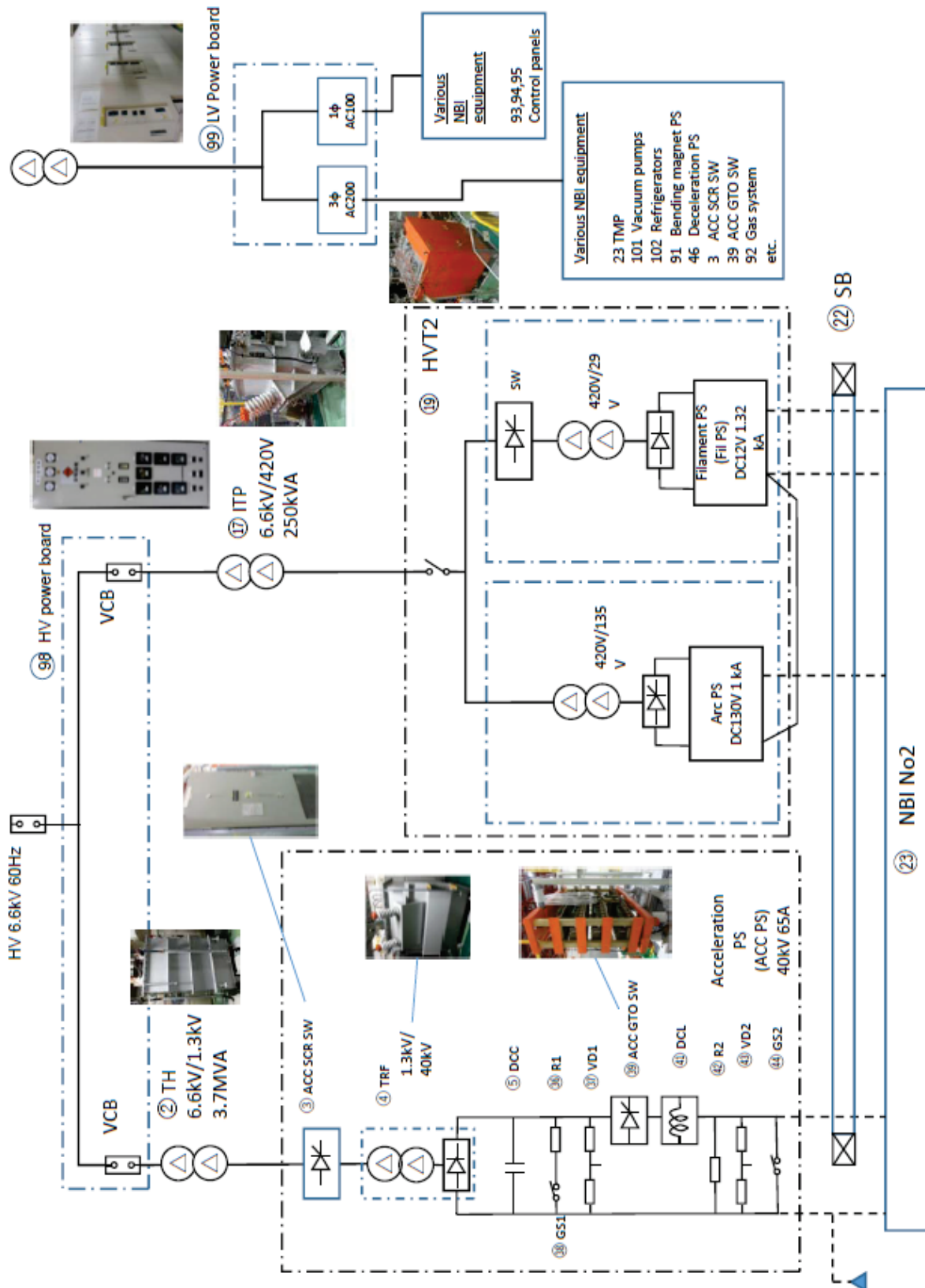


Fig. 3.4.2 One-line diagram of the NBI-2 system.

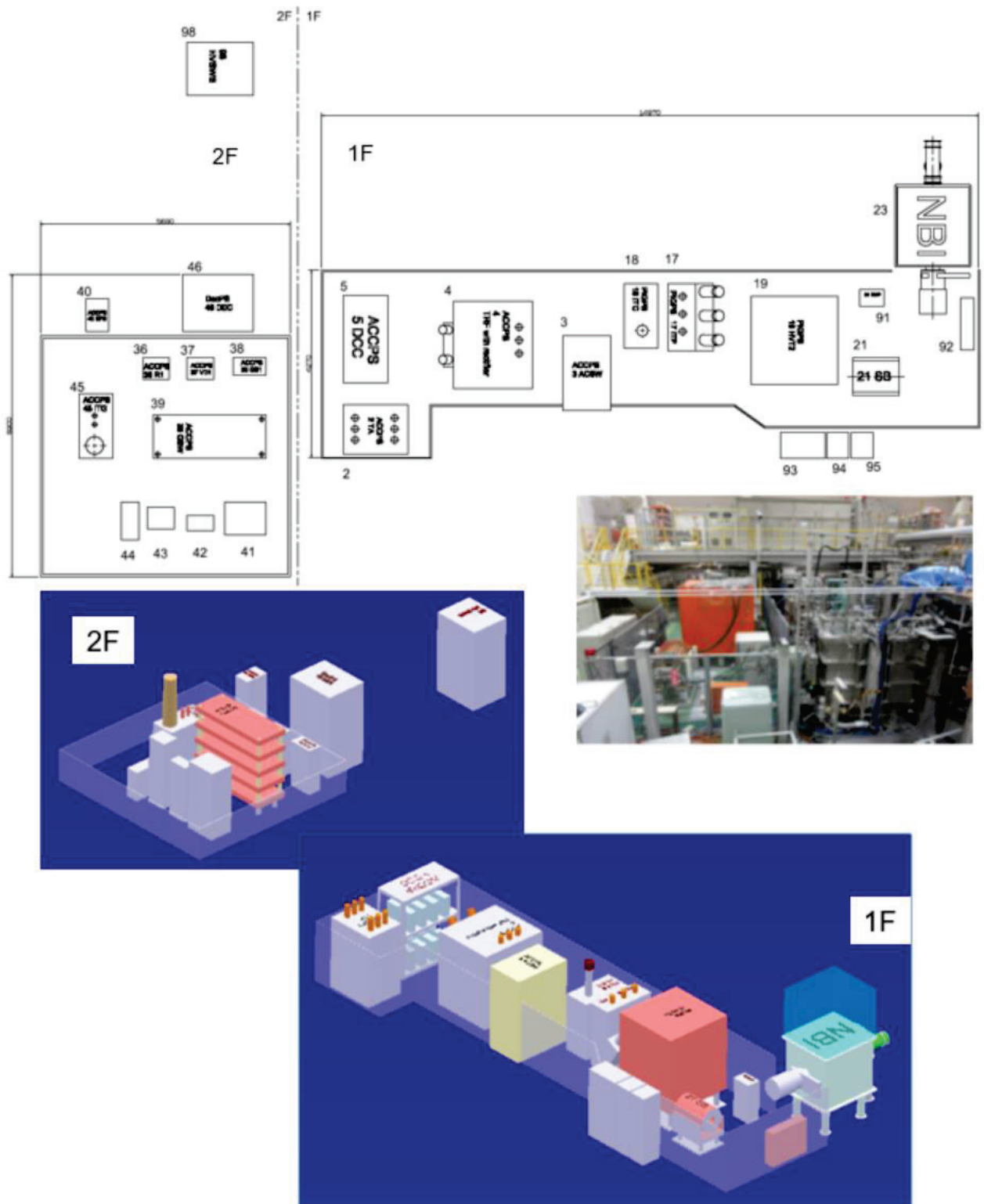


Fig. 3.4.3 Layout of the NBI-2 system.

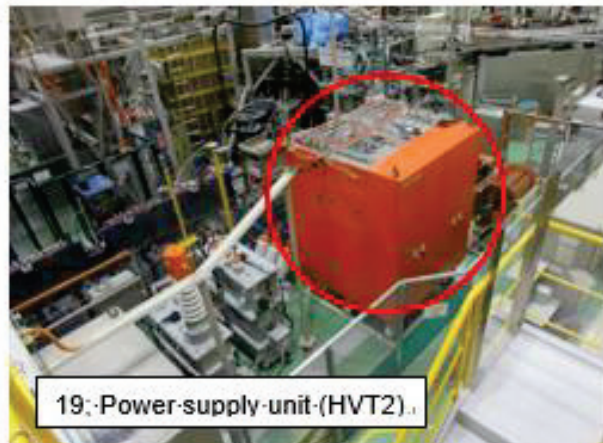


Fig. 3.4.4 Picture of main components for the NBI-2 system.

3.5 ECRH system for the CHS

There is a plan to transfer the ECRH system from the CHS to the CFQS. However, many parts are obsolete and have not been in operation for a long time and need to be rebuilt for the CFQS. A configuration of the ECRH and power supply for the CHS is shown below.

Table 3.5.1 Technical specifications of the ECRH.

No	Item	Specification
1	Power source	Gyrotron produced by a Russian company, GYCOM
2	Frequency	54.5 GHz
3	Output power	Up to 450 kW
4	Pulse length	0.1 s
5	Resonance condition	1.95 T with fundamental resonance($n=1$) 0.97 T with second harmonic resonance($n=2$)
6	Transmission line	Quasi-optical transmission line (Focusing, plane, polarizer, and 2-D steerable mirrors)
7	Magnet	Super conducting magnet with liquid helium replenishment type. It should be replaced to the new one with dedicated refrigerator.
8	Vacuum window	Sapphire window To minimize power reflection at the vacuum window, the thickness of the window d must satisfy a relation: $d = n \lambda_{in}/2$. Here, n is an integer and λ_{in} is wavelength in the window material.

Table 3.5.2 Power supply for the ECRH.

No	Item	Specification
1	Type	High voltage capacitor bank with crowbar circuit
2	Charger	Up to 100 kV DC from 200 V AC
3	Capacitor	86 capacitors with 1.5 μ F each
4	Regulator tube	EIMAC X2062K tetrode tube to supply 70 kV DC. It is very old and must be replaced to new one.
5	Ion pumps	To keep the vacuum condition inside the gyrotron and the regulator tube require DCPS of 3.5 kV
6	Heaters	To generate thermal electron beams, require ACPSs of 150 V
7	Crowbar circuit	High voltage PS used for crowbar-drive works at 8 kV DC
8	Super conducting magnet	SCM requires DCPS of 2 V/33 A

Table 3.5.3 Pure water-cooling system for the ECRH.

No	Item	Specification
1	Purpose	Removing heat load on the gyrotron and the regulator tube
2	Cooling collector	100 L/min
3	Cooling body	6 L/min
4	Cooling vacuum window	9 L/min
5	Cooling oil tank	6 L/min
6	Cooling the regulator tube	120 L/min
7	Pressure	0.2 MPa at inlet

Power Supply for Gyrotrons

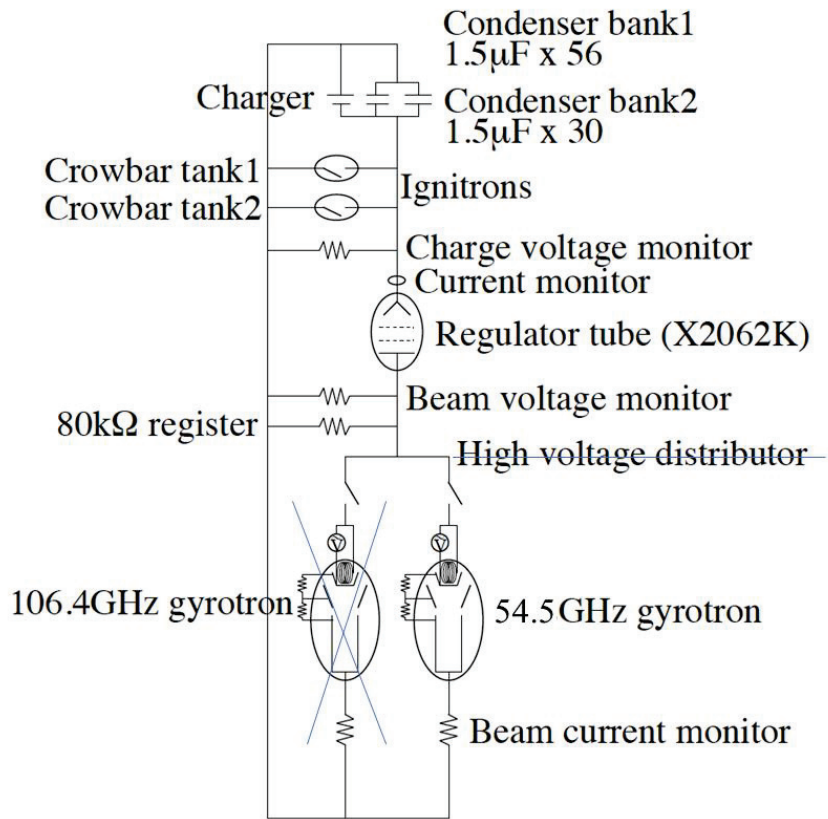


Fig. 3.5.1 One-line diagram of the ECRH system.

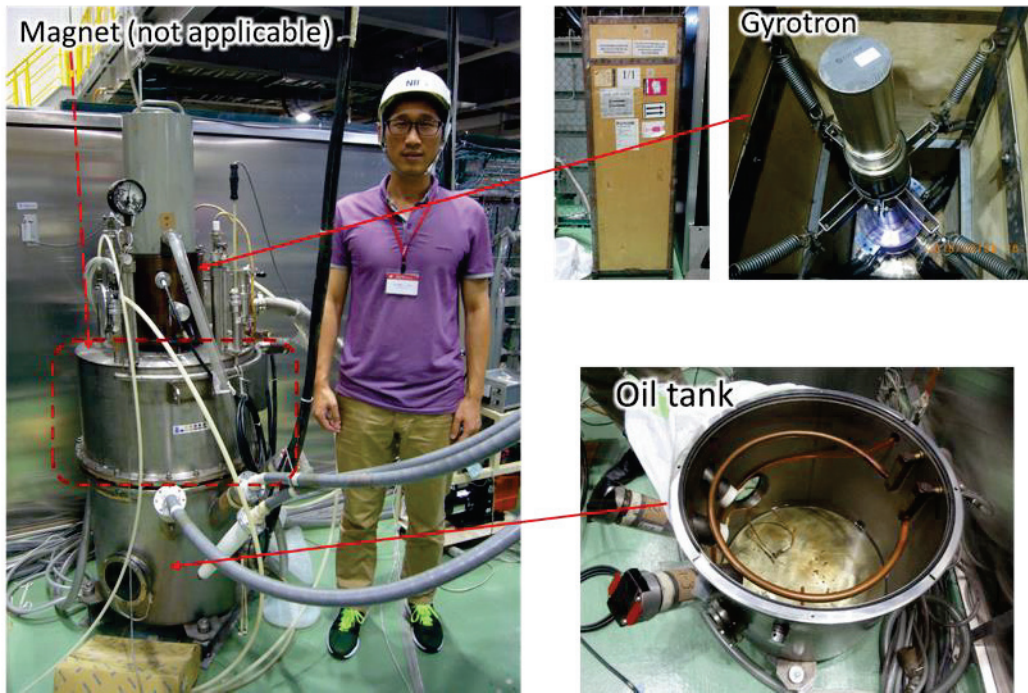


Fig. 3.5.2 54.5 GHz gyrotron.

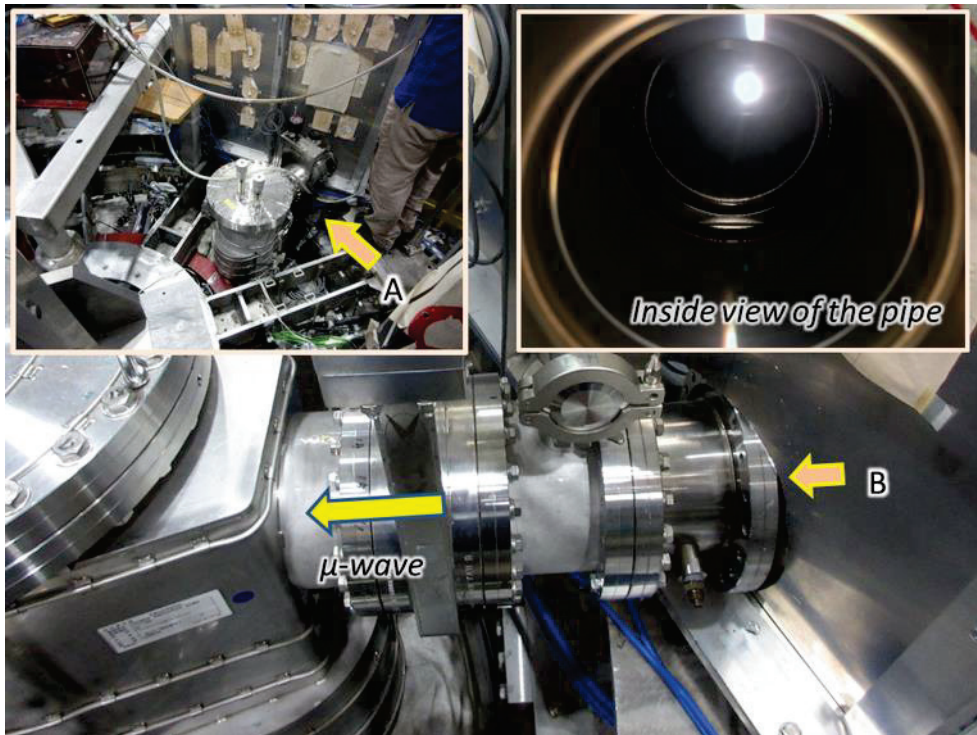


Fig. 3.5.3 Sapphire window.

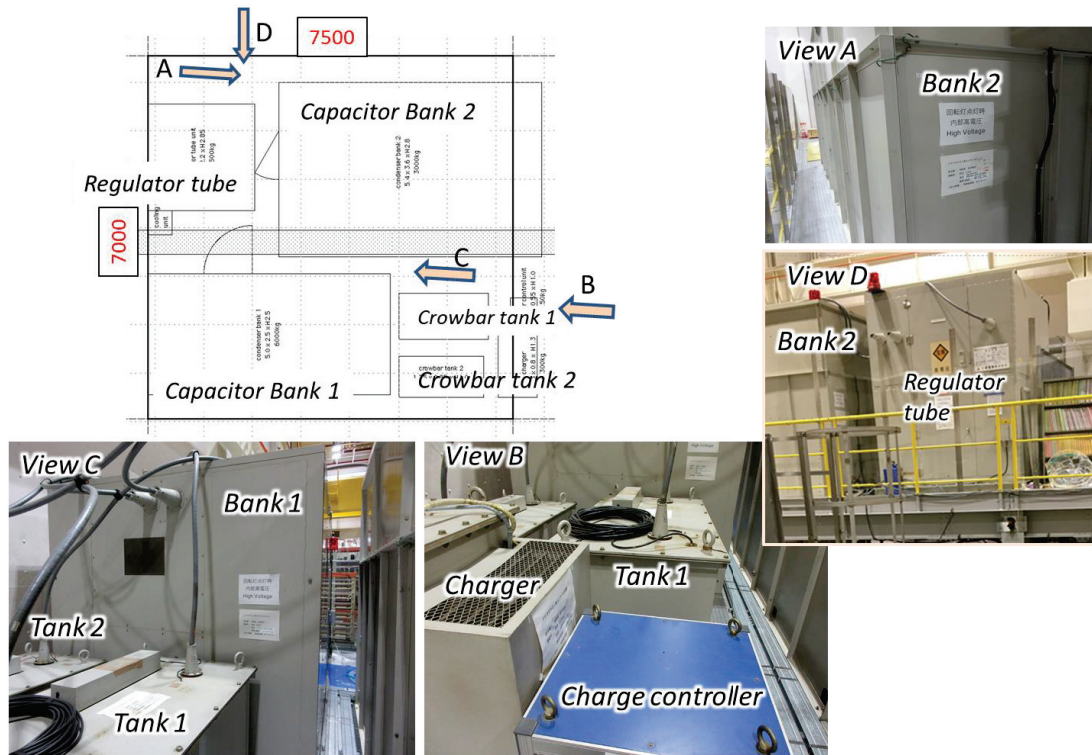


Fig. 3.5.4 Power supply for the gyrotron on the 2F.

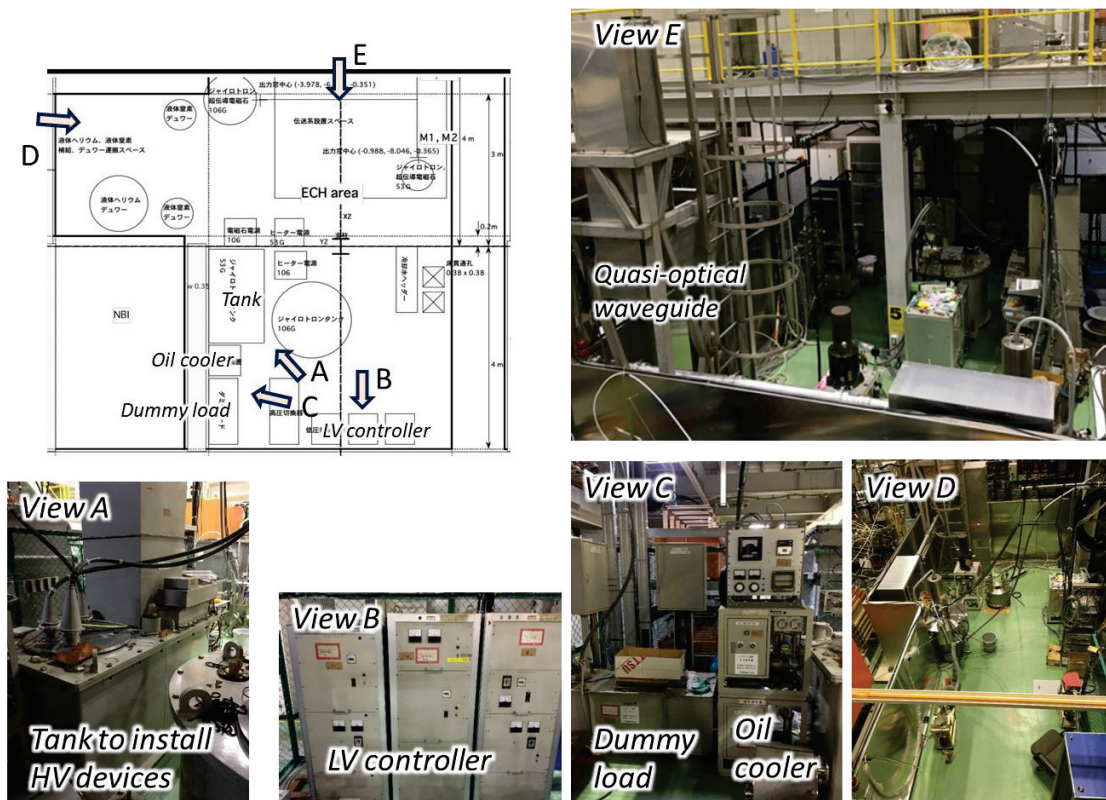


Fig. 3.5.5 Some equipment's for the ECRH system on the 1F.

3.6 Power supply to bake vacuum vessel for the CHS.



Fig. 3.6.1 Power supply for baking vacuum vessel.

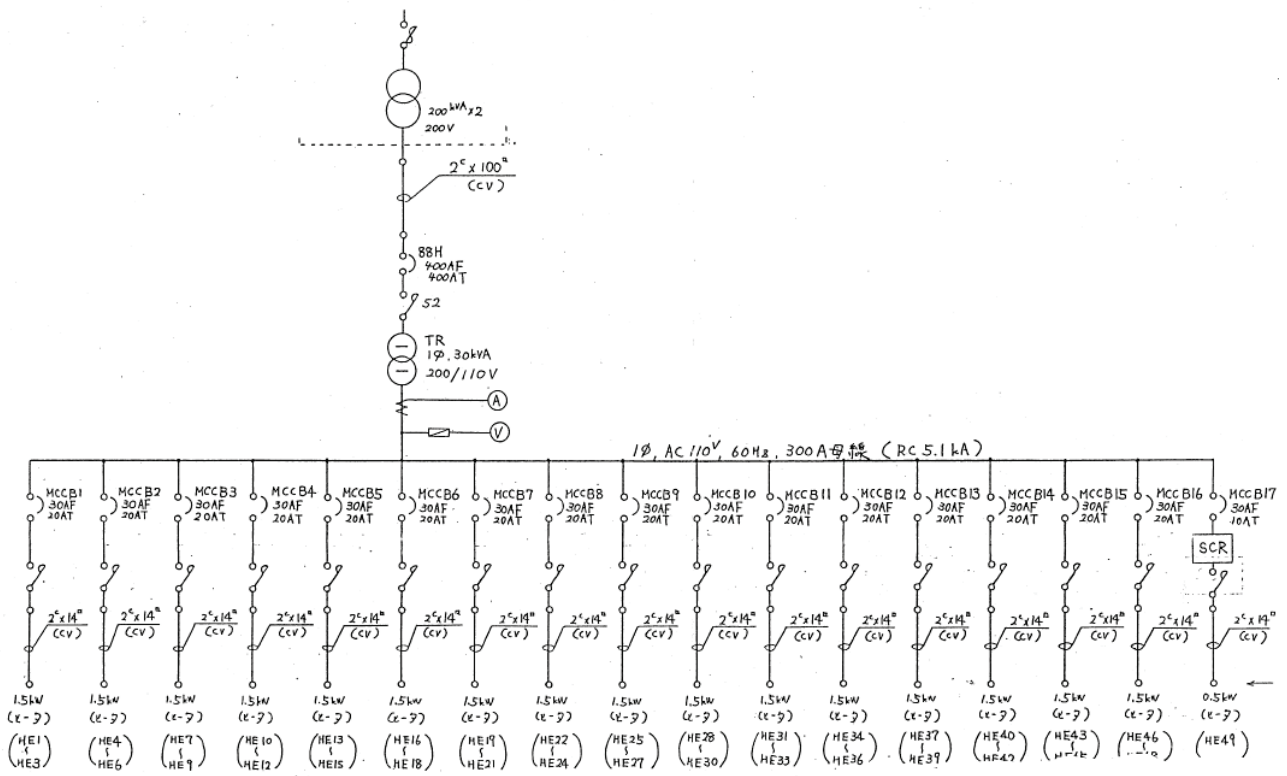


Fig. 3.6.2 One line diagram of baking power supply for the CHS.

3.7 Cooling water system for the CHS

The following figure shows the configuration of the water-cooling system for the CHS. An equivalent system is required for the CFQS.

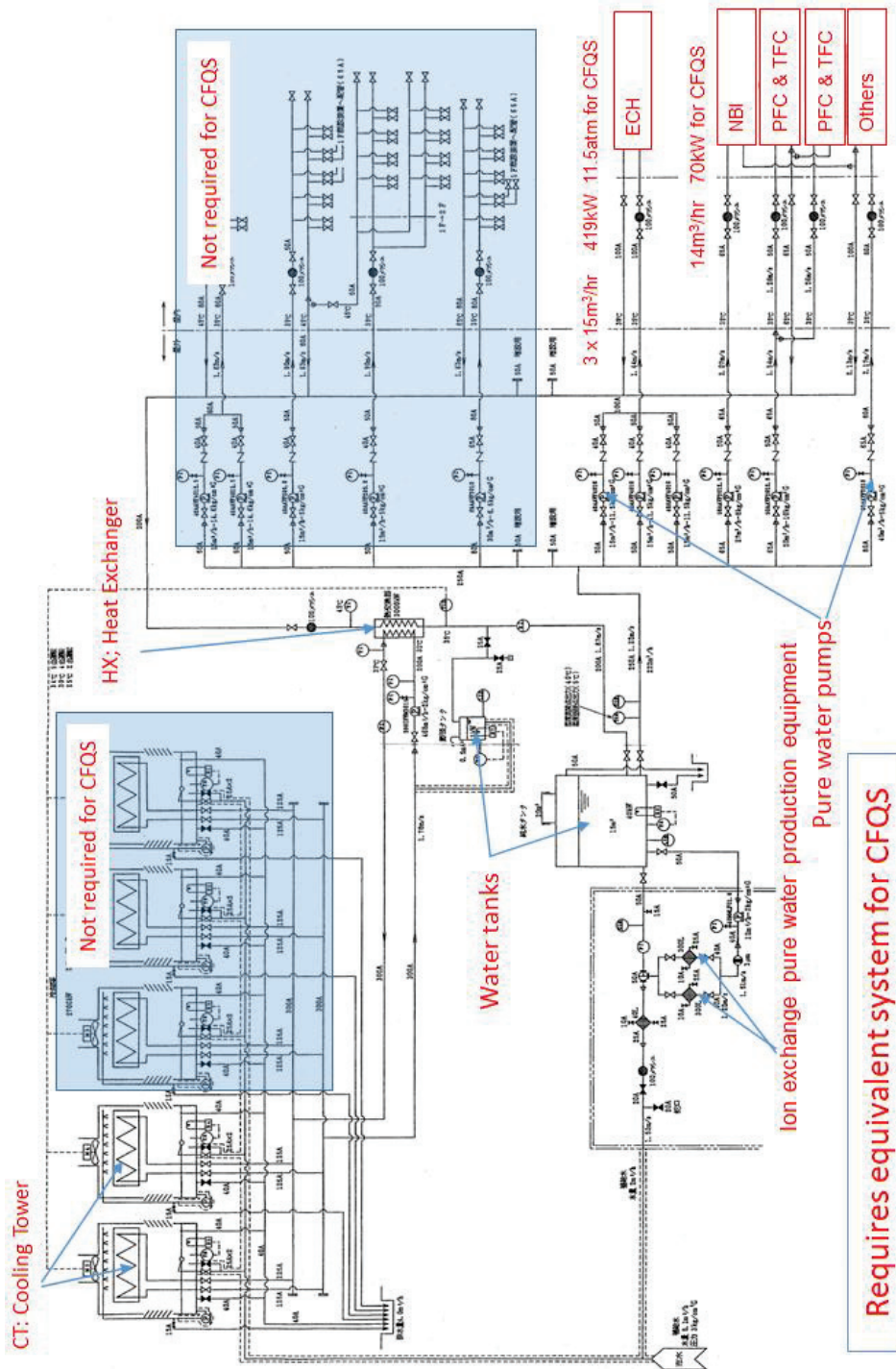


Fig. 3.7.1 Cooling water system diagram.

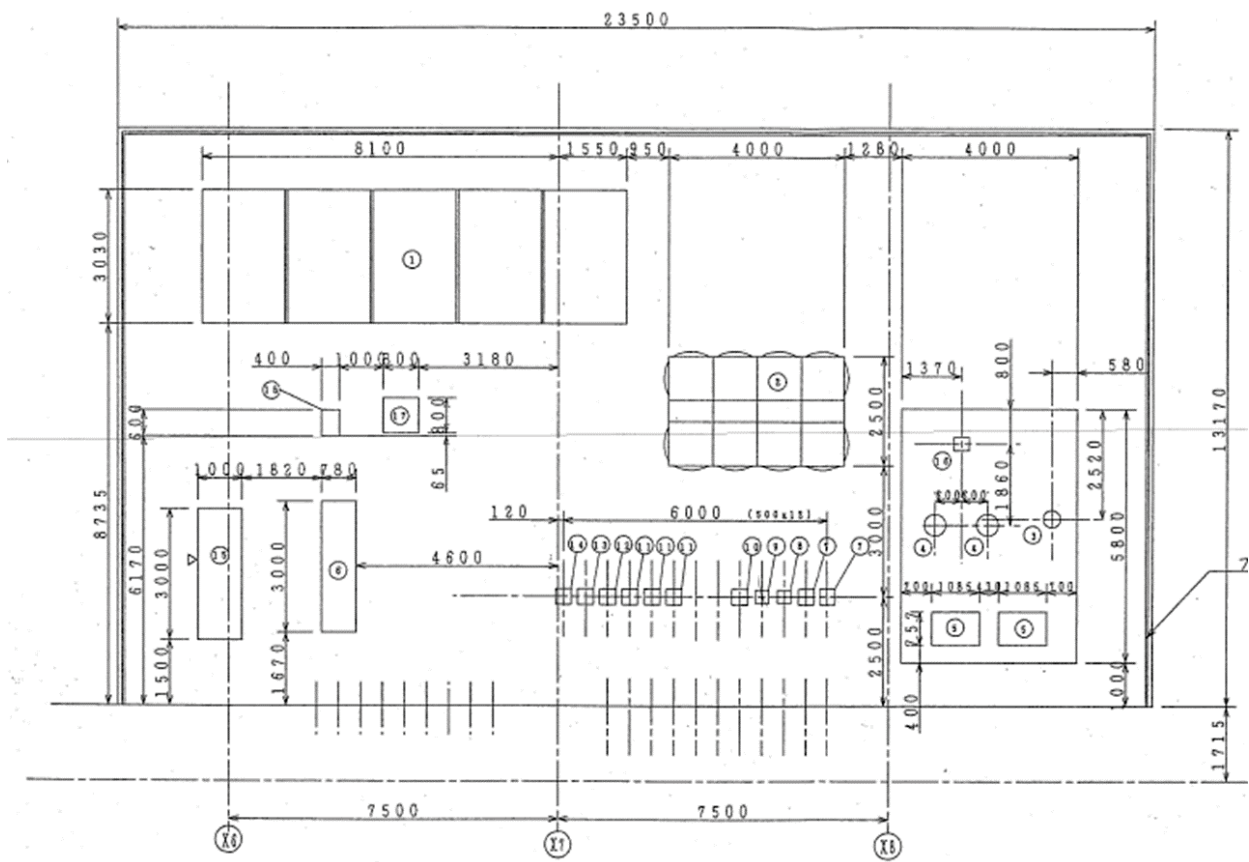


Fig. 3.7.2 Layout of cooling water system.

4 Analytical expression

4.1 Formula of adiabatic temperature rise

The temperature without cooling during pulse operation of the copper coil can be easily evaluated by the following equation. It almost matches the temperature change in a short time, because the standard thermal time constant is much longer than the pulse length.

The temperature change of the conductor is obtained from the thermal equation,

$$C \frac{dT}{dt} = Q_h - Q_c, \quad (4-1)$$

$$Q_h = I^2 R = (jS_{cu})^2 \times \rho_e L / S_{cu} = j^2 S_{cu} \rho_e L \quad [W = J/s], \quad (4-2)$$

$$Q_c = 0, \quad (4-3)$$

where C is a heat capacity, Q_h is a heating power and Q_c is a cooling power.

- Heat capacity of conductor; $C = mC_p$ [J/K]
- Mass of conductor; $m = LS_{cu}\rho$ [kg]
- Density of conductor; $\rho = 8,911\text{kg/m}^3$ [kg/m³] at room temperature (27 °C)
- Density of conductor; $\rho = 8,888\text{kg/m}^3$ [kg/m³] at 75 °C
- Specific heat of conductor; $C_p = 381$ [J/kgK] at room temperature (27 °C)
- Specific heat of conductor; $C_p = 361$ [J/kgK] at 75 °C
- Resistivity of conductor; $\rho_e = 1.724 \times 10^{-8}$ [Ωm] at room temperature (27 °C)
- Resistivity of conductor; $\rho_e = 1.895 \times 10^{-8}$ [Ωm] at 75 °C

It is as follows when the physical property value of copper is inputted.

$$\frac{dT}{dt} [K/s] = \frac{Q_h}{C} = \frac{j^2 S_{cu} \rho_e L}{LS_{cu} \rho C_p} = j^2 \frac{\rho_e}{\rho C_p} = j^2 [A/mm^2] \times 5.1 \times 10^{-3} \quad \text{at } 27^\circ\text{C}, \quad (4-4)$$

$$\frac{dT}{dt} [K/s] = \frac{Q_h}{C} = \frac{j^2 S_{cu} \rho_e L}{LS_{cu} \rho C_p} = j^2 \frac{\rho_e}{\rho C_p} = j^2 [A/mm^2] \times 5.9 \times 10^{-3} \quad \text{at } 75^\circ\text{C}. \quad (4-5)$$

For an example,

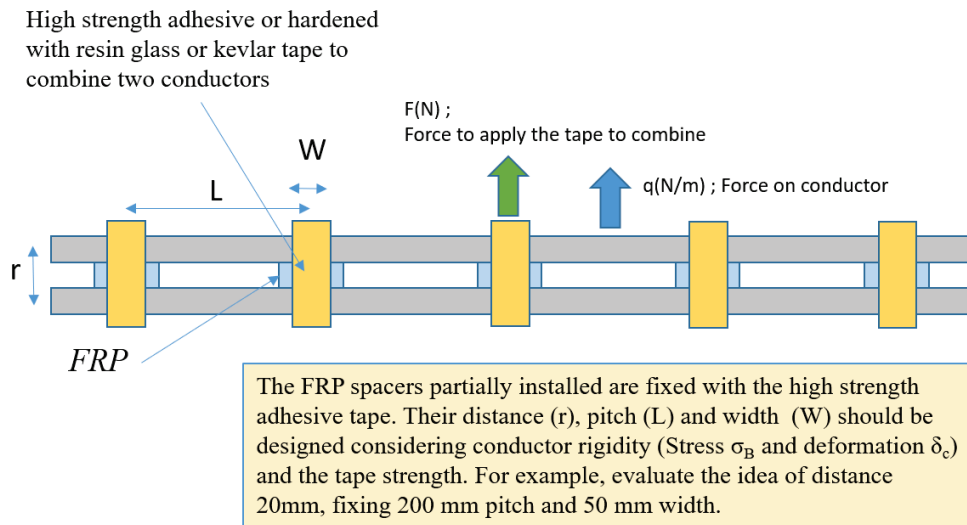
$$dT/dt = 28 \text{ K/s with } 74 \text{ A/mm}^2 \text{ at } 27^\circ\text{C}.$$

Note)

75 °C is often used as a typical temperature after heating an electric device.

25 °C = 300K is often used as a typical room temperature before heating an electric device.

4.2 Formula to combine two wires



(a) Force between parallel straight currents

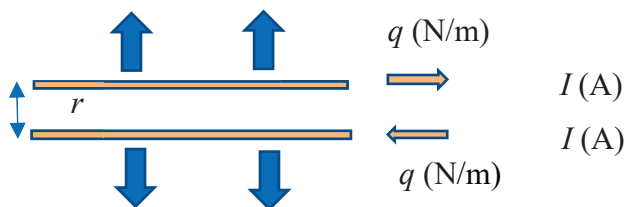
Repulsive force is generated by the reverse current,

$$q(N/m) = \frac{\mu_0 I^2}{2\pi r}, \quad (4-6)$$

where

$I(A)$; Current

$r(m)$; Distance between currents



(b) Maximum stress of the wire

It is obtained with equally distributed load both ends fixed beam model and should be smaller than 20 MPa.

$$\sigma_B(Pa) = \frac{qL^2}{2bh^2}, \quad (4-7)$$

where

$L(m)$; Support interval

$b(m) \times h(m)$; Cross section of wire

(c) Force to support

Electromagnetic force acting on the wire is applied to the support which must be designed to endure the force.

$$F(N) = qL. \quad (4-8)$$

(d) Deflection

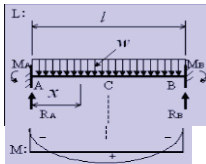
It is obtained with equally distributed load both ends fixed beam model and should be smaller than 2 mm.

$$\delta_c(m) = \frac{qL^4}{384EI_x}, \quad (4-9)$$

where

$I_x = bh^3/12$; Second moment of area of beam

$E = 100 \text{ GPa}$ (C1020-0); Longitudinal elastic modulus



(e) Lowest natural frequency

It should be larger than 40 Hz.

$$f_1 = \frac{4.73^2}{2\pi} \sqrt{\frac{EI_x}{\rho SL^4}}. \quad (4-10)$$

Where

S ; Cross sectional area (m^2)

$\rho = 8,960 \text{ kg/m}^3$ (C1020-0); Density

NIFS-SWJTU JOINT PROJECT FOR CFQS
~PHYSICS AND ENGINEERING DESIGN~

VER. 3.1
2020. NOV.

APPENDIX-C

~ DRAWING COLLECTION ~

RESULTS OF THE CFQS CONCEPTUAL DESIGN

They may change due to the progress in detailed design.



NIFS; National Institute for Fusion Science

SWJTU; Institute of Fusion Science, School of Physical Science and Technology Southwest Jiaotong University

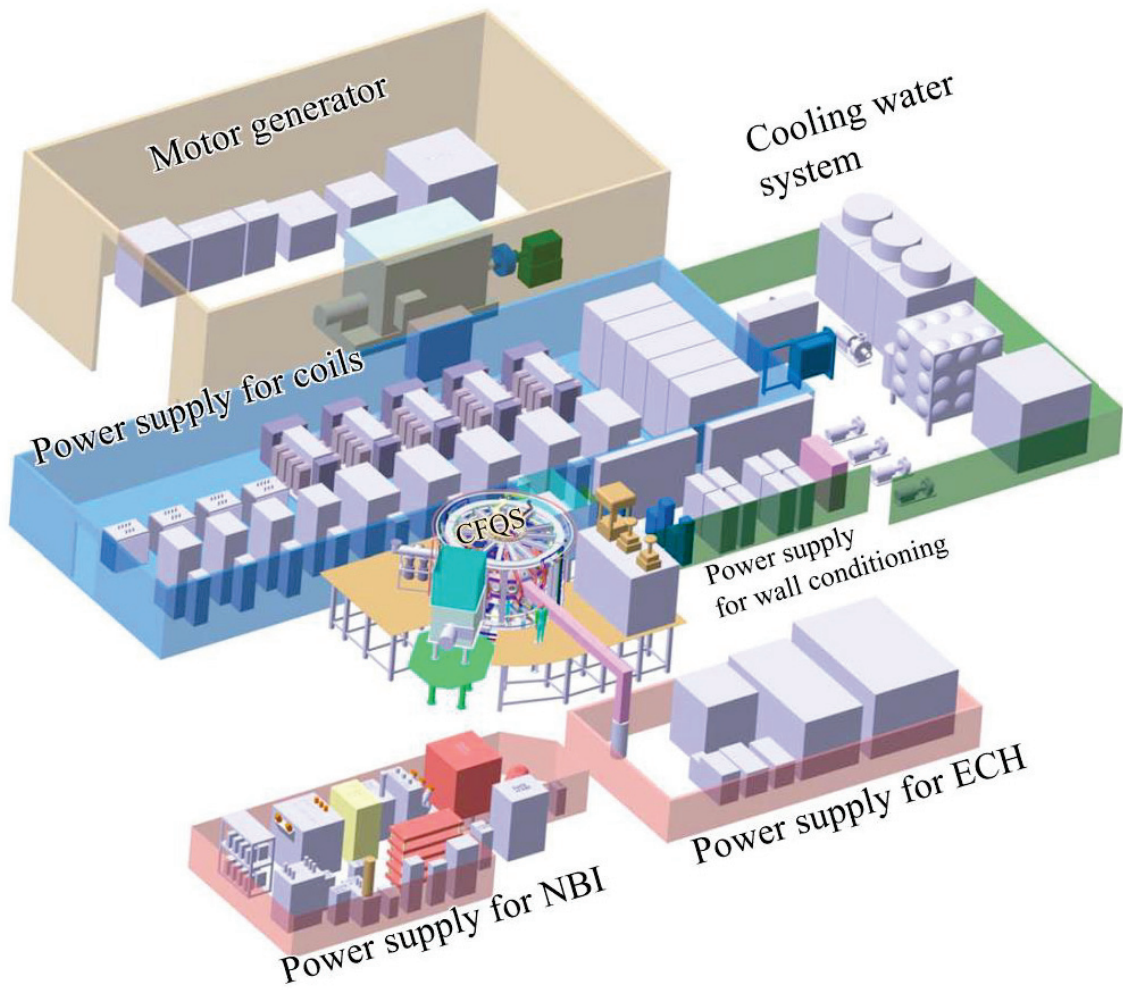
Hefei Keye; Hefei Keye Electrical Physical Equipment Manufacturing Co., Ltd.

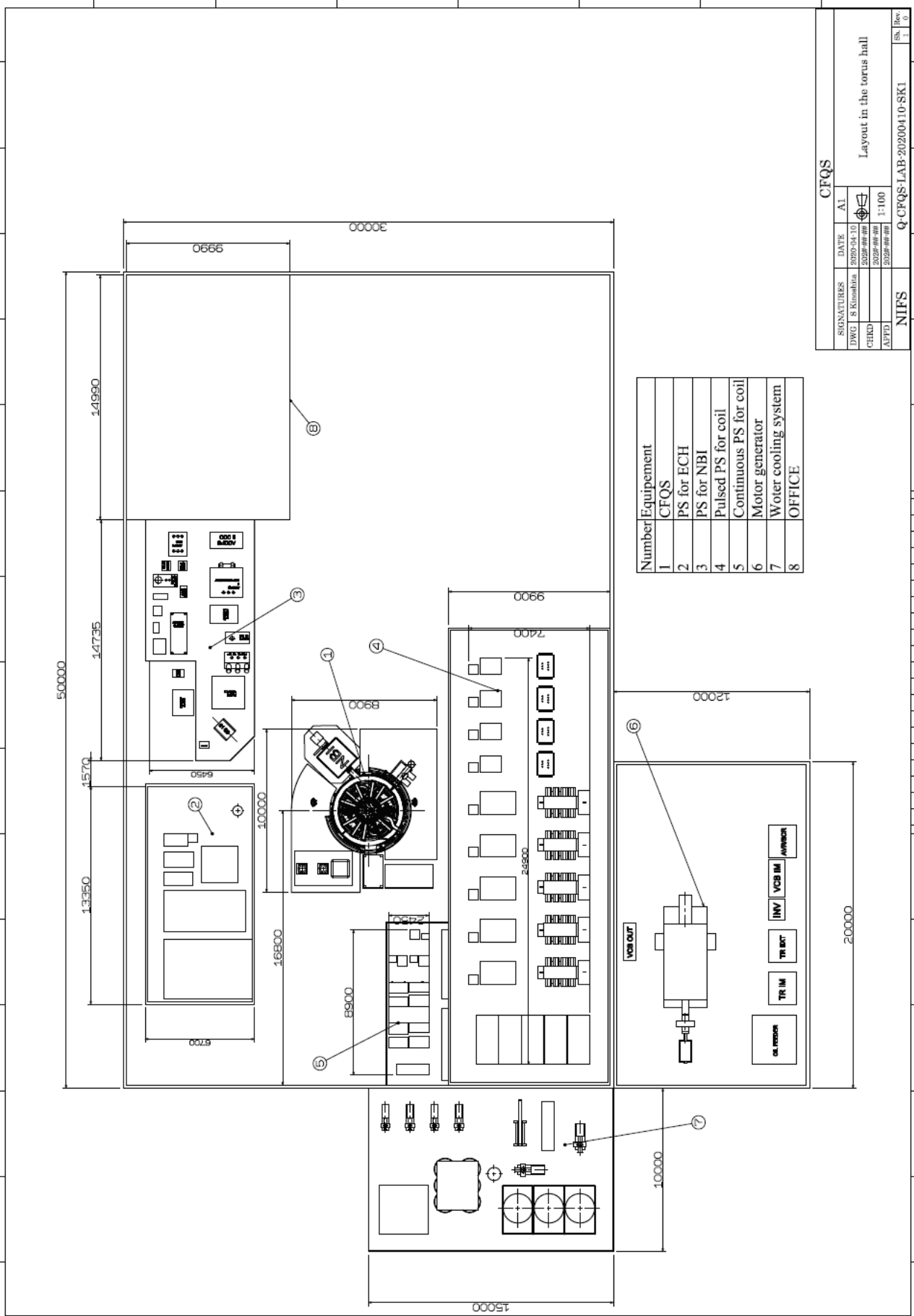
Table of contents

1	CFQS overall view	3
1.1	Layout.....	3
1.2	CFQS body	9
2	Coils	13
2.1	Modular coil	13
2.2	Toroidal field coil	24
2.3	Poloidal field coil.....	30
3	Vacuum vessel.....	33
3.1	Main body.....	33
3.2	Related device.....	37
4	Another component	42
4.1	External current lead.....	42
4.2	Support structure.....	46
4.3	Cooling water pipe.....	52

1 CFQS overall view

1.1 Layout





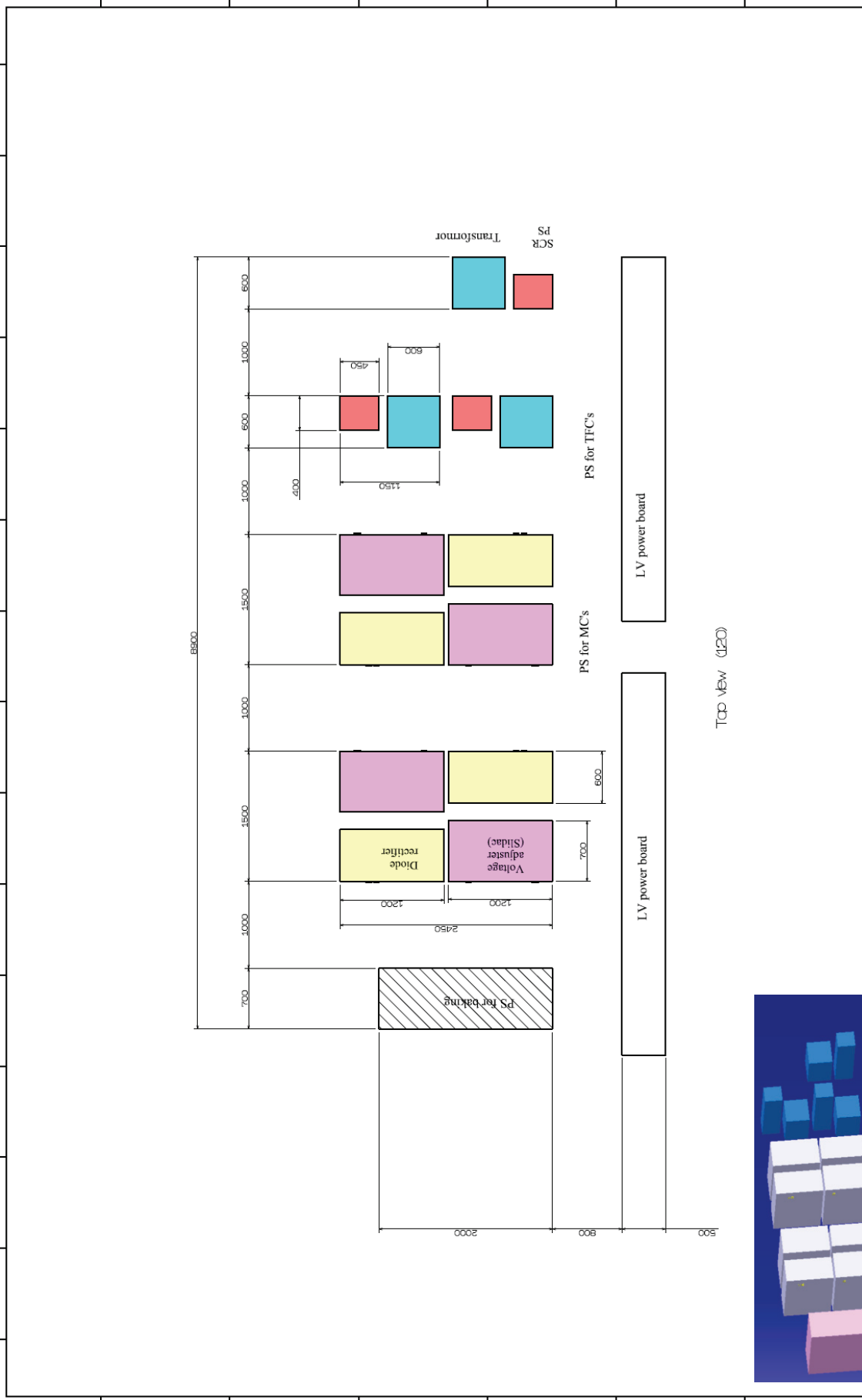
Number	Equipment
1	CFQS
2	PS for ECH
3	PS for NBI
4	Pulsed PS for coil
5	Continuous PS for coil
6	Motor generator
7	Water cooling system
8	OFFICE

SIGNATURES		DATE	AI
DWG	8 Kinoshita	2020-04-10	
CHKD		2020-04-10	
APTD		2020-04-10	
NIFS			
Q-CFQS-LAB-20200410-SK1			
sh.	1	1	3

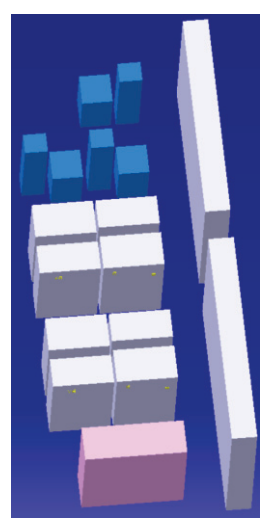
CFQS

Layout in the torus hall

1:100



TCD NEW (120)

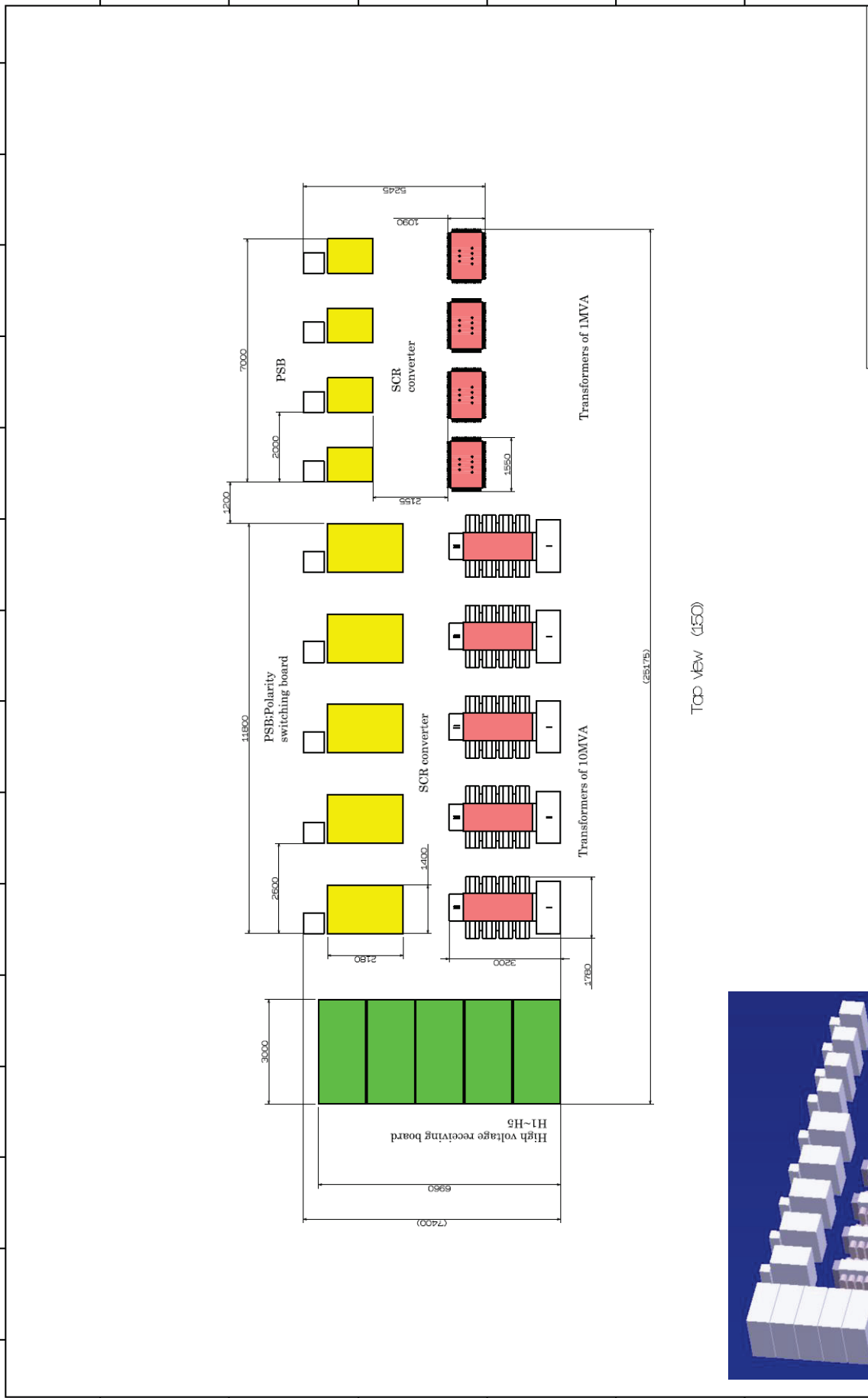


SIGNATURES		DATE	AI
DWG	S. Kurohata	2020-04-10	
CHKD		2020-04-10	
APPD		2020-04-10	

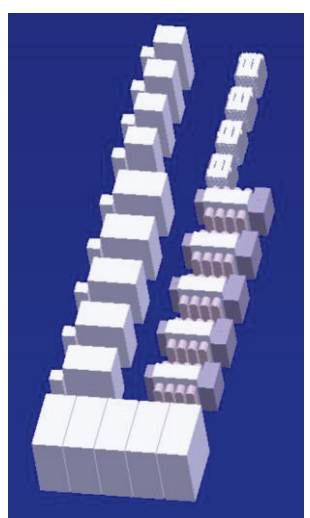
CFQS

Coil power supply for 0.1T and Baking power supply

NIFS		Sh	Rev
Q-CFQS-LAB-20200410-SK1		2	0



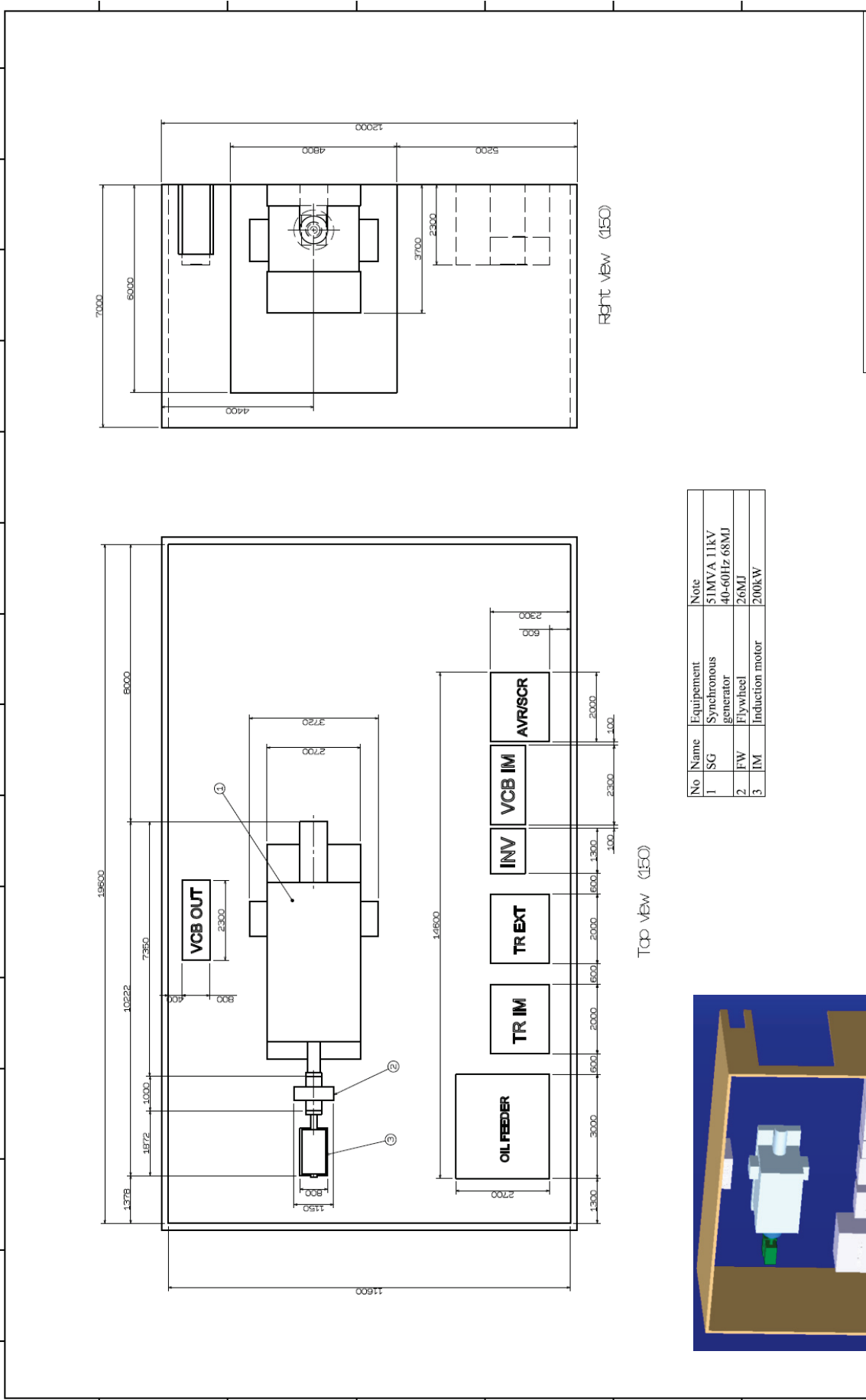
Top view (150)



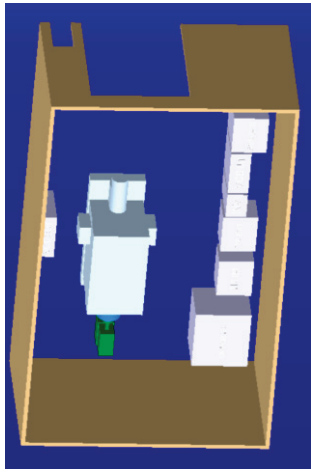
SIGNATURES		DATE		A1	
DWG	S. Kinoshita	2020-04-10			
CHKD		2020-##-##			
AUPD		2020-##-##			
NIPS					
Q-CFQS-LAB-20200410-SK1					
					Sh. Rev. 3 0

CFQS

Pulsed power supply for coil



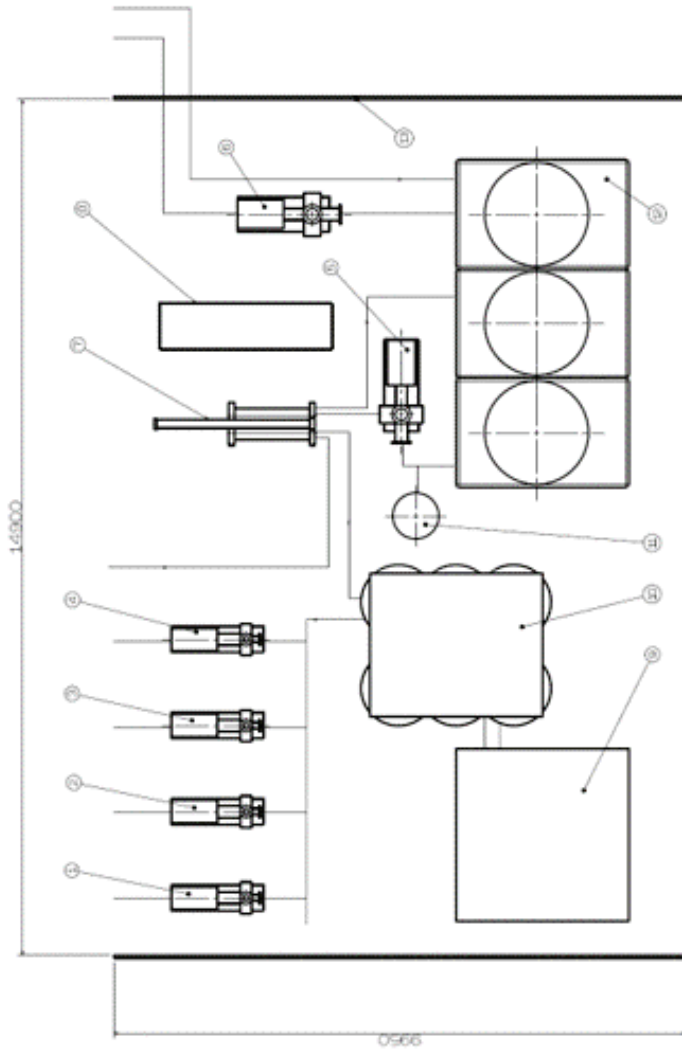
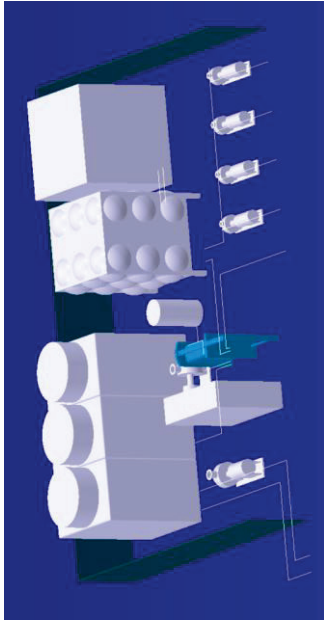
No	Name	Equipment	Note
1	SG	Synchronous generator	SIMVA 11kV 40-60Hz 68MJ
2	FW	Flywheel	26MJ
3	IM	Induction motor	200kW



SIGNATURES		DATE	AI
DWG	S. Kiranahar	2020-04-10	
CHKD		2020-##-##	
APTD		2020-##-##	

MG room

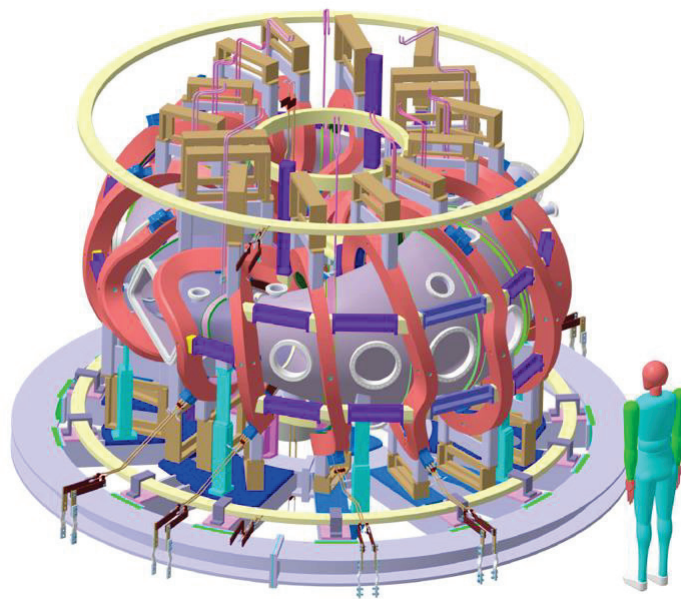
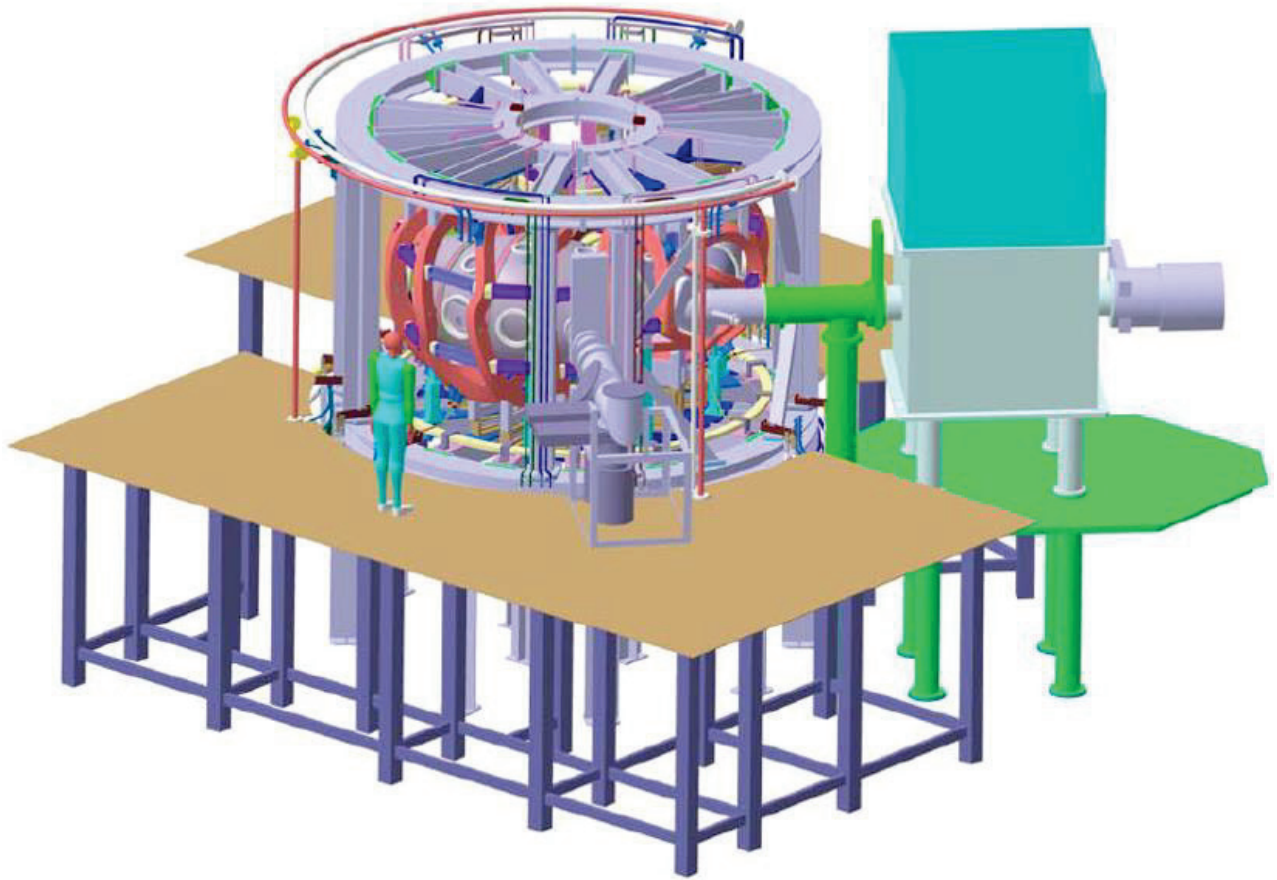
NIFS	Q-CFQS-LAB-20200410-SK1
------	-------------------------

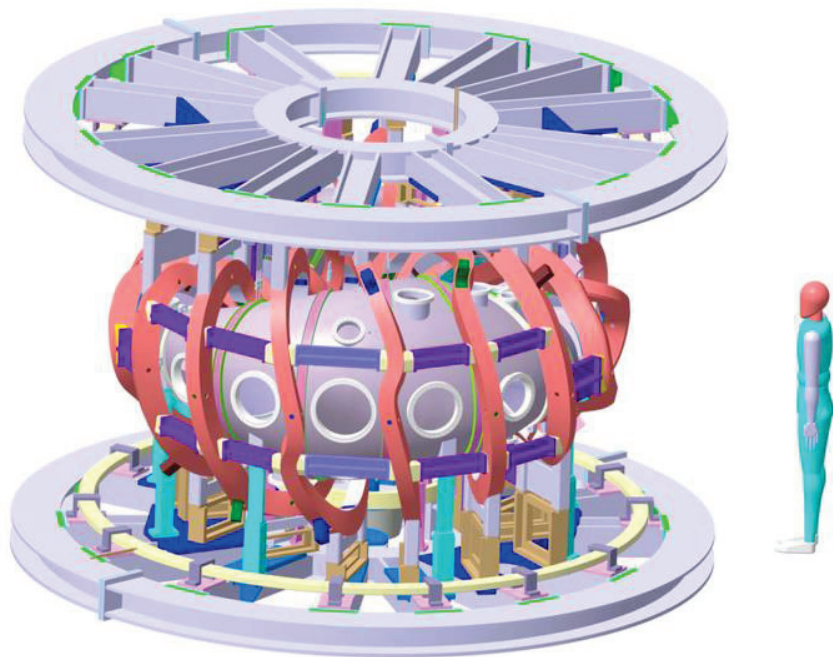
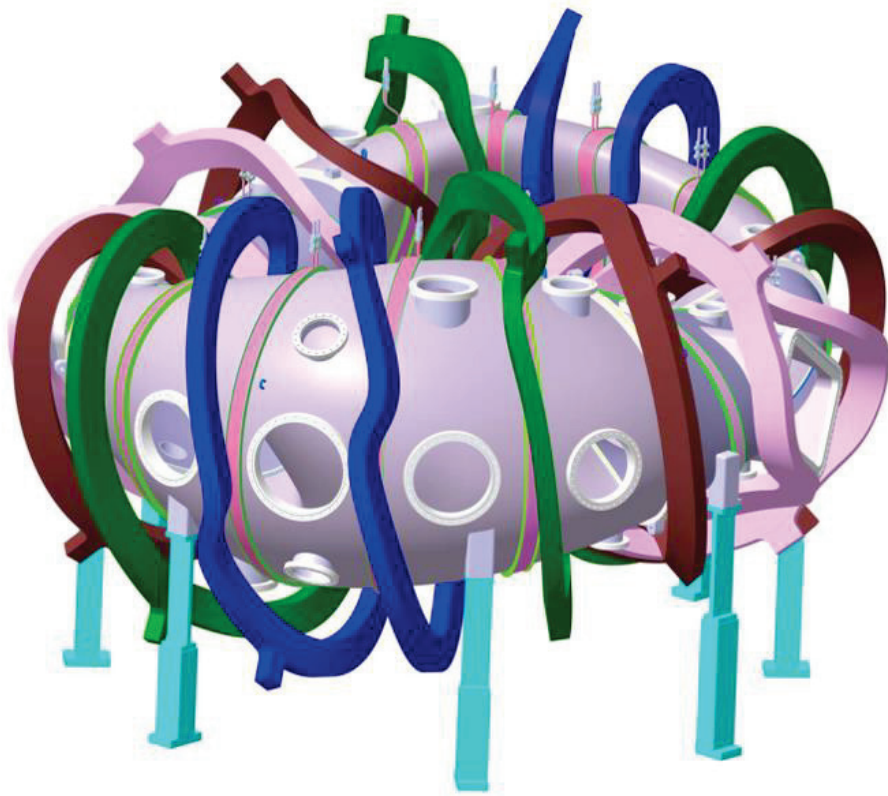


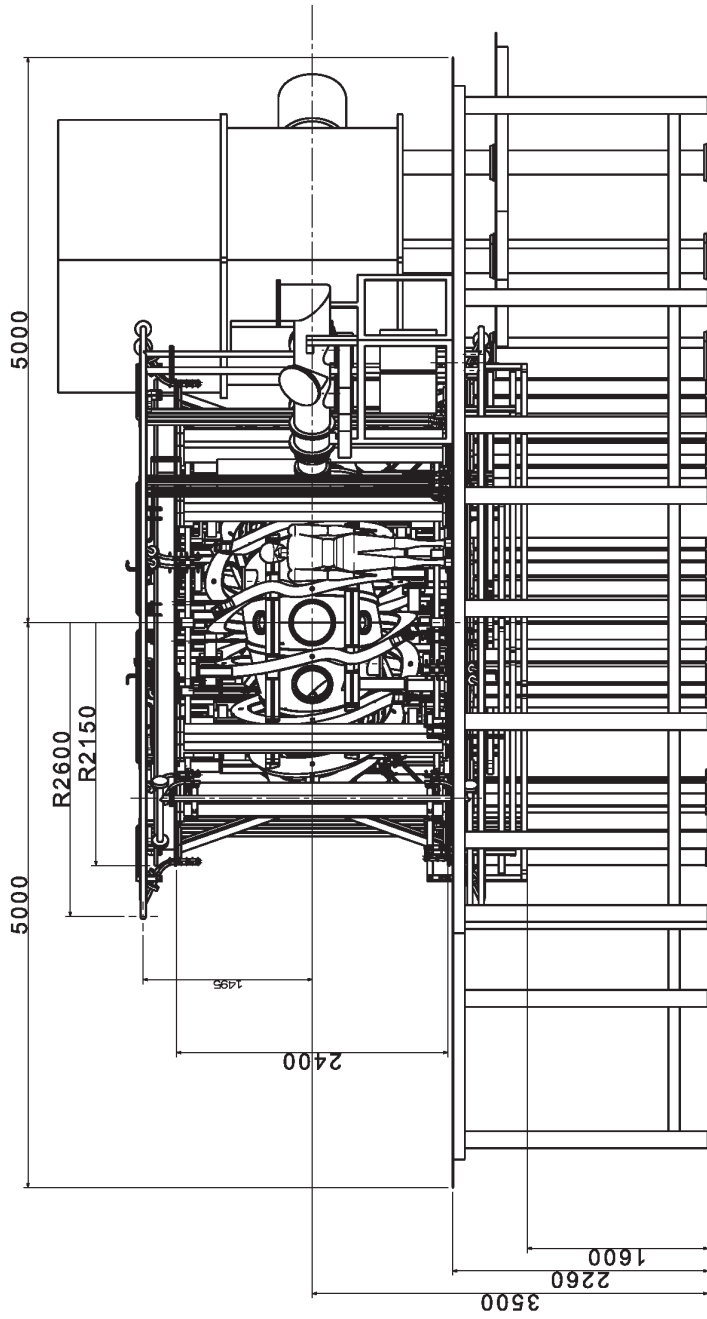
No	Name	Equipment	Quantity	Note
1	PPW	Pure water pump	1	1MPa 15m ³ /hr for an ECH
2	PPW	Pure water pump	1	1MPa 15m ³ /hr for an NBI
3	PPW	Pure water pump	1	2MPa 6m ³ /hr for coils
4	PPW	Pure water pump	1	0.6MPa 30m ³ /hr for other equipment
5	PW2	Water pump	1	0.3MPa 100m ³ /hr for secondary water
6	PMG	Water pump	1	For a motor generator
7	HX	Heat exchanger	1	2MW
8	SWB	Switch power board	1	
9	PWB	Pure water production building	1	
10	PWT	Pure water tank	1	15m ³
11	EXT	Expansion tank	1	0.5m ³
12	CT	Cooling tower	3	0.6MWx3
13	F	Fence	1	


SIGNATURES		DATE	AI
DRG: S. Kishore		2020-04-01	
CHKD:		2020-09-08	
APPD:		2020-09-08	
CFQS			
Layout of water cooling system			
NIFS			Q-CFQS-LAB-20200410-SK1
Sl. No.	3	0	

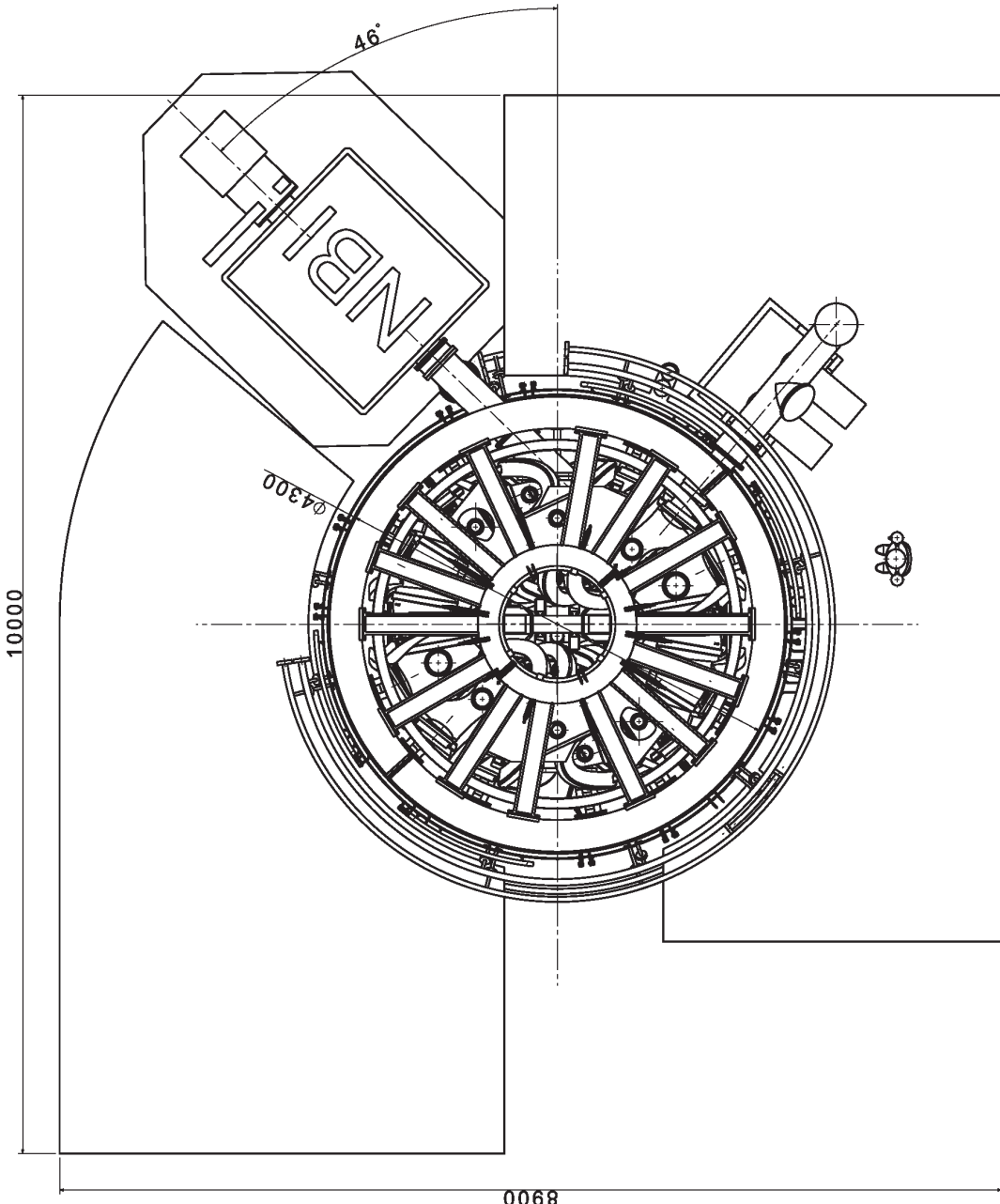
1.2 CFQS body





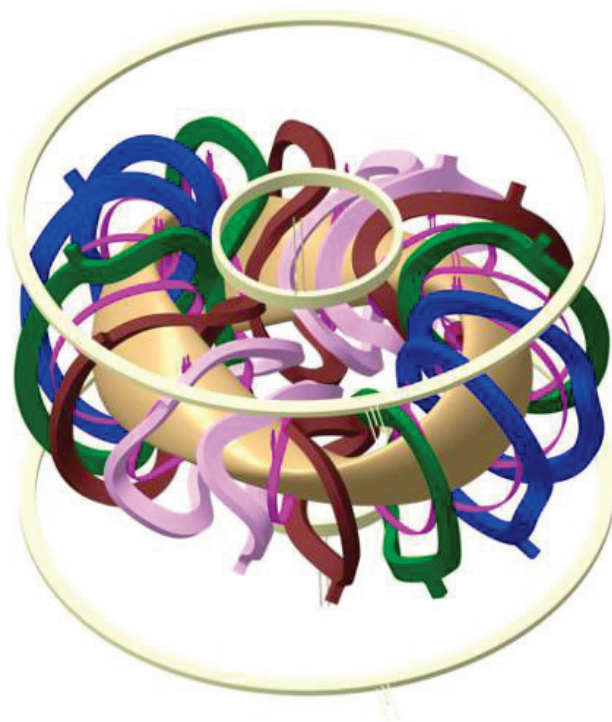


SIGNATURES		DATE	SIZE	UNIT	 CFQS BODY_1
DWG	S. Kinnablia	2020-08-05	A1	mm	
CHKD		2020-##-##			
APPD		2020-##-##			
NIFS				Q-CFQS-BODY_1-20200904	
					Rev.
					1

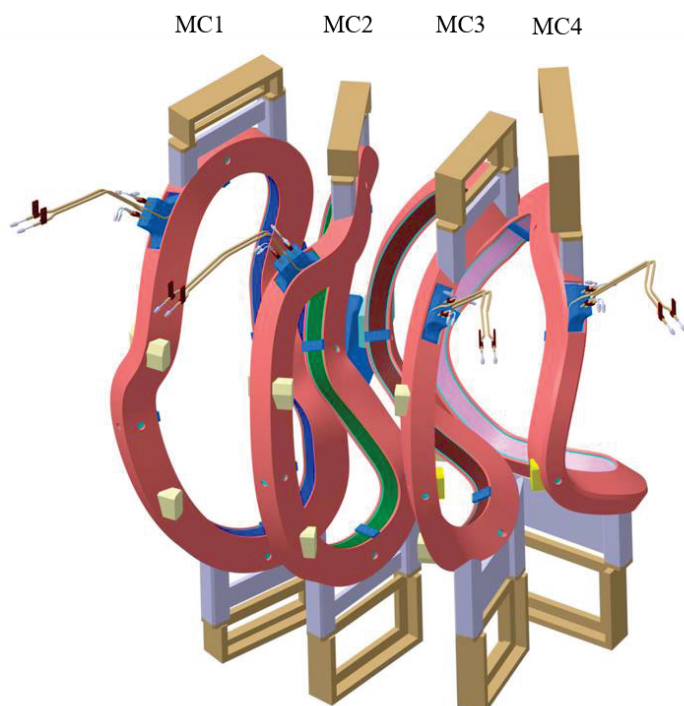


SIGNATURES		DATE	REV	CFQS
DWG	S. Escobedo	2020/04/05	A1	thd
CHKD		2020/04/05		
APPD		2020/04/05		
NIFS				Q-CFQS-BODY_1-20200904
				Sh. Rev.

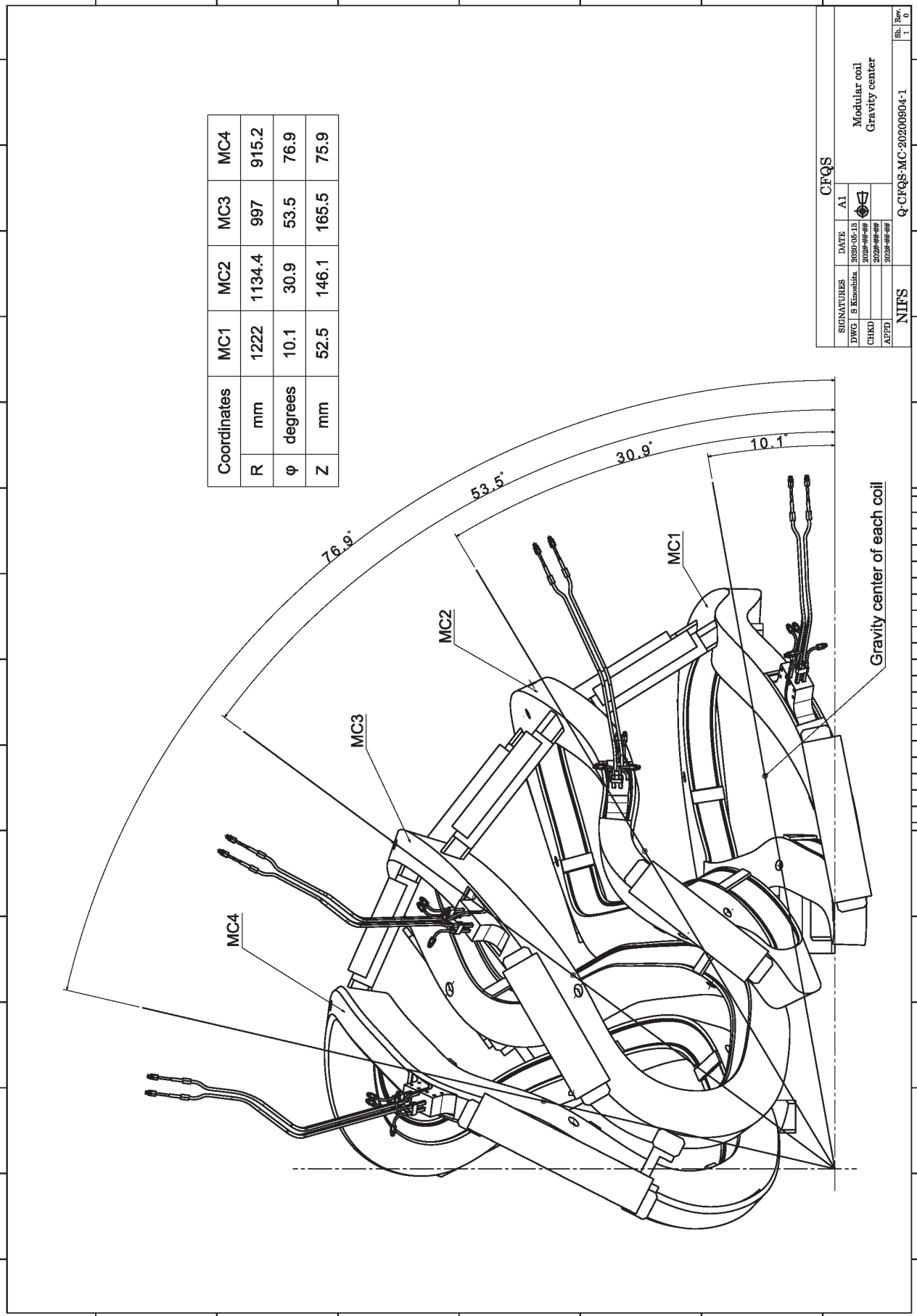
2 Coils



2.1 Modular coil



Coil name	Thickness of coil case (mm)
MC1	10
MC2	10
MC3	10
MC4	13



Coordinates		MC1	MC2	MC3	MC4
R	mm	1222	1134.4	997	915.2
ϕ	degrees	10.1	30.9	53.5	76.9
Z	mm	52.5	146.1	165.5	75.9

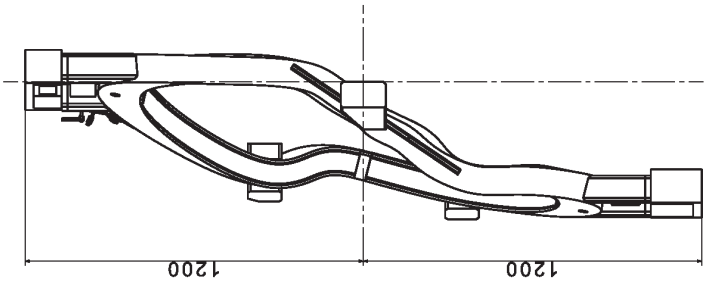
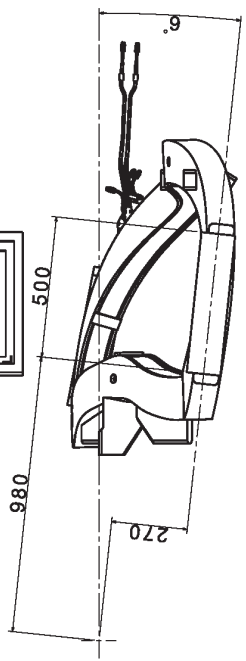
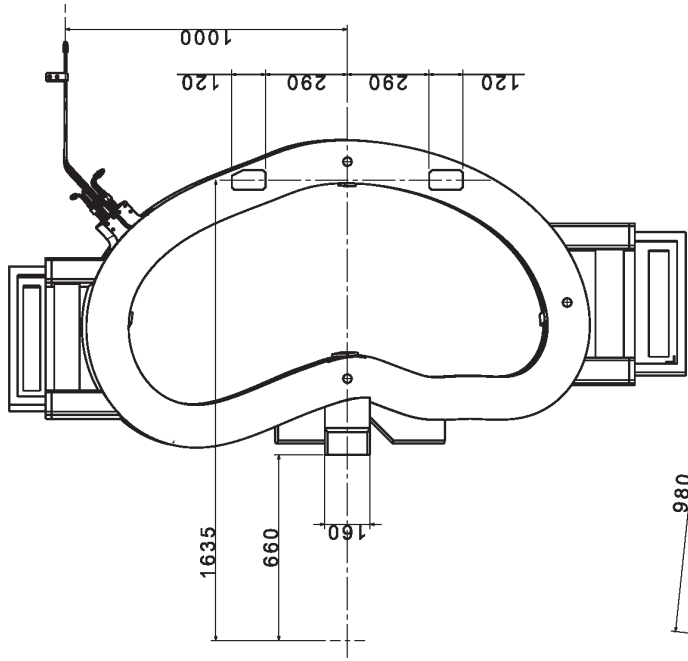
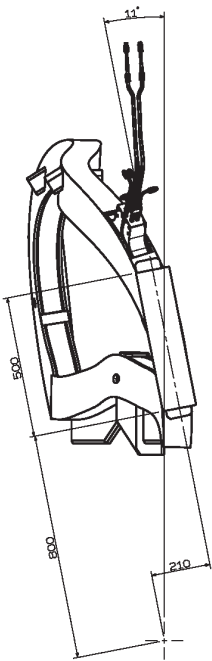
SIGNATURES		DATE	CFQS
DWG	S. Khandekar	2020-09-10	A1
CHKD		2020-09-10	
APRD		2020-09-10	

NIFS

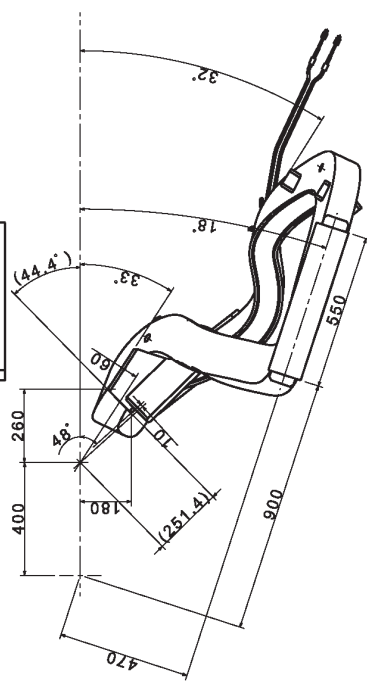
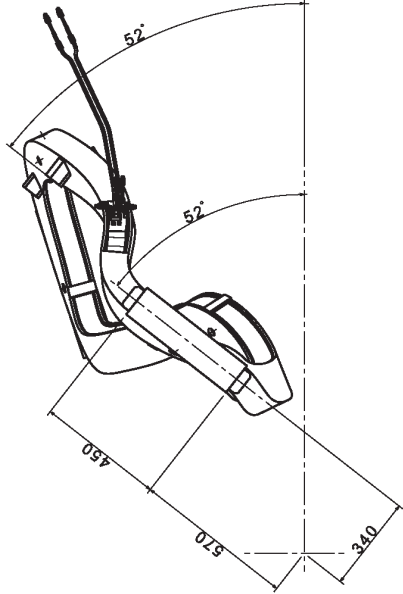
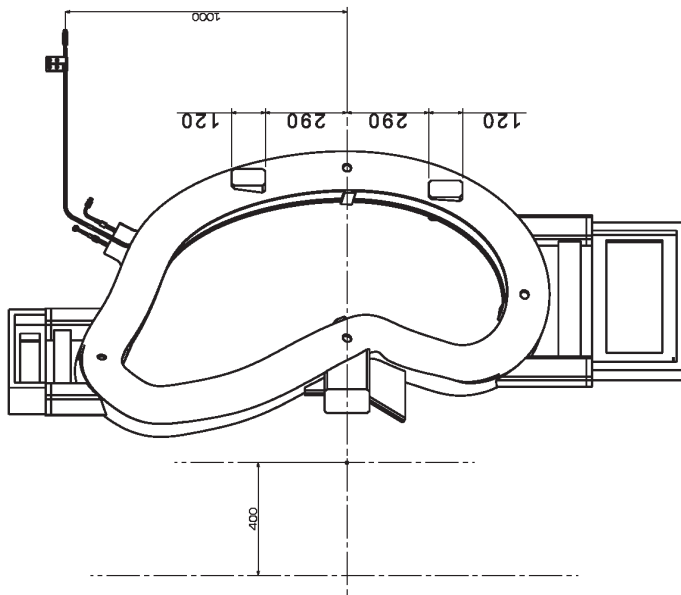
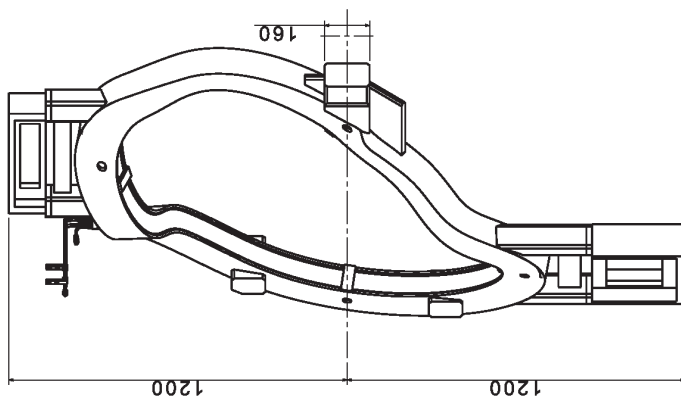
Modular coil
Gravity center

Q-CFQS-MC-20200904-1

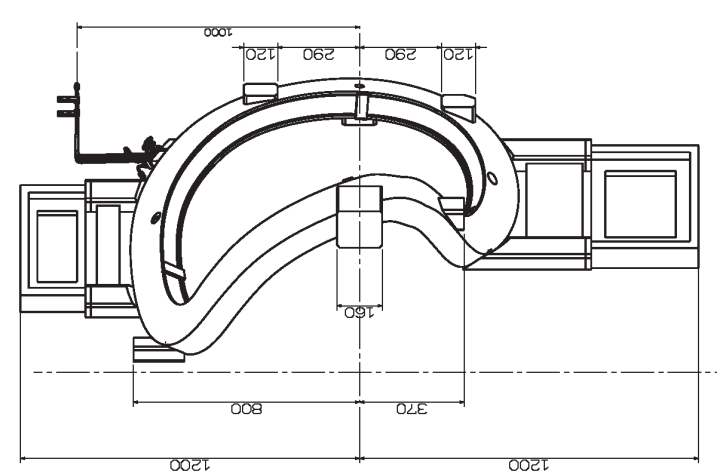
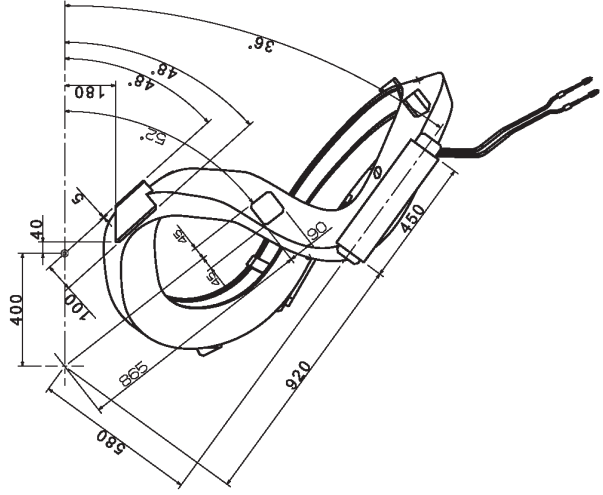
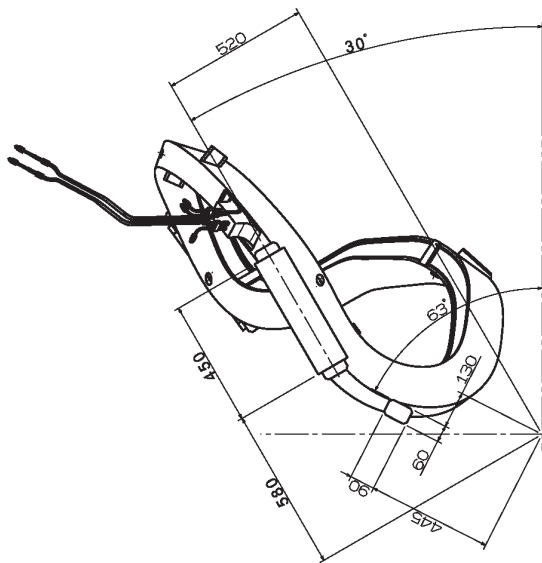
(Sh) Rev. 0
1




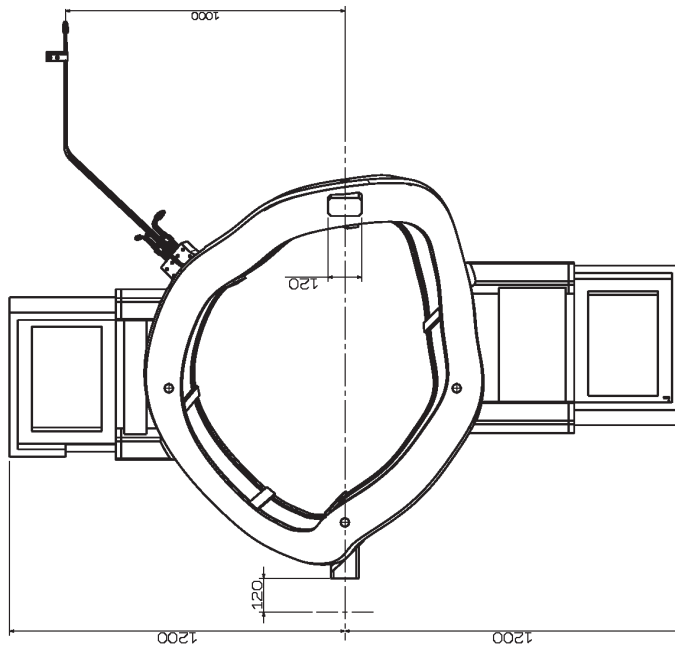
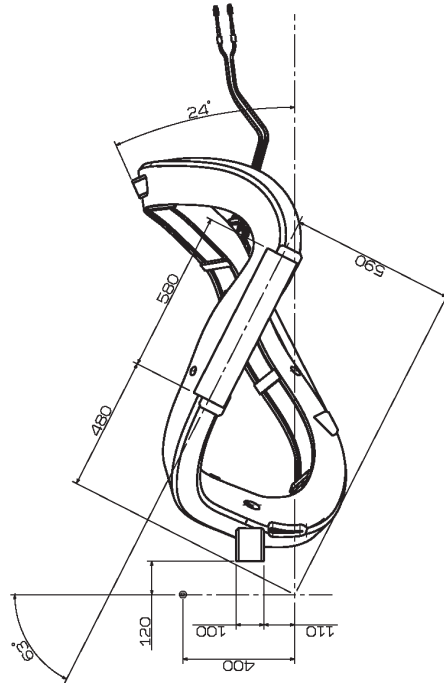
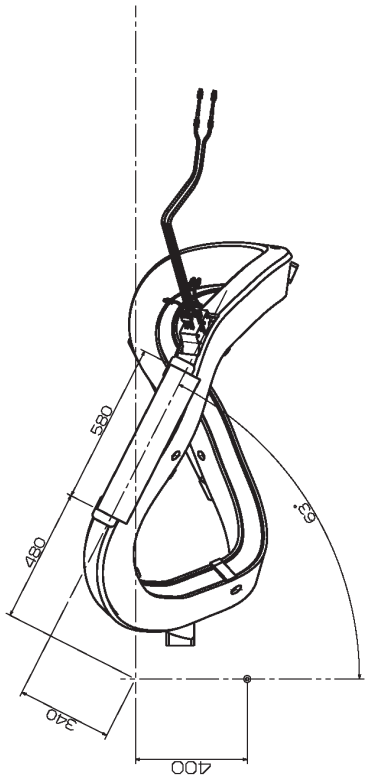
SIGNATURES		DATE	AI		Modular coil MC1
DWG	S Kinoshita	2020-05-13			
CHKD		2020-##-##			
APPD		2020-##-##			
NIFS				Q-CFQS-MC-20200904-1	Sh. Rev.
					1 0



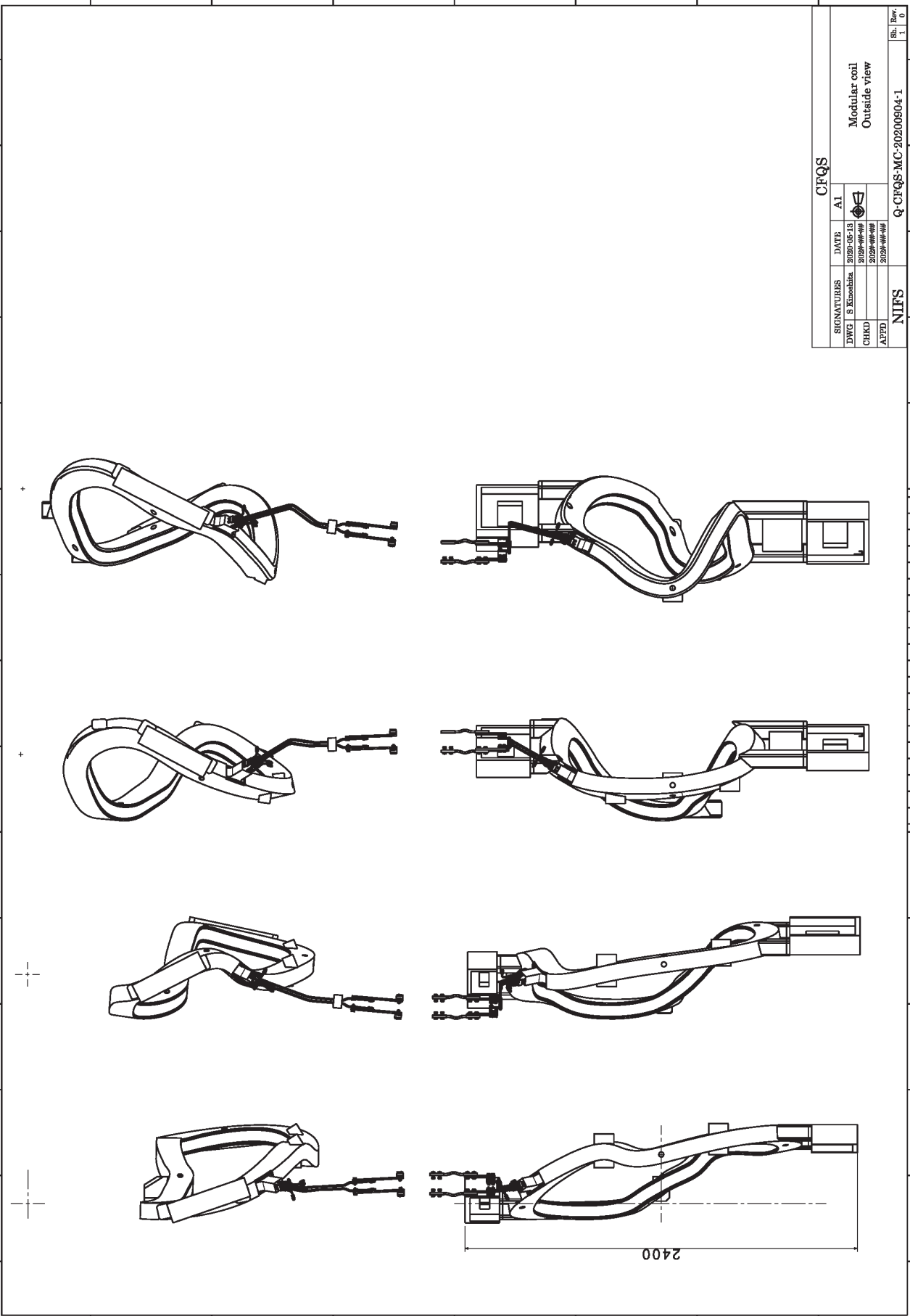
SIGNATURES		DATE	CFQS
DWG	J S Kandaia	2020/07/13	A1
CHKD		2020/07/13	
APPD		2020/07/13	
NIFS			Q-CFQS-MC-20200513-1
Modulat coil MC2			Rev 4
			0



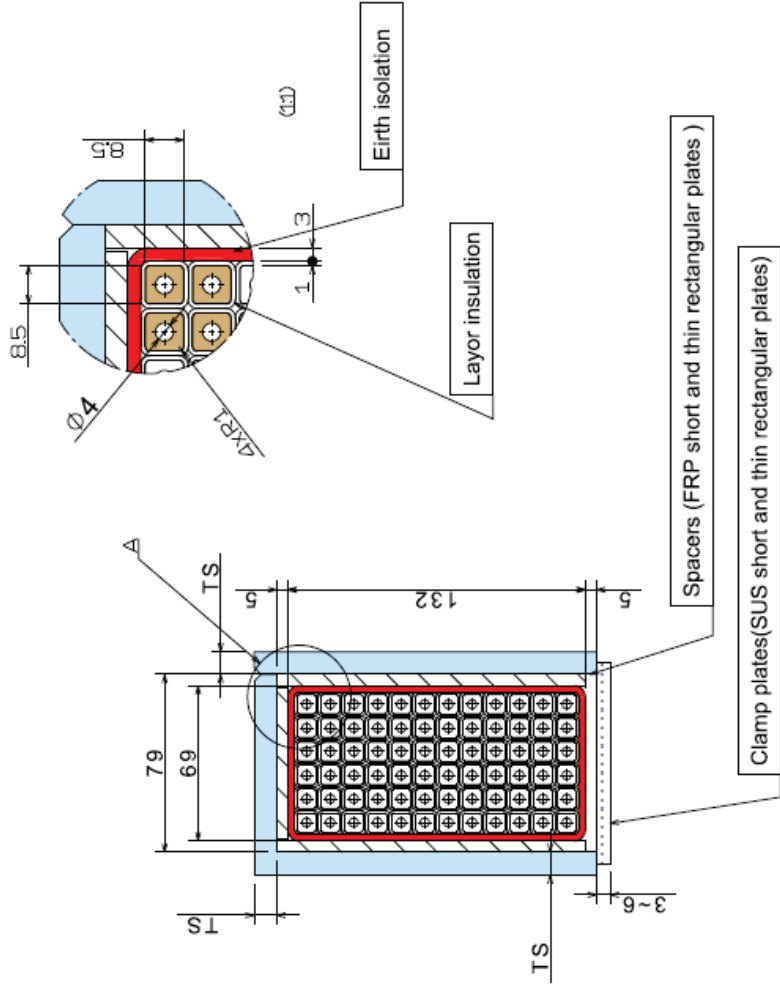
SIGNATURES		DATE	A1	 Modulate coil MC3
DWG	S. Kinnabita	2020-06-18		
CHKD		2020-##-##		
APPR		2020-##-##		
NIFS				Q-CFQS-MC-20200518-1
				Sh. 4 of 0



SIGNATURES		DATE	A1	 Modulat coil MC4
DWY	S. Kinnala	2020-02-13		
CHKD		2020-04-01		
APPD		2020-04-01		
NIFS				Q-CFQS-MC-20200513-1
				Sh. Rev.
				4 0

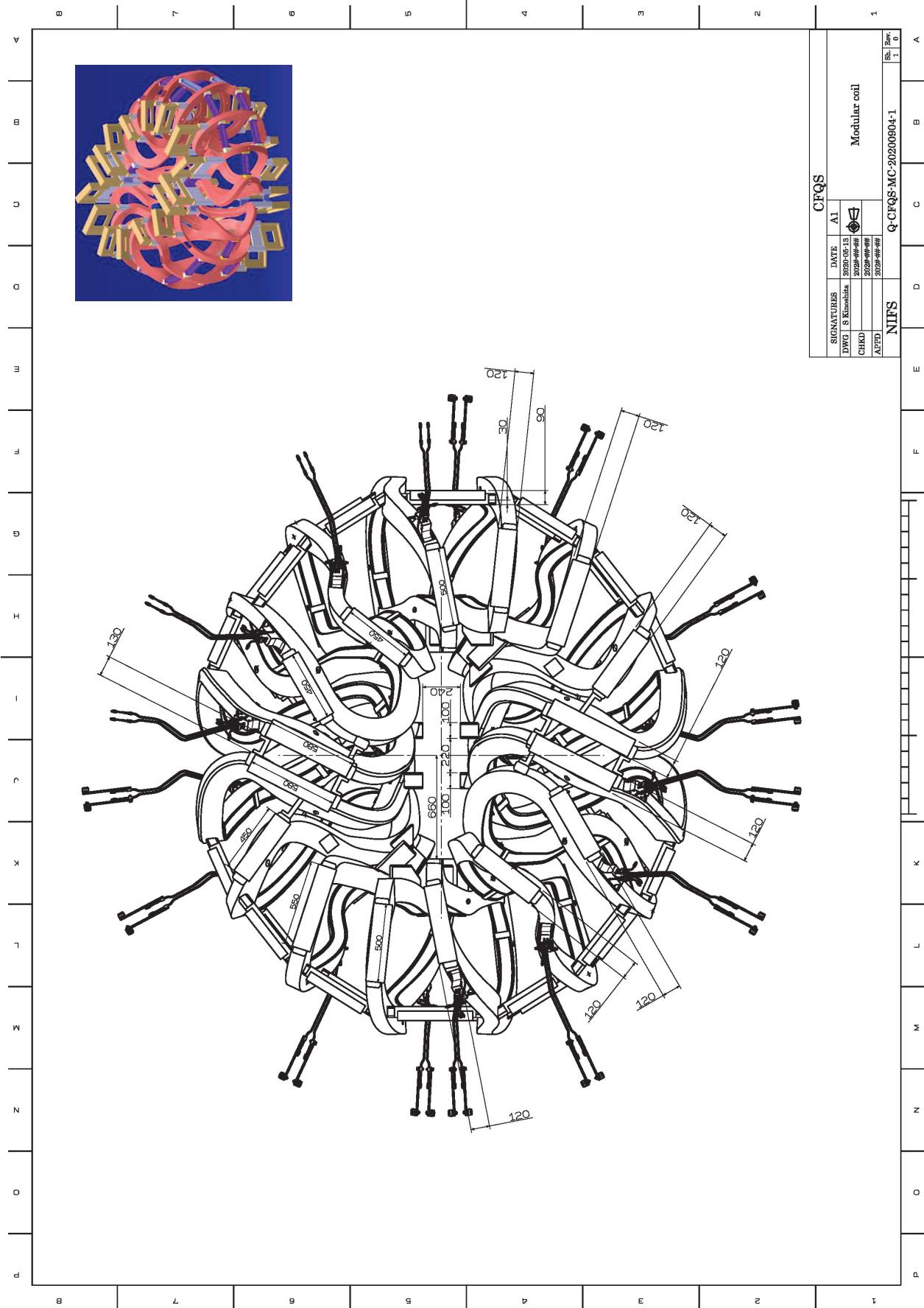


SIGNATURES		DATE	AI		Modular coil Outside view
DWG	S. Kishimoto	2020-06-15			
CHKD		2020-##-##			
APPD		2020-##-##			
NIFS		Q-CFQS-MC-20200904-1			(Rev.) 1 0

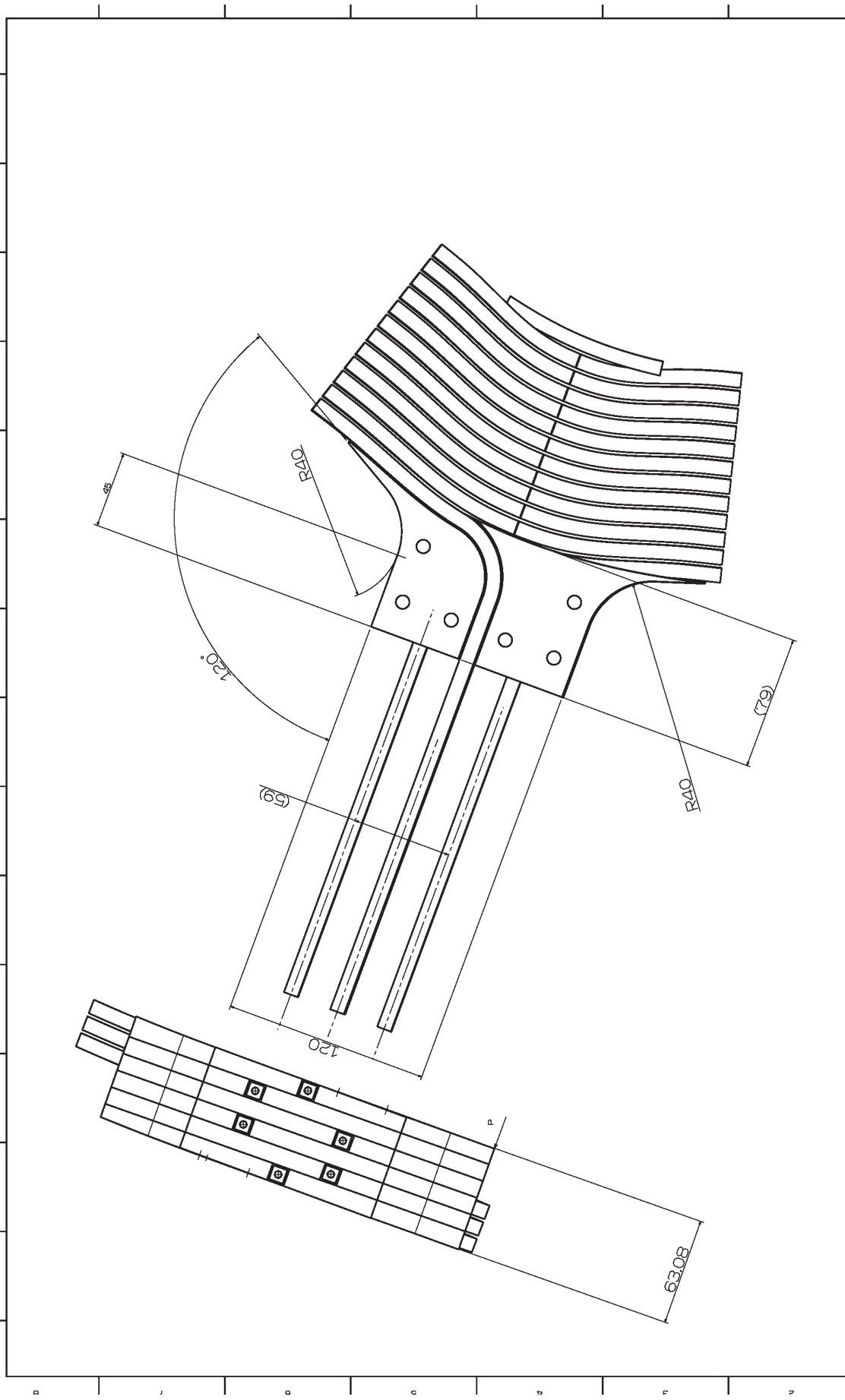


CFQS

SIGNATURES		DATE	A3	TITLE
DWG	S Kinoshita	2020-05-13		Modular coil Cross section
CHKD		202#-##-##	1:2	
APPD		202#-##-##		
NIFS			S-CFQS-MC-20200513-SK2	
				Rev. 0



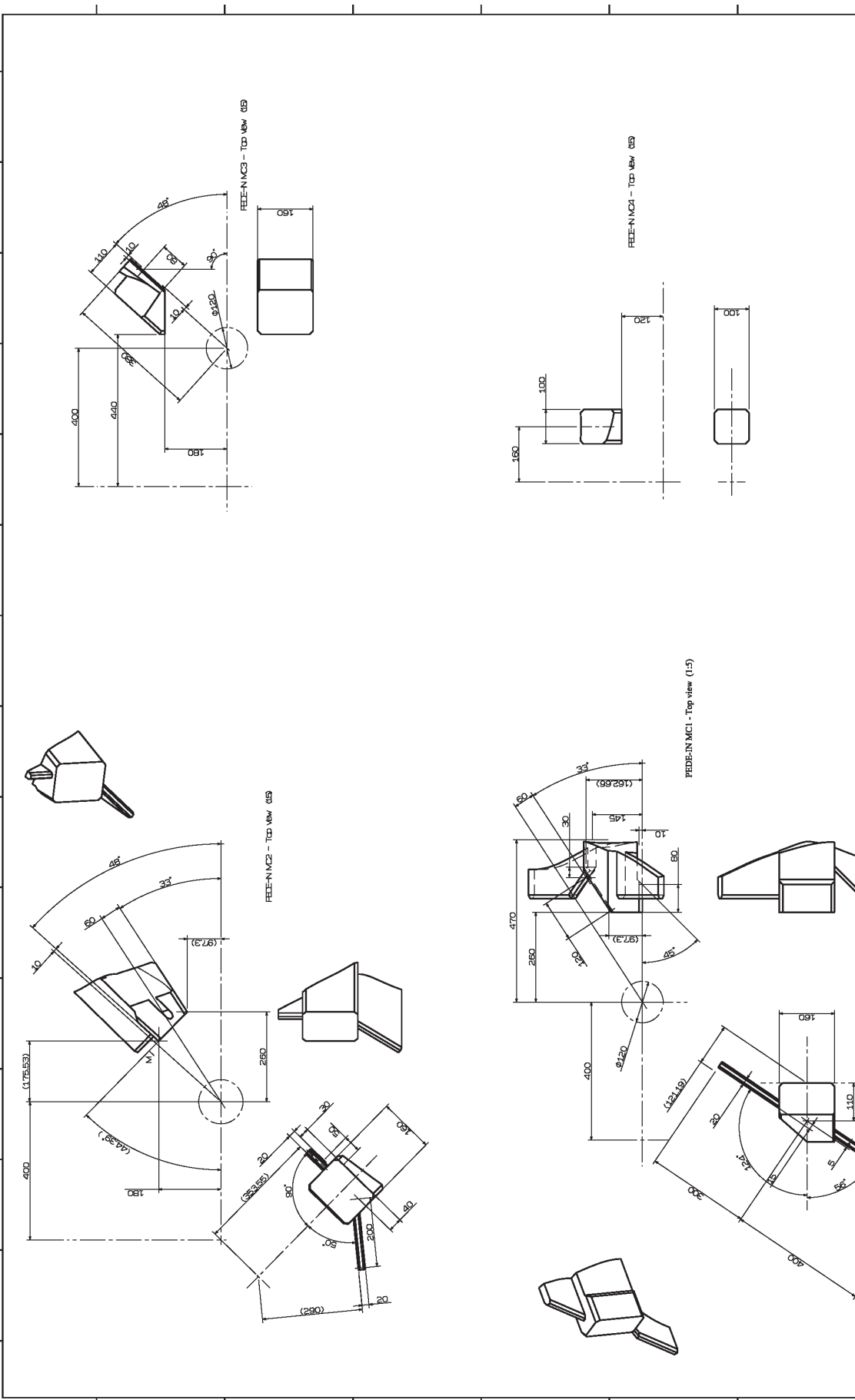
SIGNATURES		DATE		A1	
DWG S. Kurohata		2020-06-18			
CHEK		2020-##-##			
AUTD		2020-##-##			
NIFS		CFQS			
Modular coil					
Q-CFQS-MC-20200604-1					
					Rev.
					1 1 0



SIGNATURES		DATE	AI
DWC	S. Kumbhila	2020-05-13	
CHKD		2020-##-##	
APPD		2020-##-##	

CFQS

Modular coil Winding end	
NIFS	
Q-CFQS-MC-202006113-SKI	
Sh.	Rev.
6	0



SIGNATURES		DATE	AI
DWG	J S Kinnala	2020-07-15	
CHKD		2020-07-15	
APPD		2020-07-15	

CFQS

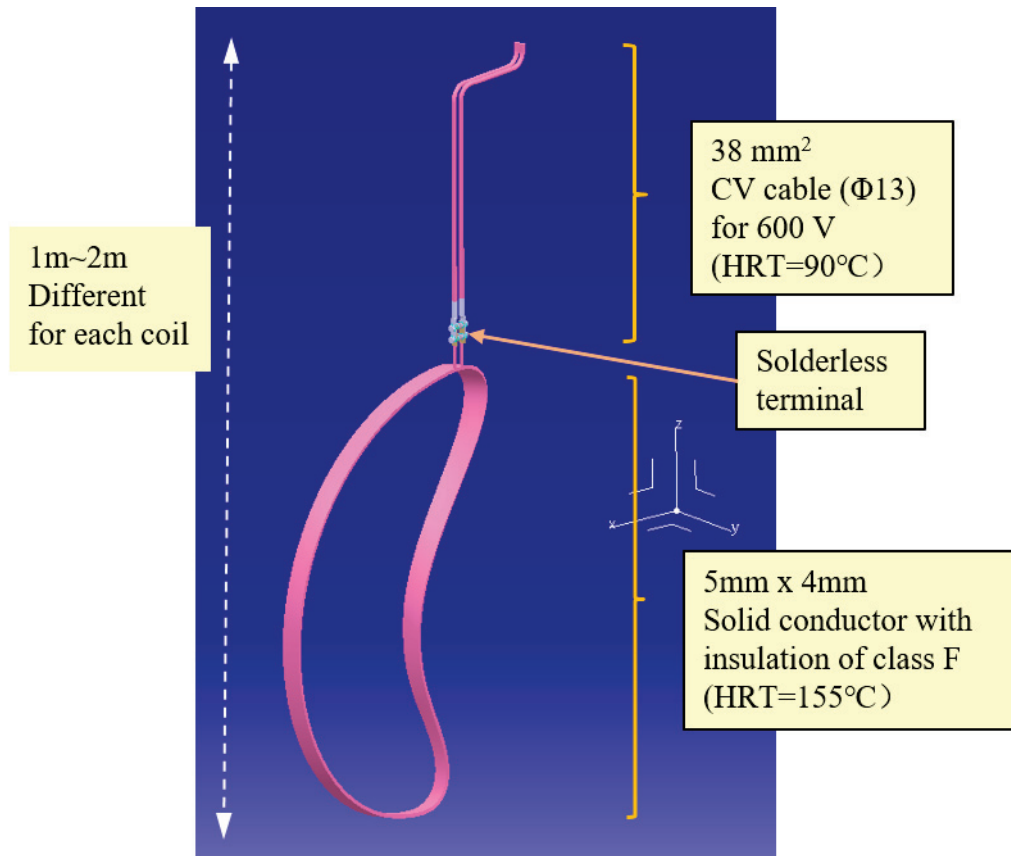
**SUPPORT STRUCTURE
FOR MODULAR COIL**

NIFS

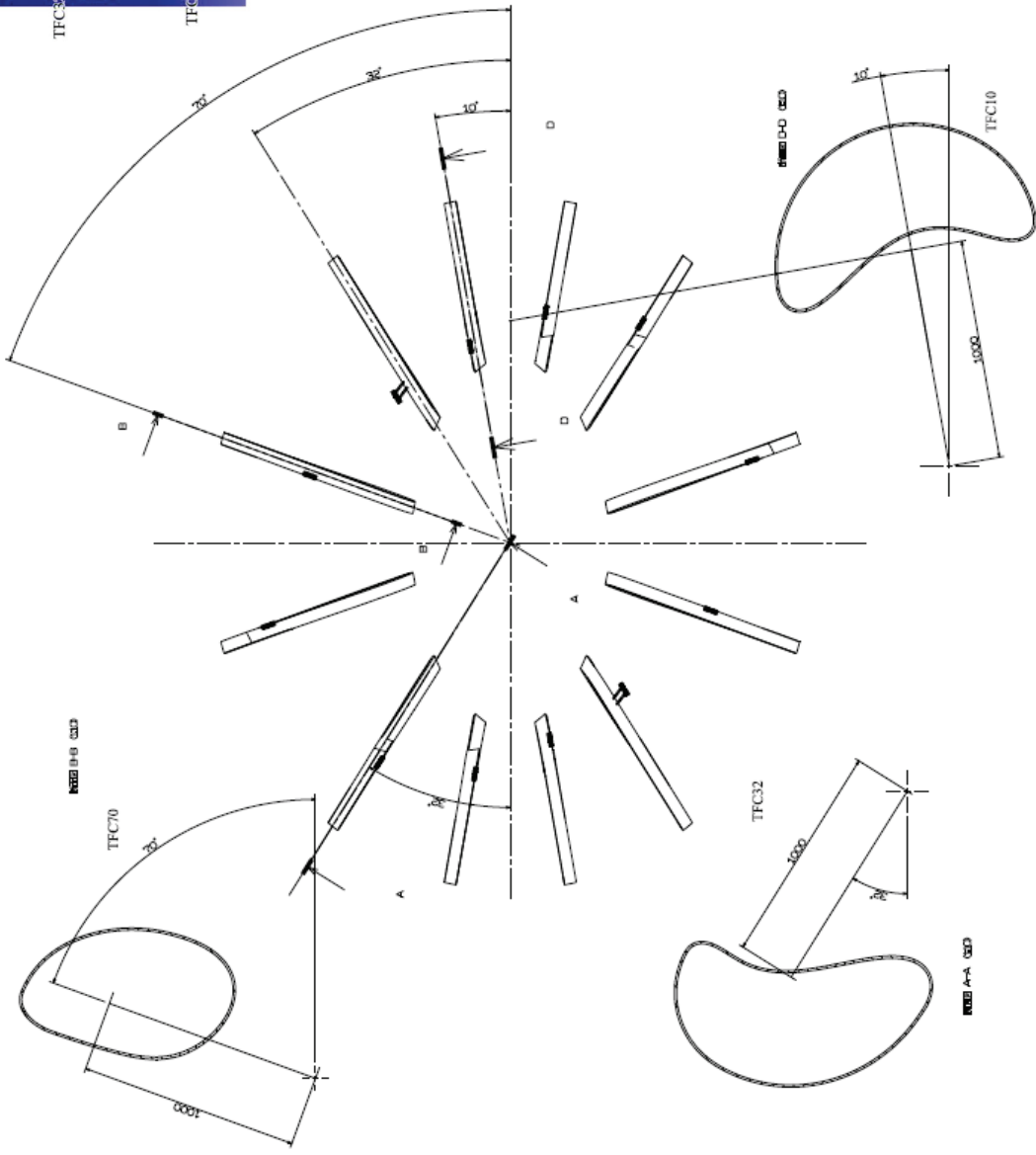
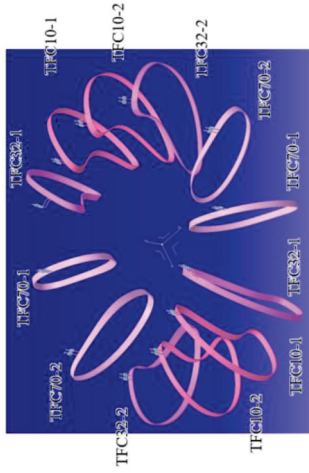
Q-CFQS-SP-202006118-SKI

Rev	1	0
-----	---	---

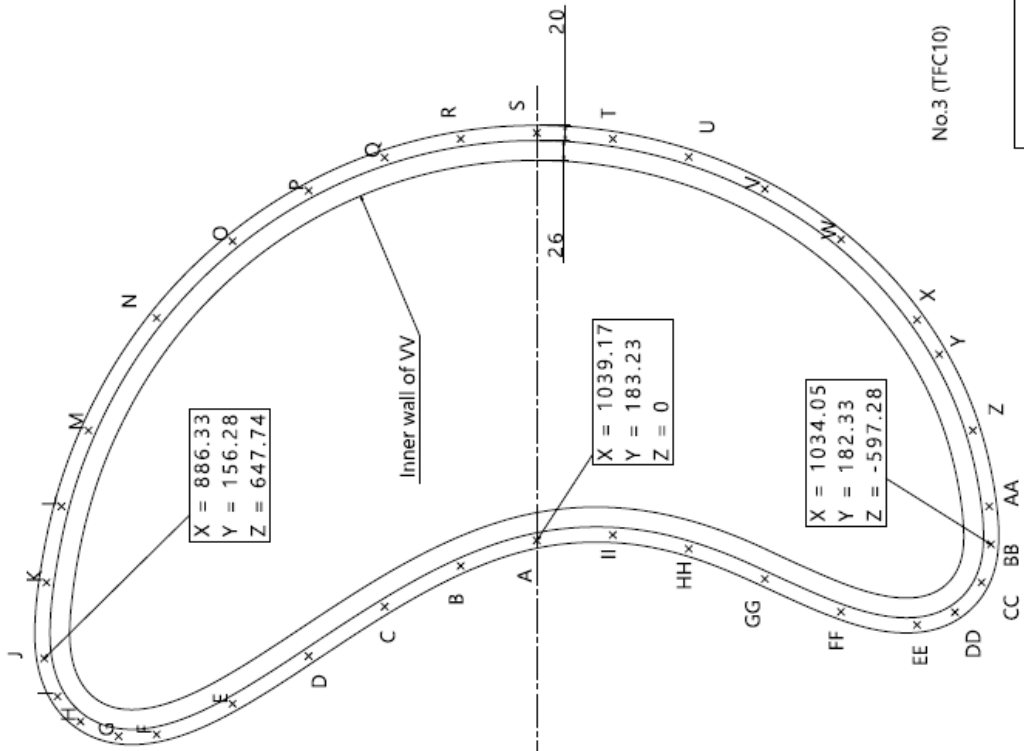
2.2 Toroidal field coil



HRT; Heat-resistant temperature



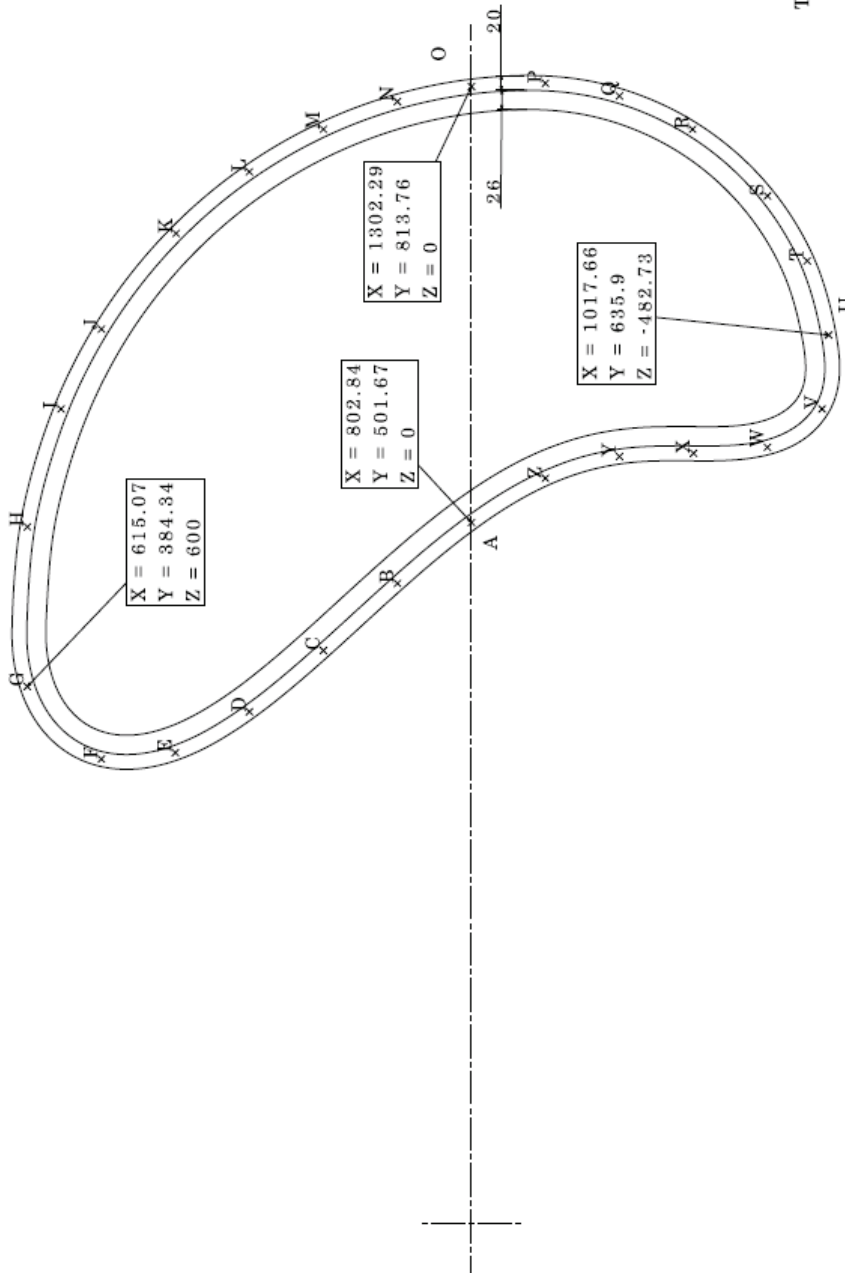
No	記号	X	Y	Z	R	S
1	A	1039.21832	0	1055.2	0	0
2	B	1006.21774	100	1021.8	105.4	
3	C	953.21681	200	968	219	
4	D	889.51568	300	903.2	338.2	
5	E	827.61459	400	840.4	456.2	
6	F	787.81389	500	800	564.1	
7	G	785.61385	550	797.7	614.1	
8	H	804.61419	600	817	667.7	
9	I	837.1147.6	630.2	850	712.4	
10	J	886.3156.3	647.7	900	765.4	
11	K	984.8173.6	644.8	1000	865.5	
12	L	1083.3191	625	1100	967.4	
13	M	1181.8208.4	589.6	1200	1073.5	
14	N	1327.5234.1	500	1348	1246.5	
15	O	1426.8251.6	400	1448.8	1388.5	
16	P	1492.5263.2	300	1515.5	1508.7	
17	Q	1535.2270.7	200	1558.9	1617.7	
18	R	1559.4275	100	1583.4	1720.7	
19	S	1567.1276.3	0	1591.2	1821	
20	T	1559.3275	-100	1583.4	1921.3	
21	U	1536270.8	-200	1559.7	2024.1	
22	V	1494.5263.5	-300	1517.6	2132.6	
23	W	1429.3252	-400	1451.4	2252.5	
24	X	1324.9233.6	-500	1345.4	2398.2	
25	Y	1280.3225.7	-529.3	1300	2452.2	
26	Z	1181.8208.4	-573.5	1200	2561.6	
27	AA	1083.3191	-595	1100	2663.8	
28	BB	1034182.3	-597.3	1050	2713.9	
29	CC	984.8173.6	-584.9	1000	2765.4	
30	DD	946.2166.8	-550	960.8	2817.9	
31	EE	929.8164	-500	944.2	2870.6	
32	FF	946.7166.9	-400	961.3	2972.1	
33	GG	989.2174.4	-300	1004.4	3081	
34	HH	1028.4181.3	-200	1044.3	3188.6	
35	II	1046.3184.5	-100	1062.5	3290.2	
			0	1055.2	3390.5	



No.3 (TFC10)

SIGNATURES		DATE	SCALE		Toroidal field coil TFC10 Node position
DWG: E. Kimahata		2025-05-13	1:3		
CHKD:		2025-05-13	1:3		
APPD:		2025-05-13			
NIFS					Q-CFQS-TF-20200513-3
					Rev. 1 1 3

NO	X	Y	Z
A	802.84	501.67	0
B	733.1	458.09	100
C	656.12	409.99	200
D	586.03	366.19	300
E	538.99	336.8	400
F	531.85	332.34	500
G	615.07	384.34	600
H	797.83	498.54	600
I	932.85	582.91	554.43
J	1024.29	640.05	500
K	1134.06	708.64	398.97
L	1204.59	752.71	300
M	1253.33	783.17	200
N	1285.05	802.99	100
O	1302.29	813.76	0
P	1305.96	816.05	-100
Q	1291.49	807.01	-200
R	1253.33	783.17	-298.76
S	1176.96	735.44	-400
T	1102.46	688.9	-453.63
U	1017.66	635.9	-482.73
V	932.85	582.91	-473.75
W	888.93	555.47	-400
X	882.12	551.21	-300
Y	878.45	548.92	-200
Z	853.56	533.37	-100

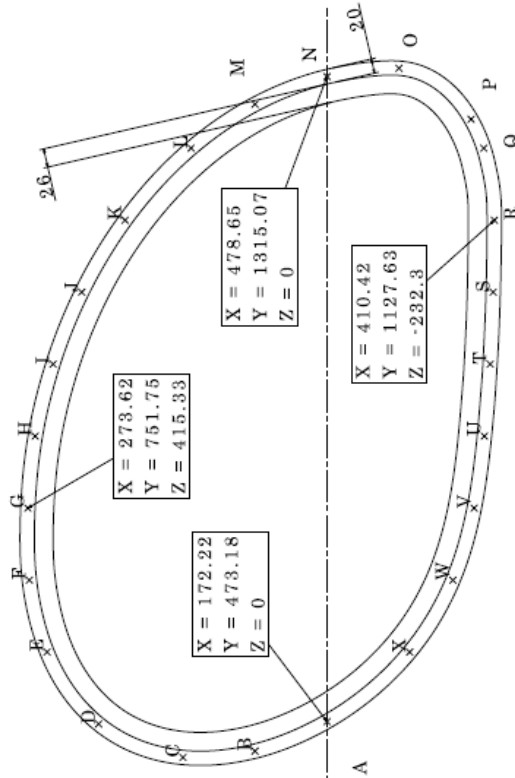


TFC32(No.2)

SIGNATURES		DATE	SCALE
DESIGN	S. Kumbar	2025-05-13	1:3
CHECKED		2025-05-13	
APPROVED		2025-05-13	

CFQS	
NO	AI
Toroidal field coil	
TFC32	
Node position	
NIFS	Q-CFQS-TF-20200513-3

NO	X	Y	Z
A	172.22	473.18	0
B	158.14	434.48	100
C	155.14	426.24	200
D	171.01	469.85	317.1
E	205.21	563.82	388.71
F	239.41	657.78	413.26
G	273.62	751.75	415.33
H	307.82	845.72	405.06
I	342.02	939.69	380.51
J	376.22	1033.66	340.54
K	410.42	1127.63	280.41
L	444.63	1221.6	188.76
M	465.5	1278.96	100
N	478.65	1315.07	0
O	482.65	1326.07	-100
P	458.38	1259.38	-200
Q	444.63	1221.6	-217.67
R	410.42	1127.63	-232.3
S	376.22	1033.66	-230.75
T	342.02	939.69	-226.4
U	307.82	845.72	-218.49
V	273.62	751.75	-204.41
W	239.41	657.78	-174.84
X	205.21	563.82	-114.77



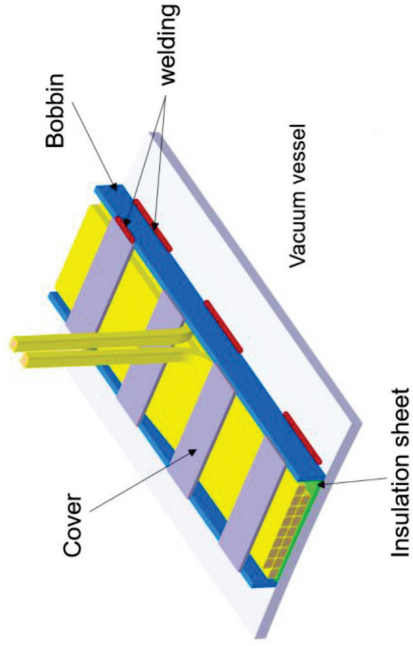
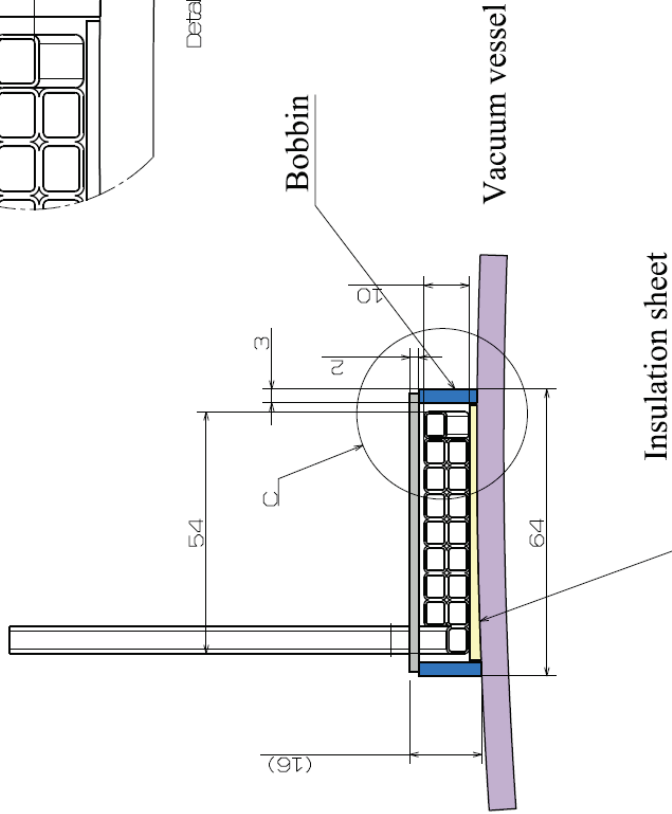
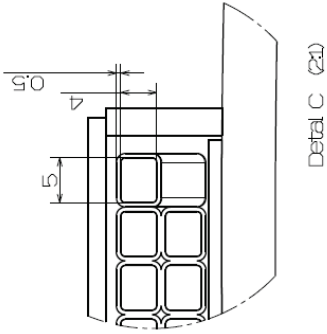
TPFC70 (No. 8)

SIGNATURES		DATE	REV	NO
DESIGN	E. Kambhata	2025-05-13	1	1
CHECK		2025-05-13		
APPD		2025-05-13		
NIFS				Q-CFQS-TP-20200513-3

CFQS
Toroidal field coil
TPFC70
Node position

Rev
1
3

Solenoid winding
8 turns x 2 solenoids
no cooling

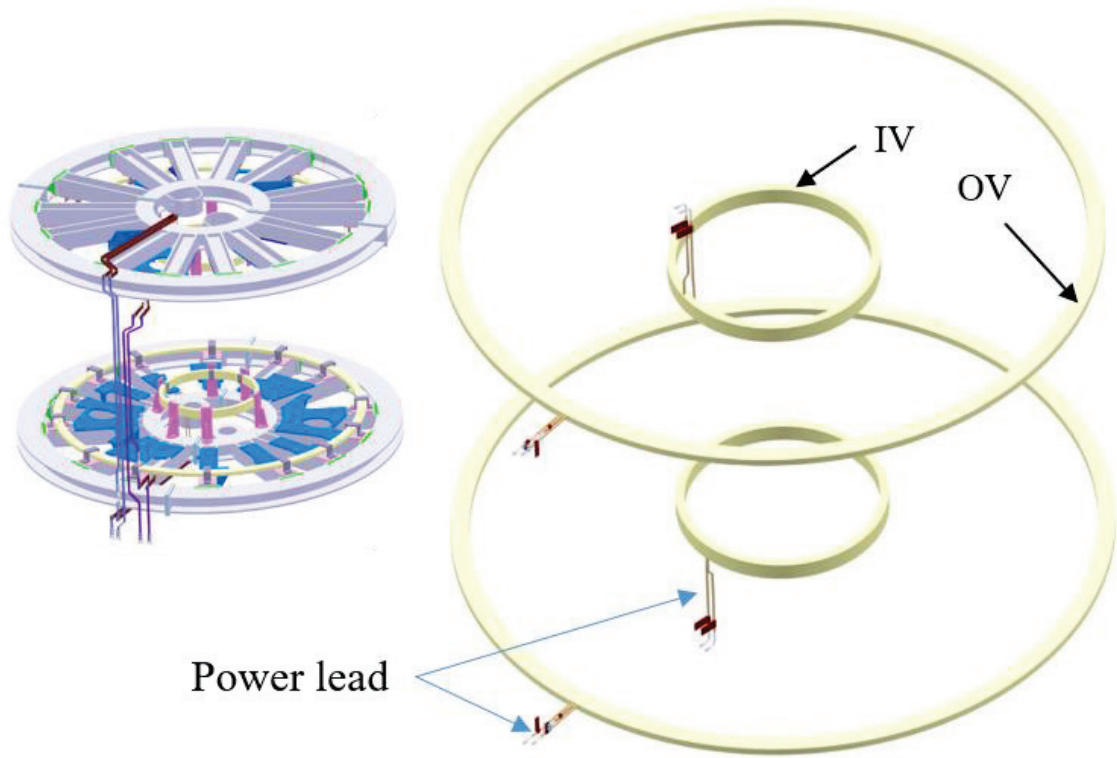


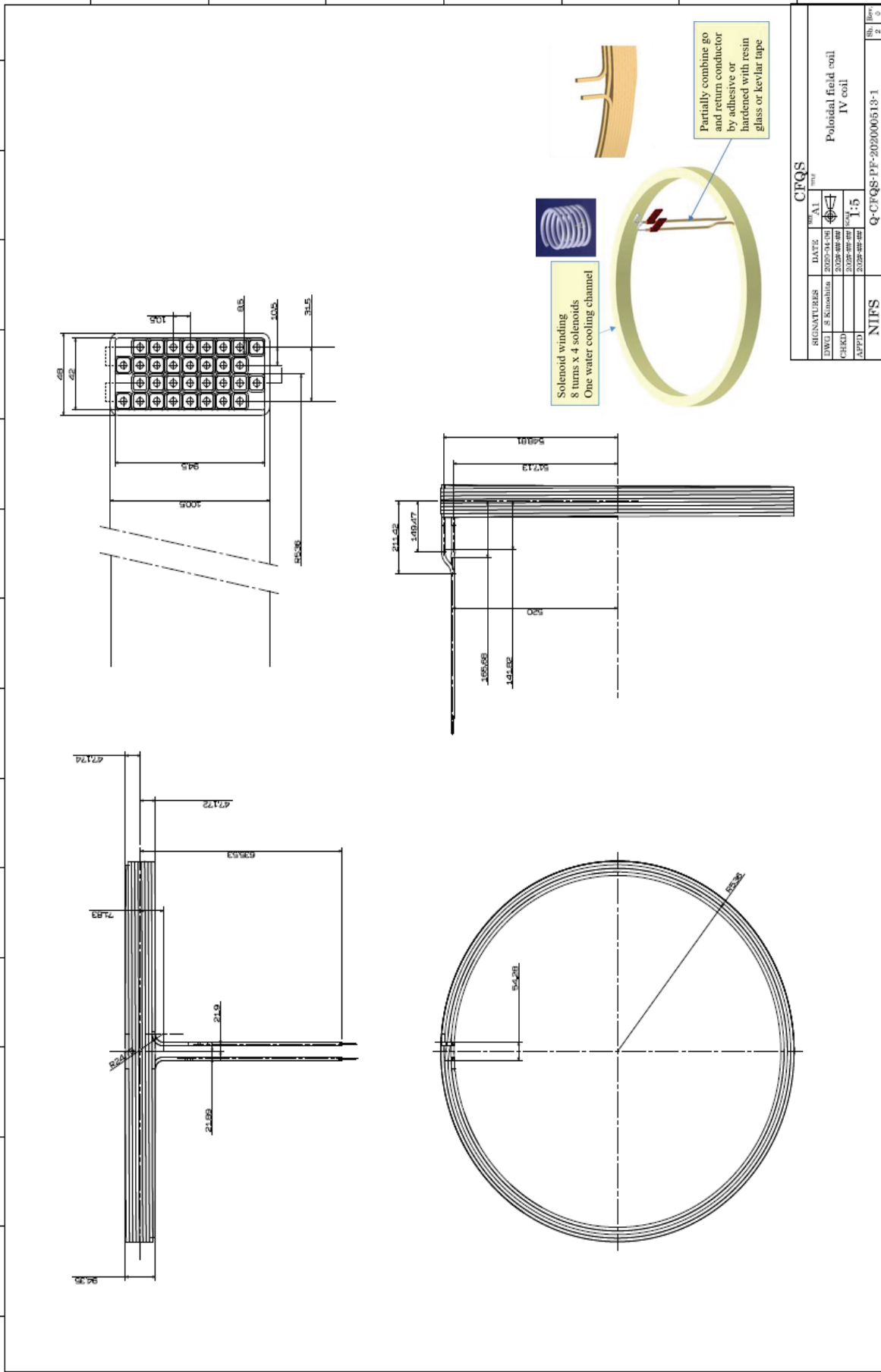
CFQS

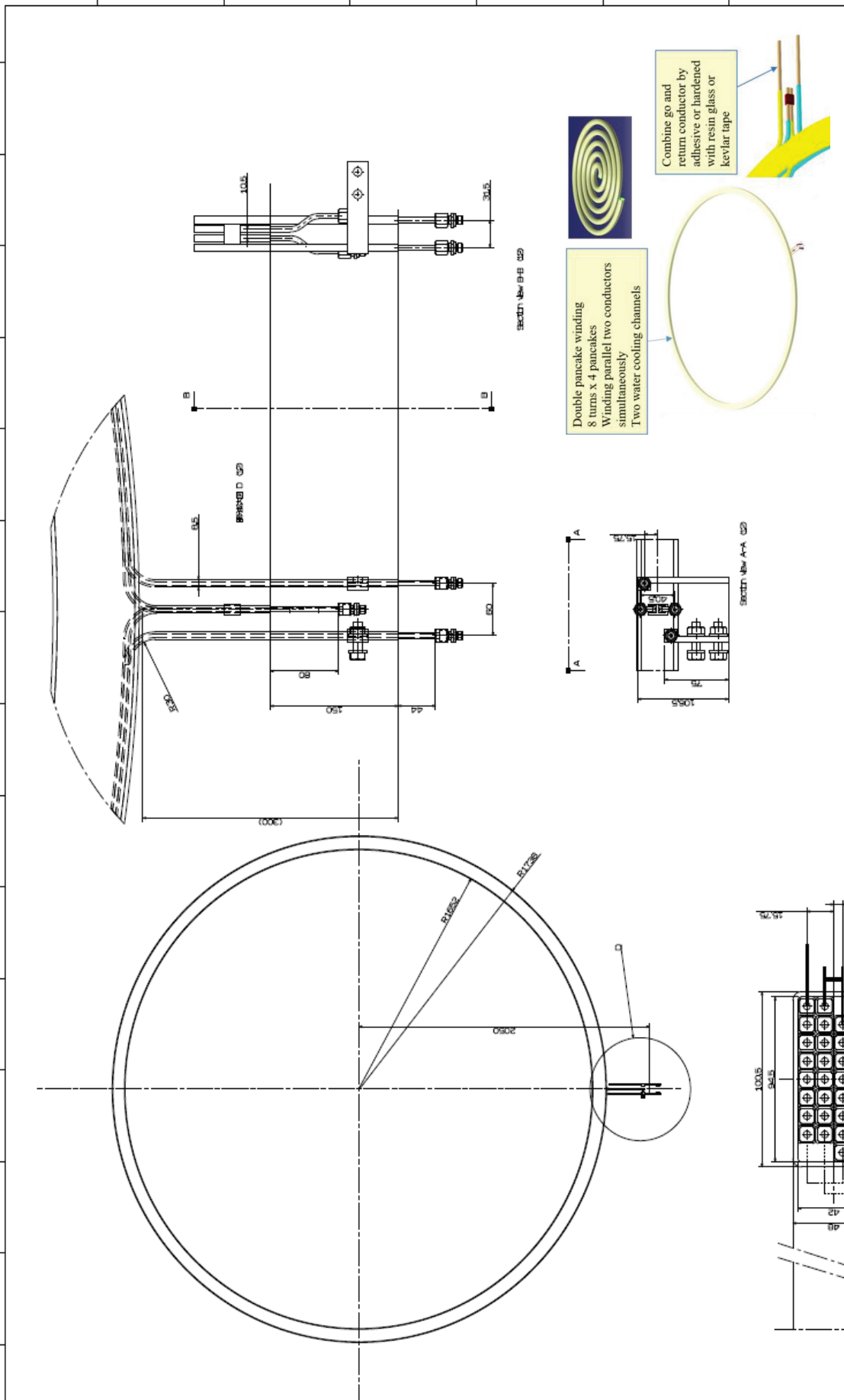
SIGNATURES	DATE	A3	TITLE
DWG S Kinoshita	2020-05-13		Toroidal field coil Cross section
CHKD	202#-##-##		
APPD	202#-##-##		
	202#-##-##		
NIFS			1:1
S-CFQS-TF-20200513-SK1			

Rev. Sh.1 0

2.3 Poloidal field coil







Double pancake winding
8 turns x 4 pancakes
Winding parallel two conductors
simultaneously
Two water cooling channels

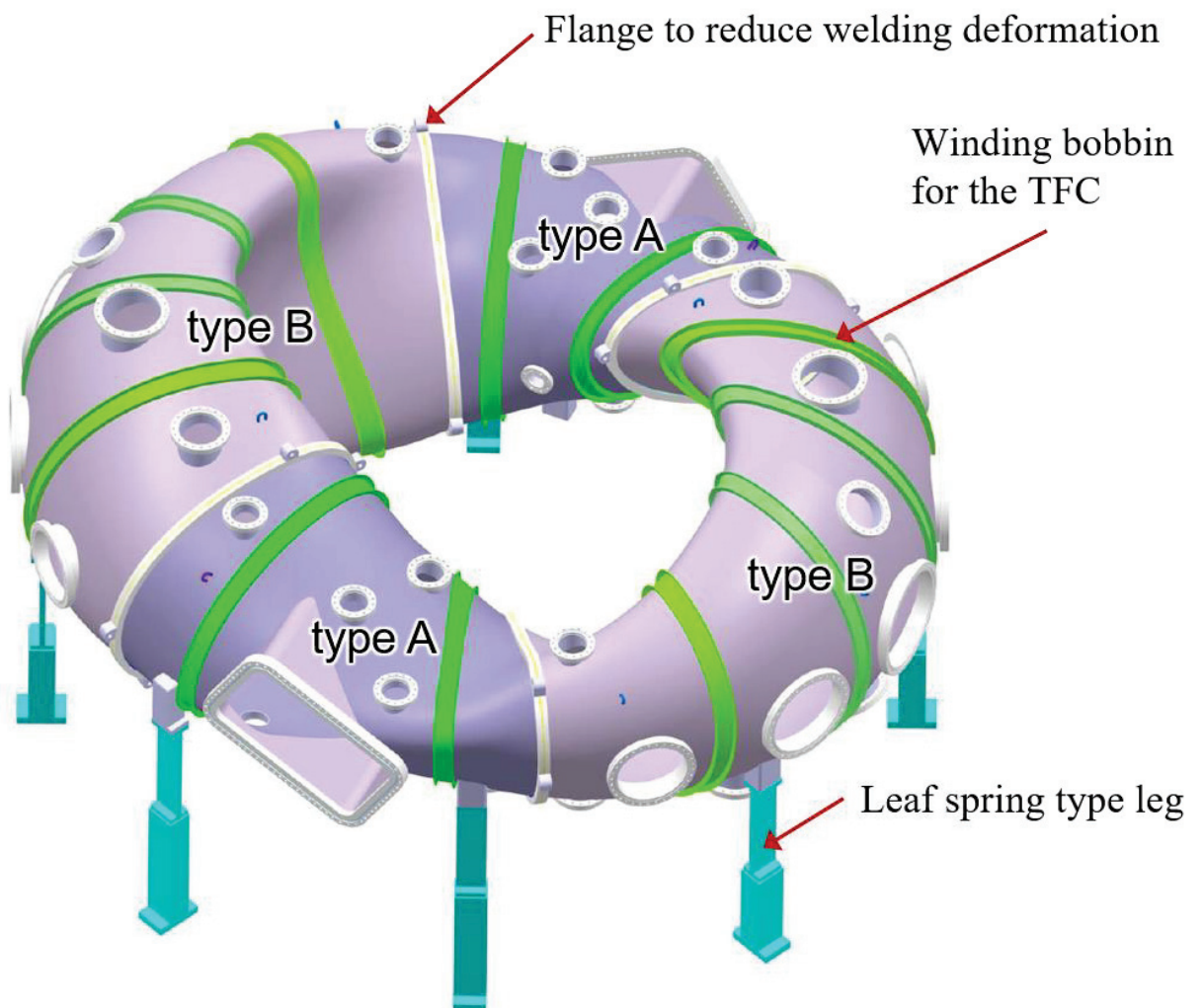
Combine go and
return conductor by
adhesive or hardened
with resin glass or
kevlar tape

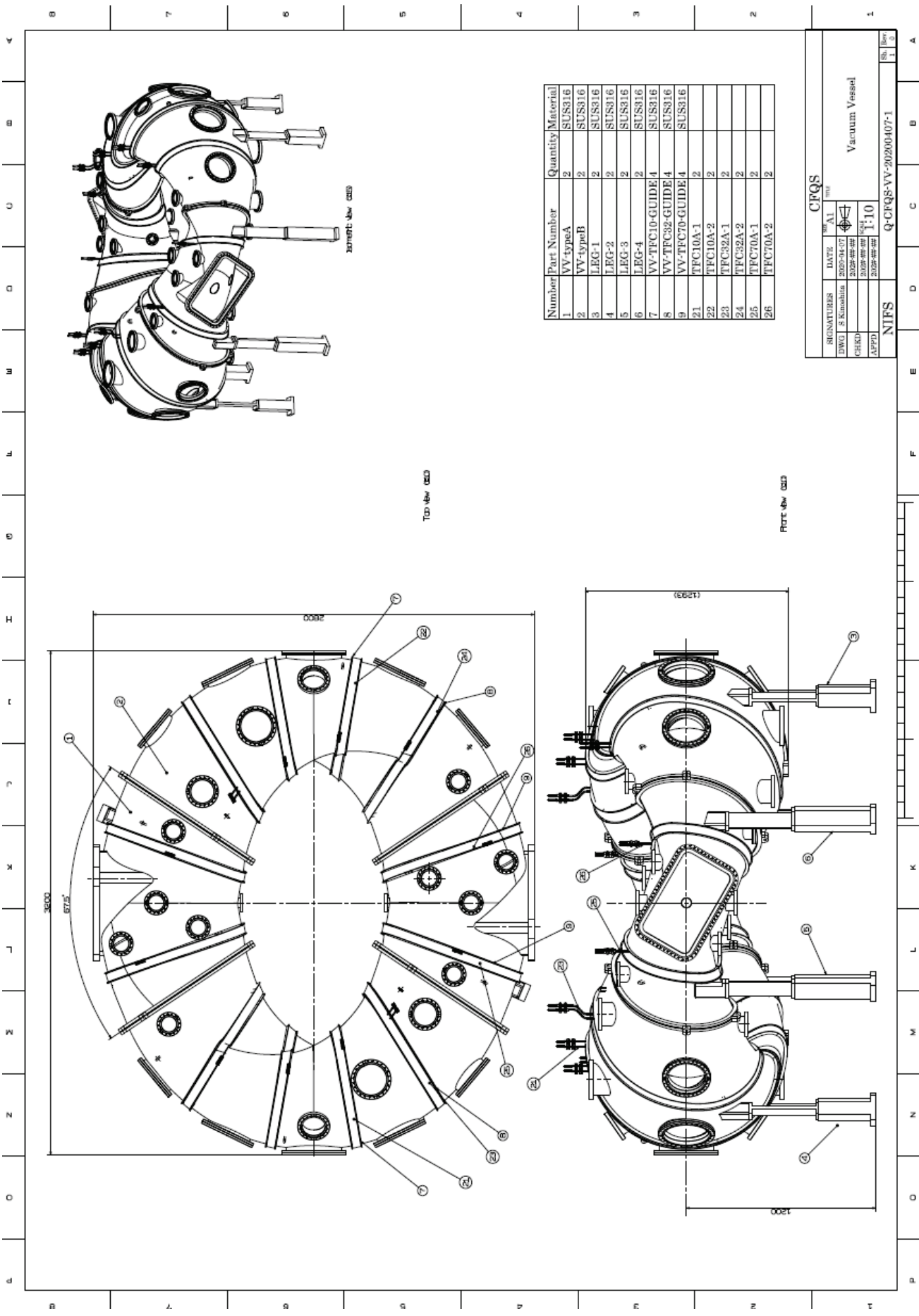
SIGNATURES		DATE		REV		CFQS	
DESIGNER	S. Kumathia	2023-11-01		01			Poloidal field coil
CHECKER		2023-11-01		02			OY coil
APPROVED		2023-11-01		03		1:12	

NIFS Q-CFQS-PF-202000513-1

3 Vacuum vessel

3.1 Main body





Number	Part Number	Quantity	Material
1	VV-typeA	2	SUS316
2	VV-typeB	2	SUS316
3	LEG-1	2	SUS316
4	LEG-2	2	SUS316
5	LEG-3	2	SUS316
6	LEG-4	2	SUS316
7	VV-TFC10-GUIDE	4	SUS316
8	VV-TFC32-GUIDE	4	SUS316
9	VV-TFC70-GUIDE	4	SUS316
21	TFC10A-1	2	
22	TFC10A-2	2	
23	TFC32A-1	2	
24	TFC32A-2	2	
25	TFC70A-1	2	
26	TFC70A-2	2	

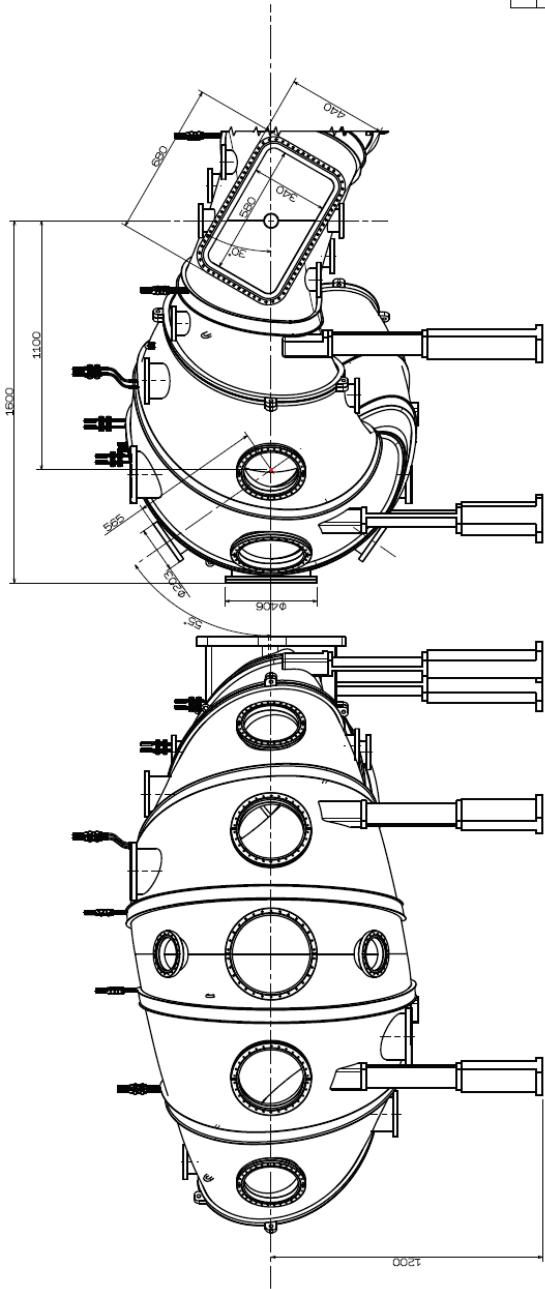
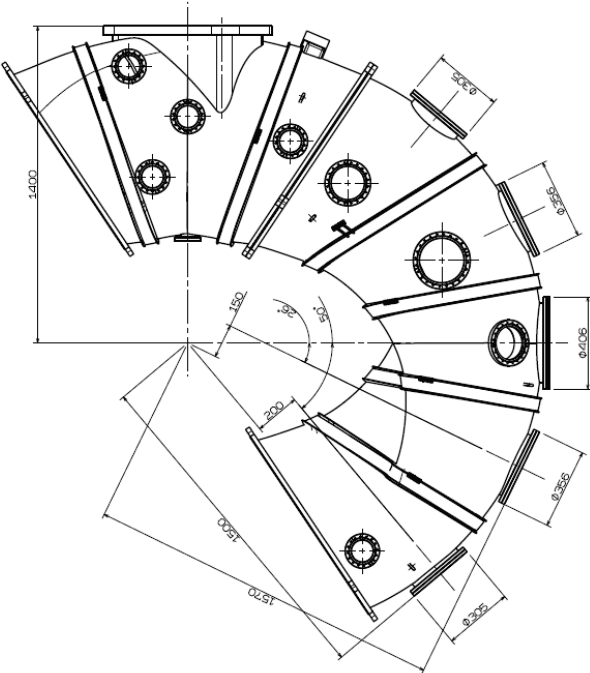
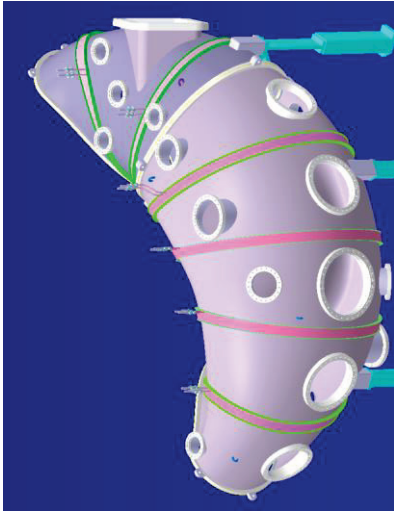
CFQS

SIGNATURES	DATE	REV	AI
DWG: S Kimoshita	2025-04-07		
CHECK:	2025-04-08		
APPD:	2025-04-08	1:10	

Vacuum Vessel

NIFS Q-CFQS-VV-20200407-1

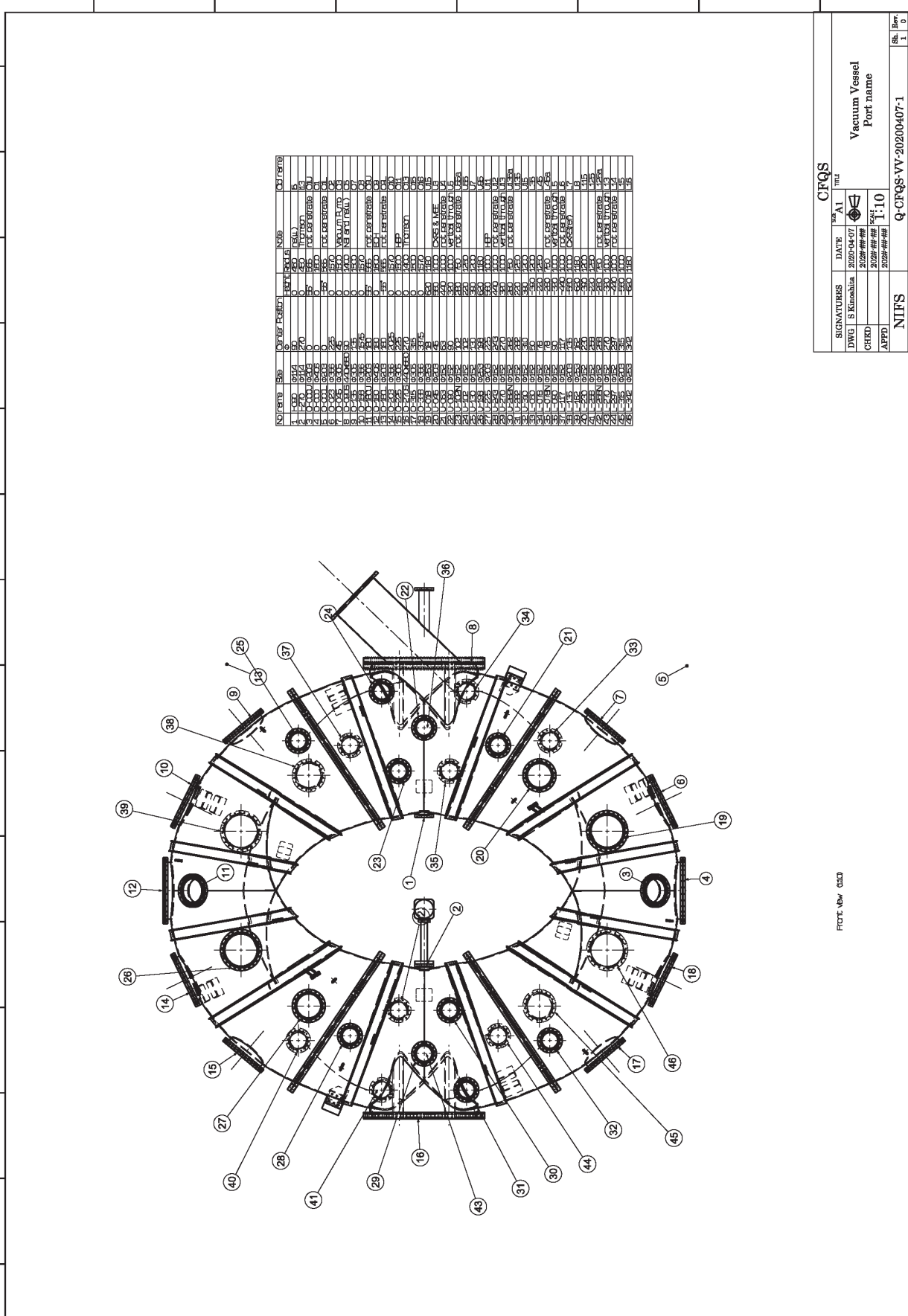
Sh. Rev. 1, 3



SIGNATURES		DATE	BY	APP'D	SCALE	CFQS MIL
DWG S Kinoshita	2020-04-07	2020-##-##	2020-##-##	2020-##-##	1:10	
NIFS						Q-CFQS-VV-20200407-1
Vacuum Vessel Horizontal Port						Sh. Rev.
						2
						0

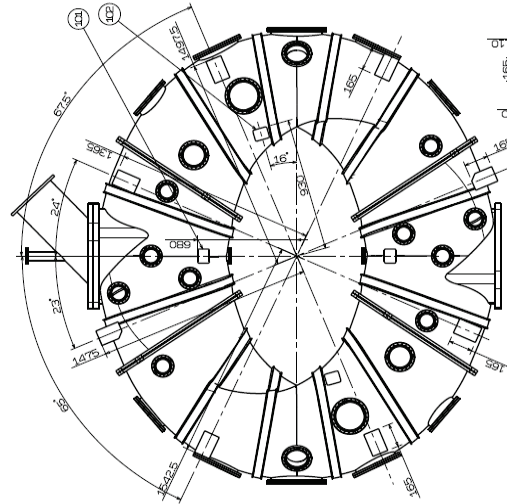
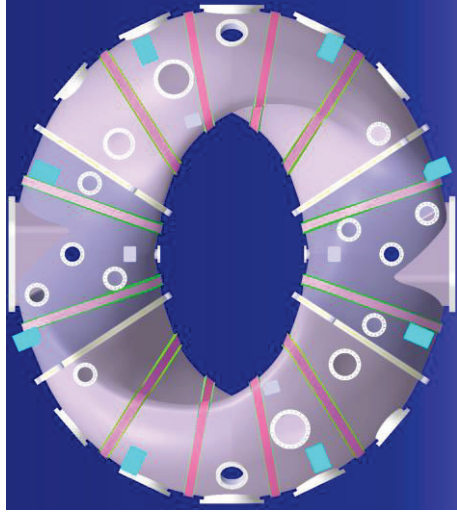
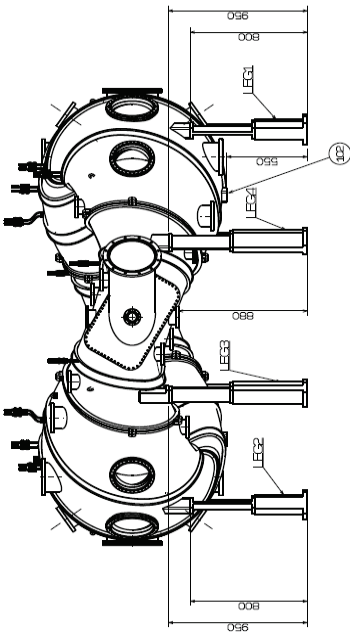
FRONT VIEW

3.2 Related device



FRONT VIEW CSD

SIGNATURES		DATE	BY	CHKD	APPD	SCALE	PROJECT
DWG: S Kimball		2020-04-07	AI			1:10	Q-CRQS-VV-20200407-1
NIFS							
Sh. Rev		1 0					



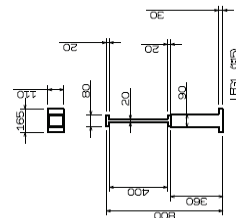
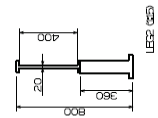
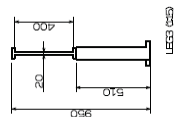
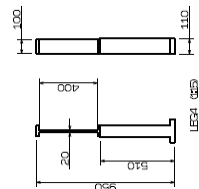
Number	Part number	Quantity	Note
101	PEDE-TMP-1	2	For production process
102	PEDE-TMP-2	2	For production process

Part label (CS)

Bottom view (CS)



External view (CS)



LEGE1 (CS)

LEGE2 (CS)

LEGE3 (CS)

LEGE4 (CS)

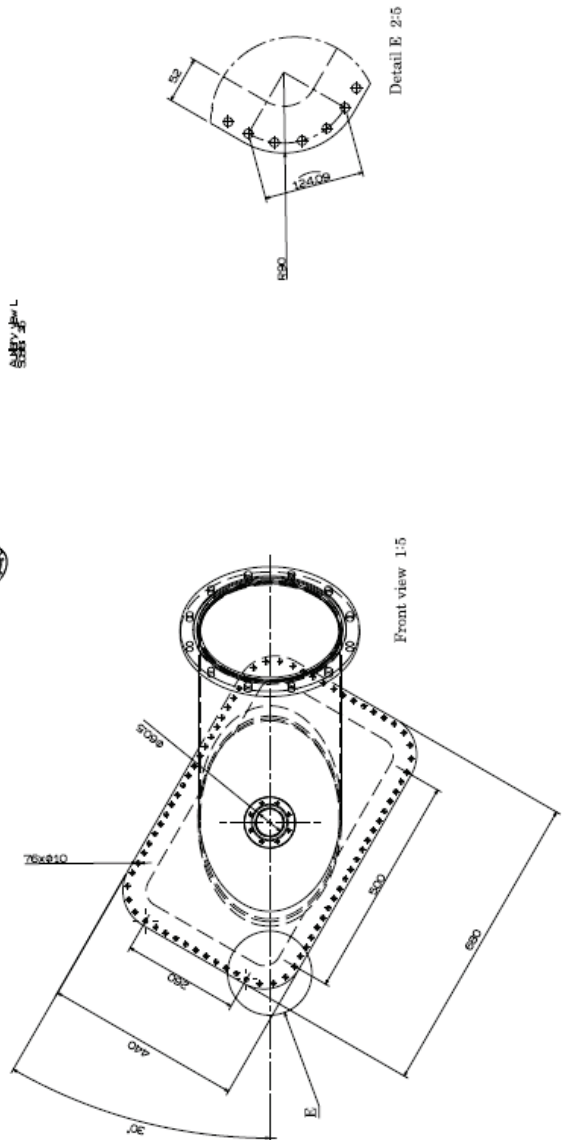
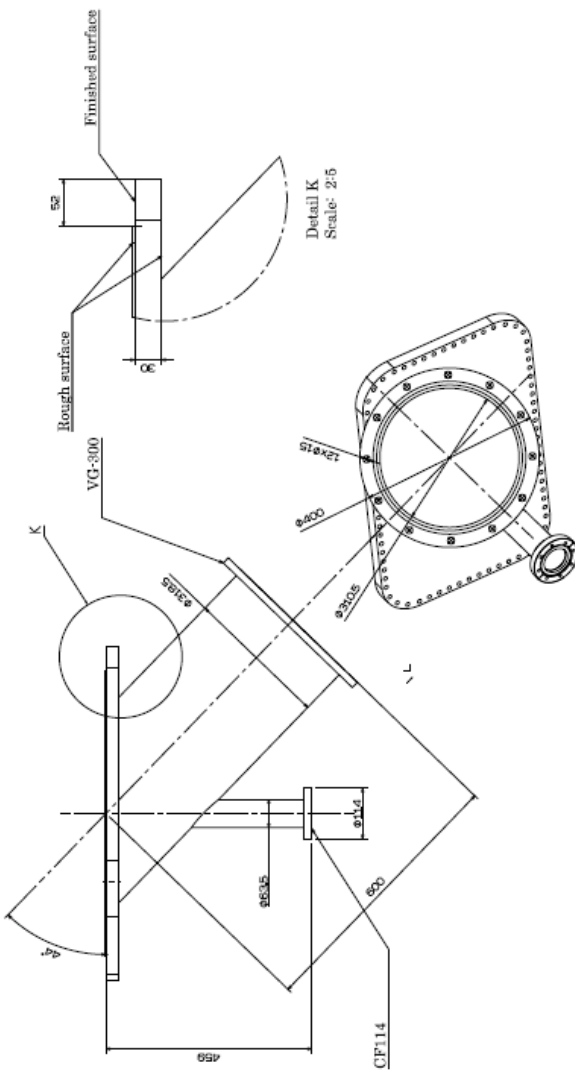
CFQS

DATE: 2020-04-07
 DWG: S Kinoshita
 CHKD: S Kinoshita
 APPR: S Kinoshita
 SCALE: 1:15
 Vacuum Vessel
 LEGS

Q-CFQS-VV-20200407-1

NIFS

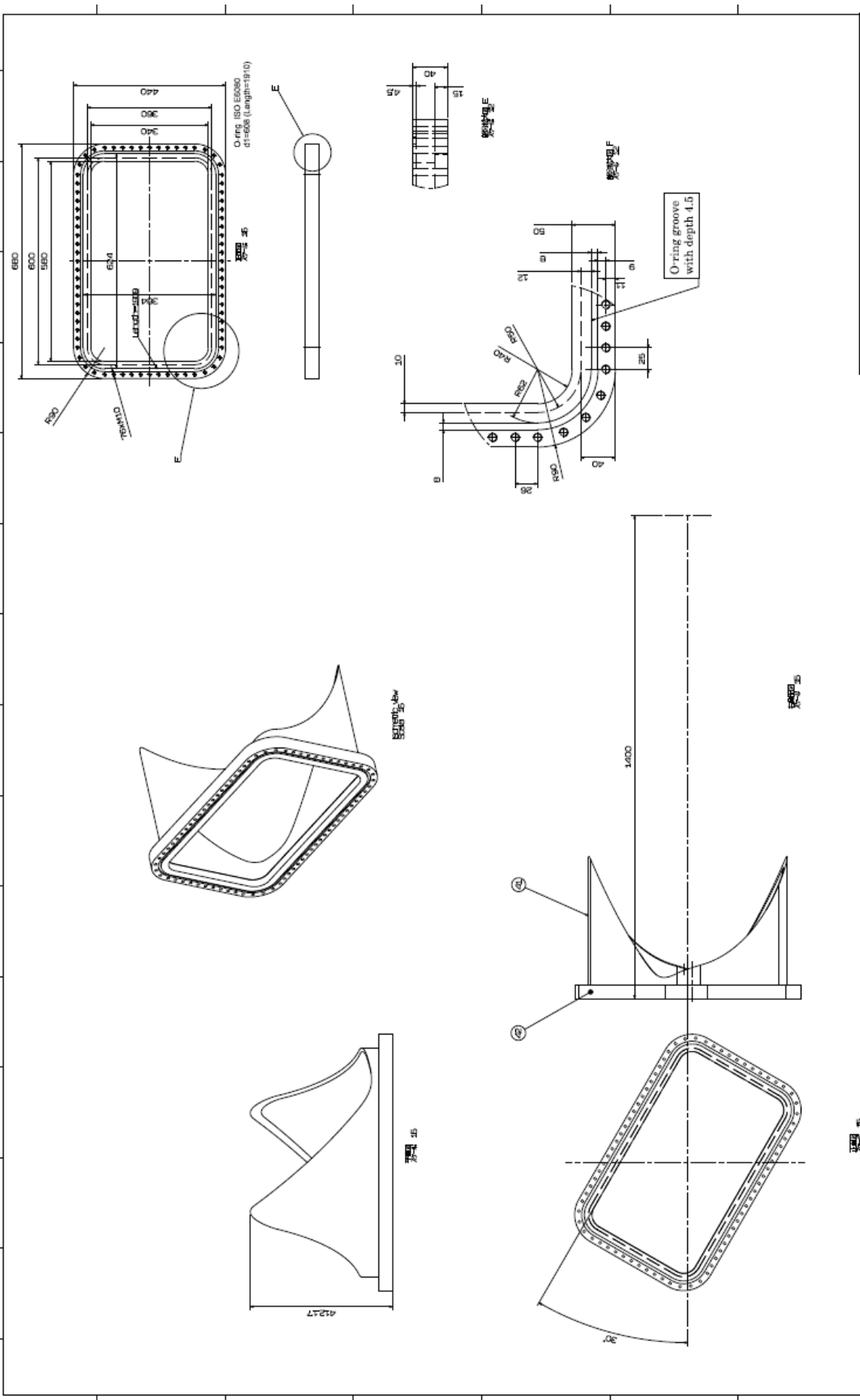
Rev
 2
 0



SIGNATURES		DATE	AI
DWG	S. Kumbhar	2023-04-05	
CHKD		2023-04-05	
APFD		2023-04-05	1:5
NIFS			Q-CFQS-VV-TYPEA-200408-1

CFQS

Vacuum vessel Type A
Conversion flange for NBI
(P-O-050)



SIGNATURES		DATE		A1	
DWG	S. Kimbata	08/01/2002			
CHECK		09/08/2004			
APPD		09/08/2004			
NIPS		Q-CFQS-VV-TYPEA-200406-1		Rev	2
				6	2

CFQS

Vacuum vessel Type A
Rectangular port (P-O-050)

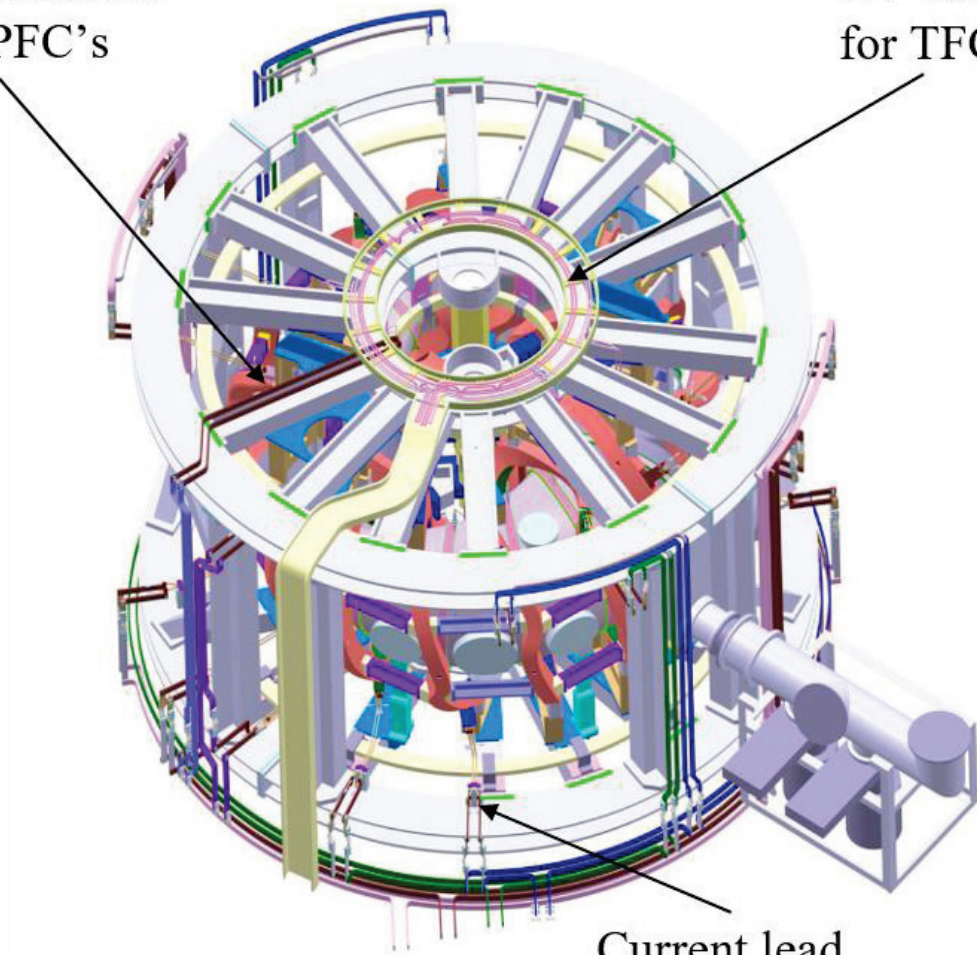
Scale: 1:5

4 Another component

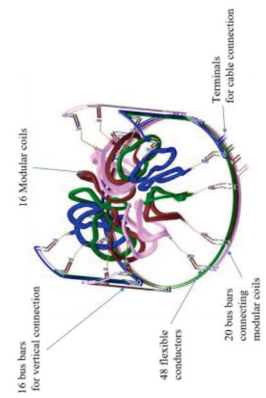
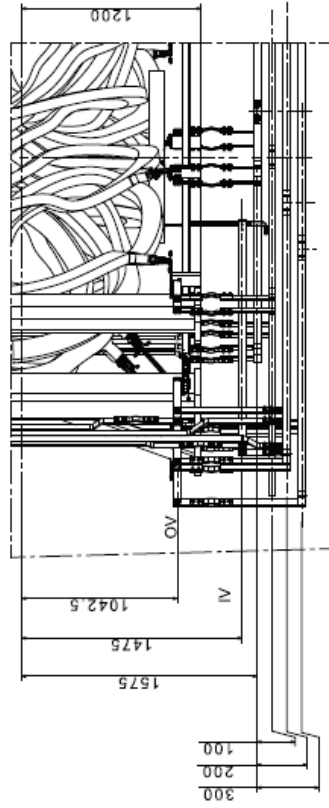
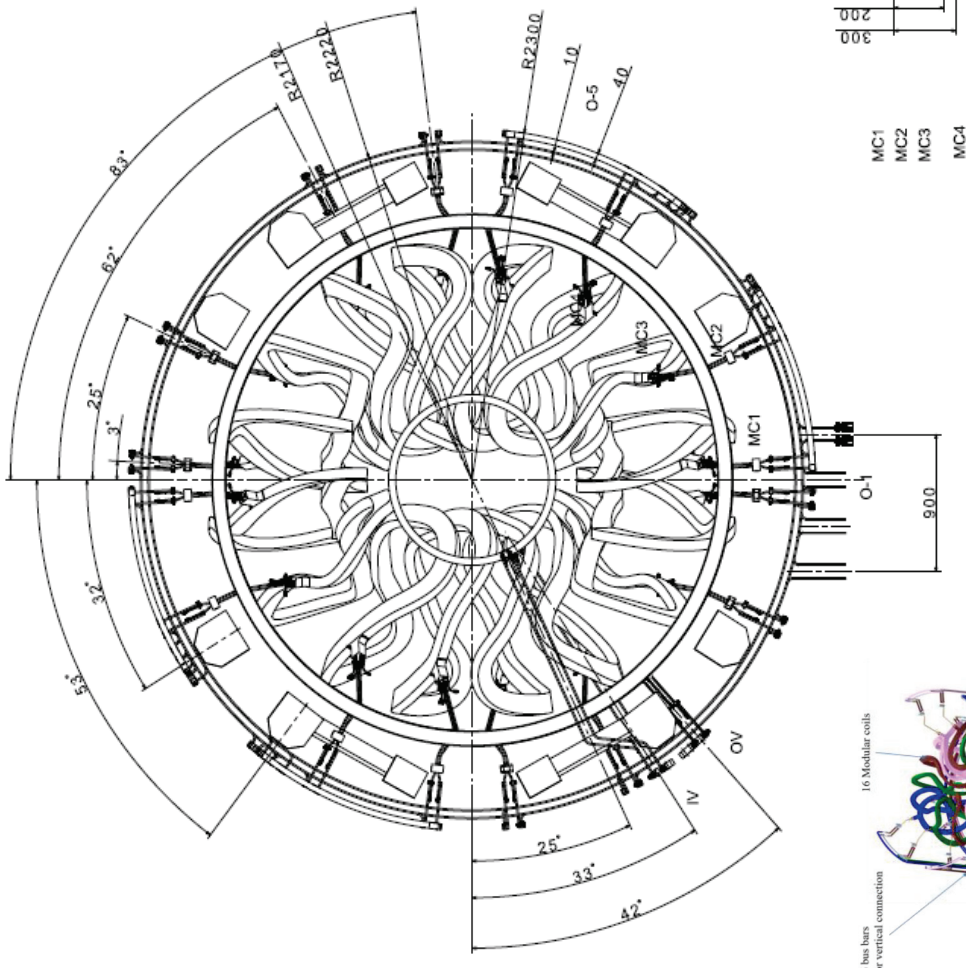
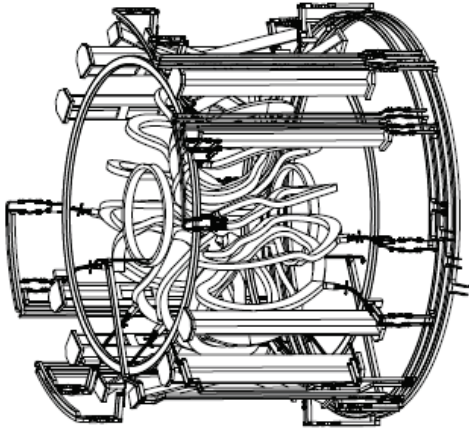
4.1 External current lead

Current lead
for PFC's

CV cable
for TFC's



Current lead
for MC's



SIGNATURES		DATE	NO	AI	REV
DWC	S. Kinnala	2025-04-03			
CHEK		2025-04-03			
APPR		2025-04-03			

CFQS

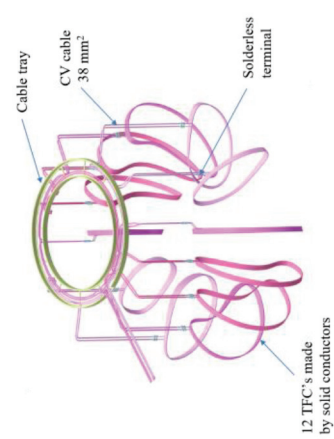
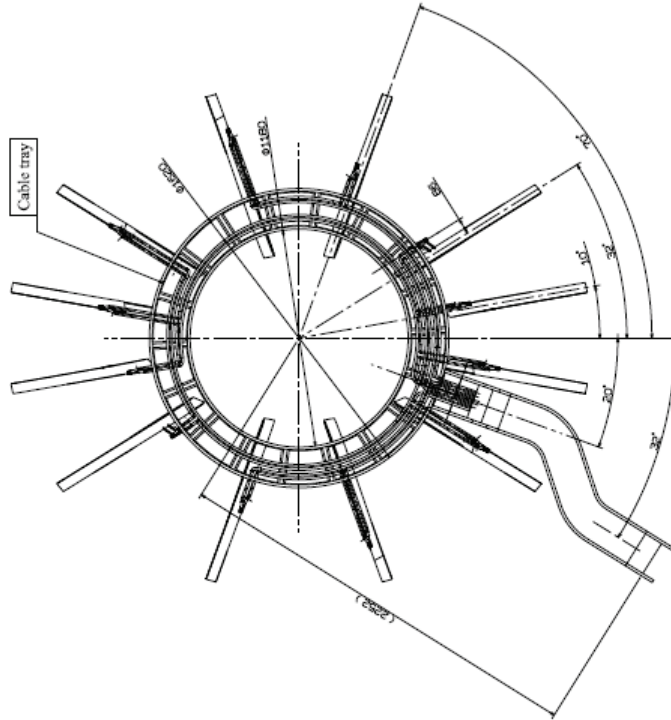
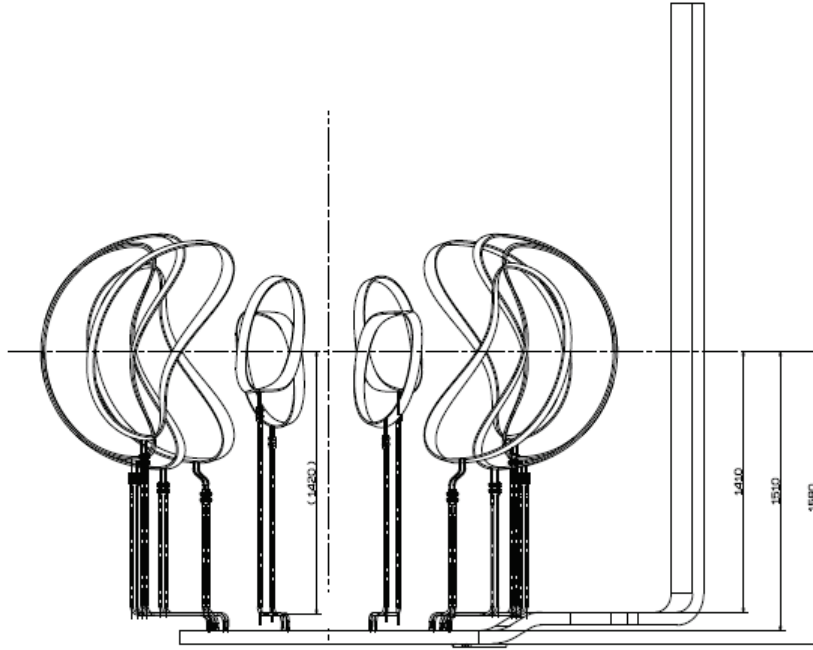
External current lead
for the MC and the PFC

Scale: 1:15

NIPS

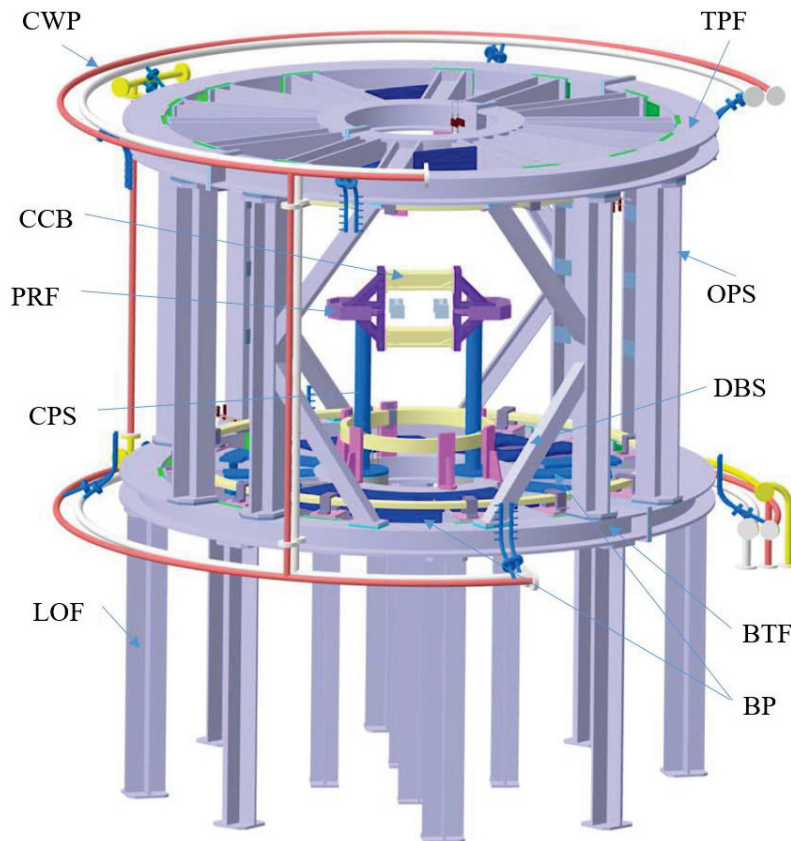
Q-CFQS-EL-20200613-1

(Rev) Rev
1 1

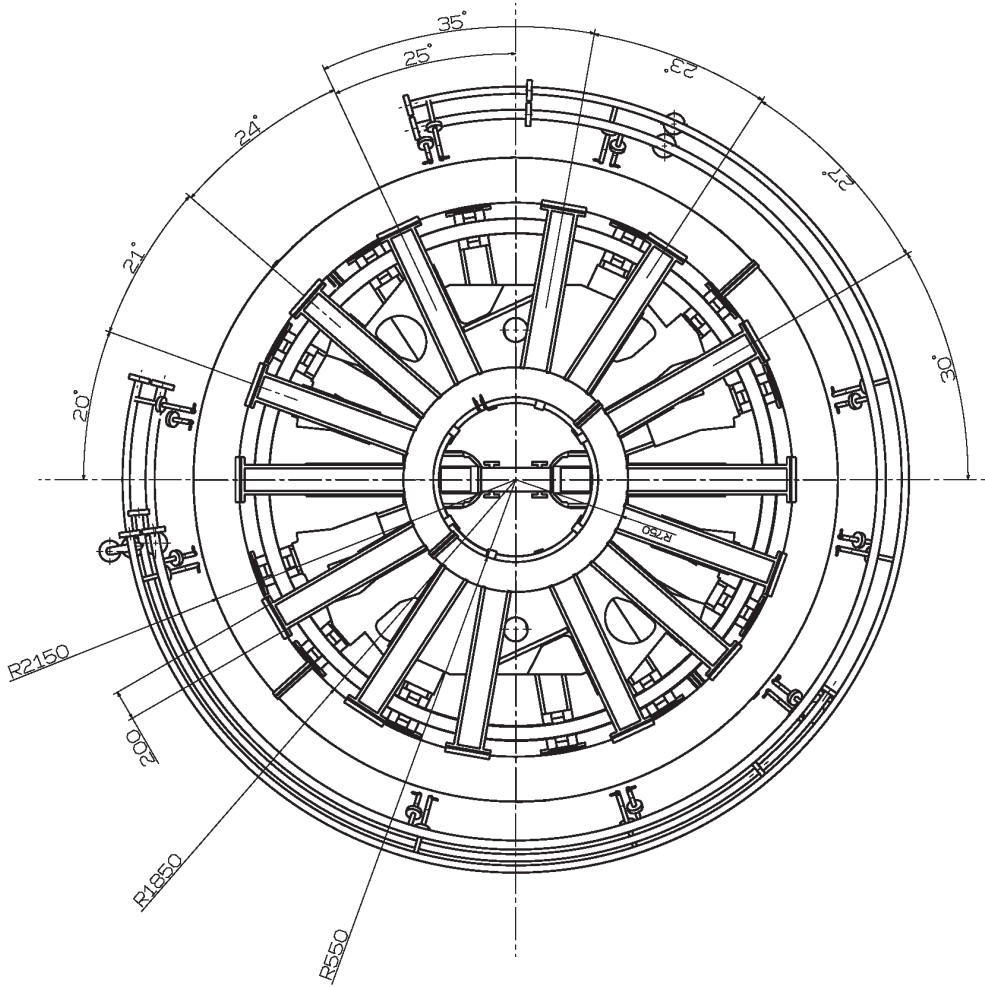


SIGNATURES		DATE	REV	CFQS External current lead for the TFC
DWG: S. Kumbhar		2025-04-08	01	
CHKD:		2025-04-08	01	
APPD:		2025-04-08	1:12	
NIFS				Q-CFQS-EL-20200519-1
				Sh. No. 2

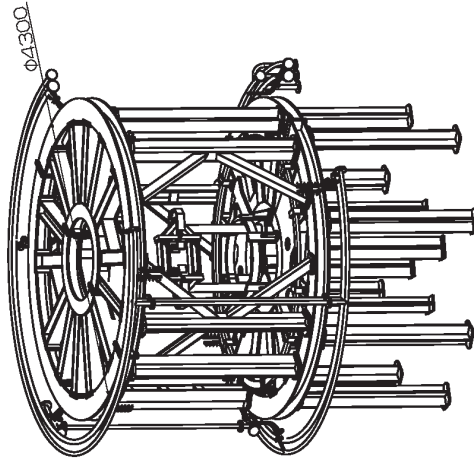
4.2 Support structure



- CWP; Cooling water pipes
- TPF; A top frame receiving the vertical force and fixing many parts.
- CPS; Central pillars
- OPS; Outer pillars
- CCB; Central connection boards
- PRF; Some pedestals receiving large centripetal force.
- DBS; Diagonal beams prevent the overturning forces rolling coils over.
- LOF; Legs of the CFQS receiving gravity.
- BTF; A bottom frame receiving the vertical force and fixing many parts.
- BP; Base pedestals as a basis for device installation. Their upper surface is necessary to be strictly controlled.



TOP VIEW (1/15)



ISOMETRIC VIEW (1/30)

SPT_STRCATDRAWING

CFQS

AI

DATE

2020-05-13

SIGNATURES

DWG: S. Kishimoto

CHKD:

APPD:

2020-05-13

2020-05-13

2020-05-13

2020-05-13

2020-05-13

2020-05-13

2020-05-13

2020-05-13

2020-05-13

2020-05-13

2020-05-13

2020-05-13

2020-05-13

2020-05-13

2020-05-13

2020-05-13

2020-05-13

2020-05-13

2020-05-13

2020-05-13

2020-05-13

2020-05-13

2020-05-13

2020-05-13

2020-05-13

2020-05-13

2020-05-13

2020-05-13

2020-05-13

2020-05-13

2020-05-13

2020-05-13

2020-05-13

2020-05-13

2020-05-13

2020-05-13

2020-05-13

2020-05-13

2020-05-13

2020-05-13

2020-05-13

2020-05-13

2020-05-13

2020-05-13

2020-05-13

2020-05-13

2020-05-13

2020-05-13

2020-05-13

2020-05-13

2020-05-13

2020-05-13

2020-05-13

2020-05-13

2020-05-13

2020-05-13

2020-05-13

2020-05-13

2020-05-13

2020-05-13

2020-05-13

2020-05-13

2020-05-13

2020-05-13

2020-05-13

2020-05-13

NIFS Q-CFQS-SP-202005113-SK1

REV

1

1

1

1

1

1

1

1

1

1

1

1

1

1

1

1

1

1

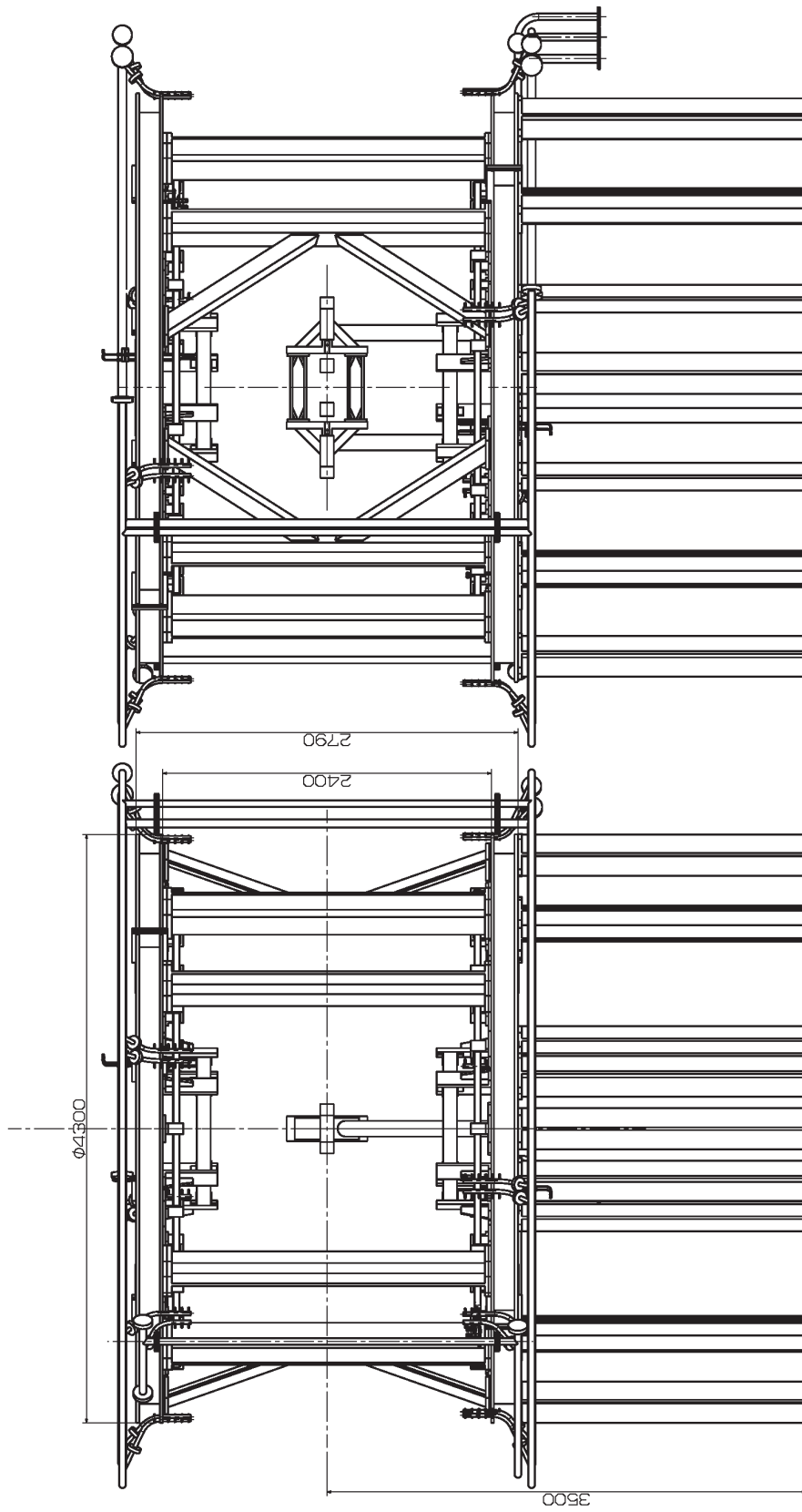
1

1

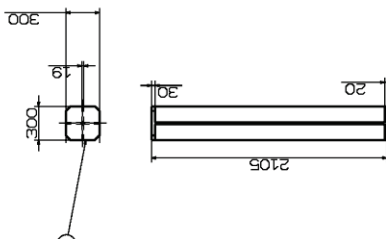
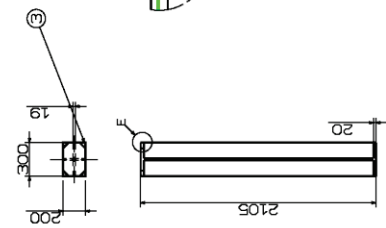
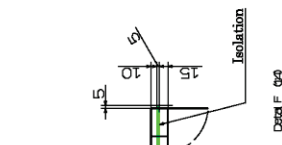
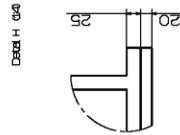
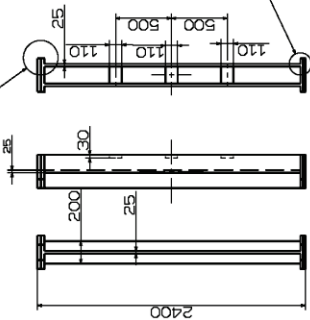
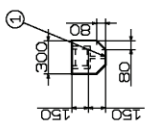
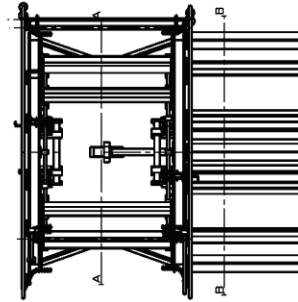
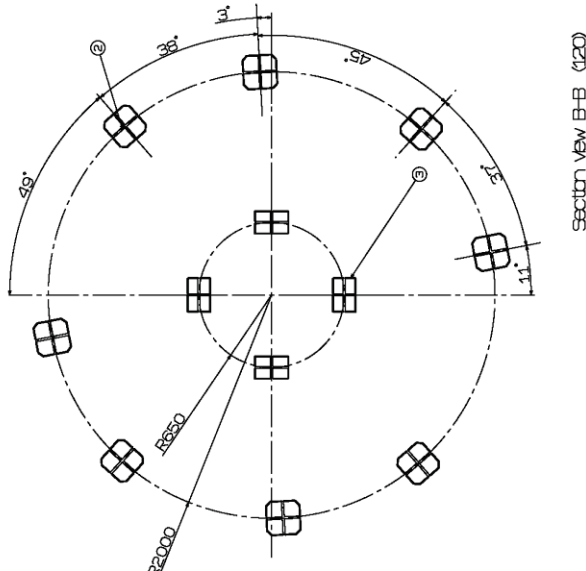
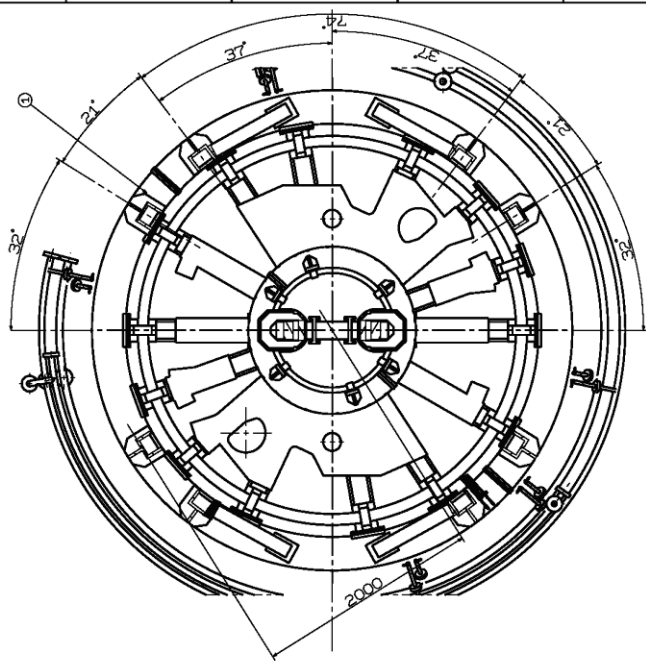
1

1

1



SIGNATURES		DATE	CFQS
DWG S. Khandhaka	2020/05/13	A1	
CHKD	2020/05/13		
APPD	2020/05/13		
NIFS			Q-CFQS-SP-20200511.3-SK1
			Rev
			2
			0



SIGNATURES		DATE	REV.
DWG	S. Kumbhar	2020-05-13	A1
CHKD		2020-05-14	
APFD		2020-05-14	

CFQS

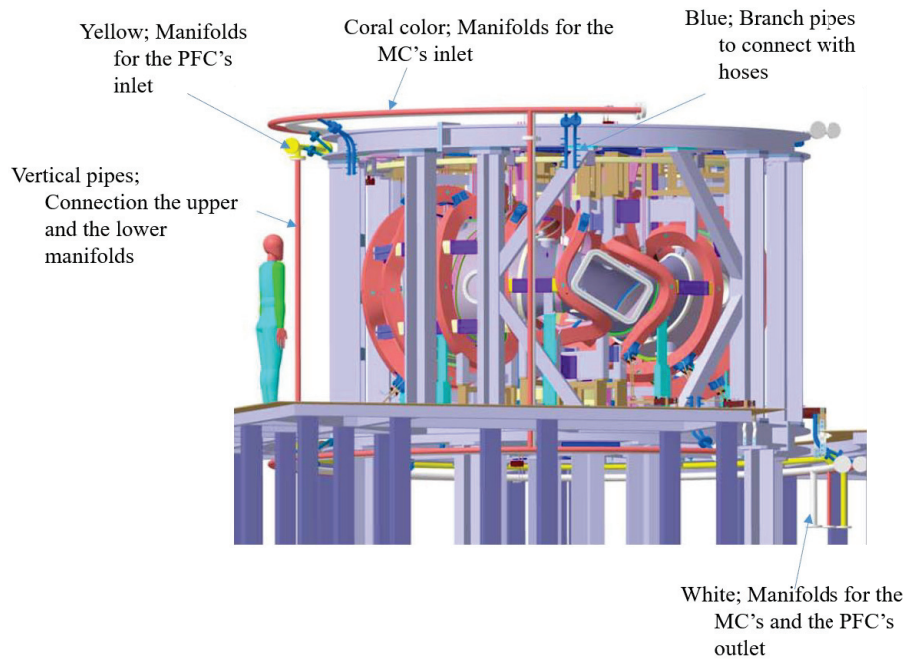
SUPPORT STRUCTURE FOR MODULAR COIL PILLARS

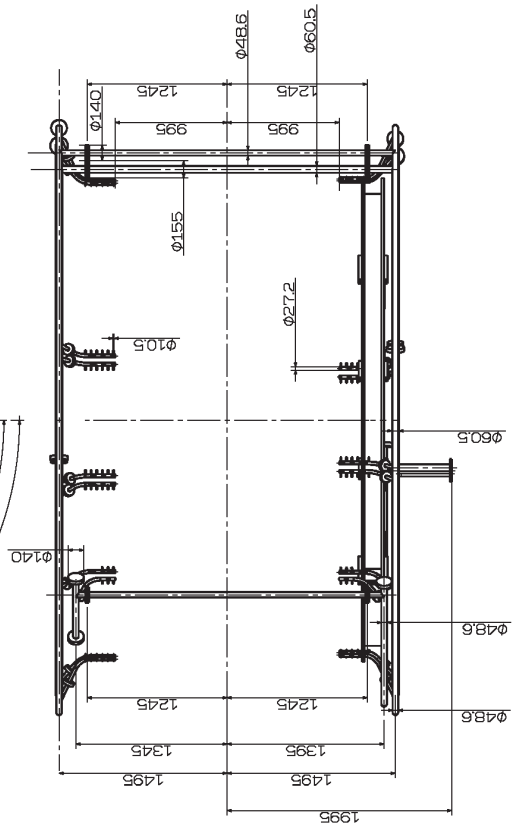
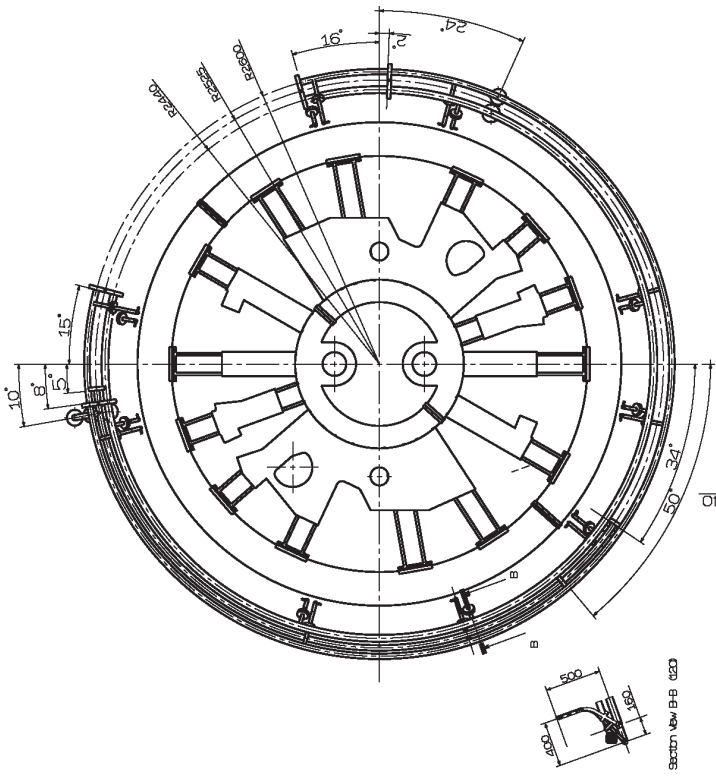
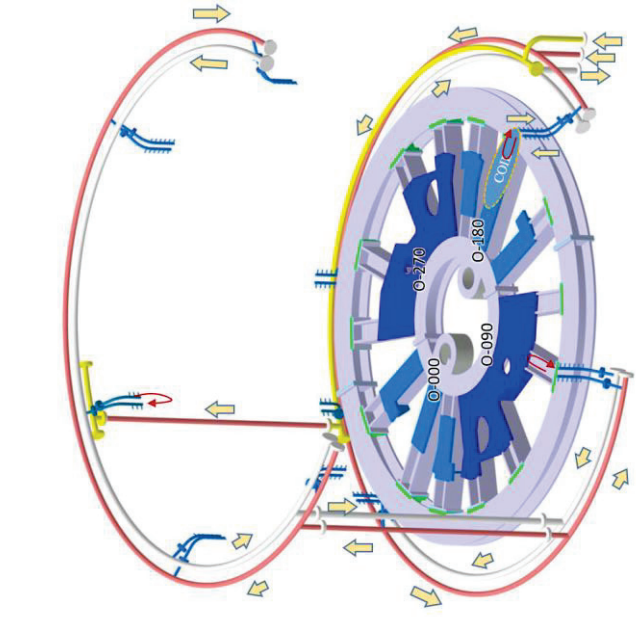
NIFS

Q-CFQS-SP-20200511.9-SKI

Sh. Rev. 8 0

4.3 Cooling water pipe





SIGNATURES		DATE	SCALE	CFQS TITLE Layout of manifold for cooling water NIFS Q-CFQS-CW-20200513-1 Sh. Rev 8 0
DWG	S. Esmailia	2020-04-06	1:1	
CHKD		2020/###/##	SCALE	
APPD		2020/###/##		

Publication List of NIFS-PROC. Series

- NIFS-PROC-104 Atsuo Iiyoshi
Fusion for Sustainable World Development
Mar. 27, 2017
- NIFS-PROC-105 Edited by Weihua Jiang
Frontiers of Applied Pulse Power Technology
Aug. 28, 2017
- NIFS-PROC-106 Edited by Keiichi Kamada and Tetsuo Ozaki
Evolution of Pulse Power and its Peripheral Technology
Nov. 01, 2017
- NIFS-PROC-107 Edited by Hiroaki Ito and Tetsuo Ozaki
Recent Progress of Pulsed Power Technology and its Application to High Energy Density Plasma
Nov. 27, 2017
- NIFS-PROC-108 Edited by Yeong-Kook OH, Shigeru MORITA and Liqun HU
Proceeding of A3 Foresight Program Seminar on Critical Physics Issues Specific to Steady State Sustainment of High-Performance Plasmas November 22-25, 2016, Jeju, Korea
Jan. 11., 2018
- NIFS-PROC-109 Edited by Shigeru MORITA, Liqun HU and Yeong-Kook OH
Proceeding of A3 Foresight Program Seminar on Critical Physics Issues Specific to Steady State Sustainment of High Performance Plasmas 11-14 July, 2017, Sapporo, Japan
Jan. 12, 2018
- NIFS-PROC-110 Edited by Jun Hasegawa and Tetsuo Ozaki
Recent Developments of Pulsed Power Technology and Plasma Application Research
Jan. 12, 2018
- NIFS-PROC-111 Edited by Liqun HU, Shigeru MORITA and Yeong-Kook OH
Proceeding of A3 Foresight Program Seminar on Critical Physics Issues Specific to Steady State Sustainment of High Performance Plasmas 12 - 15 December, 2017, Chongqing, China
Jun. 11, 2018
- NIFS-PROC-112 Edited by E. Kikutani (KEK) and S. Kubo (NIFS)
Proceedings of the meeting on Archives in Fields of Natural Sciences in FY 2017
Oct. 18, 2018 (Written in Japanese)
- NIFS-PROC-113 Pulsed Power and High-Density Plasma and its Applications
Edited by Koichi Takaki and Tetsuo Ozaki
Feb. 6, 2019
- NIFS-PROC-114 The 7th Japan-China-Korea Joint Seminar on Atomic and Molecular Processes in Plasma (AMPP2018)
Edited by Daiji Kato, Ling Zhang, and Xiaobin Ding
May 10, 2019
- NIFS-PROC-115 CFQS TEAM
NIFS-SWJTU JOINT PROJECT FOR CFQS -PHYSICS AND ENGINEERING DESIGN-
VER. 2.1 2019. SEP.
Nov. 8, 2019
- NIFS-PROC-116 Satoshi Ohdachi, Editor of the Post-CUP Workshop proceeding
Collected papers at the 2019 Post-CUP Workshop & JSPS-CAS Bilateral Joint Research Projects Workshop,
24th-26th July, 2019, Nagoya, Japan
Feb. 21, 2020
- NIFS-PROC-117 Edited by E. Kikutani (KEK) and S. Kubo (NIFS)
Proceedings of the meetings on Archives in Fields of Natural Sciences in FY2018
June. 9, 2020 (Written in Japanese)
- NIFS-PROC-118 Edited by Tetsuo Ozaki and Sunao Katsuki
New Development of Beam Physics and the Application by New Generation Pulsed Power Technology
June. 29, 2020
- NIFS-PROC-119 National Institute for Fusion Science, National Institutes of Natural Sciences
Institute of Fusion Science, School of Physical Science and Technology, Southwest Jiaotong University
Hefei Keye Electro Physical Equipment Manufacturing Co. Ltd.
NIFS-SWJTU JOINT PROJECT FOR CFQS -PHYSICS AND ENGINEERING DESIGN-
VER. 3.1 2020. NOV.
Jan. 25, 2021